INTERACTION OF THE SOLAR WIND WITH THE LOCAL INTERSTELLAR MEDIUM: A THEORETICAL PERSPECTIVE

G. P. ZANK
Bartol Research Institute, University of Delaware, Newark, DE 19716, U.S.A.;
E-mail: Zank@bartol.bartol.udel.edu

(Received 24 July 1998)

Abstract. The interaction of the solar wind with the local interstellar medium (LISM) is attracting renewed interest, thanks to the possibility that the Voyager spacecraft may, in the not too distant future, cross the heliospheric termination shock. This has spurred the development of increasingly sophisticated models which attempt to describe various aspects of the physics underlying the interaction of the solar wind and the LISM. A comprehensive review of the subject is presented here.

Table of Contents

Space Science Reviews **89:** 413–688, 1999.
© 1999 *Kluwer Academic Publishers. Printed in the Netherlands.*

1. Introduction

In the last decade, great progress has been made in our understanding of the physical processes thought to describe the outer heliosphere. Fundamental to these advances has been the recognition that the interstellar medium is coupled intimately to the heliosphere through a variety of mechanisms and that much of outer heliospheric physics cannot be understood independently of the local interstellar medium (LISM). This point has been made before of course but with the possibility that the aging spacecraft Voyager 1, 2 and Pioneer 10, 11 might encounter the heliospheric boundaries in the not too distant future, interest in the far outer reaches of our solar system and the LISM has been rekindled. A convenient, if slightly vague, definition of the outer heliosphere, and one that we adopt here, is that it is that region of the solar wind influenced dynamically by physical processes associated with the LISM. Thus, for example, neutral interstellar hydrogen is the dominant (by mass) constituent of the solar wind beyond an ionization cavity of $\sim$ 6–10 astronomical units (AU) in the upstream direction (the direction antiparallel to the incident interstellar wind). The neutral hydrogen is coupled weakly to the solar wind plasma via resonant charge exchange – a coupling which leads to the production of pickup ions that come to dominate the internal energy of the solar wind. The solar wind changes then from a small plasma β_{SW} (the ratio of plasma

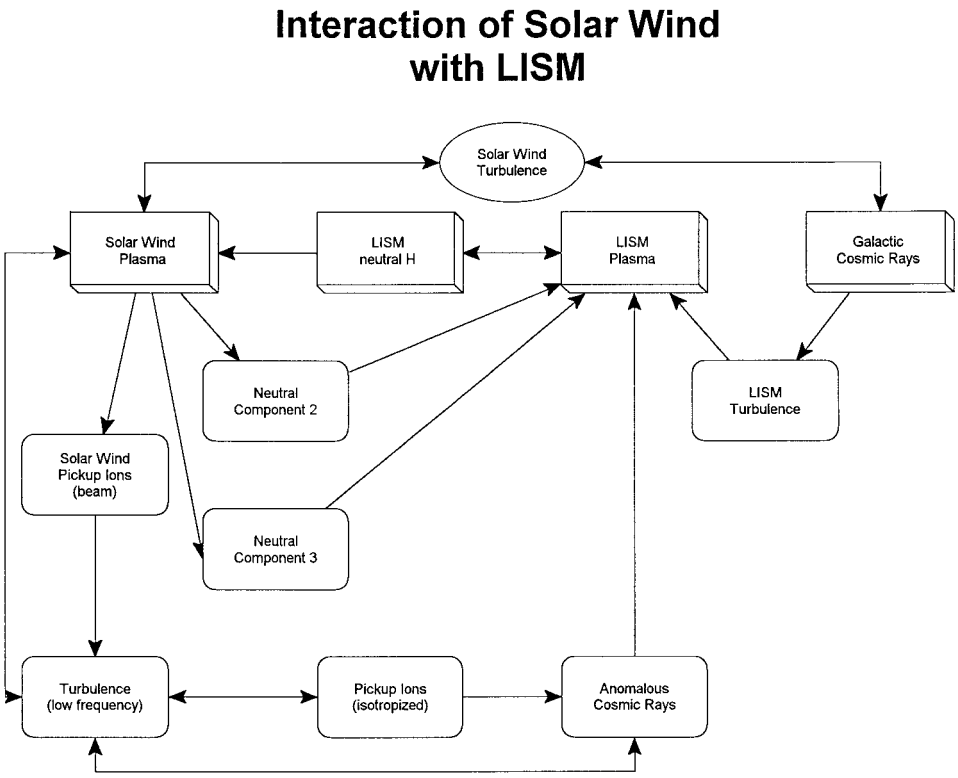

Figure 1.1. Flow chart describing the relation of the various plasma processes which couple the solar wind and the local interstellar medium.

pressure to magnetic field pressure) environment to one in which $\beta_{SW} > 3$. As a by-product of the creation of pickup ions, low-frequency turbulence is expected, so replenishing the dissipated magnetic fluctuations generated near the sun and by the interaction of streams. This has important implications for both solar wind heating and charged particle transport.

As has been illustrated above in the broadest sense, the LISM influences the outer heliosphere and this theme is pursued here in some detail and in as self-contained a fashion as possible. Several excellent and informative reviews have appeared over the years, only some of which we mention. A seminal review, still essential reading today and well worth the search through yellowing stacks in the local library, is that of Axford (1972). Many of the basic ideas and research directions for the solar wind – LISM interaction were laid out there. Subsequent reviews by Holzer (1979,1989), Suess (1990) and Baranov (1990) are also well worth perusal and the book *Physics of the Outer Heliosphere*, (1990) edited by S. Grzedzielski and D. E. Page provides an interesting collection of articles.

The purview of this review is illustrated in the 'organizational' chart of Figure 1.1. Although obviously somewhat simplistic, it serves to illustrate the complex

relationship between the four basic elements – the solar wind plasma, the LISM plasma, the LISM neutrals and the galactic cosmic-rays. The solar wind terminates at a shock whose location is determined by the balance of dynamical solar wind pressure and the external LISM pressure (Davis, 1955; Parker, 1963; Axford, 1972). Galactic cosmic-rays, which can diffuse deep into the heliosphere, are of lesser dynamical importance. Interstellar neutral hydrogen (H) is coupled to both the LISM and solar wind plasmas through resonant charge exchange, so providing an effective volumetric force and hence effecting the dynamical nature of the solar wind – LISM interaction profoundly. The two basic ways in which neutrals can modify the heliospheric and LISM plasmas are: (i) Interstellar neutrals decelerate the solar wind indirectly; (ii) Secondary very hot neutrals produced in the shocked solar wind (downstream of the termination shock) can, through secondary charge exchange, heat the LISM, as can fast neutrals produced through charge exchange with the supersonic solar wind. Newly created ions in the solar wind - the pick-up ions – are very energetic ($\sim$ 1 keV) compared to typical solar wind protons and soon come to dominate the internal energy of the solar wind in the outer heliosphere. The pick-up process itself is expected to generate significant levels of low frequency MHD turbulence which will isotropize the pick-up ion beam, dissipate and heat the solar wind and scatter cosmic-rays. Some small fraction of the pickup ions will be further energized and, probably at the termination shock, be accelerated up to MeV energies to form the anomalous cosmic-ray (ACR) component. The energy density of both anomalous and galactic cosmic-rays in the vicinity of the termination shock is expected to modify the structure and properties of the shock itself. Present day models hope to capture the fully non-linear coupled physics portrayed in Figure 1.1 within a few years. Progress has been made in capturing several of the closed loops, the most comprehensive of which is that including neutral H and solar and LISM plasma.

Although considerable progress has been made in the development and exploration of theoretical models and copious quantities of data have been returned by the outer heliospheric spacecraft (Voyager 1, 2; Pioneer 10, 11; *Ulysses*), many key parameters remain poorly constrained and much of the data is poorly understood. Thus, much remains to be learnt before we can claim that a good understanding exists of the physics of the outer heliosphere.

The review is structured as follows. Section 2 describes the basic interaction of interstellar hydrogen with the solar wind, introduces the cold and hot neutral hydrogen models and the basic equations describing the entrance of neutral hydrogen into the heliosphere. The production of pickup ions by resonant charge exchange of solar wind ions with interstellar neutral atoms or photoionization of neutrals leads to the generation of unstable waves and turbulence which, together with turbulent fluctuations already present in the solar wind, scatters pickup ions from their initial beam-like distribution and possibly heats the solar wind. These and related issues are discussed in Section 3. Section 4 describes the mediation of the 1D supersonic solar wind by pickup ions while Sections 5 and 6 consider

multi-dimensional models of the solar wind interaction with the LISM. Section 5 describes models which neglect the backreaction of either neutral hydrogen or plasma on the other component, as well as models which describe the coupling of neutral hydrogen and plasma self-consistently. Section 6 introduces magnetic fields into the global models. The acceleration and transport of pickup ions and anomalous cosmic-rays is addressed in Section 7 while Section 8 discusses the structure of the termination shock. Section 9 is concerned with the propagation of shocks in the outer heliosphere and the interaction of interplanetary disturbances with the heliospheric boundaries. Some final remarks in Section 10 bring the review to a conclusion.

2. Basic Interaction of Interstellar H with the Solar Wind

Interstellar neutral gas flows into the heliosphere relatively unimpeded and can penetrate to within several AU of the sun. Neutral atoms scatter solar radiation resonantly so that the distribution of H and Helium (He) in the heliosphere can be studied by observing sky background radiation in H I λ1216 and He I λ584. The distribution of interstellar H only is addressed here in any detail since He and the other elements have a negligible dynamical influence on the solar wind-LISM interaction. Nonetheless, since He in particular provides important and direct information about the conditions in the LISM, we discuss briefly relevent recent observations in Section 5.1.

2.1. H-PLASMA INTERACTION

The heliospheric-LISM plasma environment is composed of three thermodynamically distinct regions: (i) the supersonic solar wind, expanding more-or-less radially from the sun at speeds of $\sim$ 400 - 800 km s^{-1}, with a density that decays as $\sim r^{-2}$ (r denoting radial heliocentric distance from the sun), and a relatively low temperature ($\sim$ 10^4 K) which appears to decay adiabatically with an effective adiabatic index of $\gamma \simeq 1.1$; (ii) the shock heated subsonic solar wind, which possesses much higher temperatures ($\sim$ 10^6 K), densities ($\sim$ 10^{-3}cm^{-3}) and lower flow speeds ($\sim$ 100 km s^{-1}), and finally (iii) the LISM, where the plasma flow speed is low ($\sim$ 26 km s^{-1}) and the temperature is several $\times 10^3$ K. Here and henceforth, region 1 is taken to be the region beyond the heliopause, i.e., the LISM, and H atoms whose origin lies in region 1 shall be referred to as component 1 neutrals. Region 2 is that region occupied by the shocked solar wind plasma and component 2 neutrals are those created in region 2. Finally, region 3 refers to the supersonic solar wind and the component 3 neutrals are those born there (i.e., the 'splash' component). See Figure 2.1 for an illustration of the different regions. Quite clearly, the three neutral populations, components 1, 2 and 3, possess distinct characteritics and the complete local neutral H distribution will be highly anisotropic.

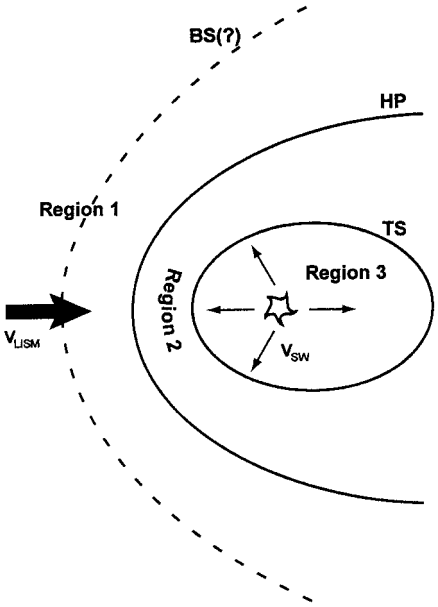

Figure 2.1. Schematic of the solar wind – LISM boundary regions which act as neutral H sources whose characteristics are clearly distinct.

TABLE I

Possible neutral hydrogen interactions in the outer heliosphere/LISM

Interaction	Cross-section σ (cm^2)	Energy range	Reference
Charge-exchange	$[7.6\times10^{-8}-1.06\times10^{-8}\log E_{\rm eV}]^2$	$10<E_{\rm eV}<5000$	1
($\mathrm{H}+\mathrm{H}^+\longrightarrow\mathrm{H}^+ +\mathrm{H}$)	$[6.5\times10^{-8}-8\times10^{-9}\log E_{\rm eV}]^2$		2
Photoionization	6.4×10^{-18}	$\mathrm{E}_{\rm eV}^{photon}>13.6$	3
($\mathrm{H}+h\nu\longrightarrow\mathrm{H}^+ +\mathrm{e}$)			
H–H$^+$ collisions	$2\sigma_{\rm CE}$		4
H–H collisions	$3.2\times10^{-15}E_{\rm eV}^{-0.11}$	$0.1<E_{\rm eV}<100$	(4), 5
E–H collisions	$1.7\times10^{-15}E_{\rm eV}^{-0.276}$	$1<E_{\rm eV}<10$	6
	$2.9\times10^{-15}E_{\rm eV}^{-1.01}$	$E_{\rm eV}>10$	5
Electron impact ionization	$2.16\times10^{-16}\ln E_{13.6}/E_{13.6}\{1-0.6\exp\left[-0.56(E_{13.6}-1)\right]\}$	$E_{13.6}>1$	7
Recombination	$\dfrac{2\times10^{-22}}{E_{13.6}(E_{13.6}+1)}$		8
H–H$^+$ Coulomb collisions	$1.6\times10^{-12}/E_{\rm eV}^2$		8

$E_{\rm eV}\equiv$ interaction energy in eV.
$E_{13.6}\equiv$ energy measured in units of 13.6 eV.
(1) Fite et al. (1962), (2) Maher and Tinsley (1977), (3) Allen (1973), (4) Dalgarno (1960), (5) Williams et al. (1997), (6) Gilardini (1972), (7) Lotz (1967), (8) Spitzer (1978)

As illustrated in Table I several interactions between H atoms, protons and electrons are possible and some important points can be made. (1) Photoionization is important within several Astronomical Units (AU) but is otherwise not (assuming that the LISM is in ionization equilibrium with the local stellar UV radiation field, as suggested by Frisch (1995)). (2) Two charge-exchange cross-sections are used in the literature, but that published by Fite et al. (1962) is a fit to observations. Nonetheless, at 1 eV, a 40% discrepancy exists between the cross-sections and, as we discuss in Section 5.5, this can effect the heliospheric H number density by a similar amount. (3) The charge-exchange cross-sections of Table I assume that no momentum transfer occurs during the interaction but, of course, non-charge-exchange H^+-H interactions can occur. The H^+-H cross-section computed by Dalgarno (1960) is the total momentum transfer cross-section and includes charge-exchange. Thus, an exclusively charge-exchange treatment of the H-H^+ interaction may underestimate the efficiency of the coupling. (4) H-H collisions have a cross-section comparable to that of charge-exchange. Such collisions may be important in the heliotail and the region upstream of the heliopause where hot component 2 and cooler component 1 neutrals can equilibrate. (5) Electron-H collisions, electron impact ionization, and recombination are unlikely to be dynamically important on 1000 AU scales. However, because electron impact ionization is sensitive to the electron distribution, it may occur in the solar wind (Isenberg, 1995). (6) Since region 1 H^+-H^+ and e–e mean free paths are $\sim$ 0.15 AU, the LISM is Coulomb collisional and the electrons equilibrate to the proton temperature.

2.2. THE HELIOSPHERIC NEUTRAL H DISTRIBUTION

The distribution of LISM neutral hydrogen drifting through the heliosphere may be calculated directly from the Boltzmann equation,

$$\frac{\partial f}{\partial t} + \mathbf{v} \cdot \nabla f + \left(\frac{\mathbf{F}}{m} \cdot \nabla_{\mathbf{v}} \right) f = P - L \, , \tag{1}$$

where $f(\mathbf{x}, \mathbf{v}, t)$ is a particle distribution function expressed in terms of position $\mathbf{x}$, velocity $\mathbf{v}$ and time t. $\mathbf{F}$ is the force acting on a particle of mass m, typically gravity and radiation pressure. The terms P and L describe the production and loss of particles at $(\mathbf{x}, \mathbf{v}, t)$, and both terms are functions of the assumed plasma and neutral distributions. In all cases of interest here, the loss term may be expressed as

$$L = f(\mathbf{x}, \mathbf{v}, t) \beta(\mathbf{x}, \mathbf{v}, t) \, , \tag{2}$$

where β is the total loss rate in s^{-1}. On defining the decay rate $\Lambda(t, t')$ as the loss of particles at a given location $(\mathbf{x}, \mathbf{v})$ between times t' and t, one has

$$\Lambda \left(\mathbf{x}, \mathbf{v}, t', t \right) \equiv \int_{t'}^{t} \beta \left(\mathbf{x}, \mathbf{v}, t'' \right) \, \mathrm{d}t'' \, . \tag{3}$$

The formal solution to (1) for the initial data $f_0(\mathbf{x}_0, \mathbf{v}_0\ , t_0)$ is then simply

$$f(\mathbf{x}\ , \mathbf{v}\ , t) = f_0(\mathbf{x}_0\ , \mathbf{v}_0\ , t_0)e^{-\Lambda(t_0,t)} + \int_{t_0}^{t} P\left(\mathbf{x}^{'}\ , \mathbf{v}^{'}\ , t^{'}\right) e^{-\Lambda(t^{'},t)}\ \mathrm{d}t^{'}\ . \tag{4}$$

The initial or boundary data is assumed typically to be a Maxwellian distribution parameterized by the bulk LISM density, velocity and temperature and the boundary condition is imposed at 'infinity'. Along the trajectory $(\mathbf{x}'\ , \mathbf{v}'\ , t')$, neutral H atoms can experience the interactions/physical processes listed in Table I.

Simple and useful estimates for the production and loss of neutral H atoms can be derived for charge-exchange production and loss (Ripken and Fahr, 1983). The neutral H loss rate due to charge-exchange is obtained by integrating over the proton distribution function, thus

$$\beta_{\mathrm{ex}}(\mathbf{x}\ , \mathbf{v}\ , t) = \int f_p(\mathbf{x}\ , \mathbf{v}_p\ , t) V_{\mathrm{rel},p}\sigma_{\mathrm{ex}}(V_{\mathrm{rel},p})\ \mathrm{d}^3\mathbf{v}_p\ , \tag{5}$$

where f_p and $\mathbf{v}_p$ refer to proton quantities, $V_{\mathrm{rel},p} \equiv |\mathbf{v} - \mathbf{v}_p|$ is the relative speed between an H atom and a proton, and σ_{ex} denotes the charge-exchange cross-section. If the proton distribution is cold with constant velocity $\mathbf{v}_{p,\mathrm{cold}}$, i.e., if $f_p(\mathbf{x}\ , \mathbf{v}\ , t) = n_p(\mathbf{x}\ , t)\delta^3(\mathbf{v} - \mathbf{v}_{p,\mathrm{cold}})$, then (5) reduces to

$$\beta_{\mathrm{ex}}(\mathbf{x}\ , \mathbf{v}\ , t) = n_p(\mathbf{x}\ , t) V_{\mathrm{rel},p}\sigma_{\mathrm{ex}}(V_{\mathrm{rel},p})\ , \tag{6}$$

and $V_{\mathrm{rel},p} \equiv |\mathbf{v} - \mathbf{v}_{p,\mathrm{cold}}|$.

The charge-exchange neutral hydrogen production term is given by

$$P_{\mathrm{ex}}(\mathbf{x}\ , \mathbf{v}\ , t) = f_p(\mathbf{x}\ , \mathbf{v}_{\mathrm{H}}\ , t) \int f_{\mathrm{H}}(\mathbf{x}\ , \mathbf{v}\ , t) V_{\mathrm{rel},H}\sigma_{\mathrm{ex}}\left(V_{\mathrm{rel},H}\right)\ \mathrm{d}^3\mathbf{v}_{\mathrm{H}}\ , \tag{7}$$

where $V_{\mathrm{rel},H} \equiv |\mathbf{v} - \mathbf{v}_{\mathrm{H}}|$ and f_{H} is the neutral H distribution. If one assumes (Ripkin and Fahr, 1983; Pauls et al., 1995) that both the neutral H and proton distribution functions are Maxwellian, then the charge exchange production and loss terms may be approximated to $\sim 5\%$ accuracy by the expressions

$$P_{\mathrm{ex}}(\mathbf{x}\ , \mathbf{v}\ , t) \simeq f_p(\mathbf{x}\ , \mathbf{v}\ , t)\left[n_{\mathrm{H}}(\mathbf{x}\ , t)\overline{V}_{\mathrm{rel},H}\sigma_{\mathrm{ex}}\left(\overline{V}_{\mathrm{rel},H}\right)\right]\ , \tag{8}$$

$$\beta_{\mathrm{ex}}(\mathbf{x}\ , \mathbf{v}\ , t) \simeq n_p(\mathbf{x}\ , t)\overline{V}_{\mathrm{rel},p}\sigma_{\mathrm{ex}}\left(\overline{V}_{\mathrm{rel},p}\right)\ . \tag{9}$$

Here the average velocity of protons (or H) relative to an H atom (or proton) with velocity $\mathbf{v}$ is (Ripkin and Fahr, 1983)

$$\begin{aligned}
\overline{V}_{\mathrm{rel},p(\mathrm{H})} &= V_{p(\mathrm{H}),\mathrm{th}}\left[\frac{\exp[-\omega^2_{p(\mathrm{H})}]}{\sqrt{\pi}} + \left(\omega_{p(\mathrm{H})} + \frac{1}{2\omega_{p(\mathrm{H})}}\right)\mathrm{erf}\left(\omega_{p(\mathrm{H})}\right)\right] \\
&\simeq V_{p(\mathrm{H}),th}\sqrt{4/\pi + \omega^2_{p(\mathrm{H})}}\ ; \\
\omega_{p(\mathrm{H})} &= \frac{1}{v_{p(\mathrm{H}),th}}\left|\mathbf{v} - \mathbf{u}_{p(\mathrm{H})}\right| \equiv \Delta\mathbf{u}/v_{p(\mathrm{H}),th}\ ,
\end{aligned}$$

and the erf(x) is the usual error function, $v_{p(\mathrm{H}),th} = \sqrt{2kT_{p(\mathrm{H})}/m}$ the thermal velocity of the proton (neutral hydrogen H), k Boltzmann's constant, and $\mathbf{u}_{p(\mathrm{H})}$ the bulk flow velocity of the plasma (H).

2.2.1. *The Cold Heliospheric H Distribution*

If one assumes that the thermal speed of H is much less than its bulk flow speed relative to the sun, then the solution of Boltzmann's equation (1) is particularly simple in the absence of production terms. The basic analysis was done by Fahr (1968), Blum and Fahr (1970), Holzer (1970), Holzer and Axford (1970, 1971) and summarized by Axford (1972). For a cold steady H distribution, subject to a spherically symmetric conservative potential

$$V(r) = -\frac{GM_{\odot}(1-\mu_{\odot})}{r}\,, \tag{10}$$

we seek a two-dimensional, axially symmetric solution to the Boltzmann equation (1). In (10), r refers to heliocentric radius, $M_{\odot}$ to solar mass and $\mu_{\odot}$ is the ratio of radiation pressure to gravitation. Any point (r,θ) in the heliospheric plane (θ is the polar angle from the assumed axis of symmetry and $\theta = 0$ is anti-parallel to the incident flow velocity) is the intersection of two hyperbolic neutral particle trajectories having the sun as focus (see Figure 2.2(a)). The cold neutral distribution at these points is therefore given by

$$f_{\mathrm{H}}(\mathbf{x}\,,\mathbf{v}) = n_{\mathrm{H},1}\delta^3(\mathbf{v}-\mathbf{v}_{\mathrm{H},1}) + n_{\mathrm{H},2}\delta^3(\mathbf{v}-\mathbf{v}_{\mathrm{H},2})\,, \tag{11}$$

where $n_{\mathrm{H},i}$ and $\mathbf{v}_{\mathrm{H},i}$ refer to the neutral hydrogen number density and velocity vectors. Since any point in the plane (r,θ) is the intersection of two trajectories having angular momentum $p_{1,2}$ or impact parameter $b_{1,2}$

$$b_{1,2} \equiv \frac{p_{1,2}}{u} = \frac{1}{2}\left\{r\sin\theta \pm \left[r^2\sin^2\theta + 4r\,(1-\mu_{\odot})\,\frac{GM_{\odot}}{u^2}\,(1-\cos\theta)\right]\right\}^{1/2}\,, \tag{12}$$

u the incident flow velocity, one may use the zeroth moment of (1) together with the loss term (6), and Equations (11) and (12), to obtain the neutral particle number density $n(r,\theta)$ at a point as (Axford, 1972)

$$n(r,\theta) = n_0\frac{b_1^2\exp\left[-\beta r^2\theta/p_1\right] + b_2^2\exp\left[-\beta r^2\,(2\pi-\theta)\,/p_2\right]}{r\sin\theta\left[r^2\sin^2\theta + 4r\,(1-\cos\theta)\,(1-\mu_{\odot})\,GM_{\odot}/u^2\right]^{1/2}}\,. \tag{13}$$

Here n_0 is the number density of neutral H at infinity. In the limit that radiation pressure balances gravitational attraction exactly, i.e., that $V(r) = 0$, expression (13) reduces to

$$n(r,\theta) = n_0\exp\left[-\frac{\beta r\theta}{u\ \sin\theta}\right] \equiv n_0\exp\left[-\frac{\lambda\theta}{r\ \sin\theta}\right]\,, \tag{14}$$

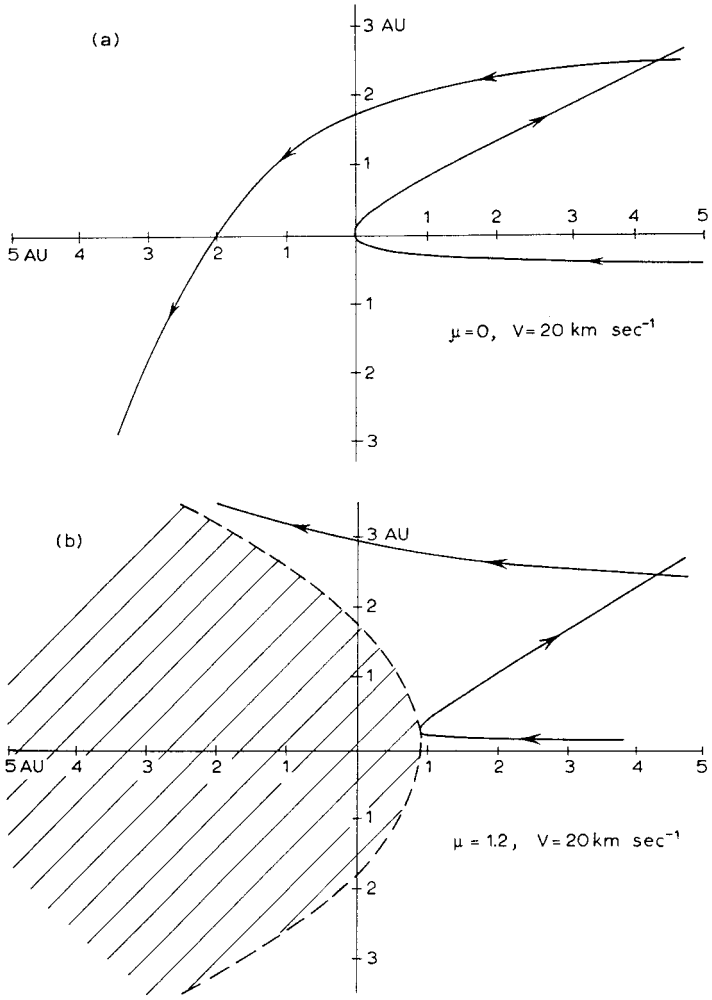

Figure 2.2. (a) Two examples of intersecting particle trajectories in the cold interstellar H approximation in the absence of radiation pressure. (b) The same as (a) but now with $\mu_\odot > 1$. The parabolic region downstream and about the sun from which cold H atoms are excluded is hatched. (Axford, 1972.)

after assuming that $\beta = \beta_0 r_0^2/r^2$, and introducing $\lambda \equiv \beta_0 r_0^2/u$. Under the assumption of a spherically symmetric and steady solar wind and solar radiation field, $\beta_0 r_0^2$ is independent of r_0 (at least if one has a minimal attenuation of the photon flux and if one ignores the accretion of interstellar protons), and the interstellar neutral hydrogen population is strongly depleted within some 6–10 AU. This region of depleted interstellar neutral hydrogen is called the ionization cavity.

Illustrated in Figure 2.2 is the motion of a single hydrogen atom subject to the potential (10). Figure 2.2(a) shows a representative single particle trajectory with a dominant gravitational force ($\mu_\odot < 1$) and Figure 2.2(b) that of a dominant solar

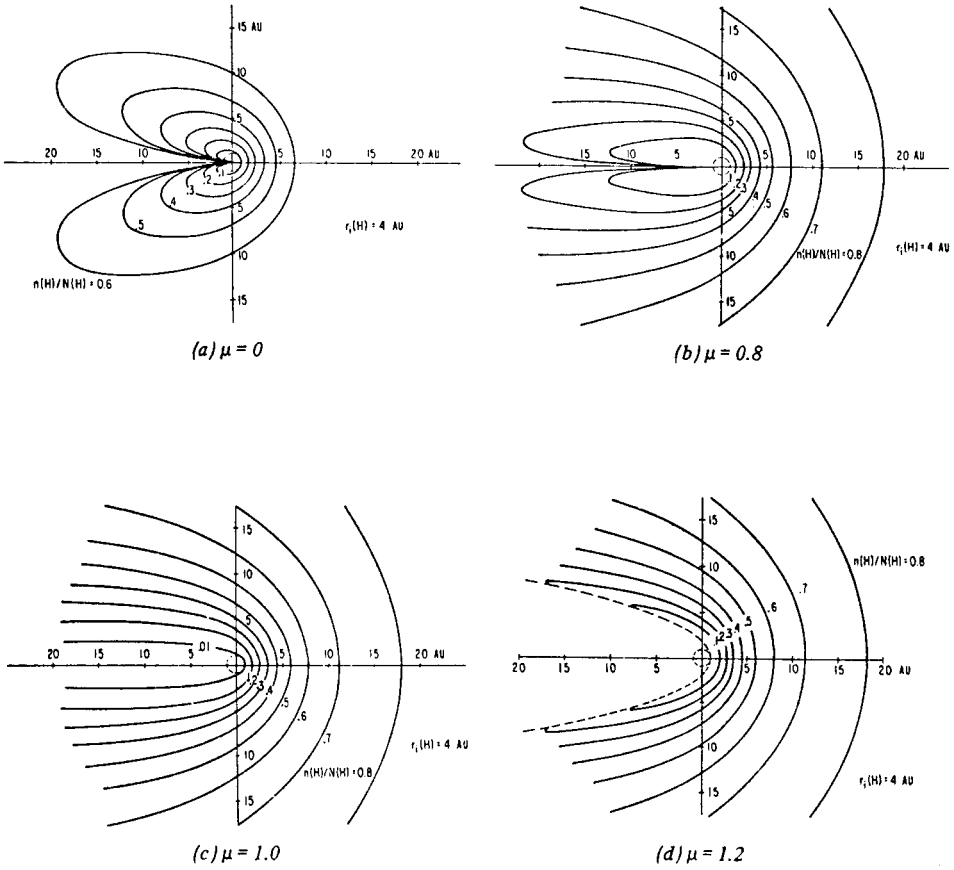

Figure 2.3. Contours of equal density of neutral H for the cold model. The Sun lies at the origin of the figure and plane corresponds to the plane defined by the interstellar wind velocity vector and the Sun. (Axford, 1972.)

Lyman-α radiation pressure ($\mu_\odot > 1$). For $\mu_\odot < 1$, one can expect that H atoms are focussed on the downward symmetry axis whereas $\mu_\odot > 1$ implies that H atoms are excluded from a parabolic regime defined by

$$r(1 + \cos\theta) \leq \frac{4GM_\odot\,(\mu_\odot - 1)}{u^2}\ . \tag{15}$$

The effect of focussing and exclusion on the heliospheric distribution of interstellar hydrogen is described by (13). In Figure 2.3, contours of equal density for neutral H are plotted for various values of $\mu_\odot$. Of note is the high density on the downstream axis of symmetry when $\mu_\odot < 1$ and the parabolic void when $\mu_\odot > 1$ (Axford, 1972).

2.2.2. *The Hot Heliospheric H Distribution*

Although a useful approximation which provides considerable insight, the cold H distribution is not completely adequate in that (i) LISM thermal speeds and bulk flow speeds are comparable, and (ii) the LISM temperature may be estimated for heliospheric resonance observations only if it is included as a model parameter. Thus, considerable efforts have been expended in extending the cold heliospheric neutral hydrogen model (e.g., Danby and Camm, 1957; Fahr, 1971; Thomas, 1972; Fahr, 1979, Wu and Judge, 1979) and useful reviews exist (Meier, 1977; Thomas, 1978).

Much the same assumptions made for the cold model are made again for the hot distribution except that now the source distribution function is assumed to be a Maxwellian, i.e.,

$$f_0(\mathbf{x}_0\ ,\mathbf{v}_0) = \frac{n_\infty}{(\sqrt{\pi}v_{\mathrm{th},\infty})^3}\exp\left[-\left(\frac{\mathbf{v}_0-\mathbf{u}}{v_{\mathrm{th},\infty}}\right)^2\right]\ , \tag{16}$$

where $\mathbf{u}$ is the bulk neutral H flow speed at infinity. Use of (16) in the formal solution (4) without the production term yields the distribution function

$$f(\mathbf{x},\mathbf{v}) = \frac{n_\infty}{(\sqrt{\pi}v_{\mathrm{th},\infty})^3}\exp\left[-\left(\frac{\mathbf{v}_0-\mathbf{u}}{v_{\mathrm{th},\infty}}\right)^2\right]\exp\left[-\Lambda\right]H\left(v_0^2\right), \tag{17}$$

where

$$v_0^2 \equiv v^2 - \frac{2GM_\odot(1-\mu_\odot)}{r}\ ,$$

and $\mathrm{H}(x)$ is the usual Heaviside step function. By solving Kepler's equation for the neutral trajectories, one has

$$\left(\frac{\mathbf{v}_0-\mathbf{u}}{v_{\mathrm{th},\infty}}\right)^2 = \frac{1}{\left(v_{\mathrm{th},\infty}\right)^2}\left[v_0^2+u^2+2v_0u\left(\frac{v_z(v_0-v_r)-V(r)\cos\theta}{v_0(v_0-v_r)-V(r)}\right)\right]\ , \tag{18}$$

where v_r and v_z are the radial and z direction components of the velocity vector $\mathbf{v}$ and $V(r)$ is the potential (10). If one assumes again that $\beta = \beta_0 r_0^2/r^2$, then

$$\Lambda = \frac{\beta_0 r_0^2\theta'}{v_0 p_0}\ , \tag{19}$$

where θ' is the angle swept out by the atom on its Keplerian trajectory and $p_0 = |\mathbf{r}\times\mathbf{v}|$ is the angular momentum.

In the limit $v_{\mathrm{th},\infty}\to 0$, the hot distribution function reduces to the cold expression (11) except on the LISM flow axis and in the forbidden region (15). Although the heliospheric H distribution is generally thought to be warm, the cold model remains useful in the physical insight that it provides. However, as we discuss in later sections, both the hot model and cold model conclusions must be tempered

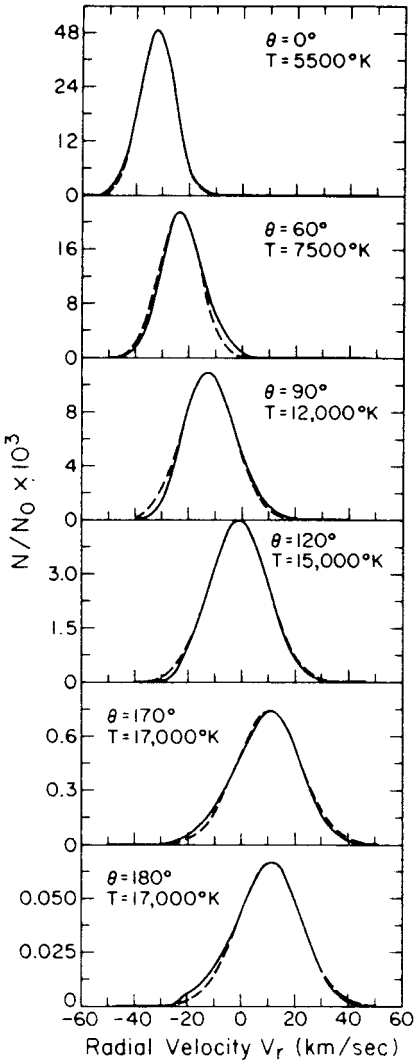

Figure 2.4. The radial velocity distribution for H at 1 AU for the hot interstellar model. The solid curve is the distribution calculated directly from the spherically symmetric Boltzmann equation and the dashed curve corresponds to a fitted Maxwellian distribution with temperature T. θ is the angle from the upwind direction. (Wu and Judge, 1979.)

with the inclusion of heliospheric boundary effects which have been neglected so-far.

The number density, velocity and temperature for the hot distribution can be obtained from (17) by taking appropriate moments, a process which is essentially numerical, although some analytic approximations can made (see Danby and Bray, 1967; Wu and Judge, 1979). Several important points emerge from the hot model for the distribution of Hydrogen in the heliosphere. (i) As illustrated in Figure 2.4,

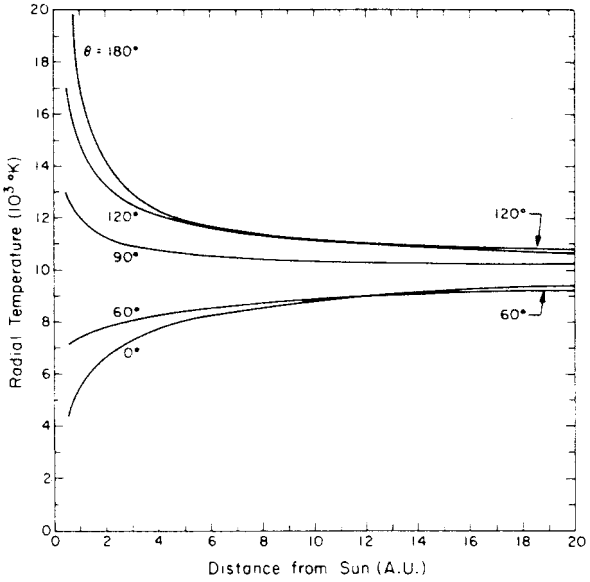

Figure 2.5. The radial temperature of H for the hot interstellar H model as a function of heliocentric distance. (Wu and Judge, 1979.)

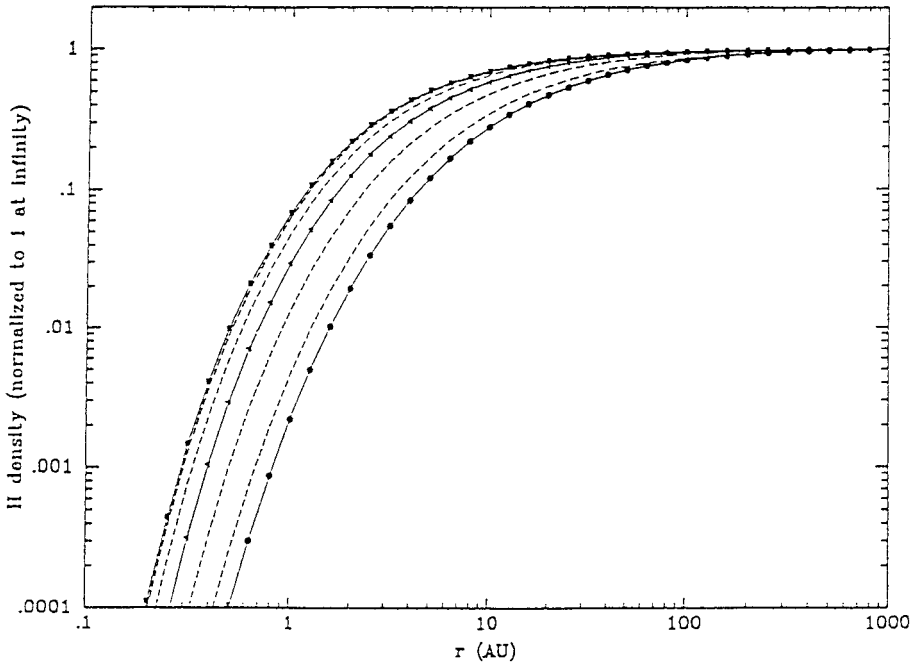

Figure 2.6. H densities as a function of heliocentric radius for the hot interstellar model, normalized to the density at 'infinity' in the upstream direction. The upstream, sidestream and downstream distributions are labelled with squares, triangles and circles respectively and intermediate angles are plotted. (Hall, 1992.)

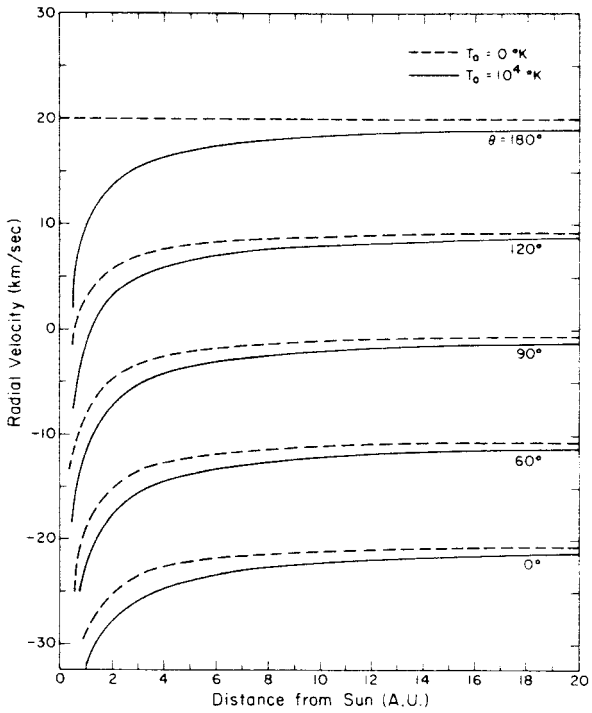

Figure 2.7. The radial velocity of H for the hot model. The solid curves correspond to a H temperature of 10^4 K and the dashed curves to a cold model. (Wu and Judge, 1979.)

(adapted from Wu and Judge, 1979), the calculated neutral radial velocity distribution $N(\mathbf{r}, v_r)$, $\mathbf{r}$ the spatial position and v_r the radial velocity, at 1 AU is very well fitted by a Maxwellian distribution (the dashed curve) for a variety of directions. This, as we shall discuss in Section 5.5, is of importance in the construction of a fully self- consistent model of the interaction of the solar wind with the LISM. (ii) An asymmetry, illustrated in Figure 2.5, in the heliospheric neutral gradient is predicted. For upwind directions, the H temperature decreases with decreasing heliocentric distance, whereas the opposite is true for the downwind direction. As discussed by Wu and Judge (1979), the H temperature increase downwind is due primarily to ionization losses. (iii) The H density as a function of radial distance for various axial angles is illustrated in Figure 2.6. The ionization cavity is evident within 6–10 AU and the cavity is elongated in the downstream direction. For $\mu_\odot > 1$, the downstream region is further depleted. Nonetheless, the downstream singularity of the cold model is eliminated by a hot neutral distribution, as is the parabaloid void when $\mu_\odot > 1$. However, these regions continue to posses the basic characteristics of the cold model. (iv) As illustrated in Figure 2.7, the interplanetary H velocity for $\mu_\odot > 1$ decreases with decreasing heliocentric distance and the hot model produces slightly lower speeds than the cold model for $v > 0$ and higher for $v < 0$.

2.2.3. *Time-Dependent Radiation Pressure and Ionization*

The models discussed above all assume that the radiation pressure $\mu_\odot > 1$ and ionization loss terms β are constant in time. Since both gravity and radiation flux vary as r^{-2}, neutral atoms at large heliospheric distances are largely unaware of changes in either the radiation pressure or photoionization rate. However, within some 10 AU upstream and $\sim$ 40–50 AU downstream, variation in $\mu_\odot$ and β can lead to significant perturbations in the neutral distribution of this region. The time spent by a neutral atom traversing such a 10 AU region is relatively short ($\sim$ 2 years compared to the $\geq$ 10 years for solar system traversal) and certainly comparable to the time-scale of solar cycle variability. Thus, several models have been developed to address the issue of solar cycle varability and the near-Earth neutral H distribution. Ruciński (1985) and Fahr et al. (1987) considered the possibility of a variable ionization rate with constant force, which is reasonable for neutral Helium but not for H. Fahr and Scherer (1990) derived a Fourier-transformed solution for a time-variable force but provided no quantitative results. Blum et al. (1993) combined the Fourier transform approach of Fahr and Scherer (1990) with a Monte-Carlo algorithm to investigate the possibility of H density modulation by means of solar cycle variability. Their analysis of the downwind heliospheric region suggested the intriguing possibility of neutral hydrogen waves driven by a variable radiation pressure. However, the conclusions advanced by Blum et al. (1993) must be tempered by the statistical limitations implicit in their analysis.

A very attractive approach has been developed by Ruciński and Bzowski (1995) which avoids the limitations of the Monte-Carlo approach. This work represents a considerable extension of the related analysis presented by Kyrölä et al. (1994) in which considered both a cold (80 K) and warm neutral gas. Here we summarize the results of Ruciński and Bzowski (1995).

Solar Lyman-α radiation is not strictly periodic, nor is it spherically symmetric and consecutive solar cycles can differ noticeably in their character. Similar comments apply also to the solar wind itself, of course. Nonetheless, by choosing typical maximum and minimum values of 1.4 and 0.7 for the normalized radiation pressure term $\mu_\odot$, Ruciński and Bzowski (1995) adopt the functional form

$$\mu_\odot(t) = \mu_\odot^0 + \hat{\mu}_\odot \cos \omega t \exp\left[\cos \omega t\right] , \tag{20}$$

where $\mu_\odot^0 = 0.75$, $\hat{\mu}_\odot = 0.243$, $\omega = 2\pi/11$ years and $t = 0$ at solar maximum. The ionization function can be described similarly although shifted by a solar cycle period. The anti-correlation of the radiation pressure and the ionization rate can be inferred from the observational data of Ajello et al. (1987) (see Kyrölä et al. (1994) and Ruciński and Bzowski (1995)). Thus, the time-dependent ionization rate is

$$\beta(t) = \beta_0 + \hat{\beta} \cos\left(\omega t + \pi\right) \exp\left[\cos\left(\omega t + \pi\right)\right] , \tag{21}$$

where $\beta_0 = 5 \times 10^{-7}$ s^{-1} and $\hat{\beta} = 10^7$ s^{-1}. The function $\mu_\odot(t)$ exhibits the observed characteristic flat minimum and well defined maximum (Lean and Skumanick, 1983).

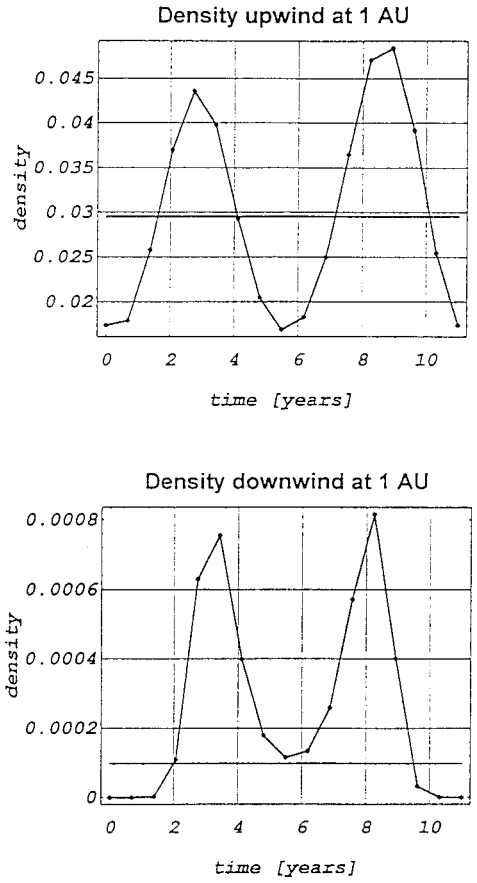

Figure 2.8. The temporal variation in the H density at 1 AU (normalized to the density at 'infinity') for the upstream (*upper panel*) and downstream (*lower panel*) directions. Time 0 corresponds to solar maximum and the solid horizontal line describes the density obtained from a classical stationary hot model with fixed mean radiation pressure and ionization rate. (Ruciński and Bzowski, 1995.)

At 1 AU, a clear temporal variability in the hydrogen distribution, in both upwind and downwind directions, is found. Illustrated in Figure 2.8 are H density waves driven by the anti-correlated radiation pressure and ionization rate. Clear minima in the neutral Hydrogen number density are observed at solar maximum and minimum. The double periodicity of the H density exhibited in Figure 2.8, at first sight surprising since the driving in (20) is singly periodic on an 11 year cycle, results from the phase shift between the radiation pressure/gravity term and the ionization rate. In Figure 2.9, the variable H density, now normalized to the H distribution results obtained from a stationary hot model (for which $\mu = 0.89$ and $\beta = 6 \times 10^{-7}$ s^{-1}), is plotted as function of heliocentric distance (upwind and downwind) at four different times – solar maximum and solar minimum and two intermediate times. Beyond $\sim$ 20 AU in the upwind direction, solar cycle variabil-

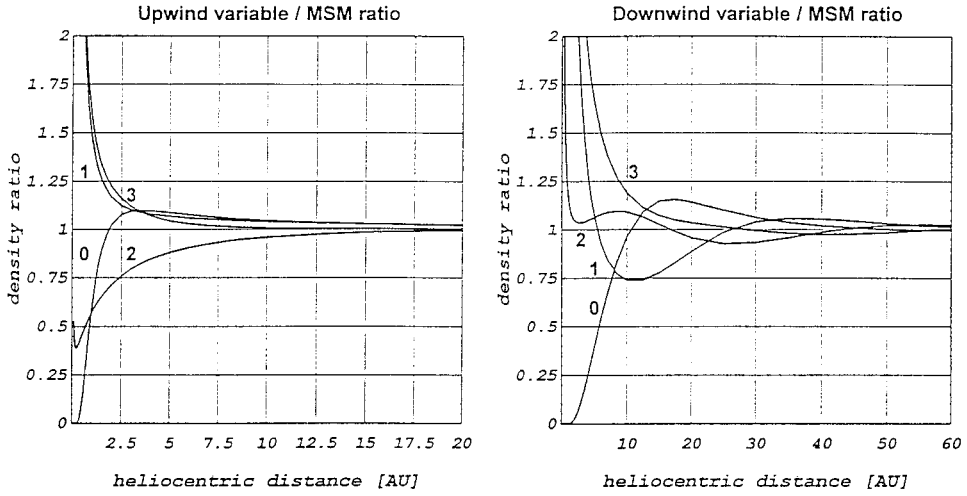

Figure 2.9. (a) Profiles of the variable radial upwind hydrogen density normalized to the density obtained from a classical stationary hot model with fixed mean radiation pressure and ionization rate. Four phases of the solar cycle are illustrated, separated in time by 2.75 years, with phase 0 describing solar maximum, 2 describing solar minimum and 1 and 3 are intermediate. (b) The same as (a) but now in the downwind direction. (Ruciński and Bzowski, 1995.)

ity is largely irrelevent and the density waves present at 1 AU have damped away. On the downstream side, however, variability in the H density can persist until some 60 AU. The latter result is less distant than suggested by Blum et al. (1993). The damping of the H density waves with heliocentric distance is a consequence of $1/r$ attenuation. Since the amplitude of the modulated H density increases with decreasing heliocentric distance, we might expect fairly significant short- term fluctuations within $\sim$ 1 AU during solar maximum.

Not surprisingly, a temporal ionization rate affects the size of the ionization cavity. During solar minimum, Ruciński and Bzowski (1995) find that the cavity is of greater extent ($\sim$ 5/26 AU in the upstream/downstream) than during solar maximum ($\sim$ 4/20 AU in the upstream/downstream).

Both the variable size of the ionization cavity and the modulated H density distribution have implications for the variability of the interplanetary Lyman- α glow.

3. Interstellar Pickup Ions in the Solar Wind

Interstellar neutral gas flows relatively unimpeded into the heliosphere, possibly experiencing some ‘filtration’ at the heliospheric boundaries. Neutral interstellar hydrogen is especially susceptible to the effects of filtration (discussed in detail in Section 5 below), being decelerated and heated in passing from the LISM into the heliosphere. The interstellar neutral gas flowing into the supersonic solar wind

can be ionized by either solar photons (photoionization) or solar particles (charge exchange, electron-impact ionization, etc.) and the new ions respond almost instantaneously to the electromagnetic fields of the solar wind. In the solar wind frame of reference, the newly born interstellar ions immediately gyrate about the interplanetary magnetic field (IMF), after which they experience scattering and isotropization by either ambient or self-generated low-frequency electromagnetic fluctuations in the solar wind plasma. Since the newly born ions are eventually isotropized, their bulk velocity is now that of the solar wind, i.e., they convect with the solar wind flow, and are then said to be 'picked up' by the solar wind. The isotropized pickup ions form a distinct population of energetic ions ($\sim$ 1 keV energies) in the solar wind whose origin is the interstellar medium.

3.1. PICKUP ION DRIVEN INSTABILITIES OF LOW-FREQUENCY WAVES

Since the neutral interstellar hydrogen gas flows into the heliosphere at $\sim$ 20 km s^{-1} (see Section 5 below), it is supersonic in the solar wind frame. Newly created pickup ions can therefore drive a host of plasma instabilities.

A newly ionized pickup ion is accelerated immediately by the motional solar wind electric field $\mathbf{E} = -\mathbf{u} \times \mathbf{B}$, where $\mathbf{u}$ is the solar wind flow velocity and $\mathbf{B}$ the ambient interplanetary magnetic field (IMF). In a Cartesian frame co-moving with the solar wind, the velocity of a pickup ion is simply $\mathbf{v}(t) = (-u_\perp \cos \Omega_i t\ , u_\perp \sin \Omega_i t\ , u_\parallel)$, where the IMF is oriented along $\hat{\mathbf{z}}$, $u_\parallel$ is parallel to $\hat{\mathbf{z}}$, $u_\perp$ is perpendicular to $\hat{\mathbf{z}}$, and $\Omega_i \equiv qB/m$ is the local pickup ion gyrofrequency (q denoting charge and m ion mass). The pickup ions therefore form a ring-beam distribution on the time scale Ω_i^{-1} which streams sunward along the magnetic field. Since the variation in both $\mathbf{u}$ and $\mathbf{B}$ in the outer solar wind can be substantial, the ring-beam should be broad, although this characteristic is not assumed typically when investigating related instabilities. However, shown in Figure 3.1 is a histogram of the measured azimuthal angle of the IMF at 35 AU obtained from hourly averaged Pioneer 11 magnetic field data (Liewer et al., 1993). While the average orientation of the IMF is perpendicular, it is nonetheless broad and a similar thickening in the pickup ion ring-beam distribution can be expected too. Subsequent scattering in the solar wind electric and magnetic field fluctuations acts to further broaden the initial ring-beam distribution.

Both the anisotropy of the ring-beam distribution and its relative streaming with the solar wind drive instabilities that remove energy from the distribution and excite waves. Wu and his colleagues (Wu and Davidson, 1972, 1986; Wu et al., 1973; Hartle and Wu, 1973; Wu and Hartle, 1974) used an idealized narrow ring-beam distribution (i.e., the pickup ions all have identical speed and pitch-angle) to show that hydromagnetic and whistler modes propagating parallel to $\mathbf{B}$ become unstable. The instability analysis of Wu and Davidson (1972) has been generalized and extended by several authors, primarily in the context of cometary pickup ions

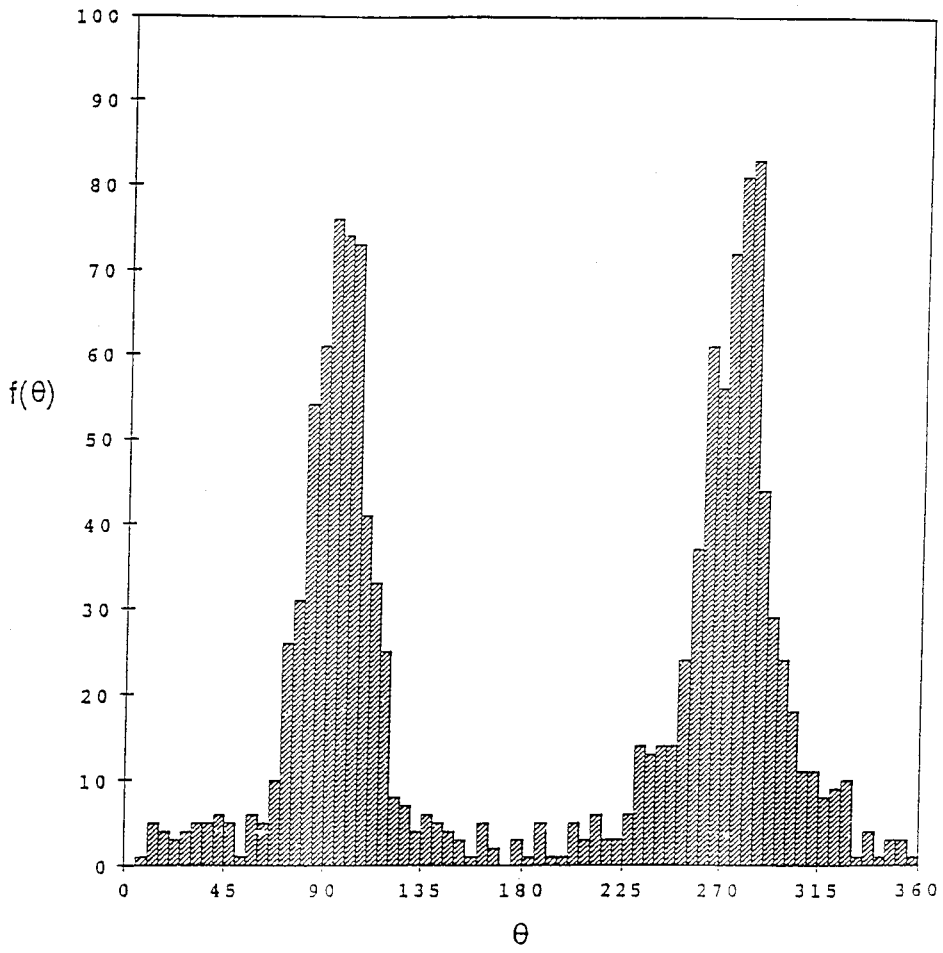

Figure 3.1. Histogram of the azimuthal angle θ of the interplanetary magnetic field at 35 AU using hourly averaged Pioneer 11 data. Pioneer 11 was approximately 15° out of the ecliptic plane. The distributions indicate that the IMF is predominantly perpendicular to the solar wind flow direction. (Liewer et al., 199?.)

(Winske et al., 1985; Winske and Gary, 1986; Sharma and Patel, 1986; Brinca and Tsurutani, 1988; Gary and Madland, 1988).

It was pointed out by Lee and Ip (1987) that the assumption of a sharp narrow ring-beam distribution was not warranted and they determined maximum growth rates for a broad ring-beam distribution. Below, we discuss both the Wu and Davidson (1972) and the Lee and Ip (1987) instability calculations although, as discussed above, the Lee and Ip estimates are to be favoured.

For a transverse electromagnetic perturbation of frequency ω and wave number k propagating parallel to $B_0\hat{\mathbf{z}}$, the dispersion relation is [e.g., *Stix*, 1992]

$$D^{\pm}(\omega\,,k) \;=\; 1-\frac{c^2k_z^2}{\omega^2}+\sum_j\frac{\omega_{pj}^2}{\omega}\int \mathrm{d}^3\mathbf{v}\frac{v_\perp}{2}\frac{1}{\omega-v_zk_z\pm\Omega_j}\times \\ \times\;\left[\frac{\partial F_j}{\partial v_\perp}-\frac{v_zk_z}{\omega}\left(\frac{\partial F_j}{\partial v_\perp}-\frac{v_\perp}{v_z}\frac{\partial F_j}{\partial v_z}\right)\right]=0\,, \tag{22}$$

and $\int \mathrm{d}^3\mathbf{v}\equiv 2\pi\int_0^\infty \mathrm{d}v_\perp\int_{-\infty}^\infty \mathrm{d}v_z$. Here, $F_j(v_\perp^2, v_z)$ is the phase-space distribution function of non-relativistic particles of species j and $\int F_j\,\mathrm{d}^3\mathbf{v}=n_j$, the particle number density. The plasma frequency for the jth species is denoted by ω_{pj} $(\equiv (n_jq_j^2/\varepsilon_0m)^{1/2})$. Depending on the functional form of $F_j(v_\perp^2, v_z)$ and on the region of interest in (ω, k_z)-space, Equation (22) is the dispersion relation for electromagnetic waves propagating parallel to $\mathbf{B}_0$, and includes Alfvén waves, the firehose instability, ion cyclotron waves, the Alfvén ion cyclotron instability, electron whistler waves, electron cyclotron waves and Wiebel-like transverse electromagnetic instabilities driven by an anisotropy in plasma kinetic energy. With the exception of Sharma and Patel (1986), who considered oblique wave propagation in the context of cometary pickup ions, all theoretical instability analyses begin with (22).

The integral in (22) contains the product of two functions which can be strongly localized in v_z for the ring-beam distribution, viz., the term in square brackets and $(\omega-v_zk_z\pm\Omega_j)^{-1}$. Wu and Davidson (1972) suppose that the pickup ion distribution F_j is strongly localized so that

$$F_{\mathrm{PI}}(v_\perp^2, v_z)\equiv F_i=\frac{n_{\mathrm{PI}}}{2\pi v_\perp}\delta(v_z-v_{z0})\delta(v_\perp-v_{\perp0})\,. \tag{23}$$

By contrast, Lee and Ip (1987) suggest instead that the pickup ion distribution is broad (for the reasons given above) and so the dominant contribution to the integral in (22) results from the resonant term $(\omega-v_zk_z\pm\Omega_j)^{-1}$. In this case, the resonant term can be evaluated using the Plemelj formula $(\omega-v_zk_z\pm\Omega_j)^{-1}=P(\omega-v_zk_z\pm\Omega_j)^{-1}-i\pi\delta(\omega-v_zk_z\pm\Omega_j)$, where P indicates the principal value. In either case, the plasma is assumed to comprise ring-beam pickup ions, cold solar wind protons and electrons.

By means of (23), the cold solar wind approximation, and integrating by parts, Wu and Davidson (1972) (see also Lee and Ip, 1972) obtained the dispersion relation

$$\overline{\omega}^2\left[\overline{\omega}^2+2\overline{\omega}\frac{v_{z0}k_z-\Omega_i}{\Omega_i}+\frac{(v_{z0}k_z-\Omega_i)^2}{\Omega_i^2}-\frac{V_{\mathrm{A}}^2k_z^2}{\Omega_i^2}\right]= \\ =\frac{\omega_{pi}^2}{\Omega_i^2}\frac{V_{\mathrm{A}}^2}{c^2}\left[\frac{v_\perp^2k_z^2}{2\Omega_i^2}-\overline{\omega}\,(\overline{\omega}-1)^2\right]\,, \tag{24}$$

in the hydromagnetic limit $\omega\ll\Omega_p$ after introducing $\overline{\omega}\equiv(\omega-v_zk_z+\Omega_i)/\Omega_i$. The subscript i refers to pickup ions and $V_{\mathrm{A}}^2\equiv B^2/\mu(\rho_p+\rho_e)$ is the square of

the Alfvén speed and $\rho_{p,e}$ the mass density of solar wind protons/electrons. In the absence of pickup ions, i.e., $\omega_{p_i} = 0$, (24) implies $\omega^2 = V_A^2 k_z^2$ (Alfvén mode) or $\overline{\omega} = 0$, i.e., $\omega = -\Omega_i + v_{z0} k_z$ (cyclotron resonant with the ring-beam). The right-hand side of (24) is small but it introduces unstable roots, depending on the magnitude of $|v_{z0} k_z - \Omega_i|$ relative to $|V_A k_z|$. The two most unstable roots occur for those values of k_z satisfying $\omega = v_{z0} k_z - \Omega_i \simeq \pm V_A k_z$. These are Alfvén waves whose growth rates are approximately

$$\gamma \sim |\Omega_i| \left[\frac{V_A}{|v_{z0}|} \frac{(1/2) n_i m v_{\perp 0}^2}{B^2/2\mu} \right]^{1/2} \tag{25}$$

(Wu and Hartle, 1974). Conversely, if instead of approximate equality, one has $|v_{z0} k_z - \Omega_i| > |V_A k_z|$, then all the roots of (24) are stable, whereas $|v_{z0} k_z - \Omega_i| < |V_A k_z|$ yields an unstable root with phase speed less than V_A and growth rate

$$\gamma = |\Omega_i| \left[\frac{(1/2) n_i m v_{\perp 0}^2}{B^2/2\mu} \right]^{1/2} \tag{26}$$

(Wu and Davidson, 1972).

Instead of using the strongly peaked distribution function (23), Lee and Ip, (1987) used a broader pickup ion ring-beam distribution whose contribution to the integral term enters primarily through the resonance condition. Subject to the assumptions that the growth rate $\gamma \ll \omega_r$ (ω_r denotes the real part of the frequency ω) and $\omega_r \ll \Omega_i$, $|v_{z0}| \geq V_A$, Lee and Ip (1987) obtain

$$\begin{aligned} \omega_r &= \pm V_A k_z; \\ \gamma &= \frac{\pi^2}{2} \frac{V_A^2}{c^2} \frac{\omega_{p_i}^2}{n_i} \int \mathrm{d}v_z \, \mathrm{d}v_\perp v_\perp^2 \left[\frac{\partial F_i}{\partial v_\perp} + \frac{k_z}{\omega_r} \left(v_\perp \frac{\partial F_i}{\partial v_z} - v_z \frac{\partial F_i}{\partial v_\perp} \right) \right] \\ &\times \delta(\omega_r - v_{z0} k_z + \Omega_i) \, . \end{aligned} \tag{27}$$

If one then assumes a Maxwellian distribution for F_i, i.e.,

$$F_i(v_\perp^2, v_z) = \frac{n_i}{2\pi^{3/2} v_\perp \sigma} \delta(v_\perp - v_{\perp 0}) \exp\left[-\frac{(v_z - v_{z0})^2}{\sigma^2} \right] ,$$

with $\sigma \ll v_{z0}$, the maximum growth rate given by (27) is

$$\gamma \sim |\Omega_i| \frac{V_A |v_{z0}|}{\sigma^2} \frac{(1/2) n_i m v_{\perp 0}^2}{B^2/2\mu} \, , \tag{28}$$

(Lee and Ip, 1987).

Comparison of (28), (25) and (26) indicate that the growth rate is smallest for the broad ring-beam distribution. Nonetheless, since the initial pickup ion distribution should be intrinsically broad by virtue of the variation in the IMF, expression (28) should be favoured.

Other instabilities, such as the firehose instability and a whistler instability were considered by Wu and Davidson (1972) on the basis of the ring-beam distribution

(23). The latter instability is however significantly reduced when a broad ring-beam distribution is assumed (Lee and Ip, 1987). Gray et al. (1996) have considered the Alfvén ion cyclotron instability in the outer heliosphere by means of a hybrid simulation. They too use a sharp ring-beam distribution but they make the important point that this instability can couple directly to the cold solar wind plasma which may lead to anisotropic heating. This is discussed further below (Section 3.6).

In concluding this discussion, we note that the investigation of ring-beam driven instabilities in the outer heliosphere has not been pursued to the extent that it should - in particular, the importance of using a broad distribution for the initial pickup ion distribution does not appear to have been fully appreciated - and much remains to be elucidated.

3.2. PICKUP ION WAVE SPECTRA

The initial ring-beam distribution scatters resonantly on both *in situ* and self-excited waves and relaxes to a stable distribution. The quasi-linear interaction of pitch-angle scattered pickup ions and their cyclotron-resonant MHD waves has been studied extensively from both an analytic (Sagdeev et al., 1986; Galeev et al., 1987, 1991; Lee and Ip, 1987) and a numerical (Gary et al., 1986, 1988, 1989, 1991; Ziebel and Yoon, 1990; Ziebel et al., 1990; Miller et al., 1991; Ye and Cravens, 1991; Yoon et al., 1991) perspective, again largely in the context of pickup cometary ions. Lee and Ip (1987) first derived the quasi-linear spectrum of waves that result from the pitch-angle scattering of interstellar pickup ions to a closed shell distribution. They predicted substantial enhancements in the solar wind wave spectrum as a result. Although the predicted spectral enhancements are consistent with wave spectra observed upstream of comets (e.g., Glassmeier et al., 1989), the Voyager and *Ulysses* data do not offer overwhelming evidence for wave enhancements due to pickup ion excited waves (Smith, 1993; Goldstein et al., 1993; Smith et al., 1994; Murphy et al., 1995).

Besides the quasi-linear approach of Lee and Ip (1987), one can utilize an attractive alternative approach developed by Johnstone et al. (1991) and Huddleston and Johnstone (1992) for the excitation of waves by pickup cometary ions. This approach, used by Williams and Zank (1994) for interstellar pickup ions and further extended by Isenberg and Lee (1996), is essentially exact provided one assumes that the bispherical distribution (Galeev and Sagdeev, 1988) represents a good approximation to the asymptotic pickup ion distribution. The pickup ions are assumed to scatter in pitch-angle by the excited and ambient waves while preserving their energy in the wave frame. If the pickup ion generated (unstable) parallel propagating modes dominate the fluctuation spectrum, then the pickup ions scatter onto a 'bispherical' shell distribution whereas elastic scattering in the solar wind frame would yield a spherical distribution. The difference in kinetic energy between the spherical and bispherical distributions is given to the waves and their free energy is $\sim V_A/u$ of the initial pickup ion energy density. The assumptions implicit in the

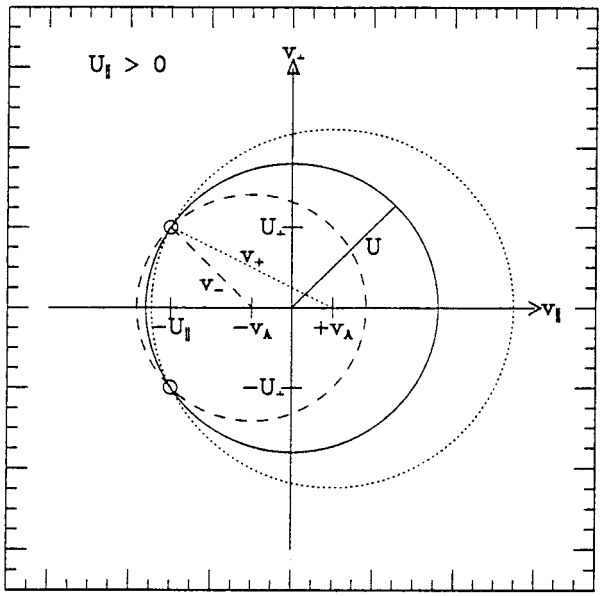

Figure 3.2. The construction of the bispherical distribution in the solar wind frame. The ring distribution is indicated by open circles. The solid line is the constant energy shell. The dotted line represents the surface of interaction between the ring and the $+V_A$ waves and the dashed line the surface of interaction between the ring and the $-V_A$ waves. The bispherical distribution is composed of the two shells within the solid line. (Williams and Zank, 1994.)

bispherical analysis are (i) that the asymptotic pickup ion distribution is bispherical and filled uniformly; (ii) that the diffusion of the ring-beam distribution onto a bisphere occurs more rapidly than the processes likely to effect either the wave spectrum (spectral transfer, etc.) or the bispherical distribution (adiabatic cooling, second-order Fermi energization) directly, and (iii) that only parallel propagating Alfvén modes resonate with the pickup ions. These assumptions have been relaxed somewhat by Isenberg and Lee (1996) who have included the effects of wave dispersion.

In Figure 3.2, the construction of the bispherical distribution in the solar wind frame, where the subscript $\parallel$ indicates parallel to the IMF, is illustrated. For parallel and anti-parallel propagating Alfvén modes only, the pickup ion-wave interaction conserves particle energy in the wave frame, so that the pickup ions move from the ring onto spheres centered on the wave velocity i.e., either $+V_A$ or $-V_A$. The ion can move off the ring in any of four directions The shell representing interaction with the anti-parallel waves is indicated by the dashed line in Figure 3.2 and that for parallel waves is dotted. The shell representing conservation of energy in the solar wind frame is solid. If an ion moves onto a shell inside the solid sphere, it gives up energy to the waves whereas an ion moving onto a shell outside the solid line takes energy from the waves. The stable state occurs when the particles have moved from the ring to the inner shells. Then, all the free energy available to the

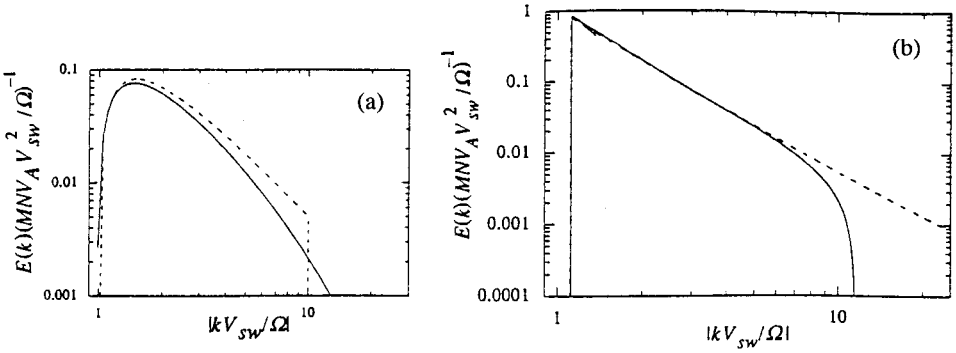

Figure 3.3. (a) Self generated wave spectra from perpendicularly picked up protons scattering on to a bispherical shell. The excited wave mode is the ion cyclotron wave. The solid line represents the dispersive result (Isenberg and Lee, 1996) and the dashed line the non-dispersive result (Williams and Zank, 1994). (b) Self-generated fast-mode spectra from parallel picked-up protons. The solid line is the dispersive result with an assumed fraction (= 0.5) of pickup ions which occupy the resonance gap and anti-sunward hemisphere (Isenberg and Lee, 1996). The dashed line illustrates the non-dispersive result (Williams and Zank), 1994]. (adapted from Isenberg and Lee, 1996.) In both figures, $V_A/u_{SW} = 0.1$ has been assumed.

waves has been taken from the pickup ion distribution. Ions with $v_z < -u_\parallel$ have given their energy to parallel propagating waves and they reside on that part of the shell centered on V_A. Conversely, ions with $v_z > -u_\parallel$ have given their energy to anti-parallel waves and they reside on that section of the shell centered on $-V_A$.

The change in $v_\perp$ ($\equiv \sqrt{v_x^2 + v_y^2}$) along the shell as a function of v_z is obviously

$$\frac{dv_\perp}{dv_z} = \frac{\pm V_A - v_z}{v_\perp} , \tag{29}$$

since pickup ions on the bispherical shell must satisfy

$$v_\perp^2 + (v_z \pm V_A)^2 = \text{const.} \tag{30}$$

The left-hand side of (30) is conserved along the characteristics of the differential operator in the square brackets of (22). The final energy density in unstable Alfvén waves with wave numbers between k and $k + dk$ is given by the energy lost by a particle as it scatters through the resonant range of $v_z(k)$ – i.e., de/dk – times the net number density of pickup ions scattering through that section of the bispherical distribution. Since the asymptotic particle distribution is assumed to be a uniformly filled bisphere, the number of pickup ions must be proportional to the fractional area $A(v_z)$ of the bispherical shell occupied by particles with values of v_z greater than that resonant with $k(v_z)$ i.e.,

$$E(k) = n_{PI} \frac{de}{dk} \frac{A(v_z)}{A_{BD}} = n_{PI} \frac{de}{dv_z} \frac{dv_z}{dk} \frac{A(v_z)}{A_{BD}} , \tag{31}$$

where A_{BD} is the total area of the bispherical distribution and $n_{\rm PI}$ is the number density of pickup ions. To compute $\mathrm{d}v_z/\mathrm{d}k$, one uses the pickup ion resonance condition

$$\omega - v_z k_z = \pm\Omega_i \ , \tag{32}$$

or $|k_z| \equiv k = \Omega_i/|V_{\rm A} - v_z|$ (since $\omega/k_z = \pm V_{\rm A}$ by assumption), to obtain

$$\mathrm{d}k/\,\mathrm{d}v_z = \pm k^2/\Omega_i \ .$$

Since the energy of a pickup ion is simply $e = 1/2m(v_\perp^2 + v_z^2)$, it follows that

$$\mathrm{d}e/\,\mathrm{d}v_z = \pm m V_{\rm A} \ ,$$

using (29). The asymptotic power spectrum is therefore given by

$$I(k) = n_{\rm PI} m V_{\rm A} \frac{\Omega_i}{k^2} \frac{A(v_z)}{A_{BD}} \ , \tag{33}$$

and $\int I(k)\ \mathrm{d}k = E_w$. The spectrum is therefore a function of k^2 and depends explicitly on the geometrical properties of the bispherical distribution in a very simple fashion. Isenberg and Lee (1996) use the cold plasma electron-proton dispersion relation $V_{ph} = \pm V_{\rm A}\sqrt{1 + \omega/\Omega_p}$ to consider the modifications introduced into the above analysis by dispersive effects.

The pickup ion generated spectra have a k^{-2}dependence for intermediate values of k, which is consistent with the wave spectra observed at comets (Glassmeier et al., 1989). Plots of the normalized intensities $I(k)$ are plotted in Figure 3.3 for a perpendicular IMF configuration (a) and a parallel configuration (b). The solid lines correspond to the dispersive analysis of Isenberg and Lee (1996) and the dashed lines to a non-dispersive analysis (Williams and Zank, 1994). In Figure 3.3, the ratio $V_{\rm A}/u = 0.1$ has been assumed and it can be seen that the non-dispersive analysis overestimates the power in the waves by between 8% and 18%, depending on the orientation of the IMF.

The quantity $I(k)$ is calculated in the solar wind frame but observations are made in the spacecraft frame. By means of the appropriate Doppler-shift for parallel propagating waves (Lee and Ip, 1987; Williams and Zank, 1994), one can determine $P(\omega)$ from the relation $I(k)\ \mathrm{d}k = I(\omega)/|V_{ph} + u_\parallel|\ \mathrm{d}\omega = P(\omega)\ \mathrm{d}\omega$, where $\mathbf{V}_{ph} = \left(\omega/k^2\right)\mathbf{k}$. Plotted in Figure 3.4 is $P(\omega)$ for a perpendicular, parallel and intermediate geometry. Ion pickup in parallel geometries excites no waves below Ω_i, unlike that in perpendicular geometries. The peak amplitude of excitation for perpendicular geometries is at frequencies much less than Ω_i, whereas for the radial and intermediate cases, the peak occurs at Ω_i. The implication of this, as noted by Williams and Zank (1994), is that pickup ion induced spectral enhancements may be masked by the higher level of ambient turbulence at these frequencies for perpendicular geometries. Enhancements to the turbulence spectra are thus likely to be seen more easily in quasi-parallel geometries, for which some

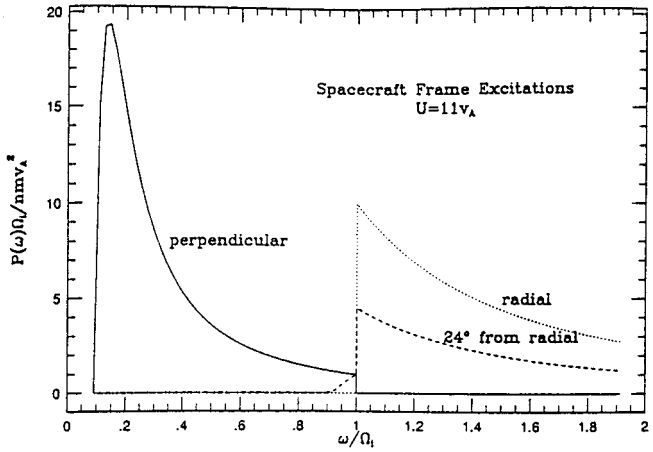

Figure 3.4. The excited wave spectra for parallel, intermediate and perpendicular pickup geometries for $V_A/u_{SW} = \frac{1}{11}$. (Williams and Zank, 1994.)

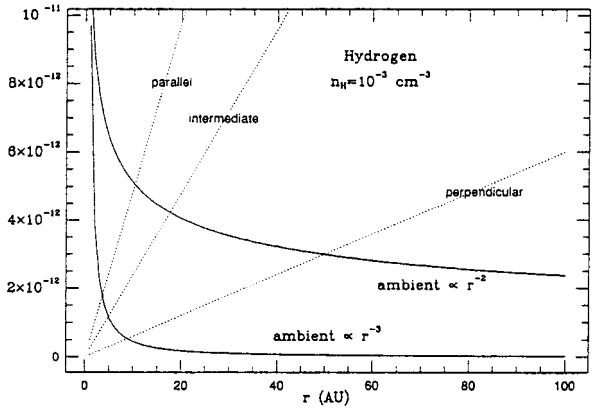

Figure 3.5. Plots of the amplitude of $P(\omega)$ at the pickup proton gyrofrequency for parallel, perpendicular and intermediate IMF configurations as a function of heliocentric distance (dotted lines). The solid lines illustrate the strength of the ambient spectra under the assumption that their decay is either $\propto r^{-2}$ or r^{-3}. $V_A/u_{SW} = 0.1$ has been assumed. (Williams and Zank, 1994.)

observational support exists (Smith et al., 1994). This is illustrated in Figure 3.5, where the peak amplitude for $P(\omega)$ is plotted as a function of radial heliocentric distance for parallel, perpendicular and intermediate IMF configurations. Plotted as solid lines is the decay of the ambient solar wind spectrum at the ion gyrofrequency under the assumption that the decay is governed either by an r^{-3} or an r^{-2} decay law. Where the dotted and solid lines intersect is an estimate for where the pickup ion driven spectral enhancement will not be masked by the *in situ* turbulence spectrum. This figure overestimates the power the in the pickup ion driven turbulence by a factor of 2 but, given the assumptions implicit in the bispherical distribution approach, this is probably irrelevant. Furthermore, if the scattering waves are dis-

persive, then as discussed above, the pickup ions tend to retain a little more of their energy than predicted by the non-dispersive treatment.

3.3. Evolution of turbulence in the outer heliosphere

The analysis of pickup ion generated wave spectra in Section 3.2 was strictly local and the spectral dynamics of the waves/turbulence in an inhomogeneous solar wind was ignored. The radial evolution of Alfvénic fluctuations in the solar wind has been described traditionally on the basis of WKB theory although, as noted by *Hollweg* (1974), the basic assumptions implicit in this theory are invariably violated in the solar wind. Nonetheless, Fisk and Goldstein (1974, unpublished manuscript) attempted to use WKB theory to determine the radial evolution of magnetic fluctuations δB^2 when pickup ion driven turbulence in the outer heliosphere was included. Not surprisingly, a considerable deviation from the well-known r^{-3} decay law for δB^2 was predicted from ~ 10 AU outward. Such a prediction is now known to be inconsistent with observations of the evolution of magnetic fluctuations in the outer heliosphere.

Zank et al. (1996) have used a turbulence-theoretic perspective to describe the evolution of arbitrary amplitude MHD fluctuations in the solar wind. The turbulence is assumed to be both 'fossil' turbulence as well as that generated locally by stream shear, shock waves, and, in the outer heliosphere, by pickup ions. The model may be expressed in spherical coordinates as (Zank et al., 1996)

$$\frac{\partial E_b}{\partial t} + u\frac{\partial E_b}{\partial r} + \frac{u}{r}E_B - \Gamma\frac{u}{r}E_B = -\frac{E_b^{3/2}}{\ell} + S\,, \tag{34}$$

where $E_b \equiv \delta B^2/\mu_0\rho$ is the magnetic fluctuation energy per unit mass, ρ and u denote the solar wind density and radial flow velocity, and Γ the MHD analogue of the Reynolds stress tensor. Γ is a function of the IMF winding angle and the assumed symmetry properties of the MHD turbulence. On the right-hand-side of (34), S denotes the turbulence source terms (including that of pickup ion driving) and $\ell(r,t)$ is the longitudinal correlation length. The turbulent decay term $-E_b^{3/2}/\ell$ of the energy-containing eddies is based on a von Karman and Howarth (1938) estimate (Zank et al., 1996; Matthaeus et al., 1996). The first three terms are, of course, identical to the usual WKB transport equation for Alfvén waves in the solar wind. The evolution equation for $\ell(r,t)$ is given by

$$\frac{\partial \ell}{\partial t} + u\frac{\partial \ell}{\partial r} + \Gamma\frac{u}{r}\ell = \frac{E_b^{1/2}}{2} - \frac{\ell}{2E_b}S\,, \tag{35}$$

(Zank et al., 1996).

Three principle sources exist for turbulence in the outer heliosphere. The first is shear associated with the interaction of fast and slow speed streams (Coleman, 1968; Roberts et al., 1992) and the second is compressional effects associated with both stream-stream interactions and blast waves (e.g., Whang, 1991). The third

source, which occurs beyond the ionization cavity, is turbulence driving/generation resulting from the ionization of interstellar hydrogen (Section 3.2). Both the shear and compressional source terms can be expressed as (Zank et al., 1996)

$$\dot{E}_{b,\mathrm{shear(comp)}} = C_{\mathrm{shear(comp)}} \frac{u}{r} E_b \ , \tag{36}$$

and $C_{\mathrm{shear(comp)}}$ is a prescribed constant. For pickup ion generated turbulence, the source term is, per unit volume, (Lee and Ip, 1987; Williams and Zank, 1994)

$$\dot{E}_{b,\mathrm{PI}} = \frac{\mathrm{d}n_{\mathrm{PI}}}{\mathrm{d}t} \frac{V_{\mathrm{A}} u}{n_{\mathrm{SW}}} = \frac{u V_{\mathrm{A}} n_{\mathrm{H}}^{\infty}}{n_{\mathrm{SW}}^{0} \tau_{\mathrm{ion}}^{0}} \exp\left[-\lambda\theta / r \sin\theta\right] \ , \tag{37}$$

where $n_{\mathrm{PI,SW}}$ denote pickup ion and solar wind number densities respectively and the time derivative refers to a creation rate rather than a convective derivative. The pickup ion creation rate is expressed in terms of the cold gas interstellar distribution for neutrals (Section 2.2.1) and n_{H}^{∞} is the interstellar neutral number density at the termination shock, τ_{ion}^{0} the neutral ionization time at 1 AU, λ the ionization cavity length scale, and θ the angle between the observation point and the upstream direction.

Remarkably, in the absence of pickup ion driven turbulence, the steady-state equations (34) and (35) can be solved analytically. Asymptotic solutions which include the effects of pickup ion driven turbulence are also easily derived. Several numerical solutions of the steady-state equations (34) and (35) are presented in Figure 3.6. Figure 3.6(a) shows the radial evolution of the magnetic fluctuation ratio $\delta B^2 / \delta B_0^2$ (δB_0^2 the normalizing value at 1 AU) as a function of heliocentric distance in the absence of driven turbulence. Four solutions are illustrated. The solid curve is a pure WKB solution (i.e., the turbulent dissipation term $-E_b^{3/2}/\ell$ in (34) is zero and the MHD Reynolds stress term satisfies $\Gamma = 0$) and the usual r^{-3} scaling is recovered. The dotted curve is a WKB solution too but now with $\Gamma = 1$. In this limit, the IMF is radial and all the fluctuation energy resides in the magnetic fluctuations (Jokipii and Kota, 1989). The remaining two solutions represent decaying turbulence solutions for different values of Γ, and, of course, these solutions decay more rapidly with increasing heliocentric distance than those of WKB theory - this due to the absence of any driving and the presence of dissipation. For the turbulence models only, the correlation length can computed, illustrated in Figure 3.6(c), and $\ell(r)$ is a modestly increasing function with increasing r. By contrast, with the addition of pickup ion driven turbulence in the outer heliosphere, the rate of the δB^2 decay with heliocentric distance is sharply arrested for the turbulence models (Figure 3.6(b)), and δB^2 now decays asymptotically as $\sim r^{-(9+\Gamma)/4}$. The WKB solutions also decay far more slowly ($\delta B^2 \sim r^{-1}$) in the outer heliosphere. Owing to the presence of strongly driven turbulence, the dissipative term in (34) assumes increasing importance and ℓ now decreases in the outer heliosphere with increasing radial distance.

By combining Voyager 1, 2 and Pioneer 11 hourly and 15-min averaged data, Zank et al. (1996) compared the various theoretical predictions with the observed

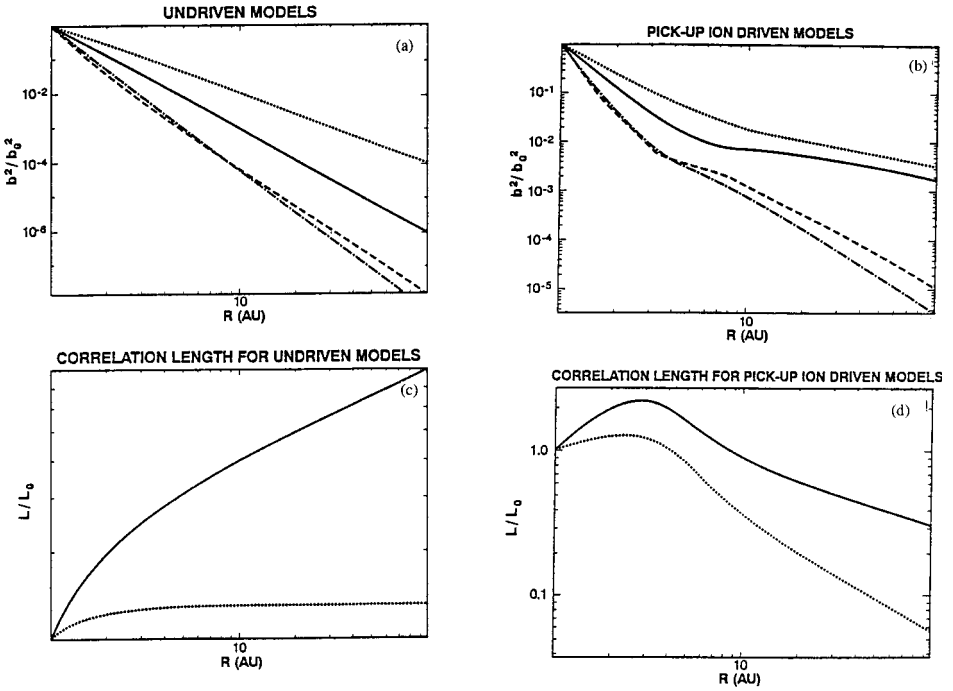

Figure 3.6. (a) Plot of the radial evolution of the magnetic fluctuation ratio b^2/b_0^2 as a function of heliocentric distance (measured in AU) in the absence of turbulent driving. The solid curve corresponds to the WKB solution, the dotted curve to the Jokipii–Kota solution, the dashed curve to the $\Gamma = 0$ solution, and the dashed-dotted curve to the $\Gamma = 1$ solution. (b) As in (a) but now with turbulence driving by stream interactions present. The solid curve corresponds to the WKB solution, the dotted curve to the Jokipii–Kota solution, the dashed curve to the $\Gamma = 0$ solution, and the dashed-dotted curve to the $\Gamma = 1$ solution. (c) Plot of the normalized correlation length ℓ/ℓ_0 as a function of heliocentric distance. The solid curve describes the $\Gamma = 0$ case, and the dotted curve describes the $\Gamma = 1$ case. (d) As with (c) but now in the presence of pickup ion driven turbulence. (Zank et al., 1996.)

magnetic field fluctuations δB^2 (normalized to 1 AU values). The results are illustrated in Figure 3.7 and four solutions are again depicted. The solid line corresponds to the WKB solution without pickup ion driving, the dotted curve to the WKB solution with pickup ion driving, the dashed line to a dissipative turbulent solution with stream driven turbulence only, and finally the dash-dotted line shows a dissipative turbulence solution when both stream and pickup driven turbulence is included. Within 6–10 AU, there is little to choose between the four solutions, but from $\sim$ 7 AU outward, the undriven WKB model and the stream- driven turbulence model underestimate the observed power in magnetic fluctuations, and the pickup ion driven WKB model is clearly inappropriate. The dissipative, stream and pickup ion driven turbulence model by contrast appears to yield reasonable agreement with the data from 1 AU to 40 AU (Zank et al., 1996).

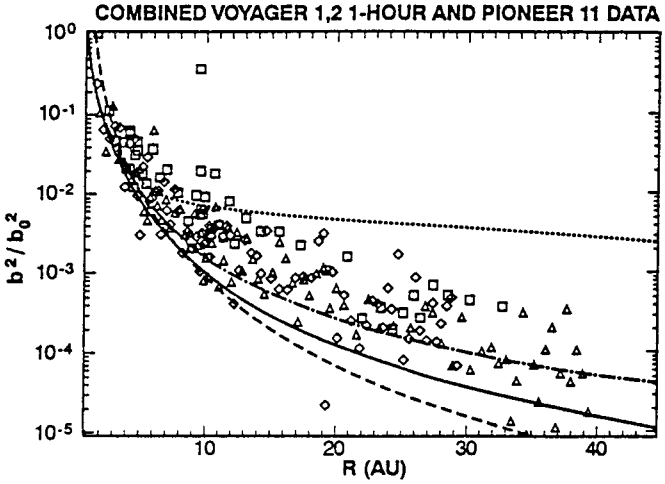

Figure 3.7. Semilog plot of b^2/b_0^2 for the combined Voyager 1 and 2 and Pioneer 11 data set (normalized to 1 AU) and four theoretical models as a function of heliocentric distance. The solid curve corresponds to the WKB solution, the dotted curve to the WKB solution with pickup ion driving, the dashed curve to a turbulent dissipative solution with driving by stream interactions and the dashed-dotted curve to a turbulent dissipative solution with driving by stream interactions and pickup ions. The triangles and diamonds denote Voyager 1 and 2 1-hour data respectively and the squares identify the Pioneer 11 15-min data. The parameters used for these solutions are drawn from solar wind observations and $\Gamma = 0.2$ has been used. (Zank et al., 1996.)

In concluding this subsection, we note that turbulence models such as that described here are of great importance in properly modelling cosmic-ray and pickup ion transport in the outer heliosphere (Zank et al., 1997; Pauls et al., 1997).

3.4. EVOLUTION OF PICKUP IONS IN THE SOLAR WIND

Consider now the evolution of the pickup ion distribution in the solar wind as it scatters in pitch-angle off the solar wind magnetic fluctuations, both those generated by the pickup ions themselves as well as *in situ* turbulence. A number of processes determine the evolution of the pickup ion distribution - primarily pitch-angle scattering and energy diffusion in the wave field, convection and adiabatic deceleration in the expanding solar wind, and the injection of newly ionized particles. These various processes all possess different time-scales, and pitch-angle scattering should dominate due to the large growth rate of the unstable waves and the high pickup ion velocities ($v \sim u$). Since $|V_A| \ll v$, classical energy diffusion, as we discuss below, is unlikely to be an important factor in determining the gross evolution of the pickup ion distribution.

Vasyliunas and Siscoe (1976) investigated the evolution of the pickup ion distribution in the absence of energy diffusion. Isenberg (1987) has since generalized this calculation by including energy diffusion.

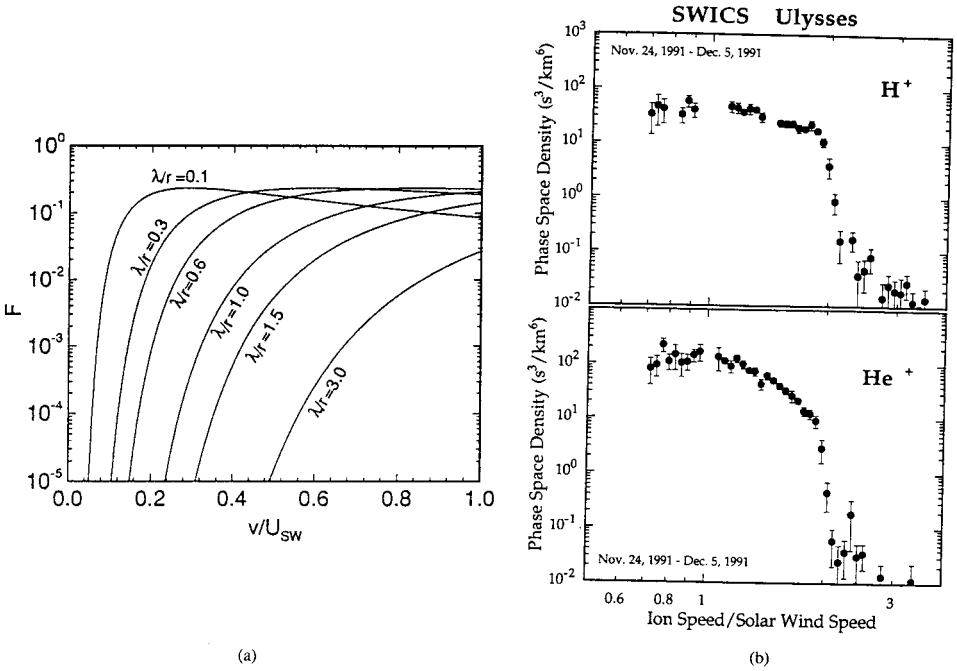

Figure 3.8. (a) The velocity distribution function for interstellar ions (40) using the cold hydrogen distribution. (After Vasyliunas and Siscoe, 1976.) (b) The phase space density of interstellar pickup protons as a function of $v/u_{\rm SW}$ in the spacecraft frame observed by the SWICS instrument on the *Ulysses* spacecraft at 4.82 AU. (Gloeckler et al., 1993.)

In a steady, spherically symmetric expanding solar wind, an isotropic distribution of pickup ions evolves as

$$\frac{\partial f}{\partial t} + u\frac{\partial f}{\partial r} - \frac{2u}{r}\frac{v}{3}\frac{\partial f}{\partial v} = \frac{1}{v^2}\frac{\partial}{\partial v}\left(v^2 D\frac{\partial f}{\partial v}\right) + \frac{n_{\rm H}}{\tau_{\rm ion}}\frac{\delta(v-u)}{4\pi v^2}\,, \tag{38}$$

where $n_{\rm H} = n_{\rm H}^{\infty}\exp\left[-\lambda\theta/r\sin\theta\right]$ and $\tau_{\rm ion} = \tau_{\rm ion}^0 r^2/r_0^2$ (Vasyliunas and Siscoe, 1976; Isenberg, 1987). In (38), it has been assumed that the isotropization of the initial ring-beam distribution is immediate so that the source term may be approximated as an isotropic shell moving at the solar wind speed. Equation (38) is solved easily using the method of characteristics in the limit that $D = 0$. In this case, the steady-state solution is given by

$$f(r,v) = \frac{3}{8\pi}\frac{n_{\rm H}(r_1)}{\tau_{\rm ion}^0 u^2}\frac{r_0^2}{r}\left(\frac{u}{v}\right)^{3/2}\,, \tag{39}$$

where $r_1 = \left(r^2v^3/u^3\right)^{1/2}$. For the simple cold distribution, (39) reduces to

$$f(r,v) = \frac{3}{8\pi}\frac{n_{\rm H}^{\infty}}{\tau_{\rm ion}^0 u^2}\frac{r_0^2}{r}\left(\frac{u}{v}\right)^{3/2}\exp\left[\frac{-\lambda}{r}\frac{\theta}{\sin\theta}\left(\frac{u}{v}\right)^{3/2}\right]\,, \tag{40}$$

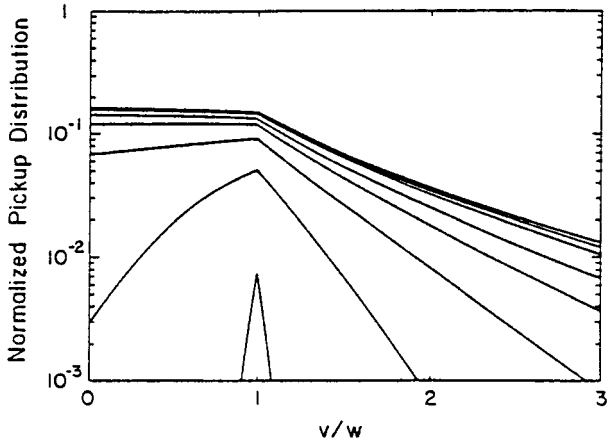

Figure 3.9. The normalized pickup ion distribution as a function of v/u_{SW} and r/r_0 for representative solar wind parameters. The curves are arranged in ascending values of r/r_0 ($r/r_0 = 1.001$, 1.05, 1.2, 1.5, 2.0, 4.0, 8.0, and ∞. (Isenberg, 1987.)

(Vasyliunas and Siscoe, 1976). Plots of $f(r, v)$ using (40) for different values of λ/r are illustrated in Figure 3.8(a) and they show that, with increasing heliocentric distance, the velocity distribution becomes increasingly flat-topped. In Figure 3.8(b), a phase-space plot (in the spacecraft frame) of pickup ions observed by *Ulysses* is shown (Gloeckler et al., 1993). The sharp cutoff at $v/u = 2$ is clearly evident.

The sharp cutoff in the pickup ion distribution (in the solar wind rest frame) indicates that adiabatic cooling dominates energy diffusion. Nonetheless, Isenberg (1987) has generalized the Vasyliunas and Siscoe (1976) solution (40) by retaining the energy diffusion term D in (38). The energy diffusion coefficient is derived from the quasi-linear theory of resonant wave-particle interactions. Subject to the assumptions that (i) the wave field is unpolarized; (ii) has zero cross-helicity; (iii) the turbulence spectrum has a power law form ($k^{-\gamma}$, k the wave number); (iv) the wave power decays with heliocentric distance as r^{-3} (i.e., WKB theory), and finally, (v) the IMF is purely azimuthal, the energy diffusion term in (38) may be expressed as (Isenberg, 1987)

$$D = Cv^{\gamma-1}r^{-1} \; . \tag{41}$$

The constant C is a function of γ, the index of the assumed wave spectrum. Remarkably, Isenberg was able to solve (38) with (41) analytically (although we do not reproduce the somewhat cumbersome expression here). Normalized pickup ion distributions are plotted as a function of v/u for different radial distances in Figure 3.9. These distributions are plotted in the solar wind frame. Initially, ($r \sim 1$ AU) the distribution remains close to the shell distribution (i.e., a delta function at $v/u = 1$). With the adiabatic cooling of the pickup ions with increasing heliocentric distance, the characteristic 'flat' distribution at energies lower than

$v/u = 1$ develops. A sharp transition to higher energies results from the energy diffusion term in (38) and the slope and maximum energy are determined by the assumed wave intensity. The sharpness of the transition is, of course, a consequence of the continual addition of new pickup ions at $v/u = 1$.

Most recently, Chalov et al. (1995, 1997) integrated both a spherically symmetric 1D and a 2D form of the pickup ion transport equation (38), but now using a neutral density source term obtained from 2D simulations of the solar wind – LISM interaction (Section 5). In only this sense does the Chalov et al. (1995) calculation differ from that of Isenberg (1987), although very different methodologies were used. Both papers arrive at the same basic conclusions.

Chalov et al. (1997) considers the 2D form of (38), retaining many of the same basic assumptions found in Chalov et al. (1995). However, the diffusion coefficient D for Alfvénic fluctuations is now modified to include a correlation length ℓ which increases as r (see Section 3.3). The novel feature of Chalov et al. (1997) is the attempt to include pickup ion energization by their interaction with multiple shocks. A diffusion theory can be derived for ion transport in a plasma populated by multiple weak shocks (supersonic turbulence) (Toptygin, 1983), and the energy gain or loss for an ion is essentially adiabatic at a weak shock or rarefaction. Energization of pickup ions in supersonic turbulence is therefore a second-order Fermi process and requires that a particle experience more compressive than rarefactive weak shock interactions. The diffusion term for large-scale supersonic or weak shock turbulence is given by

$$D_{sh} = \frac{\langle \delta u^2 \rangle^{1/2} v^2}{9 \ell_{sh}} \, , \tag{42}$$

provided that the pickup ion scattering mean free path is much less than the large-scale supersonic turbulence correlation length ℓ_{sh}. Here $\langle \delta u^2 \rangle^{1/2}$ is the large-scale correlation average of velocity fluctuations δu. It is assumed that $\langle \delta u^2 \rangle^{1/2} = u_0 \, (r/r_0)^{-0.7}$ (u_0 the solar wind speed at 1 AU) and that $\ell_{sh} = 1.5$ AU for $r < 8$ AU and 3 AU elsewhere. The D in (38) is taken to be the sum of (41) and (42).

The inclusion of D_{sh} leads both to a flattening of the pickup ion spectra compared to the results presented by Isenberg (1987) and Chalov et al. (1995), as well as maximum pickup ion energies of several 100 keV nucl^{-1}, this an order of magnitude higher than expected in the absence of supersonic turbulence. The maximum pickup ion energies appear to depend sensitively on the assumed value of $\langle \delta u^2 \rangle^{1/2}$ and the assumption that $\langle \delta u^2 \rangle_0^{1/2} = u_0$ seems somewhat large. This needs to be clarified. Nonetheless, the inclusion of ion energization by multiple weak shock waves in the outer heliosphere yields interesting results for the pre-energization of anomalous cosmic-rays which deserve further study.

In concluding this subsection, we mention a curious observation reported by Gloeckler et al. (1994) which awaits adequate explanation. Since interstellar hydrogen is ionized primarily by charge exchange with solar wind protons, a strong correlation between the pickup ion flux and the solar wind proton flux was antici-

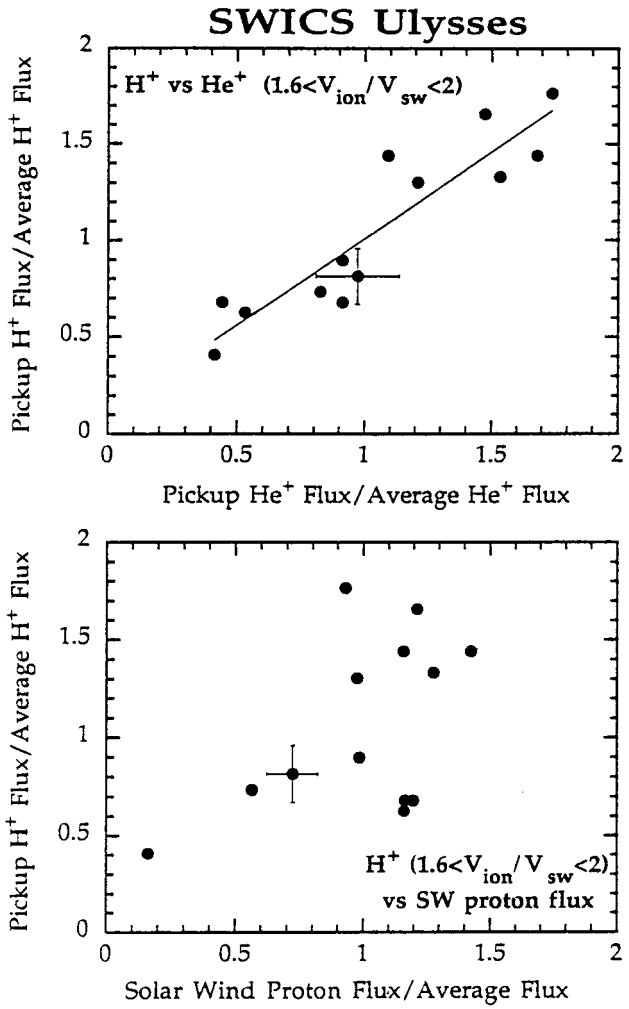

Figure 3.10. Ulysses observations showing the good correlation between the fluxes of pickup protons and He^+ (*upper panel*) and the poor correlation between pickup proton flux and the solar wind flux (*lower panel*). (Gloeckler et al., 1994.)

pated. As illustrated in Figure 3.10(b), however, this correlation is very poor. Oddly enough, the flux of pickup Helium (He^+), which is primarily photoionized, is well correlated with the flux of pickup protons (Figure 3.10). Isenberg and Lee (1995) have considered the time-dependent photoionization of pickup He^+, but the pickup proton data await elucidation.

3.5. QUASI-LINEAR MODELS.

The evolution of the pickup ion generated waves/turbulence and the pickup ions themselves have so far been treated independently. This is, of course, certainly

incorrect and one needs to couple the evolution of both waves, turbulence and pickup ions self-consistently. Such an approach was initiated in the seminal paper of Lee and Ip (1987) (see also Sagdeev et al., 1986; Galeev et al., 1987, 1991; Galeev and Sagdeev, 1988 and Lee, 1989). This work was primarily analytical and numerical models have since been discussed (Gary et al., 1988, 1989; Winske et al., 1985; Galeev et al., 1987; Gaffey et al., 1988). As with plasma instabilities driven by pickup ions, this work too was developed primarily in the context of cometary pickup ions.

The quasi-linear equations that describe the time evolution of a spatially homogeneous, gyrotropic phase space distribution of non-relativistic pickup protons in the presence of Alfvén waves propagating parallel and anti-parallel to the IMF $B\hat{\mathbf{z}}$ are (Lee, 1971; Lee and Ip, 1987)

$$\frac{\partial f}{\partial t} = \frac{\pi}{2}\left(\frac{e}{m}\right)^2 \frac{1}{v_\perp}\int_{-\infty}^{\infty} \mathrm{d}k_z \sum_{n=\pm}\left(\frac{\omega_n}{ck_z}\right)^2 \left[\frac{\partial}{\partial v_z} + \frac{k_z}{\omega_n}\left(v_\perp \frac{\partial}{\partial v_z} - v_z \frac{\partial}{\partial v_\perp}\right)\right] \times$$

$$\times \left[v_\perp \delta\left(\omega_n - v_z k_z + \Omega_i\right)\right] I_n(k_z) \left[\frac{\partial f}{\partial v_z} + \frac{k_z}{\omega_n}\left(v_\perp \frac{\partial f}{\partial v_z} - v_z \frac{\partial f}{\partial v_\perp}\right)\right], \tag{43}$$

$$\frac{\partial I_\pm}{\partial t} = 2\gamma_\pm I_\pm \,. \tag{44}$$

The wave growth rate $\gamma_\pm$ is given by (27). The wave intensities $I_\pm$ have been normalized so that $\langle \delta B^2 \rangle = \sum_{n=\pm} \int_{-\infty}^{\infty} I_n \, \mathrm{d}k_z$.

Equation (43) can be expressed in terms of the spherical velocity co-ordinates $v^2 = v_z^2 + v_\perp^2$ and $\mu = v_z/v$, and it is evident that (43) contains the effects of both scattering in pitch-angle ($\arccos(\mu)$) and diffusion in energy space. In the context of quasi-linear theory, the relevant time scale for pitch-angle scattering is $\tau_\mu \simeq |\Omega_i|^{-1} B^2/\delta B^2_{\mathrm{res}}$, where $\delta B^2_{\mathrm{res}}$ denotes the power in the magnetic field fluctuations over the cyclotron resonant range i.e., for $|k_z| \geq |\Omega_i|/u$ (on assuming that $v_z \sim u$). By approximating $k_z \sim \ell^{-1}$, ℓ the correlation length, and assuming $\delta B^2_{\mathrm{res}}/B^2 \sim 1$, one obtains $\tau_\mu \sim \ell/u$. Stochastic energization of pickup ions is due to pitch-angle scattering off Alfvén waves propagating in opposite directions so that the time scale for diffusion in energy space is $\tau_v \sim u^2/V_A^2 \cdot \tau_\mu$. Thus, since $V_{\mathrm{A}} \ll u$, pitch-angle diffusion dominates initially. Accordingly, Lee and Ip (1987) neglects all energy diffusion terms in (43) to obtain the reduced equations

$$\frac{\partial f}{\partial t} = \frac{\partial}{\partial \mu}\left[D_{\mu\mu}\frac{\partial f}{\partial \mu}\right] \,, \tag{45}$$

$$\frac{\partial I_\pm}{\partial t} = \pm \bar{\gamma} I_\pm \,, \tag{46}$$

$$D_{\mu\mu}(\mu \,, v, t) \equiv \frac{\pi}{2}\left(\frac{e}{mc}\right)^2 \frac{1-\mu^2}{v|\mu|} \sum_{n=\pm} I_n(k_r \,, t) \,,$$

$$\bar{\gamma}(k_z, t) \equiv \frac{4\pi V_A e^2}{mc^2|k|} \int_0^\infty \mathrm{d}v v^2 \int_{-1}^{1} \mathrm{d}\mu \left(1-\mu^2\right) \delta\left(\mu - \Omega_i/vk_z\right) \frac{\partial f}{\partial \mu} ,$$

where $k_r \equiv \Omega_i/\mu v$ is the resonant wave number for a proton of velocity v, pitch-angle $\arccos \mu$, and gyrofrequency Ω_i. Furthermore, $|\mu v| \gg |V_A|$ is assumed. For reasons of simplicity and tractability, the divergent behaviour at $\mu \simeq 0$ is neglected and it is assumed that the exceptional region in phase space $\mu \sim V_A/v$ neither blocks transport in pitch-angle nor invalidates the above quasi-linear model. Very low frequencies ω in the cyclotron-resonance condition are also neglected by comparison with $\mu v k_z$.

Lee and Ip (1987) assumes for simplicity the distribution $f = \delta(v-v_0)F(\mu, t)$. Equations (45) and (46) can then be integrated analytically and yield the time asymptotic wave spectrum as

$$2I_\pm(k_z, \infty) = \pm C(k_z) + \left\{\left[C(k_z)\right]^2 + 4I_+(k_z, 0) I_-(k_z, 0)\right\}^{1/2} , \tag{47}$$

where

$$\begin{aligned} C(k_z) &\equiv I_+(k_z, 0) - I_-(k_z, 0) + 2\pi n V_A m |\Omega_i| k_z^{-2} \left[\frac{\Omega_i}{v_0 k_z} - \frac{\Omega_i/v_0 k_z - \mu_0}{|\Omega_i/v_0 k_z - \mu_0|}\right] \\ &= I_+(k_z, \infty) - I_-(k_z, \infty) . \end{aligned} \tag{48}$$

For representative nominal solar wind and neutral parameters at 7.5 AU, the time asymptotic modification to the Alfvén wave spectrum (47) due to the isotropization of an initial pickup ion ring-beam distribution is illustrated in Figure 3.11. The characteristic enhancement discussed in Section 3.2 is again evident.

Thus far, the effect of continual pickup of interstellar protons in an expanding solar wind has been neglected. Since the change in pickup ion number density with radial distance is $\mathrm{d}n_{\mathrm{PI}} = n_{\mathrm{H}}(r, \theta)(r/r_0)^2/(\tau_{\mathrm{ion}}^0 u)\, \mathrm{d}r$, the expansion of (47) and (48) for small n_{PI} yields

$$\begin{aligned} \frac{\mathrm{d}I_\pm}{\mathrm{d}r} &= \pm \frac{I_\pm}{I_+ + I_-} \frac{\beta(r)}{r^3} - 3\frac{I_\pm}{r} , \\ \beta(r) &= 2\pi V_A m \frac{|\Omega_i|}{k_z^2} \frac{r_0^2}{\tau_{\mathrm{ion}}^0} \frac{r}{u} n(r, \theta) \left[\frac{\Omega_i}{v_0 k_z} - \frac{\Omega_i/v_0 k_z - \mu_0}{|\Omega_i/v_0 k_z - \mu_0|}\right] . \end{aligned} \tag{49}$$

The presence of the term proportional to r^{-1} in (49) reflects the assumption that $I_\pm$ evolves with radial distance according to a WKB decay law r^{-3}, as discussed in Section 3.3, and this may not be completely warranted in the outer heliosphere. Nonetheless, (49) can be integrated exactly (Lee and Ip, 1987) and, rather than writing out the full somewhat lengthy result, we present plots of the predicted solar wind wave spectra at 4.5 and 7.5 AU in Figure 3.12.

Bogdan et al. (1991) have considered the evolution of the pickup ion and associated wave spectrum for time scales long compared to the pitch-angle scattering/isotropization time scale τ_μ. On such long time scales, the largest terms

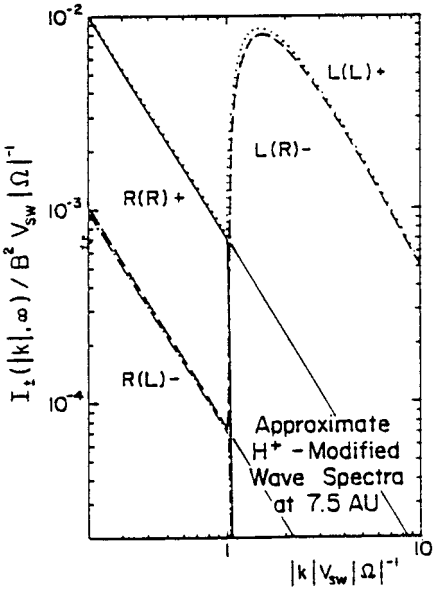

Figure 3.11. Approximate H^+-modified solar wind wave spectra at 7.5 AU plotted as a function of normalized wave number for representative parameters. Branches are labeled by solar wind polarization (R(L) denoted right(left) polarized) and propagation direction with the + sign signifying outward propagation. The solid lines correspond to the unmodified wave spectra. (Lee and Ip, 1987.)

(proportional to V_A/v) in (43) vanish, and one can show then that pitch-angle and velocity diffusion are related by (Skilling, 1975; Schlickeiser, 1989; Bogdan et al., 1991)

$$\frac{\partial f}{\partial \mu} = -V_A \frac{I_+(k_r,t) - I_-(k_r,t)}{I_+(k_r,t) + I_-(k_r,t)} \frac{\partial f}{\partial v} \,. \tag{50}$$

This relation expresses formally the result that pitch-angle scattering proceeds until the ions are isotropic in the average wave frame that propagates with velocity $\mathbf{V}_w = \mathbf{V}_A \cdot (I_+ - I_-)/(I_+ + I_-)\hat{\mathbf{z}}$. The use of (50) in (44) and (44) then eliminates the pitch-angle scattering terms and yields a diffusion equation in velocity space for the μ-averaged distribution $F(v,t) \equiv \frac{1}{2}\int_{-1}^{1} f(\mu\ ,v,t)\ \mathrm{d}\mu$,

$$\frac{\partial F}{\partial t} = \frac{1}{v^2}\frac{\partial}{\partial v}\left[v^2 D_{vv}\frac{\partial F}{\partial v}\right] + \dot{Q}_{\mathrm{PI}}(v,t)\ , \tag{51}$$

$$\frac{\partial I_\pm}{\partial t} = -\hat{\gamma}\frac{I_+ I_-}{I_+ + I_-} \pm \dot{Q}_w \frac{I_\pm}{I_+ + I_-}\ , \tag{52}$$

$$D_{vv}(v,t) \equiv \pi\left(\frac{eV_A}{mc}\right)^2 \int_{-1}^{1} \mathrm{d}\mu \frac{1-\mu^2}{v|\mu|}\frac{I_+(k_r,t)I_-(k_r,t)}{I_+(k_r,t)+I_-(k_r,t)}\ ,$$

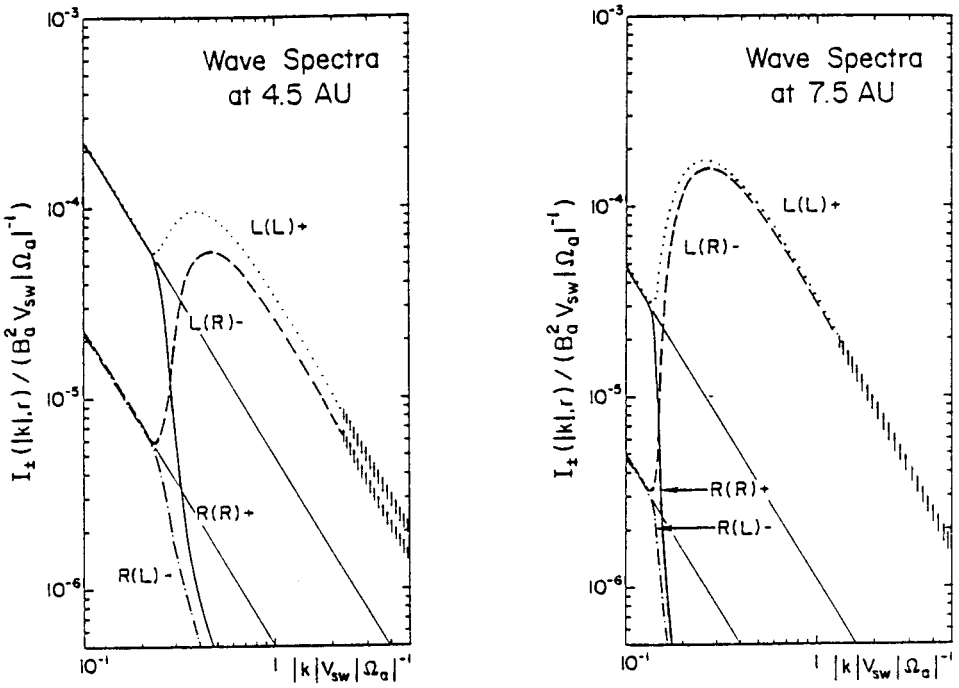

Figure 3.12. Predicted solar wind wave spectra at (a) 4.5 AU and (b) 7.5 AU assuming a WKB evolution of the total power and modification due to continual pickup of interstellar protons. (Lee and Ip, 1987.)

$$\hat{\gamma}(k_z, t) = \frac{16\pi^3 V_A^2 e^2}{mc^2|k_z|} \int_{\Omega_i/|k_z|}^{\infty} vF(v, t)\, \mathrm{d}v \ .$$

In (51) and (52), $\dot{Q}_{\mathrm{PI}}$ and $\dot{Q}_w$ denote proton and wave source terms that are introduced by the continual injection of pickup ions and their associated waves. These source terms must be chosen in such a way as to match the short time (τ_μ) evolution of both the pickup ion distribution and the waves (Bogdan et al., 1991).

By using representative parameters for pickup ions at 10 AU, Bogdan et al. (1991) solve (51) and (52) numerically. Their interstellar pickup hydrogen results are depicted in Figures 3.13 and 3.14. The time evolution of the pickup ion distribution is illustrated in Figure 3.13 and, like the results presented by Isenberg (1987), some fraction of the shell pickup ion distribution experience stochastic acceleration. As is illustrated in Figure 3.14, the large rate of hydrogen pickup ensures that the growth of waves propagating in one direction is substantial, but considerable damping occurs for oppositely propagating modes. Thus, although the wave energy density grows with time, little energy is available for the stochastic acceleration of pickup ions (which would require ideally as many inward as outward propagating waves). This led Bogdan et al. (1991) to conclude that the

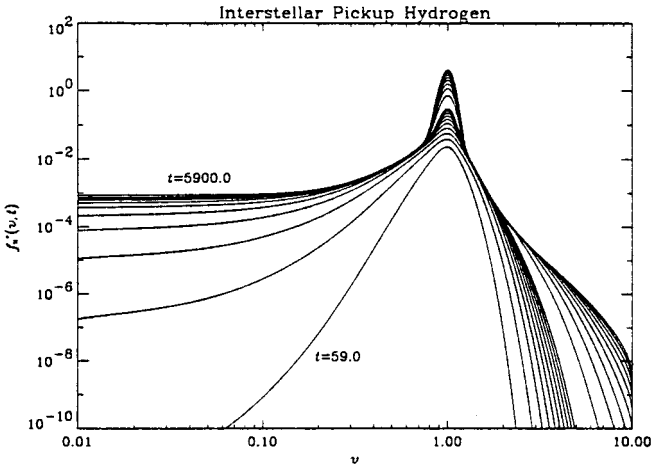

Figure 3.13. The normalized pickup hydrogen phase space distribution function as a function of $v/u_{\rm SW}$ at equally spaced times (in units of $u_{\rm SW}^2/\pi|\Omega_i|V_{\rm A}^2 = 682$ s) between 59 and 590 and 590 and 5900. (Bogdan et al., 1991.)

simpler linear analysis of Isenberg (1987) may not be appropriate since strong wave damping must eliminate one of the wave modes. This conclusion should however be interpreted cautiously since all mode couplings and nonlinear spectral transfer effects are neglected entirely in the treatment of Bogdan et al. (1991). The rate at which spectral transfer replenishes the damped Alfvén modes will presumably control the rate of stochastic energization of the pickup ions. Finally, we note that even at 10 AU, the observed cross-helicity is very low (< 0.5) in the ecliptic, indicating that forward and backward modes are almost equal in number.

3.6. DISSIPATION OF PICKUP ION DRIVEN WAVES

If pickup ions were assumed to be assimilated into the solar wind as a result of wave-particle interactions, then a substantial increase in the thermal temperature of the solar wind protons would be expected. Such a strong increase in temperature with increasing heliocentric distance is not observed, with the implication that the solar wind and pickup protons represent two distinct proton populations. In essence, the solar wind protons form a relatively cold "core" about which is superimposed a dilute halo of energetic pickup ions. Measurements of the solar wind protons which only evaluate the thermal spread of the core cannot therefore determine the effects of heating by pickup ions unless an intermediary effects the transfer of pickup ion energy to the solar wind core protons.

Fahr and Ziemkiewicz (1988) have suggested that energy diffusion associated with pickup ions should lead to strong heating of the solar wind. However, since only a very small fraction of the pickup ion excited waves are resonant with the solar wind protons, it appears difficult to heat the wind on this basis.

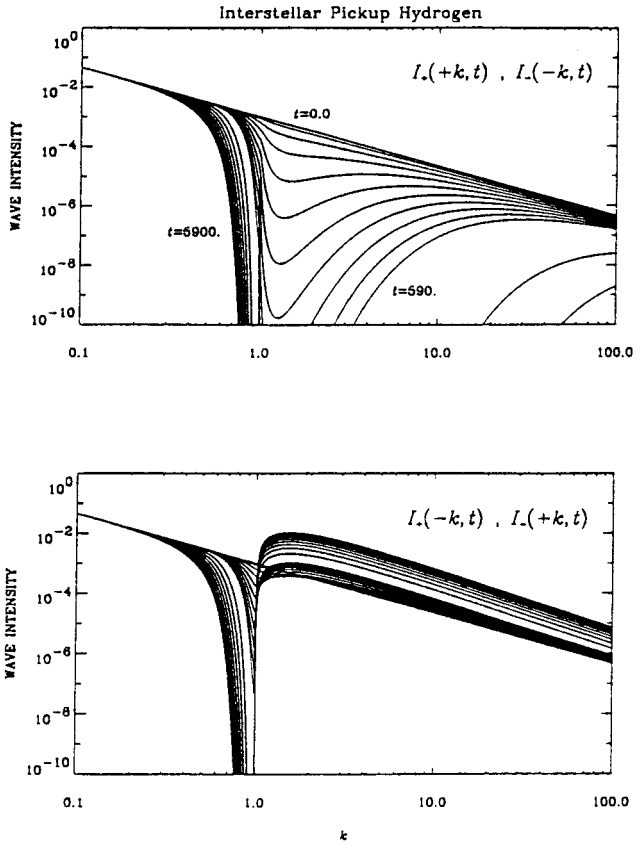

Figure 3.14. Normalized hydromagnetic wave intensities as a function of $k_z/(|\Omega_i|/u_{\mathrm{SW}})$ at equally spaced times between 0 and 590 and between 590 and 5900. Each panel corresponds to a different helicity; if $B > 0$, then the upper panel describes waves with right-handed helicity. (Bogdan et al., 1991.)

The possibility that a nonlinear turbulent cascade of magnetic fluctuation energy may lead to the heating of the core thermal solar wind proton distribution has been suggested by several authors (Isenberg, 1986; Fisk and Goldstein, 1974 (unpublished manuscript)) and was elaborated upon by Williams et al. (1995). The steady-state radial evolution of the solar wind temperature T is

$$\frac{\mathrm{d}}{\mathrm{d}r}(\kappa T) + \frac{4}{3}\frac{\kappa T}{r} = \frac{2}{3}\frac{\dot{Q}}{u n_{\mathrm{SW}}} , \tag{53}$$

where $\dot{Q}$ denotes a temperature source term and κ is Boltzmann's constant. Williams et al. (1995) assumes that the source term may be decomposed as $\dot{Q} = \dot{Q}_{\mathrm{PI}} + \dot{Q}_{\mathrm{other}}$, where $\dot{Q}_{\mathrm{PI}}$ is the heating rate associated with the local dissipation of pickup ion generated MHD waves. All other heating sources (shocks, stream shear) are included in $\dot{Q}_{\mathrm{other}}$. As discussed in Section 3.2, the waves excited by the ring-beam

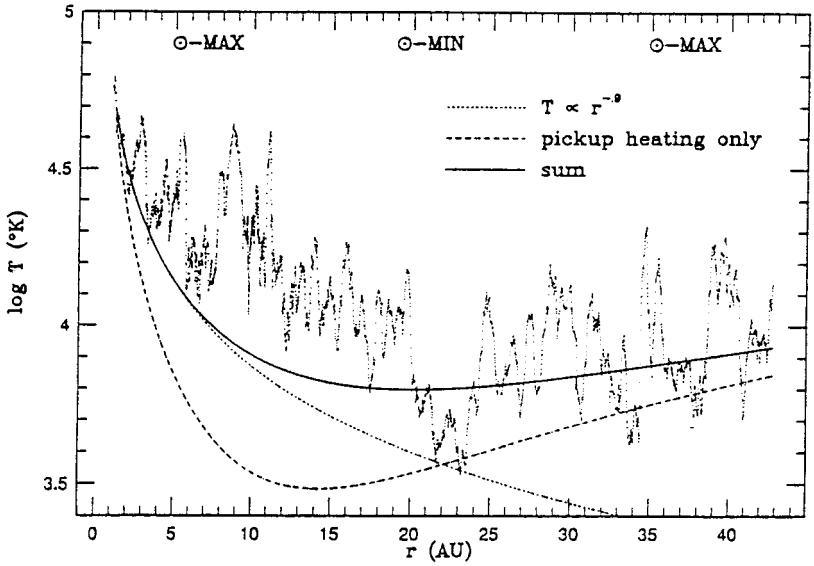

Figure 3.15. The Voyager 2 radial temperature profile (50-day averages) interpreted as the sum of two effects: power law temperature dependence in the inner heliosphere and pickup associated heating in the outer heliosphere. (Williams et al., 1995.)

pickup ion distribution contain a fraction V_A/u of the energy present in the ring distribution. For a perpendicular IMF geometry, the asymptotic wave energy is $E_w^\infty \sim mn_{PI}V_A u$ (Section 3.2) and so

$$\dot{Q}_{PI} \simeq \varepsilon m V_A u \frac{N_H}{\tau_{ion}} , \tag{54}$$

(Williams et al., 1995) and the parameter $\varepsilon < 1$. Here, ε represents the fraction of available wave energy that is dissipated in the thermal solar wind proton core and enters as a parameter.

Williams et al. (1995) makes a crude estimate of the importance of $\dot{Q}_{PI}$ relative to $\dot{Q}_{other}$ in the outer heliosphere but an adequate treatment can be achieved only on the basis of the turbulence models described in Section 3.2. This unfortunately has yet to be completed. Nonetheless, Williams et al. (1995) estimates that pickup ion driven dissipation should dominate beyond ∼10 AU, which is in accord with the correlation length plots for $\ell(r)$ (Figure 3.6) when pickup ion driving is included in the turbulence models.

The solution of (53) with (54) is simply

$$\frac{T(r,\theta)}{T(r_0)} = \left(\frac{r_0}{r}\right)^{4/3} \left[1 + \int_{r_0}^{r} \left(\frac{r}{r_0}\right)^{4/3} \{\dot{Q}_{PI} + \dot{Q}_{other}\} \frac{(2/3)\ \mathrm{d}r}{u n_{SW} \kappa T(r_0)} \right] . \tag{55}$$

For the purposes of illustration, the contribution to (55) from the term $\dot{Q}_{other}$ is taken to be $T \propto r^{-\alpha}$, where $\alpha < \frac{4}{3}$. Figure 3.15 displays three theoretical profiles

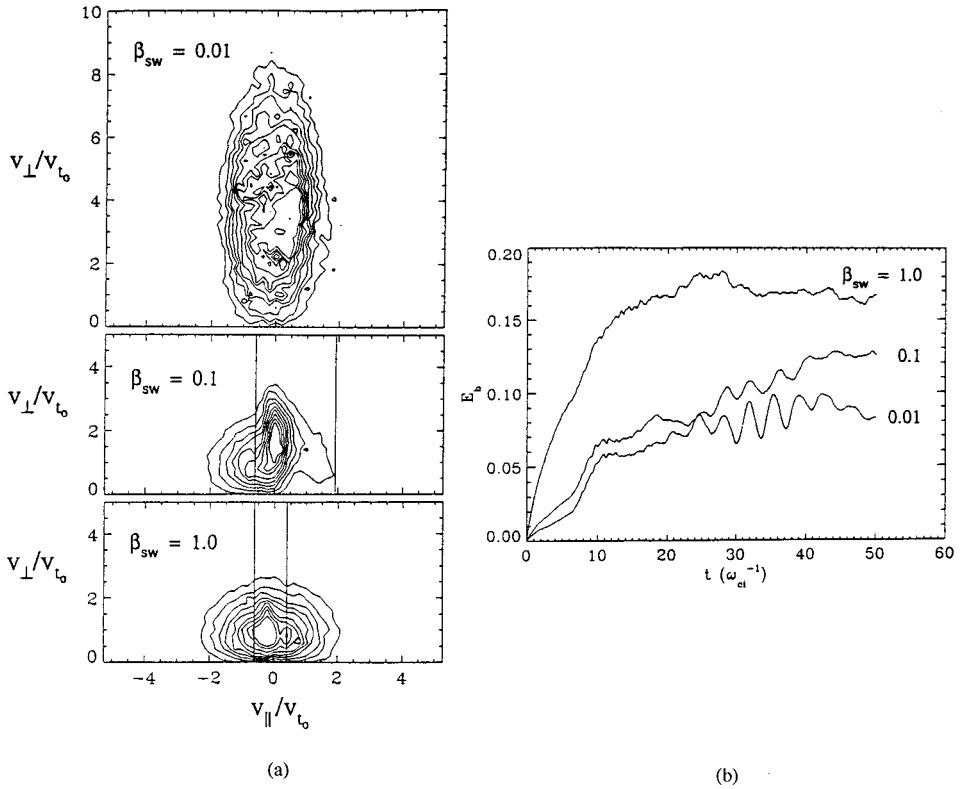

Figure 3.16. (a) Contours of the background distribution function $v_\perp f(v_\perp, v_\parallel)$ at the conclusion of the Gray et al. (1996) simulations. Approximate trapping widths about the resonant velocity are indicated by vertical lines in the bottom and middle frames. The corresponding lines for the $\beta_{SW} = 0.01$ are off the scale. (b) Evolution of the wave energy $(\delta B/B_0)^2$ for different initial choices of β_{SW}. (Gray et al., 1996.)

superimposed on Voyager 2 data (Richardson et al., 1994; Williams et al., 1995). The three theoretical temperature curves are (1) a power law $\propto r^{-0.9}$ that passes through the minimum when $\dot{Q}_{PI} = 0$, (2) the pickup ion driven solution ($\dot{Q}_{other} = 0$) which gives an adiabatic profile initially (see also a related figure in Fahr and Ziemkiewicz, 1988), and (3) a sum of profiles (1) and (2).

The theoretical profiles depicted in Figure 3.15 are, of course, steady-state solutions whereas the Voyager 2 data are a complicated function of time and distance. The important point made by this simple model is that the temperature profile can be attributed to an adiabatic expansion with possibly independent heat sources in both the inner and outer heliosphere. The current practice of fitting solar wind radial temperature profiles with a single power law may not be physically meaningful. More detailed self-consistent calculations are needed and are the subject of ongoing work.

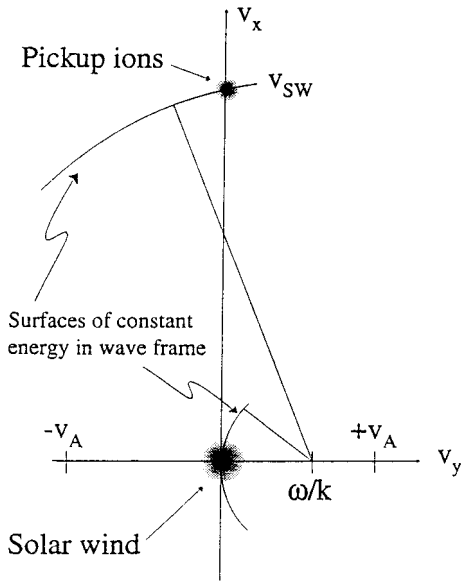

Figure 3.17. Velocity space schematic of pickup ions and background plasma in the rest frame of the solar wind. Pickup ions and solar wind particles are scattered by AIC modes along surfaces of constant energy in the wave frame. (Gray et al., 1996.)

On the basis of recent hybrid simulations, Gray et al. (1996) made the important point that an Alfvén ion cyclotron (AIC) instability generated by a pickup ion ring beam had modes with resonant velocities $v_{\rm res} \equiv (\omega - \Omega_i)/k_z$ close to the thermal speed of the solar wind. Thus, unlike the treatment by Williams et al. (1995) in which pickup ion generated wave energy is assumed to cascade to smaller scales where it then dissipates into the solar wind protons, the growing AIC mode can couple directly to the solar wind proton distribution. By means of a 2 $\frac{1}{2}$D hybrid simulation in which the initial pickup ion distribution is a cold ring beam ($\propto \delta(v_\perp - u\ \sin\theta)\delta(v_z - u\ \cos\theta)$, θ the angle between the solar wind velocity and the IMF), Gray et al. (1996) found that the growing AIC mode is damped by cyclotron resonance with solar wind protons and this leads to the perpendicular heating of the background solar wind. Shown in Figure 3.16(a) is the background solar wind distribution at the end of three simulations, each of which used a different initial solar wind plasma beta $\beta_{\rm SW}$ (i.e., excluding pickup ions). As $\beta_{\rm SW}$ decreases, the perpendicular to parallel temperature ratio $T_\perp/T_\parallel$ for the background solar wind increases markedly.

For particle motion in a circularly polarized wave, the trapping width may be estimated as (Lutomirski and Sudan, 1966)

$$v_{\rm trap} \simeq \sqrt{(\delta B/B_0)\Omega_i v_\perp/k_z}\ , \tag{56}$$

where δB is the amplitude of the wave magnetic field. In Figure 3.16(b), the temporal evolution of wave energy $\delta B^2/B_0^2$ for the three different $\beta_{\rm SW}$ values is

illustrated, showing the saturation levels. Since the AIC mode has essentially the single frequency $\omega \sim 0.7\Omega_1$ and $k_z \sim 1.5\Omega_i / V_A$, these can be used to estimate the trapping width. The trapping widths are plotted over the background solar wind distribution function in Figure 3.16(a) (the vertical lines in the plots for $\beta = 0.1$, 1.0). Particles within a trapping width of the resonant velocity will couple to the wave and scatter along constant energy surfaces in the wave frame. Figure 3.17 shows that the tangent to this surface for the background distribution is predominantly perpendicular to $\mathbf{B}_0$, and hence heating occurs preferentially in that direction too. Of course, as was discussed above, the assumption of a sharp initial ring-beam distribution is not entirely reasonable and an important extension to the work of Gray et al. (1996) would be to consider a more diffuse pickup ion source.

4. Mediation of the Solar Wind by Pickup Ions

Although number densities are too low for the direct interaction of the solar wind plasma flow with the neutral flux, appreciable momentum and energy exchange is possible nonetheless through charge exchange of solar wind protons and neutral hydrogen. As discussed in detail already, in a plasma possessing a sufficiently strong magnetic field, a newly charged particle acquires a gyrospeed equal to its initial velocity relative to the plasma and convects with the plasma flow within a gyroperiod. Although the microscopic details of this process are complicated and depend on the plasma-magnetic field configuration, the net result of ion pickup on hydrodynamic scales is qualitatively unique – there is a change in the density, momentum, and energy of the plasma flow for each act of charged particle production or destruction. The basic solar wind models which incorporated pickup ions at some self-consistent level were formulated in the seminal and far-reaching papers of Wallis (1971) and Holzer (1972), building on earlier work by Axford et al. (1963); Patterson et al. (1963); Dessler (1967); Hundhausen (1968); Fahr (1968); Blum and Fahr (1970); Semar (1970), and Holzer and Axford (1970).

In this section, we consider the mediation of the supersonic solar wind by neutral interstellar hydrogen and defer to Section 5 the global interaction of the solar wind with the LISM.

4.1. One-fluid model of the solar wind

In formulating a simple model to describe the interaction of the supersonic solar wind with interstellar neutral H, we shall follow the derivation of Khabibrakhmanov et al. (1996) who formalized the models of Wallis (1971) and Holzer (1972). This approach provides a more formal justification of the transport equation used in Section 3.4. The protons are assumed to satisfy the guiding center kinetic equation for the distribution function $f(\mathbf{x}, \mu, v_\parallel, t)$ (e.g., Kulsrud, 1983)

$$\frac{\partial f}{\partial t} + \nabla \cdot \left[\left(\mathbf{U} + v_{\parallel} \mathbf{b} \right) f \right] +$$

$$+ \frac{\partial}{\partial v_{\parallel}} \left[\mathbf{b} \cdot \nabla \left(-\frac{q_i \phi}{m_e} - \mu B + \frac{U^2}{2} \right) - v_{\parallel} \mathbf{b} \cdot \nabla \mathbf{U} \cdot \mathbf{b} \right] f = \mathcal{C}(f) \, , \tag{57}$$

where $\mu \equiv v_{\perp}^2 / 2B$ is the ion magnetic moment; $v_{\parallel}$ and $v_{\perp}$ the ion velocities parallel and perpendicular to the direction of the local magnetic field $\mathbf{B}$; $\mathbf{b} \equiv \mathbf{B}/B$ a unit vector; $\mathbf{U} = c(\mathbf{E} \times \mathbf{B})/B^2$ the solar wind drift velocity; ϕ the potential of the electric field $\mathbf{E}$ along the magnetic field lines (i.e., $\mathbf{b} \cdot \nabla \phi + \mathbf{b} \cdot \mathbf{E} = 0$); and q_i is the particle charge. The left-hand side of Equation (57) describes the particle response to the large-scale magnetic field and therefore conserves magnetic moment. All other interactions are contained in a 'collision' term $\mathcal{C}(f)$, these being Coulomb collisions, wave-particle interactions or terms describing the creation and loss of particles. The source and sink terms are proportional to the rate $\nu[F(\mathbf{v}), f(\mathbf{v})]$ of production or loss of particles with a given velocity $\mathbf{v}$, and this is, in general, a complicated functional of the distribution functions of both plasma particles $f(\mathbf{v})$ and neutral particles $F(\mathbf{v})$.

For photoionization, one has the relatively simple source term

$$\nu_{ph}(r) F(\mathbf{v}) \, , \tag{58}$$

where the rate of photoionization ν_{ph} is defined completely by the solar UV flux and is consequently $\propto r^{-2}$, assuming no appreciable extinction of photon flux.

For charge exchange, a proton with velocity $\mathbf{v}'$ and hydrogen atom with velocity $\mathbf{v}$ yields a hydrogen atom with velocity $\mathbf{v}'$ and a proton with velocity $\mathbf{v}$. The probability of this reaction occurring is determined by the charge exchange cross-section $\sigma_c \left(\left| \mathbf{v} - \mathbf{v}' \right| \right)$. The 'collision' term for charge exchange has the general form (Holzer and Banks, 1969)

$$\int |\mathbf{v} - \mathbf{v}'| \sigma_c \left(\left| \mathbf{v} - \mathbf{v}' \right| \right) \left[F(\mathbf{v}) f(\mathbf{v}') - F(\mathbf{v}') f(\mathbf{v}) \right] \, \mathrm{d}^3 \mathbf{v}' \, , \tag{59}$$

but a simpler form for production which admits an analytic treatment is (Holzer, 1972; Khabibrakhmanov et al., 1996)

$$F(\mathbf{v}) \int |\mathbf{v}'| \sigma_c \left(|\mathbf{v}'| \right) f(\mathbf{v}') \, \mathrm{d}^3 \mathbf{v}' = F(\mathbf{v}) \langle \sigma_c v \rangle \, . \tag{60}$$

Such a charge exchange production term is valid only under the assumptions that (i) the neutral velocity is much smaller than the proton velocity, which is certainly true in the supersonic solar wind but not necessarily in the shocked solar wind regime, and (ii) that the neutral thermal spread is small. The corresponding loss term may be expressed as

$$f(\mathbf{v}) |\mathbf{v}| \sigma_c \left(|\mathbf{v}| \right) \int F(\mathbf{v}') \, \mathrm{d}^3 \mathbf{v}' = f(\mathbf{v}) \sigma_c \left(v \right) v N \, , \tag{61}$$

where N is the neutral number density. The particle velocity $\mathbf{v}$ in the laboratory frame is related to the guiding center variables $(v_\perp, v_\parallel, \phi)$ by $v_\parallel = \mathbf{v}\cdot\mathbf{b}$ and $v_\perp = |(\mathbf{v}-\mathbf{U}\times\mathbf{b}|$, so allowing the source and sink terms in (57) to be expressed in terms of guiding center variables only. The gyrophase average can then be performed explicitly.

On introducing the variables

$$\mathbf{u} = \mathbf{U} + \mathbf{b}U_\parallel, \qquad U_\parallel = \int v_\parallel f(\mathbf{v})\, \mathrm{d}^3\mathbf{v} / \int f(\mathbf{v})\, \mathrm{d}^3\mathbf{v}\,,$$

one can take moments of (57) to obtain the continuity and momentum equations as

$$\frac{\partial\rho}{\partial t} + \nabla\cdot\mathbf{u}\rho = \nu_{ph} m N\,, \tag{62}$$

$$\frac{\partial\mathbf{u}}{\partial t} + \mathbf{u}\cdot\nabla\mathbf{u} + \nabla P = -\nu_{ph} m N \frac{\mathbf{u}}{\rho} - \langle\sigma_c v\rangle N\mathbf{u}\,. \tag{63}$$

As we show below, the magnetic field can be neglected to leading order in the outer heliosphere since the magnetic pressure is small compared to that of the total thermal pressure P (when the pickup ion contribution is included) and the solar wind ram pressure. However, the geometry of the pickup ion interaction and its physical properties are determined primarily by the angle between the magnetic field direction and the flow direction. If the magnetic field is orthogonal to both the solar wind and neutral flow, the newly born ions move in the plane orthogonal to $\mathbf{B}$ only and $v_\parallel = 0$. These ions have only two degrees of freedom implying that the particles behave on hydrodynamic scales as a gas with adiabatic index $\gamma = 2$. In this case, equation (57) for the distribution function takes a particularly simple form,

$$\frac{\partial f(u,\mu)}{\partial t} + \nabla\cdot\left[\mathbf{u} f(u\,,\mu)\right] = \nu_{ph} m N \delta\left(\mu - \frac{mu^2}{2B}\right) +$$

$$+\langle\sigma_c v\rangle m N\left[\delta\left(\mu - \frac{mu^2}{2B}\right) - f(u,\mu)\right]\,, \tag{64}$$

and it was assumed that the neutral particle velocity distribution is a delta function in velocity space.

Generally, however, one cannot expect the magnetic field to be orthogonal to the neutral flow and, as discussed in Section 3, bulk motion of the newly born pickup ions is possible. Such a motion is unstable to the generation of parallel propagating Alfvén waves which then scatter the pickup ions almost elastically. The rapid pitch angle scattering isotropizes the pickup ion distribution and the particles then behave as a gas with adiabatic index $\gamma = \frac{5}{3}$.

By assuming strong scattering of the pickup ion distribution, one can average (57) over θ to obtain an equation describing the isotropic part of the pickup ion distribution f (e.g., Galeev, 1991; Khabibrakhmanov et al., 1996),

$$\frac{\partial f}{\partial t} + \nabla \cdot \mathbf{u} f - \frac{1}{3v^2}\frac{\partial}{\partial v}(v^3 f \nabla \cdot \mathbf{u}) = \frac{\nu_{ph}}{v^2}\delta(u - v) -$$

$$-\sigma_c v N f + \frac{N}{v^2}\delta(u - v)\langle \sigma_c v \rangle \ , \tag{65}$$

where, for simplicity, terms involving the magnetic field have been neglected. Equation (65) is, of course, equivalent to the pickup ion transport equation (38) used by Vasyliunas and Siscoe (1976). The limiting forms (64) and (65) of the kinetic equation (57) are very different, as are the solutions for the pickup ion distribution function. However, the situation is changed considerably if, instead of solving Equations (64) and (65), we use instead the pickup ion pressure (i.e., the second moment of f). Either limiting case yields a single equation for pressure P in which the appropriate adiabatic index γ ($= 2$ or $\frac{5}{3}$) must be used. On assuming spherical symmetry, the hydrodynamic one-fluid model may therefore be expressed as (Wallis, 1971; Holzer, 1972; Khabibrakhmanov et al., 1996)

$$n_t + \frac{1}{r^2}\left(r^2 u n\right)_r = \nu_{ph} N \ , \tag{66}$$

$$\rho u_t + \rho u u_r + P_r = -\nu_{ph} m N u - \langle \sigma_c v \rangle N \rho u \ , \tag{67}$$

$$\begin{aligned} P_t + u P_r + \gamma P u_r + \frac{2}{r}\gamma u P \ &= \ (\gamma - 1)\nu_{ph} m N \frac{u^2}{2} - \\ &\quad -\langle \sigma_c v \rangle N \left[P - (\gamma - 1)\rho \frac{u^2}{2} \right] . \end{aligned} \tag{68}$$

For quasi-perpendicular geometries, $\gamma = 2$, whereas $\gamma = \frac{5}{3}$ for oblique and parallel geometries.

Equations (67) and (68) can be expressed in conservation form. If we restrict our attention to the supersonic solar wind and neglect the thermal motion of plasma particles, one can assume that the charge exchange cross section is independent of velocity and use the approximation

$$\langle \sigma_c v \rangle = \sigma_c u \ .$$

The momentum and energy equations are then

$$(\rho u)_t + \frac{1}{r^2}\left(r^2 \rho u^2\right)_r + P_r = -\sigma_c N \rho u^2 \ ,$$

$$\left(\frac{\rho u^2}{2} + \frac{1}{\gamma - 1} P\right)_t + \frac{1}{r^2}\left[r^2 u \left(\frac{\rho u^2}{2} + \frac{\gamma}{\gamma - 1} \right) \right]_r =$$

$$= -\sigma_c N u \left(\frac{1}{\gamma - 1} P + \frac{\rho u^2}{2} \right) \ .$$

It is quite straightforward to include magnetic field terms in the above equations (see, e.g., Holzer (1972) or Isenberg (1986)).

The neutral gas density should be found self-consistently. For a given neutral gas flux $N_\infty V_\infty$ at infinity, the neutral gas number density along the stagnation line can be obtained from the neutral gas continuity equation,

$$-\frac{\mathrm{d}(VN)}{\mathrm{d}r} = -\nu_{ph} N - \langle \sigma_c v \rangle N n \ . \tag{69}$$

The two continuity equations (66) and (69) can be combined as a single second-order differential equation after assuming a fixed velocity for the neutral interstellar gas V_∞, thus

$$\frac{\mathrm{d}}{\mathrm{d}r}\frac{r^2}{N}\frac{\mathrm{d}N}{\mathrm{d}r} = \frac{\sigma_c \nu_{ph} N}{V_\infty} \ , \tag{70}$$

subject to the boundary conditions

$$N(\infty) = N_\infty \ , \qquad \frac{V_\infty}{N}\frac{\mathrm{d}N}{\mathrm{d}r}(r = r_0) = \nu_{ph}^0 + \sigma_c n_0 u_0 \ , \tag{71}$$

where '0' denotes evaluation at 1 AU. The transformation

$$N/N_\infty = \exp\left[\frac{\nu_{ph}^0 + \sigma_c n_0 u_0}{r/r_0} + y(x)\right] \ , \qquad x \equiv -r_0/r \ ,$$

reduces (70) to an equation in $y(x)$ with homogeneous boundary conditions

$$x^2 \frac{\mathrm{d}^2 y}{\mathrm{d}x^2} = \frac{\sigma_c \nu_{ph}}{V_\infty} \exp\left[(\nu_{ph}^0 + \sigma_c n_0 u_0)x + y(x)\right] \ ,$$

$$y(0) = 0; \ \ y'(-1) = 0 \ . \tag{72}$$

By regarding the term $\sigma_c \nu_{ph}/V_\infty$ as a small parameter, the zeroth-order solution to (72) is the familiar result

$$N/N_\infty = \exp\left[\frac{\nu_{ph}^0 + \sigma_c n_0 u_0}{r/r_0}\right] \ ,$$

(Axford, 1972; Vasyliunas and Siscoe, 1976].

By introducing the sound speed $C_s^2 = \gamma P/\rho$ and the Mach number $M = u/c$, equations (66)–(69) can be combined as an equation for M^2 (Wallis, 1971; Holzer, 1972; Khabibrakhmanov et al., 1996)

$$\frac{M^2 - 1}{M^2}\frac{\mathrm{d}M^2}{\mathrm{d}r} = \frac{2}{r}\left[2 + (\gamma - 1)M^2\right]$$

$$+\sigma_c N \frac{\gamma + 1}{\gamma} - \frac{N}{2}\left(\sigma_c + \frac{m \nu_{ph}}{r^2 \rho u}\right)\left(\gamma M^2 + 1\right)\left[(\gamma - 1)M^2 + 2\right] \ . \tag{73}$$

TABLE II
Typical solar wind parameters

σ_c (cm^2)	5×10^{-15}
$n_0 u_0$ (cm^{-2}s^{-1})	3×10^8
N_∞ (cm^{-3})	0.1
V_∞ (km s^{-1})	20
ν^0_{ph} (s^{-1})	9×10^{-8}

Expression (73) is a little less general than that given by Holzer (1972) since magnetic and gravitational terms are neglected here but all the important points can nonetheless be made on the basis of this equation.

4.2. STEADY-STATE ONE-FLUID SOLUTIONS

A closed form solution to the wind equation (73) cannot be obtained but general properties are easily inferred and numerical solutions are straightforward to obtain. For a non-expanding flow, the wind equation shows that continuous flow through the the sonic point $M = 1$ is not possible since the right-hand side is non-zero for $M = 1$. Accordingly, a shock transition is necessary in this case. The spherical expansion of the solar wind introduces the possibility, however, of a smooth transition from a supersonic to a subsonic flow. A related extensive discussion of the deceleration of the solar wind in the vicinity of an outgassing comet also exists (e.g., Ip and Axford, 1990). The critical point at $M = 1$ (when both the left-hand side and right-hand side of (73) are zero simultaneously) is quite different from that of the familiar critical point that arises in Parker's model of the expanding and accelerating solar wind (Parker, 1958; Holzer, 1979). The sonic point near the sun is a saddle point with only one physically meaningful solution passing along a separatrix through the critical point. The topology of the steady-state solutions near the critical point admitted by (73) is more complicated.

A family of solutions to (73) can be determined numerically for the parameters listed in Table II. Initial Mach numbers of $M = 2$, 4, and 6 are assumed for the solar wind at 1 AU, and the results are plotted in Figure 4.1. As one expects from physical considerations, the Mach number profiles increase initially until the neutral hydrogen density dominates. Beyond the ionization cavity, charge exchange is sufficiently effective to both decelerate the flow and, more importantly, to increase the effective solar wind 'temperature' (by including the hot pickup ion halo). The net effect is to decrease the solar wind Mach number.

As illustrated in Figure 4.1, the radial Mach number profiles are all asymptotic to the same value as r increases. Such behaviour can be understood in terms of the nature of the critical point which exists at large heliocentric distances as the Mach number approaches 1. The critical or sonic point is an improper node with

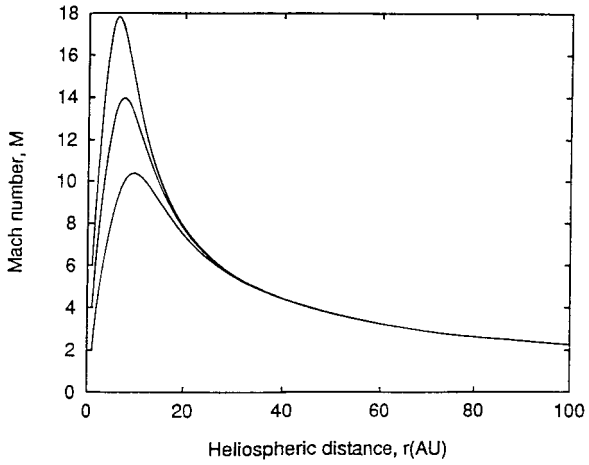

Figure 4.1. Profiles of the Mach number M for the three cases $M = 2$, 4, and 6 at $r = 1$ AU for $\gamma = 5/3$. (Khabibrakhmanov et al., 1996.)

two separatices. The physically meaningful upstream solutions all approach the critical point along the lower separatrix and the low Mach number solutions are indistinguishable from the separatrix. Following Wallis (1971), we can introduce the variable

$$\eta = \gamma \frac{M^2 - 1}{\gamma M^2 + 1} \,, \tag{74}$$

so allowing the Mach number equation (73) to be rewritten as

$$\begin{aligned} \frac{\mathrm{d}\eta}{\mathrm{d}r} \;=\; & \frac{2}{r}\frac{(\gamma^2 - \eta^2)(1-\eta)}{\gamma + 1} + \alpha N \frac{(\gamma + \eta)(1-\eta)^2}{\gamma + 1} - \\ & - \frac{N}{2}\left(\alpha + \frac{\beta}{r^2 \rho u}\right)\left(\gamma^2 - \eta^2\right) \,. \end{aligned} \tag{75}$$

The critical point occurs when the right-hand side of (75) is simultaneously zero with $\eta = 0$, i.e., $M = \pm 1$. Thus, the sonic point at $N \simeq 1$ for $r \gg 1$ is located at

$$R_s = \frac{4\gamma}{(\gamma - 1)(\gamma + 2)\alpha + (\gamma + 1)\gamma\beta/(r^2 \rho u)} \,. \tag{76}$$

When $\beta \ll \alpha$ (as is the case for the solar wind), the distance to the critical point is determined by N_∞ only and is quite independent of the initial flow conditions at 1 AU.

In the neighbourhood of the critical point, the solution for η may be expressed as (Khabibrakhmanov et al., 1996)

$$\eta^2 = a\eta(r - R_s) + b\frac{(r - R_s)^2}{2} + \cdots \,, \tag{77}$$

where

$$a = -\frac{\gamma^2}{2}\left(\alpha + \frac{\beta}{r^2\rho u}\right) - \frac{\gamma - 1}{\gamma + 1}\alpha \, ;$$

$$b = -\frac{\gamma^2(\gamma + 1)}{8}\left(\alpha + \frac{\beta}{r^2\rho u}\right)^2 + \frac{\gamma}{2}\left(\alpha + \frac{\beta}{r^2\rho u}\right)\alpha - \frac{1}{2(\gamma + 1)}\alpha^2 \, .$$

Equation (77) can be used to determine the distance to a point in the solar wind flow having a particular critical value M_c of the Mach number.

If we assume that the critical Mach number M_c of the termination shock is determined by the internal stability of the mass-, momentum-, and energy-loaded solar wind flow (Khabibrakhmanov et al., 1996), then the distance to the termination shock is determined by the interstellar neutral gas density N_∞ only. Such a criterion is quite different conceptually from from the usual manner in which the termination shock is located i.e., a balancing of the forces between the solar wind and the interstellar medium. Of course, if one simply models the solar wind as decelerating in the outer medium (e.g., Pauls and Zank, 1997) with a given radial rate, one can then balance the solar wind ram pressure against the LISM total pressure to determine the shock location. The rate at which the solar wind decelerates depends, as discussed above, on N_∞ however.

An important point not addressed by either Wallis (1971) or Holzer (1972) in their original analysis but discussed by Khabibrakhmanov et al. (1996) is that the double-valued function of (77) represents the separatrices at an improper node. Continuous flow is represented by the solution whose tangent to the function $\eta(r)$ is the same on both sides of the critical point. In principle, it is possible for the solution to 'jump' to another separatrix after crossing the the critical point. Such a flow has continuous density, velocity, and pressure but a finite jump in the first derivatives of these three parameters. Such a weak discontinuity (e.g., Landau and Lifshitz, 1987) propagates along the characteristics with a propagation speed of one of u or $u \pm C_s$. Consequently, a stationary weak discontinuity can exist only at the critical point where $u = C_s$, and the jump conditions for the derivatives are defined by the discontinuity in the tangents for the two different separatrices in (77). A weak discontinuity at the critical point may be an appropriate solution if a smooth transition behaves improperly in the subsonic region.

The introduction of a small but finite viscosity allows one to determine which of the two solution possibilities can be realized (see Owocki and Zank (1991) and Khabibrakhmanov et al. (1996)). Near the critical point $x = r - R_s$, equation (77) can be extended to include a finite viscosity μ to read (Owocki and Zank, 1991)

$$\mu\frac{\mathrm{d}^2\eta}{\mathrm{d}x^2} = \eta\frac{\mathrm{d}\eta}{\mathrm{d}x} - a\eta - b\eta \, .$$

On expanding the right-hand side in the vicinity of the equilibrium solutions $\eta = \eta_0 + y$, one obtains

$$\mu \frac{\mathrm{d}^2\eta}{\mathrm{d}x^2} = \pm\sqrt{a^2 + 4by}\ , \tag{78}$$

where positive and negative values correspond to those solutions near the corresponding separatrix. In general, for $x > 0$, solutions near one of the separatrices are unstable, while all stable solutions are attracted to the second separatrix. Thus, only those solutions corresponding to the lower separatrix for $r > R_s$ are meaningful in the limit of vanishing viscosity. On the other hand, all solutions with realistic solar wind data at $r = 1$ are attracted to the other separatrix at $r < R_s$. This suggests that the sonic transition must be a weak discontinuity when $\mu = 0$.

Plotted in Figure 4.2 is the steady-state solution to the the model equations (66) –(68) subject to the assumptions that $N(r) = N_{\mathrm{H}\infty} \exp\left[-\lambda/r\right]$, $T_{\mathrm{H}} = T_{\mathrm{H}\infty} = 10^4$ K, and $V = V_{\mathrm{H}\infty} = 20$ km s^{-1}. Here $\lambda = 4$ AU defines the ionization cavity length scale, $\nu_{ph} = 0$, and the adiabatic index $\gamma = \frac{5}{3}$. The dashed lines in Figure 4.2 depict a solution for which pickup ions are absent, i.e., the momentum and energy source terms are set to zero and the solar wind is purely adiabatic. The solid lines depict the steady-state solar wind when pickup ions are included explicitly and, while the density continues to fall off essentially as r^{-2} with increasing heliocentric distance, considerable differences in the radial profiles for pressure, temperature, Mach number and velocity are apparent. Care should be exercised in interpreting the temperature profile, however, as was discussed above. The increase in solar wind temperature corresponds primarily to the temperature of pickup ions (which have energies of $\sim$ 1 keV) and not to solar wind protons (which may experience some heating via both (weak) compression and turbulent dissipation). Nonetheless, the presence of a hot pickup ion population, whose internal energy dominates that of the solar wind and which is coupled to the solar wind by scattering off *in situ* and self-generated turbulence, can be expected to effect the dynamics of local processes in the outer heliosphere considerably. Examples include the role of pickup ion pressure in the outer heliosphere (Burlaga et al., 1994), pickup ion acceleration at interplanetary shocks (Gloeckler et al., 1994; Zank et al., 1996; Lee et al., 1996], and the propagation of shocks (Zank and Pauls, 1997).

In concluding this subsection, one should note the importance of pickup ions for the development of solar wind models in the outer heliosphere. The presence of pickup ions in the outer heliosphere allows one to adopt a primarily hydrodynamic rather than an MHD description for much of the overall dynamics. In the absence of pickup ions, the outer heliosphere is dominated by the interplanetary magnetic field and the plasma beta (ratio of gas to magnetic field pressure) $\beta(60\ AU) \simeq 0.01$. By contrast, the contribution by pickup ions yields a corresponding value of $\beta(60\ AU) \simeq 3$ (Zank et al., 1995, 1996).

4.3. Perturbation analysis of the one-fluid model

Lee (1996) presented an attractive perturbation analysis of a reduced form of the one-fluid equations (66)–(68). Since this approach is quite revealing in clarifying

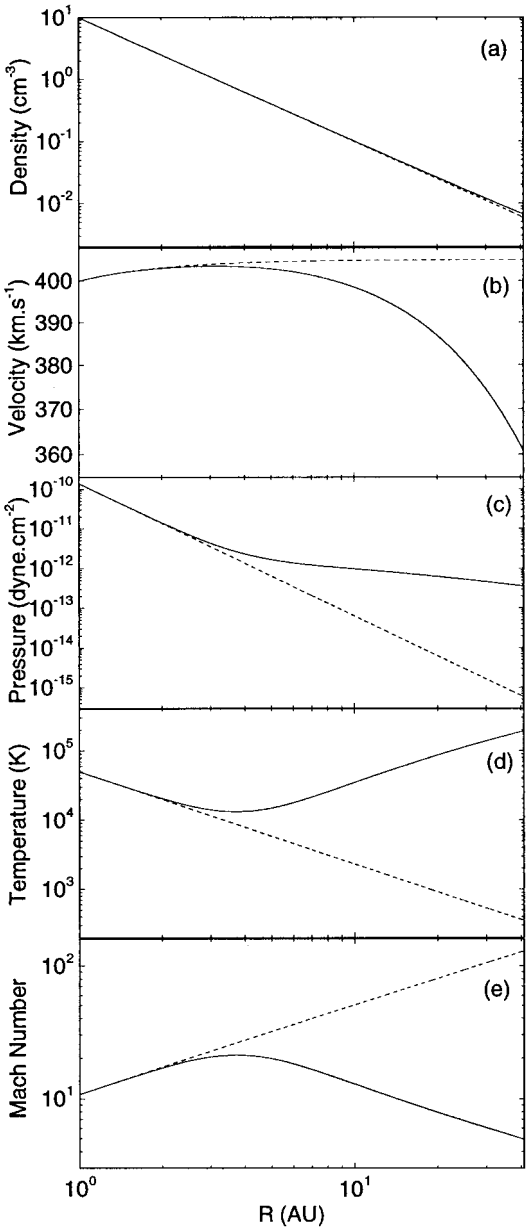

Figure 4.2. Steady state plots of (a) number density, (b) radial flow velocity, (c) gas pressure, (d) temperature, and (e) Mach number as a function of heliocentric distance R. Dashed lines correspond to an adiabatic model, and solid lines correspond to a pickup ion mediated model of the heliosphere. (Zank and Pauls, 1996.)

the role of interstellar H in the outer solar wind, we discuss this calculation briefly. A related calculation to estimate the strength of the termination shock was given too by Isenberg (1996).

The steady state, spherically symmetric hydrodynamic equations with simplified momentum and energy source terms are

$$\frac{1}{r^2}\frac{\mathrm{d}}{\mathrm{d}r}\left(r^2\rho u\right) = 0\,; \tag{79}$$

$$\frac{1}{r^2}\frac{\mathrm{d}}{\mathrm{d}r}\left(r^2\rho u^2\right) + \frac{\mathrm{d}P}{\mathrm{d}r} = -\sigma_c N\rho u^2\,, \tag{80}$$

$$\frac{1}{r^2}\frac{\mathrm{d}}{\mathrm{d}r}\left[r^2 u\left(\frac{1}{2}\rho u^2 - \frac{\gamma}{\gamma-1}P\right)\right] = -\sigma_c N\frac{\rho u^3}{2}\,. \tag{81}$$

By assuming that the total pressure P (solar wind and pickup ion) is significantly less than the solar wind ram pressure, we can introduce the scaling parameter $\varepsilon \sim P/\rho u^2$ and assume that $\varepsilon \sim \sigma N r$. At zeroth order in ε, one has the free streaming expanding solar wind solution

$$u = U_0, \qquad \rho = \rho_0\,(r_0/r)^2\,. \tag{82}$$

The first-order solution for the total pressure P and the correction to the radial fluid velocity is

$$P = \frac{\gamma-1}{2(2\gamma-1)}\frac{\rho_0 r_0^2 U_0^2}{r}\sigma_c N\,, \tag{83}$$

$$u = U_0\left(1 - \frac{3\gamma-1}{2\gamma-1}\frac{\sigma_c N}{2r}\right)\,, \tag{84}$$

so illustrating both the deceleration of the solar wind and the non-adiabatic character of the radial pressure profile (c.f., Figure 4.2). The sound speed is therefore

$$C_s^2 \equiv \gamma P/\rho = \frac{\gamma(\gamma-1)}{2(2\gamma-1)}U_0^2\sigma_c N r\,, \tag{85}$$

which increases with increasing heliocentric distance and yields a decreasing hydrodynamic Mach number

$$M = \frac{1 - [(3\gamma-1)/(2\gamma-1)]\sigma_c N/r}{\sqrt{[\gamma(\gamma-1)/2(2\gamma-1)]\sigma_c N r}}\,. \tag{86}$$

One can therefore expect the Mach number of the termination shock to be considerably smaller than that terminating an equivalent adiabatic solar wind (i.e., a wind not mediated by the presence of pickup ions).

4.4. THE THREE-FLUID MODEL

An important extension to the one-fluid solar wind model of Section 4.1 was presented by Isenberg (1986). As has been alluded to in Section 4.1, one-fluid solar wind models assume essentially that wave-particle interactions proceed sufficiently quickly that pickup ions are soon assimilated into the solar wind, becoming indistinguishable from solar wind protons. As illustrated in Figure 4.2, a substantial increase in the solar wind temperature with increasing heliocentric distance is then predicted. Such a predicted temperature increase is, of course, not observed in the outer heliosphere (Gazis, 1994; Richardson et al., 1995). As observed by Vasyliunas and Siscoe (1976) and Holzer (1977), pickup ions are unlikely to be assimilated into the solar wind completely. Instead, the pickup ion driven waves may isotropize and so stabilize the pickup ion distribution (and perhaps provide some residual heating of the solar wind protons). Thus, wave-particle interactions can be expected to produce two co-moving thermal proton populations. Further assimilation of the pickup ions into the solar wind distribution proceeds via Coulomb collisions.

The various interaction time scales accessible to the pickup ion and solar wind proton populations were analyzed carefully by Isenberg (1986). Three processes may lead to the equilibration of pickup ions with the solar wind: (i) pitch-angle scattering in the wave/turbulence field; (ii) energy diffusion in the wave/turbulence field, and (iii) Coulomb collisions with the solar wind ions. The characteristic scales may be denoted τ_μ, τ_v and τ_C respectively and these are to be compared to the characteristic solar wind flow time $\tau_f = r/u$. Estimates for τ_μ and τ_v were derived in Section 3.5. The Coulomb time scale is given by $\tau_C = 0.294/n_{\rm PI}(T_{\rm SW} + T_{\rm PI})^{3/2}$ s (Spitzer, 1962) where $n_{\rm PI}$ is the pickup ion number density and $T_{\rm SW(PI)}$ the solar wind (pickup ion) temperature in degrees K. Using reasonable parameters, Isenberg (1986) finds that $\tau_C(\sim 10^{12}s) \gg \tau_f(\sim 10^6 s)$. Thus, regardless of the relative ordering of τ_μ, τ_v and τ_f, the very large Coulomb collision time τ_C shows that pickup ions cannot be assimilated into the solar wind. If $\tau_\mu, \tau_v \ll \tau_f$ ($\ll \tau_C$), then the pickup ion distribution will not have steep or positive gradients in velocity space and the pickup ion distribution is effectively thermalized and co-moving with the solar wind flow.

In view of this ordering of time scales, a model which distinguishes the pickup ions from the solar wind ions is clearly appropriate and this can be developed in a straightforward fashion. The key assumption in the model advanced by Isenberg (1986) is that pickup ions and solar wind ions are perfectly co-moving – i.e., that there is no spatial diffusion by the pickup ions scattered in the MHD turbulence field. The pickup ion distribution is also assumed to be isotropic, so simplifying the energy equation. The one-fluid model (66)–(68) is then modified to read

$$\frac{\partial n_{\rm SW}}{\partial t} + \frac{1}{r^2}\frac{\partial}{\partial r}\left(r^2 u n_{\rm SW}\right) = -\langle\sigma_c v\rangle N n_{\rm SW}\,, \tag{87}$$

$$\frac{\partial n_{\rm PI}}{\partial t} + \frac{1}{r^2}\frac{\partial}{\partial r}\left(r^2 u n_{\rm PI}\right) = \nu_{ph} N + \langle\sigma_c v\rangle N n_{\rm SW}\,, \tag{88}$$

$$\frac{\partial}{\partial t}(\rho u) + \frac{1}{r^2}\frac{\partial}{\partial r}\left(r^2 \rho u\right) + \frac{\partial P}{\partial r} = -\langle \sigma_c v \rangle N \rho u \ , \tag{89}$$

where (89) represents a total momentum equation. The two energy equations can be expressed in conservation form as

$$\begin{aligned} \frac{\partial}{\partial t}\left(\frac{1}{2}\rho_{\rm SW} u^2 + \frac{P_{\rm SW}}{\gamma - 1}\right) \ + \ \frac{1}{r^2}\frac{\partial}{\partial r}\left[r^2 u \left(\frac{\rho_{\rm SW} u^2}{2} + \frac{\gamma}{\gamma - 1} P_{\rm SW}\right)\right] = \\ = \ -\langle \sigma_c v \rangle N \left(\frac{P_{\rm SW}}{\gamma - 1} + \frac{\rho_{\rm SW} u^2}{2}\right) \ ; \end{aligned} \tag{90}$$

$$\begin{aligned} \frac{\partial}{\partial t}\left(\frac{1}{2}\rho_{\rm PI} u^2 + \frac{P_{\rm PI}}{\gamma - 1}\right) \ + \ \frac{1}{r^2}\frac{\partial}{\partial r}\left[r^2 u \left(\frac{\rho_{\rm PI} u^2}{2} + \frac{\gamma}{\gamma - 1} P_{\rm PI}\right)\right] \\ = \ -\langle \sigma_c v \rangle N \left(\frac{P_{\rm PI}}{\gamma - 1} + \frac{\rho_{\rm PI} u^2}{2}\right) \ . \end{aligned} \tag{91}$$

Here, the total number density $\rho = mn = m(n_{\rm SW} + n_{\rm PI})$, and $P = P_{\rm SW} + P_{\rm PI}$, where $P_{\rm SW/PI} = n_{\rm SW/PI} k T_{\rm SW/PI}$ is the solar wind/pickup ion pressure. Isenberg (1986) integrated a slightly more general set of equations than (87)–(91) to obtain the steady state radial solar wind profiles illustrated in Figure 4.3. Three different values for the neutral H number density N were adopted (i: $N = 0.03$ cm^{-3}; ii: $N = 0.1$ cm^{-3}; iii: $N = 0.3$ cm^{-3}). As before, the pickup ions decelerate the solar wind, the pickup ion number density exhibits a broad maximum, and, most importantly, the pickup ions are maintained at a high temperature while the solar protons cool essentially adiabatically.

5. Global Models of the Solar Wind-LISM Interaction I. Hydrodynamic Models

The dynamical or ram pressure (ρu^2) and thermal pressure p of the solar wind decrease with increasing heliocentric distance and must reach a value which eventually balances the pressure exerted by the LISM. The relaxation towards pressure equilibrium between the solar and interstellar plasmas is characterized by (i) a transition of the supersonic solar wind flow to a subsonic state, and (ii) a divergence of the interstellar flow about the heliospheric obstacle. The transition of the supersonic solar wind is most likely accomplished by means of a shock transition, the termination shock (denoted by TS), and it is anticipated (hopefully) that at least the Voyager spacecraft will encounter this boundary in the early 21st century. The divergence of the LISM flow about the heliosphere may be accomplished either adiabatically (if the relative motion between the sun and the LISM is subsonic) or by means of a bow shock in the case of supersonic relative motion.

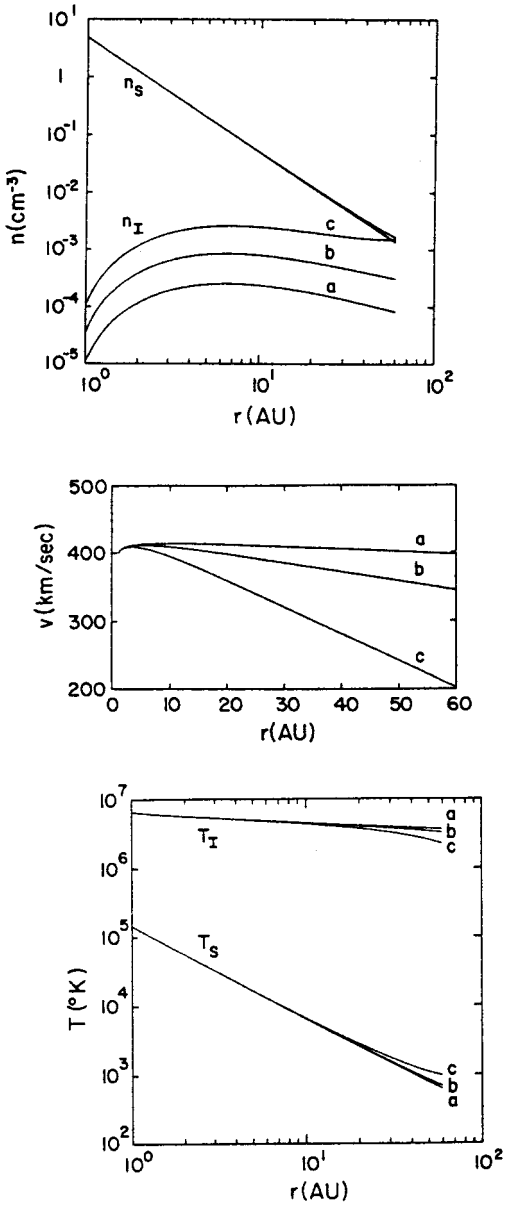

Figure 4.3. (a) Steady state solar wind and pickup proton number densities, (b) solar wind velocities, and (c) solar wind and pickup ion temperatures as a function of radial distance for three different values of the neutral H number density (i: $N = 0.03$ cm^{-3}; ii: $N = 0.1$ cm^{-3}; iii: $N = 0.3$ cm^{-3}). (Isenberg, 1986.)

Although one can estimate the location of the TS and the heliopause (HP), the discontinuity separating solar wind material from the interstellar plasma (a contact discontinuity in the case of gas dynamics), using simple pressure balance arguments, the problem of the interaction of the solar wind with the LISM is fundamentally multi-dimensional. Thus, the main advances in our understanding of global heliospheric structure since the pioneering work of Davis (1955), Parker (1961, 1963), Axford et al. (1963) and Baranov et al. (1970) have been more recent and based largely on computer simulations. The initial simulations were based on pure one-fluid gas dynamic models and only now has the inclusion of neutral interstellar Hydrogen been considered self-consistently.

In this section, we discuss first the quasi-analytic models of the heliosphere developed primarily by Parker (1961, 1963) and Baranov et al. (1970) (Section 5.2) before describing numerical gas dynamic models in the absence of interstellar neutrals (Section 5.3). This section includes both 2D and 3D models. In Section 5.4, we discuss global solutions for neutral interstellar hydrogen as it traverses a prescribed heliospheric plasma configuration. In Section 5.5, fully coupled models of the solar wind and LISM plasma and neutral interstellar hydrogen are described. Finally, in Section 5.6, the self-consistent models are used to infer the structure of the heliosphere from Lyman-α observations.

Relegated to the following section (Section 6) is a discussion about the inclusion of interplanetary and interstellar magnetic fields into models of the global heliosphere. This reflects, unfortunately, our somewhat inadequate understanding of the role magnetic fields play in determining the global structure and properties of the heliosphere and our poor knowledge of the interstellar magnetic field.

In the absence of magnetic fields, the interaction of the solar wind with the LISM is governed by the usual gas dynamic equations,

$$\frac{\partial \rho}{\partial t} + \nabla \cdot \rho \mathbf{u} = Q_\rho \ , \tag{92}$$

$$\frac{\partial}{\partial t}(\rho \mathbf{u}) + \nabla \cdot (\rho \mathbf{u}\mathbf{u}) + \nabla p = \mathbf{Q}_m \ , \tag{93}$$

$$\frac{\partial}{\partial t}\left(\frac{1}{2}\rho u^2 + \frac{p}{\gamma - 1}\right) + \nabla \cdot \left(\frac{1}{2}\rho u^2 \mathbf{u} + \frac{\gamma}{\gamma - 1}\mathbf{u}p\right) = Q_e \ , \tag{94}$$

where the charge exchange terms Q_ρ, Q_m, and Q_e represent source terms of density, momentum, and energy respectively. As before, ρ, $\mathbf{u}$, and p denote plasma density, velocity, and total pressure (electrons and ions) and the electron and ion temperatures are assumed to be equal. The adiabatic index $\gamma = \frac{5}{3}$. The source terms couple the plasma and the neutral H distribution and, in principle, one needs to compute the evolution of both distributions simultaneously.

5.1. PROPERTIES OF THE LISM

Before turning to the various models of the solar wind interacting with the LISM, we need to describe the properties of the LISM. It should be emphasized that many of the pertinent physical parameters of the LISM are poorly constrained and so, by implication, the detailed solar wind/LISM interaction is not yet well understood. We do not know, for example, whether the LISM flow is even super- or subsonic. Our best inferences about the LISM flow velocity and temperature have been made on the basis of observations of neutral interstellar H and He within the heliosphere.

As neutral interstellar hydrogen flows into the heliosphere, it experiences some deceleration and 'filtration' on its passage through the heliospheric boundaries, before it acts to decelerate the supersonic outflowing solar wind. The weak coupling of neutral interstellar hydrogen and plasma through the process of resonant charge exchange (which provides an effective volumetric force) affects both distributions in important ways. This is crucial to understanding the LISM/solar-wind interaction, and is profoundly important in determining the global structure of the heliosphere.

Besides interstellar hydrogen, interstellar helium, neon, oxygen, nitrogen and other heavy neutral atoms flow relatively unimpeded into the heliosphere but their dynamical influence on the solar wind is not very important. Conversely, the plasma may effect some of the the inflowing neutral distributions in important ways, e.g., oxygen but probably not helium.

Ionization of slow moving neutrals in the heliosphere by either photoionization or charge exchange creates pick-up ions which then respond to the various plasma physical processes in the solar wind. The average radial distance from the sun at which a significant fraction of the interstellar neutrals is singly ionized is different for different interstellar atoms and depends on the ionization rates which scale crudely with the first ionization potential of the atom. Thus, interstellar helium can flow into nearly 0.3 AU whereas neutral hydrogen, oxygen, nitrogen and neon are relatively rare within several AU.

Evidence for the presence of interstellar hydrogen and helium in the heliosphere was provided initially by the measurement of resonantly scattered solar UV light (Bertaux and Blamont, 1971; Thomas and Krassa, 1971). Subsequent measurements have tried to infer the density, temperature and (relative) velocities of hydrogen and helium (Adams and Frisch, 1977; Bertaux et al., 1985; Ajello et al., 1987). Analyses have concentrated on the strongest resonance lines, H 1216 Å (Lyman-α) and He 584 Å. Briefly described, as solar photons travel outward they scatter resonantly from heliospheric H and He atoms (Thomas, 1978). These scattered photons are detected by the Voyager and Pioneer 10 UV instruments, and the intensities vary with heliocentric distance, pointing direction, and the illuminating solar flux (Hall, 1992). H 1216 Å photons are expected to travel of order 10 AU before scattering, and He 584 Å photons scatter after traversing some 100 AU. The vast majority of H 1216 Å measurements have been obtained by spacecraft within

5 AU of the Sun, where the lines are dominated by scattering from within 10 to 20 AU. Only the Voyager and Pioneer 10 spacecraft have obtained observations of these resonance lines beyond 5 AU.

With the launch of *Ulysses*, two novel instruments now provide direct measurements for the physical parameters of the interstellar gas in the heliosphere.

(1) Close to the Sun (within ~ 5 AU), the local distribution of interstellar neutral helium has been measured, using an impact-ionization method (Witte et al., 1992), by the *Ulysses*/GAS experiment. These measurements provide the velocity and direction of the flow of interstellar He as well as its temperature and density.

(2) The densities and velocity distribution functions of the pickup ions H^+, He^+, $^4He^{++}$, $^3He^+$, N^+, O^+ and Ne^+ have been determined by the *Ulysses*/SWICS experiment (Gloeckler et al., 1993; Geiss et al., 1994; Gloeckler and Geiss, 1996). By assuming a model for the transport of interstellar neutrals within the heliosphere (e.g., the 'hot model' – Thomas, 1978; Ruciński and Bzowski, 1995), the pickup ion data can then be used to infer the neutral parameters at the heliospheric termination shock or possibly even beyond, depending on the importance of filtration.

In Table III, we summarize the hydrogen and helium parameters and their method of determination. As can be seen, there is some disagreement in the inferred number density of neutral hydrogen in the LISM and this is a result of H filtration at the heliospheric boundaries, which makes it very difficult to relate heliospheric pickup ion data directly to the LISM H. Secondly, there is some disagreement regarding the temperature of neutral hydrogen in the interplanetary medium. However, the interstellar helium temperature now appears to be well constrained and, by implication, that too of the interstellar H. The results presented in Table III provide a basis for developing and constraining global heliospheric models.

From the observations of interstellar neutrals, the bulk velocity for the LISM flow is ~ 26 km s^{-1} and the plasma temperature ~ 8000 K.

If the He density measured within the heliosphere by the *Ulysses*/GAS experiment can be related simply to its density in the LISM (as we expect, but this has to be tested in detail, especially for a one-shock model), then the combination of the local measurement (Witte et al., 1996) with H and He column densities and ratios through the Local Cloud, as measured by EUVE, yields a strong set of limits on the local interstellar densities and ionization fraction of H and He (Vallerga, 1996). Using the measurements of Dupuis et al. (1995) for $N_{\mathrm{H1}}/N_{\mathrm{He1}} \simeq 14$, $X_{\mathrm{H}} < 0.4$, $X_{\mathrm{He}} < 0.5$ (where $N_{ion/atom}$ is a column density (cm^{-2}), $X_{\mathrm{H},He}$ the ionization fraction of H and He respectively towards HZ 43) together with that of Witte et al. (1996) for local He ($n(He1) = 0.014 \pm 0.003$ cm^{-3}, $n(ion)$ the number density), one can derive upper limits on the number density of H and H1. If we assume that H is more strongly ionized than He and that the He ionization fraction is constant throughout the local cloud [e.g., Frisch, 1995], then we have locally $n(H1)/n(He1) \geq 14$ cm^{-3}. The maximum values allowed by these measurements for the local density of H and He can be derived using (Vallerga, 1996)

TABLE III
Hydrogen and Helium parameters derived from various experiments

Method	Velocity (km s^{-1})	Density ($\times 10^{-2}$ cm^{-3})	Temperature (K)	Observations
Interstellar helium				
Pickup $He^{+(1)}$	23–30	0.9–1.2	4800–7200	AMPTE
Pickup $He^{+(2)}$		1.5		ULS/SWICS
Pickup $He^{++(2)}$		1.5		ULS/SWICS
Direct[3]	25.3 ± 0.4	1.4–1.7	7000 ± 600	ULS/GAS
UV[4]	19–24	0.5–1.4	8000	Prognoz, V1, V2
Interstellar hydrogen				
Doppler-shifted absorption lines[5]	25.7			HST
Interplanetary hydrogen				
Pickup $H^{+(2)}$		11.5 ± 2.5		ULS/SWICS
UV[5]	18–20		8000	HST
UV[6]	19–21	6.5	8000	Prognoz
UV[7]			<20 000	Copernicus
UV[8]	18–20		30 000	HST (downstream)
UV[9]		14	8000	Prognoz

(1) Möbius (1996)
(2) Gloeckler (1996)
(3) Witte et al. (1996)
(4) Chassefiére et al. (1988)
(5) Lallement (1996)
(6) Bertaux et al. (1985)
(7) Adams and Frisch (1977)
(8) Clarke et al. (1995)
(9) Quémarais et al. (1995)

$$n(\mathrm{He}) = \frac{n(\mathrm{He1})}{1-X_{\mathrm{He}}} < 0.034;$$

$$n(\mathrm{He\,II}) = X_{\mathrm{He}} n(\mathrm{He}) < 0.017;$$

$$n(\mathrm{H}) = 10 n(\mathrm{He}) < 0.34;$$

$$n(\mathrm{H\,II}) = X_{\mathrm{H}} n(\mathrm{H}) < 0.14;$$

$$n_e = n(\mathrm{H\,II}) + n(\mathrm{He\,II}) < 0.15.$$

TABLE IV

Local limits of the H and He densities (in cm^{-3}) with and without the modelled effect of a stellar EUV radiation field (Valerga, 1996).

Atom/Ion	Without EUV radiation			With EUV radiation	
	Lower	Upper		Lower	Upper
He I	0.011	0.017		0.011	0.017
He II	0.004	0.017		0.004	0.0017
He	0.015	0.034	0.015		0.014
H I	0.15	0.34		0.15	0.34
H II	0.00	0.14		0.03	0.14
H	0.15	0.34		0.18	0.34

Lower limits can be derived similarly. These limits are summarized in Table IV (Valerga, 1996). A similar range of values has been derived by Gloeckler (1996). This then provides limits on both the proton and neutral H number density.

Although most models assume that the interstellar wind impinging on the heliosphere is supersonic, thus necessitating a two-shock interaction model (Baranov et al., 1971; Baranov, 1990), it is by no means clear that such an assumption is completely warranted. Our knowledge of both the local interstellar magnetic field strength and orientation and the energy density in cosmic-rays is unfortunately somewhat rudimentary. The canonical interstellar pressure contributed by cosmic-rays is $\sim 10^{-12}$ dynes/cm^2 (Ip and Axford, 1985) with perhaps $\sim (3 \pm 2) \times 10^{-13}$dynes/cm^2 contributed by cosmic-rays of energy 300 MeV nucl^{-1} and less. These estimates are very uncertain, particularly at MeV energies. It is entirely possible that low energy cosmic-rays are excluded completely from the solar wind due to enhanced scattering in the heliosheath and perhaps beyond. Such a possibility, and the attendant implications for the termination shock location, was discussed by Suess and Dessler (1985) and Zank et al. (1996). Furthermore, the degree of coupling between cosmic-rays and the thermal interstellar gas is quite obscure since we possess very little information about the turbulent local interstellar magnetic field. Adopting very reasonable LISM parameters together with a cosmic-ray pressure of 3×10^{-13} dynes cm^{-2} yields an interstellar flow that is subsonic.

Finally, little is known directly about the magnitude and direction of the magnetic field in the LISM. An upper limit on the very local interstellar magnetic field strength is derived simply from Voyager not yet having encountered the termination shock. This exercise is not particularly fruitful and yields upper limits that can range from ~ 4.3–~ 6.6 μG depending on the choice of parameters and the degree to which charge exchange decelerates the solar wind. The 'local galactic' magnetic field magnitude, derived from Faraday rotation measures of pulsars, has an average

value of $\sim$ 1.5 μG (Rand and Kulkarni, 1989; Frisch, 1994). The derivation of this estimate involves an algebraic average of the line-of-sight component of the interstellar magnetic field towards the pulsars, hundreds or thousands of parsecs distant. In addition, the interstellar field is thought to be quite turbulent, with eddy sizes perhaps as large as 50 parsecs. The random magnetic field component may have a strength of $\sim$ 5.5 μG in the very simple model of Rand and Kulkarni (1989). By considering observations of polarization in the nearest stars ($\sim$ 2–30 pc from the sun), a crude estimate for the direction of the LISM magnetic field can be made and Tinbergen (1982) and Frisch (1995) suggest that it lies perpendicular to the interstellar flow velocity vector. More recently, Gloeckler et al. (1997), using pickup hydrogen and helium data, suggest a magnetic field strength in the LISM of between $\sim$ 1.3 and $\sim$ 2 μG, assuming supersonic flow. Evidently, conclusions about the strength and direction of the local interstellar magnetic field are extremely tentative.

5.2. THE ANALYTIC MODELS

Consider first a steady, radially symmetric solar wind interacting with a static, unmagnetized interstellar gas (Davis, 1955; Parker, 1961, 1963). The deceleration of the expanding supersonic solar wind must be accomplished by a strong shock (at least within the framework of a gas dynamic solar wind in the absence of pickup ions) for which the Rankine–Hugoniot conditions normal to the shock are

$$\frac{u_2}{u_1} \simeq \frac{\gamma-1}{\gamma+1}, \quad \frac{\rho_2}{\rho_1} \simeq \frac{\gamma+1}{\gamma-1}, \quad p_2 \simeq \frac{2}{\gamma+1}\rho_1 u_1^2 \,. \tag{95}$$

The subscript 1(2) denotes upstream (downstream) states, i.e., 1 refers to the supersonic solar wind. Since the downstream Mach number is small, we may assume that the flow there is incompressible (ρ_2 constant). Along each streamline in the downstream region, the Bernoulli equation is valid, i.e.,

$$p + \rho_2 \frac{u^2}{2} = p_2 + \rho_2 \frac{u_2^2}{2} \,. \tag{96}$$

Then, since $p \to p_\infty$, the LISM pressure, and $u \to 0$ at the stagnation point, $p + \rho_2 \frac{u^2}{2} = p_\infty$. Making the further assumption that the solar wind speed $u_1 = u_0$ is constant, where the subscript 0 denotes evaluation at 1 AU, implies that

$$\rho r^2 = \rho_0 r_0^2 = \rho_t R_t^2 \,. \tag{97}$$

Here R_t denotes the location of the termination shock. It follows immediately from (95)–(97) that the TS is located at

$$\frac{R_t}{r_0} = \left[\frac{\gamma+3}{2(\gamma+1)}\frac{\rho_0 u_0^2}{p_\infty}\right]^{1/2} \,. \tag{98}$$

Behind the TS, where $\rho \simeq$ const. by assumption, the steady, spherically symmetric continuity equation (92) yields $ur^2 = u_2 R_t^2$, from which one obtains

$$u = \frac{\gamma - 1}{\gamma + 1} u_0 \left(\frac{R_t}{r} \right)^2 , \tag{99}$$

showing that the heliosphere expands slowly outward if bounded by a static interstellar plasma. For typical solar wind and LISM parameters ($u_0 = 400$ km s^{-1}, $n_0 = 5$ cm^{-3}, $p_\infty = 10^{-13}$ dyn cm^{-2}), $R_t \simeq 350$ AU.

The relative motion of the sun with respect to the interstellar plasma changes matters dramatically. Following Parker (1961, 1963), suppose that the ram pressure of the LISM is much less than the thermal pressure i.e., that $\rho_\infty u_\infty^2 \ll p_\infty$, which implies that $M_\infty \ll 1$. To determine the flow pattern of the subsonic solar wind, we follow the presentation of Suess and Nerney (1990) (see also Khabibrakhmanov and Summers, 1996). Suppose that the supersonic flow terminates at a spherical termination shock located at the radial distance R_t. Since flow downstream of the TS is incompressible, $\nabla \cdot \mathbf{u} = 0$, or in terms of the velocity potential $\mathbf{u} = \nabla\phi$,

$$\nabla^2 \phi = 0 . \tag{100}$$

The flow pattern can then be determined from the general solution of Laplace's equation (100). The velocity potential can be expressed as a linear combination of the potential of three different sources,

$$\phi_1 = u_\infty r \cos\theta , \quad \phi_2 = \frac{m \cos\theta}{4\pi r^2} , \quad \phi_3 = \frac{Q}{4\pi r} ,$$

where, respectively, they are (1) the potential of the steady flow along the z-axis, (2) the potential of the dipole, with moment $\mathbf{m}$, aligned along the z-axis at the center of the Sun, and (3) the potential of the source of strength Q located at the origin. The flow is obviously axisymmetric.

The flow components are given by

$$u_r = -\phi_r ; \qquad u_\theta = -\phi_\theta / r , \tag{101}$$

and the source term Q and dipole moment $\mathbf{m}$ are determined by the inner boundary conditions

$$u_r|_{r=R_t} = \frac{Q}{4\pi R_t^2} + \frac{2m \cos\theta}{4\pi R_t^3} - u_\infty \cos\theta = u_t . \tag{102}$$

Hence,

$$Q = 4\pi u_t R_t^2 , \qquad m = 2\pi u_\infty R_t^3 ,$$

and the velocity potential is (Suess and Nerney, 1990)

$$\phi = u_\infty R_t \cos\theta \left[\frac{1}{2} \left(\frac{R_t}{r} \right)^2 + \frac{r}{R_t} \right] + \frac{u_t R_t^2}{r} . \tag{103}$$

Since $u_\infty = -3/2 u_\infty \sin\theta$ at the termination shock (i.e., an azimuthal component of **u**), the assumption of a spherically symmetric TS is not in fact valid and one is obliged then to compute the TS geometry self-consistently with the flow pattern. The solution (103) is therefore valid only for small R_t and the term $(R_t/r)^2$ represents a correction to Parker's (1961, 1963) original point source solution ($R_t = 0$).

The stream function Ψ is defined by the equations

$$u_r = \frac{1}{r^2 \sin\theta}\frac{\partial \Psi}{\partial \theta}\,, \qquad u_\theta = \frac{-1}{r\sin\theta}\frac{\partial \Psi}{\partial r}\,,$$

which yields

$$\begin{aligned} \Psi &= -\frac{1}{2}u_\infty r^2 \sin^2\theta + \frac{m}{4\pi r}\sin^2\theta + \frac{Q}{4\pi}(1-\cos\theta) = \\ &= \frac{u_\infty R_t^3}{2r}\left[1 - \left(\frac{r}{R_t}\right)^4\right]\sin^2\theta - u_t R_t^2(\cos\theta - 1)\,, \end{aligned} \tag{104}$$

in spherical coordinates (Nerney et al., 1993; Khabibrakhmanov and Summers, 1996). The stagnation point $R_{\rm H}$ of the interstellar wind is found on the stagnation line $\cos\theta = 1$, $u_r = 0$, i.e.,

$$\frac{u_\infty}{u_t}\left[\left(\frac{R_t}{R_{\rm H}}\right)^3 - 1\right] + \left(\frac{R_t}{R_{\rm H}}\right)^2 = 0\,, \tag{105}$$

which generalizes Parker's (1961) solution $(R_t/R_{\rm H})^2 = u_\infty/u_t$. The shape of the heliopause is determined by the null surface of the streamline function $\Psi = 0$,

$$(u_\infty/u_t)\left[1 - \left(\frac{r}{R_t}\right)^3\right]\sin^2\theta - 2\frac{r}{R_t}(\cos\theta - 1) = 0. \tag{106}$$

In the limit that $r \to \infty$, the transverse dimension of the distant heliotail is

$$R_t\sqrt{2u_t/u_\infty}\,,$$

indicating that the solar wind in the heliotail is confined to a circular cylinder. Figure 5.1 shows the analytic global heliospheric structure.

The final possibility, that of a solar wind interacting with a supersonic interstellar wind, was considered by Baranov et al. (1971). In this case, two shocks are present – a bow shock through which the interstellar flow is decelerated and diverted about the heliospheric obstacle, and a solar wind termination shock. A contact discontinuity, called the heliopause, separates the heated, compressed, subsonic solar wind and the shocked LISM flows.

Baranov et al. (1971) treat the subsonic region as a thin shell separating hypersonic streams (i.e., the dense shell has negligible thickness compared to the

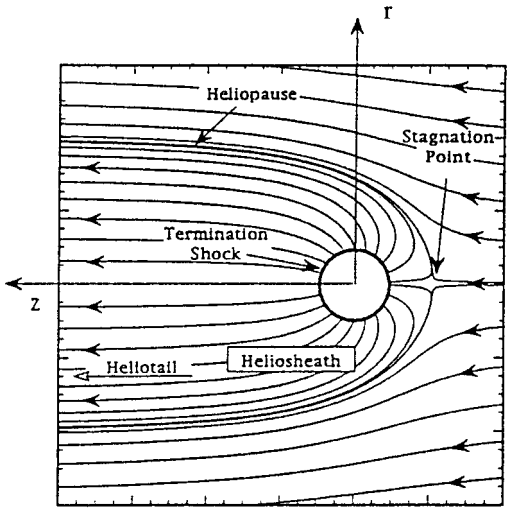

Figure 5.1. Streamline plot for the irrotational flow solution of Seuss and Nerney (1991). The termination shock, heliopause, stagnation point, heliosheath and heliotail are marked. The flow is symmetric about the stagnation axis. (Seuss and Nerney, 1991.)

distance to the sun). This approximation is sometimes called the 'thin shell' or 'Newtonian' approximation. By expressing conservation of mass and momentum for the shell, which is assumed to be described by a curve of the form $r = r(\theta)$, in directions normal and tangential to the layer, Baranov et al. (1971) (see also Ratkiewiez, 1992) were able to derive a 3rd-order ordinary differential equation

$$rr'' = \frac{F_1 - F_2'/F_3}{F_2} F_3^2 + 2rr' + 3r'r'' \,, \tag{107}$$

describing the shape of the discontinuity. Here $F_{1,2,3} = F_{1,2,3}(r, \theta)$. Equation (107) was solved numerically using the boundary conditions

$$r(\theta = 0) = R_B \,, \qquad r'(\theta = 0) = 0 \,,$$

where R_B is the heliocentric distance to the shell along the axis of symmetry. R_B is determined from

$$\rho_1 u_1^2 = \rho_\infty u_\infty^2 \,, \qquad \rho_1 u_1 R_B^2 = \rho_0 u_1 r_0^2 = \text{const.} \,, \tag{108}$$

where u_1 is the solar wind speed and the subscript 0 denotes evaluation at 1 AU. From (108), the shell length scale is given by

$$R_\mathrm{H}/r_0 = \sqrt{\frac{\rho_0 u_1^2}{\rho_\infty u_\infty}} \,. \tag{109}$$

The third boundary condition is $r'' = 2R_B/5$ (Baranov et al., 1971).

An alternative approach to determining the structure of the bow shock which is entirely analytical is possible however. Assume again the Newtonian approximation (i.e., a thin shell) which can be described entirely by the shell radius $r(\theta)$, the surface density function $d(\theta)$, and the speed $u(\theta)$ of compressed gas flowing tangentially along the shell. The angle θ is the polar angle from the axis of symmetry, as before, and $\hat{z}$ is the axis of symmetry with the LISM flow, which is in the direction $-\hat{e}_z$. Following Baranov et al. (1971), the mass flux flowing into the shell per unit time is given by

$$2\pi\Phi_\rho = \pi r^2 \rho_\infty u_\infty \sin^2\theta + 2\pi r^2 \rho_1 u_1 (1-\cos\theta)\ . \tag{11}$$

Consider now the momentum flux supplied to the thin layer by both the solar wind and the LISM flow. For an arbitrary annulus of azimuthal width $\mathrm{d}\eta$ about the symmetry axis, we can determine the surface integral of the solar wind momentum flux onto the shell by assuming that this segment of the shell is a spherical surface. Hence,

$$\begin{aligned} \Phi^{\mathrm{SW}}_{\rho u}\,\mathrm{d}\eta &= \int \rho_1 \mathbf{u}_1\mathbf{u}_1\cdot\hat{e}_n\,\mathrm{d}A \\ &= \frac{1}{2}\rho_0 u_1^2 r_0^2\,\mathrm{d}\eta\left[(\theta-\sin\theta\cos\theta)\hat{e}_y + \sin^2\theta\hat{e}_z\right]\ , \end{aligned} \tag{111}$$

where $y = r\sin\theta$ and $\hat{e}_n$ is the unit normal to the shell surface. The momentum deposited by the interstellar wind is $\Phi^{\mathrm{LISM}}_{\rho u} = -1/2\rho_\infty u_\infty^2 r^2\ \sin^2\theta\hat{e}_z\ \mathrm{d}\eta$, so that the total momentum flux impinging on the shell is

$$\begin{aligned} \Phi^t_{\rho u} &= \Phi^{\mathrm{SW}}_{\rho u} + \Phi^{\mathrm{LISM}}_{\rho u} \\ &= \frac{1}{2}\rho_0 u_1^2 r_0^2\,(\theta-\sin\theta\cos\theta)\,\hat{e}_y + \frac{1}{2}\rho_0 u_1^2 r_0^2 \sin^2\theta\left(1-\frac{r^2}{R_B^2}\right)\hat{e}_z\ . \end{aligned} \tag{112}$$

Since momentum must be conserved in the shell, the momentum flux (112) must balance the tangential momentum flux traversing the annulus of width $\mathrm{d}\eta$, i.e., $\Phi^t_{\rho u} = \phi_t\hat{e}_t$ where $\hat{e}_t$ is a tangential unit vector at constant η. Equation (112) describes the vector momentum flux and therefore the flow direction, whence the shell shape is determined from

$$\frac{\mathrm{d}z}{\mathrm{d}y} = \frac{u_z}{u_y} = \frac{\sin^2\theta - y^2/R_B^2}{\theta-\sin\theta\cos\theta}\ . \tag{113}$$

By rewriting (113) in the polar coordinates (r,θ) and using $\xi = r^2\sin^3\theta/R_B^2$, one obtains

$$\frac{\mathrm{d}\xi}{\mathrm{d}\theta} = \frac{\xi[2\theta\sin\theta + \cot\theta(\xi+3\theta\cos\theta-3\sin\theta)]}{\xi+\theta\cos\theta-\sin\theta}\ ,$$

which has the exact integral

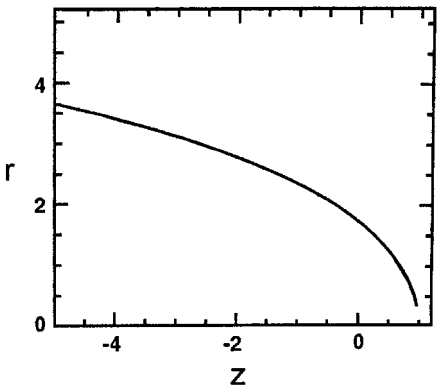

Figure 5.2. Analytic bow shock solution (Equation (114)) for the supersonic LISM model.

$$\xi = 3\,(\sin\theta - \theta\cos\theta)$$

or

$$r(\theta) = R_B \csc\theta\sqrt{3(1-\theta\cot\theta)}\,. \tag{114}$$

The solution (114) is the exact analytic form of the global structure of the bow shock in the thin layer approximation. The solution for representative parameters is illustrated in Figure 5.2.

Unfortunately, as we discuss in the following section, the Newtonian or thin layer approximation is rather poor and the distance between the bow shock and the termination shock is comparable to the distance from the sun. Nonetheless, the thin layer approximation has been used by a variety of authors to investigate different aspects of the solar wind-LISM interaction, including the effect of interstellar magnetic fields on global heliospheric structure (Section 6.1).

The analytic models, while far from satisfactory, do illustrate at least three basic results of importance for a solar wind interacting with an interstellar wind. The first is that an extended tail of subsonic solar wind should form – now called the heliotail. Secondly, the supersonic region of the heliosphere should be asymmetric. Thirdly, if we neglect the deceleration of the solar wind by resonant charge exchange effects, the minimum radius to the solar wind shock transition can be calculated from Equation (98) by assuming a value for the LISM pressure. The LISM pressure term can include the thermal gas, cosmic-rays, the interstellar ram pressure, the magnetic field pressure, dust, and MHD turbulence, and may be expressed as

$$p_\infty = \rho u^2 + p_{th} + \alpha B^2/2\mu + p_{\rm CR} + p_{\rm dust} + p(\delta B^2)\,, \tag{115}$$

where the terms are all evaluated in the LISM and the factor α attempts to include the effects of magnetic field obliquity. The analytic models are represented schematically in Figure 5.3 for both the one-shock and two-shock cases.

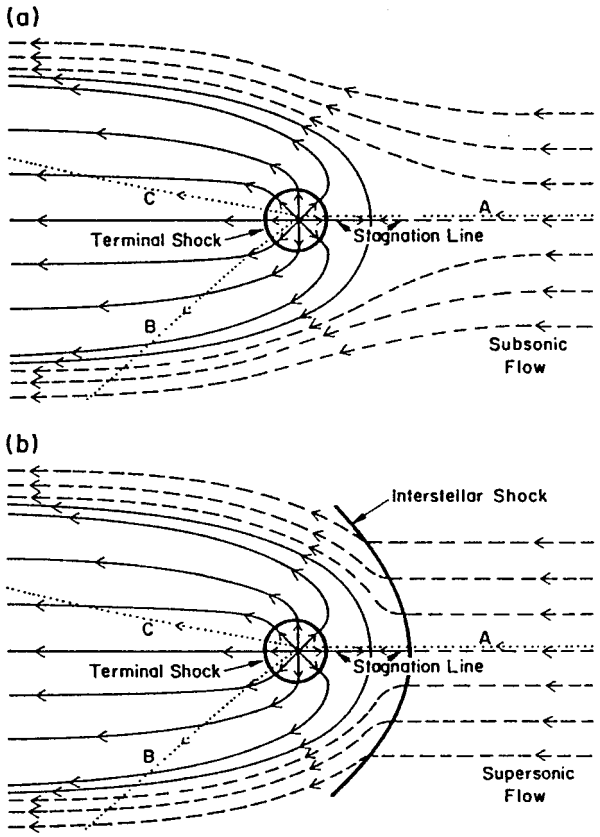

Figure 5.3. Schematic representation of the interaction of the solar wind flow with (a) a subsonic interstellar medium and (b) a supersonic LISM. The solid curves denote solar wind plasma flow and the dashed lines LISM flow. The dotted curves are trajectories of an interstellar hydrogen atom that is subjected to either a net attractive force (AB) or a net repulsive force (AC) (Section 2). (Holzer, 1989.)

5.3. GLOBAL SIMULATIONS: PLASMA ONLY

To properly understand the global structure of the heliosphere requires the use of numerical simulations. Ideally, these simulations would include self-consistently the interaction of the solar wind plasma, interstellar plasma, neutrals of both interstellar and heliospheric origin, magnetic fields, etc., all within the framework of a time-dependent, multi-dimensional, highly resolved code. Unfortunately, computer resources are not yet adequate to complete such a simulation, nor does our incomplete understanding of LISM parameters and physics warrant such an effort. Instead, more limited modelling goals have been identified and executed. In the following subsections, we shall consider each in turn. Here, we neglect interstellar and heliospheric neutrals, cosmic-rays, and magnetic fields altogether and consider the interaction of a supersonic plasma solar wind with a plasma LISM.

TABLE V

Solar wind parameters at 1 AU and LISM parameters at infinity used for the simulations illustrated in Plates 1 and 2.

	Solar wind (1 AU)	LISM
n (cm^{-3})	5.0	0.1
u (km s^{-1})	400	−26
T(K)	10^5	8000/80 000
M	7.6	1.75/0.9

5.3.1. *2D Models*

The assumption of axial symmetry along the direction of the LISM flow coupled to a spherically symmetric expanding solar wind allows one to reduce the gas dynamic equations (92)–(94) (without the source terms) to a 2D model. Such a reduced model has been investigated by several groups (Matsuda et al., 1989; Baranov and Malama, 1993; Steinolfson et al., 1994; Steinolfson, 1994; Karmesin et al., 1995; Pauls et al., 1995; Wang and Belcher, 1998) and the purely gas dynamic simulations appear now to be reasonably well understood. The solar wind and LISM parameters for the two sets of simulations illustrated in the colour plates below are tabulated in Table V. The LISM temperature is chosen so that it is either supersonic ($T = 8000$ K) or subsonic ($T = 80000$ K). Clearly, the latter temperature is an effective temperature, reflecting the pressure contribution from low energy cosmic-rays (and possibly the magnetic field). An alternative approach is to simply reduce the LISM flow velocity [e.g., Steinolfson, 1994].

Illustrated in Plate 5.1(a) is the temperature distribution (colour) of the plasma at steady-state for an assumed subsonic interstellar medium. The location of the heliopause (HP) and termination shock (TS) are labeled. Also shown in Figure 5.4 are 1D profiles of the plasma variables ρ and T in the nose (i.e., along the stagnation line) direction. The 2D Plate shows that the incoming LISM flow is decelerated and diverted far upstream of the heliospheric obstacle and some associated adiabatic compression and heating of the LISM plasma occurs ahead of the heliopause. Nonetheless, the flow lines are qualitatively consistent with the analytic streamlines derived by Parker (1961, 1963) and Suess and Nerney (1990). The interstellar and solar wind plasma meet at the heliopause where they flow at different tangential speeds. The termination shock is located at $\sim$ 70 AU in the upstream direction and is very strong (compression ratio of 4). Considerable heating of the plasma occurs and temperatures are typically $\sim 10^6$ K. Although the heliosheath, the region between the TS and HP, expands like a de Laval nozzle, the shocked solar wind does not expand sufficiently rapidly to become supersonic, remaining subsonic through-

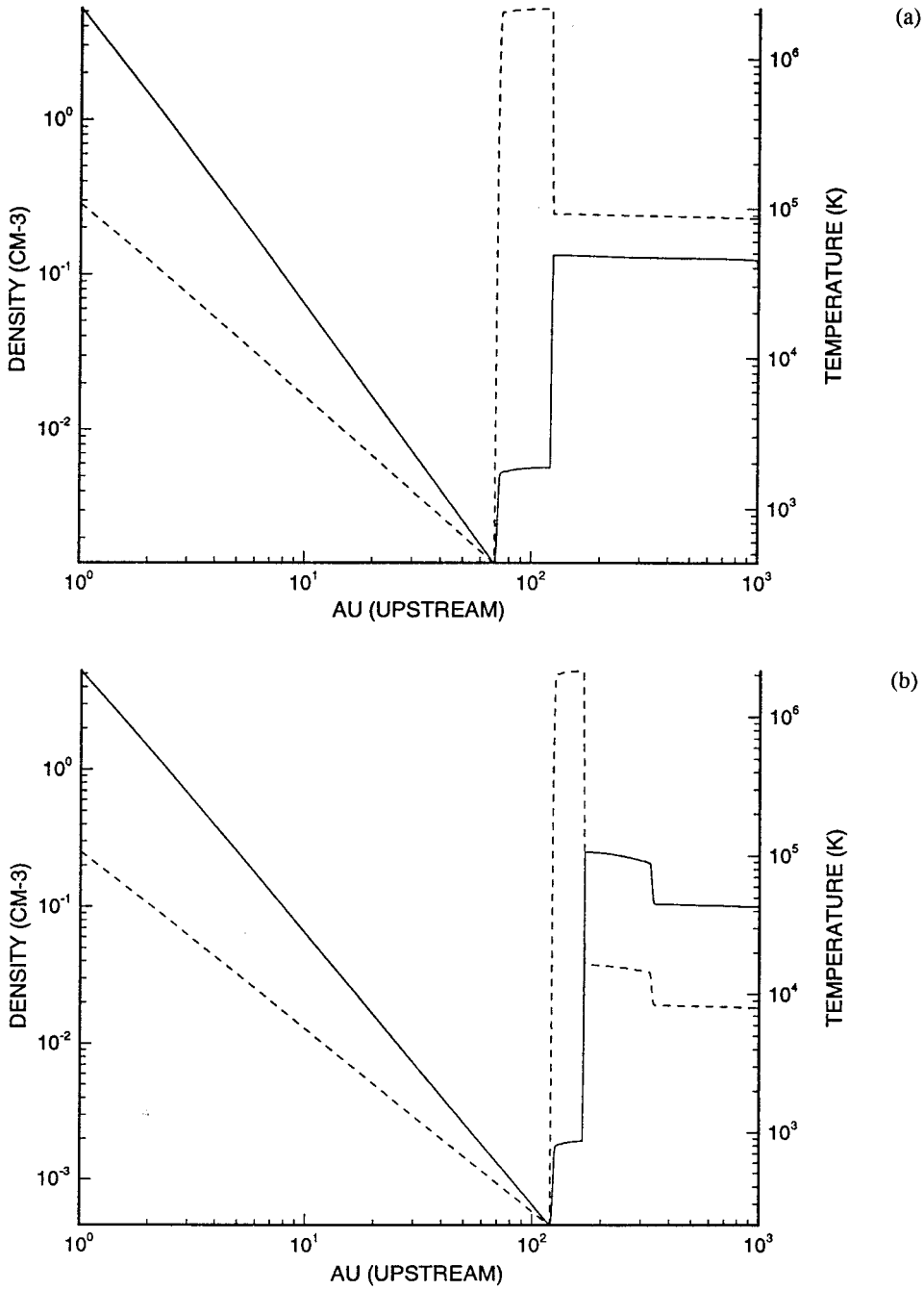

Figure 5.4. One-dimensional cuts along the stagnation axis of the plasma-only 2D simulations for (a) the one-shock model, and (b) the two-shock model. The solid line shows the plasma density and the dashed line the plasma temperature. The high LISM plasma temperature for the one-shock model is an effective temperature, reflecting the contribution of cosmic rays, for example. The TS, HP and BS are all clearly visible.

out the heliosheath. The 2D structure of the TS resembles a slightly elongated sphere. The downstream TS is located at $\sim$ 78 AU which is scarcely further than the distance in the upstream direction. The shocked solar wind in the heliotail does not cool with increasing distance from the TS and is effectively cylindrical, as expected from the analytic models.

At the heliopause, a contact discontinuity in these gas dynamic models, the density increases abruptly and dramatically from the shocked solar wind value to one almost equal to the undisturbed LISM density. A corresponding abrupt decrease in plasma temperature occurs here as well. The heliosheath is approximately 50 AU wide in the upstream direction.

Since the shocked solar wind and LISM experience a substantial velocity shear across the HP, a Kelvin-Helmholtz instability might be expected to develop in this region. The Kelvin-Helmholtz instability was investigated analytically by Baranov et al. (1992) and the stability of the nose region was investigated by Chalov (1996). Indeed, Matsuda et al. (1989) had found in their simulations that the HP appeared to be non-stationary. Subsequent simulations of the solar wind-LISM interaction using a variety of numerical schemes did not reproduce the instability. The simulations shown in Plate 1 do however exhibit a weakly non-stationary HP (these simulations being similar to those of Pauls et al. (1995) except at slightly higher resolution). However, Wang and Belcher (1998), using a PPM scheme which has significantly less dissipation at discontinuities than typical hydrodynamic smoothing schemes, find that the heliopause is unstable. The instability begins in the near-nose region on time scales of less than 50 years with a growth rate roughly consistent with that predicted from analytic linear incompressible theory (Chandrasekhar, 1961). As the Kelvin-Helmholtz instability saturates, a non-linear oscillation or shear wave on the HP develops and advection along the HP towards the heliotail occurs. A figure illustrating the time-dependent HP for the one-shock case is shown in Figure 5.5(a).

Suppose now that the LISM flow is supersonic. In this case, as discussed above, a bow shock is necessary to divert the approaching LISM flow about the heliosphere. Plate 5.1b shows the plasma temperature at steady-state when charge exchange with neutrals is neglected. The positions of the TS, HP and BS are indicated on the plot. For this purely gas dynamic (GD) case, the TS is axisymmetric and bullet shaped (Baranov and Malama, 1993; Steinolfson, 1994; Steinolfson et al., 1994; Pauls et al., 1995; Steinolfson and Gurnett, 1995; Wang and Belcher, 1998). The TS has a compression ratio of $r = 4$ independent of polar angle, while the BS on the other hand is a weak shock ($r = 1.7$ at $\theta = 0°$). The supersonic solar wind flow velocity is radial and constant, resulting in an adiabatic expansion of the plasma ($\rho \propto r^{-2}$, $T \propto r^{-4/3}$) up to the TS, where the density, pressure and velocity of the plasma jump discontinuously to a subsonic flow and and is deflected towards the heliotail ($\theta = 180°$). The LISM and solar wind plasmas meet at the HP where the interstellar and shocked solar wind pressures are balanced, while the density of the plasma jumps discontinuously. The width of the heliosheath (distance between

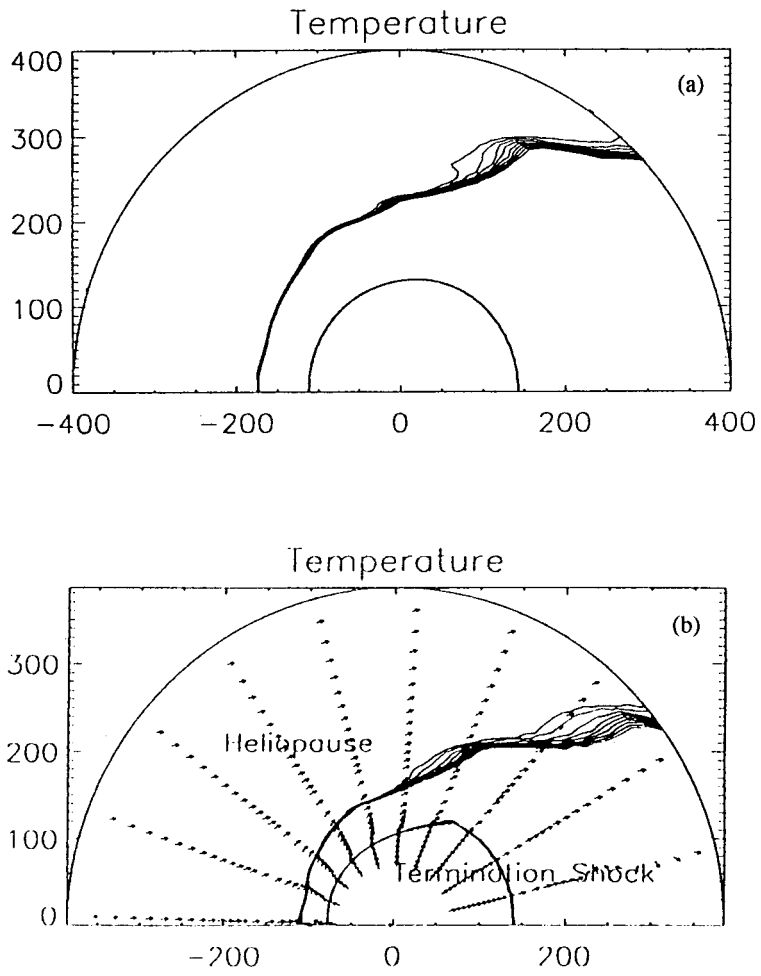

Figure 5.5. Nonlinear evolution of the Kelvin-Helmholtz instability along the heliopause for (a) a one-shock model, and (b) a two-shock model. Contours denote temperature and arrows flow direction. The perturbation is advected down the HP toward the tail. (Wang and Belcher, 1998.)

the TS and HP) at the nose ($\theta = 0°$) is $\sim$ 50 AU and the upstream TS is located at $\sim$ 120 AU. The heliocentric distance of the BS along the stagnation axis is $\sim$ 330 AU.

Consider the supersonic solar wind flow at $\theta = 0°$, as shown in Plate 5.1(b). The plasma shocks at the TS, and this subsonic suprathermal material starts to flow in the heliosheath to the tail region. Moving about the flanks of the TS, the flow accelerates to a supersonic state as shown by the presence of a sonic line (Mach number $M = 1.0$) in the heliosheath (Pauls et al., 1995). Since the supersonic heliosheath flow must eventually accommodate to the subsonic flow in the heliotail, a shock wave attached to the TS is necessary together with an additional contact

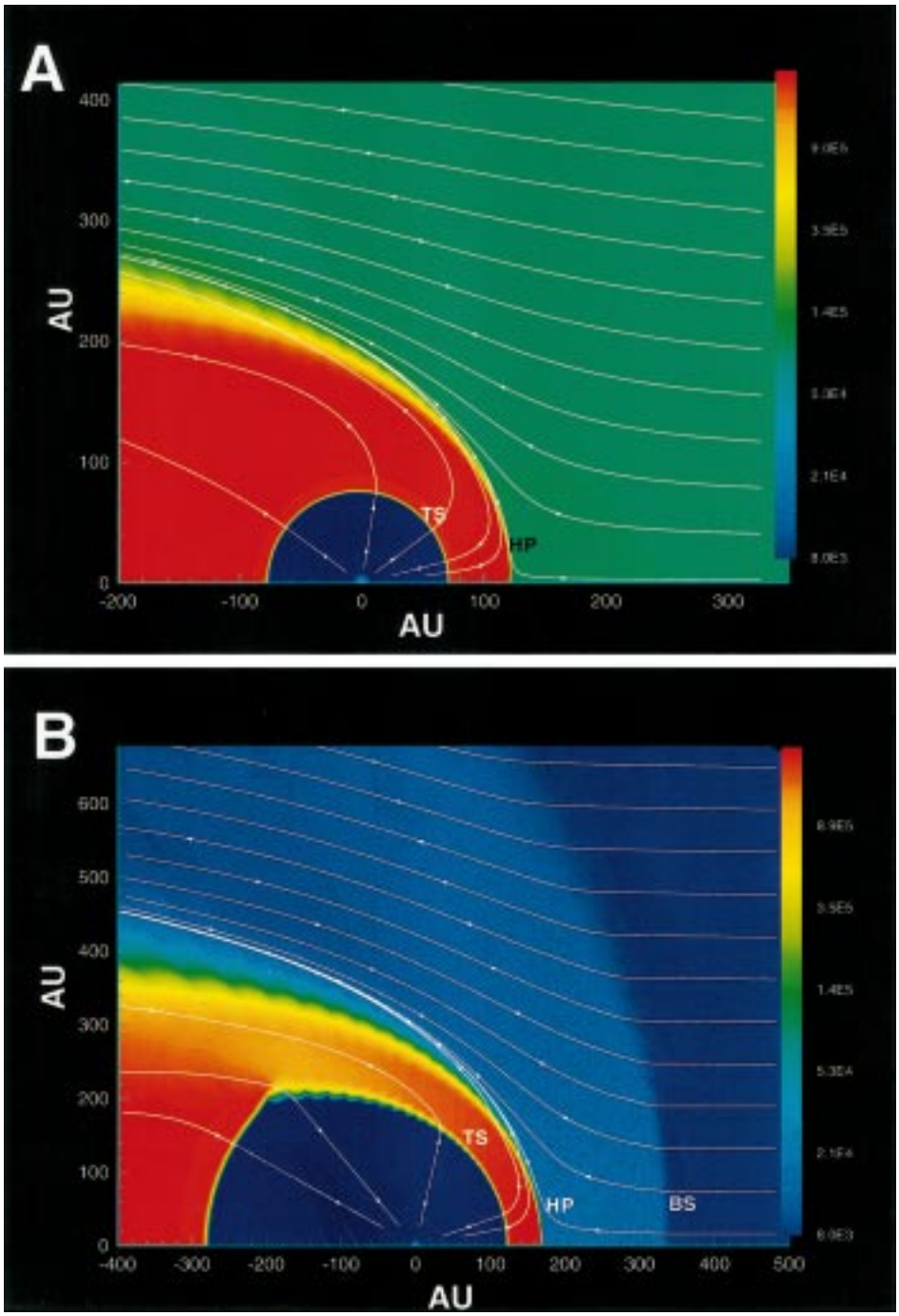

Plate 5.1. (a) Colour plot of the Log[Temp] for a 2D one-shock model. The termination shock (TS) and and heliopause (HP) are shown. (b) As with (a) except now for a two-shock model. A bow shock (BS) is now present.

discontinuity. As is evident from Plate 5.1(b), the supersonic flow shocks once again at the reflected shock and the re-shocked material meets the heliotail flow at a contact discontinuity.

Like the one-shock case discussed above, Wang and Belcher (1998) find that the HP is again Kelvin-Helmholtz unstable, an example of which is illustrated in Figure 5.5(b). However, it should be noted that the entire issue of the Kelvin-Helmholtz instability is far from resolved since both the magnetic field and resonant charge-exchange of ions with interstellar neutrals may stabilize some of the excited modes.

Karmesin et al. (1995) have considered briefly the effect of the solar wind ram pressure varying with solar cycle within a purely gas dynamic framework, both for a one-shock and a two-shock model. Lazarus and McNutt (1990) used 200-day averaged solar wind plasma data from Voyager 2 to show that the ram pressure can vary by about a factor of two over the solar cycle. By using a sinusoidally varying solar wind ram pressure over an 11 year period, Karmesin et al. (1995) found that the termination shock in the upstream direction oscilated about its mean position with a similar period, the excursions from equilibrium being typically $\sim$ 5% for a two-shock model and $\sim$ 8% for a one-shock model. The typical TS speeds are $\sim$ 12 - 14 km s^{-1}, which is close to the estimated 17 km s^{-1} speed of the Voyager 1 spacecraft.

5.3.2. *3D Models*

The 2D models discussed above assumed the solar wind to be isotropic, that is independent of heliolatitude. However, with the recent pass of *Ulysses* over the southern pole of the Sun (Smith et al., 1995), the three-dimensional structure of the solar wind can no longer be ignored. Measurements of the solar wind speed during this polar pass indicate that the solar wind speed increases from $\sim$ 400 km s^{-1} in the ecliptic plane to $\sim$ 700 km s^{-1} over the Sun's pole, while the proton number density decreases from $\sim$ 8 to $\sim$ 3 cm^{-3} in going from ecliptic to pole. The observed proton temperature also increases from $\sim$ 50 000 K to $\sim$ 200 000 K from ecliptic to pole (Phillips et al., 1995a). As shown by Phillips et al. (1995b), the heliolatitudinal variation results in an increase, by a factor of about 1.5, in the observed momentum flux in going from the ecliptic plane to the solar pole. These observations correspond to a solar wind consisting of two components, the first being a steady, long-lived hot, low-density, high-speed wind emanating from two large polar coronal holes, one in each hemisphere and extending down to about 35° heliolatitude, and bounding a cool, sluggish, high-density, somewhat turbulent solar wind. These conditions probably pertain to solar minimum only.

Pauls and Zank (1996) have extended their 2D gas dynamic models to 3D, thus including heliolatitudinal variation in the solar wind. Subsequently, Barnes (1998) investigated analytically the shape of the termination shock when latitudinal variation of the solar wind ram pressure is included. Both papers are discussed here.

5.3.2.1. *Analytical Model.* By means of a suitable generalization of the analysis outlined in Section 5.2 (Parker, 1961), Barnes (1998) was able to determine analytically the geometry of the TS as a function of colatitude θ. By assuming now that the radial velocity of the solar wind flow and density are functions of the spherical coordinates r and θ,

$$\mathbf{u} = u(\theta)\hat{\mathbf{r}} \quad \text{and} \quad \rho = \rho(r, \theta) \ ,$$

we may determine the TS geometry $r = R_t(\theta)$ as a function of $u(\theta)$ and $\rho(\theta)$. The normal to the termination shock is

$$\mathbf{n} = \frac{1}{\sqrt{1 + (R_t'/R_t)^2}} \left(1, -R_t'/R_t\right) \ , \tag{116}$$

and the angle between the upstream solar wind velocity and the shock normal is simply

$$\tan\alpha(\theta) \equiv -R_t'/R_t \ . \tag{117}$$

Use of the strong shock conditions for an oblique shock,

$$\begin{aligned} \frac{\rho_2}{\rho_1} &= \frac{u_1 \cos\alpha(\theta)}{u_1 \cos\beta(\theta)} = \frac{\gamma+1}{\gamma-1}, \quad w_1 \sin\alpha(\theta) = w_2 \sin\beta(\theta) \ ; \\ p_2 &= \frac{2}{\gamma+1}\rho_1 u_1^2 \cos^2\alpha \ , \end{aligned} \tag{118}$$

in the Bernoulli equation (96) yields the generalization of (98) as (Barnes, 1998)

$$\frac{(\gamma+1)^2}{R_t^2} - \frac{4}{R_t^2 + (R_t')^2} = \frac{2(\gamma^2-1)}{\rho u^2} p_\infty \ . \tag{119}$$

Unlike (98), Equation (119) is an ordinary differential equation for the shape of the TS which depends explicitly on the ram pressure profile $\rho u^2(\theta)$. Barnes (1998) does not solve (119) either analytically or numerically, but uses instead parameterized models for $R_t(\theta)$ from which $\rho u^2(\theta)$ can be determined and then compared to *Ulysses* observations. One such parametric representation is

$$\begin{aligned} &\frac{R_t(\theta)}{R_t(0^\circ)} = \\ &= \left\{1 - \frac{0.35}{2}\left(\frac{\pi}{12}\right)^{1/2}\left[\mathrm{erf}\left(\sqrt{12}\,\{-0.5 - \cos 2\theta\}\right) + \mathrm{erf}\left(1.5\sqrt{12}\right)\right]\right\} \ , \end{aligned}$$

which is illustrated in Figure 5.6. For reference, a spherical shock is plotted. Also plotted is the corresponding curve associated with assuming that $R_t(\theta) \propto [\rho u^2(\theta)]^{1/2}$. Evidently, the latitudinal dependence of the solar wind ram pressure requires that the TS must be oblique at some latitudes, so leading to an outward 'bulge' in the global shape of the termination shock. This follows immediately from the α

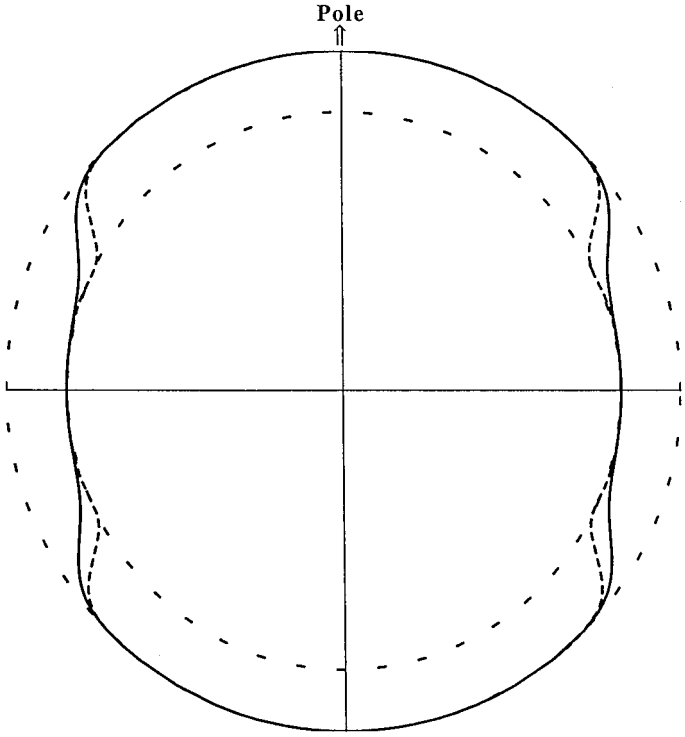

Figure 5.6. Polar plot of the position of the normalized TS location, $R_t(\theta)/R_t(0°)$ (solid curve). The short-dashed curve shows the TS position were $R_t(\theta) \propto [\rho u^2(\theta)]^{1/2}$ assumed. For reference, spherical shocks are plotted. (Barnes, 1998.)

dependence of the oblique shock conditions. Furthermore, there is a fairly substantial difference in the shock shapes for different assumed dependences of $R_t(\theta)$ on $\rho u^2(\theta)$.

By regarding the post-shock flow as incompressible, the streamlines in the heliosheath can again be determined from potential theory. Like Suess and Nerney (1991) and Khabibrakhmanov and Summers (1996), we are concerned here with the post shock flow and not the LISM flow. As before, there exists a scalar function $\phi(r, \theta)$ such that $\mathbf{q} = \rho^{1/2}\mathbf{u} = \nabla\phi$, and $\nabla^2\phi = 0$. Barnes (1998) expands ϕ in Legendre polynomials and assumes that $\mathbf{q} \to 0$ as $r \to \infty$. Thus, since $\phi(r, \theta) \simeq C + A/r + B\cos\theta/r^2$ for large r, A, B and C are constants to be determined. For $r \to \infty$,

$$\mathbf{q} = \rho^{1/2}\mathbf{u} \simeq -\frac{1}{r^2}\left(\left[A + \frac{2B}{r}\cos\theta\right]\hat{\mathbf{r}} + \frac{B}{r}\sin\theta\hat{\theta}\right) , \tag{120}$$

and $|\mathbf{q}|$ is essentially independent of θ for large r. The flux of $\mathbf{q}$ over that part of the shock surface lying poleward of colatitude θ is, from (116), (119) and (120),

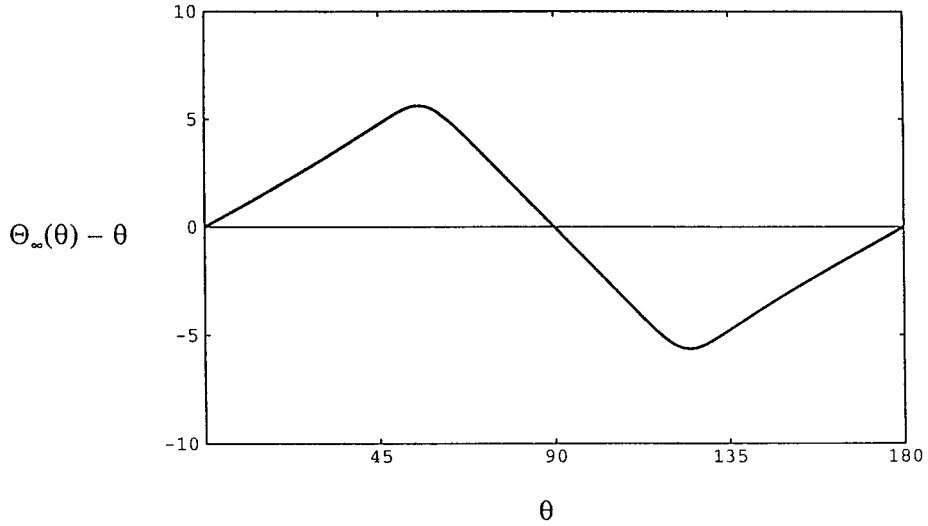

Figure 5.7. Equatorward deflection of the post-shock flow as described by $\theta_\infty(\theta)$. The figure shows that a streamline that intersects at colatitude 60° will bend toward the equator, asymptotically approaching a colatitude of $\sim 66°$ at large heliocentric distances. (Barnes, 1998.)

$$\begin{aligned} F_q(\theta) &= \int\limits_{\substack{\text{colat}<\theta \\ r=R_t}} \mathbf{q}\cdot\mathbf{n}\,\mathrm{d}A \\ &= 2\pi\left(\frac{\gamma-1}{\gamma+1}\right)^{1/2}\int\limits_0^\theta \left[\rho(\theta')u^2(\theta')\right]^{1/2} R_t(\theta')\sin(\theta')\,\mathrm{d}\theta' \,. \end{aligned} \tag{121}$$

The flux through the entire surface is $F_q(\pi)$ and has the same value on all surfaces outside the shock. Thus, since $|\mathbf{q}|$ is independent of θ as $r \to \infty$, the flux of $\mathbf{q}$ poleward of θ on the sphere at infinity is

$$F_q^\infty(\theta) = \int\limits_{\substack{\text{colat}<\theta \\ r\to\infty}} \mathbf{q}\cdot\mathbf{n}\,\mathrm{d}A = \frac{1}{2}F_q(\pi)(1-\cos\theta)\,. \tag{122}$$

From equations (121) and (122), it follows that a streamline which intersects the shock surface at colatitude θ tends to colatitude

$$\theta_\infty(\theta) = \cos^{-1}\left[1 - \frac{2}{F_q(\pi)}F_q(\theta)\right]\,, \tag{123}$$

as $r \to \infty$. Expression (123) indicates that the post-shock flow is deflected towards the equator, as illustrated in Figure 5.7, for a prolate termination shock.

5.3.2.2. *Numerical Model* A comprehensive 3D simulation of both one-shock and two-shock heliospheric configurations has been presented by Pauls and Zank

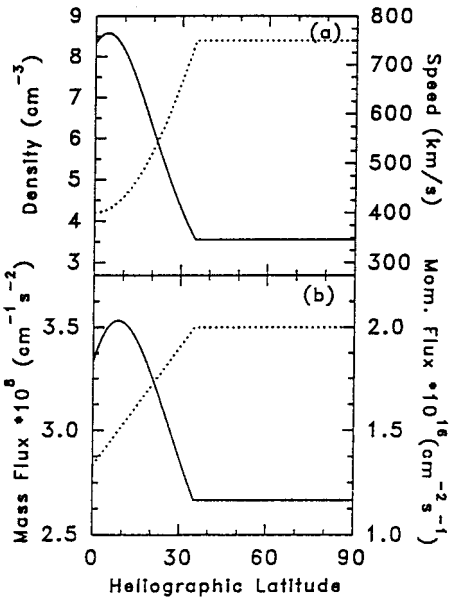

Figure 5.8. Solar wind boundary conditions used at Earth as a function of heliolatitude for the 3D simulations of Pauls and Zank (1996, 1997). The solid lines in both plots refer to the left y-axis and the dashed line to the right y-axis. (Pauls and Zank, 1996.)

TABLE VI

LISM parameters used for the simulations

	Two-shock model	One-shock model
n, cm^{-3}	0.1	0.1
v, km s^{-1}	26	26
T, K	8000	74, 000
M	1.75	0.74

(1996) using initial data that correspond to the *Ulysses* heliographic plasma observations (illustrated in Figure 5.8). The LISM parameters are tabulated in Table VI. Pauls and Zank (1996) present a detailed comparison of models which assume either an isotropic solar wind or an anisotropic solar wind. Both the one-shock and two-shock isotropic solar wind models are essentially identical to those described in Section 5.3.2 and we concentrate here on the anisotropic models.

Shown in Plates 5.2 and 5.3 are two planar cuts through the three-dimensional heliosphere for a supersonic LISM. Plate 5.2 shows the log T and normalized flow vectors in a cut through the ecliptic plane, while Plate 5.3 shows these values in the polar plane. Comparing these two plots, one observes that the TS is bullet-shaped and elongated along the poles of the Sun. The elongation results from the increased

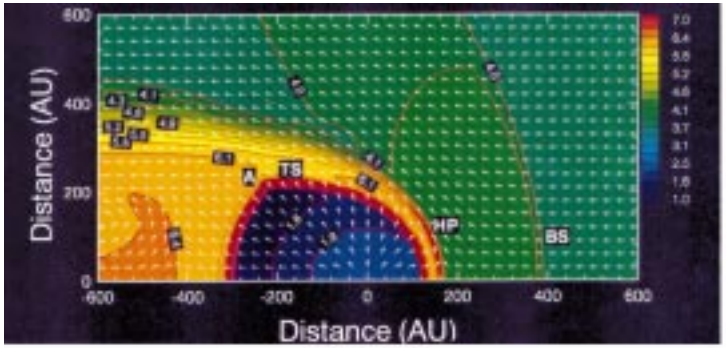

Plate 5.2

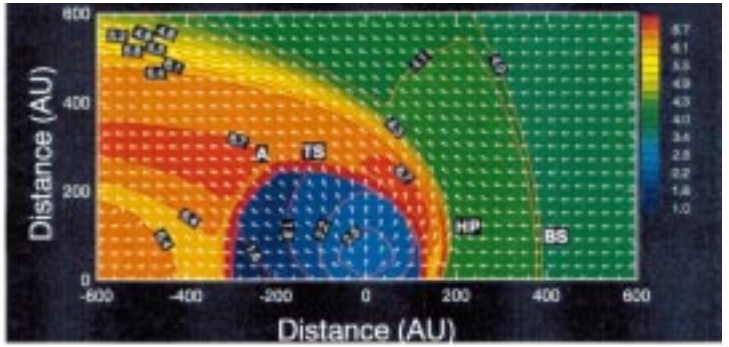

Plate 5.3

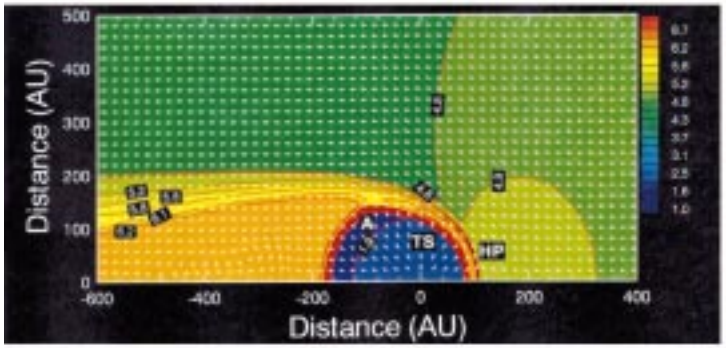

Plate 5.4

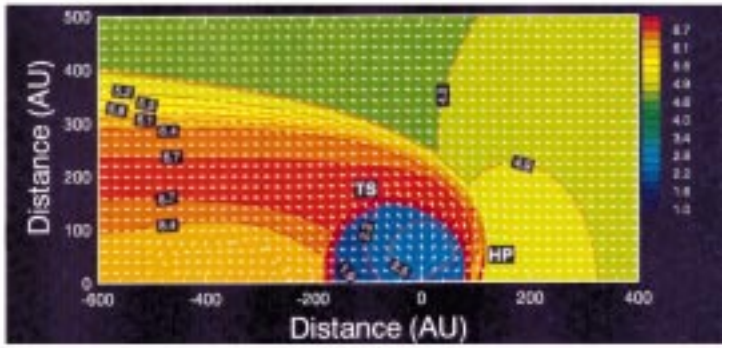

Plate 5.5

Plate 5.2. (a) Log[Temp] (contour and colour) and normalized flow vectors in the ecliptic plane for a two-shock anisotropic solar wind. The position of the triple point in the flow is identified by A. (Pauls and Zank, 1996.) (Plate 5.3) As in Plate 5.2 except now for the polar plane. (Pauls and Zank, 1996.) (Plate 5.4) Log[Temp] (contour and colour) and normalized flow vectors in the ecliptic plane for a one-shock anisotropic solar wind. Note the presence of the triple point in the flow, identified by A. The bow shock (BS) is absent. (Pauls and Zank, 1996.) (Plate 5.5) As with Plate 5.4 except now for the polar plane. (Pauls and Zank, 1996.)

TABLE VII

Distances to the boundaries for the case of a supersonic LISM. Heliocentric distances are given in astronomical units. TS is the termination shock, HP is the heliopause, and BS is the bow shock

	Isotropic solar wind				Anisotropic solar wind			
	Nose	Ecliptic	Pole	Tail	Nose	Ecliptic	Pole	Tail
TS	133	186	186	300	133	195	230	320
HP	186	290	290	–	163	240	360	–
BS	350	–	–	–	380	–	–	–

solar wind ram pressure with heliolatitude, hence the increase in distance to the TS and consequently the HP over the poles of the Sun (see Table VII for a list of the distances to the boundaries). The shocked solar wind and interstellar material at the nose flow to the tail region in the ecliptic plane, rather than taking the longer route over the poles of the Sun. Streamlines for an isotropic and an anisotropic solar wind are illustrated in Figure 5.9. In the isotropic case, the streamlines diverge uniformly over the heliosphere, both in the post-TS and in the post-BS regions. By contrast, the anisotropic solar wind model has streamlines which congregate in the ecliptic plane region. This is a consequence of the $-\nabla P$ force in the region of the stagnation point, in the direction of the flow along the HP, being much greater in the ecliptic plane than in the polar plane. Hence the shocked solar wind and the shocked interstellar wind in the region of the nose is forced to flow to the tail in the ecliptic plane rather than over the poles of the Sun.

Since the solar wind ram pressure increases as a function of heliolatitude, the distance to the TS in the polar plane (shown in Plate 5.3) increases more rapidly with heliolatitude than that in the case of an isotropic solar wind. This leads to a slightly higher pressure at the stagnation point for the anisotropic solar wind than an isotropic solar wind. The higher pressure forces the BS further out (350 AU for the isotropic solar wind compared to 380 AU for the anisotropic solar wind). Another consequence of the ram pressure increase with heliolatitude is the rapid increase in distance to the HP with latitude in the region of the nose, as can be seen from Plate 5.3. Although not shown, a cut through the three-dimensional solution in a plane perpendicular to the stagnation line through the origin, reveals an hour glass shape for the HP, with the elongation along the solar poles. This is also seen from Table VII by comparing the sidestream distances to the HP in the ecliptic plane (240 AU) to that over the poles of the Sun (360 AU).

From Table VII, it is seen that the width of the heliosheath at the nose decreases from 53 AU in the isotropic solar wind case to 30 AU for the anisotropic solar wind. The reason for this decrease is a consequence of an increase in the LISM ram pressure acting on the HP. The shocked LISM flow for the anisotropic solar

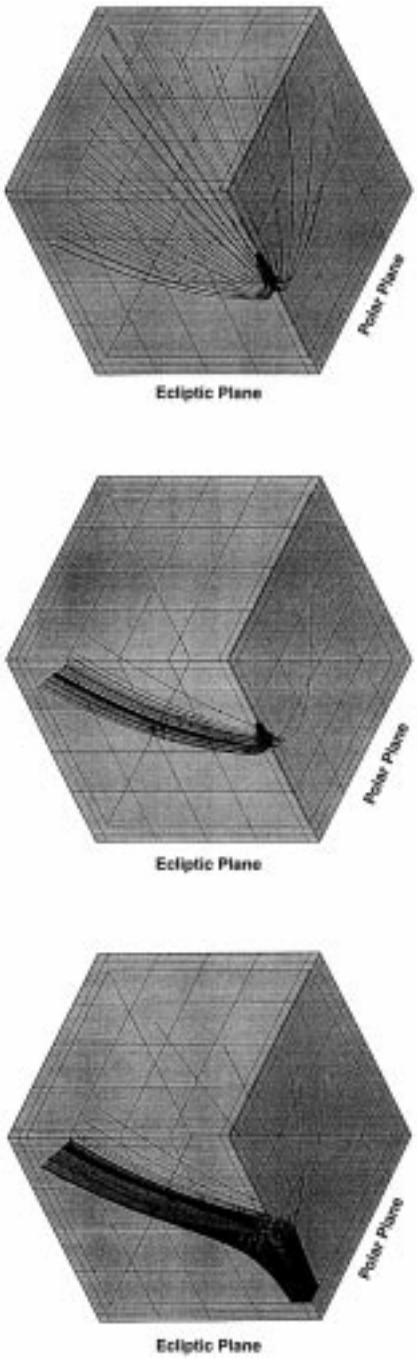

Figure 5.9. Streamline plots for the anisotropic 3D simulations of Pauls and Zank (1996). (a) The shocked solar wind streamlines for an assumed isotropic solar wind. (b) the shocked solar wind streamlines for an anisotropic solar wind. (c) The shocked LISM flow streamlines for an anisotropic solar wind. The ecliptic and polar planes are labeled.

wind case is forced to flow to the heliotail in the ecliptic plane rather than uniformly over the heliosphere (Figure 5.9) as is the case for the isotropic solar wind. This then leads to an increase in the LISM ram pressure acting on the interstellar side of the HP. The same argument holds for the heliosheath flow, but to a lesser extent. This enhanced shocked LISM ram pressure forces the HP closer to the Sun.

The increased heliosheath flow in the ecliptic plane results in a weakly time-dependent, turbulent flow in the heliotail, as can be seen from the roll-ups in the heliotail flow pattern (Plates 5.2 and 5.3). The shocked solar wind flow, rather than diverging equally in all directions as it does in the isotropic solar wind case, remains predominantly in planes parallel to the ecliptic plane. The rotational heliotail flow also occurs in planes parallel to the ecliptic. The axis of rotation of the flow is perpendicular to the ecliptic plane. Pauls and Zank (1996) ascribe the existence of vortices in the heliotail to gradients in the pressure and density, exacerbated by an anisotropic solar wind, acting as vortical source terms.

One-dimensional profiles of the number density, flow speed, and temperature as a function of heliocentric distance at the nose (solid line), sidestream in the ecliptic plane (dashed line), pole (dotted-dashed line), and in the tail (dotted line) are shown in Figure 5.10. The vortices in the tail flow are seen as a jump in density and temperature, with the flow speed becoming negative (i.e., flowing toward the Sun). The shocked polar solar wind also has a higher temperature than that in the ecliptic plane, this a consequence of the very strong polar TS and high ram pressure over the poles.

By modifying the LISM conditions appropriately (Table VI), a one-shock 3D gas dynamics model was also investigated by Pauls and Zank (1996). Planar cuts through the three-dimensional solution for this simulation are shown in Plates 5.4 and 5.5. Plate 5.4 shows the $\log T$ contours and normalized flow vectors in the ecliptic plane, while Plate 5.5 shows these values in the polar plane. The ram pressure increase with heliolatitude elongates the TS along the poles. This elongation forces the solar wind and LISM flow at the nose to flow in the ecliptic plane for the same reasons as discussed above. The increased flow in the ecliptic plane forces the heliosheath flow to become supersonic, thereby necessitating the introduction of a triple point (A) in the region close to the ecliptic plane (see Plate 5.4). The triple point vanishes for heliolatitudes greater than $\sim 30°$, yielding a Mach disc with a 'pie slice' structure, centered on the stagnation line, and tracing the triple point up to $\pm 30°$ in heliolatitude.

When compared to the isotropic solar wind model, the heliosheath width in the ecliptic plane is reduced for the anisotropic solar wind. Since the TS is elongated along the poles of the Sun, the shocked LISM material is forced to flow to the heliotail in the ecliptic plane, increasing the ram pressure acting on the HP at the nose. The same process also acts on the solar wind side of the HP, but to a lesser extent, and hence the HP moves closer to the Sun.

The increased flow in the ecliptic plane as well as the enhanced pressure and density gradients generate turbulent flow in the heliotail, just as in the two-shock

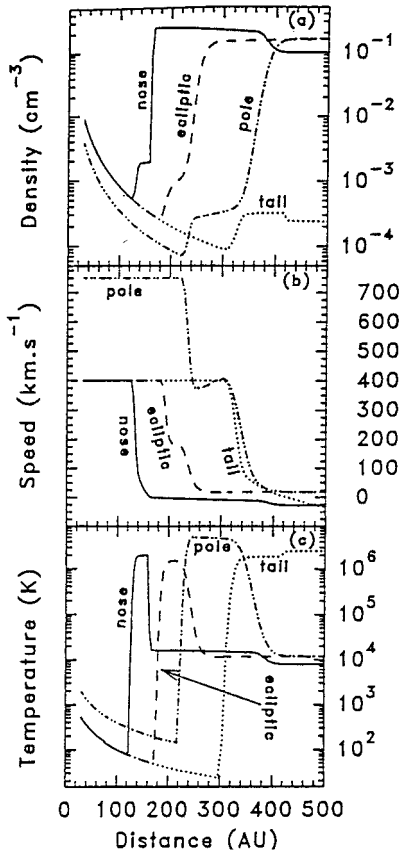

Figure 5.10. (a) Density, (b) speed, and (c) temperature as a function of heliocentric distance for the two-shock anisotropic solar wind case. Nose refers to flow along the direction of the nose/stagnation point, ecliptic to the sidestream flow in the ecliptic plane, pole to the sidestream flow in the polar plane, and tail to the flow in the direction of the tail. (Pauls and Zank, 1996.)

model. The continuous shedding of shocked solar wind material yields a weakly time-dependent solution of the gas dynamic equations and a periodically oscillating TS in the tail, the oscillation having amplitudes of $\sim$ 20 AU with a period of $\sim$ 100 years. As in the two-shock simulation, the time-dependent behaviour is confined to the heliotail and does not influence the nose or sidestream distributions.

Finally, Figure 5.11 shows the number density, flow speed, and temperature as a function of heliocentric distance at the nose (solid line), sidestream in the ecliptic plane (dashed line), pole (dotted-dashed line), and in the tail (dotted line) for the one-shock model. The distance to the boundaries for both an isotropic and anisotropic solar wind are listed in Table VIII.

TABLE VIII

Distances to the boundaries for the case of a subsonic LISM. Heliocentric distances are given in astronomical units. TS is the termination shock, HP is the heliopause, and BS is the bow shock

	Isotropic solar wind				Anisotropic solar wind			
	Nose	Ecliptic	Pole	Tail	Nose	Ecliptic	Pole	Tail
TS	87.6	120	120	165	87.6	125	150	175
HP	125	180	180	–	110	150	230	–

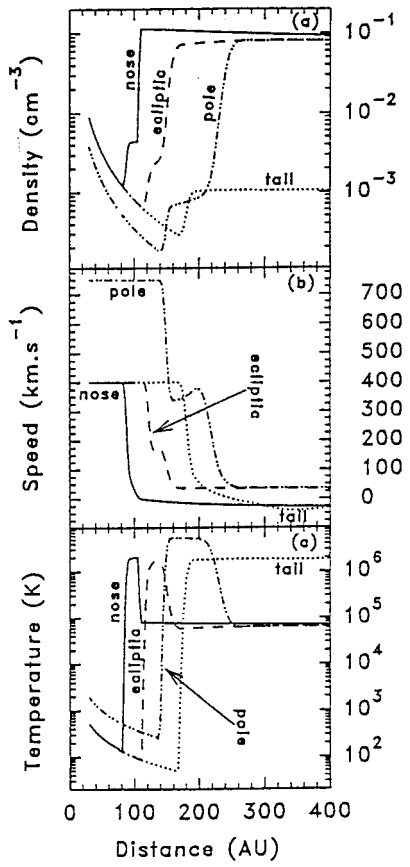

Figure 5.11. (a) Density, (b) speed, and (c) temperature as a function of heliocentric distance for one two-shock anisotropic solar wind case. (Pauls and Zank, 1996.)

5.4. GLOBAL SIMULATIONS: NEUTRAL HYDROGEN (H) ONLY

To enter the heliosphere, a hydrogen atom has to cross three thermodynamically distinct regions, as discussed in Section 2.1. Through resonant charge exchange, the diverging LISM flow and the shocked solar wind flow act to divert some fraction of the incident interstellar neutral H flux away from the heliosphere. This effective swapping of trajectories by an interstellar neutral and a proton can also lead to an enhancement in the neutral interstellar density and temperature in the vicinity of the solar wind-LISM stagnation region. As discussed by Wallis (1984), the charge exchange process should be regarded as a scattering rather than an extinction process since charge exchange effectively produces a new neutral population with a velocity distribution that resembles that of the source plasma distribution. One may then, by analogy with isotropic photon scattering by a non-absorbing plane-parallel layer, estimate the depletion of incident neutral H. For interstellar neutral hydrogen, the density is reduced by a factor (Wallis, 1984; Holzer, 1989)

$$\mathcal{F} = 1 - \left[1 - f_1/f_0\right](1 - \exp[-\tau_{\rm H}]) \equiv 1 - F\,(1 - \exp[-\tau_{\rm H}])\ , \qquad (124)$$

where f_1 is the fraction of newly produced neutral H that enters the heliosphere and f_0 is the fraction of the incident neutral H that enters. The 'optical depth' $\tau_{\rm H} \equiv \beta n_p L$ depends on the plasma number density n_p and the characteristic length scale L over which the LISM flow is diverted. β is a parameter $\sim 5 \times 10^{-2}$. For typical parameters, Holzer (1989) finds $F \leq 0.15$ and $\mathcal{F} > 0.95$.

The same scattering process can be applied to neutral H experiencing charge exchange in the subsonic solar wind. The newly created neutrals will have a high temperature ($\sim 10^6$ K) and a Maxwellian velocity distribution like that of the heated solar wind protons. Holzer (1989) estimated an exclusion factor of $F \geq 0.4$ and the 'optical depth' is now approximately $\tau_{\rm H} \sim (9/R_t)[(R_{\rm H} - R_t)/R_t]$, where $R_{\rm H}$ is the minimum heliocentric distance to the heliopause. Taking $R_{\rm H}/R_t \sim 2$, and $R_t \sim 100$ AU, Holzer finds that $\mathcal{F} > 0.95$.

The precise factor for the reduction in neutral H density as it crosses the heliospheric boundaries into the heliosphere, as determined above, is not especially important. What is clear from elementary arguments is that the heliospheric boundaries form quite an effective barrier to interstellar neutral hydrogen. Thus, to relate the interstellar H distribution to that observed in the solar system (by either Lyman-α backscatter observations or by direct satellite measurements) requires that the assumed background plasma distribution include the solar wind – LISM interaction region at some level. In this subsection, we describe two approaches to the multi-dimensional test-particle modelling of the flow of interstellar neutral gas through the heliospheric interface. The first is a method, developed by Fahr and his collaborators (for a review, see e.g., Fahr, 1996), which solves the Boltzmann equation by expanding the distribution function into collision hierarchies. The second approach that we discuss is a particle-mesh method developed by Lipatov et al. (1998).

5.4.1. *The Direct Boltzmann Method*

The basic approach to solving the Boltzmann equation (1) by means of collision hierarchies was described in Ripkin and Fahr (1982) and Fahr and Ripkin (1984). A more sophisticated and rigorous representation of the collisional production term has since been developed by Osterbart and Fahr (1992), whose approach we follow. This approach addresses the criticisms that Wallis (1984) directed at the original simpler approach.

The stationary Boltzmann equation (1) can be expressed in terms of the characteristic s as

$$\frac{\mathrm{d}}{\mathrm{d}s} f(\mathbf{x}, \mathbf{v}) = \frac{1}{v}\left[\mathbf{v}\cdot\nabla + \frac{\mathrm{d}\mathbf{v}}{\mathrm{d}t}\cdot\nabla_{\mathbf{v}}\right] f(\mathbf{x}, \mathbf{v}) = \frac{1}{v}\left[P(\mathbf{x}, \mathbf{v}) - L(\mathbf{x}, \mathbf{v})\right] , \tag{125}$$

and L can be factored according to (2) as before. The distribution function f is expanded in a series

$$f(\mathbf{x}, \mathbf{v}) = \sum_j f_{j-1}(\mathbf{x}, \mathbf{v}) , \tag{126}$$

where the f_j correspond to atoms that have experienced resonant charge exchange j times already (i.e., prior to their arrival at $\mathbf{x}$, the atom has exchanged charge j times already). Equation (125) may then be separated into a system of equations for each f_j,

$$\frac{\mathrm{d}f_j}{\mathrm{d}s} = \frac{1}{v}\left[P_{j-1} - \beta_{\mathrm{ex}} f_j\right] . \tag{127}$$

The production term depends only on f_{j-1}, i.e.,

$$P_{j-1} = P_{j-1}(f_{j-1}(\mathbf{x}, \mathbf{v})) ,$$

and is given by expression (8). Equation (127) therefore admits the solution

$$\begin{aligned} f_j(\mathbf{x}, \mathbf{v}) \;=\; & f_{j,\infty}(\mathbf{v}_\infty) \exp\left(-\int_\infty^s \beta'_{\mathrm{ex}} \frac{\mathrm{d}s'}{v'}\right) + \int_\infty^s P'_{j-1} \frac{\mathrm{d}s'}{v'} \\ & \times \exp\left(-\int_{s'}^s \beta''_{\mathrm{ex}} \frac{\mathrm{d}s''}{v''}\right) , \end{aligned} \tag{128}$$

from which $f(\mathbf{x}, \mathbf{v}) = \sum_j f_j(\mathbf{x}, \mathbf{v})$. The function $f_{j,\infty}$ is the LISM distribution at infinity and, of course, $f_{j,\infty} = 0$ for all $j \neq 0$.

To evaluate the series of equations (127) requires the explicit assumption of a thermodynamic model of the heliosphere and its boundaries. Fahr and his colleagues (Ripkin and Fahr, 1982; Osterbart and Fahr, 1992; Fahr and Osterbart, 1993; Fahr et al., 1995; Fahr, 1996) adopt analytic models of the heliosphere described in Section 5.2 and illustrated in Figure 5.3. It is also assumed that the

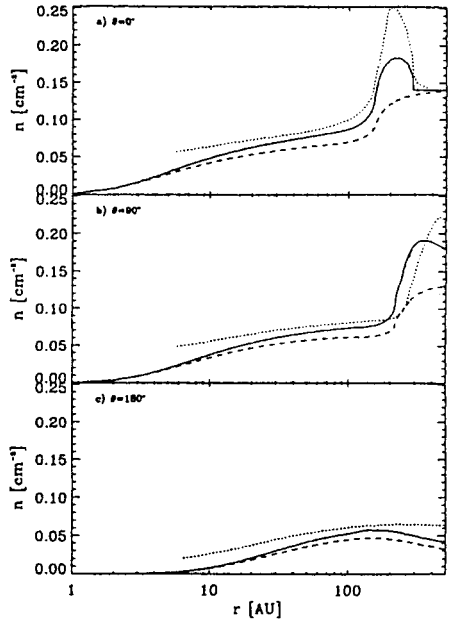

Figure 5.12. Hydrogen densities obtained using a one-shock model (dashed curve), a two-shock model (solid curve), and, for comparison, results from a self-consistent 2D simulation (Baranov and Malama, 1993). (Fahr, 1996.)

proton distribution function in each of the thermodynamically distinct regions (regions 1, 2, and 3) is Maxwellian, allowing $P_{j-1}(\mathbf{x}, \mathbf{v})$ in (127) to be expressed as equation (9). Similarly, for an assumed Maxwellian proton distribution, β_{ex} can be approximated adequately by (11). Additional ionization processes such as electron impact ionization can be included in the collision hierarchy scheme in a relatively straightforward fashion (Osterbart and Fahr, 1992).

Both the one-shock and two-shock models are considered, although using analytic approximations for the global heliospheric structure. Using LISM values of $u_\infty = 25$ km s^{-1}, $n_{\text{H},\infty} = 0.14$ cm^{-3}, $T_{\text{H},\infty} = 10^4$ K, the 2D neutral H densities obtained numerically from (127) are illustrated in Figure 5.12 for three sightlines (upstream, sidestream, downstream). The one-shock model is depicted by the dashed lines, the two-shock model by solid lines, and, by way of comparison, a model by Baranov and Malama (1993) (see Section 5.5). The two-shock model is seen to produce a clear enhancement in the neutral number density upstream of the HP. The enhancement persists into the sidestream direction and a 'hydrogen wall' upstream of the direction of heliospheric motion is formed. In the heliotail region, the neutral hydrogen is considerably depleted compared to its undisturbed LISM value. By contrast, the one-shock model produces no enhancement or wall in the upstream direction but the boundaries again act to filter neutral interstellar H as it enters the heliosphere. Typical interplanetary number densities are roughly half or less than those in the undisturbed LISM.

Quite significant differences exist between the two-shock neutral densities of Fahr (1996) and those of Baranov and Malama (1993). It is possible that part of the discrepancy between the two approaches has to do with the assumed incompressible flow in the analytic models used by Fahr and his collaborators. Nonetheless, it should be recognized that modelling the passage of interstellar neutral H through the heliosphere is exceedingly difficult and different approaches by various groups have yet to be synthesized into a set of consistent results. Certainly, the absence of a hydrogen wall in the one-shock case may be ascribed to the somewhat simple incompressible analytic model of the LISM flow in the vicinity of the heliosphere.

5.4.2. *Particle-Mesh Boltzmann Simulations*

In the preceding subsection (see also Section 2.2), it was assumed that both the neutral and proton distribution functions are Maxwellian in the different thermodynamic regions (1, 2, and 3). This assumption allowed for the simplification of the charge exchange production and loss terms, which simplified the integro-Boltzmann equation significantly. However, while the characteristic scale of the ionized components is determined usually by the typical ion gyroradius, which is much less than characteristic global heliospheric scales of interest, the mean free path of neutral particles is comparable to characteristic heliospheric scales such as the distances separating the bow shock and heliopause, the heliopause and termination shock, and even the radial extent of the supersonic solar wind. Consequently, the Knudsen number $Kn = \lambda/L$ (λ the mean free path of neutral particles and L a characteristic heliospheric scale), which is a measure of the distribution relaxation distance, satisfies $Kn \approx 1$. Thus, it is difficult to simply assume that the neutral H distribution can relax to a Maxwellian distribution and one needs ideally to solve the full Boltzmann equation for the neutral component without the simplifying assumptions described above.

Lipatov et al. (1998) have adopted a particle-mesh method to simulate the interaction of neutral H with the heliosphere. The particle-mesh method exploits a force-at-a-point formulation and a field equation for the potential. Field quantities are represented approximately by values on a regular array of mesh points and differential operators are replaced by finite-difference expressions on the mesh. Potentials and forces at particle positions are obtained by interpolating on the array of mesh-defined values. Mesh-defined densities are obtained by assigning particle attributes to nearby mesh points to create the mesh-defined values (see e.g., Lipatov, 1996; Hockney and Eastwood, 1981).

Lipatov et al. (1998) assume that the distribution function for centers of the neutral macroparticles may represented by a set of δ functions,

$$f = \sum_{i=1}^{N_p} \alpha_i \delta(\mathbf{x} - \mathbf{x_i})\delta(\mathbf{v} - \mathbf{v_i}) \ , \tag{129}$$

where $\alpha_i = \alpha_i(t)$ denotes the weight of an individual macroparticle with number i and $\mathbf{x}_i = \mathbf{x}_i(t)$, $\mathbf{v}_i = \mathbf{v}_i(t)$ are the coordinates of macroparticles in phase space.

Summation is over all macroparticles N_p. The neutral macroparticle is described by 7 (i.e., a 2.5D model) scalar components *viz.*, the weight of a macroparticle α_i, the position $\mathbf{x}_i$, velocity $\mathbf{v}_i$, and the survival probability w of the ith macroparticle against photoionization and charge-exchange. The equation of motion for the neutral particles is, of course,

$$\frac{\mathrm{d}\mathbf{v_i}}{\mathrm{d}t} = \mathbf{F}_i/M_n; \quad \frac{\mathrm{d}\mathbf{x_i}}{\mathrm{d}t} = \mathbf{v}_I \ , \tag{130}$$

where the force acting on the neutral particle $\mathbf{F}_i = \mathbf{F}_g + \mathbf{F}_r$ results from a balance of the solar gravitational force $\mathbf{F}_g$ and radiation pressure $\mathbf{F}_r$. Here M_n is the mass of the atom.

The survival probability against a charge exchange event is given by

$$w_{ex,i} = \exp\left[-\int_{t_0}^{t} \beta_{ex,i}\ \mathrm{d}t \right] \ , \tag{131}$$

and the index i indicates that integration is over the ith particle trajectory. The term β_{ex} is defined again by equation (11).

At the time of creation (either at the boundary of the calculation box, or at the moment of charge exchange), a neutral macroparticle has initial coordinates $\mathbf{x}_i(t_0) = \mathbf{x}_{i,0}$, $\mathbf{v}_i(t_0) = \mathbf{v}_{i,0}$, a weight $\alpha_i(t_0) = \alpha_{i,0}$, and a survival probability $w_{ex,i}(t_0) = 1$. For each new neutral particle i, the critical probability $w^*_{ex,i}$ when charge exchange will occur must be determined and this is done using the relation

$$w^*_{ex,i} = \xi \ , \tag{132}$$

where ξ is random number drawn from the interval [0, 1]. Those particles for which the probability of survival satisfies the condition

$$w_{ex,i} \leq w^*_{ex,i} \ , \tag{133}$$

must exchange their (macroparticle) velocity with the velocity of a proton from the ionized component of the LISM or the solar wind. This is accomplished using a random generator for a Maxwellian proton distribution. If charge exchange occurs, then a new neutral macroparticle begins its motion with $w_{ex,i} = 1$.

By means of (129), the appropriate source term for the neutral distribution can be computed, together with the total loss rate (Lipatov et al., 1998).

Lipatov et al. (1998) consider two different two-shock configurations, differing only in the LISM temperature assumed. The H parameters used are $n_{\mathrm{H},\infty} = 0.14$ cm^{-3}, $u_{\mathrm{H},\infty} = 26$ km s^{-1}, and either $T_{\mathrm{H},\infty} = 8000$ K or 10 900 K. The ionized LISM parameters differ only in that $n_{\mathrm{H}^+,\infty} = 0.07$ cm^{-3} (see Section 5.5.1). Unlike the heliospheric model used by e.g., Fahr (1996), the background plasma model for the heliosphere used by Lipatov et al. was calculated using the multi-fluid

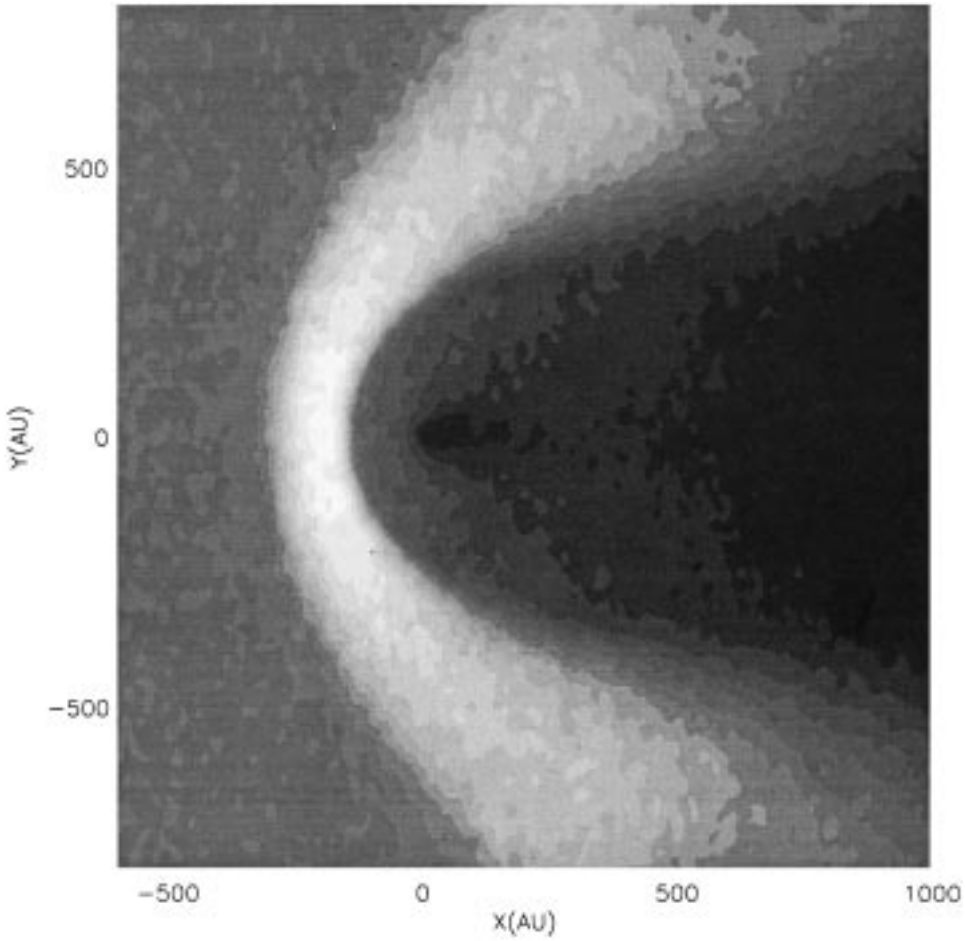

Figure 5.13. A two-dimensional distribution of the neutral hydrogen density obtained using a 2D Boltzmann simulation. (Lipatov et al., 1998.)

model of Zank et al. (1996) (see Section 5.5). The Zank et al. (1996) model incorporates neutral hydrogen self-consistently at a hydrodynamic level and can therefore be expected to provide a reasonably realistic plasma background. Nonetheless, the (Lipatov et al. (1998) approach is a test-particle calculation for the neutral H since there is no dynamical coupling of plasma to the neutrals.

Upstream of the detached bow shock, charge exchange does not greatly change the velocity distribution function of the neutral component. Nonetheless, a small increase in the neutral density ahead of the bow shock occurs thanks to atoms created in the solar wind which stream radially outwards. Between the bow shock and the heliopause, the neutral component is affected strongly by charge exchange with the (weak) shock heated, LISM ionized component. Figure 5.13 shows the two-dimensional distribution of the H density in the 2-D plane and Figure 5.14

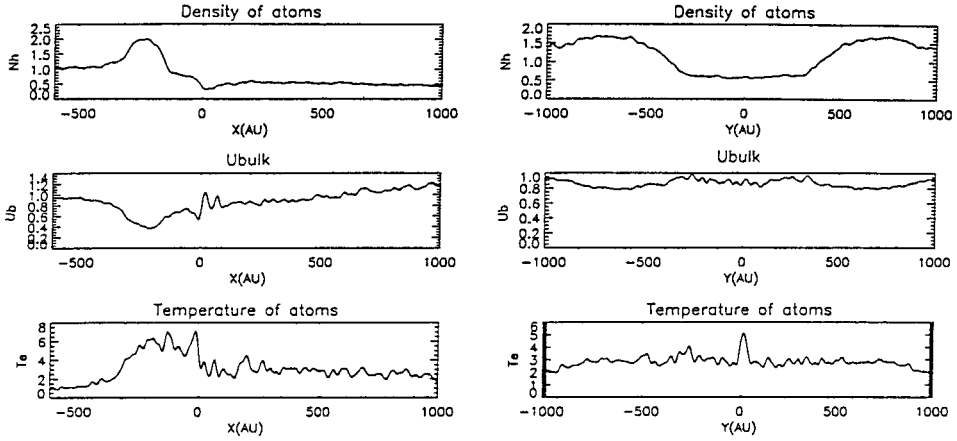

Figure 5.14. One-dimensional central cuts (from top to bottom) of the H density, the x component of the bulk velocity $u_{\rm bulk}$, and the temperature T_H in the $x(y = 0)$ direction (first column) and in the $y(x = 0)$ direction (second column). (Lipatov et al., 1998.)

illustrates 1-D line-of-sight profiles along and orthogonal to the stagnation axis for the H density $n_{\rm H}$, the bulk H velocity $u_{\rm bulk}$, and the effective temperature $T_{\rm H} \propto < \frac{1}{3}(\mathbf{V} - \mathbf{u}_{\rm bulk})^2 >$. Ahead of the bow shock, the neutral density and temperature increase significantly up to values of $n_{{\rm H},max} \approx 2n_{{\rm H}\infty}$ and $T_{\rm H} \approx 3 - 6T_{{\rm H}\infty}$, while the bulk velocity decreases.

At the heliopause ($x = 130AU$) the density of H decreases to $0.9n_{{\rm H}\infty}$, the temperature decreases slightly, $T_{\rm H} \approx 5T_\infty$, and the bulk velocity decreases to $0.3u_{{\rm H}\infty}$.

Between the termination shock and the heliopause, the density of H atoms decreases to $\sim 0.8 - -0.9n_{{\rm H}\infty}$ while the bulk velocity is reduced to $u_{\rm bulk} = (0.35 - 0.6)u_{{\rm H}\infty}$. The temperature of H atoms increases significantly from a heliopause value of $T_{\rm H} \approx 5T_{{\rm H},\infty}$ to $T_{\rm H} \approx 7T_{{\rm H},\infty}$ at the termination shock.

The global plasma configuration using the 8000 K temperature is a little different from that obtained from the 10 900 K simulations in that one has a slightly stronger bow shock, and a smaller separation distance between the bow shock and heliopause. As a result, the increase in the H density downstream of the bow shock is about 12% higher than in case with $T_\infty = 10\,900$ K, illustrated explicitly in Figure 5.15. The thickness of the H density profile at the heliopause is also much smaller than that of the high $T_{{\rm H},\infty}$ case. Furthermore, Lipatov et al. (1998) find that diffusion of neutral hydrogen through the bow shock and heliopause is smaller for the $T_\infty = 8000$ K case than for the higher temperature LISM model. In the supersonic solar wind, the H density profile does not depend strongly on the assumed LISM neutral hydrogen temperature.

The central and very important result of Lipatov et al. (1998) was their determination of the neutral hydrogen velocity distribution throughout the heliosphere. This is discussed in some detail here. The typical velocity distribution function

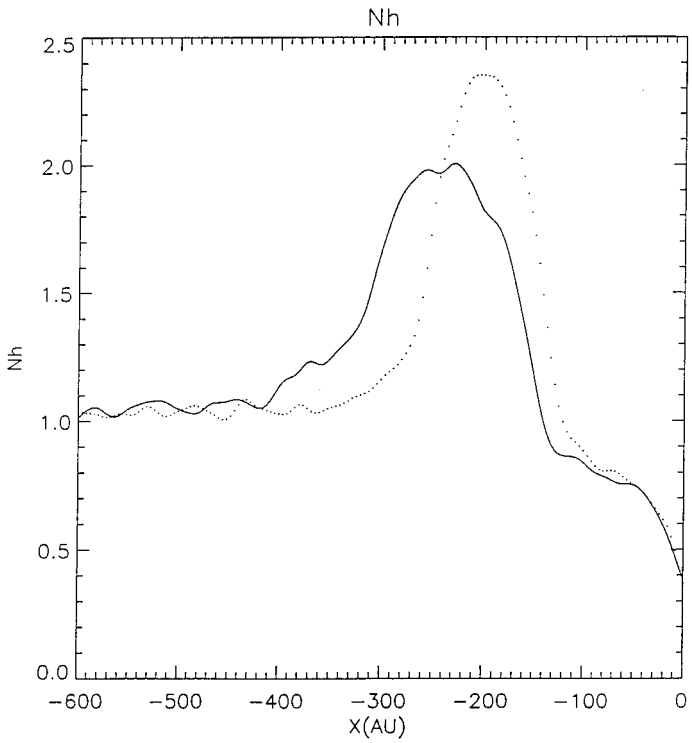

Figure 5.15. One-dimensional central cuts of the H density profile along the axis x for a Boltzmann simulation with $T_{H\infty} = 10,900$ K (solid line) and $T_{H\infty} = 8,000$ K (dotted line). (Lipatov et al., 1998.)

consists of several fairly distinct components: a large core, which corresponds to atoms originating in the LISM, slightly broadened by charge exchange with bow shock heated LISM material; a beam of hot neutral atoms originating from the subsonic solar wind, and a cooler beam of neutral H produced in the supersonic solar wind. Figure 5.16 shows the projection of the H velocity distribution function for different sections along the axis $x(y = 0)$, ordered according to the radial distances listed below. The initial LISM neutral H distribution is assumed to be a Maxwellian.

(1) Outside the bow shock, the H velocity distribution function consists of a strong core of slightly heated atoms originating in the LISM and a weak beam of neutral atoms produced by charge exchange in the heliosheath and the supersonic solar wind. Typical velocities in the beam are about $18u_\infty = 468$ km s^{-1} (Figure 5.16 (sect 1), $x = -300$ AU).

(2) Inside the bow shock, the H velocity distribution function consists of a core of heated atoms that are created by charge exchange between inflowing neutral atoms and the bow shock heated plasma, together with a tongue-like distribution produced by charge exchange in the heliosheath and supersonic solar wind.

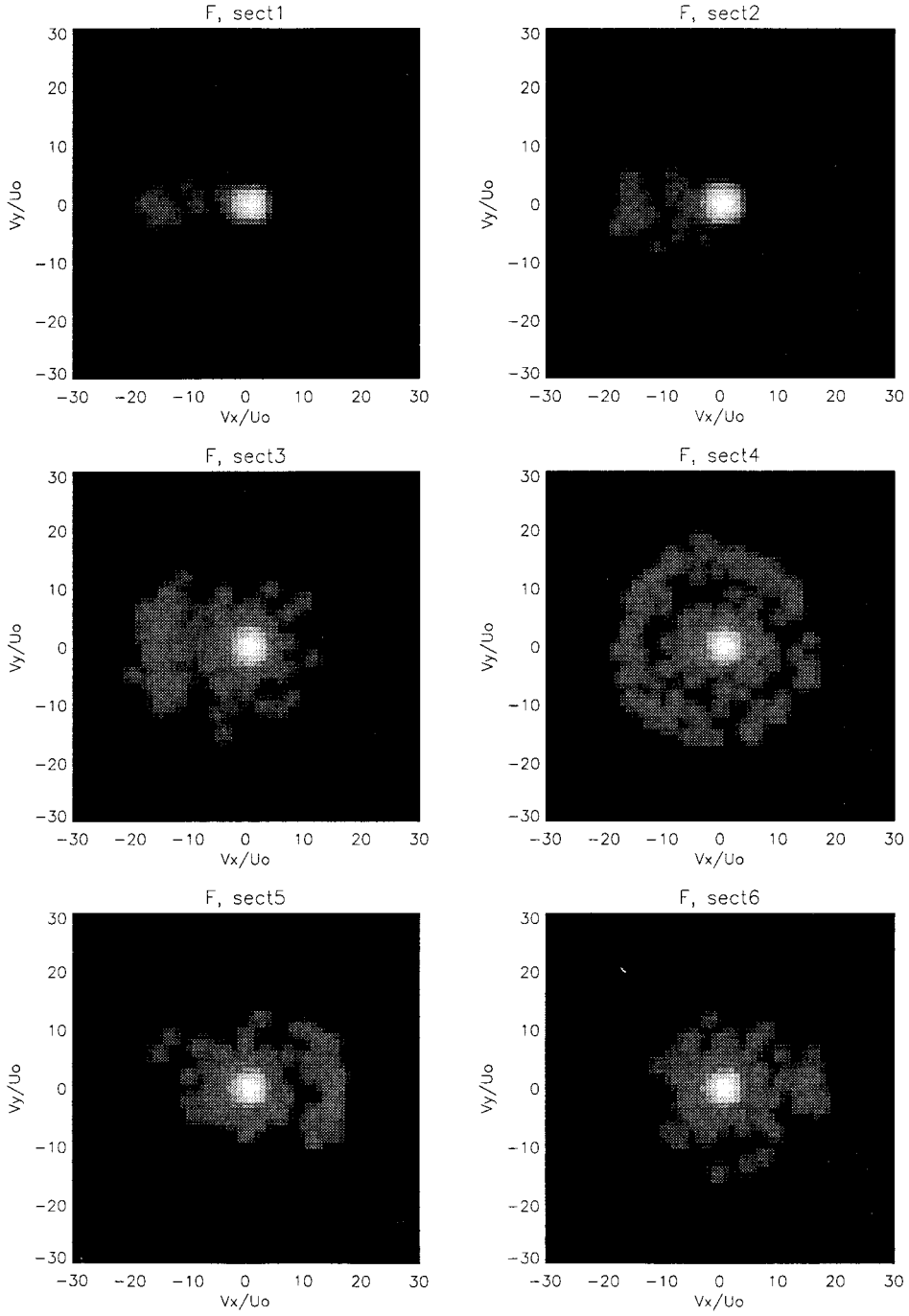

Figure 5.16. The projection of the neutral hydrogen velocity distribution function in the (v_x, v_y)-plane for different sections along the $x(y = 0)$ axis at different distances. From top to bottom: $x = -300$ AU, -200 AU, -100 AU; $+100$ AU; $+200$ AU (Lipatov et al., 1998).

The core is component 1 and the secondary or tongue component is component 2 (Zank et al., 1996b). The distribution is displayed in Figure 5.16 (sect 2) for $x = -200$ AU.

(3) Just downstream of the termination shock in the heliosheath, the H velocity distribution function (sect 3) consists of a component 1 core and a strong tongue-like beam (component 2), and a halo of heated atoms produced by charge exchange between H atoms and the supersonic solar wind (component 3/'splash' component). The velocity of halo atoms is comparable with the thermal velocity of supersonic solar wind protons.

(4) In the vicinity of the Sun, the H velocity distribution function consists of the component 1 core, the heated component 2 neutrals, and component 3 atoms (Figure 5.16 (sect 4) for $x = 0$ AU). Since the velocity distribution is smoothed over a large grid about the sun, component 3 exhibits a halo distribution rather than a tongue-type of distribution.

(5) In the heliotail region just downstream of the termination shock, the H atom velocity distribution function has a core of LISM atoms, a halo of component 2 heated atoms (with the thermal velocity now slightly smaller than found in the equivalent upstream heliosheath region), and a tongue of atoms, produced in the supersonic solar wind (component 3).

The Boltzmann simulations of Lipatov et al. (1998) describe for the first time the detailed neutral hydrogen velocity distribution function as it traverses the heliosphere. The basic decomposition of neutral H into components distinguished by their origin is clearly demonstrated by the simulations. Thus, the typical neutral H distribution observed within the neighbourhood of the heliosphere consists of a thermal core of LISM H (component 1), somewhat heated by charge exchange in the region between the bow shock and heliopause, a hot tongue-like distribution produced by charge exchange with the hot shock solar wind plasma in the heliosheath (component 2), and finally a more halo-like distribution whose origin is the supersonic solar wind (component 3). The relative density of these three fairly distinct components differs, of course, with location within the heliosphere/heliospheric boundaries but the essential features of the velocity distribution function are unchanged.

The basic global features of the neutral hydrogen density distribution in the two-shock heliosphere model are in basic accord with those found by Fahr and his colleagues, recognizing of course the differences in the nature of the plasma models.

5.5. Self-consistent global models

As has become abundantly clear, the weak coupling of neutral gas and plasma (which provides an effective volumetric force) affects both distributions in important ways, and this self-consistent coupling is crucial in modelling the interaction of the solar wind with the LISM. Baranov and Malama (1993, 1995) developed

such a coupled model using a Monte-Carlo algorithm to evaluate the neutral H distribution and a 2D steady-state fluid description of the plasma. An alternative series of models which are based on a multi-fluid description of the neutrals has been developed by Pauls et al. (1995, 1996), Zank et al. (1996a, b, c), Williams et al. (1997) and Liewer et al. (1997). The need for modelling the neutrals as a multi-fluid stems from the variation in the charge exchange mean-free-path for H in different regions of the heliosphere and LISM. Large anisotropies are introduced in the neutral gas distribution by charge exchange with the solar wind plasma (both sub- and supersonic) and the multi-fluid approach represents an attempt to capture this characteristic in a tractable and computationally efficient manner.

5.5.1. *The 2D Multi-Fluid Models*

As discussed in Section 2.1, the heliosphere-LISM environment can be described as three thermodynamically distinct regions; the supersonic solar wind (region 3), the very hot subsonic solar wind (region 2), and the LISM itself (region 1). Each region acts a source of neutral H atoms whose distribution reflects that of the plasma distribution in the region. Accordingly, Zank et al. (1996) identify neutral components 1, 2, and 3 with neutral atoms originating from regions 1, 2, and 3. Each of these three neutral components is represented by a distinct Maxwellian distribution function appropriate to the characteristics of the source distribution in the multi-fluid models. This observation allows the use of the simpler production and loss terms (9) and (11) for each neutral component. The complete highly non-Maxwellian H distribution function is then the sum over the three components, i.e.,

$$f(\mathbf{x}, \mathbf{v}, t) = \sum_{i=1}^{3} f_i(\mathbf{x}, \mathbf{v}, t) , \tag{134}$$

and for each component, the integral equation (4) must, in principle, be solved (Hall, 1992; Zank et al., 1996c). Instead of solving (4), Zank et al. (1996) use (134) in (1) to obtain three Boltzmann equations corresponding to each neutral component. This is an extension of the procedure developed in Pauls et al. (1995). For component 1, both losses and gains in the interstellar medium need to be included, but only losses are needed in the heliosheath and solar wind. Similarly for components 2 and 3. Thus, for each of the neutral H components i ($i = 1, 2$ or 3)

$$\frac{\partial f_i}{\partial t} + \mathbf{v} \cdot \nabla f_i = \begin{cases} P_1 + P_2 + P_3 - \beta_{\rm ex} f_i & \text{region i} \\ -\beta_{\rm ex} f_i & \text{otherwise} \end{cases} , \tag{135}$$

where $P_{1,2,3}$ means that $P_{\rm ex}$ is to be evaluated for the parameters of components 1, 2, or 3 respectively. Under the assumption that each of the neutral component distributions is approximated adequately by a Maxwellian, one obtains immediately from (135) an isotropic hydrodynamic description for each neutral component,

$$\frac{\partial \rho_i}{\partial t} + \nabla \cdot (\rho_i \mathbf{u}_i) = Q_{\rho i} \; ; \tag{136}$$

$$\frac{\partial}{\partial t}(\rho_i \mathbf{u}_i) + \nabla \cdot \left[\rho_i \mathbf{u}_i \mathbf{u}_i + p_i \mathbf{I}\right] = \mathbf{Q}_{mi} \; ; \tag{137}$$

$$\frac{\partial}{\partial t}\left(\frac{1}{2}\rho_i u_i^2 + \frac{p_i}{\gamma - 1}\right) + \nabla \cdot \left[\frac{1}{2}\rho_i u_i^2 \mathbf{u}_i + \frac{\gamma}{\gamma - 1}\mathbf{u}_i p_i\right] = Q_{ei} \; . \tag{138}$$

The source terms Q are appropriate moments of (9) and (11) and are listed in Pauls et al. (1995) and Zank et al. (1996). The subscript i above refers to the neutral component of interest ($i = 1, 2, 3$), ρ_i, $\mathbf{u}_i$, and p_i denote the neutral component i density, velocity, and isotropic pressure respectively, $\mathbf{I}$ the unit tensor and γ ($= \frac{5}{3}$) the adiabatic index.

The plasma is described similarly by the 2D hydrodynamic equations

$$\frac{\partial \rho}{\partial t} + \nabla \cdot (\rho \mathbf{u}) = Q_{\rho p} \; ; \tag{139}$$

$$\frac{\partial}{\partial t}(\rho \mathbf{u}) + \nabla \cdot \left[\rho \mathbf{u}\mathbf{u} + p \mathbf{I}\right] = \mathbf{Q}_{mp} \; ; \tag{140}$$

$$\frac{\partial}{\partial t}\left(\frac{1}{2}\rho u^2 + \frac{p}{\gamma - 1}\right) + \nabla \cdot \left[\frac{1}{2}\rho u^2 \mathbf{u} + \frac{\gamma}{\gamma - 1}\mathbf{u} p\right] = Q_{ep} \; , \tag{141}$$

where $Q_{(\rho,m,e),p}$ denote the source terms for plasma density, momentum, and energy. They too are listed in Pauls et al. (1995) and Zank et al. (1996). The remaining symbols enjoy their usual meanings. The proton and electron temperatures are assumed equal in the multi-fluid models.

The coupled multi-fluid system of Equations (136)–(141) are solved numerically. Pauls et al. (1995) use a two-fluid reduction of the equations (136)–(141) in that components 2 and 3 are neglected entirely. This simplified approach has the virtue of computational efficiency while still retaining the basic features of the full model.

In this subsection, three models for the LISM are considered, and are listed in Table IX, and the parameters for the solar wind at 1 AU are standard ($n = 5$ cm^{-3}, $u = 400$ km s^{-1}, and proton temperature $T_p = 10^5$ K). The parameter α in Table IX describes the 'effective' temperature of the LISM and accounts for the added contribution of electrons, cosmic-rays, and perhaps a magnetic field. More precisely, if P_T denotes total pressure, then α is defined implicitly by

$$P_T = k_B(n_p T_p + n_e T_e) + P_{\rm CR} + P_{\rm mag} + P_{\rm dust} + \cdots \simeq \alpha n_p k_N T_p \; ,$$

where the subscript $p(e)$ refers to proton (electron) quantities and k_B to Boltzmann's constant. For a plasma comprising only non-relativistic electrons and protons, $\alpha = 2$. For a subsonic LISM where cosmic-rays, for example, may contribute

TABLE IX
Model inflow parameters for the LISM

Model	Mach No.	n_e (cm^{-2})	$n_{\rm H}$ (cm^{-2})	T (K)	v (km s^{-1})	α
1	1.5	0.07	0.14	10900	−26	2
2	0.7	0.07	0.14	10900	−26	9.1
3	0.9	0.1	0.14	7600	−26	7.9

to the total pressure, $\alpha > 2$. In the solar wind, $\alpha = 2$ always. Several other models besides those listed in Table IX are investigated in Williams et al. (1997).

5.5.1.1. *Two-Shock Case.* Consider now the case of a supersonic interstellar wind incident on the heliosphere.

Plate 5.6(a) shows the normalized density, flow direction and temperature (colour plot) for the H^+ fluid at steady-state, this time including charge exchange with the H gas self-consistently. The positions of the three interfaces are indicated on the plot. A major effect of charge exchange on the heliospheric interfaces is to decrease the distances to the TS, HP and BS. These distances, for $\theta = 0°$ and $\theta = 180°$ are listed in Table X for the charge exchange case and can be compared to the distances listed in Table VII. The reason for the decrease in distance results primarily from the decrease in the solar wind ram pressure, this due to the mediation of the wind by charge exchange (Section 4.2). Two sets of distances are tabulated in Table X. The one set of distances correspond to the full multi-fluid model of Zank et al. (1996) and the second set, identified as PZW, corresponds to the reduced two-fluid model of Pauls et al. (1995) and the importance of component 2 is illustrated clearly.

Besides the distance to the various heliospheric boundaries, charge exchange effects the shape of the termination shock, making it more spherical than the purely gas dynamic model. This is due to charge exchange in the heliosheath, which decelerates the shocked solar wind plasma in this region. Thus, the heliosheath flow remains subsonic throughout the region and the need for a triple umbilic point disappears when the neutral hydrogen density is nonzero.

Owing to the deposit of interstellar protons in the solar wind when charge exchange is included, the solar wind flow now departs slightly from simple spherical symmetry. The departure can scarcely be seen in Plate 5.6a but a comparison of Plates 5.1 and 5.6(a) shows clearly the contribution to the internal energy of the supersonic solar wind by pickup ions. The tail region is also cooler when the proton fluid and neutral fluid are coupled compared to the no-charge exchange model. The cooling is a consequence of the very hot heliotail being cooled by charge exchange with cooler component 1 neutrals.

Illustrated in Plate 5.6(b) is a 2D plot of the component 1 neutral distribution. The basic features can be summarized as follows.

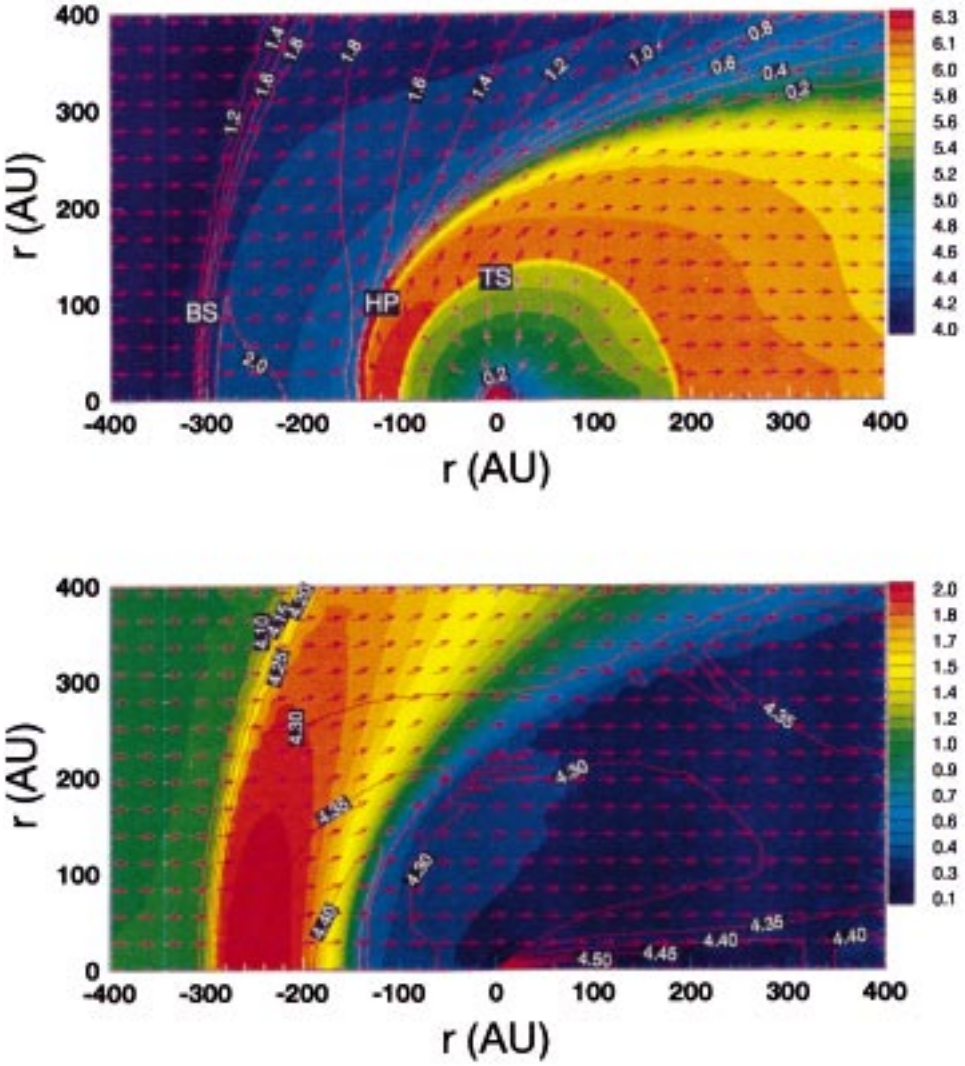

Plate 5.6. (a) A 2D plot of the global plasma structure for the two-shock model when neutral H is included self-consistently. The colour refers to Log[Temp]. The streamlines are included. (b) A 2D plot of the corresponding component 1 neutral distribution. The colour now refers the number density. The hydrogen wall is clearly visible between the bow shock (BS) and heliopause (HP). (Zank et al., 1996.)

Inflowing component 1 neutrals are decelerated substantially and filtered by charge exchange with the interstellar plasma between the BS and HP in the upstream direction. This leads to the formation of a hydrogen wall with maximum densities $\sim$ 0.3 cm^{-3}, column densities $\sim 10^{14}$ cm^{-2} and temperatures ranging from 20 000 K to 30 000 K. The pile-up in the neutral gas results from the deceleration and deflection of the neutral flow by charge exchange with the interstellar

TABLE X

Distances to the boundaries for the case of a supersonic LISM. Heliocentric distances are given in AU. TS is the termination shock, HP is the heliopause, and BS is the bow shock

	$\theta = 0°$			$\theta = 90°$	$\theta = 180°$
Model	TS	HP	BS	TS	TS
Multifluid	95	140	310	140	190
PZW	90	122	230	135	170

plasma, which is itself decelerated and diverted due to the presence of the heliosphere. Note that the charge exchange mean-free-path is typically less than the separation distance between the heliopause and bow shock and so a large part of the incident interstellar neutrals experience charge exchange.

Component 2, produced via charge exchange between component 1 and hot shocked solar wind plasma between the TS and HP, streams across the HP into the cooler shocked interstellar gas and heats the interstellar plasma through a second charge exchange. This leads to an extended thermal foot abutting the outside edge of the HP. This heating of the plasma by component 2 serves to broaden the region between the BS and HP, as well as to (indirectly) further heat the component 1 interstellar neutrals after subsequent charge exchanges. Some minor heating of the unshocked LISM also occurs upstream of the BS, thereby marginally reducing the Mach number of the incident interstellar wind.

The temperature of component 1 neutrals once inside the heliosphere remains fairly constant in the upstream region, at $T \sim 20\,000$ K, a substantial increase over the assumed LISM temperature of 10 900 K assumed for Model 1. A further increase in the component 1 temperature occurs in the downstream region.

The number density of component 1 crossing the TS is ~ 0.07 cm^{-3}. This is approximately half the assumed incident LISM number density, an effect termed 'filtration'. Between the TS and 10 AU from the Sun in the upstream region, this density varies only weakly, following a rough power law ($\sim R^{0.25}$, with R the heliospheric radius). In the downstream direction, component 1 densities are lower within the heliosphere and the gradient is somewhat more pronounced, with density increasing with $R^{0.35}$. The precise value of the component 1 density at the TS can vary with parameters and an example is presented below. A further effect of filtration is to decelerate the upstream neutral gas from -26 km s^{-1} in the LISM to -19 km s^{-1} at the TS in the region of the nose. Deflection of the flow also reduces the radial velocity component at angles away from the nose. Such a deceleration is in accord with Lyman-α backscatter observations (Lallement et al.), 1993).

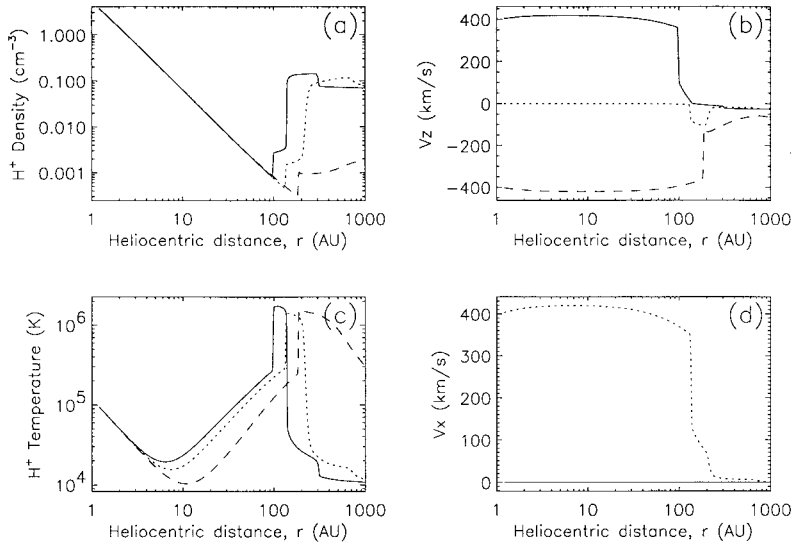

Figure 5.17. Lines-of-sight profiles for the two-shock model plasma in the upstream direction (solid line), sidestream direction (dotted line) and downstream direction (dashed line). Shown are (a) the density profiles; (b) the plasma velocity v_z; (c) the temperature, and (d) the velocity v_x profiles. (Zank et al., 1996.)

Finally Zank et al. (1996a) and Liewer at al. (1996) have pointed out the possibility that the HP is time dependent due to an inwardly directed ion-neutral drag term which provides an effective 'gravitational' term for a stratified fluid (which then introduces the possibility of Rayleigh-Taylor-like instabilities). The time scale of 180 years and the $\sim$ 3 AU amplitude of the oscillation suggest that this is unlikely to be important, but a more detailed analysis is warranted.

Line-of-sight profiles for the plasma and component 1 neutrals are presented in Figures 5.17 and 5.18.

The results of the Boltzmann simulation of Lipatov et al. (1998) can be compared with corresponding results obtained in a four-fluid simulation using the same LISM ($T_\infty = 8000$ K) and solar wind parameters. Figure 5.19 shows a one-dimensional cut of the H atom density profile along the upstream stagnation axis $x(y = 0)$ for the Boltzmann (solid line) and four-fluid (dotted line) simulations. The four-fluid model gives a slightly different distribution of H density. Far upstream of the bow shock, the Boltzmann code and the four-fluid model give approximately the same distribution except for 'shot noise' fluctuations in the Boltzmann simulation. Just ahead of the bow shock, the Boltzmann solution demonstrates strong diffusion of the neutral H compared to the four-fluid solution. The amplitude of the hydrogen wall is comparable in both models and the filtration is similar with a slightly smaller density crossing the termination shock in the four-fluid simulation. At distances $r \leq 30$ AU from the Sun, the neutral H number density in the Boltzmann simulation is about of 30% higher than in the four-fluid

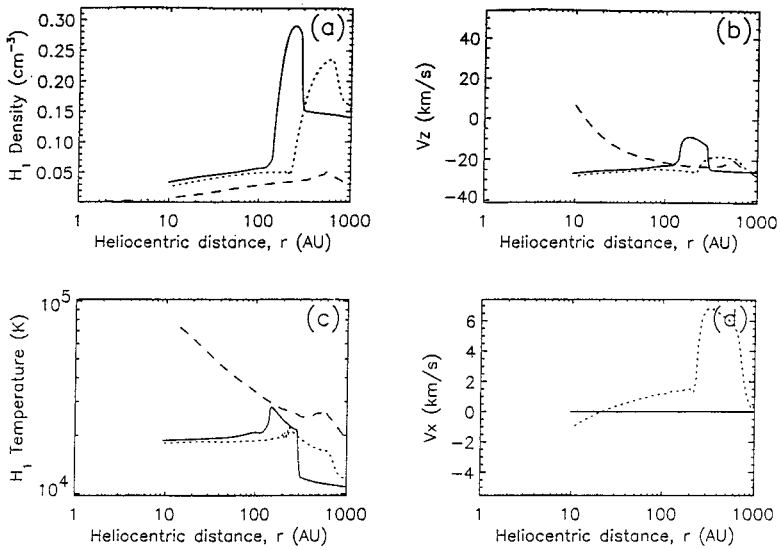

Figure 5.18. Lines-of-sight profiles for the two-shock model component 1 neutrals in the upstream direction (solid line), sidestream direction (dotted line) and downstream direction (dashed line). Shown are (a) the density profiles; (b) the plasma velocity v_z; (c) the temperature, and (d) the velocity v_x profiles. (Zank et al., 1996.)

model. This is due in part to the course inner grid adopted in the simulations of Lipatov et al. (1998). The comparison described here indicates that the simpler multi-fluid model captures the basic features of the solar wind – interstellar neutral interaction.

Finally, we should note that the choice of which charge-exchange cross section to use in simulations (Fite et al., 1962 or Maher and Tinsley, 1977) can lead to neutral hydrogen distributions that are different from one model to another. Williams et al. (1994) showed explicitly that large differences in the neutral number density and temperature could result if only the charge-exchange cross section were varied, this because at 1 eV, a 40% difference exists between the Fite et al. and Maher and Tinsley cross-sections.

5.5.1.2. *One-Shock Model* It is important to note that a cosmic-ray pressure of 3×10^{-13} dyne cm^{-2}, combined with the interstellar plasma thermal pressure from Table IX (2×10^{-13} dyne cm^{-2}) yields a total pressure of 5×10^{-13} dyne cm^{-2}. We expect that on LISM scales, cosmic-rays with energy $\leq$300 MeV will be coupled to the interstellar plasma. This would be sufficient to increase the LISM sound speed to $\sim$ 27 km s^{-1} and force the LISM inflow to be barely subsonic. Alternatively, a magnetic field strength of 3 μG with n$_e$=0.05 cm^{-3} gives an Alfvén speed of v_a=29 km s^{-1}, which would enhance the magnetosonic speed and also invalidate a two-shock model.

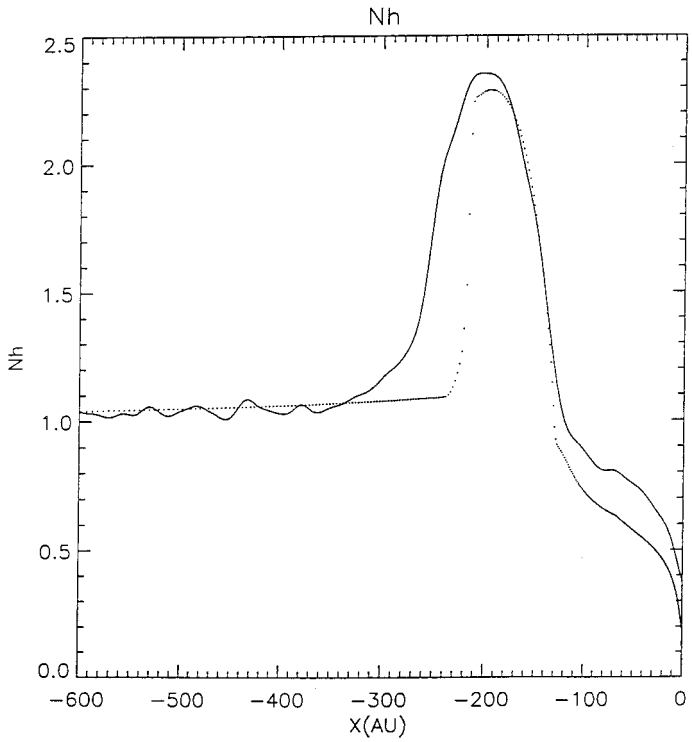

Figure 5.19. One-dimensional central cut of the H number density profile along the stagnation axis for a Boltzmann simulation (solid line) and a four-fluid (dotted line). (Lipatov et al., 1998.)

In view of the comments above, Zank et al. (1996) consider models with subsonic LISM flow. These do not have a bow shock and may therefore resemble the Parker (1963) model. For model 2, $n_e = 0.07$ cm^{-3}, n_H=0.14 cm^{-3}, and T=10 900 K (see Table VIII) is used to be consistent with model 1, but a larger 'effective' temperature is used to account for the added contribution from cosmic-rays (and perhaps the magnetic field). The value $\alpha = 9.1$ has been chosen for model 2, so the upstream Mach number is reduced from 1.5 (as in model 1) to 0.7. The implied interstellar plasma pressure is 10^{-12} dyne cm^{-2}. No charge exchange is assumed to occur between the cosmic-rays and neutrals due to the former's very low number density and the cosmic-ray contribution is neglected within the heliosphere.

Plate 5.7(a) shows the 2D proton temperature, density, and flow directions for the one-shock model. The heliopause (HP) and termination (TS) are labelled. Plate 5.7(b) shows the corresponding neutral hydrogen density, temperature, and flow directions. The diffuse hydrogen wall is clearly visible beyond the heliopause. Figures 5.20 and 5.21 are line-of-sight profiles for the density, velocity and temperature of the plasma and component 1 neutrals. The basic results that emerge from the one-shock models are summarized (see Zank et al. (1996) for further details).

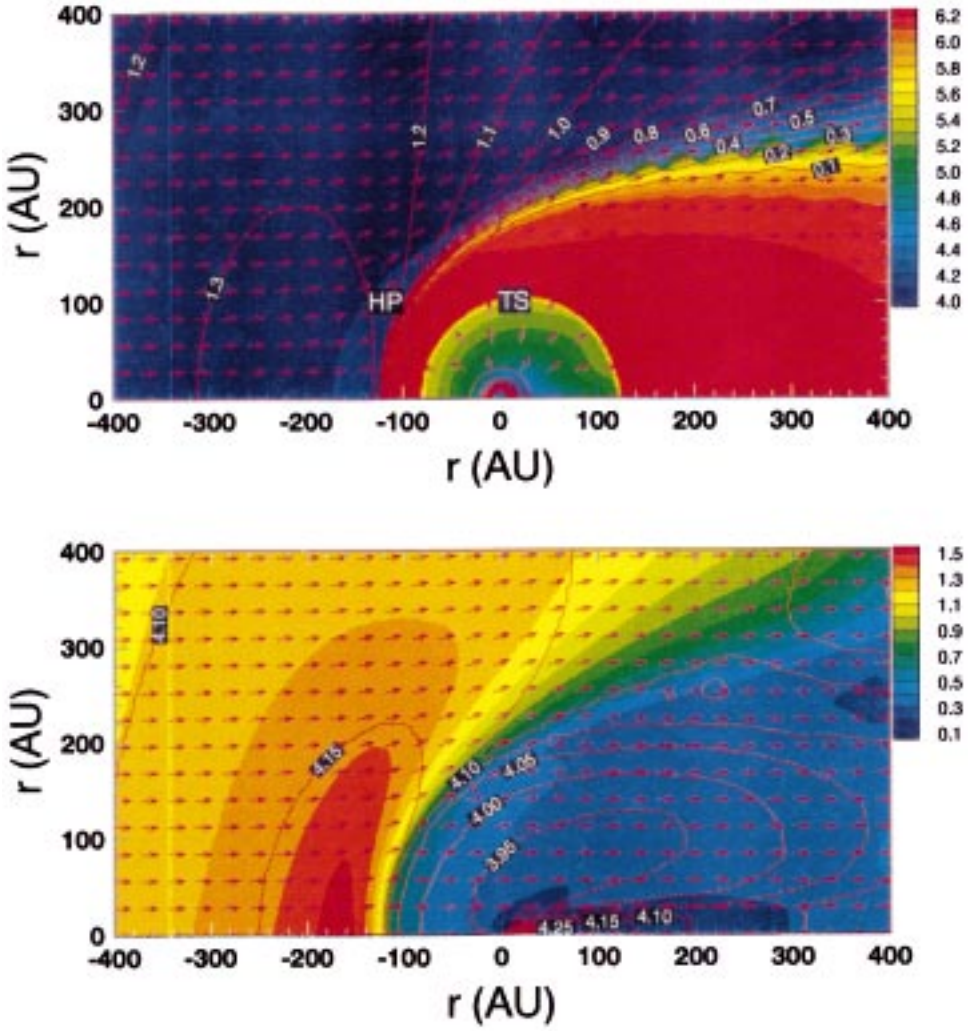

Plate 5.7. (a) A 2D plot of the global plasma structure for the one-shock model when neutral H is included self-consistently. The colour refers to Log[Temp]. The streamlines are included. (b) A 2D plot of the corresponding component 1 neutral distribution. The colour now refers the number density. The hydrogen wall is clearly visible beyond the heliopause. (Zank et al., 1996.)

Although a bow shock is absent, some adiabatic compression of the incident interstellar flow is evident. This more gradual compression leads to the formation of a lower amplitude hydrogen wall that is more extended in the radial direction. It is also less extended in the tangential direction because of the localized nature of the adiabatic compression. The density of the wall in the upstream direction is only ~ 0.21 cm^{-3} (though still larger than the incident LISM n_H=0.14 cm^{-3}). However, because it is wider, its column density is comparable to the two-shock case.

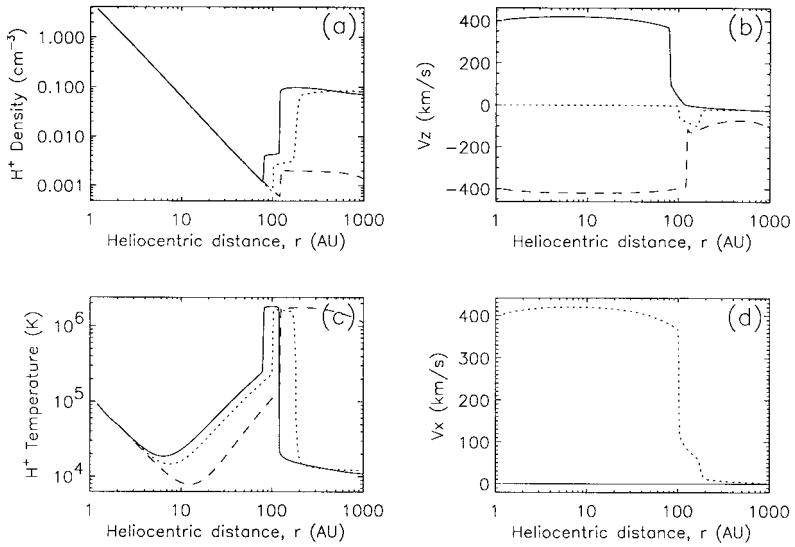

Figure 5.20. Lines-of-sight profiles for the one-shock model plasma in the upstream direction (solid line), sidestream direction (dotted line) and downstream direction (dashed line). Shown are (a) the density profiles; (b) the plasma velocity v_z; (c) the temperature, and (d) the velocity v_x profiles. (Zank et al., 1996.)

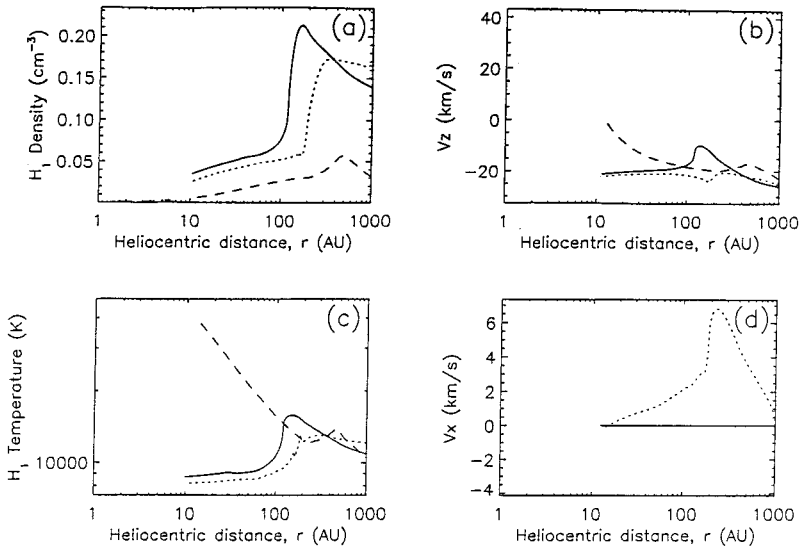

Figure 5.21. Lines-of-sight profiles for the one-shock model component 1 neutrals in the upstream direction (solid line), sidestream direction (dotted line) and downstream direction (dashed line). Shown are (a) the density profiles; (b) the plasma velocity v_z; (c) the temperature, and (d) the velocity v_x profiles. (Zank et al., 1996.)

The heliosphere is less distorted along the axis of symmetry than for the two-shock case, and is smaller due to the higher assumed LISM pressure.

In the vicinity of the nose, the number density of component 1 flowing across the TS is ~ 0.06 cm^{-3} with a velocity of ~ -20 km s^{-1}, almost identical to the two-shock model.

Since the H wall has a smaller transverse extent than the two-shock model, it is less pronounced along the sidestream sightline. This may allow the one- and two-shock models to be observably different, not only upstream, but sidestream as well.

Finally, the upstream and downstream temperature characteristics of the heliospheric component 1 differ significantly between the one- and two-shock models. In the upstream direction of the one-shock model, some possible cooling of the neutrals is predicted. A temperature asymmetry between upstream and downstream heliospheric neutrals is again present, but the downstream temperatures are markedly lower than predicted by the two shock model.

To bridge the gap between models 1 and 2, Gayley et al. (1997) computed a third model for which the inflow Mach number was chosen to be the intermediate value 0.9 (model 3, Table VIII). However, the inflow temperature was reduced to the more realistic value $T = 7600$ K, and, to compensate, the plasma density was increased slightly to n_e=0.1 cm^{-3} so as to preserve the incident plasma heat flux.

The model 3 results for the component 1 neutrals are depicted by dot-dashed curves in Figure 5.22. The overall structure and distribution are similar to model 2, underscoring the qualitative connection between subsonic models. The quantitative attributes of the hydrogen wall are generally intermediate to models 1 and 2, presumably owing to the intermediate value of the Mach number, which appears to be the most important single parameter. Note that unlike Figures 5.18 and 5.21, Figure 5.22 shows neutral profiles along the α Cen sightline (see Section 5.6 below).

5.5.2. *The 3D Multi-Fluid Model*

The 3D gas dynamic model of Section 5.3.2 has been extended by Pauls and Zank (1997) to include self-consistently interstellar neutral H in the multi-fluid framework. In modeling the neutral component, the simpler two-fluid approach of Pauls et al. (1995) is adopted, this to circumvent the considerable computational demands imposed by the 3D simulation.

Before proceeding to the simulation results, one can anticipate the effects of interstellar neutral charge exchange on the anisotropic solar wind. From Section 5.3.2, recall that the presence of an anisotropic solar wind with a high velocity, low density, high temperature polar steam diverts both the subsonic solar wind and the LISM plasma flow into the ecliptic region of the heliosphere. The presence of a high density band of fluid/plasma about the ecliptic plane must increase the filtration of neutrals compared to the higher polar regions. With an increased neutral flux of H over the poles, the polar wind must experience comparatively greater

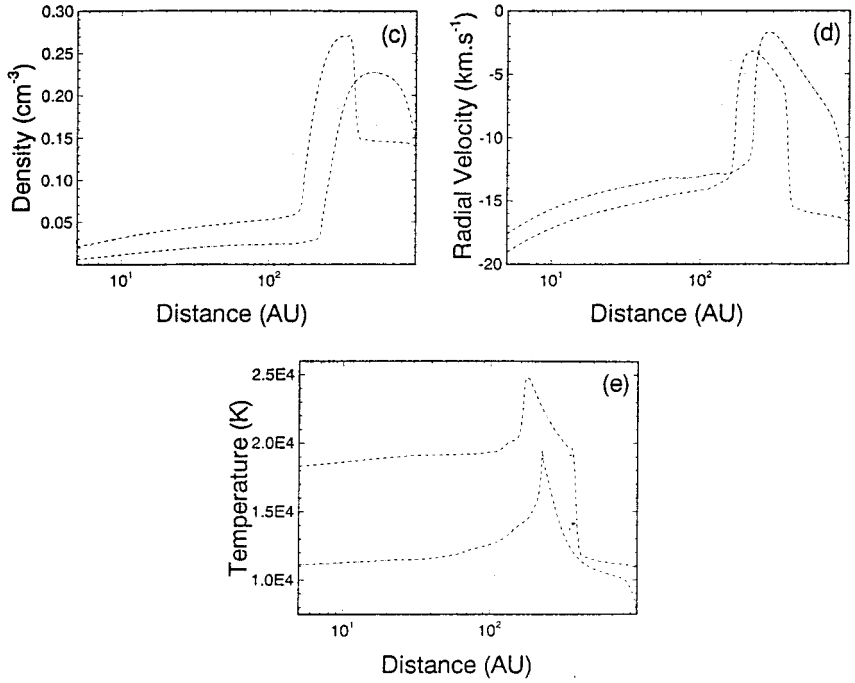

Figure 5.22. A comparative plot of component 1 neutrals from the 2D models in Table 5.6. The density, radial velocity, and temperature profiles along the α Cen sightline are illustrated for model 1 (dashed), model 2 (dotted), and model 3 (dot-dash). (Gayley et al., 1997.)

deceleration, so reducing the degree of anisotropy seen in the 3D gas dynamic simulations. In addition, the global distribution of neutral H should also be anisotropic in heliolatitude. Of course, it should be bourne in mind that these remarks pertain primarily to the period of solar minimum.

Pauls and Zank (1997) use the same boundary conditions as used in their 3D gas dynamic study (Pauls and Zank, 1996).

Shown in Figure 5.23 are sightline plots of the density, speed, and temperature from the steady state plasma solution at the nose (solid line), side-stream in the ecliptic plane (dashed line), over the poles of the sun (dash-dotted line) and toward the heliotail (dotted line). In Figure 5.23(a), the first discontinuity in the density (in the direction away from the sun) corresponds to the termination shock, the next to the heliopause, and the last to the bow shock. The solar wind density decreases almost adiabatically until the TS, mediated slightly by ion pickup. As before, the hot pickup ions yield an increasing solar wind temperature profile for the one-fluid plasma model. Some cooling of the heliotail is evident from Figure 5.23(c).

Plate 5.8 shows the normalized flow vectors and the log(H^+ temperature) contours of the steady state solution as a function of distance. The top panel shows a cut through the three-dimensional data set in the polar plane, while the bottom panel is a cut in the ecliptic plane. One immediately obvious difference between

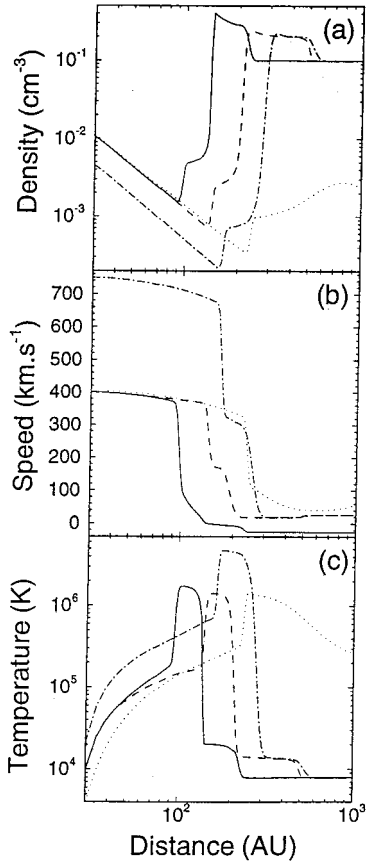

Figure 5.23. (a) Proton density, (b) speed, and (c) temperature, as function of heliocentric distance along the nose (solid line), sidestream in the ecliptic plane (dashed line), over the solar poles (dash-dotted line), and toward the heliotail (dotted line). (Pauls and Zank, 1997.)

this solution and the no-charge-exchange solution is that the vortices present in the heliotail of the latter simulation are absent. This is a consequence of the dissipative character of the charge exchange source terms.

The distances to the boundaries (TS, HP, and BS) are again greatly reduced by charge exchange, as seen in Table XI which compares these distances for both the gas dynamic and the multi-fluid simulations. Once again, the decrease in distance to the TS is due mainly to the reduction in solar wind ram pressure associated with the deceleration of the supersonic wind by charge exchange.

Another interesting result, illustrated in Plate 5.8, is the presence of a triple point (letter A on the Plate) attached to the termination shock in the ecliptic plane. Only for a two-dimensional gas dynamic simulation of a supersonic LISM interacting with the solar wind does a triple point occur. However, the same 2D simulation with the self-consistent inclusion of interstellar neutrals does not have a triple point

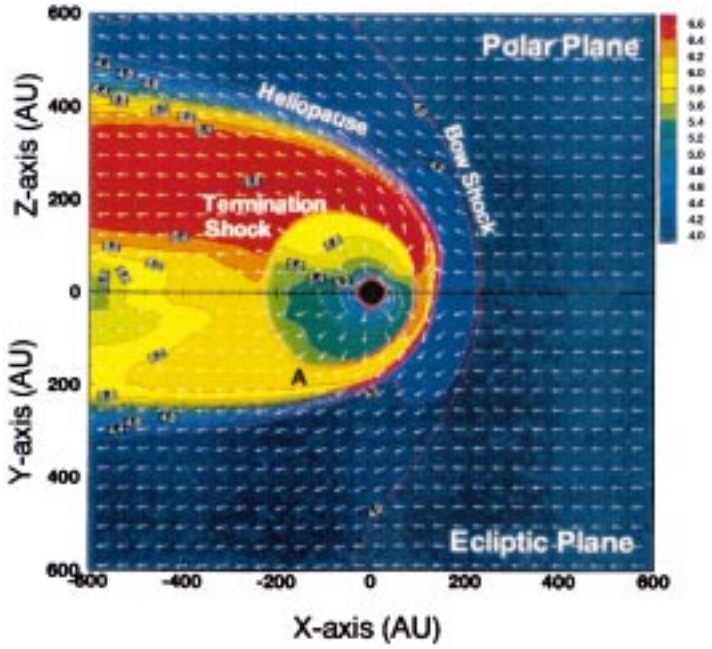

Plate 5.8. Log[Temp] (contour and colour) and normalized flow vectors as a function of distance in the polar plane (top panel) and in the ecliptic plane (bottom panel). A denotes the position of a triple point. (Pauls and Zank, 1997.)

TABLE XI

Distances to the boundaries for both the no-charge-exchange and charge-exchange cases for a supersonic LISM. Heliocentric distances are given in AU. TS is the termination shock, HP is the heliopause, and BS is the bow shock. Ecliptic refers to the side-stream direction in the ecliptic plane, perpendicular to the pole direction

	No charge exchange				Charge exchange			
	Nose	Ecliptic	Pole	Tail	Nose	Ecliptic	Pole	Tail
TS	133	195	230	320	95	145	165	240
HP	163	240	360	–	138	205	280	–
BS	380	–	–	–	230	–	–	–

(Section 5.3 and 5.5), this due to the heliosheath flow never attaining supersonic speeds. However, the elongation of the heliosphere over the poles of the sun causes the flow to be focussed in the ecliptic plane, both with and without the inclusion of interstellar neutrals. Thus, the ecliptic plane heliosheath flow speed is higher (high enough for the flow to become supersonic, so necessitating a triple point) than the flow speed over the poles. Plate 5.8 also shows cooling of the heliotail region.

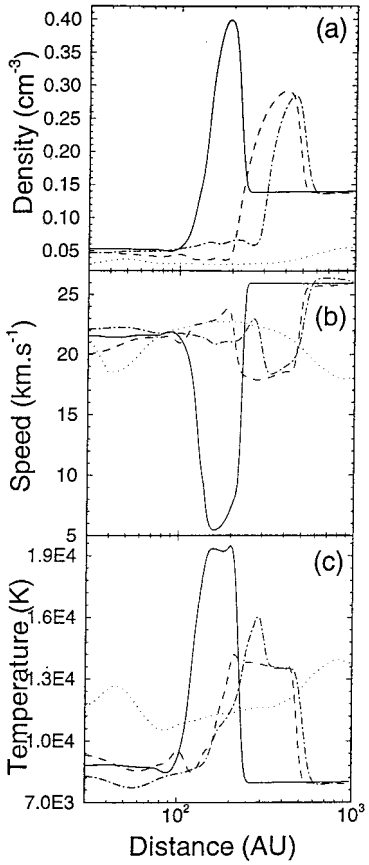

Figure 5.24. (a) Neutral H density, (b) speed, and (c) temperature, as function of heliocentric distance along the nose (solid line), sidestream in the ecliptic plane (dashed line), over the solar poles (dash-dotted line), and toward the heliotail (dotted line). (Pauls and Zank, 1997.)

The neutral H distribution corresponding to the plasma distribution described above is shown in Figure 5.24 and Plate 5.9. Figure 5.24 gives the H sightline plots of the density, speed, and temperature at the nose (solid line), side-stream in the ecliptic plane (dashed line), over the solar poles (dash-dotted line), and towards the heliotail (dotted line), while Plate 5.9 shows the density contours and normalized flow vectors of the H fluid.

The elongation of the heliosphere along the solar poles leads to a greater shocked LISM flow in the ecliptic plane compared to that over the poles. This 10% increase in plasma density is evident between the HP and BS when the two side-stream flows are compared (Figure 5.23). Since the charge exchange source terms are proportional to the plasma density, charge exchange is enhanced between the HP and BS in the ecliptic plane compared to the polar plane. This, in turn, causes a greater deceleration of the neutral H fluid in the ecliptic plane compared to the polar

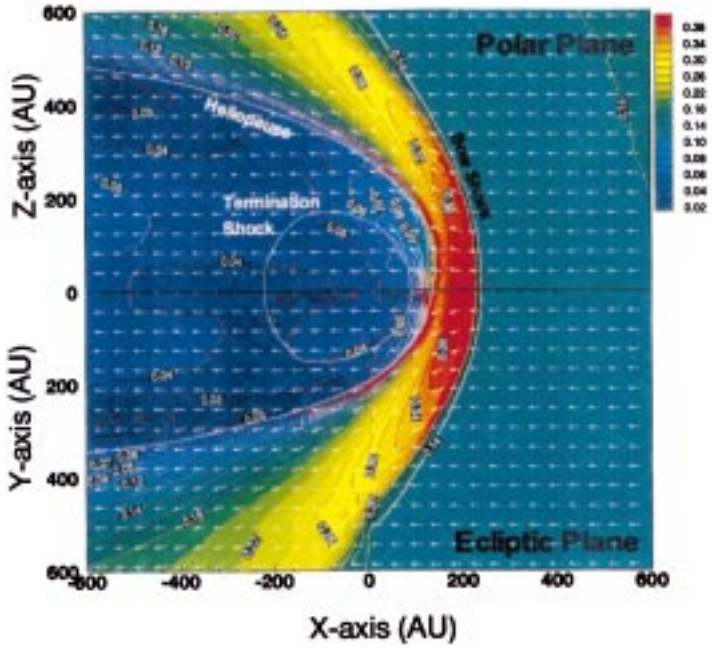

Plate 5.9. Interstellar neutral hydrogen density (cm^{-3}) (contour and colour) and normalized flow vectors as a function of distance in the polar plane (top panel) and in the ecliptic plane (bottom panel). The positions of the plasma boundaries are indicated. (Pauls and Zank, 1997.)

plane (Figure 5.24), and leads to a denser H pileup in the ecliptic plane compared to the solar poles.

Since the density of the hydrogen wall is a maximum in the ecliptic plane, one has more effective neutral H filtration here. Thus, less interstellar neutral H can be expected to flow into the heliosheath in the ecliptic plane than at high solar latitudes (Figure 5.24(a) and Plate 5.9).

Besides the enhancement of the LISM flow in the ecliptic region, the shocked solar wind too is diverted into the ecliptic plane. This, together with the assumed decrease in supersonic solar wind density with increasing heliolatitude, leads to increased charge exchange in the ecliptic plane in the heliosheath (not enough, however, to prevent the ecliptic flow from becoming supersonic). Thus, less interstellar H flows into the supersonic solar wind in the ecliptic regions compared to the polar regions. The higher H density over the poles of the sun reduces the elongation of the TS in the charge exchange case compared to the no-charge-exchange case (see Table XI which shows a 33% decrease in distance to the TS over the poles, compared to a 29% decrease in the ecliptic plane when charge exchange is included in the 3D model).

Thus, in summary, the elongation of the heliosphere over the solar poles, caused by a ram pressure increase in this region, results in an increased flux of interstellar H flowing into the heliosphere in the high heliolatitude regions compared to

the ecliptic plane. This decreases, in turn, the elongation of the heliosphere over the poles. If, in fact, the neutral interstellar hydrogen density were much higher, the heliosphere might revert to a more spherical structure (and possibly be time dependent).

5.5.3. *The 2D Monte-Carlo models*

As was discussed in Section 5.4, one should ideally calculate the interstellar neutral distribution at a kinetic level since the Knudsen number $Kn \simeq 1$ for neutral H. Extending the original hydrodynamic-like model of Baranov et al. (1981), Baranov and Malama (1993, 1995) used a Monte-Carlo approach to solve the neutral H Boltzmann equation and coupled this self-consistently to a steady-state 2D hydrodynamic model of the solar wind and LISM plasma.

The steady-state gas dynamic equations are as usual

$$\begin{aligned} &\nabla \cdot \rho \mathbf{u} = 0 \ , \\ &\rho \mathbf{u} \cdot \nabla \mathbf{u} + \nabla p = \rho \mathbf{F}_1 \left(f_{\mathrm{H}}(\mathbf{x}, \mathbf{v}), \rho, \mathbf{u}, p \right) \ , \\ &\nabla \cdot \left[\rho \mathbf{u} \left(\frac{u^2}{2} + \frac{\gamma}{\gamma - 1} \frac{p}{\rho} \right) \right] = F_2 \left(f_{\mathrm{H}}(\mathbf{x}, \mathbf{v}), \rho, \mathbf{u}, p \right) \ , \end{aligned} \tag{142}$$

where $f_{\mathrm{H}}(\mathbf{x}, \mathbf{v})$ is the neutral H distribution function.

Neutral H trajectories in the solar wind and LISM plasma are computed using the trajectory splitting Monte-Carlo method developed by Malama (1991), from which the source terms $\mathbf{F}_1$ and F_2 can be evaluated. The approach of Malama (1991) is equivalent to solving the Boltzmann equation (1) with the integral production and loss terms (2) and (8). It is assumed that the plasma can be described as a Maxwellian distribution $f_p(\mathbf{x}, \mathbf{v})$ with respect to the gas dynamic values determined by (142). The source terms in (142) are then computed from Equations (2), (5), and (8) after integrating over the neutral H velocity space. The gas dynamic equations (142) and the Boltzmann equation (1) are then solved iteratively until the solution converges. The LISM neutral H distribution is assumed to be Maxwellian. Besides charge exchange and photoionization, Baranov and Malama (1996) now include electron impact ionization in the region between the termination shock and heliopause. The Monte-Carlo scheme is inherently steady-state.

Illustrated in Figure 5.25 are three possible solutions for the global heliospheric structure obtained by Baranov and Malama (1993, 1996). Examples 1 and 3 correspond to models which incorporate the effects of resonant charge exchange, photoionization, gravity, and electron-impact ionization. Model 2 excludes electron-impact ionization and photoionization but is otherwise identical to model 1. The parameters used for these models are tabulated in Table XII. The ratio of solar radiation pressure to gravitational force is $\mu = F_r / F_g = 0.8$.

The solutions illustrated in Figure 5.25 show that the TS in the upstream direction lie in the range 65–85 AU and some differences exist between the models that

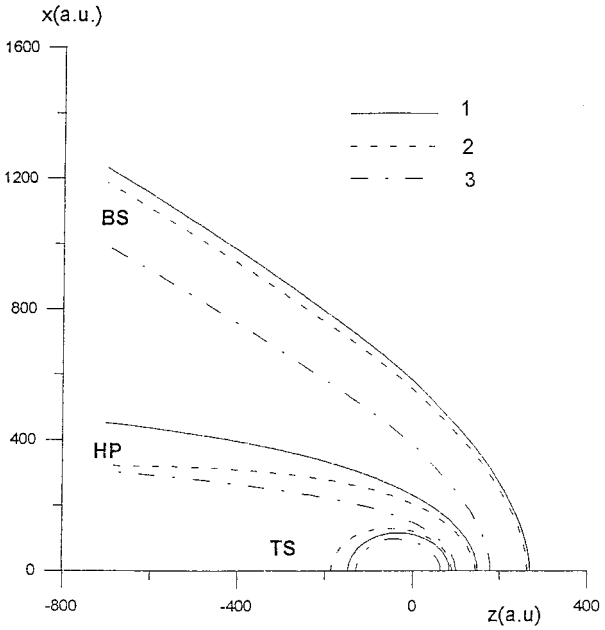

Figure 5.25. The boundaries of the termination shock, heliopause, and bow shock for undisturbed LISM plasma and neutral H densities (1) $n_p = 0.1$ cm^{-3}, $n_H = 0.2$ cm^{-3}, (2) $n_p = 0.1$ cm^{-3}, $n_H = 0.2$ cm^{-3}, and (3) $n_p = 0.3$ cm^{-3}, $n_H = 0.3$ cm^{-3}. Curves (1) and (2) differ in that the (1) includes the effects of electron impact ionization. (Baranov and Malama, 1996.)

TABLE XII

Solar wind and LISM parameters. 1 ≡ Model 1, 2 ≡ Model 2, 3 ≡ Model 3

	1 AU	H^+_∞	H_∞
n (cm^{-3})	7	0.1^1, $0.2^{2,3}$	0.2^1, $0.3^{2,3}$
u (km s^{-1})	450	26	26
M	10	1.9 ($T = 6700$ K)	

include or exclude electron-impact ionization. These pertain primarily to the location of the termination shock, indicating that in the heliosheath, electron-impact ionization may play an important role. Of course, given the nature of the shock heating of electrons and protons, it is unclear whether a Maxwellian description of the shocked solar wind plasma is entirely appropriate and this may well alter the quantitative conclusions that one draws from Figure 5.25. One-dimensional profiles of the number density in the upstream direction for each of models 1, 2, and 3 are

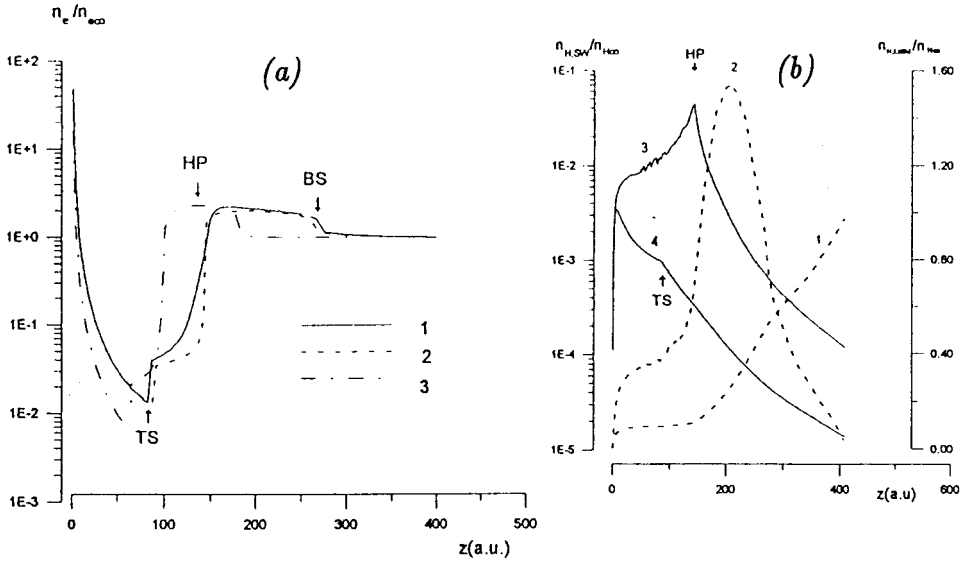

Figure 5.26. (a) Plasma number density (normalized to that of the undisturbed LISM) as a function of heliocentric radius for the three different models of Figure 5.25. (b) Neutral number density as a function of heliocentric distance for $n_p = 0.1$ cm^{-3}, $n_H = 0.2$ cm^{-3} in the upwind direction. The dashed lines are for neutral H whose source is the LISM (curve 1 is for primary LISM H and curve 2 for secondary LISM H i.e., component 1) and the the solid lines are for neutral H whose source is the solar wind (curve 3 is for component 2 H and curve 4 for component 3 H). (Baranov and Malama, 1996.)

presented in Figure 5.26(a) and the basic characteristics have been discussed at length already.

The neutral H number density in the upstream direction is illustrated in Figure 5.26(b) for model 1. Four sets of curves are plotted, the dashed curves corresponding to interstellar neutral H and the solid curves to H born in the solar wind. Curve 1 denotes primary LISM H atoms and curve 2 is for the secondary atoms. Curve 1 illustrates clearly how the incident interstellar H atoms are depleted strongly by charge exchange in the region between the bow shock and heliopause. These H atoms are replaced by secondary atoms, shown by curve 2 in Figure 5.26(b), whose characteristics are determined by the shocked interstellar plasma. This leads, as discussed above, to the formation of the hydrogen wall, which consists of those neutral H atoms which experience charge exchange upstream of the HP. Curve 3 shows the number density of component 2 neutrals and curve 4 of component 3 neutrals. The energetically important component 2 neutrals peak in the vicinity of the HP and experience secondary charge exchange as they stream into the LISM, significantly heating the LISM plasma in the immediate vicinity of the HP, as described above.

5.5.4. *Analytical Model of the Heliopause*

Many of the effects described in the preceding subsection can be elucidated by means of a simple 1D analytic model (Khabibrakhmanov et al., 1996b). The basic model consists of a hydrodynamic plasma coupled via resonant charge exchange to a neutral fluid whose density varies self-consistently but whose velocity is prescribed and constant. Using again the simplified source terms of Section 4.1, but without assuming supersonic solar wind flow, we now have

$$\begin{aligned}
&\frac{\partial \rho}{\partial t} + \nabla \cdot (\rho \mathbf{u}) = 0 \; ; \\
&\rho \frac{\partial \mathbf{u}}{\partial t} + \rho \mathbf{u} \cdot \nabla \mathbf{u} + \nabla p = -\langle \sigma v \rangle N \rho (\mathbf{u} - \mathbf{V}) \; ; \\
&\frac{\partial p}{\partial t} + \mathbf{u} \cdot \nabla p + \gamma p \nabla \cdot \mathbf{u} = -\langle \sigma v \rangle N \left(p - \frac{\gamma - 1}{2} \rho (\mathbf{u} - \mathbf{V})^2 \right) \; ; \\
&\frac{\partial N}{\partial t} + \nabla \cdot (N \mathbf{V}) = -\frac{\langle \sigma v \rangle}{m} \rho N \; ,
\end{aligned} \tag{143}$$

where N is the neutral number density and $\mathbf{V}$ the corresponding velocity. In the supersonic solar wind, one can assume incompressibility although the solenoidal condition is no longer valid in the presence of charge exchange. Hence,

$$\gamma \nabla \cdot \mathbf{u} = -\langle \sigma v \rangle N \; . \tag{144}$$

For steady flow along the stagnation line, we thus obtain the model equations

$$\begin{aligned}
&u \frac{\mathrm{d}\rho}{\mathrm{d}r} = \frac{\langle \sigma v \rangle N}{\gamma} \rho \; , \\
&\rho u \frac{\mathrm{d}u}{\mathrm{d}r} + \frac{\mathrm{d}p}{\mathrm{d}r} = -\langle \sigma v \rangle N \rho (u + V) \; , \\
&u \frac{\mathrm{d}p}{\mathrm{d}r} = \langle \sigma v \rangle N \frac{\gamma - 1}{2} \rho (u + V)^2 \; , \\
&\frac{\mathrm{d}(NV)}{\mathrm{d}r} = -\frac{\langle \sigma v \rangle}{m} \rho N \; ,
\end{aligned} \tag{145}$$

after assuming that the neutral H flows against the subsonic solar wind plasma with a constant velocity $-V$. Khabibrakhmanov et al. (1996b) integrate (145) to obtain

$$\rho = \rho_c \left[\frac{1}{1+x} \left(\frac{xa+1}{1+x} \right)^{(\gamma-1)/2} \right]^{2/[\gamma(\gamma+1)]} \equiv \rho_c f(x) \; , \tag{146}$$

where $x = u/V$ and $a = (\gamma+1)/(\gamma-1)$. The plasma density remains finite, say ρ_c, at the contact discontinuity (on the inner side) at $x_c = 0$ for a finite neutral particle velocity V. By taking $V = 20$ km s^{-1} and the solar wind speed downstream of the TS, $u_2 = 100$ km s^{-1}, the density increases from a value ρ_2 at the TS to ρ_c where

$$\frac{\rho_c}{\rho_2} = 1.8\ , \qquad x_2 = \frac{u_2}{V} = 5.$$

The neutral number density is given by

$$N = N_2 \left[1 + \frac{\gamma n_c}{N_2} \int_{x_2}^{x} t \frac{\mathrm{d}f(t)}{\mathrm{d}t}\, \mathrm{d}t \right] \equiv N_2 f_N(x)\ , \tag{147}$$

where the constant of integration is specified by the neutral density N_2 on the downstream side of the termination shock. In the case of complete stagnation at the heliopause, $u_c = 0$ at $x_c = 0$. The net increase in the neutral H density from the termination shock to the heliopause is given by

$$\Delta N \equiv N_c - N_2 = \gamma n_c \int_{x_2}^{0} t \frac{\mathrm{d}f(t)}{\mathrm{d}t}\, \mathrm{d}t \simeq 0.8\ . \tag{148}$$

By further calculating the plasma pressure p from (145) and using the approximation

$$\langle \sigma v \rangle = \sigma v_T \propto \sigma \sqrt{\gamma p/\rho}\ ,$$

together with the plasma continuity equation, Khabibrakhmanov et al. (1996b) estimated the separation distance between the the TS and HP to be

$$R_{\mathrm{HP}} - R_{\mathrm{TS}} \simeq \frac{1.2\gamma}{\sigma N_2} \frac{V}{u_2} \sqrt{\frac{\rho_c}{\rho_2}} M_2 \equiv 1.2 R_L = 38\ \mathrm{AU}\ , \tag{149}$$

($\gamma = \frac{5}{3}$, $M_2 = 0.5$, $\sigma = 5 \times 10^{-15}$ cm^{-2}, $N_2 = 0.07$ cm^{-3}). The separation distance is consistent with the simulations described above.

Although we do not discuss it in detail here, Khabibrakhmanov and Summers (1996) generalized the potential flow analysis of Section 5.2 to include ion pickup in the heliosheath. In view of (144), one now has to solve the Poisson equation for the velocity potential, i.e.,

$$\nabla^2 \phi = -\frac{\langle \sigma v \rangle}{\gamma} N\ . \tag{150}$$

The analysis, while straightforward, is somewhat involved and simple expressions analogous to those derived in Section 5.2 are not readily available. The interested reader is referred to Khabibrakhmanov and Summers (1996) for details.

5.6. Inferred structure of the heliosphere

In principle, we should already be in a position to decide observationally whether the heliosphere is a one- or a two-shock heliosphere. Bertaux et al. (1985) inferred the characteristics of neutral interstellar hydrogen in the interplanetary medium

using PROGNOZ 5 and 6 interplanetary Lyman α line profile measurements. Their estimates for hydrogen flow speeds and directions are consistent with subsequent measurements of these quantities presented by Lallement et al. (1993) and Clarke et al. (1995). Bertaux et al. (1985) suggested an upwind interstellar neutral temperature in the interplanetary medium of 8000 $\pm$ 1000 K and Clarke et al. (1995) suggest a downwind temperature of 30 000 K. This appears to be roughly consistent with the one-shock model expectations. Adams and Frisch (1977), using Copernicus data, obtained an upper limit of $\sim$ 20 000 K for upstream H temperature which, while not inconsistent with the one-shock model, may favour the two-shock model.

The most promising approach, however, to determining remotely the global structure of the heliosphere is to use the Lyman-α absorption line in the direction of nearby stars. A neutral hydrogen pileup or wall may be detectable in directions where the decelerated H is red-shifted out of the shadow of the interstellar absorption if the interstellar column density is sufficiently low. Linsky and Wood (1996) and Frisch et al. (1996) attributed the red-shifted excess absorption in Hubble Space Telescope (HST) GHRS Lyman-α observations towards α Cen (seen previously by Copernicus and IUE, Landsman et al., 1984) to the solar hydrogen wall. Shown in Figure 5.27 are the Linsky and Wood (1996) observations. The solid curves are the observed profiles for α Cen A and B, and the wavelength scale is relative to the Lyman-α line center in the heliocentric rest frame. The dashed curve is the assumed intrinsic stellar Lyman-α emission profile. In both the analysis of Linsky and Wood (1996) and Gayley et al. (1997) (below), the accurate representation of the intrinsic stellar profile is unimportant since the absorption features of interest vary sharply. The dotted curves in Figure 5.27 give the attenuation of the stellar Lyman-α emission by interstellar H with column depth $N = 4.5 \times 10^{17}$ cm^{-2}, velocity $V = -18$ km s^{-1} and a Doppler broadening $b = 9.3$ km s^{-1}. The value for N was fixed by scaling to the Deuterium column density, assuming the commonly accepted value of D/H $= 1.6 \times 10^{-5}$ (Linsky et al., 1995). Figure 5.27 shows very clearly that additional absorption is required both redward and blueward of the interstellar feature if the fit is to be completed. Furthermore, the fit must be applied preferentially to the redward side, so arbitrarily changing the D/H ratio is unacceptable. Linsky and Wood (1996) and Frisch et al. (1996) interpreted the additional redward absorption as evidence for the detection of the hydrogen wall. The blueward absorption suggests the possibility of a hydrogen wall about α Cen A and B.

To see why the H wall should produce an observable signature in the Lyman-α absorption data, consider the optical depth of the H wall,

$$\tau_{hw}(\lambda) = \frac{7.5 \times 10^{-13}}{b_{hw}} N_{hw} e^{-(247\lambda - v_{hw})^2/b_{hw}^2}\,, \tag{151}$$

where v_{hw} and b_{hw} are in km s^{-1} (and negative v_{hw} corresponds to motion toward the Sun), and λ is in Å from line center in the heliocentric frame. The narrow absorption domain of interest in Figure 5.27 appears in the vicinity of +0.1 Å,

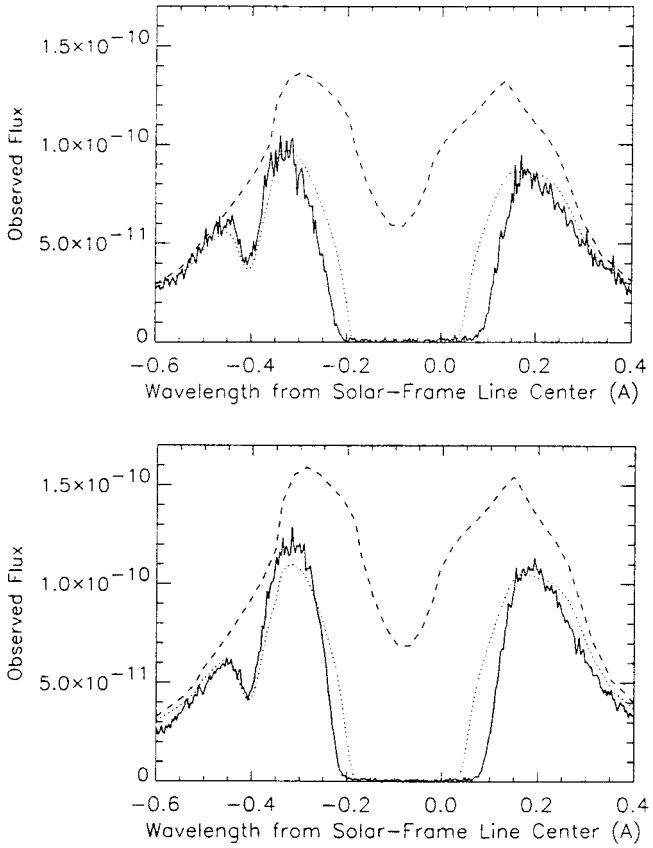

Figure 5.27. The solid curves are GHRS Lyman-α profiles towards (a) α Cen A and (b) α Cen B. The upper dashed curve is the assumed intrinsic stellar Lyman-α emission profile. The dotted curve shows the intrinsic stellar emission line after absorption by a purely LISM cloud with $N_H = 4.5 \times 10^{17}$ cm^{-2}, $b = 9.3$ km/s, and $v = -18.2$ km/s, with D/H $= 1.6 \times 10^{-5}$. (Linsky and Wood, 1996.)

corresponding to a Maxwellian sub-population moving at $+25$ km s^{-1} away from the Sun. Linsky and Wood (1996) found they could achieve a reasonable fit to the profile in this domain using $N_{hw} = 3 \times 10^{14}$ cm^{-2}, $b_{hw} = 22$ km s^{-1}, and $v_{hw} = -8$ km s^{-1}. Using these parameters, equation (151) yields $\tau_{hw} = 1.12$ at $\lambda = +0.1$. Thus, a simple constraint is that any heliospheric model invoked to explain this absorption feature must yield an optical depth of roughly unity at $\lambda = +0.1$ in the heliocentric frame.

Since the column depth of the hydrogen wall is three orders of magnitude smaller than the column depth in the LISM toward α Cen, it may be surprising at first glance that the heliospheric optical depth at +0.1 Å is of the same order as the LISM optical depth at that wavelength. The key difference is that the hydrogen wall is heated and decelerated, which both broadens and redshifts the heliospheric

component away from the -0.07 Å centroid of the LISM absorption and toward the $+0.1$ Å wavelength of interest.

To compare the relative importance of the temperature increase and the velocity shift in allowing the hydrogen wall to be visible, one finds from Equation (151) that decelerating the projected velocity of the hydrogen wall along the α Cen sightline by an additional 1 km s^{-1} (from -8 km s^{-1} to -7 km s^{-1}) has the same effect as increasing the temperature by 2300 K (if b_{hw} is purely thermal, so that $T_{hw} = 61 b_{hw}^2$). Each would increase the optical depth by 15%. Since the Linsky and Wood v_{hw} is redshifted by 10 km s^{-1} relative to the LISM, and heated by about 24 000 K, extrapolating the above analysis suggests that each of these effects contributes about equally in making the hydrogen wall visible. However, the nonlinear response to temperature rapidly becomes important as the temperature falls, and equation (151) indicates that $\tau_{hw}(0.1)$ falls by a factor of 5 if b_{hw} is reduced to 16 km s^{-1}, corresponding to $T_{hw} \simeq 16,000$ K. For this reason, the temperature is the parameter that shows the most significant variation, and is therefore the most critical discriminant.

Gayley et al. (1997) used Equation (151) locally in conjunction with the modelled heliospheres of Section 5.5.1 (specifically, models 1, 2, and 3 listed in Table IX) and the Linsky and Wood (1996) assumptions about the interstellar H parameters to obtain synthetic Lyman-α absorption spectra. Figure 5.28 shows the Lyman-α absorption at the red edge of the LISM feature for each of the three heliospheric models listed in Table IX. The modeled results can then be compared directly to the GHRS data of Linsky and Wood (1996) (the solid curve).

The primary and very important conclusion to emerge from the Gayley et al. (1997) study is that the synthetic Lyman-α profiles support the detection of the hydrogen wall by Linsky and Wood (1996). Thus, it appears that the hydrogen wall has indeed been observed!

Comparing the results of models 1–3 with the observations demonstrates the following points, all of which are robustly insensitive to variations in the plausible intrinsic profile. (1) Heliospheric Lyman-α absorption in the supersonic model (model 1) is too strong due to the stronger deceleration and especially the increase in temperature of the interstellar neutrals in the hydrogen wall. (2) Heliospheric Lyman-α absorption in the subsonic model with low Mach number (model 2) is too weak, since the more gradually diverted interstellar plasma flow leads to less deceleration and less heating of the interstellar neutrals. (3) The model with a barely subsonic Mach number of 0.9 (model 3) and a larger plasma density (see Table IX) does yield a favorable fit, giving compression and charge exchange heating of the neutrals intermediate to the results of Models 1 and 2.

The consistency with GHRS data given by the parameters of model 3 should not be expected to be unique, and other combinations may well suffice. However, Gayley et al. (1997) suggest that the incident interstellar gas flow can be neither highly supersonic nor highly subsonic, since these possibilities lead rather inevitably to Lyman-α absorption that is either too strong or too weak respectively.

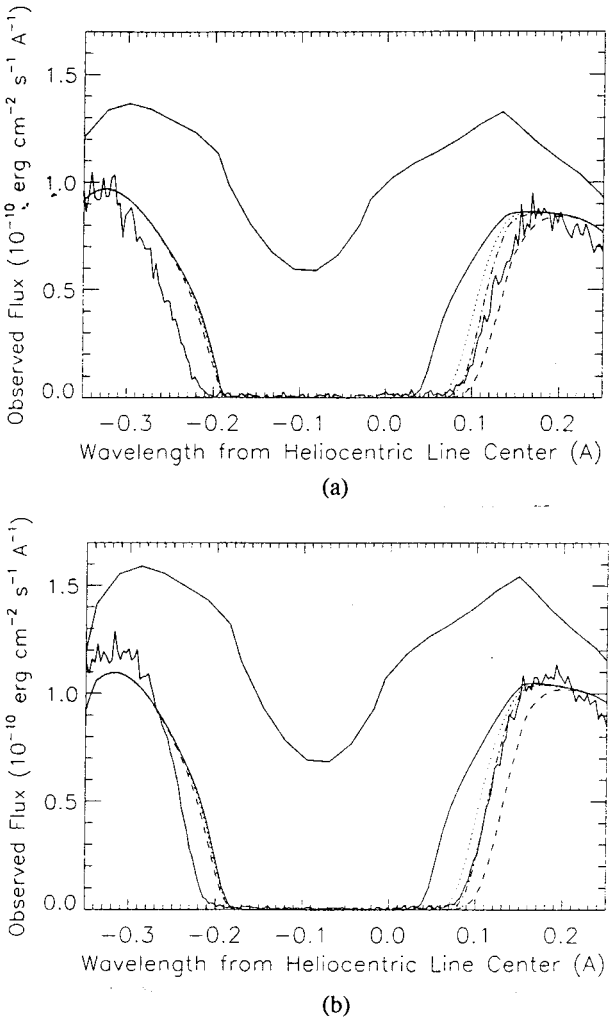

Figure 5.28. Similar to Figure 5.26, except that absorption from the three heliospheric models is included. All curves from Figure 5.26 are reproduced as solid lines, while the dashed curve is for model 1 (M=1.5), dotted for model 2 (M=0.7), and dot-dashed for model 3 (M=0.9). Again, (a) and (b) refer to α Cen A and B respectively. The red edge of the LISM absorption feature is fitted best by model 3, and note that none of the models can fit the blue edge. This raises the possibility that α Cen A and B also possess a hydrogen wall. (Gayley et al., 1997.)

On the other hand, it appears that a barely subsonic interstellar wind provides the proper degree of both deceleration and heating of the neutrals to fit the data. More detailed constraints on the interstellar Mach number and inflow density imposed by these data clearly need to be explored in future models.

Finally, Richardson (1997) has used the solar cycle variability of the solar wind ram pressure to suggest the possibility that this may cause the HP to move in and

out. If the heliopause speed is large compared to that of the LISM, the possibility that the heliosphere will alternate between a one- and two-shock heliosphere was suggested. By considering IMP 8 and Voyager 1 and 2 data, estimates of the possible movement of the HP were derived which appeared to support the possibility that the global heliospheric structure might alternate with solar cycle between a one- and two-shock state. To support this idea, however, more extensive theoretical modelling efforts are needed.

6. Global Models of the Solar Wind-LISM Interaction II. Magnetohydrodynamic Models

The role of both interplanetary and interstellar magnetic fields was neglected entirely in Section 5. Unfortunately, compared to our present understanding of hydrodynamical models of the heliosphere, efforts to include magnetic fields into these models are at a somewhat preliminary stage. At present, only a handful of papers have simulated the 3D MHD structure of the heliosphere and much remains to be explored. Here, we survey briefly some analytic approaches that have been developed and describe the few simulations that exist.

To model the interaction of the solar wind with a partially ionized LISM, the following 3D set of MHD equations must be solved,

$$\frac{\partial \rho}{\partial t} + \nabla \cdot \rho \mathbf{u} = Q_\rho \,, \tag{152}$$

$$\rho \frac{\partial \mathbf{u}}{\partial t} + \rho \mathbf{u} \cdot \nabla \mathbf{u} + (\gamma - 1) \nabla e + (\nabla \times \mathbf{B}) \times \mathbf{B} = \mathbf{Q}_m \,, \tag{153}$$

$$\frac{\partial}{\partial t}\left(\frac{1}{2}\rho u^2 + e + \frac{B^2}{8\pi}\right) + \nabla \cdot \left[\left(\frac{1}{2}\rho u^2 + \gamma e\right)\mathbf{u} + \frac{1}{4\pi}\mathbf{B} \times (\mathbf{u} \times \mathbf{B})\right] = Q_e \,, \tag{154}$$

$$\frac{\partial \mathbf{B}}{\partial t} - \nabla \times (\mathbf{u} \times \mathbf{B}) = 0 \,, \tag{155}$$

$$\nabla \cdot \mathbf{B} = 0 \,, \tag{156}$$

together with the equation of state $e = \alpha n k_B T/(\gamma - 1) = p/(\gamma - 1)$. Here the choice of $\alpha = 1$ or 2 (or greater) corresponds to either the neutral or plasma population. The remaining variables have their usual definitions and the source terms Q_ρ, $\mathbf{Q}_m$, and Q_e serve to couple the neutral hydrogen and proton populations.

Subject even to the assumption of an isotropic solar wind, the problem (152)–(156) is inherently 3D thanks to the solar magnetic field and the current sheet. The

little that we know about the orientation and strength of the LISM magnetic field is summarized in Section 5.1.

6.1. KINEMATIC MAGNETIC FIELD MODELS

Magnetic fields do not play a major role in the dynamics of the supersonic solar wind, their pressure contribution being much less than that of the solar wind ram pressure. However, in the presence of a solar wind decelerated by ion pickup, the magnetic field can deviate slightly from the expectations of the familiar Parker (1963) interplanetary magnetic field. Recall that subject only to the assumption of $B_\theta = 0$ and axial symmetry ($\partial B_\phi/\partial\phi = 0$ in spherical co-ordinates (r, θ, ϕ)), the IMF spirals according to [Parker, 1963]

$$\begin{aligned} B_\phi(r) &= B_r(r_c)\left(\frac{r_c}{r}\right)^2 \frac{\Omega(r - r_c)}{u}\,; \\ B_r(r) &= B_r(r_c)\left(\frac{r_c}{r}\right)^2\,, \end{aligned} \tag{157}$$

where r_c is an inner boundary. The total magnetic intensity is $|\mathbf{B}| = (B_r^2 + B_\phi^2)^{1/2} \propto r^{-1}$ for $r \gg r_c$. In deriving (156), it was not assumed that the radial solar wind speed u was a constant in heliocentric radial distance. With charge exchange, u decays approximately as $u_0(1 - Ar^{-1})$ for some constant A (see Section 4.3), indicating that $B_\phi(r)$ is correspondingly larger at a given location in the outer heliosphere than its nominal Parker value. This is an obvious result of the compression of the solar wind as it decelerates. By using the solar wind – LISM models of Section 5.5.1, the difference between B_ϕ for a solar wind mediated by charge exchange and one without charge exchange can be determined. Illustrated in Figure 6.1 is the 10% increase in B_ϕ compared to the B_ϕ expected from a constant velocity solar wind. Smaller differences can be expected in the downstream direction since the deceleration of the solar wind is less pronounced in this direction.

Much more interesting is the role of the magnetic field in the heliosheath, especially in the upstream region where the flow is subsonic and approximately incompressible. It was observed by Axford (1972) and Cranfill (1971) that downstream of the termination shock, the flow velocity $u \propto r^{-2}$ for a flow that is spherically symmetric, radial and incompressible ($\rho \sim const.$). Hence, since

$$ru B_\phi = \text{constant}\,, \tag{158}$$

(B_r can safely be neglected), the azimuthal or transverse component increases according to

$$B_\phi \propto r \sin\theta\,. \tag{159}$$

Evidently, the magnetic field energy density must increase downstream of the termination shock until it begins to exert an appreciable dynamical effect on the diverted shocked solar wind flow and the interstellar flow.

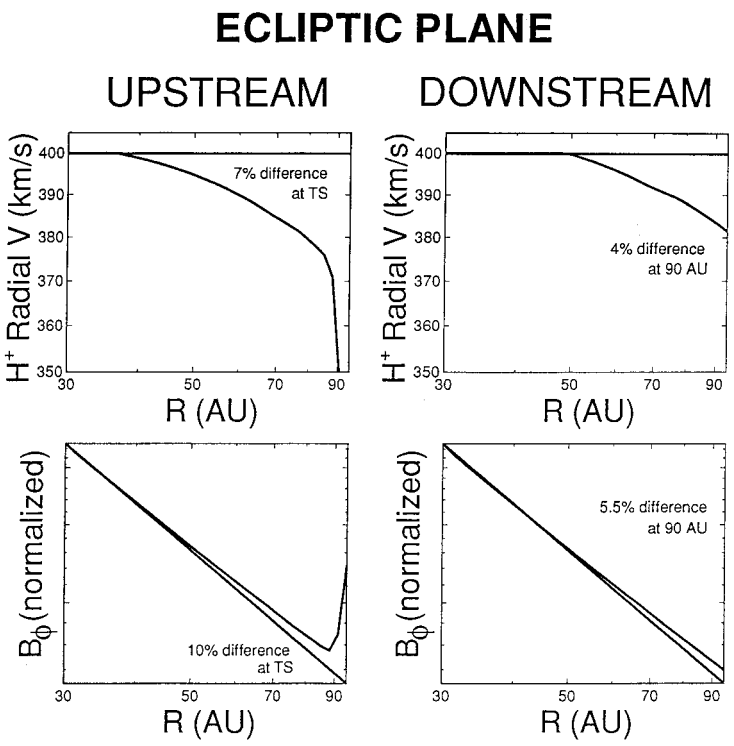

Figure 6.1. Plot of the upstream and downstream radial flow velocity obtained from the axisymmetric models of Section 5.3 (no LISM neutrals, constant flow speed) and Section 5.5.1 (self-consistent inclusion of LISM neutrals, decelerating solar wind) and the corresponding azimuthal magnetic field component B_ϕ as a function of heliocentric distance.

By following Axford (1972), Cranfill (1971), and Nerney et al. (1991; 1993), the steady spherically symmetric equations (152)–(156) can be integrated from the TS outward. The boundary conditions at the TS are determined from the normalized Rankine–Hugoniot conditions for an MHD shock, i.e.,

$$\begin{aligned}
&\bar{\rho}_2\bar{u}_2 = 1\,,\\
&\bar{\rho}_2\bar{u}_2^2 = \bar{p}_2 + \bar{B}_2^2/\beta_p = 1 + \beta_p^{-1}\,,\\
&\frac{1}{2}\bar{u}_2^2 + \frac{\gamma}{\gamma-1}\frac{\bar{p}_2}{\bar{\rho}_2} + \frac{2}{\beta_p}\frac{\bar{B}_2^2}{\bar{\rho}_2} = \frac{1}{2} + 2\beta_p^{-1}\,,\\
&\bar{B}_2\bar{u}_2 = 1\,,
\end{aligned} \tag{160}$$

after assuming that the solar wind is cold ($p_1 \simeq 0$) and that the solar wind magnetic field is purely azimuthal. In (160), $\beta_p \equiv \rho_1 u_1^2/B_1^2$ is the plasma beta and $\bar{\rho} = \rho/\rho_1$, $\bar{u} = u/u_1$, $\bar{B} = B/B_1$, and $\bar{p} = p/\rho_1 u_1^2$. The subscripts 1/2 denote upstream/downstream, as before. The integrated equations of motion in the subsonic regime are

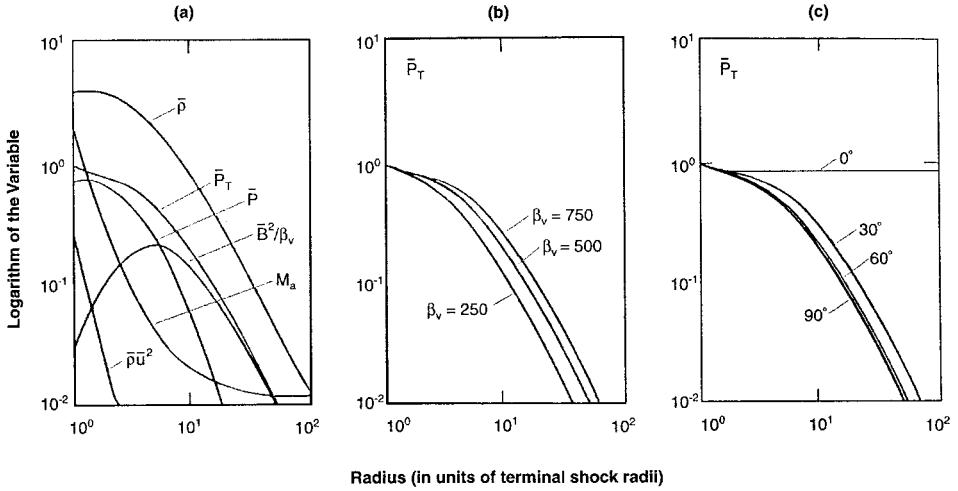

Figure 6.2. (a) The Axford-Cranfill effect. $\beta_p = 500$. (b) The normalized total pressure $\bar{p}_T$ as a function of normalized radius for $\beta_p = 250$, 500, and 750. As the magnetic field strength increases, the total pressure decreases. (c) $\bar{p}_T$ for $\beta_p = 500$ at polar angles $\theta = 0°$, 30°, 60°, and 90°. The 0° case is the same as the zero-field solution and the solution for 90° corresponds to panels (a) and (b). (Nerney et al., 1991.)

$$\bar{\rho}\bar{u}\bar{r}^2 = 1\,,$$

$$\frac{1}{2}\bar{u}^2 + \frac{\gamma}{\gamma-1}\frac{\bar{p}}{\bar{\rho}} + 2\beta_p^{-1}\bar{B}^2 = \frac{1}{2} + 2\beta_p^{-1}\,,$$

$$\bar{p}/\bar{\rho}^{\gamma} = \bar{p}_2/\bar{\rho}_2^{\gamma}; \tag{161}$$

$$\bar{r}\bar{u}\bar{B} = 1\,,$$

where $\bar{r} = r/R_t$. The reason for expressing the Rankine–Hugoniot conditions (160) and the equations of motion (161) in normalized form is to emphasize that the plasma beta β_p is the only parameter in the problem. Equations (160) and (161) are solved easily for different values of β_p. Illustrated in Figure 6.2 are solutions for different values of β_p (Nerney et al., 1991; Axford, 1972). Here $\bar{p}_T$ is the normalized total pressure (kinetic, thermal and magnetic) and $M_{\rm A}$ is the Alfvén Mach number. It was observed by Cranfill and Axford that $\bar{p}_T$ is reduced relative to the thermal pressure in the absence of a magnetic field. This effect should therefore move the TS in towards the sun for a given interstellar pressure, but only if the distances are large ($r > 5R_t$). The azimuthal field increases downstream of the termination shock until the magnetic field gradient begins to drive the flow outwards so that, asymptotically, the flow does not stagnate.

The amplification of the azimuthal magnetic field in the heliosheath has been called the 'Axford–Cranfill' effect. Clearly, the very simplified analysis presented

above needs to be considered in the context of more realistic heliospheric geometries. Nerney et al. (1991, 1993, 1995) have used the heliospheric model of Suess and Nerney (1991) (Section 5.2) to compute kinematically the interplanetary magnetic field in the heliosheath. In particular, they suggested on the basis of their gas dynamic generalization of Parker's model that the distance separating the heliopause and termination shock might be $R_{\rm H}/R_t \simeq 2$ (Equation (105)), with the implication that the Axford–Cranfill effect might be negligible.

To quantify the importance of the Axford–Cranfill effect, Nerney et al. (1991) solved the induction and solenoidal equations (154) and (156) in the (kinematic) limit in which the force on the fluid due to the magnetic field is ignored. By writing **B** in streamline coordinates,

$$\mathbf{B} = B_s\hat{e}_s + B_t\hat{e}_t + B_\phi\hat{e}_\phi \,, \tag{162}$$

$$\hat{e}_s = \mathbf{u}/|\mathbf{u}| \,, \qquad \hat{e}_t = \hat{e}_\phi \times \hat{s} \,,$$

for the unknown scalar components B_s, B_ϕ, and B_t, one can use the model of Suess and Nerney (1990) (Section 5.2) in the induction equation (154). In cylindrical coordinates (r, ϕ, z), it may be shown explicitly that B_ϕ and B_t can be derived from the streamline constants (104), and that the component along the streamline B_s satisfies the first-order differential equation

$$\mathbf{u}\cdot\nabla\left(\frac{B_s}{u}\right) - \frac{2B_t}{ru^2}\nabla\psi\cdot\nabla\mathbf{u} = 0 \,. \tag{163}$$

Equation (163) must be integrated numerically subject to the determination of (B_s, B_t, B_ϕ) on the shock. This is accomplished by using the asymptotic form of (156) ($r \gg r_c$) and converting to the streamline coordinate system.

Nerney et al. (1991) find that in the downstream direction, the magnetic field energy density never becomes large enough to dominate either the kinetic or internal energy density. In the upstream direction, however, this is no longer the case, even though the separation distance between the HP and TS is not very large. The reason for the larger than expected amplification of the azimuthal magnetic field is the stronger deceleration of the heliosheath flow before it turns along the face of the heliopause. The stronger deceleration then leads to additional compression and hence amplification of the magnetic field.

Pauls and Zank (1997c) used their 3D hydrodynamical model of an isotropic solar wind interacting with the supersonic LISM (Pauls and Zank, 1997a) to investigate the kinematic magnetic field topology under more realistic flow conditions. The interstellar magnetic field is assumed to be parallel to the solar rotation axis with a magnitude of 0.15 nT, while the interplanetary magnetic field is a Parker spiral with a magnitude of 5 nT at 1 AU. Plate 6.1(a) (Pauls and Zank, unpublished) illustrates the 2D projection of the IMF, and the Parker spiral is clearly evident, extending in a symmetric fashion until the TS in the upstream direction. Thereafter, the magnetic field is compressed at the TS and the field line which passed through

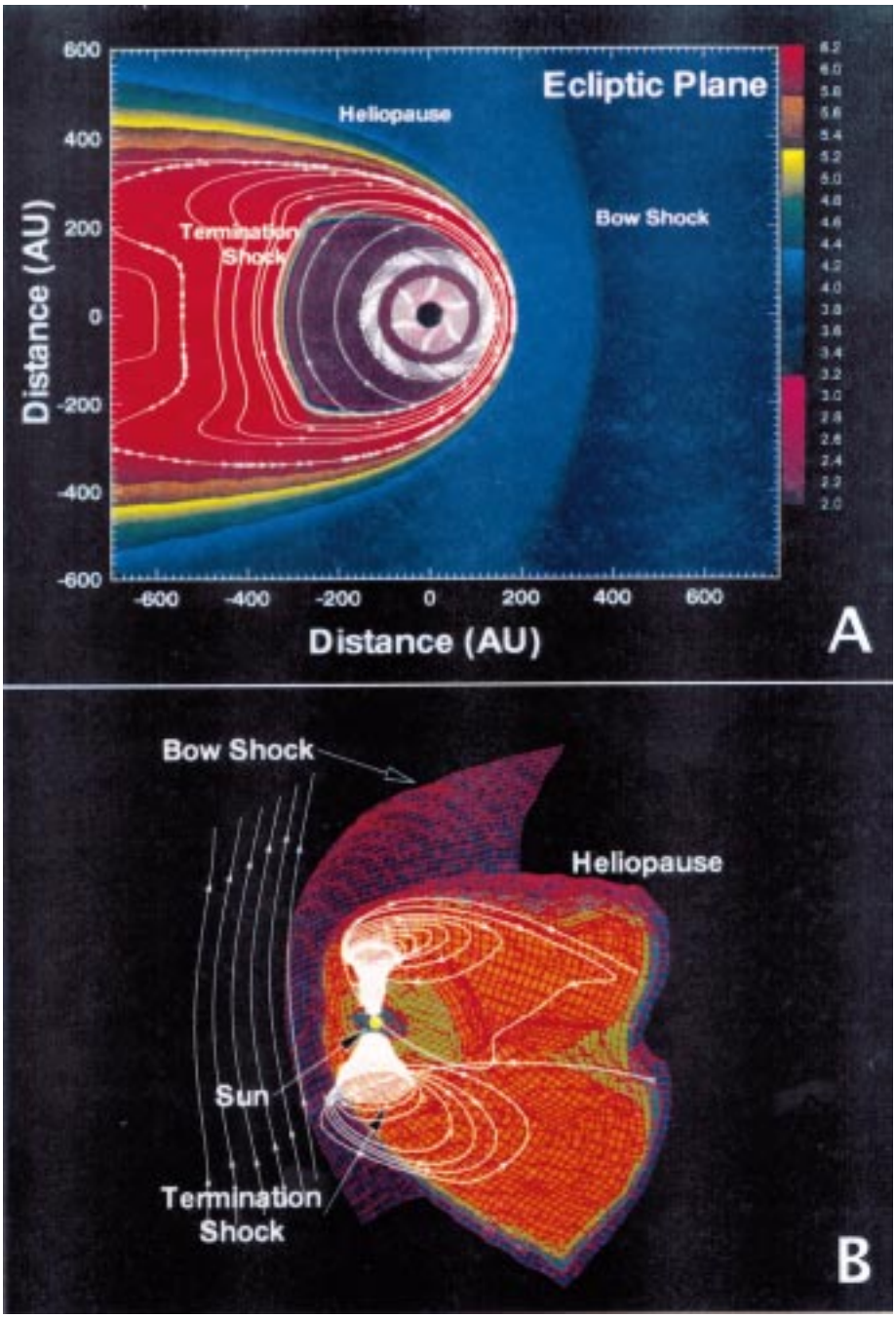

Plate 6.1. (a) Shown in white are the interplanetary Parker magnetic field lines in the ecliptic plane. The colour corresponds to the Log[plasma temperature (K)] as a function of distance. The model heliosphere corresponds to the 3D isotropic gas dynamic simulations of Pauls and Zank (1996). (b) A 3D depiction of the interplanetary and LISM magnetic field showing the characteristic 'tornado'-like structure of the IMF. Of note is the repeated crossing of the termination shock by the spiral magnetic field. (Pauls and Zank, unpublished.)

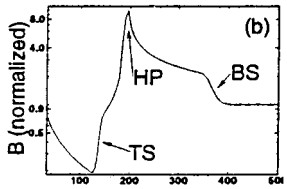

Figure 6.3. The normalized magnetic field strength along the nose. (Pauls and Zank, 1997.)

the upstream TS can re-enter the unshocked heliosphere at a higher latitude further down the TS. Indeed, as is evident from Plate 6.1a, a magnetic field line can cross the termination shock multiple times. One implication of this, is that the TS cannot be approximated as a perpendicular shock throughout most of the heliosphere. The 3D projection of Plate 6.1a is shown in Plate 6.1b, showing the tornado-like character of the interplanetary magnetic field. Plate 6.1(b) shows especially clearly how the high latitude magnetic field crosses the TS multiple times before being dragged out by the subsonic heliotail and supersonic heliosheath flow. The draping of the interstellar magnetic field about the heliopause can also be seen.

The magnetic field topology revealed in Plates 6.1a and 6.1b has intriguing implications for both the acceleration of the anomalous cosmic-ray component and the transport of cosmic-rays in the heliosphere. To date, these have scarcely been appreciated although Nerney et al. (1995) have made similar points.

The amplification of the azimuthal magnetic field along the stagnation line is illustrated in Figure 6.3 as a function of radial distance. The interstellar field is compressed by a factor of $\sim$2 at the weak bow shock and then increases almost tenfold over the assumed LISM magnetic field before meeting the interplanetary magnetic field at the heliopause. The Axford–Cranfill effect is clearly evident. The magnitude of the LISM magnetic field in the vicinity of the HP in the ecliptic region indicates that the $\mathbf{J} \times \mathbf{B}$ force should certainly not be neglected here and that the kinematic model breaks down. Nonetheless, the kinematic models provide considerable insight into the expected behaviour of the IMF in the heliosheath.

Before turning to those simulations in which the magnetic field is included self-consistently, it should be mentioned that Nerney et al. (1995) consider the effect of the 22-year solar cycle on the heliosheath magnetic field. Since the heliosheath flow speed is subsonic for large regions of the two-shock model and throughout the one-shock model, it can take almost one solar cycle for the shocked solar wind to convect down the heliosheath/heliotail. Thus, the changing polarity of the solar magnetic field over the solar cycle can influence the overall magnetic field structure in the heliosheath. Nerney et al. (1995) show that streamlines in the heliosheath carry an imprint of the 11-year magnetic polarity cycle, which they name ‘magnetic polarity envelopes.’ The polarity envelopes are mappings of the unipolar regions lying at either pole of the sun. During solar minimum, the polarity envelopes grow to their maximum latitudinal extent and shrink to zero at solar maximum. This leads to alternating polarities of the envelopes in the heliosheath.

6.2. ANALYTIC TWO-SHOCK MHD MODEL

The thin layer or Newtonian approximation method for determining the structure of the heliospheric bow shock (Baranov et al., 1971; Section 5.2) for a supersonic LISM has been extended to include a homogeneous interstellar magnetic field of arbitrary magnitude and orientation (Fahr et al., 1988; Ratkiewiez, 1992). As in Section 5.2, for a two-shock model, the heliopause curve defined by $r = r(\theta)$ satisfies a third-order ordinary differential equation of the form (107), where now $F_{1,2,3} = F_{1,2,3}(\theta, \rho_\infty, \mathbf{u}_\infty, \mathbf{B}_\infty)$ depends also on the LISM magnetic field parameters. The initial conditions are (108) and $r''(0) = f(M_A)$ (Ratkiewiez, 1992). The minimum heliocentric distance to the HP is now given by

$$(R_H/r_0)^2 = \rho_0 u_0^2 / \left(\rho_\infty u_\infty^2 \cos^2\theta_s - B_\infty^2 \cos 2(\theta_0 - \theta_s)\right) , \tag{164}$$

(compare to Equation (109)) where θ_0 is the LISM magnetic field inclination angle relative to the LISM flow vector and θ_s is the deviation angle of the heliospheric stagnation line from the LISM flow vector. The angle θ_s can be obtained from (Fahr et al., 1988)

$$\rho_\infty u_\infty^2 \sin 2\theta_s = 2B_\infty^2 \sin 2(\theta_s - \theta_0), \qquad -\pi/2 \le \theta_s \le \pi/2 . \tag{165}$$

For a given Alfvén Mach number, the appropriate third-order equation (107) can be solved numerically, and examples for a magnetic field parallel to the LISM flow are illustrated in Figure 6.4. As M_A increases from 1, the HP curvature decreases. For $M_A \simeq 1$, the thin layer approximation predicts an almost spherical structure. Shown in Figure 6.5 are curves of the minimum heliocentric distance to the HP as a function of magnetic field inclination angle. For all M_A, the minimum distance occurs for an inclination angle of $\theta_0 = 90°$, i.e., for a LISM magnetic field perpendicular to the interstellar flow, and the maximum distance occurs for a LISM magnetic field parallel to the flow vector. The deviation angle θ_s plotted as a function of magnetic field inclination angle θ_0, Figure 6.6, shows that the stagnation line can deviate substantially from the LISM flow direction. The deviation depends critically on whether M_A is greater or less than 1.

Mullan and Arge (1996) have suggested that the structure of the bow shock should be determined by dissipative processes associated with ion-neutral friction. A 1D two-fluid transverse MHD model (i.e., an MHD fluid coupled to a neutral H fluid by charge exchange) was was used to explore this possibility. For a significant range of plausible LISM electron number densities and magnetic field strengths, Mullan and Arge (1996) found that the heliosphere bow shock can be mediated by ion-neutral drifts. Since the primary dissipation mechanism in the model is ion-neutral damping, the length scale for the shock thickness can be hundreds (or more) of AU. This is depicted in Figure 6.7 which plots contours of the bow shock thickness as a function of upstream LISM ion density and magnetic field strength. If the bow shock is indeed mediated strongly by ion-neutral drift, this may effectively ensure a one-shock structure for the heliosphere. However, the results of Mullan

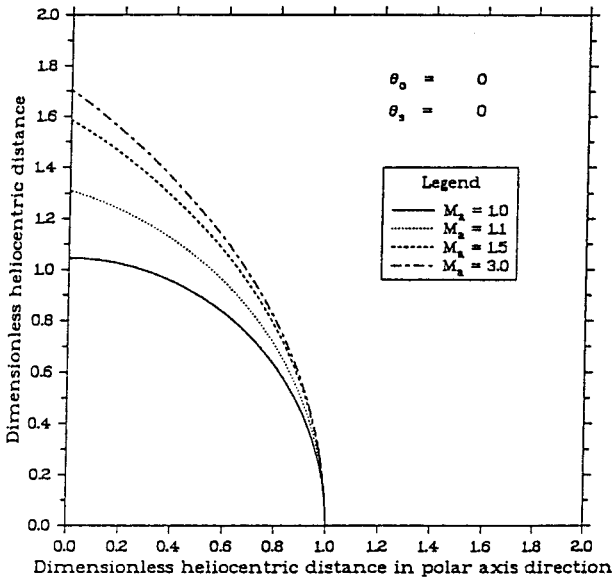

Figure 6.4. Examples of heliopause geometry for different Alfvén Mach numbers M_A in the MHD thin layer approximation ($\theta_0 = 0°$, $\theta_s = 0°$). (Ratkiewicz, 1992.)

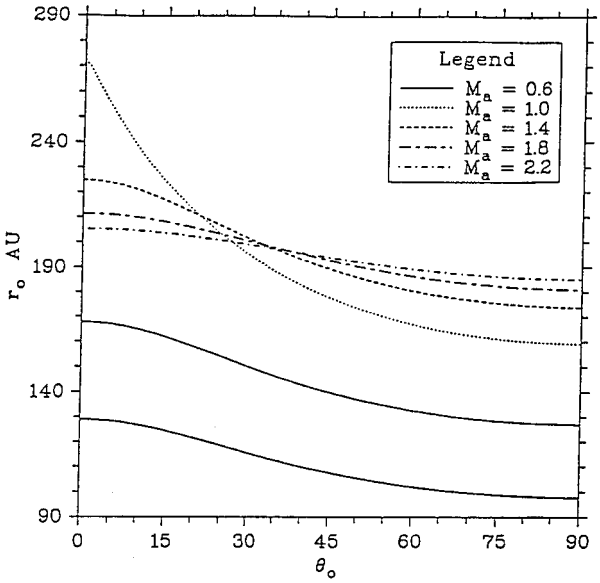

Figure 6.5. Heliocentric distance to the heliopause as a function of inclination angle θ_0 for different Alfvén Mach numbers. (Ratkiewicz, 1992.)

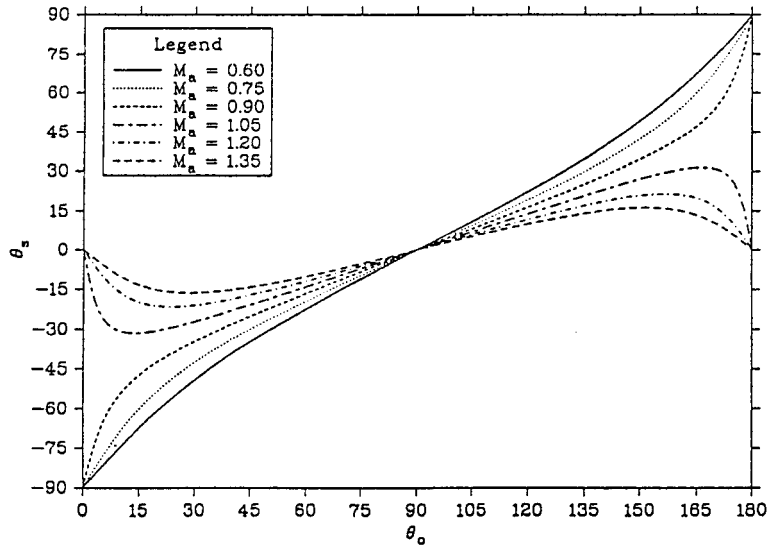

Figure 6.6. Deviation angle θ_s as a function of inclination angle θ_0 for different values of the Alfvénic Mach number. (Ratkiewicz, 1992.)

and Arge (1996) are 1D only and the scale length of the shocks they investigate are comparable to the global heliospheric-LISM system and multi-dimensional effects should not be neglected.

6.3. 3D MHD MODELS

The number of papers attempting to simulate the full 3D structure of the magnetized solar wind interacting with a magnetized LISM is small. The inclusion of magnetic fields renders the problem of heliospheric structure fully three-dimensional. Nonetheless, some efforts have been made to include magnetic fields into axisymmetric models (Fujimoto and Matsuda, 1991; Baranov and Zaitsev, 1995; Pogorelov and Semenov, 1997), assuming that the LISM magnetic field is parallel to the interstellar flow and that the solar wind is not magnetized. Since such a field orientation is not expected of the LISM and since some controversy exists about the possibility that the bow shock can split into several shocks (fast, slow and normal), we do not discuss these models here. Indeed, we should emphasize that the relative paucity of MHD simulations makes it difficult to draw firm conclusions about heliospheric structure in a magnetized environment. Instead, we shall describe the basic 3D results that have been presented by Washimi (1993), Washimi and Tanaka (1996), Ratkiewicz et al. (1998), Pogorelov and Matsuda (1998), and Linde et al. (1998).

Ratkiewicz et al. (1998) assume an unmagnetized solar wind and consider the variation of interstellar magnetic field strength and orientation. Thus, the fundamental role of the Axford–Cranfill effect is neglected. No interstellar neutral com-

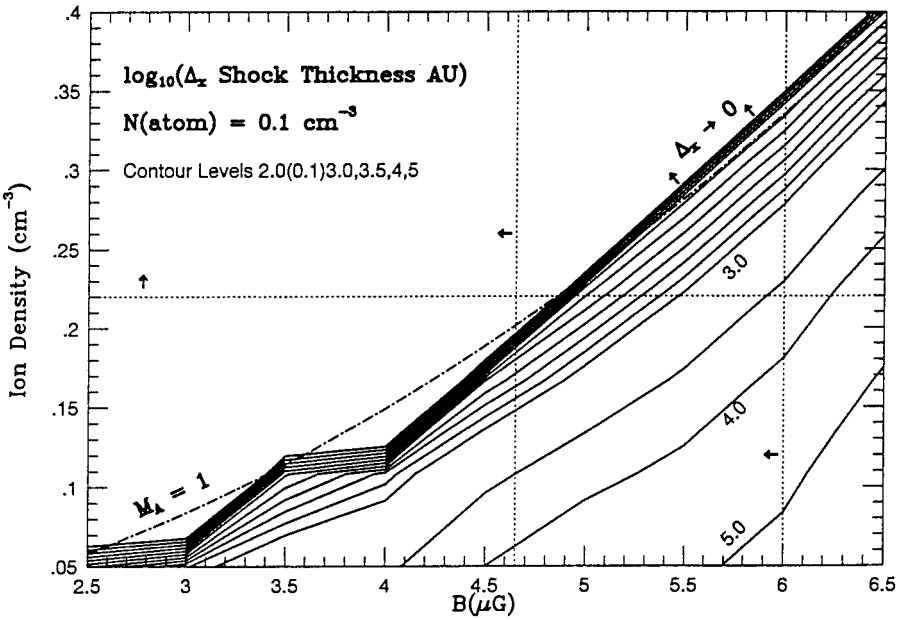

Figure 6.7. The solid lines depict contours of the logarithm[shock thickness (AU)] of ion-neutral mediated shocks as functions of initial proton number density and initial magnetic field strength. The narrowest shocks (top contour) are $\sim$ 100 AU wide. Above the top curve, ion-neutral friction is insufficient to completely mediate the shock and the shocks are narrower. (Mullan and Arge, 1996.)

ponent is included either. These authors concentrate on relating the analytic two-shock results of Section 5.2 above to the simulations, specifically the orientation of the stagnation line and the stand-off distance of the heliopause. Illustrated in Figure 6.8 are the pressure contours for a 3D simulation in which the magnetic field inclination angle θ_0 is 30°. Figure 6.8 is plotted in the symmetry plane defined by the magnetic field and LISM flow vectors. The BS, HP, and TS, while not very clearly resolved, are marked. Both the HP and BS exhibit a marked asymmetry and the TS appears to also be somewhat asymmetric. The heliopause nose and BS nose are in opposite directions and the TS does not appear to be bullet-shaped even though the simulations exclude LISM neutrals. Ratkiewicz et al. (1998) find generally that for magnetic field inclination angles $0° < \theta_0 < 90°$, the heliopause/heliosphere is asymmetric, and that the minimum distance to the HP (TS) occurs for $\theta_0 = 90°$. For the BS, the minimum distance occurs for $\theta_0 = 0°$. These results are in basic agreement with those derived from the analytic thin-layer two-shock models, although the thickness of the heliospheric boundary regions appears to invalidate the Newtonian approximation. Reasons for the asymmetry of the HP and BS are presented by Ratkiewicz et al. (1998).

Pogorelov and Matsuda (1998) considered too the influence of the LISM magnetic field inclination angle on the global heliospheric structure. In their simulations, they also neglect the interplanetary magnetic field and interstellar neutrals.

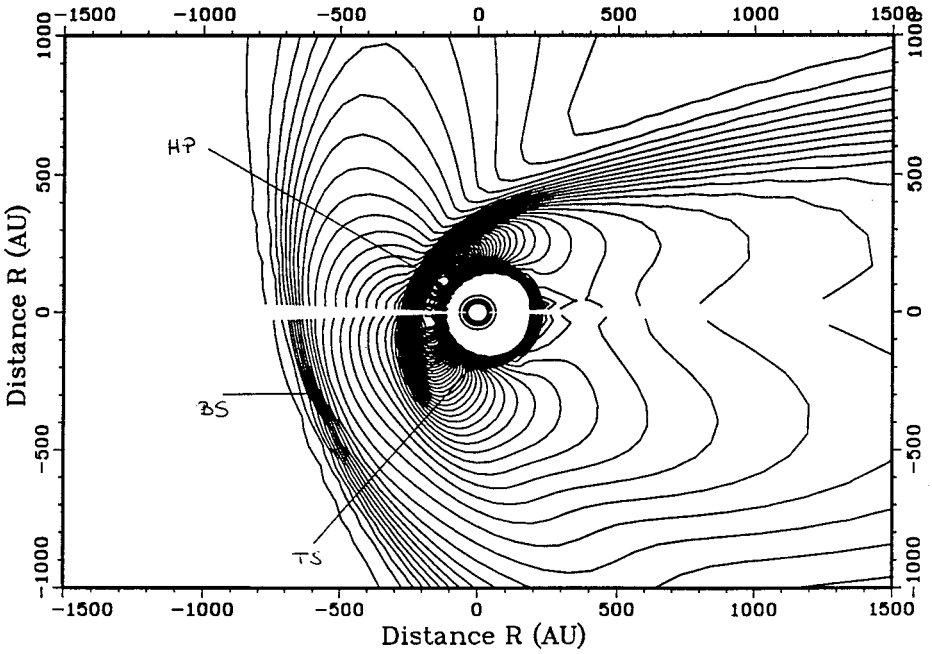

Figure 6.8. Thermal pressure contour plots for inclination angle $\theta_0 = 30^0$, LISM Mach number $M_A = 1.5$, and solar Mach number 10. The positions of the bow shock, heliopause, and termination shock are labeled. (Ratkiewicz et al., 1997.)

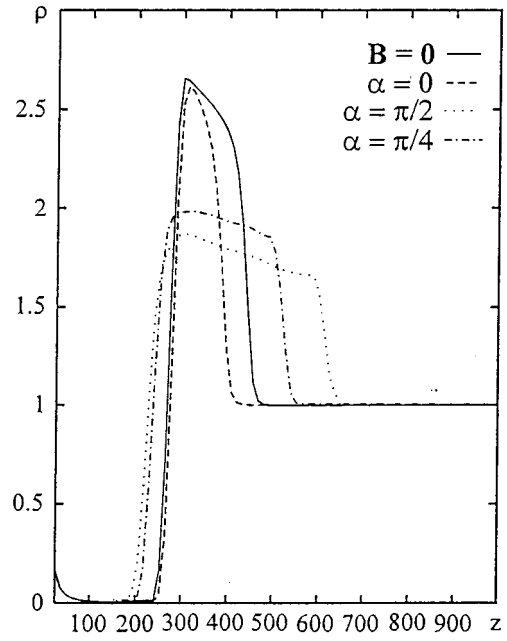

Figure 6.9. Density profiles along the stagnation axis for different magnetic field inclination angles θ_0. (Pogorelov and Matsuda, 1998.)

TABLE XIII

Solar wind and LISM plasma parameters used for the 3D simulations of Washimi and Tanaka (1996). Solar wind parameters are for 1 AU except for T which corresponds to 50 AU

	Solar wind	LISM
$n(\mathrm{cm}^{-3})$	5	0.1
u (km s^{-1})	400	25
T(K)	10^4	10^4
$\|B\|$ (nT)	2.8	0.15

Like Ratkiewicz et al. (1998), they find that the asymmetry of the heliopause is roughly consistent with the analytic Newtonian approximation model. In Figure 6.9, the density profile along the Sun–LISM flow direction axis is plotted for three inclination angles θ_0 and for $\mathbf{B} = 0$. Unfortunately, the profile is not plotted on a logarithmic scale and the TS location is not easily read off the graph. Altogether, the same basic conclusions arrived at by Ratkiewicz et al. (1998) appear to hold in the analysis of Pogorelov and Matsuda (1998).

Washimi and Tanaka (1996) and Linde et al. (1998) have developed fully 3D MHD simulations which include the interplanetary magnetic field. We consider first the simulations of Washimi and Tanaka (1996) since, unlike those by Linde et al. (1997), no neutral hydrogen model is included at any level.

The parameters of the Washimi and Tanaka (1996) simulations are listed in Table XIII. The LISM magnetic field is perpendicular to the LISM flow and parallel to the solar rotation axis. The global structure is illustrated in Figure 6.10, and the bow shock, heliopause and termination shock are evident. The characteristic bullet-shape of the TS seen in the gas dynamic simulations is recovered. In Figure 6.11, the magnetic field components and magnitude are plotted. The interplanetary toroidal component B_y is enhanced in the heliosheath. An interesting result is that the neutral sheet in the heliosheath is bent upwards, so that the amplitude of B_y is greater on the equatorial than on the meridional plane. The equipressure contours are a minimum in the middle region of the upstream heliosheath and the pressure depression is more evident on the equatorial than on the meridional plane. The depressions are due to a magnetic pressure effect and the pressure depletion in Figure 6.10 coincides exactly with the B_y enhancements of Figure 6.11. This corresponds to the formation of a 3D magnetic shell or wall in the outer regions of the upstream heliosheath. The outward flow of the shocked solar wind (the u_x component) is rapidly curtailed, indicating that the magnetic wall in the middle and high latitudes diverts the flow tailward. Only on the up-

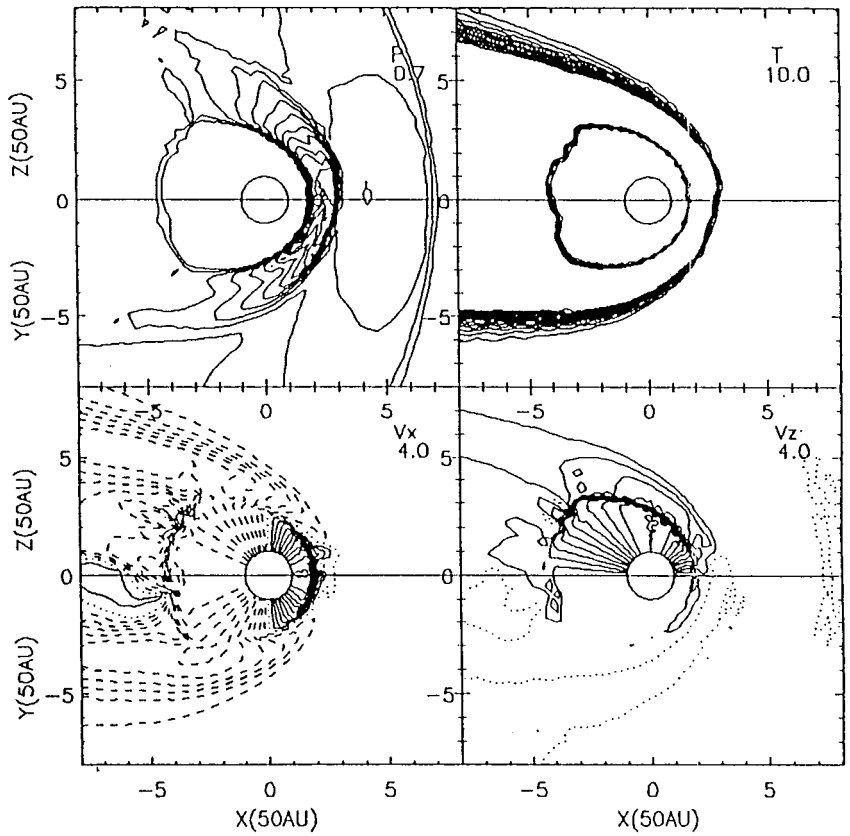

Figure 6.10. Global structure of the 3D MHD solar wind-LISM interaction. The upper and lower halves of each panel correspond to the meridional (x, z) and equatorial (x, y) planes respectively. From the upper left in clockwise order, the panels show pressure, temperature, u_x velocity, and u_z velocity contours respectively. Solid and dashed lines correspond indicate positive and negative values. Regions of positive and negative maximum/minimum values are indicated by a p or m. (Washimi and Tanaka, 1996.)

wardly distorted heliospheric current sheet is u_x positive almost all the way to the heliopause. Thus, Washimi and Tanaka (1996) find that the region between the TS and the magnetic wall is occupied by solar wind originating from the middle and high latitudes whereas the region between the magnetic wall is composed of solar wind originating from the equatorial neutral sheet region.

Profiles of the ram pressure, thermal pressure, and magnetic pressure are shown in Figure 6.12 and the location of the termination shock, heliopause, and bow shock is identified. The TS is located at ∼90 AU and the HP at ∼145 AU. Observe the peak in the magnetic pressure at the HP, which balances approximately the solar wind thermal pressure. The magnetic wall, located at ∼115 AU, corresponds to a local minimum in thermal pressure and to a virtual stagnation of the solar wind flow. The presence of a subsequent peak in the subsonic solar wind ram pressure

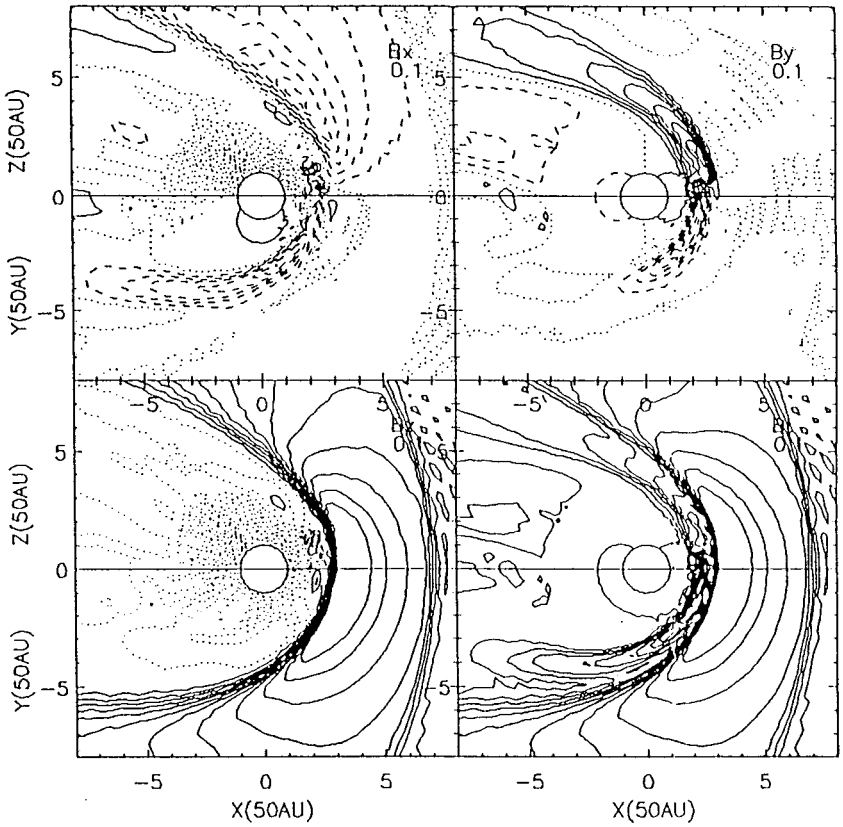

Figure 6.11. The global structure of the magnetic field corresponding to Figure 6.10. As before, in clockwise order, the panels show B_x, B_y, B_z, and $|B|$ contours. Dotted lines depict zero values of a variable. (Washimi and Tanaka, 1996.)

beyond the magnetic wall indicates that this plasma does not originate locally i.e., it comes from the equatorial current sheet region, as discussed above.

Thus, the major result to emerge from the Washimi and Tanaka (1996) study is that the subsonic/heliosheath solar wind is effectively partitioned by a magnetic wall. The inner plasma, between the TS and magnetic wall, has its origin in the higher latitude solar wind whereas the outer shocked solar wind plasma originates from the equatorial region where the magnetic field is weaker.

The magnetic pressure effect and the subsequent bending of the current sheet can be understood as a straightforward consequence of the $\mathbf{J}\times\mathbf{B}$ force, the Axford–Cranfill amplification of the azimuthal magnetic field component, and the presence of a current sheet. In the equatorial region of the heliosheath, B_ϕ increases much more than elsewhere in the heliosheath. Present in the same region, however, is the magnetic neutral sheet at which $B_\phi = 0$ and across which B_ϕ is oppositely oriented. A phenomenological representation of the Parker field in the heliosheath may be

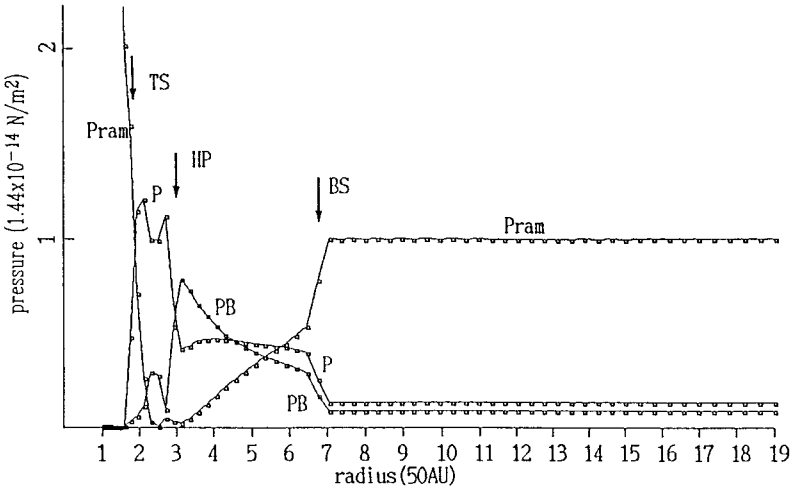

Figure 6.12. Spatial variation of the ram pressure P_{ram}, thermal pressure P, and magnetic pressure PB along the line $\theta = 80°$ (colatitude) in the meridional plane (x, z) along the stagnation axis. (Washimi and Tanaka, 1996.)

$$\mathbf{B} = \left[\frac{B_0}{r^2}\hat{\mathbf{r}} - B_0\frac{\sin\theta}{r}\hat{\phi}\right] f(\theta) \,, \tag{166}$$

where, by way of example and for the sake of simplicity, we have assumed $f(\theta) \equiv \tanh\left[a(\pi/2 - \theta)\right]$ for some amplitude a. The B_ϕ component of the magnetic field as a function of co-latitude is plotted in Figure 6.13(a) and it illustrates how B_ϕ increases as one approaches the equator from the pole before decreasing to zero at the current sheet. From (166), we have

$$\mathbf{J} \times \mathbf{B} = \left\{\frac{B_0^2}{2r^5}\frac{\mathrm{d}}{\mathrm{d}\theta}\left[f(\theta)\right]^2 + \frac{B_0^2}{2r^3}f(\theta)\frac{\mathrm{d}}{\mathrm{d}\theta}\left[\sin^2\theta f(\theta)\right]\right\}\hat{\theta} \,, \tag{167}$$

and this expression is plotted in Figure 6.13(b). If θ_0 denotes the angle at which B_ϕ peaks with respect to the co-latitude, it is positive for $\theta < \theta_0$ and $\theta > \pi - \theta_0$ and negative for $\theta_0 < \theta < \pi - \theta_0$. Thus, the magnetic pressure drives the plasma both polewards and toward the ecliptic plane (Figure 6.13(c)), which results in the neutral sheet bending northward (or southward, depending on solar cycle) in the heliosheath.

The effect on the global MHD model of an 11-year solar cycle variation in magnetic field polarity has been addressed briefly by Washimi and Tanaka (1996) as well. Like Nerney et al. (1995), they find that the polarity of the magnetic field in the heliosheath reflects the solar cycle dependence and the heliosheath consists of a series of magnetized 'plasma bubbles' or 'magnetic polarity envelopes.' The neutral sheet is found to extend between the bubbles in a very complicated fashion that is certainly not well understood.

Linde et al. (1998) include interstellar neutral hydrogen in their 3D MHD simulations and investigate three possible LISM magnetic field orientations. The neutral

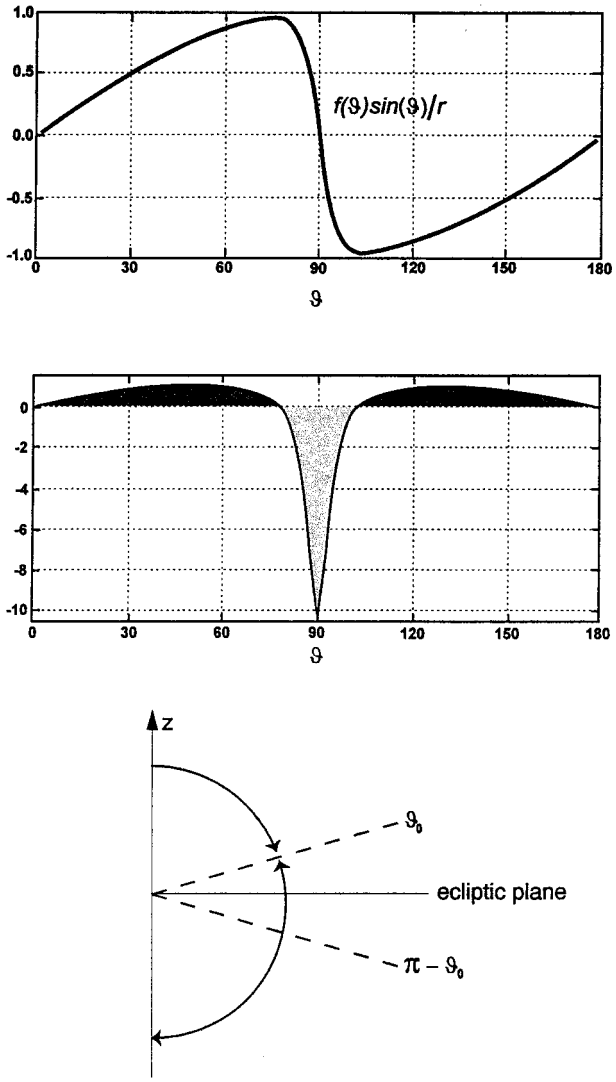

Figure 6.13. The magnetic pressure effect. (a) B_ϕ plotted as a function of colatitude. (b) The $\mathbf{J} \times \mathbf{B}$ force acting on the plasma as a function of colatitude θ. (c) Schematic to illustrate the force exerted by the magnetic pressure to push the plasma both poleward and towards the ecliptic plane for $\theta = \theta_0$ and $\theta = \pi - \theta_0$. The neutral sheet bends northward in the heliosheath (or southward, depending on solar cycle.)

H model is very simple in that it is assumed that the neutral H velocity and temperature remain constant and that interstellar H is lost only inside the HP. This then allows the solar wind to be mediated by the interstellar medium, so leading to a reduction in solar wind ram pressure. Such a neutral model clearly cannot

TABLE XIV

Solar wind and LISM plasma parameters used for the 3D simulations of Linde et al. (1996)

	Solar wind (30 AU)	LISM
n (cm^{-3})	7.8×10^{-3}	0.07
u (km s^{-1})	450	26
T(K)	3×10^4	7500
$\|B\|$ (nT)	0.2	0.15

reproduce the complicated neutral physics described by the self-consistent models of Section 5, but it has the virtue of being relatively inexpensive computationally.

The three LISM magnetic configurations considered by Linde et al. (1998) are $\mathbf{B}_{\rm LISM} \parallel \mathbf{u}_{\rm LISM}$ and $\mathbf{B}_{\rm LISM} \perp \mathbf{u}_{\rm LISM}$, the latter case with $\mathbf{B}_{\rm LISM}$ either in the equatorial plane or anti-parallel to the solar rotation axis. The last case corresponds to the model of Washimi and Tanaka (1996). The plasma parameters are listed in Table XIV.

Consider first the case of $\mathbf{B}_{\rm LISM} \parallel \mathbf{u}_{\rm LISM}$. Plate 6.2 is a meridional slice through the solution and shows the temperature distribution (a) and the total magnetic field intensity (b). Unlike the gas dynamic simulations, a noticeable cooling of the heliosheath flow occurs in the low latitude regions near the HP, but not in the equatorial plane (nor over the poles). This is a direct consequence, as discussed above, of the presence of the magnetic wall, clearly evident in Plate 6.2b in these lower latitude regions, and the current sheet (the dark blue strip around the equatorial plane). The magnetic wall deflects the mid-latitude flow before it reaches the HP, leading to a ridge of cooler flow. The equatorial plasma can flow beyond the magnetic wall, as was discussed in the context of the Washimi and Tanaka (1996) simulations.

To compare the results of Linde et al. (1998) and Washimi and Tanaka (1996), and thereby evaluate the role of the LISM mediated solar wind more clearly, we consider as a final case, $\mathbf{B}_{\rm LISM} \perp \mathbf{u}_{\rm LISM}$ and anti-parallel to the solar rotation axis. As before, meridional cuts of the plasma temperature and magnetic field intensity are shown (Plates 6.3a and b respectively). Comparison of Figure 6.9 and Plate 6.3(a) shows that the heliosheath flow remains subsonic when neutrals are included, and the bullet-shaped TS becomes more spherical, consistent with the gas dynamic simulations. The magnetic wall is clearly present in Plate 6.3b (in fact, two walls). Magnetic reconnection appears to occur where the magnetic field has to re-orient across the HP. Interestingly, the tilt of the neutral sheet appears to be

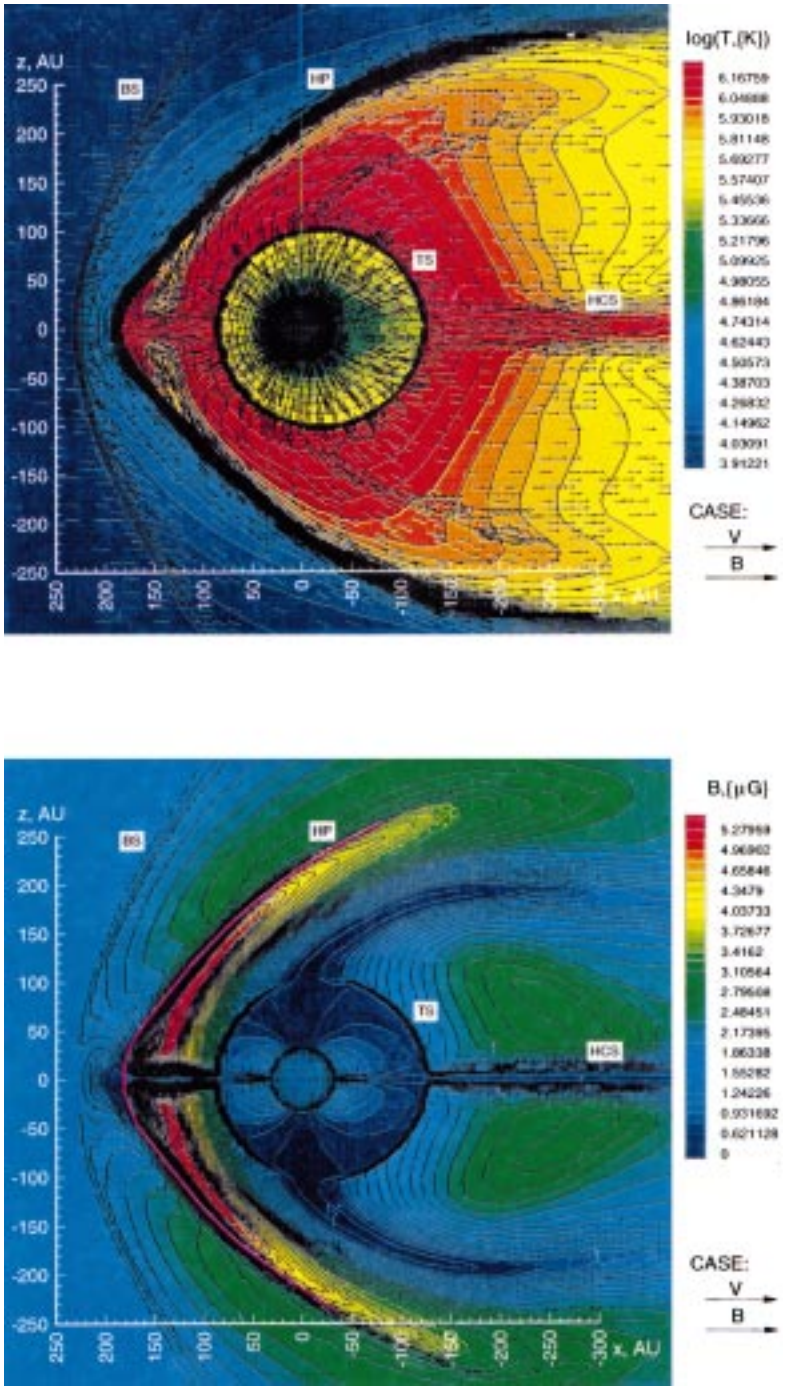

Plate 6.2. Model $\mathbf{B}_{\mathrm{LISM}} \parallel \mathbf{u}_{\mathrm{LISM}}$. (a) Contours of the Log[plasma temperature (K)] along the meridional plane. Small arrows indicate the plasma velocity field. (b) Contours of the total magnetic field intensity along the meridional plane. Small arrows indicate the magnetic field. (Linde et al., 1998.)

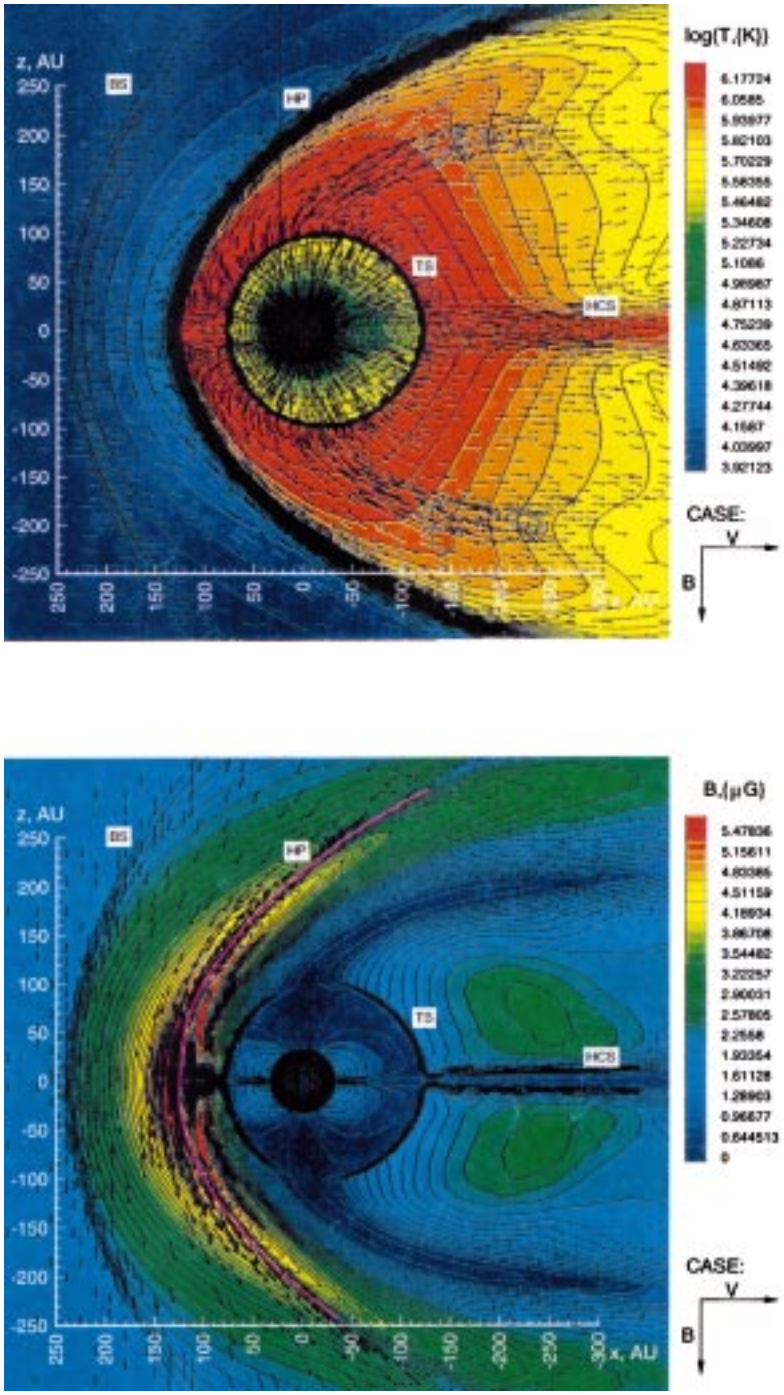

Plate 6.3. Model $\mathbf{B}_{\mathrm{LISM}} \perp \mathbf{u}_{\mathrm{LISM}}$. (a) Contours of the Log[plasma temperature (K)] along the meridional plane. Small arrows indicate the plasma velocity field. (b) Contours of the total magnetic field intensity along the meridional plane. Small arrows indicate the magnetic field. (Linde et al., 1998.)

TABLE XV

Distances to the heliospheric boundaries in the 3D simulations of Linde et al. (1998).

Case	TS (up)	TS (down)	HP	BS
$\mathbf{B}_{\rm LISM} \parallel \mathbf{u}_{\rm LISM}$	88	124	188	227
$\mathbf{B}_{\rm LISM} \perp \mathbf{u}_{\rm LISM}$	79	124	137	237

less pronounced in the simulations of Linde et al. (1998) than in those of Washimi and Tanaka (1996).

Finally, the distances to the heliospheric boundaries for the two Linde et al. (1998) models discussed above are listed in Table XV. This illustrates the role of LISM magnetic fields parallel and perpendicular to the LISM flow vector in determining global heliospheric structure. As discussed in Section 6.2, the minimum distance to the HP occurs when the LISM magnetic field is perpendicular to the flow direction. It is also evident that the Newtonian approximation is somewhat difficult to justify.

7. The Acceleration and Transport of Pickup Ions

The detection of an anomalously high cosmic-ray flux was reported first by Garcia-Munoz et al. (1973), and it was subsequently observed that the excess or anomalous component consisted of pure ^4He, unlike the galactic cosmic ray component which is composed of both ^4He and ^3He. Anomalously high fluxes of oxygen (Hovestadt et al., 1973) and nitrogen (McDonald et al., 1974) were also detected. The anomalous component of cosmic-rays (ACRs) is now thought to be comprised of fluxes of helium, neon, argon, nitrogen, oxygen, carbon, and hydrogen (Klecker, 1995) which are enhanced in an energy spectrum ranging from $\sim$20 MeV to $\sim$300 MeV. The ACRs are predominantly singly ionized (see Mewaldt et al. (1996) and Jokipii (1996) for a discussion of multiply ionized ACRs) and have a positive radial intensity gradient to the most distant spacecraft. Observed energy spectra of anomalous cosmic-ray oxygen, helium, and protons are illustrated in Figure 7.1 (Cummings and Stone, 1988).

Since the anomalous component consists of singly charged ions, it can be detected using mass and charge measurements. Furthermore, since the rigidity of ACRs and galactic cosmic-rays is different, one expects ACRs and galactic cosmic-rays to be modulated differently and their spectral peaks to occur at different energies. Such differences do not exist for hydrogen however and the existence of anomalous hydrogen was much more difficult to detect (Christian, 1989; Christian et al., 1988) and the effects of cosmic-ray modulation need to be considered very

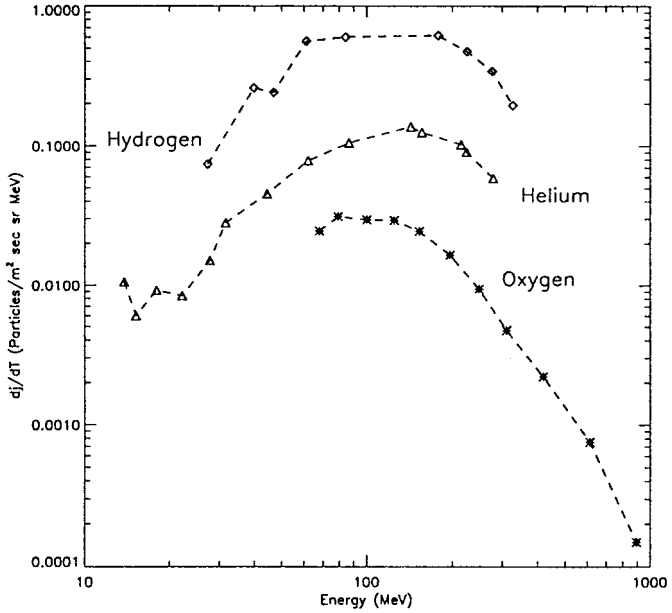

Figure 7.1. Energy spectra of anomalous oxygen, helium and hydrogen observed at 21 AU in 1985. (Cummings and Stone, 1987, 1988.)

carefully. These issues are not addressed directly here (see e.g., Potgieter, 1997 for a review). Instead, we concentrate on reviewing the direct connection that is thought to exist between interstellar pickup ions and the anomalous cosmic-ray component.

In a seminal paper, Fisk et al. (1974) proposed that anomalous cosmic ray fluxes should occur for those elements with high first ionization energies. These particles are more likely to enter the heliosphere as interstellar neutral atoms whereas those elements with low first ionization potentials are more likely to be ionized in the LISM, entering the heliosphere (if at all) in an ionized state. Unlike interstellar or solar ions, interstellar neutrals which experience ionization in the heliosphere produce singly ionized pickup ions with typical energies of $\sim$1 keV. By some process, not yet well understood, a fraction of the pickup ions are energized to form the anomalous cosmic-ray component. It is generally thought that pickup ions are accelerated primarily at the termination shock to ACR energies. The Fisk et al. (1974) model provides a very attractive explanation for the composition of the ACR component but the mechanism whereby some pickup ions become ACRs, increasing their energy by 4–6 orders of magnitude, has yet to be elucidated completely.

7.1. Fermi acceleration and modulation of anomalous cosmic-rays

Following Jokipii and Giacalone (1996), we address the question of pickup ion acceleration by considering two distinct energy ranges. Historically, the first problem considered was the acceleration of already energetic ions (> 100 keV), this reflecting the better understood physics of charged particle acceleration and transport at these energies. We defer to Section 7.2 a discussion of the initial energization of pickup ions up to these energies.

7.1.1. *The Cosmic-Ray Transport Equation*

The transport of energetic charged particles in the solar wind is governed almost entirely by ambient electric and magnetic fields (both large-scale and random fluctuations), and can be described by the cosmic-ray transport equation (Parker, 1965; Axford, 1965; Jokipii, 1966; Gleeson and Axford, 1967; Jokipii and Parker, 1969, and many others) for the omni-directional distribution function $f(\mathbf{x}, p, t)$

$$\frac{\partial f}{\partial t} - \nabla \cdot (\kappa \nabla f - \mathbf{u} f) - \frac{1}{3p^2} (\nabla \cdot \mathbf{u}) \frac{\partial}{\partial p} \left(p^3 f \right) = Q(\mathbf{x}, p, t) \, , \tag{168}$$

where, as usual, $\mathbf{u}$ denotes the solar wind velocity, p the particle momentum, $Q(\mathbf{x}, p, t)$ a source term, and

$$\kappa = \begin{pmatrix} \kappa_{\parallel} & 0 & 0 \\ 0 & \kappa_{\perp} & \kappa_{\mathrm{A}} \\ 0 & -\kappa_{\mathrm{A}} & \kappa_{\perp} \end{pmatrix} \, , \tag{169}$$

is the spatial diffusion tensor. In (169), $\kappa_{\perp}$ and $\kappa_{\parallel}$ refer to diffusion perpendicular and parallel to the mean magnetic field $\mathbf{B}$. The transport equation (168) describes four distinct effects; (i) convection with the large-scale flow field; (ii) gradient and curvature drifts due to the large-scale variation of the background magnetic field; (iii) particle energy change due to the compression or expansion of the flow, and finally (iv) spatial diffusion due to particle scattering on random magnetic irregularities. The gradient and curvature drifts can be related to the anti-symmetric elements of the diffusion tensor (169) by

$$\mathbf{v}_D \equiv \nabla \times (\kappa_{\mathrm{A}} \mathbf{B}/B) \tag{170}$$

(Jokipii, 1993). For weak scattering, $\kappa_{\mathrm{A}} = v R_L/3$, v the particle velocity and R_L the Larmor radius, which implies

$$\mathbf{v}_D = \frac{pv}{3q} \nabla \times \frac{\mathbf{B}}{B^2} \, , \tag{171}$$

for a particle of charge q. Evidently, since $\nabla \times \mathbf{B}$ determines the drift direction, it can change with solar polarity and during positive and negative solar cycles ($A > 0$ or $A < 0$), anomalous cosmic rays can either drift in or out from the polar region and out or in along the current sheet (see Figure 7.2).

For solar modulation models, the radial diffusion coefficient

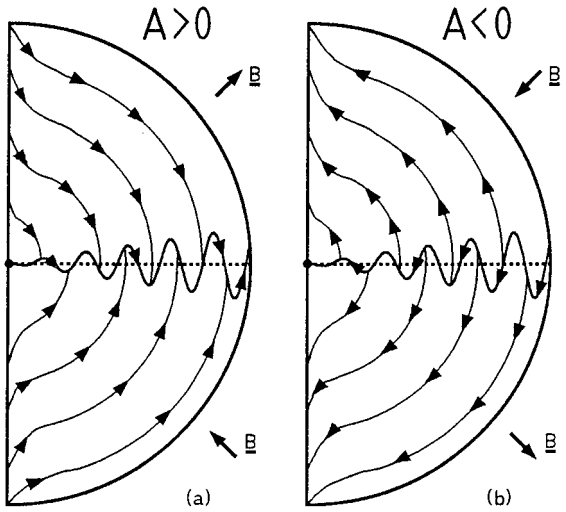

Figure 7.2. The drift directions due to IMF gradients, curvature and the neutral current sheet for positively charged particles for (a) the $A > 0$ epoch, and (b) the $A < 0$ epoch. The direction of the IMF is shown. (Haasbroek, 1996.)

$$\kappa_{rr} \equiv \kappa_{\parallel} \cos^2 \Psi + \kappa_{\perp} \sin^2 \Psi \ , \tag{172}$$

is of particular relevance. Here Ψ is the usual winding angle between the mean IMF and the radial direction (Parker, 1958)

$$\tan \Psi = \frac{\Omega r_c}{u} \, (r/r_c - 1) \sin \theta \tag{173}$$

(θ the colatitude with respect to the solar rotation axis). It is convenient to discuss the diffusion tensor in terms of the equivalent length scales $\lambda_{\parallel,\perp,A} \equiv 3\kappa_{\parallel,\perp,A}/v$. These length scales can be referred to somewhat colloquially as parallel, perpendicular and drift ($\lambda_{\rm drift}$) mean free paths (mfps).

To evaluate the spatial diffusion tensor (169), one has to make certain assumptions about the properties and character of the underlying turbulence. Bieber et al. (1994) have argued on the basis of observed cosmic-ray mfp observations in the solar wind ecliptic plane that a purely 'slab' model of interplanetary magnetic turbulence (Jokipii, 1966) is inappropriate, suggesting instead a composite model comprising a superposition of a dominant two-dimensional (2-D) component and a minor slab component. Such a perspective is in accord with the observations of magnetic fluctuation correlation functions and power spectra in the solar wind (Matthaeus et al., 1990; Bieber et al., 1996) as well as with theoretical studies of nearly incompressible turbulence (Zank and Matthaeus, 1992, 1993; Ghosh and Goldstein, 1997). All three perspectives suggest that approximately 80% of the inertial range turbulent magnetic fluctuation energy should reside in the 2-D component and the remainder in slab fluctuations (see Matthaeus et al. (1996) for a review).

For cosmic-rays resonant with MHD turbulence in both the inertial and energy ranges, the 2-D component is effectively invisible. The parallel component of the diffusion tensor can be estimated directly from the Fokker-Planck coefficient for pitch-angle scattering $\Phi(\mu)$ (Zank et al., 1998, who extend a similar calculation by Bieber et al., 1995),

$$\lambda_{\parallel} = \frac{3}{2} v \int_0^1 \frac{(1-\mu^2)^2}{\Phi(\mu)}\, \mathrm{d}\mu \ , \tag{174}$$

where μ the cosine of the particle pitch angle and (Jokipii, 1966)

$$\Phi(\mu) = \frac{2v}{R_L^2 B^2} \frac{(1-\mu^2)}{|\mu|} \pi P\left(\frac{1}{|\mu| R_L}\right) \ . \tag{175}$$

In (175), $P(k) = (2\pi)^{-1} \int_{-\infty}^{\infty} R(z) \exp[-ikz]\, \mathrm{d}z$ is the turbulence power spectrum in terms of the wave number k and is related to the slab fluctuations $\delta B_{x,\mathrm{slab}}^2$ by

$$\delta B_{x,\mathrm{slab}}^2 = 2 \int_0^{\infty} P(k)\, \mathrm{d}k \ .$$

In $P(k)$, $R(z)$ denotes the two-point, two-time correlation function specialized to slab turbulence and z is the spatial lag parallel to the mean magnetic field. For $P(k)$, one can use the approximate form

$$P(k) = 2\pi C \lambda \left(1 + k^2 \lambda^2\right)^{-5/6} \ , \tag{176}$$

for C an appropriately chosen constant. Expression (176) contains both a Kolmogorov inertial range contribution for high values of k ($\gg \lambda$) and an energy containing range for smaller values of k ($\ll \lambda$).

The slab correlation length is defined by

$$2\pi P(0) = \int_{-\infty}^{\infty} R(z)\, \mathrm{d}z = 2\delta B_{x,\mathrm{slab}}^2 \ell_{\mathrm{slab}}$$

and thus ℓ_{slab} is related to λ by $\ell_{\mathrm{slab}} = 0.746834\lambda$. Observations at 1 AU (Bieber et al., 1994) indicate that $C = 0.5\,\mathrm{nT}^2$, $\delta B_x^2 = 13.2152\,\mathrm{nT}^2$ and $\ell_{\mathrm{slab}} = 3.4 \times 10^9$ m. The values for C and δB_x^2 are appropriate if all the measured turbulence is assumed to be in slab modes. For composite 2-D/slab models, these numbers should be reduced correspondingly.

Use of (174)–(176), together with some manipulation, yields (Zank et al., 1998)

$$\lambda_{\parallel} = 3.1371 \frac{B^{5/3}}{\delta B_{x,\mathrm{slab}}^2} \left(\frac{P}{c}\right)^{1/3} \ell_{\mathrm{slab}}^{2/3} \left\{1 + \frac{7/9A}{(q+1/3)(q+7/3)}\right\} \ , \tag{177}$$

where

$$B = B_r\,(r_c/r)^2\left[1 + (\Omega r_c/U)^2\,(r/r_c - 1)^2\sin^2\theta\right]^{1/2}\ ,$$

is the magnitude of the interplanetary magnetic field. Here

$$A = (1+s^2)^{5/6}\hat{u}1\ , \quad s \equiv 0.746834 R_L/\ell_{\rm slab}\ , \quad q = \frac{5s^2/3}{1+s^2-(1+s^2)^{1/6}}\ ,$$

r is the radial heliocentric distance, $\delta B^2_{x,\rm slab}$ the variance of the x component of slab geometry fluctuations, and $P \equiv pc/Ze$ the particle rigidity (p momentum, c the speed of light, and Ze particle charge). Finally, $\ell_{\rm slab}$ is the correlation length for slab turbulence. Although an approximation, expression (177) is in very close accord with the exact Fokker–Planck result. In Figure 7.3, the analytic approximation and the exact Fokker–Planck form of $\lambda_\parallel$ are plotted as a function of rigidity in MV. Three curves are shown. The solid curve is the exact Fokker-Planck result. The full analytic approximation, which includes both the inertial and energy-containing range contributions (i.e., using (177)), is plotted as the dashed line, and clearly the approximation is excellent over the full range of rigidities. Also plotted, as the dotted curve, is an approximation which is based on a model for $P(k)$ which contains only an inertial range. Evidently, such an approximation fails when particle gyroradii are sufficiently large that they resonate with the energy-containing range.

The expression for $\lambda_\parallel$ may not be completely valid for very small rigidities when dynamical MHD turbulence effects can be important (Bieber et al., 1994). The fractional term in braces is of particular importance in the outer heliosphere when the particle Larmor radius can become comparable to or greater than the correlation length $\ell_{\rm slab}$. In this case, the ion no longer scatters resonantly with turbulent MHD fluctuations in the inertial range but rather with fluctuations that reside in the much flatter energy-containing range. As a result, depending on how the correlation length evolves with heliocentric distance, the scaling of $\lambda_\parallel$ with respect to both rigidity P and correlation length can change from inner to outer heliosphere. This is discussed further below in the context of pickup ion driven turbulence in the outer heliosphere (see also Section 3.3).

Three different approaches to deriving the mean free path $\lambda_\perp$ and the drift length scale $\lambda_{\rm A}$ exist and all lead to the same basic form. By introducing a relaxation time approximation, one can utilize a hard sphere scattering approach (Axford, 1965; Gleeson and Axford, 1967; Jones, 1990) to derive expressions formally equivalent to those obtained on the basis of quasi-linear theory (QLT) (Jokipii, 1966; Jokipii and Parker, 1968, 1969; Forman et al., 1974),

$$\lambda_\perp = R_L\frac{\Omega\tau}{1+(\Omega\tau)^2}\ ; \tag{178}$$

$$\lambda_{\rm A} = \Omega\tau\lambda_\perp\ . \tag{179}$$

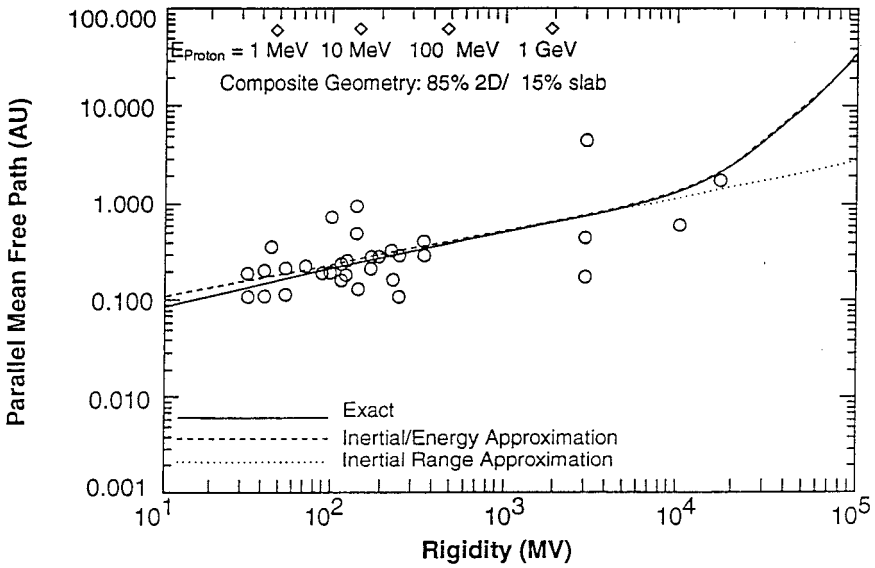

Figure 7.3. Cosmic-ray mean free path versus particle rigidity in composite slab/2-D turbulence. The solid curve shows the exact Fokker-Planck result. The full analytic approximation, which includes both the inertial and energy-containing range contributions (i.e., using (??)), is plotted as the dashed line, and the approximation is excellent over the full range of rigidities. Plotted as the dotted curve is an approximation which assumes only an inertial range. The latter approximation fails for large rigidities. (Zank et al., 1998.)

Here, τ is a 'scattering' or 'relaxation time', and Ω the particle gyrofrequency. A third approach developed recently by Bieber and Matthaeus (1997) (see also Forman (1977)) begins with a Green-Kubo-Taylor form of the particle diffusion coefficient $D_{ij} \equiv \int_0^\infty \langle v_j(t) v_i(t+t') \rangle \, \mathrm{d}t'$, where the angle brackets denote ensemble averaging, v_i the particle velocity and t' a lagged time. The key insight of Bieber and Matthaeus (1997) is to suggest that the *Ansatz* $v^2/3 \exp\left[-\nu t'\right] \cos \Omega t'$ be used for the ensemble-averaged particle velocity correlation to derive $\lambda_\perp$ and $v^2/3 \exp\left[-\nu t'\right] \sin \Omega t'$ for λ_A. The sine and cosine terms describe charged particle motion along a magnetic field, while the exponential term describes the 'decorrelation' with time of the magnetic field seen by the particle. Remarkably, these simple *Ansätze* render the diffusion coefficient integrable and expressions (178) and (179) are recovered exactly without the QLT limitation to the $\Omega\tau > 1$ regime. Thus, the key to understanding (178) and (179) lies in describing the so far formal term $\Omega\tau$ as a function of rigidity and heliocentric distance. Hard sphere scattering provides little insight in identifying an appropriate form of $\Omega\tau$.

Bieber and Matthaeus (1997) suggest

$$\Omega\tau = \frac{2}{3} R_L / D \,, \tag{180}$$

where D denotes a magnetic field line diffusion coefficient. By prescribing D appropriately, one can recover the usual quasi-linear (QLT) form for $\Omega\tau$ (Jokipii, 1966; Jokipii and Parker, 1968, 1969; Forman et al., 1974).

More recently, a nonperturbative approach to the diffusion of magnetic fields has been developed by Matthaeus et al. (1995) and Gray et al. (1996). For a two-component model (slab plus 2-D turbulence, i.e., $\delta\mathbf{B} = \delta\mathbf{B}_{2D}(x, y) + \delta\mathbf{B}_{\rm slab}(z)$, where $\hat{z}$ is the assumed direction of the mean magnetic field $\mathbf{B}$), the magnetic field line diffusion coefficient is found to be

$$2D_\perp = D_{\rm slab} + \sqrt{D_{\rm slab}^2 + 4D_{2D}^2}\,; \tag{181}$$

where

$$D_{\rm slab} = \frac{\delta B_{\rm slab}^2}{2B^2}\ell_{\rm slab}\,, \qquad D_{2D} = \frac{\delta B_{2D}}{B}\tilde{\ell}\,.$$

In (181), $D_{\rm slab}$ describes magnetic field line wandering for slab turbulence, and $\ell_{\rm slab}$ is the parallel correlation length (Matthaeus et al., 1995). Observe that if $\delta B_{2D} = 0$, one then obtains the classical diffusion result of Jokipii and Parker (1968, 1969). The term D_{2D} describes the contribution to magnetic field line wandering associated with 2-D fluctuations and $\tilde{\ell}$ is a ('mesoscale' or 'ultrascale') correlation weighted by the 2-D magnetic fluctuations. A physical interpretation of $\tilde{\ell}$ is that it describes the length scales for poloidal magnetic fields. In this interpretation, the physical effects that determine the length scale of $\tilde{\ell}$ are likely to be large-scale solar wind fluctuations associated with shocks, merged interaction regions and the like and are thus, in some sense, external to a self-consistent theory of the CR diffusion tensor. Unfortunately, even with this interpretation, the correlation $\tilde{\ell}$ is a very poorly constrained and understood quantity, and neither observations nor existing theoretical analyses provide much insight (Zank et al., 1998).

Dependent on the weighting of the slab and 2-D components, it is easily seen that $D_\perp$ can converge to either the slab or the 2-D magnetic field line diffusion coefficients (181). An important distinction between the slab or quasi-linear theory and the nonperturbative interpretation of magnetic field line diffusion resides in the small-amplitude $\delta B/B$ limit. If the ratio of slab to 2-D fluctuation energy is fixed, together with the ratio of $\ell_{\rm slab}$ to $\tilde{\ell}$, then the limit as $\delta B/B \longrightarrow 0$ yields $D_\perp \longrightarrow D_{2D}$. Thus, for the two-component model, the 2-D diffusion coefficient D_{2D} and not the QLT/slab result represents the correct limit for small-amplitude magnetic field fluctuations.

In using expression (180) for $\Omega\tau$, two basic approaches to investigating the radial and latitudinal dependence of the diffusion length scales in the heliosphere were adopted by Zank et al. (1998).

(1) By analogy with QLT, as developed by Jokipii (1966), Jokipii and Parker (1968, 1969), Forman et al. (1974) and Fisk (1979), Zank et al. (1998) suggest the approximation

$$D \equiv D_{QLT} = \frac{\delta B^2}{2B^2}\ell_{\rm slab}\,. \tag{182}$$

Here, δB^2 refers to the total fluctuating magnetic field and not to the power resident in the slab component only. This distinguishes the model (182) from the classical QLT model.

(2) The fully self-consistent two-component model adopts the relation

$$D \equiv D_\perp \,, \tag{183}$$

and one then has to prescribe $\tilde{\ell}$ independently.

These latter models, introduced by Zank et al. (1998), are referred to as non-perturbative models.

Evidently, pickup ion generated turbulence in the outer heliosphere (Section 3.3) must play a fundamental role in determining the radial and latitudinal dependence of the cosmic-ray tensor and hence the modulation properties of the ACR component. Generally, however, the specific role of turbulence in determining the form of the cosmic-ray tensor is neglected in almost all studies of ACR acceleration and modulation. These coefficients typically take the form [e.g., *Reinecke and Moraal*, 1992]

$$\begin{aligned} \lambda_\parallel &= \lambda_{\parallel 0}\beta \left(\frac{P}{P_0}\right)^{b\parallel} \left(\frac{B_e}{B}\right)^{a\parallel} \,, \\ \lambda_\perp &= \lambda_{\perp 0}\beta \left(\frac{P}{P_0}\right)^{b\perp} \left(\frac{B_e}{B}\right)^{a\perp} \,, \end{aligned} \tag{184}$$

where $\beta \equiv v/c$ and $b_{\parallel\,,\perp}$, $a_{\parallel\,,\perp}$, and $\lambda_{\parallel 0,\perp 0}$ are prescribed parameters.

7.1.2. *Acceleration of Particles at Shocks*

In a remarkable development, it was recognized independently by Axford et al. (1977), Bell (1978a, b), Blandford and Ostriker (1978) and Krymsky (1977) that solutions to the cosmic-ray transport equation (168) at a planar collisionless shock wave yielded a power law solution $f(\mathbf{x}, p) \propto p^{-q}$, where $q = 3r_s/(r_s - 1)$ is a function of the shock compression ratio r_s. For strong shock waves ($r_s \simeq 4$), such a spectrum is very similar to the inferred cosmic-ray source spectrum. Diffusive shock acceleration or first-order Fermi acceleration of particles can occur for an arbitrarily oblique shock and the energization results, in general, from both compression and drift effects. However, as discussed by Jokipii (1990), diffusive acceleration at a quasi-perpendicular shock is more closely related to particle drift in the motional $\mathbf{u} \times \mathbf{B}$ electric field at the shock front than to compressive Fermi acceleration. If the particle scattering frequency is much less than the particle gyrofrequency but sufficient to maintain both isotropy and prevent all particles from being convected away from the shock, the particle energy gain at a quasi-perpendicular shock is simply (Jokipii, 1990)

$$\Delta\mathcal{E} \simeq Ze\Delta\phi \,, \tag{185}$$

where $\Delta\phi$ is the electrostatic potential. The maximum ACR energy that can be expected from diffusive acceleration at an assumed quasi-perpendicular termination shock is therefore determined by the change in electrostatic potential in going from the ecliptic to the pole region. Thus, singly charged ions can achieve a maximum energy of $\sim$ 350 MeV for a termination shock located at $\sim$ 65 AU.

At a steady planar 1D shock, assuming that the upstream flow velocity and diffusion coefficient are spatially independent, the transport equation (168) becomes

$$\frac{\partial^2 f}{\partial x^2} - \frac{u}{\kappa}\frac{\partial f}{\partial x} = Q \; . \tag{186}$$

Equation (186) must be solved subject to (i) the cosmic-ray continuity condition at the shock

$$f_1 = f_2 \; , \tag{187}$$

(where the subscripts 1(2) denote upstream(downstream), as usual), and (ii) the flux diverging from the shock must originate at the shock i.e.,

$$\nabla \cdot \mathbf{S}(\mathbf{x}, p) = Q \; , \tag{188}$$

where

$$\mathbf{S} = \kappa \nabla f + \mathbf{u}\frac{p}{3}\frac{\partial f}{\partial p} \; .$$

For a distributed upstream source term Q, and assuming no diffusion in the upstream region, (188) implies that

$$\frac{u_1 - u_2}{3} p \frac{\partial f}{\partial p}(0, p) = -\kappa_1 \left(\frac{\partial f}{\partial p}(0, p)\right)_1 \; . \tag{189}$$

If we have a delta function source on the shock, then (189) should include Q. Since (186) admits the solution

$$\begin{aligned} f(x, p) \; = \; & f(-\infty \, , p) + \left[f(0, p) - f(-\infty \, , p)\right] \exp\left[ux/\kappa\right] + \\ & + \left[\left(1 - \exp\left[ux/\kappa\right]\right) \int_x^{-\infty} Q \, \mathrm{d}x' - \left[ux/\kappa\right] \int_0^x Q \left(1 - \left[ux'/\kappa\right]\right) \, \mathrm{d}x' \right] \; , \end{aligned} \tag{190}$$

in the upstream region $x < 0$,

$$\left(\frac{\partial f}{\partial p}(0, p)\right)_1 = \frac{u}{\kappa_1}\left[f(0, p) - f(-\infty \, , p)\right] - \frac{1}{\kappa_1}\int_0^{-\infty} Q \, \mathrm{d}x \; .$$

Hence, writing $r_s = u_1/u_2$ and $q = 3r_s/(r_s - 1)$ yields

$$f(0,p) = qp^{-q}\int_0^p \left[f(-\infty\,,p') + \frac{1}{u_1}\int_0^{-\infty} Q(x,p')\,\mathrm{d}x \right] p'^{q-1}\,\mathrm{d}p'\,, \qquad (191)$$

and the complete solution is given by

$$f(x,p) = \begin{cases} f(0,p) & x \geq 0 \\ \text{equation(190)} & x < 0 \end{cases} \qquad (192)$$

The solution (192) yields a power law solution whose spectral index depends only on the shock compression ratio r_s. The universal character of the accelerated spectrum suggested to Pesses et al. (1981) that many features of the anomalous cosmic-ray component could be explained by invoking diffusive shock acceleration of pickup ions at the termination shock. Numerous authors have since investigated the acceleration of energetic pickup ions at the termination shock, both analytically (extending the above simple 1D calculation to a spherically symmetric TS, for example [e.g., (Drury, 1983)) and numerically (e.g., Jokipii, 1986; Moraal, 1993, and references therein). This is discussed further below.

A further point concerning the acceleration of anomalous cosmic-rays relates to a result described by Adams and Liesing (1991) and subsequently reinterpreted interestingly by Jokipii (1992). Adams and Liesing showed that if 10 Mev nucl^{-1} singly charged oxygen propagates a distance greater than 0.2pc in the local interstellar medium, the charge state will be increased by electron stripping. They interpreted this result as limiting the site of ACR acceleration to the interaction region of the solar wind and LISM. Although Adams and Liesing based their estimates on the neutral density of the LISM, the neutral density is unlikely to differ too significantly in the outer heliosphere (Section 5.5). Jokipii (1992) argued that one could instead reinterpret the Adams and Liesing result as providing an upper limit on the age of the energetic ions and, by implication, a constraint on the characteristic acceleration time at this energy. For an observed energy of 10 MeV nucl^{-1}, this constraint corresponds to a time of 4.6 years. Of the known acceleration mechanisms, Jokipii demonstrated that only Fermi acceleration is capable of achieving such acceleration times. Indeed, since the acceleration time scale τ_{acc} is

$$\tau_{\mathrm{acc}} = \left(\frac{1}{p}\frac{\mathrm{d}p}{\mathrm{d}t}\right)^{-1} \simeq \frac{3r_s\kappa_{rr}}{u_1^2(r_s-1)}\,, \qquad (193)$$

the acceleration time is minimized when κ_{rr} is very small. If one uses the so-called 'Bohm limit' for $\kappa_\parallel$ i.e., $\kappa_B \equiv 1/3\ vR_L$, then Jokipii showed that the acceleration time at a parallel shock far exceeded the 4.6 year acceleration time constraint. However, since

$$\kappa_\perp = \frac{\kappa_\parallel}{1+\eta_c^2}\,,$$

(where $\eta_c \equiv \lambda_\parallel/R_L$) one can significantly reduce $\kappa_\perp$ below $\kappa_\parallel$ by demanding that $\eta_c \gg 1$. Clearly, η_c is a measure of the scattering strength and $\eta_c \gg 1$ represents

the weak scattering limit. By making η_c suitably large at a perpendicular shock, the acceleration time (193)) can be reduced well below the acceleration time constraint [Jokipii, 1992]. Thus, since it is generally thought that the termination shock is quasi-perpendicular (although see Section 6.1), the TS is thought to be an ideal location for the prompt acceleration of pickup ions to high ACR energies.

7.1.3. *Anomalous cosmic-ray modulation simulations*

In this subsection, we discuss the 2D numerical solution of the cosmic-ray transport equation (168) in a model heliosphere. We focus here on the results of Jokipii and Giacalone (1996), this providing a representative example of the status of modern ACR acceleration and modulation studies, and those of Steenberg and Moraal (1997) and Steenberg et al. (1997), who consider the phenomenological form of the cosmic-ray diffusion tensor in modulation models. We mention too the work of Fichtner et al. (1994; 1996) who use a hydrodynamic form of the cosmic-ray transport equation (168).

The heliospheric configuration in which (168) is solved numerically is that of a radial solar wind with constant velocity, terminating at a spherical shock of radius $R_{\rm TS} \sim 70$ - 100 AU. The shock compression ratio is typically 4, and the heliosheath flow velocity decreases as r^{-2} until some prescribed spherical outer escape boundary for the cosmic-rays is reached. The outer boundary is typically some 30% - 50% beyond $R_{\rm TS}$. A spiral interplanetary magnetic field and neutral current sheet are included and Jokipii and Giacalone (1996) modify the polar IMF in accordance with the results of Jokipii and Kóta (1989) and Jokipii et al. (1995). Compared to the heliospheric models described in Section 5 and Section 6, the heliospheric models used to investigate cosmic-ray transport and acceleration are highly idealized.

The parameters adopted by Jokipii and Giacalone (1996) are $\kappa_\parallel = 1.5 \times 10^{22}$ $P^{1/2}\beta$ cm^2/s, $\kappa_\perp = 0.1\kappa_\parallel$, $u = 400$ km s^{-1}, $R_{\rm TS} = 70$ AU with an escape boundary at 130 AU (P is particle rigidity in GV). Low energy (100 keV) particles are injected uniformly in space at the shock. In Figure 7.4, theoretical ACR spectra are illustrated, both at the shock and at 10 AU. At the shock, the power law form of the spectrum is evident, extending to some 10–20 MeV nucl^{-1}, followed by an exponential cut-off. The effect of modulation is clear, and obviously effects the lower energy ACRs the most.

Figure 7.5 shows contour plots of the intensity of anomalous oxygen as a function of heliocentric distance in the solar meridional plane. Not surprisingly, the intensity increases with radius out to the termination shock, after which it decreases to the escape boundary. Along the shock, the maximum intensity occurs at a latitude which depends on the solar polarity. If $A > 0$ particles drift along the shock towards the pole and then down the polar axis to the current sheet. Hence the maximum ACR intensity during the $A > 0$ epoch occurs near the poles. For an $A < 0$ period, the intensity maximum lies in the equator.

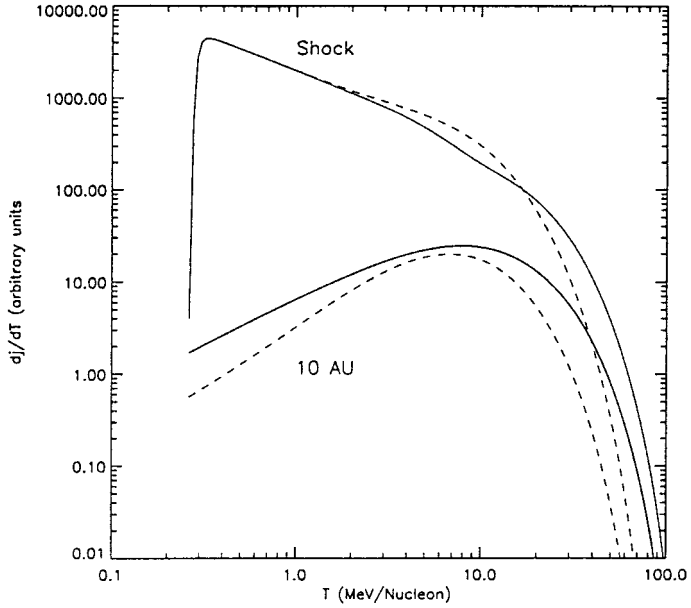

Figure 7.4. Plot of the computed cosmic ray energy spectra near the heliospheric equator, for two radii and two IMF epochs ($A > 0$ depicted by the solid line, $A < 0$ by the dashed line). (Jokipii and Giacalone, 1996.)

Radial and latitudinal gradients computed from the model appear to be consistent with observed ACR radial and latitudinal gradients reported by McKibben et al. (1979), McDonald and Lal (1986), and Cummings et al. (1987, 1995). Furthermore, the latitudinal gradient near the current sheet should change sign in

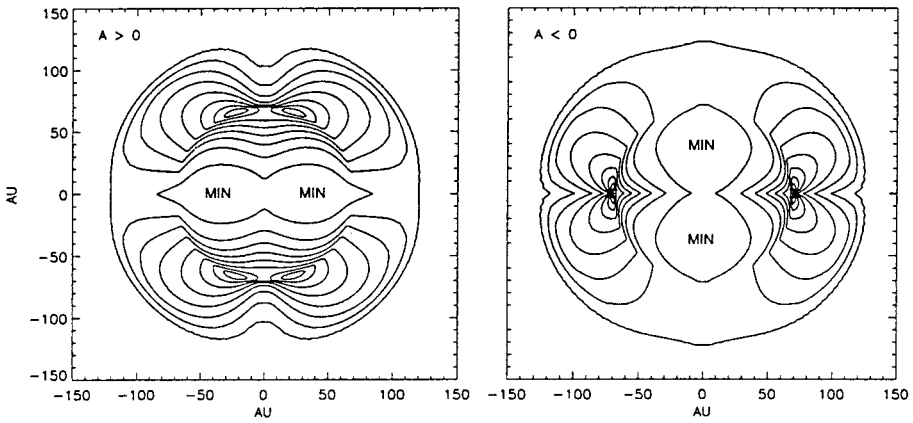

Figure 7.5. Equal intensity contours plotted for 8 MeV/nuc. anomalous oxygen, as a function of position in the meridional plane ($A > 0$ corresponds to the left panel, $A < 0$ to the right panel). (Jokipii and Giacalone, 1996.)

alternate sunspot minima. For example, during the present and 1975 sunspot minima, the ACR intensity should increase away from the current sheet whereas the opposite will occur during the 1986 sunspot minimum.

The radial and rigidity (P) dependence of the effective radial diffusion coefficient κ_{rr} has been emphasized in the modeling studies of Steenberg and Moraal (1997) and Steenberg et al. (1997). Using near-Earth observations together with those of the Pioneer/Voyager spacecraft in the outer heliosphere, they argue that the radial dependence of κ_{rr} imposed by an underlying heliospheric field model is too restrictive. Accordingly, they abandon an *a priori* prescribed background heliospheric field model and use instead spatial and rigidity dependences for the diffusion coefficients that provide the best fit to observations during solar minimum conditions in 1987 and 1996. Their preliminary results are enumerated as follows.

(1) When drift effects are suppressed, both galactic and anomalous cosmic-ray components are surprisingly well fitted with an almost spatially independent radial diffusion coefficient. Specifically, for $\lambda_{rr} \propto r^a$ (r the radial heliocentric distance), best fits to GCR spectra are obtained for for $a = 0.5$, while $a \simeq 0$ best fits the ACR component.

(2) An approximately linear rigidity dependence for $\lambda_{rr} \propto P$ is all that is needed to fit GCR spectra. The 1996 ACR spectra observed by Pioneer/Voyager in the outer heliosphere are, however, best fitted with a rigidity dependence of approximately P^2 or even P^3. This result is in general agreement with the modeling efforts of Cummings et al. (1994) who suggested a rigidity dependence of $\lambda_{rr} \propto R^{1.8}$. Bieber and Matthaeus (1997) have interpreted such a rigidity dependence as consistent with a κ_{rr} dominated by perpendicular diffusion and strong scattering in the outer heliosphere. However, this can be consistent too with dominant parallel diffusion in the outer heliosphere (Zank et al., 1998; see below).

(3) The above two results are modified by the inclusion of poleward diffusion and drifts, but not dramatically. The reason appears to be that poleward gradients may be so moderate that perpendicular diffusion in the poleward direction and drift fluxes have a smaller influence on the cosmic-ray intensities than hitherto thought.

In the models discussed above, two important effects are neglected generally in the study of ACR modulation in the solar wind. The first, discussed by Fahr et al. (1992), Grzedzielski et al. (1992) and Fichtner et al. (1994, 1996a), concerns the strong upwind-downwind heliospheric asymmetry of the pickup ion population (Section 5). Thus, assuming that pickup ions provide the seed particles for ACRs, one might expect an asymmetric source ACR distribution throughout the outer heliosphere. The second effect is the asymmetric global structure of the termination shock, the region where ACRs are thought to be accelerated. This too should introduce asymmetries into the anomalous cosmic-ray distribution function throughout the outer heliosphere.

By taking moments of the cosmic-ray transport equation (168) (see Section 8.1 for further discussion), one can derive a diffusive equation describing the energy density of ACRs. Such an equation was integrated numerically by Fichtner et al.

(1994, 1996a, b) for both an asymmetric pickup ion source distribution and an asymmetric termination shock. Relatively small longitudinal gradients are found for ACRs in the outer heliosphere, differences that should only become apparent well beyond $\sim$ 60 AU.

7.1.4. *Anomalous Cosmic-Ray Modulation Using a Self-Consistent Diffusion Tensor*

The work of Steenberg and Moraal (1997) and Steenberg et al. (1997) emphasizes the important role of the functional form of the cosmic ray spatial diffusion tensor in providing good fits to the solar minimum cosmic-ray observations. To provide a theoretical basis for the radial and rigidity dependences of the diffusion tensor, Zank et al. (1998) used the driven MHD turbulence models for an expanding solar wind developed by Zank et al. (1996) (Section 3.3) to evaluate equations (177) and (178)–(183). A similar approach was used by Morfill et al. (1979) in the context of WKB models for the magnetic field fluctuations.

For the quasi-linear model, Zank et al. (1998) assume that $\ell_{\rm slab} = \ell$ (Equation (35), Section 3.3) in (182), while for the non-perturbative models, they assume either $\tilde{\ell} \simeq \ell$ (called NP1) or $\tilde{\ell} = 10^2 \ell$ (called NP2), the latter scaling corresponding to a physical interpretation of the mesoscale correlation length. On theoretical grounds, the NP2 model is to be favoured.

By evaluating (34) and (35) throughout the heliosphere, and using the QLT, NP1, and NP2 models, Zank et al. (1998) determine the dependence of the cosmic-ray diffusive length scales $\lambda_{rr,\perp,A}$ on heliocentric radius and latitude. The parameters used are $\ell(1\ {\rm AU}) = 3.4 \times 10^9$ m, $E_B(1\ {\rm AU}) = 1.2 \times 10^9$ m^{2}s^{-2}, and results for 100 MeV particles only are displayed. In Figure 7.6(a), $\lambda_{rr,\perp,A}$ is plotted as a function of heliocentric distance r for an undriven turbulence model. λ_{rr} is clearly dominated by $\lambda_\parallel$ for all heliocentric distances and $\lambda_\perp$ is unimportant. In Figure 7.6(b), the corresponding QLT, NP1, and NP2 mfps for a fully driven turbulence model in the ecliptic plane are plotted and λ_{rr} now no longer increases with r but is approximately constant until $\sim$ 10 AU. Thereafter, the QLT and NP1 λ_{rr} models experience some radial variation – the later increase in λ_{rr} is due to resonant scattering with turbulence in the energy containing range rather the inertial range – but remains dominated by $\lambda_\parallel$. By contrast, the NP2 model for λ_{rr}, is strongly influenced by $\lambda_\perp$ beyond $\sim$ 20 AU (at 100 MeV energies). This implies that for NP2, the rigidity dependence of $\lambda_{rr} \propto P^2$. However, in the presence of pickup ion driven turbulence, for which the correlation ℓ decreases with increasing distance, Zank et al. (1998) show from (177) that $\lambda_\parallel \propto P^2$ in the outer heliosphere too. Thus, all three models yield $\lambda_{rr} \propto P^2$, although for quite different reasons.

Finally, in Figure 7.7(a), $\lambda_{rr}(r)$ is plotted at different latitudes for the QLT model. The corresponding NP2 results are plotted in Figure 7.7(b). In the higher polar regions, stream shear driven turbulence is assumed to be absent and Zank et al. (1998) therefore consider pickup ion driven turbulence only. In Figures 7.7, $90^\circ \equiv$ ecliptic and $0^\circ \equiv$ pole. In the inner polar regions, the absence of stream

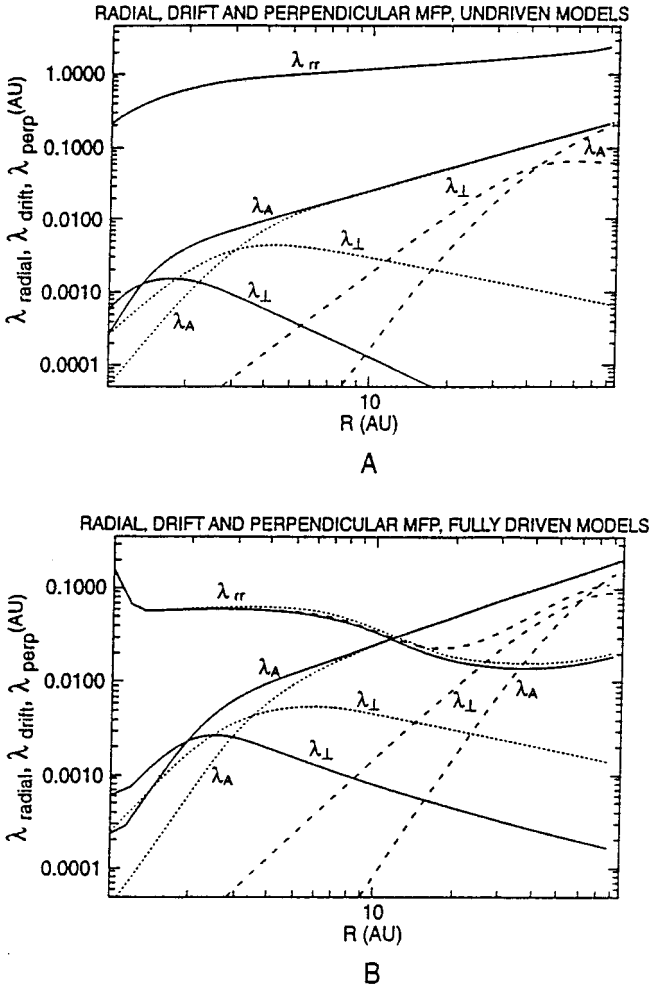

Figure 7.6. (A). The radial (λ_{rr}), perpendicular ($\lambda_{\perp}$) and drift ($\lambda_{\rm drift}$) length scales for an undriven turbulence model in the ecliptic plane. The solid lines depict the three scale lengths in the quasi-linear approximation; the dotted lines the scales for NP1 and the dashed lines are appropriate to NP2. The length scales are a function of heliocentric distance and all lengths are measured in terms of Astronomical Units. A particle rigidity of 445 MV (corresponding to a 100 MeV proton) has been assumed. (B). Cosmic ray diffusion length scales for a fully-driven (streams plus pickup ions) turbulence model in the ecliptic plane. (Zank et al., 1998.)

driven turbulence implies that polar turbulence decays more rapidly than ecliptic turbulence ($\sim r^{-3.5}$) [Zank et al., 1996], which is consistent with observations (Forsyth et al., 1996). This then leads to an increase in the radial CR mfp compared to that in the ecliptic. In the presence of pickup ion driven turbulence beyond the ionization cavity, λ_{rr} decreases until resonant scattering with the energy containing range causes λ_{rr} to increase again with increasing r. For the NP2 model, the

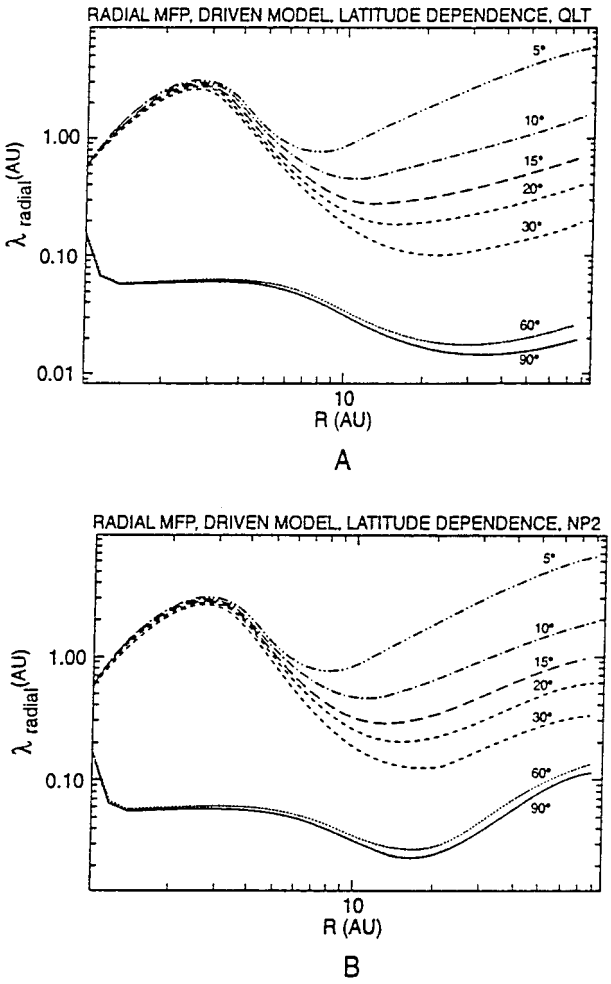

Figure 7.7. (A). The radial dependence of the radial mfp for different latitudes in the QLT approximation. (B). Plots of λ_{rr} corresponding to those of Figure 7.6(a) but now for the NP2 model. The NP1 results are not plotted since they are effectively identical to those of the QLT calculation. (Zank et al., 1998.)

additional influence of $\lambda_\perp$ in the outer heliosphere acts to increase the radial CR mfp. For the QLT model, we find again that λ_{rr} is dominated at all latitudes by $\lambda_\parallel$ unlike the NP2 models where the influence of $\lambda_\perp$ is felt at all but the very highest latitudes.

Pauls et al. (1997) used the three forms of the cosmic-ray diffusion tensor derived by Zank et al. (1997, 1998) when solving the spherically symmetric form of the cosmic-ray diffusion equation (168). They compared non-acceleration solutions for the cases of (i) no turbulence generation (i.e., decaying *in situ* turbulence), and (ii) fully driven turbulence (i.e., stream shear and pickup ion driven turbulence).

Pauls et al. (1997) distinguish between four sets of diffusion coefficients using (1) the QLT model for strictly decaying turbulence ($\text{Decay}_{\text{QLT}}$); (2) the QLT model for fully driven turbulence (pickup ion and stream shear driven – Full_{QLT}); (3) the NP2 model for decaying turbulence ($\text{Decay}_{\text{NP2}}$); and (4) the NP2 model for fully driven solar wind turbulence (Full_{NP2}).

Figure 7.8 shows the differential cosmic-ray intensity ($p^2 f$) of protons as a function of kinetic energy per nucleon, calculated using the four sets of diffusion coefficients at three different radial positions [(a)(b) at 1 AU, (c)(d) at 30 AU, and (e)(f) at 50 AU], in the ecliptic plane [(a)(c)(e)] and over the solar poles [(b)(d)(f)]. In each of these plots, the solid line depicts the assumed initial cosmic-ray spectrum, the dashed lines the spectra from the decaying turbulence diffusion coefficients (both QLT and NP2), and the dotted lines the spectra obtained from the fully driven diffusion coefficient models (QLT and NP2).

At all three radial positions in the ecliptic plane, the fully driven models predict intensities 2–3 orders of magnitude smaller than predicted by the purely decaying MHD turbulence models (for energies of $10-10^3$ MeV nucl^{-1}). This is evident from Figures 7.6 and 7.7 which show that the fully driven turbulence cosmic-ray models are smaller than their corresponding freely decaying counterparts. This holds for all rigidities and distances in the domain of interest. Since the diffusion in the ecliptic plane for the fully driven QLT model is smaller than the fully driven NP2 model diffusion coefficient, intensities obtained from the QLT model might be less than those obtained from the fully driven NP2 model. This is illustrated in Figures 7.8(a, c, e). Furthermore, since the diffusion coefficients for the freely decaying turbulence models are identical, the calculated spectra from these models are also identical (dashed lines in Figure 7.8(a, c, e)). The cosmic-ray spectrum is only slightly modulated in this case. The low energy or adiabatic limit and the 'bulging' spectra at intermediate energies are also clearly visible in the Figures 7.8(a, c, e) for the fully driven solutions (see Reinecke and Moraal (1992) for a detailed discussion of these effects).

The diffusion coefficients over the solar poles are always larger than their ecliptic plane counterparts in the outer heliosphere. This leads to much weaker modulation over the poles compared to the ecliptic plane, as is seen clearly by comparing Figures 7.8(a) and 7.8(b). Figures 7.8(a–f). As with the ecliptic plane results, the modulation predicted by the fully driven models is much higher than that predicted by the decaying MHD turbulence models.

Obviously, the turbulence generated by the ion pickup process in the outer heliosphere plays a fundamental role in determining not only the acceleration properties but also the modulation characteristics of anomalous cosmic-rays and this will need to be included eventually in more sophisticated cosmic-ray transport models.

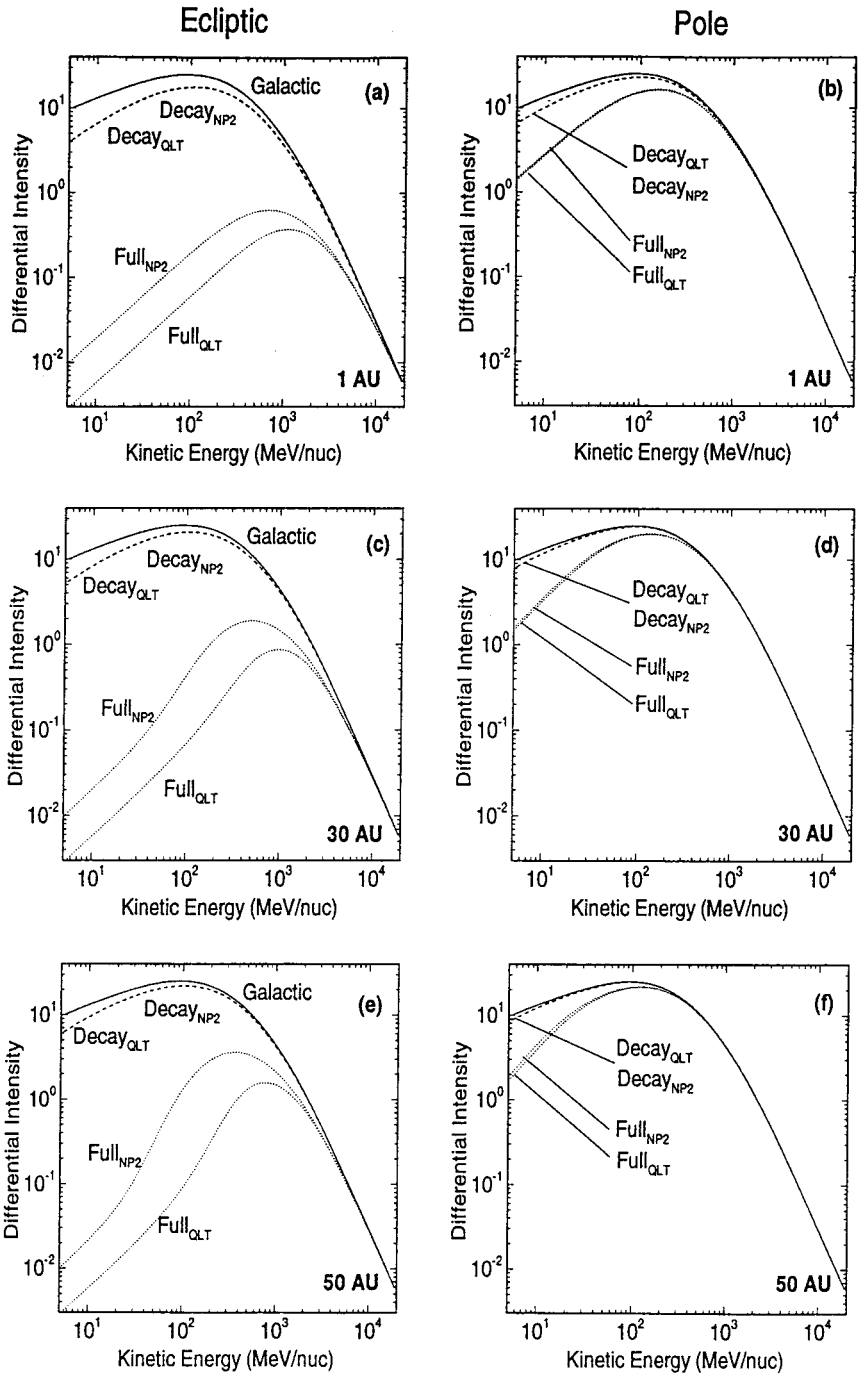

Figure 7.8. Differential proton intensities as a function of kinetic energy in the ecliptic plane and over the solar poles at three radial positions. (Pauls et al., 1997.)

7.2. THE ACCELERATION OF PICKUP IONS

In Section 7.1, the acceleration (and modulation) of ACRs was considered. Diffusive shock acceleration, at least to first-order, appears to account for the observations reasonably well. However, our understanding of the physics underlying the initial stage of diffusive acceleration is rudimentary at best and several quite distinct approaches have been advocated. As discussed in Section 7.1.2 above, to account for a predominantly singly charge ACR component, acceleration of ions at the termination shock must be prompt, and this can be achieved best by Fermi acceleration at a quasi-perpendicular termination shock in the presence of weak scattering (Jokipii, 1992). However, besides the question of shock stability (Zank et al., 1990), there arises a serious problem regarding the injection of pickup ions into a diffusive Fermi acceleration process when scattering is assumed weak. For diffusive shock acceleration to be a viable process, an ion must scatter many times as a field line convects through a shock. As discussed in detail by Webb et al. (1995), this is tantamount to requiring that the scattering frequency ν_c satisfy

$$\nu_c \gg V_{sh}/R_L \ ,$$

where V_{sh} is the shock speed (Jokipii, 1987). Rewriting this in terms of the particle velocity v, one has the equivalent requirement that

$$v \gg V_{sh}\eta_c \ . \tag{194}$$

Inequality (194) represents an injection constraint on the particle speed. A similar constraint can be obtained by requiring that the escape probability downstream of a shock be small, or

$$v \gg \frac{4V_{sh}(1+\eta_c^2)^{1/2}}{r} \ . \tag{195}$$

In either case, the injection constraint is severe in the weak scattering limit ($\eta_c \gg 1$) although not serious in the case of strong scattering ($\eta_c \sim 1$). For the scattering required by Jokipii (1992) ($\kappa_\perp = 3 \times 10^{-2}\kappa_B$) to meet the time constraint of 4.6 years, conditions (194) or (195) indicate that only those particles whose energies are much greater than about 1 MeV nucl^{-1} can possibly be accelerated by a Fermi mechanism at a perpendicular termination shock. Of course, one should recognize that the time scale constraint above is a rather crude estimate, but nonetheless, since a pickup ion is born in the solar wind with an energy of about 1keV, it is clear that the injection threshold is not easily surmounted. This is the so-called 'injection problem'.

Observations of interstellar pickup ions accelerated by a forward shock have been made by *Ulysses* at 4.5 AU (Gloeckler et al., 1994). The shock was only weakly perpendicular ($\theta_{\rm BN} = 50^\circ \pm 11^\circ$, where $\theta_{\rm BN}$ denotes the angle between the shock normal and the upstream magnetic field) and rather weak (an inferred compression ratio of only ~ 2.4) yet the conclusions of Gloeckler et al. (1994) should

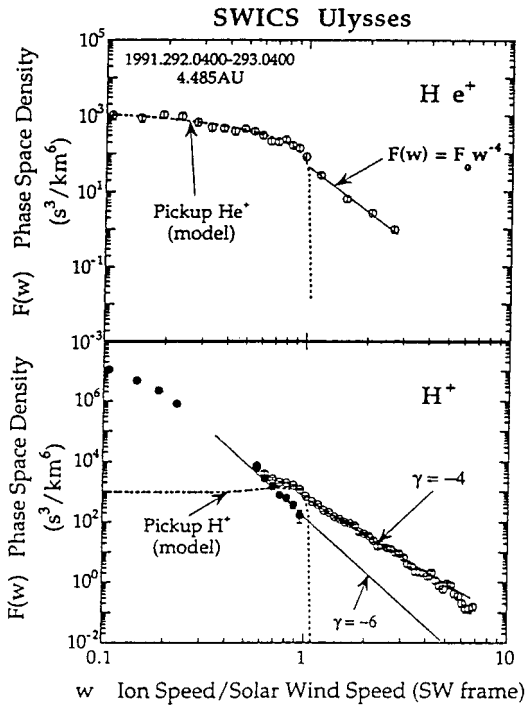

Figure 7.9. Normalized velocity distribution function of (upper) interstellar pickup He^+ and (lower) solar wind protons plus interstellar pickup H^+ in the solar wind frame. (Gloeckler et al., 1994.)

remain at least qualitatively valid at more perpendicular shocks (since reflected ions always return to the shock – see Gosling et al. (1982) and Zank et al. (1996)) They find (i) that injection efficiencies for pickup ions are much higher than for solar wind ions; (ii) that pick-up H^+ is the most abundant suprathermal ion species and carries a large fraction of particle thermal pressure; (iii) that the injection efficiency is greatest for pick-up H^+, lowest for He^+, and intermediate for alpha particles; (iv) that both H^+ and He^+ have identical spectral shapes above the cutoff speed for pickup ions, and (v) that the solar wind frame velocity distribution function for accelerated pickup ions is significantly harder than might be expected from conventional first-order Fermi shock acceleration at a weak shock. Figure 7.9 shows the observed velocity distribution function of both pickup-helium, and pickup H as function of particle speed and illustrates the emergence of the accelerated power law distribution from the thermal pickup ion population. As noted by Gloeckler et al. (1994), if these observations are in fact common to all quasi-perpendicular shocks in the outer heliosphere (i.e., wherever pickup ions are present), then they should be equally true at the TS. This should then have important implications for the acceleration of anomalous cosmic-rays at the TS as well as for the strength and structure of the TS.

Since propagating interplanetary shocks often have speeds that are not significantly faster than the solar speed, the injection criteria (194) or (195) are more easily met there i.e., Fermi acceleration can occur at an interplanetary shock for particle energies lower than the 1 MeV nucl^{-1} needed at the termination shock, for example. Thus, it is possible that pickup ions accelerated at interplanetary shocks may be boosted to energies sufficiently large ($>$ 1 MeV) that they can be injected directly into a Fermi mechanism at the quasi-perpendicular termination shock. Nonetheless, even at an interplanetary shock, a pickup ion has to be energized considerably above its initial pickup energy ($\sim$1 keV) before it can be Fermi accelerated at the shock.

Relatively few approaches to the injection problem at quasi-perpendicular shocks have been considered, and we discuss each in turn. The possibility of second-order Fermi or stochastic acceleration throughout the heliosphere has been discussed already in Section 3 and is not repeated here.

7.2.1. *Shock Drift Acceleration of Pickup Ions*

Shock drift acceleration (SDA) is a well studied charged particle acceleration mechanism, both theoretically and observationally (Armstrong et al., 1985; see the review by Decker, 1988), and the energization results from the particle crossing a narrow shock several times in the course of its gyromotion (and thus being effectively accelerated in the motional electric field).

As discussed by Webb et al. (1983), SDA can be treated rather simply at a perpendicular shock on the basis of conservation of adiabatic moment. We follow the treatment of Webb et al. (1983) but consider only non-relativistic ions. In the fluid frame Σ^a, the particle adiabatic moments are conserved, i.e.,

$$v^a_{\parallel 1} = v^a_{\parallel 2}\,,\; v^2_{\perp 1}/B^a_1 = v^2_{\perp 2}/B^a_2\,, \tag{196}$$

where $v^a_{\parallel,\perp}$ denotes the particle velocity parallel or perpendicular to the mean magnetic field. It then follows that

$$\begin{aligned} v^{a2}_2 &= v^{a2}_1\left[1+\left(B^a_2/B^a_1-1\right)\,\sin^2\theta^a_1\right]\,; \\ \cos^2\,\theta^a_2 &= \frac{\cos^2\theta^a_1}{1+\left(B^a_2/B^a_1-1\right)\sin^2\theta^a_1}\,, \end{aligned} \tag{197}$$

from which one finds that the energy gain in Σ^a_2 (i.e., downstream) is

$$\frac{\varepsilon^a_2}{1/2\;mu^2_1} = \frac{v^{a2}_1}{u^2_1}\left(1+(r-1)\sin^2\theta^a_1\right) = 1+(r-1)\sin^2\theta^a_1\,. \tag{198}$$

The latter equality in (198) is valid for pickup ions which have not been reflected at the shock (i.e., for which $v^a_1 = u_1$). Clearly, the energy gain for a drift accelerated (but not reflected) pickup ion is rather modest, with

$$\frac{\Delta\varepsilon^a}{1/2\;mu^2_1} = (r-1)\sin^2\theta^a_1\,,$$

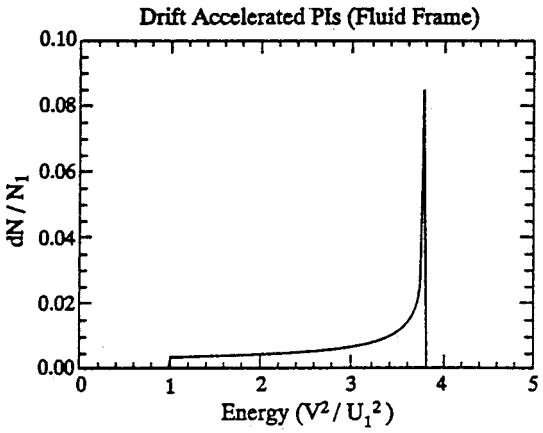

Figure 7.10. The downstream energy spectrum for shock drift accelerated pickup ions in the fluid frame. An upstream shell distribution was assumed and the shock was perpendicular with a compression ratio of $r_s = 3.8$. (Zank et al., 1996.)

giving at most $\Delta\varepsilon^a = 3\left(1/2\ mu_1^2\right)$ for a strong shock and $\theta_1^a = \pi/2$. To determine the downstream pickup ion energy in the shock frame due to SDA, one is obliged to average over gyrophase, so obtaining

$$\begin{aligned} \frac{\langle \varepsilon_2 \rangle}{1/2\ mu_1^2} &= \frac{v_1^{a2}}{u_1^2}\left(1 + (r-1)\sin^2\theta_1^a\right) + 1/r^2 \\ &= \frac{r^2+1}{r^2} + (r-1)\sin^2\theta_1^a\ , \end{aligned} \tag{199}$$

where, again, the latter equality refers to the absence of pickup ion reflection at a shock. Thus, in the shock frame, there is no formation of an energetic particle population although in the fluid frame a spreading of the distribution from $v/u_1 = 1$ to a region of energy space bounded by $(v/u_1)^2 = 1$ to ~ 4 (depending on the shock compression ratio) occurs, illustrated in Figure 7.10.

By means of (198), one can derive the transmitted drift accelerated pickup ion number density and energy downstream of the perpendicular shock. The pickup ion distribution far upstream of a shock is represented adequately by the shell distribution

$$f(v) = \frac{n}{4\pi\, v^2}\delta(v - u_1)\ , \tag{200}$$

where v is the ion speed, and u_1 the solar wind speed in spherical coordinates. Not surprisingly,

$$n_{PI,2} = \iiint \frac{n_{PI,1}}{4\pi\, v^2}\delta(v-u_1)v_2^{a2}\ \sin\theta_2\ \mathrm{d}v_2\ \mathrm{d}\theta_2\ \mathrm{d}\phi_2 = r\ n_{PI,1}\ , \tag{201}$$

where r_s is of course the shock compression ratio. More interestingly, the drift accelerated downstream energy for pickup ions is given by

$$\begin{aligned} \varepsilon_{PI,2} &= \int_0^{2\pi}\int_0^{\pi}\int \frac{n_{\mathrm{PI},1}}{4\pi v^2}\delta(v-u_1)\varepsilon_2^a v_2^{a2}\,\sin\theta_2\,\mathrm{d}v_2\,\mathrm{d}\theta_2\,\mathrm{d}\phi_2 \\ &= 2/3\,(r-1)\,\frac{n_{\mathrm{PI},1}mu_1^2}{2}\,, \end{aligned} \tag{202}$$

(Zank et al., 1996; see also McLoud and Moraal, 1990). Expression (202) is useful in that it provides an estimate for the increase in downstream pickup ion pressure due to SDA across a perpendicular shock. Clearly, from (202), the net energy gain due to SDA is rather modest, and by itself, is unlikely to boost pickup ion energies sufficiently high that they can overcome the injection problem, even at an interplanetary shock.

Two possibilities exist to overcome the injection problem for pickup ions. The first, advocated by Giacalone and Jokipii (1996) and Jokipii and Giacalone (1996), is that weak scattering of a slightly energized pickup ion will eventually allow the pickup ion to be overtaken again by the interplanetary shock, and hence further energized. This however is tantamount to Fermi acceleration with weak scattering and the arguments given above suggest that pickup ions cannot reach injection energies in this model. A second possibility, advocated by Zank et al. (1996) and Lee et al. (1996), is that the internal structure of a collisionless quasi-perpendicular shock (termination shock or interplanetary shock) can give rise to the repeated reflection of pickup ions and hence to a large energy gain in the motional electric field. The possible importance of such a reflection process for pickup ions appears to have been recognized first by Lee and Axford (1988). Zank et al. (1996) suggest that interplanetary shocks may in fact be the source of all ≤ 1 MeV nucl^{-1} ions in the solar wind.

7.2.2. *Multiply Reflected Ion Acceleration of Pickup Ions*

A fairly well-developed theory, at least compared to quasi-parallel shocks, exists for high $\beta_p \sim O(1)$ perpendicular shocks (e.g., Leroy, 1983) and a self-sustaining mechanism of ion reflection at the electrostatic cross shock potential is thought to be the primary dissipation mechanism. Recall that the electrostatic shock potential forms as a result of charge separation induced by the overshoot at the shock of the more massive ions. Such an overshoot effect is observed to be present at both quasi-perpendicular and quasi-parallel shocks.

As recognized by Zank et al. (1995, 1996) and Lee et al. (1996), an important property of the pickup ion distribution is that part of the distribution function in the shock frame has very small normal velocity components at the shock interface which prevents their overcoming the electrostatic cross shock potential. By estimating or prescribing the shock potential (Leroy, 1983), one can estimate the fraction of incident solar wind or pick-up ions that are reflected. The velocity V_{spec}, below which ions are reflected at a given shock, can be estimated from the electrostatic shock potential ϕ, which is approximated usefully at a perpendicular shock as

$$e\phi \simeq \eta \frac{1}{M_{A1}^2} \frac{\delta B}{B_1} m u_1^2 , \tag{203}$$

where $\delta B \equiv B_2 - B_1$ is the difference between downstream (2) and upstream (1) magnetic fields and M_{A1} is the upstream Alfvénic Mach number. Equation (203) is derived from the momentum equation for electrons (which are assumed massless) and the parameter η has been introduced to approximate the contribution to ϕ of the deflected bulk velocity u_y (which arises through ion reflection at the shock ramp) and the jump in the electron pressure (Leroy, 1983). For a particle to be reflected specularly at the shock, its velocity component in the shock normal direction v_x must satisfy $(e\phi)_{shock} \geq 1/2\ m v_x^2$. This of course neglects the particle's Lorentz force but for the low particle speeds under consideration and the assumed structure of the shock potential (see below) this is adequate. For a pickup ion shell distribution ahead of the shock, the fraction of the distribution $R_{\rm ref}$ that is incapable of surmounting the cross shock potential barrier is found to be (Zank et al., 1995, 1996)

$$R_{\rm ref} = \left[\frac{Zm}{M} \frac{\eta}{2M_{\rm A1}^2} (r-1) \right]^{1/2} , \tag{204}$$

where m refers to the proton mass and M and Z to the mass and charge of the particle of interest (pick-up H^+, He^+, etc.). Zank et al. (1996) and Lee et al. (1996) argue that these reflected ions are capable of being accelerated to large energies. Several points can then be inferred if we interpret reflection efficiency as injection efficiency. (i) Heavier pickup ion species, i.e., with $M > m$, are less efficiently injected, and (ii) injection efficiency increases with increasing particle charge state. Thus, pick-up H^+ should be injected twice as efficiently as pick-up He^+, and, if we assume that the alpha particle distribution is shell-like, then the injection efficiency of He^{++} should be intermediate to the aforementioned pick-up species. This appears to be what is observed by the *Ulysses* spacecraft at a forward shock (Gloeckler et al., 1994).

To examine the possibility that pickup ions are reflected multiple times before overcoming the electrostatic potential (i.e., if the pickup ion is trapped at the quasi-perpendicular shock by the particle Lorentz force and the shock electrostatic potential), Zank et al. (1996) and Lee et al. (1996) integrate particle orbits of a pickup ion analytically at a shock. Two examples of possible individual pickup ion trajectories at shock are plotted in Figure 7.11, one of which shows the phenomenon of multiple reflection. In the fluid frame of reference (chosen to ensure that the motional electric field $\mathbf{E} = 0$), the general gain in energy for a reflected particle is

$$\frac{\varepsilon^a}{1/2\ m u_1^2} = v^2/u_1^2 + 4\ v/u_1\ \sin\theta \cos\phi + 4 , \tag{205}$$

For a steady shock with velocity $\mathbf{V}_{sh} = -u_1 \hat{\mathbf{x}}$, a reflected particle will reencounter the shock at a time $t^* > 0$ such that

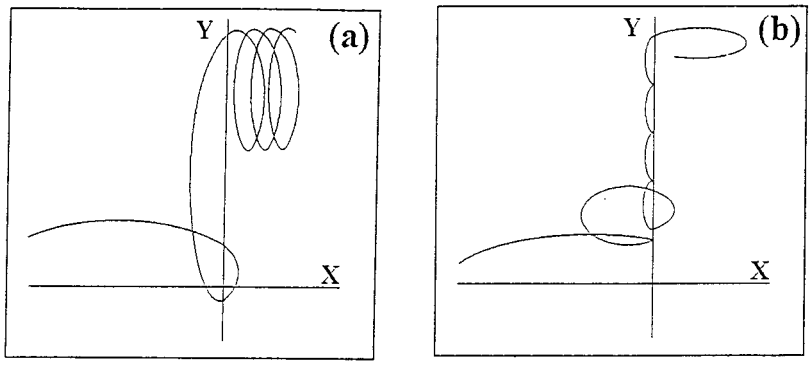

Figure 7.11. Examples of exact integrated individual pickup ion trajectories at a perpendicular shock located at $x = 0$ with an assumed step-like electrostatic cross-shock potential. The ion trajectories are projected into the (x, y) plane. Here (**a**) illustrates the trajectory of a shock drift accelerated particle and (**b**) illustrates a single reflection followed by SDA, followed by multiple reflection and then transmission. (Zank et al., 1996.)

$$\Omega t^* - 2\sin\Omega t^* + v/u_1 \ \sin\theta\left[\sin\phi - \sin(\Omega t^* + \phi)\right] = 0\ . \tag{206}$$

Lee et al. (1996) solved the pickup ion equations of motion with (206) approximately, while Zank et al. (1996) solved (206) numerically, using the exact equations of motion. Both sets of authors find that the domain of multiply reflected pickup ions can be quite substantial, due largely to the assumed (broadened) bispherical character of the pickup ion distribution.

Depending on the initial conditions, incident pickup ions can be (i) reflected at the shock potential until they gain sufficient energy to overcome the barrier, after which they may experience some drift energization; (ii) transmitted directly through the shock with some associated SDA, or (iii) partially shock drift accelerated before being reflected. The downstream or transmitted pickup ion distribution is then easily computed (by assuming as the initial conditions an upstream shell distribution for the pickup ions, Zank et al., 1996) and is illustrated in Figure 7.12. Figure 7.12(a) refers to the distribution in the fluid frame and Figure 7.12(b) to the shock frame and clearly there is little difference. The normalized differential number density $\mathrm{d}N/N_1$ ($\equiv f\mathrm{d}^3v$, f the computed downstream pickup ion distribution) is plotted as a function of normalized energy (v^2/u_1^2) for interstellar pick-up H^+. The first peak in the spectrum ($E/E_1 = 4$) of Figure 7.12(a) corresponds to those pickup ions which have not experienced any reflections but have been drift accelerated only – note the similarity to Figure 7.10. The remaining part of the spectrum corresponds to multiply reflected and energized pickup ions. The first lobe corresponds to singly reflected ions. The power law tail in energy produced by multiply reflected ion (MRI) acceleration is evidently extremely hard. For reference, an $E^{-1.5}$ power law is drawn through the spectrum. As discussed below, there is no limit to pickup ion energy gain from this mechanism when a step function electrostatic potential is assumed.

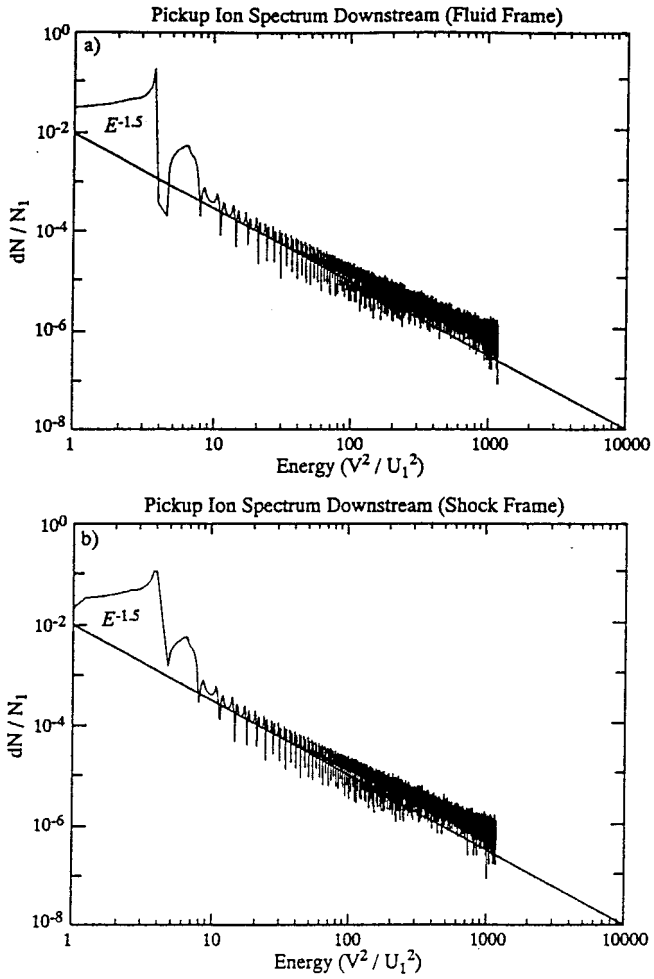

Figure 7.12. The transmitted pickup ion spectrum at a perpendicular shock in the (**a**) fluid and (**b**) shock frames. An $E^{-1.5}$ power law has been plotted over the computed spectrum for the purposes of illustration. (Zank et al., 1996.)

The spectra obtained from MRI acceleration are very different from the spectra expected of a first-order Fermi shock acceleration mechanism. For Fermi acceleration, the non-relativistic energy spectrum is $\propto v^{-q}$, where $q = 3r_s/(r_s - 1)$ as before. The hardest spectra, $q = 4$, are therefore associated with the strongest shocks ($r_s = 4$) whereas, even for weak shocks, MRI acceleration yields spectra much flatter (harder) than this. For example, from Figure 7.12, $f \sim v^{-3}$.

Three effects conspire against a reflected pickup ion gaining unlimited energy from the motional electric field. The first is obviously that the particles' incident normal velocity v_x must satisfy $1/2\ mv_x^2 \leq e\phi$. The second is escape from the shock environment due to any of several effects including finite shock extent,

obliquity of the magnetic field (MRI acceleration cannot work at a quasi-parallel shock), magnetic field fluctuations scattering reflected ion trajectories significantly and perturbations associated with the shock itself. The third effect is that, as the reflected pickup ions acquire a large velocity v_y in the transverse direction associated with the motional electric field, the Lorentz force ev_yB becomes increasingly important in the vicinity of the electrostatic barrier. The particle Lorentz force must eventually exceed the force exerted by the electrostatic potential $-e\nabla\phi$ so allowing the reflected ion to escape downstream. Evidently, the gradient of the electrostatic shock potential is crucial in determining the maximum pickup ion energy gain from MRI acceleration. By introducing the shock ramp thickness $\Delta x \equiv L_{\rm ramp}$, the balancing of the particle Lorentz force against the electrostatic potential gradient yields

$$ev_yB \simeq e\phi/L_{\rm ramp}. \tag{207}$$

On using the estimate (203) for the shock potential, one has (Zank et al., 1996; Lee et al., 1996)

$$v_y = \frac{\eta}{M_{A1}^2}\,\frac{\delta B}{B_1}\,\frac{mu_1}{eB_1}\,\frac{u_1}{L_{\rm ramp}}\,, \tag{208}$$

where mu_1/eB is the gyroradius of a particle moving at the solar wind speed. Thus, the maximum energy gain is proportional to the ratio of an ion gyroradius (whose velocity is that of the solar wind) to the smallest characteristic electrostatic shock potential length scale. Clearly, v_y can become very large as $L_{\rm ramp} \to 0$.

If the length scale $L_{\rm ramp}$ is that of the thermal solar wind ion gyroradius, the initially very low velocity pickup ions will be accelerated up to no more than the ambient solar wind speed. However, our current (not very good) understanding of the micro-structure of quasi-perpendicular shocks is that fine structure in the shock potential can be on the order of electron inertial scales, so yielding

$$v_y = \eta V_{A1}\frac{\delta B}{B_1}\left(\frac{m}{m_e}\right)^{1/2}\,. \tag{209}$$

Subject to the assumption (209), MRI acceleration can yield pickup ion energies of $\sim 10^5$–10^6 eV at even weak interplanetary shocks.

Lipatov et al. (1998) and Zilbersher and Gedalin (1997) used direct particle simulations to explore the acceleration of pickup ions at collisionless quasi-perpendicular shocks with an assumed fixed profile for the transition layer, demonstrating several new features as well as providing support for the basic analysis of Zank et al. (1996) and Lee et al. (1996). Their results may be enumerated as follows. (1) The energy spectrum of accelerated H^+ pickup ions at quasi-perpendicular shocks may be approximated by the power law $N \approx (E/E_0)^{-k}$, where k varies from 0.92 to 1.2. This spectrum is a little harder than that obtained by the quasi-analytical approach of Zank et al. (1996). Lipatov et al. (1998) provide plots which show

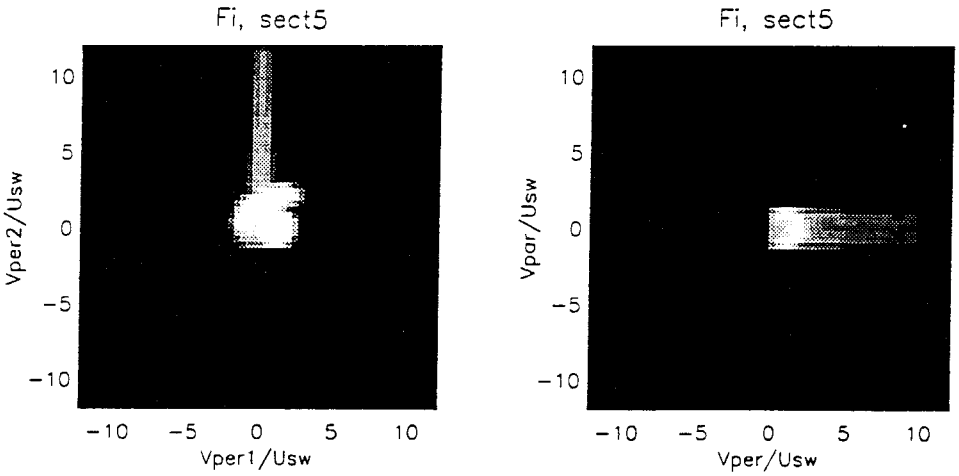

Figure 7.13. The projection of the pickup ion distribution onto the velocity plane just ahead of the ramp of a structured perpendicular shock. $v_\perp$ and $v_\parallel$ are the velocity components perpendicular and parallel to the magnetic field. (Lipatov et al., 1998.)

the the projected pickup ion distribution in velocity space as a function of distance from the shock. In the immediate upstream vicinity of the shock, the pickup ion distribution acquires a large v_y component (Figure 7.13). (2) The fine structure of the shock may slightly decrease the maximum energy of accelerated pickup ions compared to a step-like transition layer. (3) A flat turbulence spectrum in the shock transition layer results in an increased maximum pickup ion energy for of particles downstream of the shock, whereas power law turbulence reduces the maximum pickup ion energy gain. The basic mechanism of MRI acceleration is however preserved and hard spectra result. (4) The energy spectrum of accelerated He^+ pickup ions at quasi-perpendicular shocks may also be approximated by the power law $N \approx (E/E_0)^{-k}$, where k varies between 1.2 to 1.3. As expected, the injection efficiency of pickup He^+ is substantially less than that of pickup H^+. (5) For oblique shocks with $\theta_{bn} = 60° \sim 70°$, a strong beam of pickup ions is formed along the magnetic field. In a self-consistent simulation, the reflected pickup ion beam might be expected to drive further low frequency plasma instabilities. The key factor determining the efficacy of MRI acceleration is the existence of a strong steep ramp inside the shock transition layer. However, under more realistic circumstances, the ramp structure in a quasi-perpendicular shock, even with a large θ_{bn} ($\theta_{bn} \sim 80 - -90°$), may be nonstationary, experiencing cyclical changes which are characterized by a progressive steepening and smoothing of the electromagnetic field in the shock transition layer. This behaviour may result in the appearance of sporadic bursts of accelerated pickup ions at the shock front.

In concluding this subsection, we note that Savopulos and Quenby (1997), using an earlier model (Savopulos et al., 1995), have investigated the acceleration of He^+ based on the transport equation (168) in an effort to identify the role of

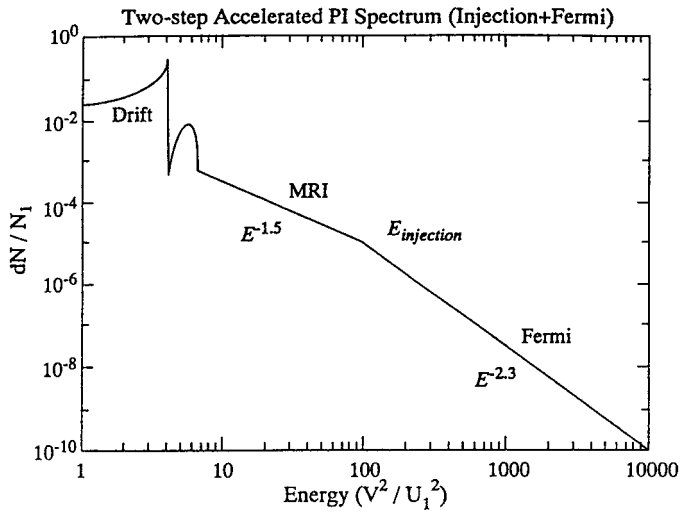

Figure 7.14. A schematic spectrum for pickup ions transmitted through the TS in a two-step acceleration process. That part of the upstream pickup ion shell not reflected by the shock potential barrier is drift accelerated up to energies 2–4 times that of $1/2\ mu_1^2$ (the precise value depending on the shock compression ratio). Multiply reflected pickup ions are then accelerated up to energies perhaps several 100 times that of $1/2\ mu_1^2$ – the injection energy necessary to initiate a second stage Fermi acceleration process. The transmitted pickup ion spectrum will be extremely hard until $E_{\rm inj}$ ($\sim E^{-1.5}$) whereupon a softer spectrum might develop ($\sim E^{-2.4}$) whose slope is consistent with Fermi acceleration at a weak TS. (Zank et al., 1996.)

injection energy and the associated injection/pre-acceleration schemes that have been advanced. This appears to be an important direction to explore in the near future. In Figure 7.14, a schematic spectrum for pickup ions accelerated from their pickup energy ($\sim$ 1 keV) up to ACR energies is depicted for a two-step acceleration process (in this case, MRI plus Fermi acceleration).

7.3. SIMULATIONS

To explore the full nonlinear character of the pickup ion injection and acceleration process at a collisionless shock requires the use of particle simulations. Of course, such simulations are limited too by the assumptions imposed by the modelling approach and the available computational resources. Thus, while simulations are an invaluable tool in guiding and developing our understanding of particle acceleration at collisionless shocks, one should be well aware of their implicit limitations. We describe here three approaches that have been adopted in the investigation of the injection and acceleration of pickup ions at either the termination shock or at interplanetary shocks.

7.3.1. *Hybrid Simulations*

Liewer et al. (1993, 1995) and Kucharek and Scholer (1995) used 1D hybrid simulations (kinetic ions and fluid electrons) to investigate the injection and initial stages of pickup ion energization at the termination shock. All simulations assume a shell distribution for the pickup ions initially and a Maxwellian solar wind ion distribution. The Alfvén Mach number and solar wind plasma β_p are specified.

The simulations of Liewer et al. (1993) concentrate primarily on shock structure although results about particle acceleration at a quasi-perpendicular shock can be inferred. For nearly perpendicular shocks ($\theta_{\rm BN} = 80°$), it is found that, with a pickup ion population 10% that of the background solar wind ions, an extended foot ahead of the shock ramp is formed, this with a scale length comparable to the pickup ion gyroradius. The pickup ion temperature increase was essentially adiabatic and no evidence for particle injection or acceleration was seen. The formation of the pickup ion foot resulted from pickup ion reflection at the shock electrostatic potential. The absence of an energetic pickup ion sub-population suggests that specular reflection of pickup ions occurred once only.

By contrast, the hybrid simulations of Liewer et al. (1995) and Kucharek and Scholer (1995) for shocks with $\theta_{\rm BN} < 60°$ show evidence that low-energy pickup ions can be accelerated efficiently. These authors find that pickup ions form an ion beam streaming back upstream after reflection at the shock. The reflection efficiency is shown to decrease with increasing $\theta_{\rm BN}$, where Kucharek and Scholer (1995) define reflection to mean particles that stream upstream to some prescribed distance ($= 30c/\omega_p$). The beam drives a cyclotron instability (Liewer et al., 1995), which then contributes to the scattering of pickup ions. For $\theta_{\rm BN} \leq 60°$, Liewer et al. and Kucharek and Scholer find that the turbulence levels are sufficiently high to keep the scattered pickup ions in the vicinity of the shock and this leads to the Fermi acceleration of pickup ions up to relatively modest energies (this due in part to computational limitations). An example of the accelerated pickup ion spectrum for $\theta_{\rm BN} = 50°, 60°$, and $70°$ (Kucharek and Scholer, 1995) is illustrated in Figure 7.15. The dotted line shows the solar wind distribution function and the other lines show the accelerated pickup ion distribution for the three $\theta_{\rm BN}$ values. At low energies, there is little difference between the pickup ion distributions for the three obliquities but for $\theta_{\rm BN} > 60°$, virtually no additional energization of the pickup ions occurs at the termination shock. By studying the orbits of individual pickup ions, Liewer et al. (1995) find that pickup ions are energized primarily by shock drift acceleration coupled to repeated downstream scattering which returns the pickup ions to the shock. This is consistent with theoretical expectations for Fermi acceleration at a quasi-perpendicular shock (Jokipii, 1992). Finally, Kucharek and Scholer (1995) find He^+ to be less efficiently injected (by a factor of ~ 2) than H^+.

As was discussed at some length by Liewer et al. (1993, 1995) and Kucharek and Scholer (1995), the termination shock is expected to be predominantly perpendicular (Figure 3.1), in which case injection can occur sporadically, when large-scale magnetic field fluctuations ensure that $\theta_{\rm BN} < 60°$. This is estimated to occur

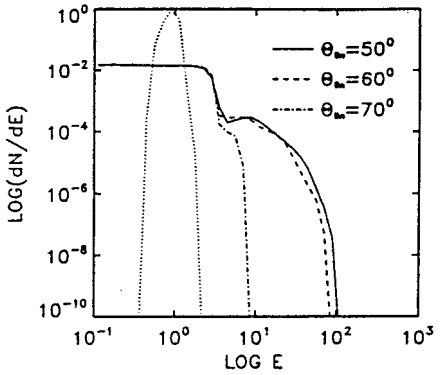

Figure 7.15. Differential densities (dN/dE) upstream of a quasi-perpendicular shock with $M_A = 8$ as a function of energy for different shock normal angles θ_{BN}. The energy is normalized to the shock ram energy and the dotted line shows the solar wind distribution. (Kucharek and Scholer, 1995.)

only 10% of the time (Kucharek and Scholer, 1995). The very sporadic nature of such an injection model is a drawback. However, as discussed in Section 6.1, it is possible that the termination shock is not strictly perpendicular as often as is expected.

The question of why accelerated pickup ions are not seen in the quasi-perpendicular simulations discussed above has been addressed by Lipatov et al. (1998). As described in Section 7.2.2, highly perpendicular shocks favour MRI acceleration. However, the thickness of the ramp plays a crucial role in determining the maximum energy gain possible for a pickup ion. The maximum pickup ion energy and the shock ramp thickness are related by $\log_{10}(E_{max}/E_0) = 2\log_{10}(\eta/M_A^2 \cdot (r_s - 1)) - 2\log_{10}(L_{ramp}/R_L)$ (Equation (208)), and Figure 7.16 illustrates this graphically. Here, * denotes results obtained from the particle-mesh simulations of Lipatov et al. (1998) and the solid line is the estimated maximum pickup ion energy. The simulation demonstrates reasonable quantitative agreement with the analytical estimate. It is clear from Figure 7.16 that hybrid or particle simulations that do not resolve the shock ramp very well (i.e., hybrid codes which effectively resolve the shock ramp numerically, often with $L_{ramp} >> 0.01R_L$) are inadequate to investigate the MRI acceleration mechanism. This appears to be the case for all published simulations.

In an effort to overcome this shortcoming, Lipatov and Zank (1999) used a one-dimensional, (1+2/2)D hybrid kinetic electromagnetic code which included anomalous resistivity and electron inertia terms. Spatial variation along the z direction only was assumed, but all three components of the electromagnetic fields and particle velocities were retained. The shocks studied by Lipatov and Zank (1999) used upstream parameters expected of the solar wind in the transition layer of the termination shock: $M_A = 3 - 5$, $\beta_{e,p} = 0.1$, $n_{PI}/n_0 = 0.001 - 0.1$, $M/m = 1840$, $M_{PI}/M = 1$, $DZ = 10r_{ci}$, $\Delta_z = (0.006 - 0.0125)c/\omega_{pi}$, $\theta_{BN} = 90°$, and $l_d = (0.00625 - 0.25)c/\omega_{pi}$, where M_A is the Alfvén Mach Number, $\beta_{p(e)}$ denotes

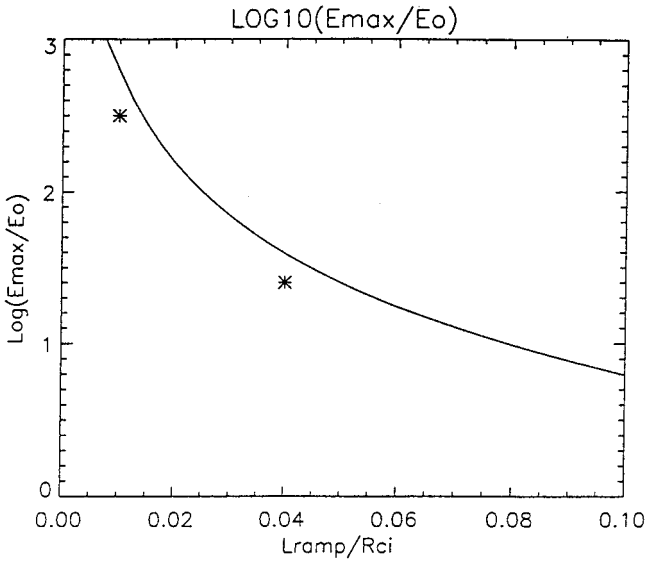

Figure 7.16. The dependence of the maximum energy of MRI accelerated pickup ions on shock ramp thickness. (Lipatov et al., 1998.)

the solar wind proton(electron) plasma beta, $n_{\rm PI}/n_0$ is the ratio of PI to proton density, M/m is the ratio of proton to electron mass, $M_{\rm PI}/M$ is the ratio of PI to proton mass, DZ is the size of simulation box, Δ_z is the cell size, $r_{ci} = u_0/\Omega_i$ is the proton cyclotron radius ($r_{ci} = r_{cH^+}$), and $l_d = \eta c^2/4\pi u_0$ is the resistive diffusion length (Leroy et al., 1982), where η is the anomalous resistivity. For example, the resistivity η, taken as constant $\eta/4\pi = 1.2^{-4}\omega_{pi}^{-1}$, corresponds to a collision frequency $\nu/\omega_{pi} = \eta\omega_{pe}^2/4\pi\omega_{pi} = 0.22$ and to a diffusion length $0.15c/\omega_{pi}$. The chosen range of the resistive diffusion length is reasonable and consistent with observational and theoretical studies of instabilities at shock fronts (see, for example, Scudder, 1986; Kennel et al., 1985; Winske, 1985). Initially, the proton velocity distribution function was taken to be Maxwellian by Lipatov and Zank (1999), with a broadened pickup ion shell velocity distribution in velocity space. The simulation time step assumed in the simulation of Lipatov and Zank was $5 \times 10^{-5} T_{ci}$, where $T_{ci} = 2\pi/\Omega_i$ and Ω_i is the proton gyrofrequency. Such small spatial and time scales were chosen to resolve the ramp on an electron inertial length scale and to provide an accurate calculation of pickup ion trajectories as they are transmitted across the ramp.

Figure 7.17 illustrates a simulation (Lipatov and Zank, 1999) of a shock with $M_{\rm A} = 5, n_{\rm PI}/n_0 = 0.01$, and $l_d = 0.006c/\omega_{pi}$ at time $t = 3.8T_{ci}$. The velocity, magnetic field, density, and electron pressure are normalized to the upstream velocity, magnetic field, proton density, electron pressure. The electric field and electrostatic potential are normalized to the upstream motional electric field $u_0 B_0/c$ and the kinetic energy of incoming protons $Mu_0^2/2$. The simulation illustrates the

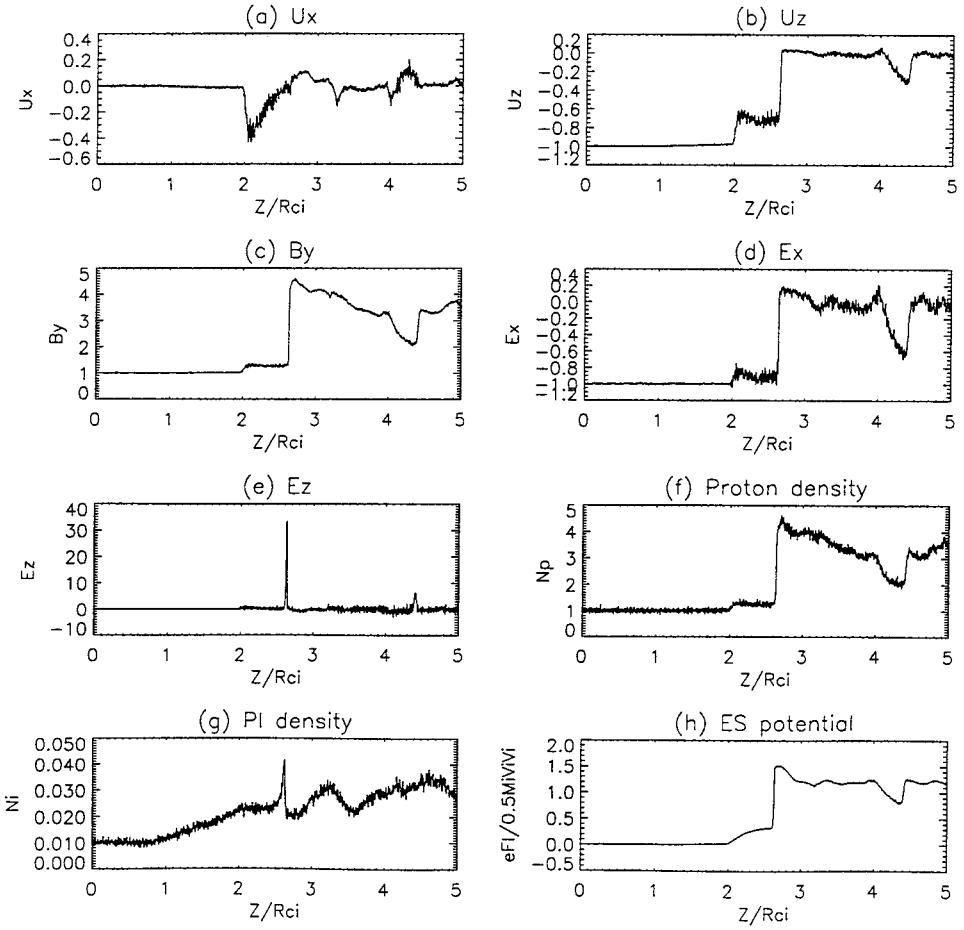

Figure 7.17. Typical profiles of the bulk velocity components u_x and u_z, the magnetic field component B_y, the electric components E_x and E_z, the proton n_p and PI n_{PI} densities, and electrostatic potential $e\phi/Mu_0^2/2$. (Lipatov and Zank, 1999.)

formation of a shock transition layer with a strong foot in the pickup ion density profile (g) and a thin ramp, $\Delta_{\text{ramp}}/r_{ci} < 0.05$ in the magnetic field and electrostatic potential profiles (Figures 7.17(c) and 7.17(h)). An additional jump forms at a distance $\delta z \approx 0.6 r_{ci}$ before the ramp in the electromagnetic field, bulk velocity and proton density profiles. It is clearly seen that the peak in pickup ion density corresponds to accelerated pickup ions and the peak is located inside the shock ramp due to temporary trapping of pickup ions (Figure 7.17(g)).

Figure 7.18 shows $v_{\perp 2}$ vs $v_{\perp 1}$ for the protons and H^+ pickup ions at different locations relative to the shock ramp. The panels of Figure 7.18 are arranged in ascending order from the bottom according to position as follows: far upstream (bottom panel), on the shock front, just downstream of the shock, and, the top

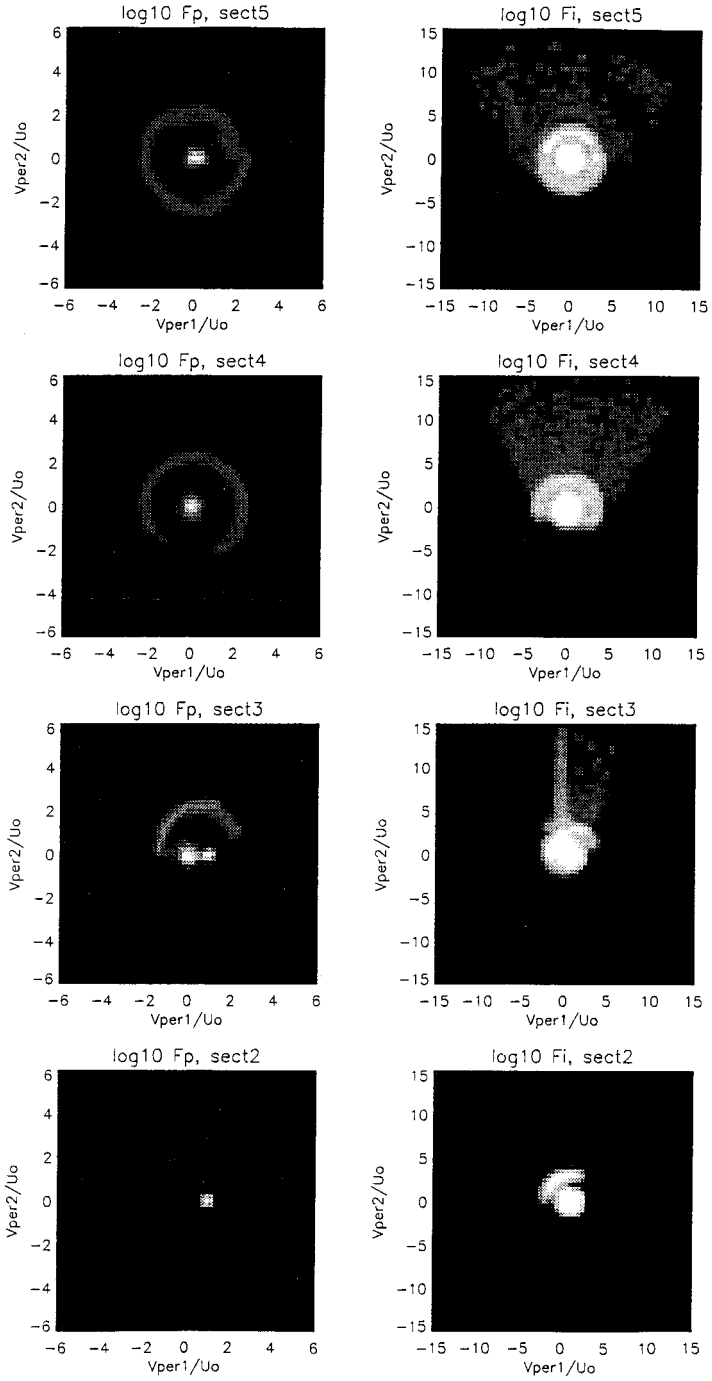

Figure 7.18. The projection of the protons (left column) and the H^+ pickup ion (right column) distribution onto the velocity plane for spatial sections ranging from downstream to upstream. Here $v_{\perp 1} \parallel \mathbf{v}_z$ and $v_{\perp 2} \parallel \mathbf{v}_x$ are the velocity components perpendicular to the magnetic field. (Lipatov and Zank, 1999.)

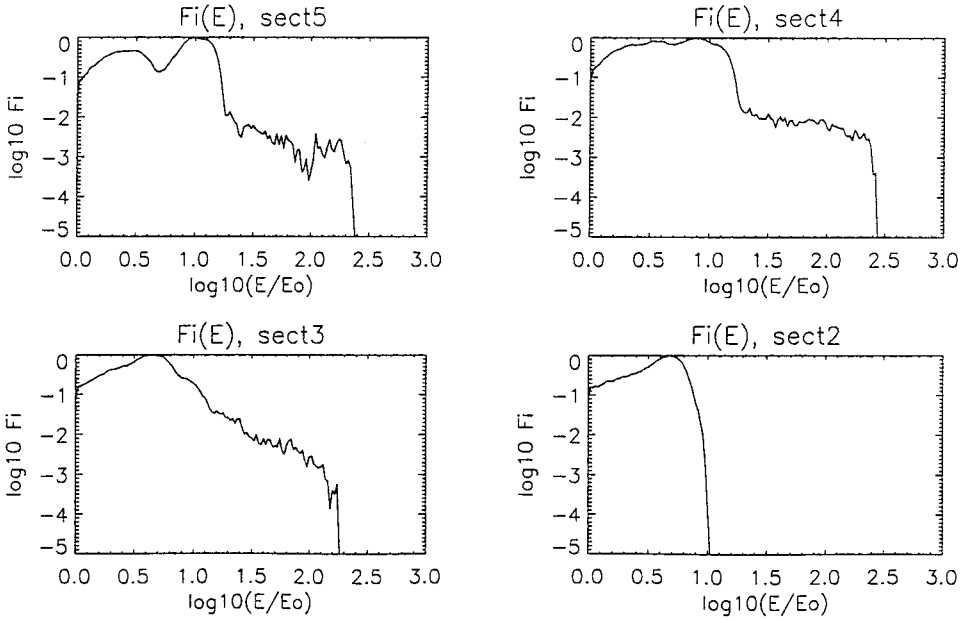

Figure 7.19. The energy spectrum of accelerated H^+ pickup ions for spatial sections ranging from downstream to upstream. (Lipatov and Zank, 1999.)

panel, far downstream. The left column illustrates the projected proton distribution in the plane $(v_{\perp 1}, v_{\perp 2})$ at various distances from the shock ramp, where $v_{\perp 1}$ and $v_{\perp 2}$ are the velocity components, perpendicular to the magnetic field. The proton distribution function has a supersonic core ahead of the ramp and a subsonic core downstream of the shock front. Before the ramp, we see reflected protons while downstream, the transmitted protons form a halo due to phase mixing. The right column shows the projected pickup ion distribution in the plane $(v_{\perp 1}, v_{\perp 2})$ at various distances from the shock ramp, where $v_{\perp 1}$ and $v_{\perp 2}$ are the velocity components, perpendicular to the magnetic field. The bottom right panel illustrates a very typical distribution which results from ion reflection at a perpendicular shock. Such distributions are seen at virtually all quasi-perpendicular shocks, both observationally (e.g., Sckopke, 1995) and in simulations (e.g., Leroy et al., 1982) and contribute essentially to the formation of the ion shock foot. If the number and energy density of the reflected pickup ions were sufficiently high at the termination shock, the foot structure and length scales would be determined primarily by reflected pickup ions rather than the colder more numerous solar wind protons (Liewer et al., 1993; Zank et al., 1996). The second panel from the bottom shows the pickup ion distribution at the shock ramp and a strong transverse acceleration of pickup ions along the shock front is evident with the formation of an extended 'tongue' along $v_{\perp 2}$. Finally, phase mixing occurs far downstream.

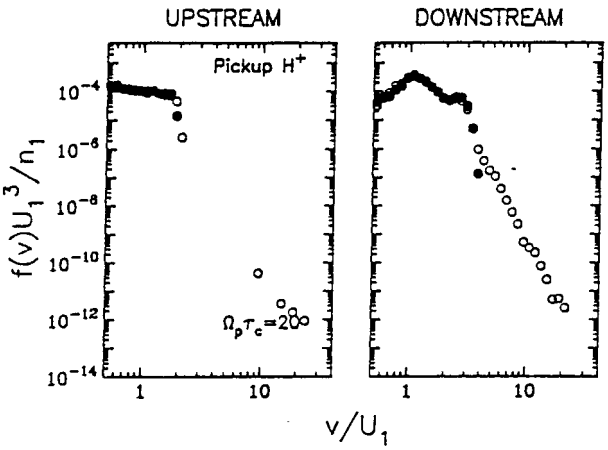

Figure 7.20. Upstream and downstream velocity distribution functions of pickup protons in the absence of scattering (solid circles) and with scattering (open circles). (Giacalone et al., 1994.)

Figure 7.19 illustrates the energy spectrum of accelerated H^+ pickup ions for spatial sections ranging from downstream to upstream. The pickup ion energy spectrum has two parts, as discussed already (Zank et al., 1996) – a shell-like distribution with an energy cut-off at about $E_0 = M_{\rm PI}u_0^2/2$ in the solar wind frame and an accelerated pickup ion component which emerges from the shell distribution as a hard/flat power law spectrum. The accelerated pickup ion energy spectrum may be approximated by the power law $F_i \propto {\rm d}N/N \sim (E/E_0)^{-k}$, where the energy E is calculated in the solar wind frame and N denotes the pickup ion number density. In the present case, the index k is about 1.0–1.3 in the vicinity of the ramp. The similarity between the spectra produced by the hybrid simulation of Lipatov and Zank (1999), the test particle-mesh simulation (Lipatov et al., 1998), and those obtained from the quasi-analytical approach (Zank et al., 1996) is close.

Thus, kinetic hybrid simulations of the acceleration of H^+ pickup ions at low-β collisionless quasi-perpendicular shocks (with a low pickup ion density ($n_{\rm PI}/n_0 < 0.1$) and appropriate anomalous resistivity $0.006c/\omega_{pi} < l_d < 0.25c/\omega_{pi}$) demonstrate several new features, as well as providing support for the basic test-particle analysis of Zank et al. (1996) and Lee et al. (1996).

7.3.2. *Injection at Quasi-Perpendicular Shocks*

The simulation of ion injection and acceleration at quasi-perpendicular shocks has been described in several papers by Giacalone and Jokipii (1996a, b) and Giacalone et al. (1994). The important feature of these simulations is the inclusion of either synthetic turbulent magnetic fields (Giacalone and Jokipii, 1996a, b) or a phenomenological cross-field scattering model (Giacalone et al., 1994).

Jokipii et al. (1993) (see also Jones et al., 1998) have argued that the diffusion of particles across a magnetic field is suppressed in 1D and 2D hybrid simulations. To avoid this limitation, since cross-field diffusion is essential to particle acceleration

at quasi-perpendicular shocks, Giacalone et al. (1994) introduce an *ad hoc* particle 'scatter' at some time τ which conserves particle speed and pitch-angle in the local plasma frame but randomizes the gyrophase. Whether this rather crude model over- or underestimates cross-field transport of ions in their 1D hybrid simulations is unclear. Nonetheless, such an assumption leads to the acceleration of pickup ions at a perpendicular shock. Shown in Figure 7.20 is a pickup ion spectrum with (open circles) and without (solid circles) the phenomenologically prescribed cross-field scattering model. In the presence of scattering, a power law accelerated pickup ion population emerges from the assumed pickup ion shell distribution downstream of the perpendicular shock. Conversely, solar wind ions are not seen to be accelerated at the perpendicular shock even thought the simulations show a substantial specularly reflected proton population upstream of the shock. The reason for pickup ion acceleration without solar wind ion acceleration is largely a consequence of the assumed scattering model (gyrophase randomization) and the assumed pickup ion and solar wind proton distribution functions (shell and Maxwellian respectively). The specularly reflected solar wind ions possess a small range of velocities perpendicular to the magnetic field, unlike the pickup ions, and cannot remain in the vicinity of the shock for any significant length of time when only gyrophase scattering is assumed. This may indicate yet again that the shell distribution is rather special in alleviating the 'injection problem' at quasi-perpendicular shocks. However, the nature of the scattering model introduced by Giacalone et al. (1994) must temper such a conclusion.

It is clear that the heart of the injection problem resides in the nature of low-energy particle scattering, either by MHD turbulence or specularly, and in the nature of the pickup ion distribution. In an effort to determine whether a realistic turbulence field could provide the necessary pickup ion scattering at a shock needed to inject and accelerate ions to large energies, Giacalone and Jokipii (1996a, b) performed test-particle simulations using synthetic MHD turbulence spectra. Two models for the turbulence were investigated, the first assuming that the correlation length $\ell \gg R_L$ (R_L the particle gyroradius), and the second that $\ell \sim R_L$. In the first case, field-line random walk essentially determines particle diffusion, unlike the second model.

Illustrated in Figure 7.21 is the downstream omni-directional pickup ion flux. The solid line corresponds to the $\ell \sim R_L$ model and the dashed line to a $\ell \sim 100 R_L$ model. The structure in the spectrum can be interpreted as one, two, and multiple particle encounters with the shock (one encounter gives rise to the drift acceleration feature – compare with Figure 7.10), especially for the $\ell \sim R_L$ model. In the $\ell \sim 100 R_L$ model, thanks to the random walk of the magnetic field, the acceleration process becomes diffusive after the particle encounters the shock more than once. The subsequent spectral slope is approximately consistent with the expectations of diffusive shock acceleration theory. The $\ell \sim R_L$ model produces far steeper spectra. In both cases, the number of accelerated ions is two orders of magnitude smaller than the number experiencing one encounter with the shock.

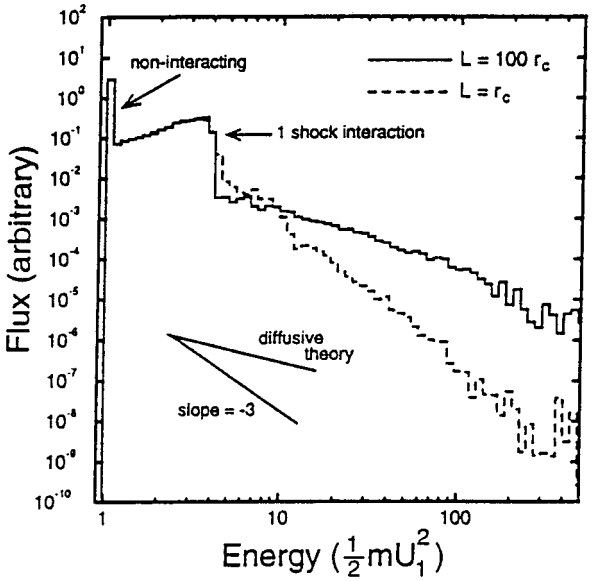

Figure 7.21. Downstream particle flux as function of energy, normalized to the solar wind ram energy. (Giacalone and Jokipii, 1996b.)

Giacalone and Jokipii (1996a, b) conclude that the motion of low-energy pickup ions is not well described by diffusion theory. Consequently, the spectral slope of accelerated particles was steeper at low energies than expected from Fermi acceleration theory. This, they suggested, implies that simple scattering off convected magnetic fluctuations cannot readily account for the acceleration of freshly ionized pickup ions.

The final set of simulations that we discuss are Monte Carlo simulations of ion acceleration at interplanetary shocks. These are not directly relevant since pickup ions are not included in these models (Baring et al., 1997) and only the injection of solar wind ions is considered. However, the suggestion has been made (Ellison et al., 1995; Baring et al., 1997) that there is no difficulty in injecting thermal particles into the Fermi acceleration scheme, even for quasi-perpendicular shocks ($\theta_{\rm BN} > 70°$). For this reason, we consider the Monte Carlo simulations a little more closely.

Baring et al. (1997) compare modelled accelerated solar wind ion spectra with *Ulysses* SWICS H^+ data and obtain good fits. The Monte Carlo model relies on several key assumptions. Firstly, it is assumed that the particle scattering is elastic and isotropizes particle momenta in the local fluid frame, and therefore mimics large-angle scattering. The scattering mean-free-path is assumed to be

$$\lambda = \lambda_0 \, (R_L/R_{L1}) \propto p \, , \tag{210}$$

where R_{L1} is the far upstream particle gyroradius. Secondly, the ratio λ_0/R_{L1} is prescribed and, since $\kappa_\perp = \kappa_\parallel/(1 + (\lambda/R_L)^2)$, defines the magnitude of the cross-

field diffusion. To obtain the fit of model to data, Baring et al. (1997) have to use $\lambda_0/R_{L1} \sim 1$, implying that the scattering is very strong (since $\kappa_\perp \simeq \kappa_\parallel$). If $\lambda_0/R_{L1} \gg 1$, then no acceleration occurs at the quasi-perpendicular shock at all.

Recognizing that the Baring et al. (1997) model does not address the issue of pickup ion injection and acceleration directly, their model raises several disturbing issues. (1) The adopted phenomenological form of the scattering mean-free-path model (210) is not consistent with either the parallel or perpendicular mfp models derived in Section 7.1.1. For low energy ions, $\lambda_\parallel \propto p^{1/3}$ and, for strong scattering, $\lambda_\perp \propto p^{1/3}$. For weak scattering, $\lambda_\perp \propto p^2$. Thus, the choice of the scattering law (210) appears to be neither well motivated nor consistent with the assumption of strong scattering. Equation (210) also favours the injection of low-energy particles since it overestimates their mobility compared to a $\lambda \propto p^{1/3}$ scattering law. (2) As discussed by Jokipii (1992), to accelerate ions rapidly at a quasi-perpendicular shock requires that $\lambda/R_L \gg 1$, which appears to be in conflict with the requirement of $\lambda/R_L \sim 1$ that Baring et al. (1997) need for injection and acceleration. (3) As discussed above in the context of the Giacalone and Jokipii (1996a, b) simulations, the nature of the turbulence scattering field is essential in deciding whether scattering alone is sufficient to provide the injection particles for Fermi shock acceleration and the prescription of an *ad hoc* scattering law cannot circumvent this plasma physical question. In this respect, the results of Giacalone and Jokipii (1996a, b) appear to be in conflict with the Monte Carlo model of Baring et al. (1997). If nothing else, this illustrates the complexities and subtleties of the injection problem for cosmic-rays.

8. Nonlinear Theory of Termination Shock Structure

The question of what the Voyager spacecraft might see when crossing the heliospheric termination shock has assumed increasing importance and many studies have now addressed this issue. These studies fall typically into two classes: (1) What role do pickup ions play in determining shock structure? and (2) How do anomalous and galactic cosmic-rays help to determine termination shock structure? Although the disparate length scales between ~ 1 keV pickup ions and MeV ACRs suggest that the role of one is independent of the other, pickup ions provide presumably the seed population for ACRs and one needs therefore to assess the importance of injection too in the dynamics of the shock structure. It is easy to convince oneself that both the test particle pickup energization and the ACR acceleration models discussed in Section 7 lead to energy densities for the accelerated pickup ions and ACRs that are comparable to or exceed the thermal energy density of solar wind ions. The nonlinear backreaction of energized ions on the solar wind and termination shock structure must therefore be included self-consistently. We shall begin this section by considering the effects of pickup ions on the termination shock.

Thereafter, shock structure will be considered from the perspective of cosmic-ray mediation.

8.1. Effect of pickup ions on the termination shock

In an analysis of anomalous cosmic-ray spectra observed during 1994, Stone et al. (1996) suggested that the termination shock should be located at ∼85 AU and the shock compression ratio $r_s \simeq 2.6$. Such a weak shock corresponds to a sonic Mach number $M \simeq 2.4$ for the solar wind flow just ahead of the shock. Although the termination shock is expected to be much weaker, due both to the deceleration of the wind by ion pickup and the increase in effective sound speed, such a small compression ratio is not consistent with simulations (Sections 5, 6). It is possible that assumptions regarding the ACR acceleration model at the TS may contribute to the somewhat low compression ratio of the TS. Nonetheless, Isenberg (1997) (see also Zank et al., 1995, 1996) used both a perturbation model (Section 4.3) and his three-fluid model (Section 4.4) to evaluate the (fast magneto)sonic Mach number M_f for the solar wind as a function of radial distance. Illustrated in Figure 8.1 is a plot of $M_f(r)$. The parameters used to produce Figure 8.1 were $N = 0.125$ cm^{-3} (the neutral number density assumed at the TS and not in the LISM), $u(1\text{ AU}) = 400$ km s^{-1}, $n(1\text{ AU}) = 5$ cm^{-3}, $T_p(1\text{ AU}) = 1.4 \times 10^4$ K, and $B = 2.5\gamma$. In order to achieve such a low Mach number, it was essential to assume a high neutral number density at the TS. Gloeckler et al. (1995) and Gloeckler (1996) suggest that such values are reasonable although earlier estimates Gloeckler et al. (1993) suggested lower values ($N = 0.06$ cm^{-3}). A high value for N is very difficult to understand theoretically – either filtration is completely unimportant or the LISM value of the neutral number density N of hydrogen is much higher than often assumed or inferred. If the latter is in fact correct, then the extent of the heliosphere should be much smaller than predicted by the global 2D and 3D models of Section 5. In general, the global models predict a TS that is located at $\sim$ 70–80 AU. Although the ACRs act to push the shock further out, the inwardly directed galactic cosmic ray pressure gradient tends to nullify this effect. Thus, it is difficult to place the shock at $\geq$ 85 AU and simultaneously impose a large value of N at the TS, as required in the analysis of Isenberg (1997). The resolution to this difficult lies in any of several directions. (i) Inferences drawn from the ACR data may depend too strongly on the cosmic-ray acceleration and injection model. (ii) ACR modulation in the outer heliosphere is not yet fully understood and inferences from the spectra may be difficult to draw. (iii) Neutral number densities may have been overestimated, both those derived from Lyman-α observations and pickup ion data. (iv) The LISM plasma density may be lower than assumed generally.

To summarize, one expects theoretically that the TS should be weakened considerably by pickup ions in the solar wind. The precise strength of the termination shock is however unclear since neither the multi-dimensional simulations nor the inferences and implications from observations are consistent.

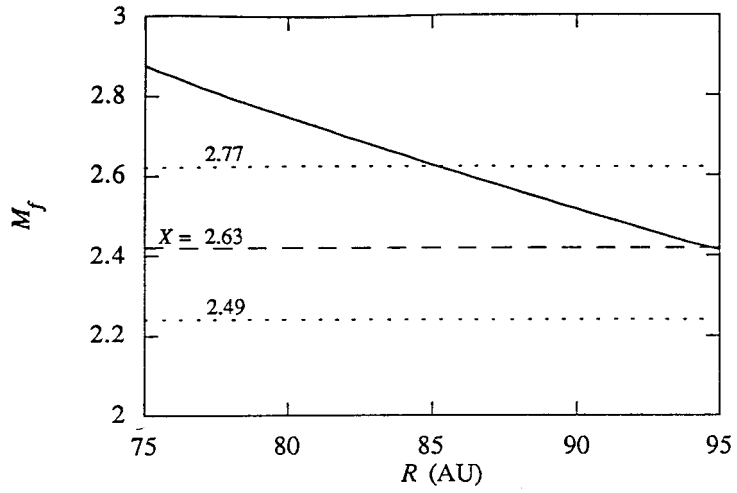

Figure 8.1. Solar wind fast-mode Mach number in the radial range 75–95 AU (solid line), calculated using the three-fluid model of Isenberg (1986). The range of shock compression ratios X derived by Stone et al. (1996) are shown by the dashed lines (Isenberg, 1997.)

8.1.1. *Termination Shock Structure: Theory*

The very interesting simulations presented by Liewer et al. (1993) of a quasi-perpendicular termination shock in the presence of a pickup ion population prompted the development of a fairly detailed theoretical termination shock model based on pickup ion reflection (and MRI acceleration) at the cross-shock electrostatic potential (Zank et al., 1996) We consider first the simplified theoretical analysis before discussing the simulations.

Based on the three-fluid model of Isenberg (1986) (Section 4.4), Zank et al. (1996) consider four TS models, these distinguished by the termination shock location and the assumed thermal temperature dependence on heliocentric distance. These models are contrasted with a pure MHD solar wind model (i.e., no neutral H, and hence no pickup ions, included). Model 1 assumes a termination shock location of 60 AU and the TS of Model 2 is at 100 AU. Models 1a and 2a assume an adiabatically cooled solar wind whereas Models 1b and 2b assume that $T \propto r^{-0.55}$ (Richardson et al., 1995). Models 1 and 2a assume that $N = 0.1$ cm^{-3}, and Model 2b assumes $N = 0.01$ cm^{-3}. The expected sound speeds, Mach numbers and plasma beta values are tabulated in Table XVI, obtained using values for the temperature, density, and magnetic field strength listed in Zank et al. (1996). Several points are immediately apparent from Table XVI and the plasma parameters on which it is based. (i) Charge exchange, and the lesser effect of mass-loading, can decelerate the solar wind significantly, with the implication that the TS shock strength can weaken dramatically with increasing heliocentric distance. (ii) The thermal solar wind temperature (i.e., excluding pickup ions) is very low, even when non-adiabatic thermal expansion is assumed (Model 1b) and several

TABLE XVI

Derived sound speeds (V_A and V_f correspond to the Alfvén and fast magnetosonic speeds), Mach numbers (M_A and M_f to the Alfvén and fast magnetosonic Mach numbers) and plasma β's ($\beta_{PI/SW}$ refer to the plasma beta with and without pickup ions) for the TS models.

	V_A (km s^{-1})	V_f (km s^{-1})	M_A	M_f	β_{SW}	β_{PI}
Model 1a	50	98	6.9	3.5	6.6×10^{-3}	3.3
Model 1b	50	99	6.9	3.5	0.15	3.45
MHD (60AU)	51	51	7.8	8	0.005	
Model 2a	62.5	110	4.5	2.5	2.4×10^{-3}	2.6
Model 2b	68.5	100	5.6	3.8	2.4×10^{-3}	1.4
MHD (100AU)	71	71	5.6	5.6	2.4×10^{-3}	

orders of magnitude lower than that of the pickup ions. The solar wind distribution function becomes increasingly narrow in velocity space. By contrast, the continued addition of energetic pickup ions serves to offset the effects of adiabatic expansion, so leading to an almost constant pickup ion temperature and pressure in the outer heliosphere all the way out to the TS (Isenberg, 1986). (iii) pickup ions constitute merely 15–20% of the total number density at 60AU and 20–25% at 100AU yet are the dominant outer heliospheric plasma pressure (excluding the solar wind ram pressure, of course). (iv) With the exception of Model 2a, the number density of pickup ions is sufficiently small that the Alfvén speed V_A is not greatly changed from the canonical MHD value. The associated deceleration of the solar wind speed does however reduce the Alfvén Mach number compared to the purely MHD models. (v) The addition of hot pickup ions to the outer heliosphere reduces the fast magnetosonic Mach number of the TS considerably, implying that the TS is significantly weakened by the inclusion of pickup ions. (vi) Finally, it is evident from Table XVI that the plasma beta is determined almost entirely by the pickup ion contribution. In the absence of pickup ions, the plasma beta β is negligibly small unless there is significant heating (Model 1b), in which case β is merely small.

A phenomenological classification of quasi-perpendicular shocks into laminar, quasi-laminar, turbulent and quasi-turbulent has been made by Greenstadt (1974), Formisano (1977) and Mellott (1985) (and references therein) based on observational studies of the terrestrial bow shock and interplanetary shocks. The classes are determined by the upstream plasma beta and the fast magnetosonic Mach number. In Figure 8.2, the Greenstadt/Formisano scheme is used to classify the TS models of Table XVI. (It should be noted that Figure 8.2 applies only to quasi-perpendicular shocks – a similar parametric classification scheme for quasi-parallel shocks does not exist.) All four of the pickup ion modified TS models fall into the

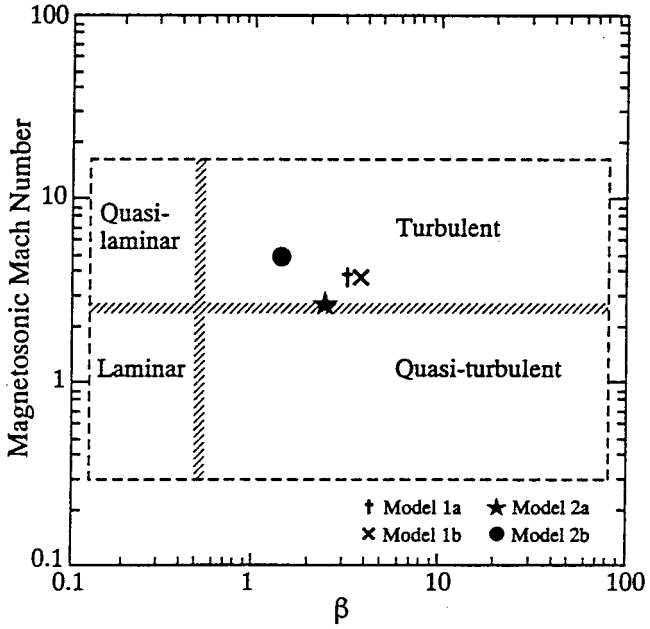

Figure 8.2. The classification scheme proposed by Greenstadt (1974) and Formisano (1977) which divides quasi-perpendicular shocks into four classes depending on the plasma β and magnetosonic Mach number (after Mellott, 1985). The classification of Models 1a,b and 2a,b within this scheme is illustrated by a † (Model 1a), a $\times$ (Model 1b), a $\star$ (2a) and a $\bullet$ (2b). The purely MHD models at 60 and 100 AU are not in the figure since they have $\beta \ll 0.1$ (Zank et al., 1996.)

turbulent regime. However, due to increasing heliocentric distance, the TS Model 2a is so weak that it borders the quasi-turbulent category. The much smaller pickup ion number density assumed for Model 2b ensures that the TS in this case is fully turbulent, like those of Models 1a and 1b. In principle, the dissipation necessary to form quasi-turbulent (and laminar) shocks derives from dispersive effects and/or anomalous resistivity. For shocks with Mach numbers greater than some critical Mach number ($\sim 2-3$), resistivity alone is insufficient to provide structure to the shock. Consequently, additional dissipative mechanisms are required to form the shock. Thus, Figure 8.2 suggests that the TS is likely to be supercritical, although perhaps only marginally. Note that if the pickup ion density were slightly larger or if the TS were located somewhat beyond 100 AU, the magnetosonic Mach number would be so reduced as to render the TS subcritical! Even for the much better studied terrestrial bow shock, it remains unclear which wave modes provide the anomalous viscosity at a subcritical shock – a situation which can only be rendered more uncertain by the presence of hot pickup ions.

Zank et al. (1996) assume that the termination shock is supercritical and quasi-perpendicular. It is shown that the narrowness of the cold solar wind distribution makes the reflection of solar wind ions at a weak TS very inefficient. Pickup H^+, on the other hand, is much more efficiently reflected and, using the parameters of

TABLE XVII

Specular reflection and pickup ion injection characteristics for the different TS models

	% reflected H^+	% overall efficiency (%)
Model 1a,b	22	3.5
Model 2a	30	6
Model 2b	29	1

Table XVI and the results of Section 7.2.1, we summarize the pickup ion injection efficiencies (percentage of reflected to incident pickup H^+) and the overall injection efficiency, i.e., the percentage of reflected to incident pickup plus solar wind protons, for each of the models (Table XVII). Under the assumption that the solar wind ion distribution is Maxwellian, injection efficiencies of $\ll 1\%$ for reflected solar wind protons are achieved.

Table XVII suggests that the perpendicular structure of the TS is determined largely by pickup ions. In all cases, a significant fraction of the incoming pickup ion population is reflected at the TS – a percentage that corresponds to a modest fraction of the total incident ion population. Furthermore, the percentage of reflected ions is probably sufficiently small that the TS remains stable (Leroy, 1983). Pickup ions may therefore provide the primary dissipation mechanism for a perpendicular TS with solar wind ions playing very much a secondary role. The length scale of the TS foot should also be determined by the gyroradii of the reflected pickup ions. Initially, reflected pickup ions will have gyroradii on the order of several $\times 10^4$ km. If one assumes that MRI acceleration can accelerate pickup ions up to MeV energies with gyroradii $\sim 10^{-2}$ AU, then the thickness of the foot should be on the order of several $\times 10^6$ km. The energy density of the reflected pickup ions will determine the strength of the precursor relative to the ramp and, given the flatness of the reflected pickup ion energy spectrum, this may well be substantial.

Simple estimates for the expected heating of the pickup ions and solar wind ions and electrons can be made (Zank et al., 1996). The bulk of the pickup ions are heated by shock drift acceleration for which the energy increase is given by (202) (this neglects the energization due to MRI acceleration). One can estimate the solar wind ion heating from either a simple cross shock potential calculation or from the appropriate Rankine-Hugoniot conditions. Empirically, the heating of electrons averages about 20% of the total temperature change implied by the Rankine-Hugoniot conditions (Schwartz et al., 1988) although this fraction can increase for lower values of the magnetosonic Mach number. Zank et al. (1996) also estimate the energy density of reflected pickup ions in the foot. The various estimates are collected together in Table XVIII.

TABLE XVIII

Derived structural properties of the TS models when MRI acceleration is taken into account. Here r_s refers to the shock compression ratio, L_f to the foot length scale, P_{foot} to the reflected pickup ion pressure in the foot, $T_{\text{SW}_2}^{\text{ion/electron}}$ to the downstream solar wind ion and electron temperatures, P_{foot}/P_1 to the ratio of foot to upstream pressures, and $T_{\text{PI}2}$ to the downstream pickup ion temperature for the shock drift accelerated component

	r_s	L_f (km)	P_{foot} (eV cm^{-3})	$T_{\text{SW}_2}^{\text{ion}}$ (K)	$T_{\text{SW}_2}^{\text{electron}}$ (K)	P_{foot}/P_1	T_{PI_2} (K)
Model 1a	3.2	$\geq 10^6$	1.3×10^{-1}	2.4×10^5	6.2×10^4	1.6	1.4×10^6
Model 1b	3.2	$\geq 10^6$	1.3×10^{-1}	2.4×10^6	5.9×10^5	1.6	1.4×10^6
Model 2a	2.7	$\geq 10^6$	7.6×10^{-2}	1.7×10^6	4.2×10^5	1.6	1.2×10^6
Model 2b	3.6	$\geq 10^6$	3.5×10^{-2}	2.1×10^6	5.3×10^5	1.4	2.8×10^6

TABLE XIX

The injection efficiencies (measured in percentages) of different pickup ion species for the four TS models

	H^+	He^+	C^+	N^+	O^+	Ar^+
Model 1a,b	22	10.7	6.2	5.8	5.4	3.4
Model 2a	30	14.5	8.4	7.7	7.2	4.6
Model 2b	29	14.4	8.3	7.65	7.2	4.55

Before discussing the simulations of Liewer et al. (1993), consider briefly the implications of the MRI acceleration mechanism for the relative abundance's of the ACR component. Zank et al. (1996) and Lee et al. (1996) suggest multiply reflected pickup ions might form the ACR injection component (i.e., they assume that the reflected particles are injected into a second-stage acceleration process from which the ACR component is then produced). Using their models 1 and 2, Zank et al. (1996) calculate the fraction of the solar wind pickup ion population that can become ACRs. The mass/charge ratio implicit in (203) differentiates the injection efficiencies of the various species according to mass, as is illustrated in Table XIX for H^+, He^+, C^+, N^+, O^+ and Ar^+ in each of the four TS models.

The simple results collected here suggest that a primary dissipation mechanism at the perpendicular termination shock or subshock (see below) is the reflection and subsequent MRI energization of pickup ions.

8.1.2. *Termination Shock Structure: Simulations*

Liewer et al. (1993) simulate the structure of the termination shock in the presence of a pickup ion shell distribution. Subsequent simulations by Liewer et al. (1995),

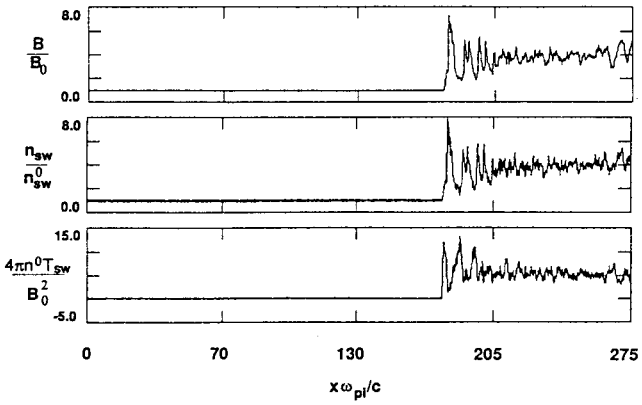

Figure 8.3. Simulation results for a $M_{\rm A} = 8$ quasi-perpendicular shock with no pickup ions. The total magnetic field magnitude, solar wind density ($n_{\rm SW}$), and solar wind ion temperature $T_{\rm SW}$ (normalized to upstream values) as a function of $x\omega_{pi}/c$ (ω_{pi} the ion plasma frequency) (Liewer et al., 1993.)

Kucharek and Scholer (1995), and Giacalone and Jokipii (1996a, b) concentrate on the issue of ion injection and acceleration. Liewer et al. (1993) modified a standard 1D hybrid plasma particle simulation code with particle ions and massless fluid electrons by including a second (pickup) ion species. The pickup ions were initialized with a spherical shell distribution in velocity space. Three cases were considered : (i) no pickup ions; (ii) 10% of the ions are pickup H^+, and (iii) 20% are pickup ions.

Consider first a simulation without pickup ions. For this simulation, the Alfvén Mach number $M_{\rm A} = 8$ and the shock is strong ($M_f \simeq 6.1$). The plasma variables are illustrated in Figure 8.3. The magnetic field and density experience a jump with compression ratio $r_s \sim 4$. A foot can be discerned in the magnetic field profile of Figure 8.3, which is due to the reflection of solar wind ions. The solar wind ions experience significant heating, thanks to the strong shock.

With the inclusion of a 10% pickup ion population, the magnetosonic Mach number $M_f \simeq 3$ although $M_{\rm A} = 8$. The results of the simulation are displayed in Figure 8.4. The density and magnetic field jump at the shock are appreciably smaller than their no pickup ion counterparts and the pickup ion temperature increase across the shock is essentially adiabatic. The thickness of the ramp, a consequence of the assumed phenomenological resistivity, is too broad to allow MRI acceleration. The magnetic and density profile of Figure 8.4 shows the presence of a foot whose length scales with the pickup ion gyroradius. Some solar wind ion reflection occurs too, introducing a small bump on the foot.

Figure 8.5 compares the magnetic foot and ramp on a finer scale for the three simulations. The extended foot due to pickup ion reflection at the electrostatic shock potential is clearly visible, as is the second small bulge that is produced by solar wind ion reflection in the 10% pickup ion case. The apparent absence of

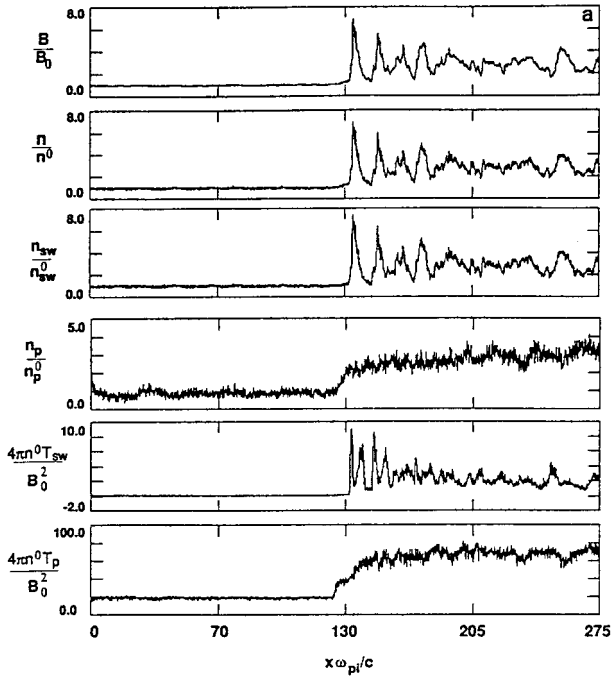

Figure 8.4. Simulation results for a quasi-perpendicular shock with 10% pickup hydrogen. $\theta_{BN} = 80°$ and $M_A = 8$. The total magnetic field magnitude, the total number density, solar wind density (n_{SW}), pickup ion (n_p) and solar wind T_{SW} and pickup (T_p) ion temperatures (normalized to upstream values) as a function of $x\omega_{pi}/c$ (ω_{pi} the ion plasma frequency). Note the presence of the foot ahead of the main shock ramp caused by backstreaming pickup ions (Liewer et al., 1993.)

reflected solar wind ions in the third case (20% pickup ion population) is most likely a consequence of the very low Mach number of the shock ($M_f \simeq 2.6$).

Liewer et al. (1993, 1995) and Kucharek and Scholer (1995) discuss the structure of an oblique TS. For $\theta_{BN} = 50°$, $M_A = 8$, but now with no resistivity, a 'no pickup ion' case is simulated (Figure 8.6). A characteristic broad shock transition is seen. By contrast, a simulation with a 10% pickup ion population is shown in Figure 8.7. A noticeable fraction of the incident pickup ion population is reflected and these ions stream away from the shock. Solar wind ions experience little reflection. A large-amplitude compressive magnetosonic wave, excited by the streaming pickup ions (Liewer et al., 1993; Barnes, 1970), propagates upstream. Such large-amplitude waves steepen as they convect into the shock, possibly forming 'shocklets', as well as scattering streaming pickup ions. This may have implications for the injection and energization of pickup ions at the TS but this has yet to be explored.

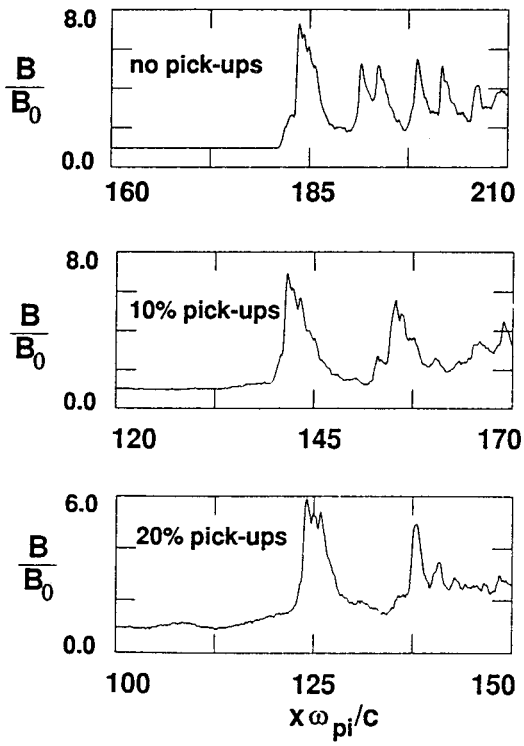

Figure 8.5. A comparison of the magnetic ramps for three cases, no pickup ions, 10% pickup hydrogen, and 20% pickup hydrogen (Liewer et al., 1993.)

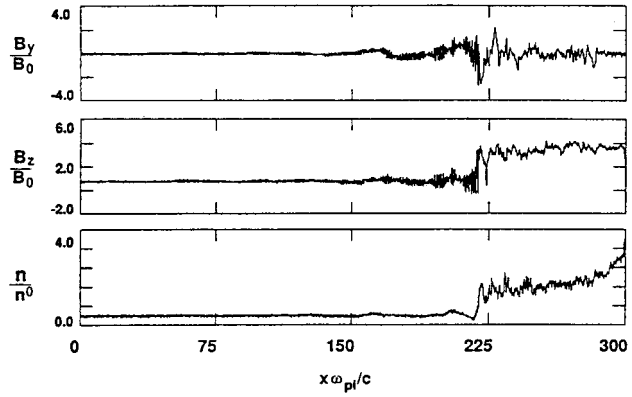

Figure 8.6. Simulation results for an oblique shock ($\theta_{\mathrm{BN}} = 50°$) in the absence of pickup ions. Plotted as a function of x are the transverse magnetic field components B_y and B_z and the solar wind density. No large amplitude magnetosonic wave appears ahead of the shock (Liewer et al., 1993.)

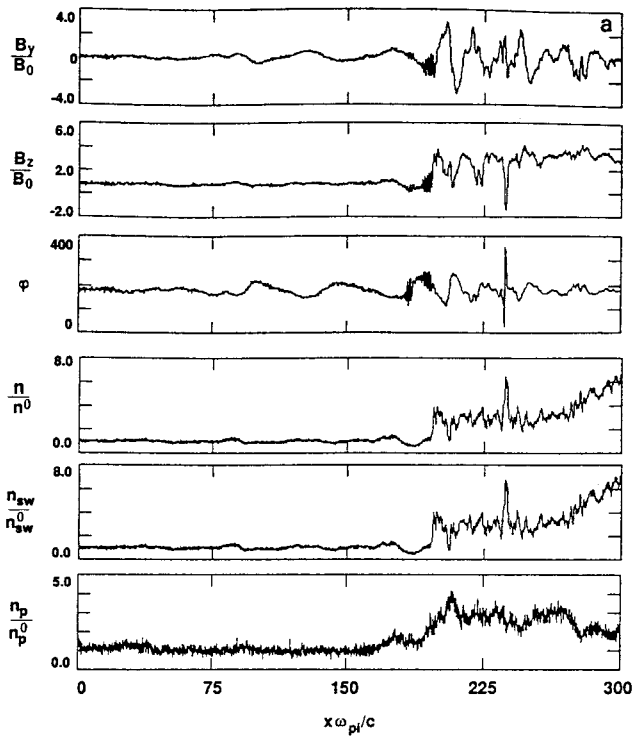

Figure 8.7. Simulation results for an oblique shock ($\theta_{BN} = 50°$) with 10% pickup hydrogen and $M_A = 5$. Plotted as a function of x are the transverse magnetic field components B_y and B_z, the phase angle ϕ between B_y and B_z (in degrees), and the total, solar wind and pickup ion number densities, all in normalized units. A compressional magnetosonic wave, excited by reflected pickup ions, is apparent ahead of the shock (Liewer et al., 1993.)

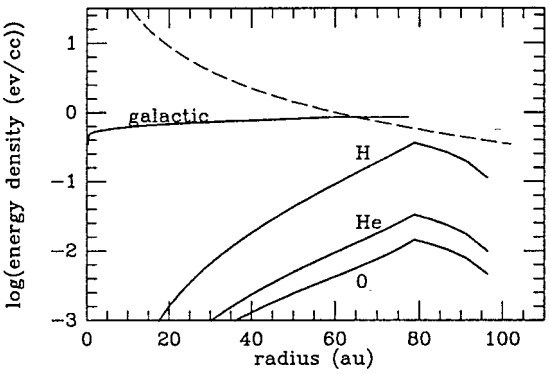

Figure 8.8. The solid lines show the computed energy density computed from the observed spectra shown in Figure 7.1 as a function of heliocentric distance. The dashed line corresponds to the solar wind energy density, using standard parameters (Jokipii, 1989.)

8.2. Effects of cosmic-rays on the termination shock

Consider now the role of anomalous and galactic cosmic-rays scattered by *in situ* and self-generated magnetic fluctuations. Such a scattering environment ensures that the cosmic-rays convect with the super-Alfvénic solar wind, with which they exchange momentum via the MHD turbulence intermediary. The pressure of cosmic-rays in the solar wind adds a non-thermal pressure contribution to the dynamics of the solar wind. The energy density of the ACR component is surprisingly large and increases with radius. By evaluating moments of a modulation solution to the cosmic-ray transport equation (168), Jokipii (1989) obtained the radial energy density profiles of anomalous H, He, O and galactic cosmic-rays illustrated in Figure 8.8. The solar wind proton energy density is plotted too. The solar wind calculation neglects the effects of pickup ions, which will dominate. Nonetheless, the ACR component can be expected to be important in the outer heliosphere, especially in view of the steep gradients expected in the vicinity of the TS. With the additional energization of anomalous cosmic-rays at the termination shock, ACRs represent a primary dissipation mechanism that can act to determine termination shock structure on scales larger than those of pickup ion gyroradii.

Early studies which included a dynamical cosmic-ray component focussed primarily on the deceleration of the solar wind by the galactic cosmic-ray pressure gradient [see, for example, Axford, 1965; Axford and Newman, 1965; Sousk and Lenchek, 1969; Babayan and Dorman, 1977). The models did not include the adiabatic exchange of energy between cosmic-rays and solar wind, which therefore precluded a study of the mediated termination shock itself. Lee and Axford (1988), Ko and Webb (1987), and Ko et al. (1988) used the full cosmic-ray pressure equation in spherical geometry to study both the deceleration of the solar wind and the structure of the termination shock. Lee and Axford (1988) assumed that the solar wind was cold, unlike Ko and Webb (1987), but the latter authors included a solar gravitational term which complicated the analysis unduly. The studies of Lee and Axford (1988), Ko and Webb (1987), and Ko et al. (1988) all demonstrated that galactic cosmic-rays could decelerate the solar wind marginally, causing the TS to move inward slightly, and that the termination shock was mediated by cosmic-rays. These basic cosmic-ray models have since been refined and extended considerably, and we shall review these more recent models in some detail below.

8.2.1. *The Basic Equations*

Before turning to specific models of a termination shock mediated by cosmic rays, we describe briefly the underlying non-linear models which couple the solar wind flow and cosmic-rays. Of particular importance is the method by which particle injection is introduced. Proper injection models must depend ultimately on the specific form of the distribution function. As a step in that direction, Zank et al. (1993) suggested a ‘thermal leakage’ type of injection model, a model which has

since been extended by several authors (Kang and Jones, 1995; Chalov and Fahr, 1994; Ko et al., 1997).

Within the two-fluid model, injection can be introduced consistently by assuming that all particles are described by a single distribution function $f_{\text{total}}(\mathbf{x}, t, p)$ (e.g., pickup ions and ACRs) and regarding only those particles with momenta $p > p_0$ as energetic. The transport of the energetic particles is assumed to be described adequately by the cosmic-ray transport equation (168). Such energetic particles represent those found in the tails of the overall distribution function, while the background thermal gas is assumed to comprise those cooler particles found in the core of the distribution. To obtain a closed 'hydrodynamic' system, it is necessary to take moments of the transport equation for the energetic particles, integrating over momentum from the lower to the upper bound. Such an integrated cosmic-ray energy density equation was written down first by Eichler (1979, 1984), although his analysis was concerned primarily with particle escape and its consequent dynamical implications for the shock and the particle distribution function. We consider only injection here. With the inclusion of a lower momentum boundary at p_0, the cosmic-ray energy density equation acquires an injection term proportional to the gradient of the flow velocity. In a nonuniform decelerating flow, this merely expressed the fact that the incoming fluid is compressed, and consequently a fraction of the particles in the cool thermal core are energized sufficiently to cross the lower momentum boundary and thus become 'energetic particles.' Obviously, the steeper the flow velocity gradient, the stronger the compression and hence the greater the injection rate. Thus, injection is of particular importance at subshocks.

As usual in the two-fluid formulation, energetic particles (ACRs or GCRs) are described in terms of a pressure p_c and energy density E_c, both of which are related via a specific heat ratio γ_c. The energetic particles are assumed to have negligible mass density. This explicit assumption implies that one cannot model the injection of, e.g., energetic pickup ions into the ACR component by using a number density based model, at least within the context of the standard two-fluid model (e.g., Chalov and Fahr, 1994).

Energetic particles embedded in a fluid with comoving scattering centers satisfy the transport equation (168), repeated here for convenience

$$\frac{\partial f}{\partial t} + \mathbf{u} \cdot \nabla f - \nabla (\kappa \cdot \nabla f) = \frac{1}{3} \nabla \cdot \mathbf{u} p \frac{\partial f}{\partial p} , \tag{211}$$

provided that the energetic particle distribution function remains nearly isotropic. The transport equation can be written in conservation form using the particle streaming flux **S**,

$$\mathbf{S} = -\kappa \cdot \nabla f - \mathbf{u} \frac{p}{3} \frac{\partial f}{\partial p} . \tag{212}$$

There are two important points to note about Equation (211). The first concerns the absence of the momentum diffusion term (the 'second-order Fermi' term).

Although this term is typically neglected in two-fluid and shock acceleration calculations, it is potentially important for highly turbulent shocks possessing extremely tangled fluctuating magnetic fields. In a two-fluid formulation, the momentum diffusion term in the transport equation will assume the form of a pressure source term. The second point concerns the absence of a 'source term' in Equation (211) – such a source term is generally included in studies which involve particle injection (Falle and Giddings, 1987; Kang and Jones, 1990). The reason for excluding such a source term is essentially that described above. Like Eichler (1979, 1984), Ellison and Eichler, 1984; Jones and Ellison (1991), Zank et al. (1993) assume that in principle no particular distinction exists between the thermal (e.g., pickup ions) and non-thermal (ACRs) particle populations, and that all particles are described by a single distribution function, however complicated. Zank et al. (1993) do not consider the full distribution function but instead separate the particles into a high energy bin (those having momenta $p > p_0$) and a low energy bin ($p < p_0$). Particles are allowed to migrate from one bin to the other. It is assumed for simplicity that the high energy particles propagate diffusively in the sense described by the transport equation (211). It is clear that in this model, no distinct source term is allowed in Equation (211) unless ACRs are created spontaneously. Instead, a 'source term' will enter through an integrated form of Equation (211) and will represent a measure of the particle flux across the momentum boundary p_0.

If we introduce the standard definitions

$$E_c = 4\pi \int_{p0}^{\infty} Ep^2 f \, \mathrm{d}p, \qquad p_c = \frac{4\pi}{3} \int_{p0}^{\infty} vp^3 f \, \mathrm{d}p \, , \tag{213}$$

for the cosmic-ray energy density and pressure, respectively, ($v \equiv$ particle velocity, $E \equiv$ particle energy), then multiplying Equation (211) by energy and integrating with respect to $p^2 \, \mathrm{d}p$ yields the hydrodynamical form of the cosmic-ray transport equation or cosmic-ray energy equation

$$\frac{\partial E_c}{\partial t} + \nabla \cdot (\mathbf{u} E_c) + p_c \nabla \cdot \mathbf{u} - \nabla \cdot (\bar{\kappa} \cdot \nabla E_c) = -\alpha \nabla \cdot \mathbf{u} \, , \tag{214}$$

where $\bar{\kappa}$ is an averaged hydrodynamical form of the spatial diffusion tensor [e.g., *Drury*, 1983]. The term α is the injected 'energetic particle pressure' crossing the lower momentum boundary, and is defined as

$$\alpha = \frac{4\pi}{3} E(p_0) p_0^3 f(p_0). \tag{215}$$

The source term $\alpha \nabla \cdot \mathbf{u}$ represents a growth term for the cosmic ray energy density in a decelerating flow. Thus, particle injection via thermal leakage is regulated by the large-scale fluid flow. Although α is prescribed in terms of a lower momentum boundary p_0, there is no reason to assume that α should be constant. Zank et al. (1993) suppose that away from a subshock, however, $\alpha = constant$. At a subshock, they allow α to change discontinuously. Ko (1995), Ko et al. (1997), and

Chalov and Fahr (1994) suggest that $\alpha = \eta_1 + \eta_2 p_g$ might be an alternative choice, especially since it is analytically tractable.

To derive a closed system of equations, one needs to relate the cosmic-ray energy density E_c to the cosmic-ray pressure p_c. As is usual in two-fluid models, an energetic particle adiabatic index γ_c is introduced such that

$$E_c = \frac{p_c}{\gamma_c - 1} , \tag{216}$$

where $\frac{4}{3} \leq \gamma_c \leq \frac{5}{3}$, the two limits being those appropriate to fully relativistic and non-relativistic energetic particles respectively. Strictly speaking, since one injects from a non-relativistic thermal pool, γ_c should be less than $\frac{4}{3}$. Indeed, Axford et al. (1982), and especially Achterberg et al. (1984), have noted and discussed the rather sensitive dependence of shock solutions on γ_c. Unfortunately, a completely consistent treatment can come only at the transport equation level, and two-fluid models use a prescribed and constant γ_c.

From Equations (216) and (214), we obtain

$$\frac{\partial p_c}{\partial t} + \mathbf{u} \cdot \nabla p_c + \gamma_c p_c \nabla \cdot \mathbf{u} - \nabla \cdot (\kappa \cdot \nabla p_c) = -\alpha(\gamma_c - 1)\nabla \cdot \mathbf{u} , \tag{217}$$

for the energetic particle pressure. The remaining equations are the continuity equation

$$\frac{\partial \rho}{\partial t} + \nabla \cdot (\rho \mathbf{u}) = 0 , \tag{218}$$

the total momentum equation

$$\rho \left(\frac{\partial \mathbf{u}}{\partial t} + \mathbf{u} \cdot \mathbf{u} \right) + \nabla p_g + \nabla p_c = 0 , \tag{219}$$

and the total energy equation for the system,

$$\begin{aligned} &\frac{\partial}{\partial t}(E_g + E_c + \tfrac{1}{2}\rho u^2) \\ &+\nabla \cdot [\mathbf{u}(E_g + \tfrac{1}{2}\rho u^2 + p_g) + \mathbf{u}(E_c + p_c) - \kappa \cdot \nabla E_c] = 0 , \end{aligned} \tag{220}$$

where ρ is the mass density of the thermal plasma only, p_g the thermal gas pressure and $E_g = p_g/(\gamma_g - 1)$.

For smooth flows, the total energy equation can be reduced to

$$\frac{\partial p_g}{\partial t} + \mathbf{u} \cdot \nabla p_g + \gamma_g p_g \nabla \cdot \mathbf{u} = \alpha(\gamma_g - 1)\nabla \cdot \mathbf{u} , \tag{221}$$

which is often simpler to use. Equation (221) yields the thermal gas equation of state

$$p_g = A\rho^{\gamma_g} + \frac{\gamma_g - 1}{\gamma_g}\alpha , \tag{222}$$

where A is a constant of integration. The important implication of equation (222) is that the gas sound speed of the system is reduced when $\alpha \neq 0$, since

$$\left(\frac{\partial p_g}{\partial \rho}\right)_S = \frac{\gamma_g p_g}{\rho}\left(1 - \frac{\gamma_g - 1}{\gamma_g}\frac{\alpha}{p_g}\right) \equiv C_s^2, \tag{223}$$

at constant entropy S. Conversely, if $\alpha = C\rho^{\gamma_g}$, then (Chalov and Fahr, 1994; Ko et al., 1997)

$$p_g = A\rho^{\gamma_g'}, \qquad \gamma_g' \equiv \gamma_g - C(\gamma_g - 1)\ . \tag{224}$$

Equations (218)–(220) form the basic hydrodynamic equations for two-fluid cosmic-ray hydrodynamics. To close the hydrodynamic equations, one has to use either the transport equation (211) directly and take moments of the calculated distribution function to compute E_c and p_c, or one can use the hydrodynamic version of the transport equation (217). The two-fluid equations are easily generalized to include the presence of a magnetic field.

The two-fluid cosmic-ray equations can be used to study both the solar wind response to cosmic-ray pressure gradients as well as the non-linear structure of the termination shock. The diffusion term $\nabla(\kappa\nabla f)$ introduces a diffusive length scale over which particle acceleration at a shock acts to smoothly decelerate the incident supersonic flow. However, Fermi acceleration need not lead to completely smoothed shocks (Drury and Völk, 1981; Axford et al., 1982) and a subshock is often present.

To determine the jump conditions at the subshock, it is assumed that the energetic particle momentum and energy fluxes are continuous across the very thin gas shock (Section 7.1.2). This is reasonable, at least to this order, because the cosmic-rays possess a diffusion coefficient significantly larger than that corresponding to any length scale appropriate to the thermal gas. The nature of the two-fluid model indicates that some care must be exercised when deriving the jump conditions for the cosmic-rays. In particular, the cosmic-ray mass flux is assumed negligible and cosmic-rays contribute only to the overall energy density. On taking moments of the energetic particle streaming flux **S** (212) between the same limits as used in deriving the cosmic-ray energy equation (214), one obtains the normal (1D) energetic particle jump conditions as

$$[p_c] = 0\ , \qquad [F_c] \equiv \left[\frac{\gamma_c}{\gamma_c - 1}up_c - \frac{\bar{\kappa}}{\gamma_c - 1}\frac{\mathrm{d}p_c}{\mathrm{d}x} + \alpha u\right] = 0\ . \tag{225}$$

Equation (225) can therefore be written as

$$\left[\frac{\gamma_c}{\gamma_c - 1}up_c - \frac{\bar{\kappa}}{\gamma_c - 1}\frac{\mathrm{d}p_c}{\mathrm{d}x}\right] = -[\alpha u]\ , \tag{226}$$

which demonstrates that the injection source term across the shock is proportional to the weighted difference in the upstream and downstream flow velocities (which is therefore related obviously to the shock compression ratio). As discussed above,

α is unlikely to be constant, particularly at a (sub)shock where the heating of the inflowing gas must result in a significant change to f_c. Thus, an enhanced energy flux across the lower momentum boundary into the cosmic-ray gas can be anticipated as a consequence of the nonadiabatic heating of the thermal gas at a subshock. It follows then that, if the subscripts a and b designate ahead of and behind the shock, we must have $\alpha_b > \alpha_a$ and

$$[\alpha u] = \alpha_a u_a - \alpha_b u_b \ .$$

In view of (225) and (226), the normal (1D) Rankine–Hugoniot conditions appropriate to the gas subshock take the form

$$[\rho u] = 0 \ , \tag{227}$$

$$\left[\rho u^2 + p_g\right] = 0 \ , \tag{228}$$

$$\left[\rho u \left(\frac{1}{2}u^2 + \frac{\gamma_g}{\gamma_g - 1}\frac{p_g}{\rho}\right)\right] = [\alpha u] \ . \tag{229}$$

The basic 'thermal leakage' model above was used by Zank et al. to investigate shock structure, extending earlier studies by Drury and Völk (1981) and Axford et al. (1982).

Before concluding this subsection, we stress again that the two-fluid model (and variations thereof) assumes at a fundamental level that the energetic particles (cosmic-rays) are massless. To include a cosmic-ray source term in the continuity equation violates the basic conservation laws of the hydrodynamic system and leads to unphysical results. If injection is to be addressed at the level of mass flux rather than energy flux, as is done above, then the two-fluid model needs to be revised to incorporate cosmic-rays with mass. Such a study was initiated by Zank et al. (1993, 1994) and Story and Zank (1996) in the context of cometary shocks where the massive water group ions dictate the need for such an approach. This approach can be used to relate pickup ions and ACRs but has yet to be pursued in any detail (see Zank et al., 1995 for the rudimentary basis of the model). The resulting model differs in important ways from the standard two-fluid massless cosmic-ray model.

8.2.2. *Termination Shock Structure: Two-Fluid Models*

Donohue and Zank (1993) used the basic two-fluid model of Section 8.2.1 to investigate the steady and dynamical structure of the termination shock in the presence of cosmic-rays. This in many respects is a direct extension of the simpler model used by Lee and Axford (1988) to investigate termination shock structure. The model of Donohue and Zank (1993) does not distinguish between the ACR flux and the GCR flux and a single relativistic value of γ_c is assigned. The ACR and GCR species are therefore assumed to satisfy the single hydrodynamic transport equation (217), even though, strictly speaking, the ACRs are not relativistic. Unlike Lee and

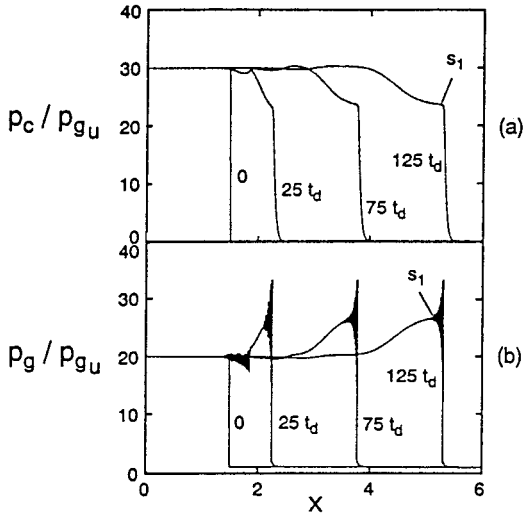

Figure 8.9. Time dependent evolution of the (a) cosmic ray and (b) thermal gas pressures from the initial condition to the steady-state S_1. The time intervals are expressed as diffusion time units $t_d = \kappa / V_{sh}^2$. Both pressures are normalized to the upstream gas pressure (the preshocked solar wind). The spatial scaling is arbitrary. The shock overshoot and oscillations are unphysical and due to numerical instability (Donohue and Zank, 1993.)

Axford (1988), Donohue and Zank (1993) consider only the structure of the TS, neglecting spherical symmetry and the expansion of the solar wind. Donohue and Zank (1993) do not, however, assume that the solar wind is cold.

Here we follow Donohue and Zank (1993) and examine the steady state structure of a solar wind termination shock under the assumption that the wind is decelerated at the shock by interstellar cosmic-ray pressure. Drury and Völk (1981) and Axford et al. (1982) found that the nonlinear two-fluid equations admit three possible downstream solutions for a shock. For the downstream cosmic-ray (thermal gas) pressure p_{cd} (p_{gd}), these correspond to (1) the gas dynamic limit ($p_{cd} = 0$), which we may call S_0; (2) comparable downstream gas and cosmic-ray pressures ($p_{cd} \simeq p_{gd}$), or S_1, and (3) dominant gas pressure ($p_{gd} > p_{cd}$), or S_2. Under certain circumstances, the solution S_1 may also approach a cosmic-ray dominated state with $p_{cd} > p_{gd}$, as discussed below. Donohue and Zank (1993) examine the structure and stability of these solutions using a time-dependent computational model.

Consider first the evolution of the two-fluid equations (217)–(220) to a steady shock solution in the absence of injection i.e., $\alpha = 0$. Figure 8.9 shows the time evolution of the cosmic-ray (a) and thermal gas (b) pressures for a shock which settles to the solution S_1. Initially, the downstream cosmic-ray pressure exceeds the gas pressure. When the system reaches steady state, the two are approximately equal. Note that in the downstream region, the sum of the two pressures is approximately conserved as the shock evolves in time. This results from momentum

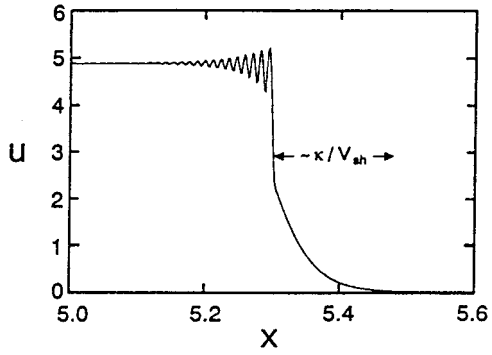

Figure 8.10. Detail of the steady-state velocity transition to S_1 for the simulation of Figure 8.9 in the Lagrangian frame i.e., the upstream velocity is zero and the shock moves supersonically (from left to right) into the unshocked upstream gas. The foreshock, with length scale κ / V_{sh} is clearly visible, as is the subshock. The downstream oscillations are unphysical (Donohue and Zank, 1993.)

conservation since the downstream momentum flux is dominated by the pressure terms for a strong shock. Figure 8.9 also illustrates the smoothing effect of the cosmic-ray pressure on the initially sharp shock transition. In the steady state structure, the momentum exchange between the thermal fluid and cosmic rays leads to the formation of a diffusive precursor upstream of the shock. The velocity precursor is shown in expanded detail in Figure 8.10. The width of the precursor corresponds to the diffusion scale of the cosmic-rays, κ / V_{sh}. The thermal gas is decelerated in the precursor by a cosmic-ray pressure gradient, and subsequently undergoes a subshock transition to the final downstream state. This structure is the most fundamental result of the cosmic-ray mediated shock model and is likely to be of considerable importance in any TS encounter. The two-fluid model predicts a cosmic-ray dominated ($p_{cd} > p_{gd}$) state for higher shock Mach numbers, and in such a case, the large cosmic-ray pressure gradient completely smooths the flow, and a subshock is absent (Drury and Völk. 1981; Axford et al., 1982; Lee and Axford, 1988). Hence there exists the possibility that no sharp discontinuity will be observed at the termination boundary.

Figure 8.11 shows a second simulation (Donohue and Zank, 1993) in which the initial cosmic-ray pressure (p_{cd}) is less than the equilibrium pressure S_1 corresponding to Figure 8.9. As the simulation progresses, the system first attempts to converge to the intermediate or gas-dominated solution S_2. The intermediate solution is an unstable equilibrium (Donohue et al., 1994), and the system subsequently converges to S_1, but on a considerably longer timescale. The primary effect of the intermediate solution is to extend the convergence time for shocks which begin near a gas dynamic state. This result may well be relevant to the evolution of the termination shock if some external process induces the shock to change continually from a cosmic-ray mediated to a gas dynamic state. This is discussed in Section 9. Figures 8.9 and 8.11 illustrate that if the termination shock has a hydrodynamic Mach number of 6.0 or greater, then cosmic-rays should play a significant role

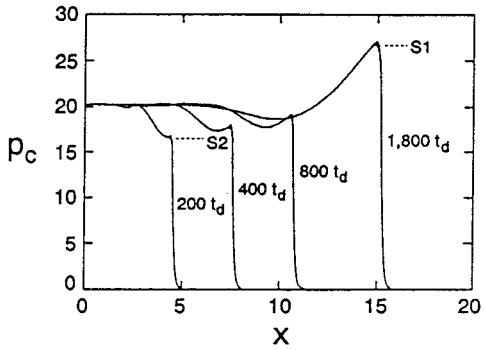

Figure 8.11. Time dependent evolution of the cosmic ray pressure from an initial state below the equilibrium solution S_1. The shock first converges to the unstable solution S_2. Note that the timescale for convergence to S_1 is much greater than that illustrated in Figure 8.9 (Donohue and Zank, 1993.)

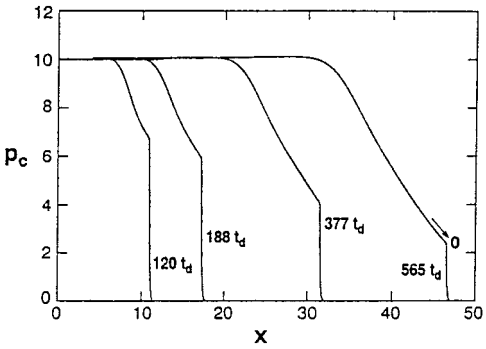

Figure 8.12. Time dependent evolution of the cosmic ray pressure from an initial state well below the unstable solution S_2. The shock converges towards the gas dynamic limit ($p_c = 0$) on a very long timescale (Donohue and Zank, 1993.)

in determining the structure and dynamics of the shock. As a result, cosmic-rays cannot be regarded as a minor component.

An interesting question concerning the time evolution of the shock is whether the purely gas dynamic limit ($p_{cd} = 0$) can be reached by beginning with a small nonzero cosmic-ray pressure downstream. Figure 8.12 (Donohue and Zank, 1993) show that, beginning with an initial p_{cd}, the system can indeed converge towards the gas dynamic limit, although exceedingly slowly. While some fraction of the cosmic-ray pressure is convected downstream, the shock continues to trap and accelerate both the remaining cosmic-rays and the upstream diffusive flux. This balance between convection, diffusion, and acceleration is insufficient to maintain a small equilibrium cosmic-ray pressure. However, the time scale for the removal of cosmic-rays from the shock is far longer than that in progressing from a gas dynamic state to a cosmic-ray dominated shock in the presence of particle injection. Consequently, the TS is unlikely to ever be found in a purely gas dynamic state.

Finally, Donohue and Zank (1993) show that the acceleration of the anomalous cosmic-ray component may also affect the steady state structure of the shock. The acceleration is modelled using the thermal leakage mechanism of Section 8.2.1. Physically, since particle injection provides a new source of energetic particles, besides the diffusive component, the equivalent Mach number is able to maintain a higher downstream cosmic-ray pressure p_c in the steady state. This is confirmed by the simulation shown in Figure 8.13, which uses the same initial configuration as used in Figure 8.9 but now with particle injection. Comparing the downstream cosmic-ray and thermal gas pressures from Figures 8.9 and and 8.13 reveals an increase in the fractional pressure contributed by cosmic-rays. The partial pressure of the injected or ACR component may therefore be quite significant at the shock, although this result depends on the choice of the injection parameter α. Since total pressure must still be approximately conserved downstream, one also observes an additional injection driven decrease in p_{g_d}. Therefore, the Mach 6.0 shock with particle injection is even more strongly cosmic-ray dominated. Thus, Donohue and Zank (1993) argued that cosmic-rays must play an essential role in determining the structure and dynamics of the termination shock.

8.2.3. *Termination Shock Structure: Three-Fluid Model*

In an effort to identify more clearly the distinct role of ACRs and GCRs in determining the structure of the termination shock, Ziemkiewicz (1994), Ziemkiewicz and Banaszkiewicz (1996), and Banaszkiewicz and Ziemkiewicz (1997) introduced a three-fluid model comprising solar wind plasma, ACRs and GCRs. The latter two papers also included pickup ions in a one-fluid solar wind description. This approach is an important extension to that used by Lee and Axford (1988), Ko and Webb (1987, 1988), and Donohue and Zank (1993) in that ACRs are not treated as relativistic particles.

A steady state, 1D spherically symmetric MHD model is considered. The suitable generalization of the equations of Section 8.2.1 is

$$\nabla \cdot (\rho \mathbf{u}) = Q_\rho \ ,$$

$$\rho \mathbf{u} \cdot \nabla \mathbf{u} = -\nabla (p_S + p_{\mathrm{A}} + p_G) - \frac{1}{\mu} \mathbf{B} \times \nabla \times \mathbf{B} + \mathbf{Q}_M ; \tag{230}$$

$$\nabla \cdot \left[\rho \mathbf{u} \left(\frac{1}{2} u^2 + \frac{\gamma_S}{\gamma_S - 1} \frac{p_S}{\rho} \right) + \frac{1}{2\mu} u B^2 + \frac{\gamma_{\mathrm{A}}}{\gamma_{\mathrm{A}} - 1} u p_{\mathrm{A}} + \frac{\gamma_G}{\gamma_G - 1} u p_G \, \hat{\mathrm{u}} \right.$$
$$\left. - \frac{1}{\gamma_{\mathrm{A}} - 1} \kappa_{\mathrm{A}} \nabla p_{\mathrm{A}} - \frac{1}{\gamma_G - 1} \kappa_G \nabla p_G \right] = Q_E \ .$$

In (230), Q_ρ, Q_M, and Q_E denote pickup ion source terms (Section 4) for the supersonic and subsonic solar wind, $p_{S,A,G}$ the solar wind, anomalous, and galactic cosmic-ray pressures, and $\gamma_{S,A,G}$ the respective adiabatic indices ($\gamma_{S,A} = \frac{5}{3}$ and $\gamma_G = \frac{4}{3}$).

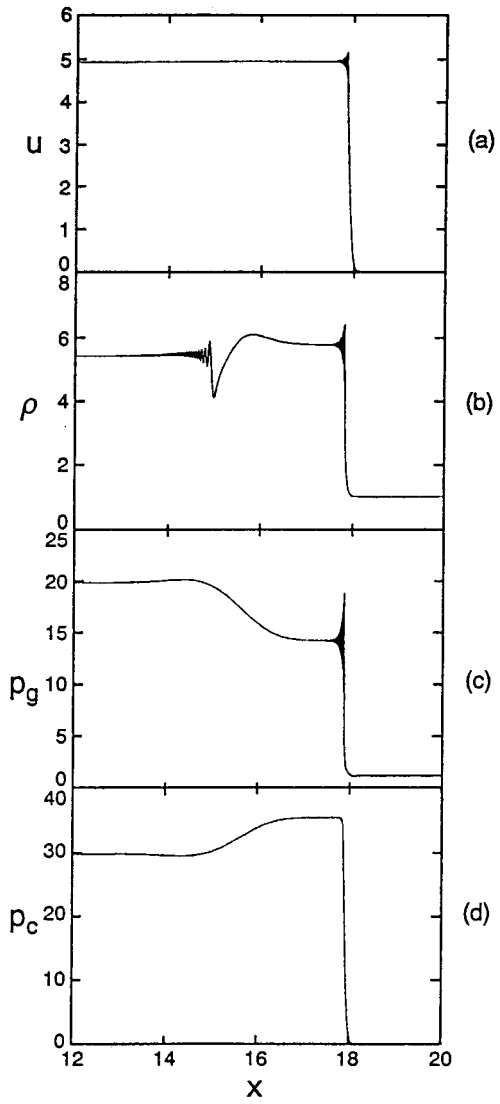

Figure 8.13. The equilibrium state for a termination shock model incorporating seed particle (anomalous cosmic ray) injection. (a) Gas velocity, (b) density, and (c) pressure, and (d) cosmic ray pressure (Donohue and Zank, 1993.)

The ACR component in this model is produced only at the subshock of the termination shock with an efficiency ε. Thus, the hydrodynamic steady state transport equation for both cosmic-ray populations is simply

$$\nabla \cdot \left(\frac{\gamma_{A,G}}{\gamma_{A,G} - 1} \mathbf{u} p_{A,G} - \frac{1}{\gamma_{A,G} - 1} \kappa_{A,G} \nabla p_{A,G} \right) = \mathbf{u} \cdot \nabla p_{A,G} \, . \tag{231}$$

TABLE XX

Plasma parameters at 1 AU used by Banaszkiewicz and Ziemkiewicz (1997). The pressures are measured in erg cm^{-3}

	n (cm^{-3})	u (km s^{-1})	p_S	p_G	p_A
Equator	8	400	4.4×10^{-11}	1.8×10^{-13}	1.8×10^{-17}
Polar	3.5	750	2.2×10^{-10}	1.8×10^{-13}	1.8×10^{-17}

If we denote the solar wind, magnetic, ACR, and GCR fluxes by $\mathbf{F}_S$, $\mathbf{F}_B$, $\mathbf{F}_A$, and $\mathbf{F}_G$ respectively, the 1D termination shock jump conditions can be expressed as the system of differential equations

$$[\rho u] = 0; \qquad \left[\rho u^2 + p_S + p_B + p_A + p_G\right] = 0 ,$$

$$\left[p_A\right] = 0; \qquad \left[p_G\right] = 0 , \tag{232}$$

$$[F_S + F_B] \equiv -[F_A] = \tfrac{1}{2}\varepsilon\rho_1 u_1^3; \qquad [F_G] = 0 .$$

Such an injection condition represents a fixed choice of α at the subshock and $\alpha = 0$ elsewhere. The subscript 1 denotes values upstream of the shock.

Ziemkiewicz and Banaszkiewicz (1996) and Banaszkiewicz and Ziemkiewicz (1997) do not use the galactic cosmic-ray and LISM thermal pressures as boundary conditions but instead assume a TS location and solve the coupled system of ordinary differential equations (230)–(232) as an initial value problem at 1 AU.

Banaszkiewicz and Ziemkiewicz (1997) investigate an exhaustive range of possible parameters and shock locations. We describe here two sets of results, one appropriate to the slow equatorial solar wind and the other to a polar solar wind. The assumed solar wind parameters at 1 AU are tabulated (Table XX).

The pickup ion production rates are calculated for two extreme cases, corresponding to either a solar minimum photoionization rate and a low density LISM ($\nu_{ph}^{\circ} = 9 \times 10^{-8}$ s^{-1}, $N = 6 \times 10^{-2}$ cm^{-3}) or a solar maximum photoionization rate and a high density LISM ($\nu_{ph}^{\circ} = 1.5 \times 10^{-7}$ s^{-1}, $N = 0.12$ cm^{-3}. For the equatorial wind, two distinct spatial diffusion coefficient models are considered: (i) $\kappa_G = 6\times10^{22}+0.1\times10^{20} r$ [AU] cm^2 s^{-1}, and (ii) $\kappa_G = 4\times10^{22}+0.5\times10^{20} r$ [AU] cm^2 s^{-1}, and $\kappa_A = 0.1\kappa_G$. For the polar wind, $\kappa_G = 10^{23}$ cm^2 s^{-1}, and $\kappa_A = 1.18 - 1.5 \times 10^{22}$ cm^2 s^{-1}.

The solutions obtained by Ziemkiewicz and Banaszkiewicz (1996) and Banaszkiewicz and Ziemkiewicz (1997) are parameterized by both the assumed shock location and the injection efficiency ε. By considering only those solutions which yield acceptable values of the GCR pressure downstream of the TS ($p_G \simeq 0.33$ eV cm^{-1}), a total pressure equal to the assumed LISM pressure ($\sim$ 1 eV cm^{-1}),

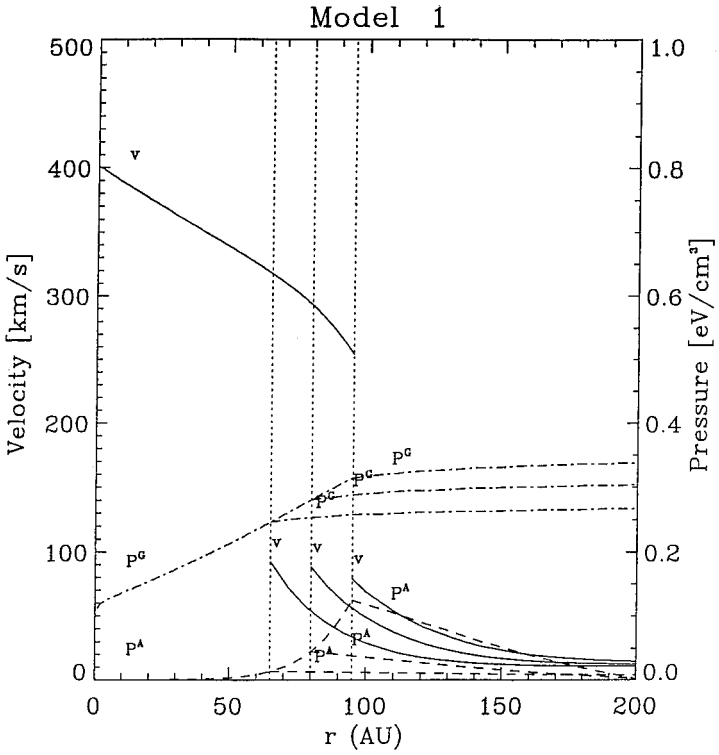

Figure 8.14. Velocity and gas and cosmic ray pressures as a function of radial distance. The vertical dotted lines identify three possible termination shock locations. The production efficiency ε is equal to 0, 0.01, and 0.06 for the shocks located at 65, 80 and 95 AU respectively. ε is chosen for each shock as a maximum possible value from the range (0,0.15) which yields a non-negative ACR pressure downstream (Banaszkiewicz and Ziemkiewicz, 1997.)

and a non-negative ACR pressure downstream, one can estimate values for ε. Banaszkiewicz and Ziemkiewicz (1997) find that for a shock located at 65 AU, the production rate for ACRs is less than 1%, increasing to $\sim$ 5% for $R_{\rm TS} = 80$ AU, and 15% for $R_{\rm TS} = 95$ AU.

To obtain solutions for the polar solar wind, Banaszkiewicz and Ziemkiewicz (1997) find that an increase in both the GCR and ACR diffusion coefficients was necessary to (1) maintain p_G^∞ within reasonable limits and (2) to prevent the occurrence of singular solutions in the model. The values for κ_G and $\kappa_{\rm A}$ cited above are probably as large as one can justify.

Illustrated in Figure 8.14 is a set of model solutions for an equatorial solar wind with three different TS locations. As usual, pickup ions decelerate the solar wind, with a modest contribution from the GCR and ACR pressure gradients. The shock compression ratio decreases with increasing shock distance, from $r_s = 3.5$ at $R_{\rm TS} = 65$ AU to 3.25 at $R_{\rm TS} = 95$ AU. The downstream galactic cosmic-ray pressure is almost constant downstream of the TS ($\sim$ 0.33 eV cm^{-3}). The solar

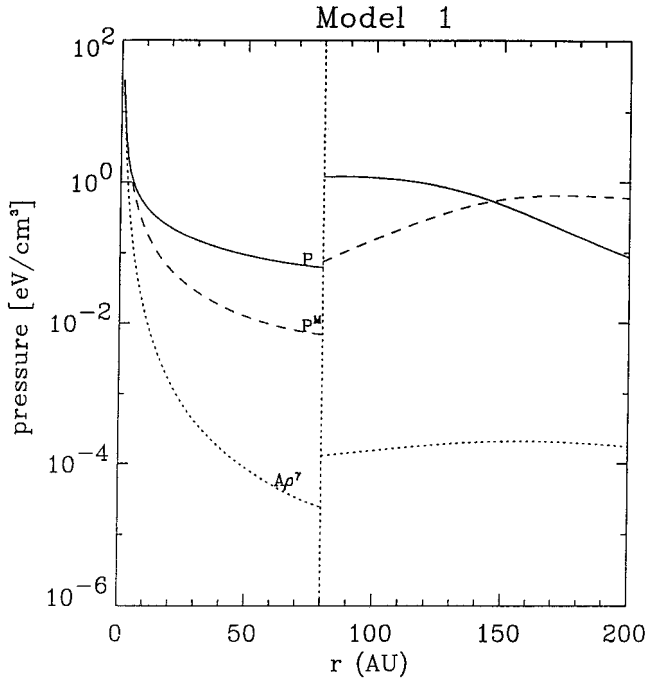

Figure 8.15. Gas pressure p and magnetic pressure p^M as a function of heliocentric distance for a TS located at 80 AU. The adiabatic pressure is shown for comparison (Banaszkiewicz and Ziemkiewicz, 1997.)

wind and magnetic pressure corresponding to the parameters of Figure 8.14 and a TS at 80 AU are shown in Figure 8.15. It is evident that the pickup ion pressure dominates that of the magnetic field in the upstream region and immediately downstream of the termination shock. The sum of the two pressures balances that of the LISM approximately. The Axford–Cranfill amplification of the magnetic field leads eventually to a plasma beta satisfying $\beta_p < 1$ in the heliosheath.

In choosing the termination shock location, Banaszkiewicz and Ziemkiewicz (1997) assume that the enhanced polar ram pressure (compared to that in the ecliptic) will place the shock in the interval 80–120 AU. The radial solar wind velocity and radial GCR and ACR pressures of the polar model are displayed in Figure 8.16. The polar models are sensitive to assumptions about the magnitude of κ_A, and downstream ACR pressures can differ by a factor of 5 for a 25% change in κ_A. The strong deceleration of the solar wind between 80 and 120 AU is a consequence of the large ACR pressure gradient. This leads to the possibility of a very weak TS for the more distant location, e.g., $r_s \simeq 1.7$ and $R_{TS} = 120$ AU. However, the entire region dominated by the ACR pressure, i.e., where the strong decrease in solar wind speed occurs, should be thought of as forming the precursor of a cosmic-ray mediated termination shock.

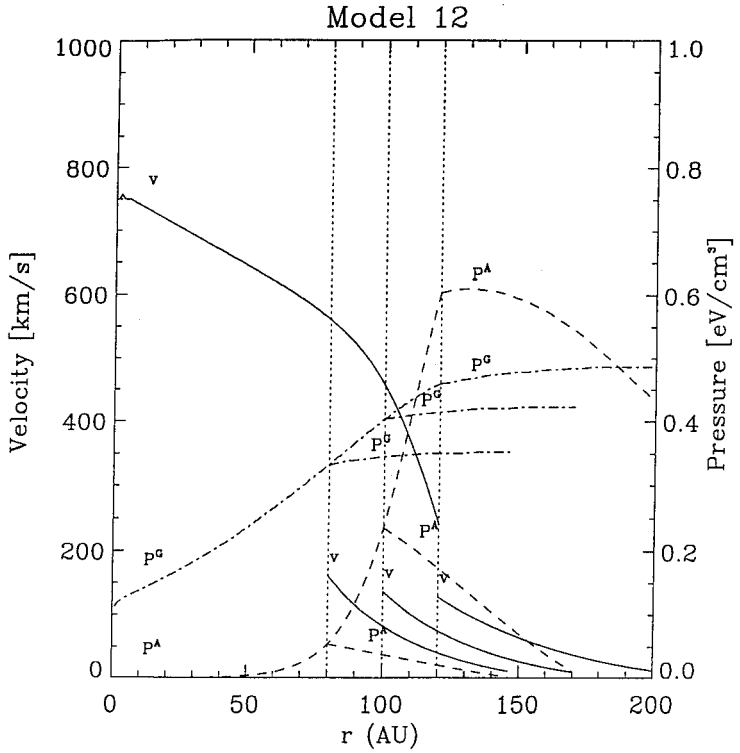

Figure 8.16. As with Figure 8.14 but now for ε values of 0, 0.07, and $\geq$ 0.15 (Banaszkiewicz and Ziemkiewicz, 1997.)

The results of Ziemkiewicz and Banaszkiewicz (1996) and Banaszkiewicz and Ziemkiewicz (1997) are interesting from several perspectives. It provides one of the more detailed analyses of the termination shock structure problem. However, it is unclear, for example, why the polar solar wind models should be so sensitive to assumptions about the diffusion coefficients. Such a sensitivity leads to ACR production rates which can vary widely and to ACR pressures which can be much smaller or larger than the GCR pressure. Thus, although Figures 8.14 and 8.16 indicate that for most TS locations, the GCR pressure is larger than the ACR pressure at the TS, it remains unclear which component provides the basic dissipation mechanism at the shock. Also, it is unclear whether the singular nature of the flow for smaller diffusion coefficients indicates that the flow is time dependent. Alternatively, it is possible that the radial form of the (hydrodynamic) diffusion coefficient needs revision. These, and other, intriguing issues raised by Banaszkiewicz and Ziemkiewicz (1997) suggest that we are far from a full understanding of the role that ACRs play in determining the dynamics of the outer solar wind and termination shock.

8.2.4. *Stability of the Termination Shock*

Although the analysis so far has focussed on the steady-state structure of the termination shock, it was recognized by Drury and Falle (1986) and Zank and McKenzie (1987) that the cosmic-ray mediated shock precursor could be driven unstable by backward propagating compressive waves with length scales shorter than that of the cosmic-ray diffusion length scale κ / V_{sh}. This work has been extended considerably in several directions (see Webb et al., 1997, 1998 and references therein).

Short-wavelength modes admitted by the two-fluid description (217)–(220) are decoupled from the cosmic-ray gas and propagate at the thermal sound speed (appropriately modified to include injection). In the presence of a large-scale energetic particle gradient (effectively the precursor of the energetic particle modified shock), the dynamical time scale associated with the short wavelength waves is much shorter than that associated with energetic particle diffusion, consequently $\kappa \nabla p_c$ is approximately constant as far as the short wavelength acoustic modes are concerned. Thus, the ∇p_c term in the total momentum equation (219) assumes the role of an effective 'gravity' in the stratified fluid (the shock) and introduces a local acceleration proportional to $(\kappa\rho)^{-1}$. Unless $(\kappa\rho)^{-1}$ is constant, small density fluctuations will induce velocity fluctuations which can amplify the original density fluctuations in a variety of ways. It transpires that a good analogy can be drawn between the stability properties of stratified fluids and those of energetic particle modified shocks (Zank et al., 1990).

For a one dimensional shock problem, the evolution of the wave action $\mathcal{A} \equiv \rho_0 u_1^2/\omega'$ (ρ_0 the background inhomogeneous density profile, u_1 the fluctuation about the inhomogeneous background velocity field and ω' the Doppler shifted frequency of the short wavelength acoustic mode) for the acoustic mode can be written as

$$\begin{aligned} \frac{\partial \mathcal{A}}{\partial t} + \frac{\partial}{\partial x}\left(\frac{\omega}{k}\mathcal{A}\right) &= -\mathcal{A}\left[\frac{C_c^2}{\kappa} \pm \frac{M_0^2 - 1}{M_0}\frac{\mathrm{d}u_0}{\mathrm{d}x}\right] = \\ &= -\mathcal{A}\left[\frac{C_c^2}{\kappa} \mp \frac{1}{\rho_0 C_s}\frac{\mathrm{d}p_{c0}}{\mathrm{d}x}\right]. \end{aligned} \tag{233}$$

The definitions $C_s^2 \equiv \gamma_g p_{g0}/\rho_0 \cdot \left[1 - (\gamma_g - 1)/\gamma_g \cdot \alpha/p_{g0}\right]$, $C_s^2 \equiv \gamma_c p_{c0}/\rho_0 \cdot \left[1 + (\gamma_c - 1)/\gamma_c \cdot \alpha/p_{c0}\right]$ and $M_0 \equiv u_0/C_s$ have been used in (233) and represent the appropriate form for the 'sound speeds' in a two-fluid injection model (Section 8.2.1). From (233), it is apparent that forward propagating modes are unstable provided the background flow is sufficiently supersonic and decelerating. Observe from (233) that if the thermal background gas is cold (and so the gas pressure restoring forces are absent and $M_0 \to \infty$), then the instability assumes its maximum growth rate. However, in the cold gas limit, the cosmic-ray mediated shock is smoothed completely, having no subshock, yet is the most unstable to acoustic perturbations. The instability has been suggested as a mechanism for heating the

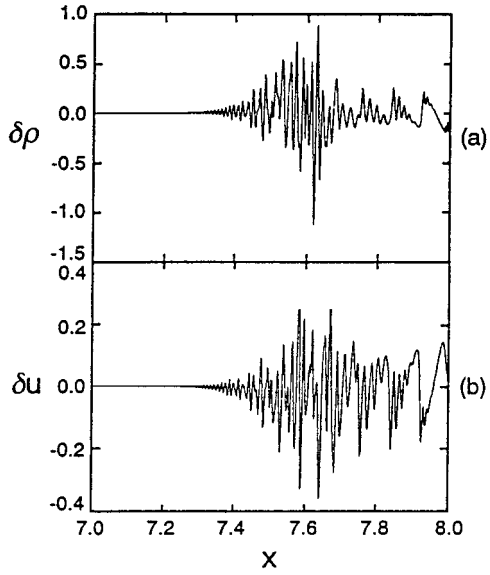

Figure 8.17. The amplification of an acoustic wave train as it convects through the cosmic ray foreshock. The background steady-state termination shock profile has been subtracted in order to illustrate the amplification more clearly. In the units used, the subshock location is approximated $x = 7.62$ (Donohue and Zank, 1993.)

thermal population in the foreshock region of a cosmic-ray mediated shock (Zank et al., 1990; Chalov, 1990).

To illustrate the 'squeezing' instability described by (233), Donohue and Zank (1993) propagated a small amplitude short wavelength wave into a steady-state cosmic-ray modified termination shock. Figure 8.17(a) illustrates the growth in density fluctuations as the wave propagates through the shock (after the background mediated shock has been subtracted out in order to illustrate the wave amplification more clearly). Although the initial upstream wave amplitude was only 0.1 in the normalized units, the corresponding amplification can be as much as $7-8$ times that. It should be noted that the acoustic perturbations are damped in a background cosmic-ray fluid (via the dissipation term $\sim C_s^2/\kappa$ in (233)), so that wave amplification exceeding the shock compression is a clear indication of unstable growth. The instability appears to be relatively minor effect at a cosmic-ray mediated termination shock, at least for the parameters considered by Donohue and Zank (1993). For more strongly cosmic-ray mediated shocks, we can expect to see the smoothed structure almost completely eradicated by the instability (Ryu et al., 1993). The associated fluctuations in the velocity field u are illustrated on Figure 8.17(b).

Although multi-dimensional effects are not discussed here in any detail, we describe some properties of the instabilities present in a 2D cosmic-ray mediated shock which are of particular interest to the termination region. By including the off-diagonal terms in the multi-dimensional diffusion tensor describing cosmic-ray

transport, several unstable wave modes can be found which have no 1D analogue (Zank et al., 1990, Table I; Chalov, 1990) and these depend critically on the strength of the particle scattering. Of particular interest for quasi-perpendicular shocks is the so-called 'drift instability' of Zank et al. (1990) since this unstable mode propagates orthogonally to both the plasma velocity and the magnetic field vectors. When the sun is in a state of positive polarity (i.e., $A > 0$), the unstable wave modes propagate away from the equatorial plane whereas when the polarity reverses (as it did during the mid 1980's) ($A < 0$), the direction of wave propagation reverses. Thus, the solar wind plasma in the vicinity of the equatorial plane is likely to be significantly more disturbed during the $A < 0$ phase than during that of the $A > 0$ cycle. It also follows from the general instability analysis [Zank et al., 1990] that the cosmic-ray diffusion coefficient should be smaller in the neighbourhood of the equatorial region during the $A < 0$ polarity phase. One implication of a reduced diffusion coefficient, assuming that the acceleration of the anomalous component occurs mainly near the equatorial region, is that a shift in the anomalous cosmic-ray intensity peak towards higher energies should occur whenever the polarity reverses from an $A > 0$ cycle to a $A < 0$ cycle. This shift in the peak of the anomalous cosmic-ray intensity reflects the enhanced efficiency of cosmic-ray acceleration associated with a smaller diffusion coefficient (see Jokipii, 1992).

8.2.5. *Termination Shock Structure: Kinetic Cosmic-Ray Model*

The hydrodynamic models described above have been extended by solving the cosmic-ray transport equation (211) directly instead of using moments and closure assumptions to obtain a reduced description (LeRoux and Ptuskin, 1995a, b; LeRoux and Fichtner, 1997). Such an approach offers several advantages over the simpler hydrodynamic models in that (i) closure assumptions about γ_c can be avoided; (ii) one does not need to use an averaged hydrodynamical form of the cosmic-ray diffusion tensor, and (iii) calculated cosmic-ray spectra can be compared directly with observed modulated cosmic-ray spectra.

The model considered by LeRoux and Fichtner (1997) consists of the spherically symmetric equations (218)–(219), together with pickup ion source terms, i.e.,

$$\frac{\partial \rho}{\partial t} + \frac{1}{r^2}\frac{\partial}{\partial r}\left(r^2 \rho u\right) = m Q_{ph} \,, \tag{234}$$

$$\frac{\partial}{\partial t}(\rho u) + \frac{1}{r^2}\frac{\partial}{\partial r}\left(r^2 \rho u^2\right) = -\frac{\partial}{\partial r}(p + p_c) - mu Q_{ce} \,, \tag{235}$$

$$\frac{\partial}{\partial t}\left(\frac{1}{2}\rho u^2 + \frac{p}{\gamma - 1}\right) + \frac{1}{r^2}\frac{\partial}{\partial r}\left[r^2 u\left(\frac{1}{2}\rho u^2 + \frac{\gamma}{\gamma - 1}p\right)\right] = -u\frac{\partial p_c}{\partial r} +$$

$$+\alpha \frac{1}{r^2}\frac{\partial}{\partial r}(r^2 u) - \frac{1}{2}m\left[u^2 H(R_{\mathrm{TS}} - r) + v_{\mathrm{rms}}^2 H(r - R_{\mathrm{TS}})\right] Q_{ce} \,. \tag{236}$$

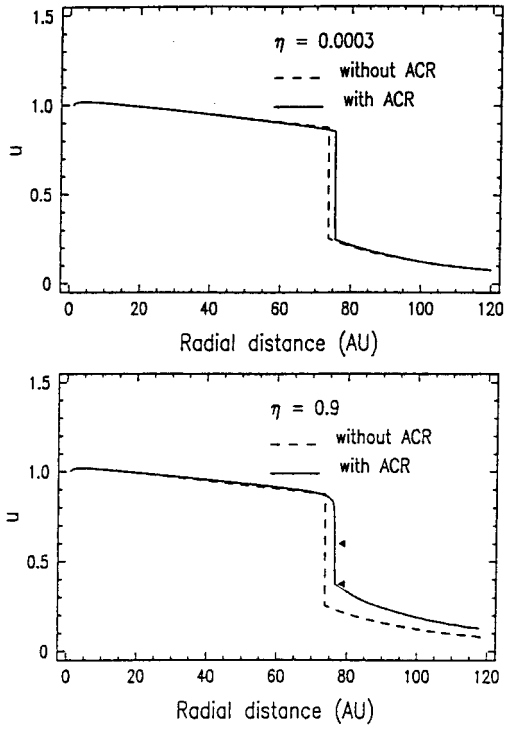

Figure 8.18. Solar wind speed (normalized to 400 km s^{-1}) as a function of heliocentric distance in the upwind direction. The dashed curve is a reference solution which includes pickup ions whereas the solid solution contains both pickup ions and ACRs. The top panel corresponds to the low injection efficiency solution $\eta = 3\times 10^{-4}$ and the lower panel to the high injection efficiency solation $\eta = 0.9$. The solid triangles identify the subshock (LeRoux and Fichtner, 1997.)

The solar wind protons, electrons and pickup ions are assumed to be a single fluid while both ACRs and GCRs form a second (massless) fluid. The presence of the Heaviside step functions H in (236) results from the assumption that the energy loss rate is dominated by flow energy upstream and thermal energy downstream of the termination shock. The parameter α is given by (215) and models the energy gain or loss of the background fluid when ion transfer occurs between the pickup ions and ACRs.

To close the model equations (234)–(236), LeRoux and Fichtner (1997) use the spherically-symmetric cosmic-ray transport equation

$$\frac{\partial f}{\partial t} + u\frac{\partial f}{\partial r} - \frac{1}{r^2}\frac{\partial}{\partial r}\left(r^2\kappa_{rr}\frac{\partial f}{\partial r}\right) - \frac{1}{3r^2}\frac{\partial}{\partial r}\left(r^2u\right)p\frac{\partial f}{\partial p} = \eta Q_{\rm PI}\,, \tag{237}$$

where $Q_{\rm PI} = \pi/4N\nu_{\rm CE}\delta(p - p_{\rm inj})/p_{\rm inj}^2$ is a source term for newly ionized isotropically distributed pickup ions and η denotes the injection efficiency for pickup ions to be shock accelerated at the termination shock. This source term needs to be interpreted carefully since the parameter α already describes the injection process

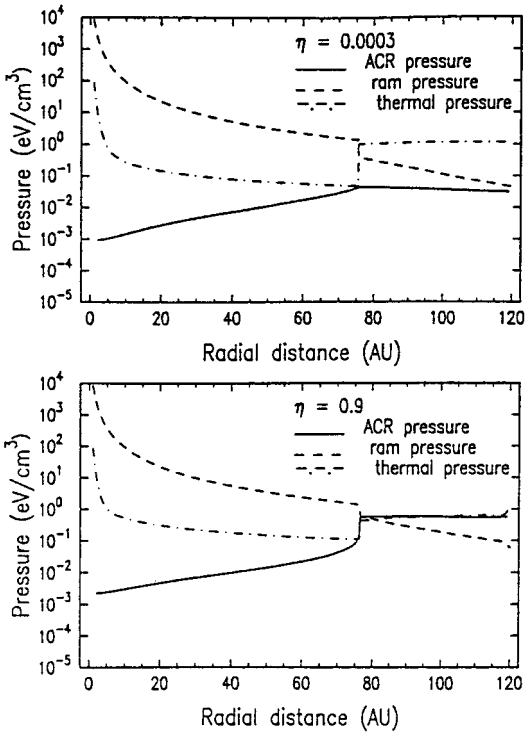

Figure 8.19. Solar wind ram (dashed line), thermal (dash-dot) and ACR (solid) pressure profiles in eV cm^{-3} for the low (top panel) and high (bottom panel) efficiency solutions (LeRoux and Fichtner, 1997.)

in the solar wind. $Q_{\rm PI}$, in the absence of pickup ion energization in the solar wind, is only non-zero at the TS and can be thought of as corresponding to a jump in α at the subshock. Equation (237) is used to evaluate the total cosmic-ray (ACR and GCR) pressure in (234)–(236) for momenta $p > mu$.

A phenomenological model for the radial diffusion coefficient is assumed, with $\lambda_\parallel = dR_L$ for some parameter d (= 56). The parameters were chosen to match solar wind cosmic-ray proton spectra obtained during the 1987 solar minimum. This gives

$$\kappa_{rr} = \kappa_\parallel \cos^2\Psi + \kappa_\perp \sin^2\Psi \ , \tag{238}$$

$$\kappa_\parallel = \kappa_0 \beta\,(R/R_0)\,(B_0/B) \ , \qquad \kappa_\perp = \frac{b\kappa_\parallel}{1+d^2} \ ,$$

where $\kappa_0 = d \cdot 6 \times 10^{20}$ cm^{2}s^{-1}, rigidity $R_0 = 1$ GV, $B_0 = 5$ nT, and $b = 47$.

LeRoux and Fichtner (1997) integrate equations (234)–(238) numerically for several models. Following their analysis, we consider first the role of anomalous cosmic-rays and neglect the galactic cosmic-ray population. Illustrated in Figure 8.18 are two models which include the injection and acceleration of some

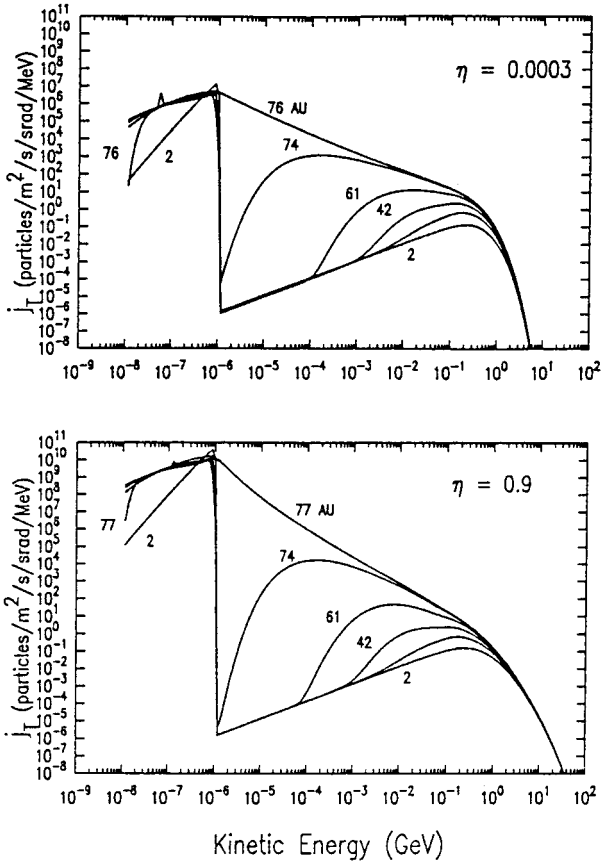

Figure 8.20. Combined pickup ion and ACR differential intensities in particles m^{-2} s^{-1} $srad^{-1}$ MeV^{-1} as a function of kinetic energy in GeV in the upwind direction for the low (top) and high (bottom) efficiency solutions. The distance at which the spectra are determined appears as a label on the curve. 76 AU is just downstream of the TS (LeRoux and Fichtner, 1997.)

fraction of the pickup ion population to ACR energies once they cross a threshold momentum $p_{\rm inj} = mu$. Both the low ($\eta = 3 \times 10^{-4}$) and the high ($\eta = 0.9$) injection efficiency solutions show that the TS is pushed out by the ACR pressure gradient (1.9–2.7 AU displacement). The high efficiency model yields a termination shock possessing a large ($\sim$ 4 AU) precursor, with a significantly weaker subshock ($r_s \sim 1.6$) than a corresponding model without ACRs. The ACR and solar wind pressure gradients are shown in Figure 8.19, and these show quite graphically the reason for the existence of a strongly mediated cosmic-ray termination shock in the case of high injection efficiency.

The ACR spectra at different radial distances are plotted in Figure 8.20 for the high and low injection models and the intensity levels between the two models are quite different. For the weakly mediated TS, the accelerated ACR spectrum is

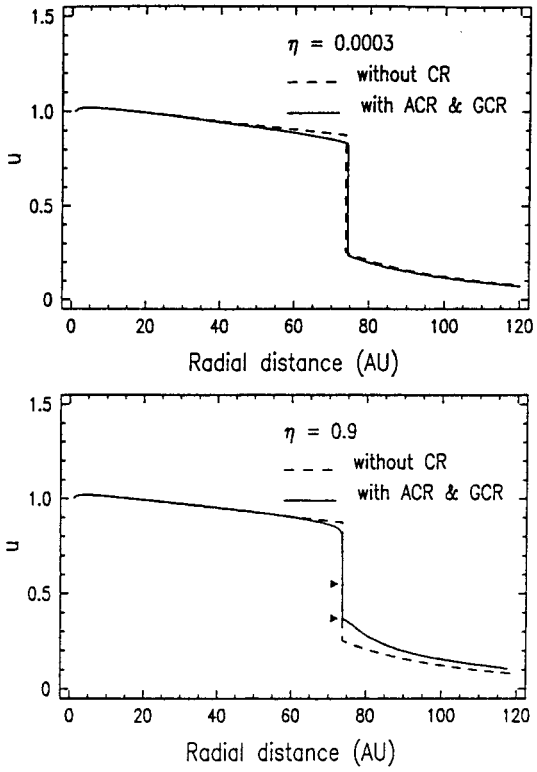

Figure 8.21. Solar wind speed (normalized to 400 km s^{-1}) as a function of heliocentric distance in the upwind direction. The dashed curve is a reference solution which includes pickup ions whereas the solid solution contains pickup ions, ACRs and GCRs. The top panel corresponds to the low injection efficiency solution $\eta = 3\times10^{-4}$ and the lower panel to the high injection efficiency solution $\eta = 0.9$. The solid triangles identify the subshock (LeRoux and Fichtner, 1997.)

a power law in energy, reflecting particle acceleration at a relatively sharp termination shock. By contrast, the high injection model spectra exhibits a pronounced concavity, indicative of less energetic ACRs experiencing only the subshock compression (i.e., a steeper low energy spectrum) and the higher energy particles experiencing the full mediated shock compression (i.e., a flatter spectrum at high energies). Both sets of spectra roll over at approximately the same energy ($\sim$ 200 MeV) and intensity level. The rollover energy, determined by the condition $\kappa/u > R_{\rm TS}$, is the same because κ is the same for both efficiencies. Thus, the spectra at rollover energies are essentially independent of the detailed TS structure. That intensity levels at the rollover energy are similar is a consequence of choosing the two injection efficiencies. Within $\sim$ 60 AU, the modulated spectra, because they are determined largely by the properties of the spectral rollover, are very similar for both injection efficiencies. At larger heliocentric distances, the two cosmic-ray spectra have very different slopes and intensities. Thus, cosmic-ray measurements

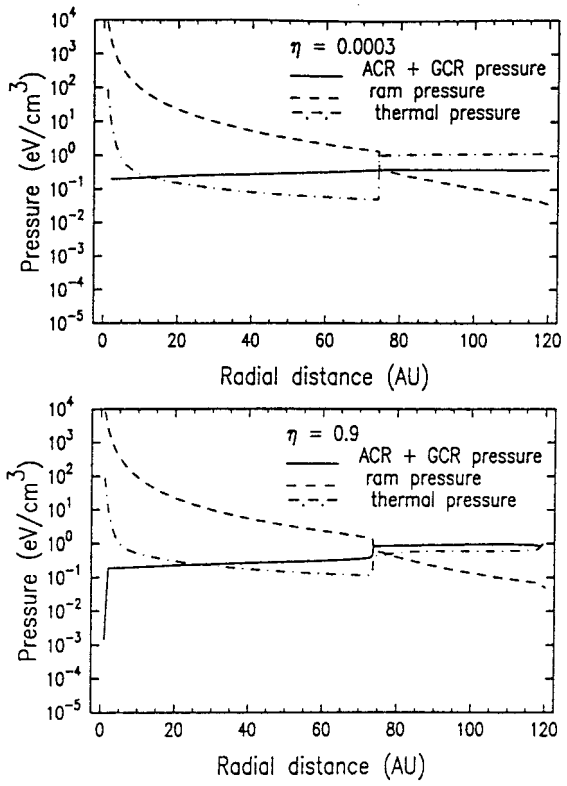

Figure 8.22. Solar wind ram (dashed line), thermal (dash-dot) and ACR-GCR (solid) pressure profiles in eV cm^{-3} for the low (top panel) and high (bottom panel) efficiency solutions (LeRoux and Fichtner, 1997.)

being made currently by Voyager 1 may shed considerable light on the structure of the TS and on cosmic ray injection efficiency.

LeRoux and Fichtner (1997) consider too the role of GCRs in determining termination shock structure and location. The interstellar GCR pressure acts to push the termination inward, thus counteracting the ACR pressure gradient. This is illustrated in Figure 8.21. It is evident that GCRs contribute more strongly to the formation of a precursor than ACRs and hence determine the basic length scale. Nonetheless, pickup ions continue to play the primary role in determining the overall compression ratio, although ACRs continue to reduce the subshock strength significantly in the high injection model. The radial pressure profiles for the various components are illustrated in Figure 8.22. For the low injection model, GCR pressure dominates throughout the solar wind, whereas GCRs only dominate upstream of the TS in the high injection model.

From the work of LeRoux and Fichtner (1997), it is unclear which of the two models, high or low injection, is to be favoured. For the high injection model, an extremely efficient injection mechanism needs to be identified. Finally, it is

also unclear how strongly the rollover results depend on the simplified form of the diffusion coefficients (238). As discussed in Section 7.1.4, modulation properties can be effected by assumptions in the form of κ_{rr}.

9. Interplanetary Disturbances and the Termination Shock

Although almost all the preceding discussion has focussed on the steady-state location and structure of the termination shock, it is most unlikely that the termination shock will be motionless. The solar wind exhibits temporal variations with fluctuation amplitudes that can be substantial. The scales on which these fluctuations vary range from minutes and less to the solar cycle period. Thus, as has been observed by numerous authors (e.g., Barnes, 1993; Suess, 1993; Whang and Burlaga, 1993; Donohue and Zank, 1993), our first detection of the termination shock is likely to occur as the shock sweeps in and over the Voyager 1, 2 spacecraft. The first encounter is likely to be followed by successive outward and inward encounters. However, the response of the termination shock to interplanetary disturbances is unlikely to be simple and a complicated compound structure of shocks, contact/tangential discontinuities and rarefaction waves is likely to result (Story and Zank, 1995, 1997; Ratkiewicz et al., 1996). It may therefore be very difficult to identify conclusively which structure corresponds to the termination shock itself. This difficulty can only be compounded with the inclusion of cosmic-rays and this has interesting and important implications for the cosmic-ray mediated termination shock (Donohue and Zank, 1993).

This section begins by considering shocks in the outer heliosphere and the role played by pickup ions in determining their propagation characteristics. Thereafter, the interaction of interplanetary disturbances with the termination shock is addressed on the basis of gas dynamical, MHD, and two-fluid cosmic-ray models.

9.1. Shock propagation in the outer heliosphere: role of pickup ions

Whang (1991) has reviewed shock propagation beyond 1 AU in considerable detail, and the results and conclusions described therein can be expected to remain valid within the ionization cavity. However, since pickup ions dominate the internal energy of the solar wind beyond the ionization cavity, we may expect the properties of shocks propagating in the inner and outer heliosphere to be quite different. The most obvious difference has to do with the sound speed. In the inner heliosphere, the temperature T decreases as a power law (more or less adiabatically, (e.g., Liu et al., 1995)), whereas in the outer heliosphere, if one were to include the hot pickup ions, the temperature should increase with heliocentric distance beyond the ionization cavity. Such a temperature increase cannot, unfortunately, be measured directly by the plasma instruments on board the Voyager or Pioneer

spacecraft, and indirect detection of pickup ions is only possible (Burlaga et al., 1994). Theoretically, the sound speed, after initially decreasing, is expected to increase significantly in the outer heliosphere. By regarding shocks as essentially steepened sound waves, it is clear that (1) shock propagation speeds should be higher in a pickup ion modified heliosphere compared to shocks propagating in an 'adiabatic' wind; (2) the shock compression ratio (which depends on Mach number) should decay more rapidly for a shock propagating in a PI mediated solar wind than in an adiabatic wind, and (3) the forward-reverse shock formation and propagation characteristics (i.e., corotating and merged interaction regions) will be different for an adiabatic compared to a pickup ion modified heliosphere. Each of these points has been developed and discussed by Zank and Pauls (1997) in the context of gas dynamics. Extensions to MHD are awaited. Nonetheless, some insight into the effect of the IMF is gained by setting the adiabatic index to $\gamma = 2$ in the gas dynamic model since the equations of MHD for a magnetic field perpendicular to the flow direction are isomorphic to the gas dynamic equations.

Zank and Pauls (1997) consider shock propagation in the context of the spherically symmetric, model equations

$$\frac{\partial \rho}{\partial t} + \frac{1}{r^2}\frac{\partial}{\partial r}\left(\rho u r^2\right) = 0 \,, \tag{239}$$

$$\frac{\partial}{\partial t}\left(\rho u\right) + \frac{1}{r^2}\frac{\partial}{\partial r}\left(\rho u^2 r^2\right) + \frac{\partial p}{\partial r} = Q_M \,, \tag{240}$$

$$\frac{\partial}{\partial t}\left(\frac{1}{2}\rho u^2 + \frac{p}{\gamma - 1}\right) + \frac{1}{r^2}\frac{\partial}{\partial r}\left[\rho u r^2 \left(\frac{1}{2}u^2 + \frac{\gamma}{\gamma - 1}\frac{p}{\rho}\right)\right] = Q_E \,, \tag{241}$$

where the photoionization of neutral hydrogen H has been neglected. The symbols have their usual meanings. Zank and Pauls (1997) assume that the cold neutral distribution (Axford, 1972; Vasyliunus and Siscoe, 1976)

$$n_{\rm H}(r) = n_{{\rm H}\infty} \exp[-\lambda/r] \,, \quad T_{\rm H} = T_{{\rm H}\infty} \,, \quad \mathbf{u}_{\rm H} = \mathbf{u}_{{\rm H}\infty}$$

is unchanged in the heliosphere. The subscript ∞ refers to the boundary values (the boundary being the termination shock), and the cold model is quite reasonable provided one specifies appropriate boundary data. The specific source terms can be found in the appendix of Pauls et al. (1995). The parameters used by Zank and Pauls (1997) are standard: $\langle n\sigma_{ce}\rangle = 2.5 \times 10^{-16}$ cm^{-5} for the charge exchange cross-section, $T_{{\rm H}\infty} = 10^4$ K, and $u_{{\rm H}\infty} = 20$ km s^{-1}. For a nominal value of $n_{{\rm H}\infty} = 0.1$ cm^{-3} at the termination shock, this corresponds to a constant charge exchange cross section of $\sigma_{ce} = 2.5 \times 10^{-15}$ cm^{-2}. Finally, $\lambda = 4$ AU is used.

The steady-state solution to equations (239)–(241) without the above parameters is illustrated in Figure 4.2. Recall that this figure illustrates both an adiabatic solar wind model and a solar wind mediated by pickup ions (solid lines). While the density falls off essentially as r^{-2} for both models, considerable differences in

the radial profiles for pressure, temperature, Mach number, and velocity exist, as discussed in Section 4. Since the sound speed $C_s \propto \sqrt{T}$, Figures 4.2(d) and 4.2(e) suggest that very different propagation characteristics can be expected for waves in either an adiabatic or pickup ion-mediated solar wind.

9.1.1. *Shock Propagation: Theory*

A nonlinear theory for the propagation of shocks in a solar wind whose density decays quadratically with heliocentric distance, whose velocity is approximately constant, and whose radial pressure/temperature corresponds to either an adiabatic or pickup ion mediated profile was developed by Zank and Pauls (1997). The idea behind their approach is that in a local frame of reference moving with the fluid velocity u, the fluid variables change in accordance with linear theory. On the scale of a pulse length, the disturbance will propagate along a tube whose undisturbed cross section $A_0(x)$, sound speed $C_0(x)$, and density $\rho_0(x)$ vary gradually, where x denotes the spatial or 'radial' coordinate.

Assume that there exist equilibrium solutions to (239)–(241) for which $p_0 = p_0(x)$, $\rho_0 = \rho_0(x)$, and u_0 is constant (Figure 4.2), and write $\Psi \equiv (\rho\ , p, u)$ as $\Psi = \Psi_0 + \Psi_e$. Then it follows that the gas dynamic momentum equation becomes

$$\rho\left(\frac{\partial u_e}{\partial t} + u_e\frac{\partial u_e}{\partial \overline{x}}\right) = -\frac{\partial p_e}{\partial \overline{x}}\ , \tag{242}$$

where u_e is the fluid velocity accelerated by the excess pressure (p_e) gradient. Note that in (242), the comoving frame $\overline{x} = x - u_0 t$ has been introduced. We shall henceforth neglect the bar for convenience, it being understood that we are in the solar wind frame of reference. Similarly, the continuity equation may be expressed in the comoving frame as

$$\frac{\partial}{\partial t}(\rho A) + \frac{\partial}{\partial x}(\rho A u_e) = 0\ , \tag{243}$$

and the equation for entropy S is

$$\frac{\partial S}{\partial t} + u_e\frac{\partial S}{\partial x} = 0\ . \tag{244}$$

In (243), A denotes the cross-sectional area of a flux tube in the solar wind. Equations (243)–(244) can be used to describe wave and shock propagation analytically in an inhomogeneous wind provided specific radial profiles for ρ_0 and T_0 are assumed.

Assuming that the variation in density over a cross section of the flux tube is negligible (i.e., ρ varies with radial distance only), suppose that ρ and the cross-sectional area A vary with the local excess pressure p_e according to

$$\rho = \rho\,(p_e\ , S)\ , \qquad A = A\,(p_e\ , x)\ . \tag{245}$$

These equations specify the compressibility of the fluid for a given entropy S and the distensibility of the flux tube at a given location.

The linearized wave equation for p_e is

$$\frac{\partial^2 p_e}{\partial t^2} = \frac{C_0(x)}{K(x)} \frac{\partial}{\partial x} \left(C_0 K \frac{\partial p_e}{\partial x} \right) , \tag{246}$$

where $K(x) = A_0/(\rho_0 C_0)$.

Under the assumption that $A_0(x)$, $\rho_0(x)$, and $C_0(x)$ are slowly varying (and hence $K(x)$), one may seek solutions to (246) of the form

$$p_e = K^{-a} f(x \pm C_0 t) . \tag{247}$$

It follows that to leading order, (247) is a solution to (246) provided the 'attenuation index' a satisfies

$$\frac{1}{C_0} \frac{\partial C_0}{\partial x} + (-2a + 1) \frac{1}{K} \frac{\partial K}{\partial x} = 0 . \tag{248}$$

Some simple results for linear waves propagating in both adiabatic and PI-mediated solar winds are easily derived. Note first that for a spherically symmetric wave propagating into a constant atmosphere (i.e., with $A_0(x) \sim x^2$, $\rho_0(x)$, $C_0(x)$ constant), one obtains $a = \frac{1}{2}$ and hence the well-known result $p_e \propto f(x \pm C_0 t)/x$ [Whitham, 1974]. Suppose now that $p_0 \propto \rho_0^\gamma$ and that the density decays as x^{-2}. For general values of γ, one finds that $a = 2/(\gamma + 3)$ and thus for any wind, $p_e \propto f(x \pm C_0 t)/x^2$. Thus, although the wave speeds can be different for either an adiabatic or a pickup ion mediated solar wind, the attenuation experienced by the wave in the comoving frame is independent of the model, provided the background density decays quadratically.

As observed by Whitham (1974), it is often a good approximation to consider the nonlinear evolution of simple waves when one wishes to study gas dynamic shocks of moderate strength. For 1D gas dynamic simple waves propagating outward in an expanding wind from an initial disturbance, the quantity propagated forward unchanged is not now p_e but rather $p_e K^a$ (see (247)). It follows then that $p_e K^a$ satisfies the nonlinear wave equation

$$\left[\frac{\partial}{\partial t} + (u_e + C) \frac{\partial}{\partial x} \right] \left(p_e K^a \right) = 0 , \tag{249}$$

and (249) is a general description for the nonlinear propagation of a simple wave in an inhomogeneous flow with variable sound speed. By utilizing the approximation $u_e \simeq p_e/\rho_0 C_0$, and the definitions

$$w \equiv \frac{\gamma + 1}{2} \frac{p_e}{\rho_0 C_0^3} , \qquad V(x) \equiv A_0^{-a} \rho_0^{a-1} C_0^{a-3} ,$$

equation (249) then reduces to the well-known nonlinear wave equation (Zank and Pauls, 1997)

$$\frac{\partial \mathcal{F}}{\partial \xi} + \mathcal{F} \frac{\partial \mathcal{F}}{\partial X} = 0 , \tag{250}$$

where $\mathcal{F} \equiv w/V$. Equation (250) is a remarkably general description of wave and shock propagation in a flux tube of arbitrary cross section in a wind of arbitrary sound speed and density variation in the radial direction. Observe that the choice of coordinates in (250) gives the radial rather than the temporal evolution of the wave form since

$$X \equiv \int_0^x C_0^{-1}\, \mathrm{d}x' - t; \qquad \xi \equiv \int_0^x V(x')\, \mathrm{d}x' \,,$$

for $\gamma \geq \frac{2}{3}$, and $X \equiv \int_x^\infty C_0^{-1}\, \mathrm{d}x' - t$, $\xi \equiv \int_x^\infty V(x')\, \mathrm{d}x'$ for $\gamma < \frac{2}{3}$.

Equation (250) is a well-known classical equation which has been studied extensively. Zank and Pauls (1997) use (250) to study analytically the evolution of shocks (shock strength, velocity and density jumps, etc.) propagating in the outer heliosphere. As discussed by Whitham (1974), an initial compression pulse (such as generated by a piston moving into the fluid a certain distance and then coming to rest again) will be distorted with distance, forming eventually a head shock wave moving into the undisturbed fluid followed by a gradual decay (the rarefaction) back into the ambient state. The asymptotic structure is a triangular pulse. Use of Whitham's 'equal area' law for shock waves (Whitham, 1956) applied to a single compression pulse shows that the amplitude of the head shock wave decays asymptotically as

$$\delta\mathcal{F} \sim (2\mathcal{P}/\xi)^{1/2} \,, \tag{251}$$

which is the familiar inverse-square-root law for the decay of shock wave strength with 'time' ξ. Here $\mathcal{P}$ is the area of the initial pulse. Since the pulse length increases asymptotically as $(2\xi)^{1/2}$, the total wave energy in the shock pulse tends to zero as $(2\mathcal{P})^{3/2}/\xi^{1/2}$ and so the rate of decrease is proportional to $\xi^{-3/2}$.

Relation (251) can be expressed in terms of the velocity jump δu_e as

$$\delta u_e \sim \frac{\delta\mathcal{F}}{K^a \rho_0 C_0} \,. \tag{252}$$

A similar simple scaling law for the evolution of the density jump at a propagating shock can be derived. For a slowly varying background, the density satisfies

$$\frac{\partial\rho}{\partial t} + (u \pm C)\,\frac{\partial\rho}{\partial x} = 0 \,. \tag{253}$$

Since $\delta u_e \simeq 2/(\gamma - 1)\delta C$, linearization of (253) and adopting the co-moving frame yields a differential relation between the (weak) density jump and velocity jump,

$$\frac{\partial}{\partial x}\,(\delta\rho) = \frac{\gamma+1}{\gamma-1}\left(-\frac{\partial\rho_0}{\partial x}\right)\frac{\delta u_e}{C_0(x)} \,, \tag{254}$$

or, equivalently, with $M_{sh} \equiv \delta u_e / C_0$.

Assume that $A_0(x) \sim x^2$. For an adiabatic solar wind $\rho_0(x) \sim x^{-2}$ and $p_0(x) \propto \rho_0^\gamma$ $(1 < \gamma \leq 2)$. Hence $C_0(x) \sim x^{-(\gamma-1)}$, $a = 2/(\gamma + 3)$, and the shock front evolves with increasing radial distance x according to

$$\delta u_e \sim x^{-\gamma/2}, \quad M_{sh} \sim x^{\gamma/2-1}, \quad \delta\rho \sim x^{\gamma/2-3} . \tag{255}$$

For a pickup ion mediated solar wind, $\rho_0(x) \sim x^{-2}$ and $T \sim x$ beyond some 6 AU (the extent of the ionization cavity). Hence $C_0 \sim x^{1/2}$ and

$$\delta u_e \sim x^{-1/4}, \quad M_{sh} \sim x^{-3/4}, \quad \delta\rho \sim x^{-11/4} . \tag{256}$$

Recall that for a $\gamma = 2$ gas and a perpendicular (to the flow vector) magnetic field geometry, the MHD equations and the gas dynamic equations are isomorphic provided that the total pressure is interpreted as the sum of the magnetic and thermal pressures. The choice of $\gamma = 2$ therefore provides some idea of the shock propagation characteristics when an interplanetary magnetic field is included. The full MHD analysis has yet to be developed however.

From (255) and (256), we may conclude that (1) the velocity jump of a propagating shock pulse decays much less rapidly for a PI-mediated solar wind than for an adiabatic heliosphere $(1 < \gamma \leq 2)$, and (2) the shock Mach number decays faster in a pickup ion mediated heliosphere than in an adiabatic heliosphere.

The analytic results for the density jump scaling at a shock propagating in the outer heliosphere show that (1) in an adiabatic heliosphere, the decay is inhibited as γ increases (by the presence of a magnetic field, for example) and (2) that the density jump decays faster in a pickup ion mediated heliosphere than for an adiabatic heliosphere of any index $(1 < \gamma \leq 2)$. Thus shock decay is controlled and hastened in the outer heliosphere by pickup ions – that is, shocks propagating in the outer heliosphere are weakened by the pickup ion component of the solar wind. The decay laws (255) and (256) have been compared to simulations (Zank and Pauls, 1997) and are found to be surprisingly accurate asymptotically, especially for $\delta\rho$.

9.1.2. *Shock Propagation: Simulations*

Shock propagation in an adiabatic solar wind has been well studied (see the reviews by, e.g., Hundhausen, 1985, or Whang, 1991) and these results remain valid within the ionization cavity. Consider now blast wave propagation beyond the ionization cavity. Depicted in Figure 9.1 is a blast wave at an early time in the simulation, so that the blast wave is well within the ionization cavity. One observes a forward or head shock where the speed, density, pressure, and temperature increase abruptly, followed by a density depletion (the radially expanding analogue of the 1-D gas dynamic contact discontinuity), and then a reverse shock propagating sunward while convecting outward in the supersonic solar wind. Abrupt increases in the density, pressure, and temperature occur at the reverse shock, and the overall velocity profile resembles the well-known N wave solution. For the adiabatic solar wind, the

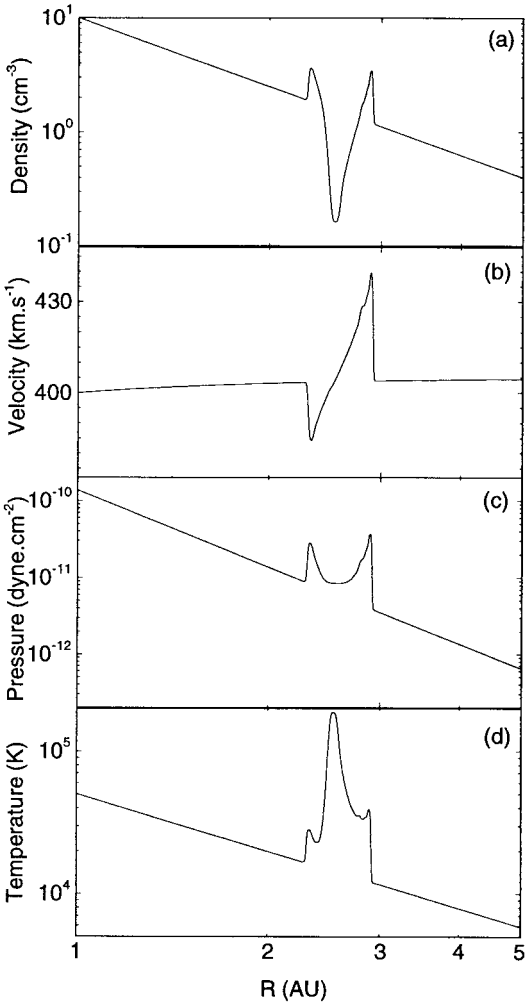

Figure 9.1. Example of a blast wave (generated at 1 AU) propagating within the ionization cavity. The plasma parameters, as a function of radial distance R, are plotted for (a) number density (cm^{-3}); (b) radial velocity (kilometers per second); (c) pressure (dyne/cm^2); and (d) temperature (Kelvin) (Zank and Pauls, 1997.)

N wave structure does not change structurally with radial distance, experiencing only broadening and damping.

Shortly after the heliospheric radial temperature profile (Figure 4.2(d)) changes from adiabatic to pickup ion dominated in the pickup ion heliosphere model, shock propagation characteristics change dramatically. The shock speed is seen to increase and the existing forward and reverse shocks separate faster than they would in an adiabatic model. The adiabatic (dashed line) and the PI-mediated (solid line) shocks are plotted in Figure 9.2. The shocks, which had identical initial conditions for both model heliospheres, have propagated for an identical time. The propaga-

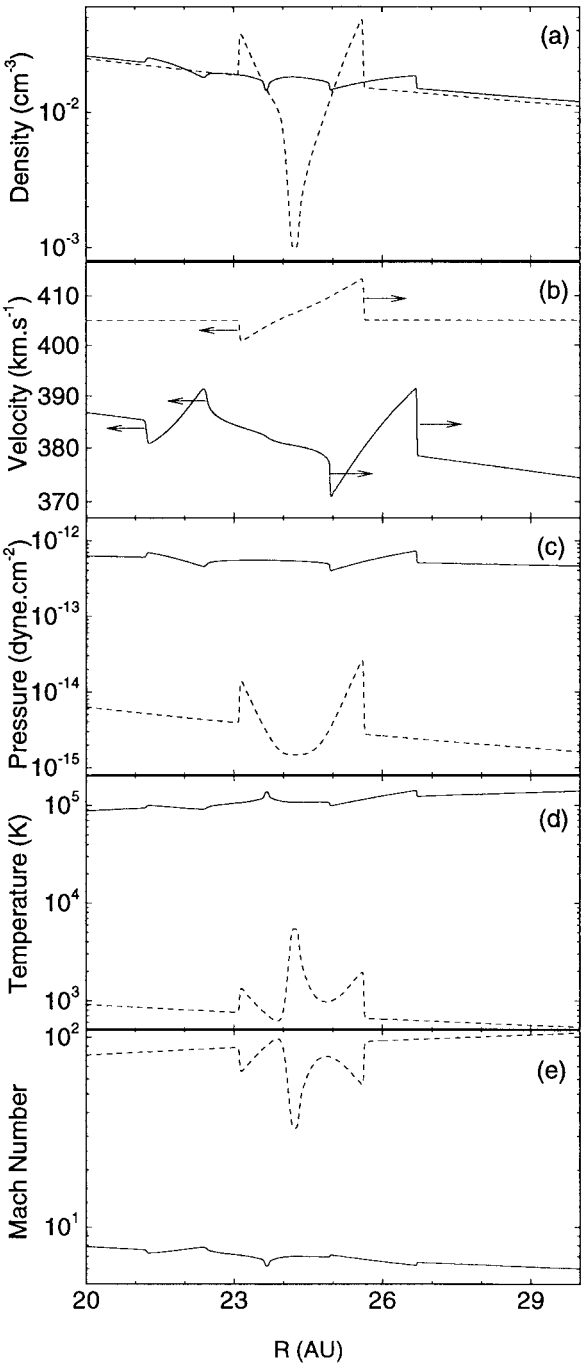

Figure 9.2. Dashed and solid lines illustrate blast wave propagation in an adiabatic and a PI-mediated solar wind, respectively, both taken at identical times and for which identical initial conditions were used. See text for details. (a) Number density; (b) radial velocity; (c) pressure; (d) temperature, and (e) Mach number, all as a function of heliocentric radius R (Zank and Pauls, 1997.)

tion speed of both the forward and reverse shocks in the pickup ion mediated wind is higher than that of their adiabatic counterparts. When the propagating shocks encounter the boundary of the ionization cavity where the temperature increases, the shocks bounding the *N* wave accelerate apart. The original *N* wave now splits into a double forward-reverse shock pair: two adjacent forward shocks and two adjacent reverse shocks. This split is illustrated clearly in Figures 9.3(a) and 9.3(b), where the arrows indicate the shock propagation direction. Much more density structure results from this dynamical change too, generally of rather small amplitude. Such a splitting of the original gas dynamic forward shock into two forward shocks, with an analogous splitting of the original reverse shock, is quite distinct from blast wave evolution in an adiabatic heliosphere. As the blast wave continues to propagate through the pickup ion mediated heliosphere, no new structure is generated, and the double N wave simply broadens while decaying.

Zank and Pauls (1997) suggest several possible tests for determining whether interplanetary shock properties are changed by the presence of pickup ions in the outer heliosphere. These might be (1) structural, such as the existence of forward (or reverse) shock pairs beyond the ionization cavity; and (2) statistical, since the correlation of velocity and density jumps within and without the ionization cavity will be different. The velocity jump for shocks in the pickup ion mediated heliosphere decays more slowly with radial distance than its counterpart in the adiabatic wind. Accordingly, one should see at least as much velocity structure, and perhaps more because of the splitting effect described above, in the outer heliosphere as in the inner regions. The density jump, should, however, decay much more rapidly in the pickup ion mediated heliosphere than in the adiabatic wind. The large density depletions and enhancements characteristic of the adiabatic model are much smaller when pickup ions are included in the solar wind, and the solar wind density profile should tend towards a more uniform state with only small-scale structure present. Thus pickup ions in the outer heliosphere should leave the velocity fluctuations with characteristics relatively similar to those observed in the inner regions but the density fluctuations, which might be strongly associated with shocks in the inner heliosphere, should no longer correlate very well with velocity jumps in the outer heliosphere, thanks to both an increased decay rate with heliocentric distance and to the generation of new density structure during shock 'splitting.' Such a prediction is quite at variance with the expectations of either gas dynamic or MHD (e.g., Whang, 1991) heliospheric models.

Zank and Pauls (1997) explore several other 1D initial conditions besides those appropriate to blast wave propagation. Only one additional case is described here, that of stream-driven shocks. To model the formation of shocks driven by high-speed, low-density, high-temperature streams, Zank and Pauls introduce a square pulse in velocity at the left boundary (from 400 to 800 km s^{-1} for 39.6 hours) while decreasing the density from 10 to 2 cm^{-3} and increasing the temperature from 5×10^4 to 20×10^4 K. This example is particularly interesting since it illustrates how very different shock formation and propagation can be in a pickup ion

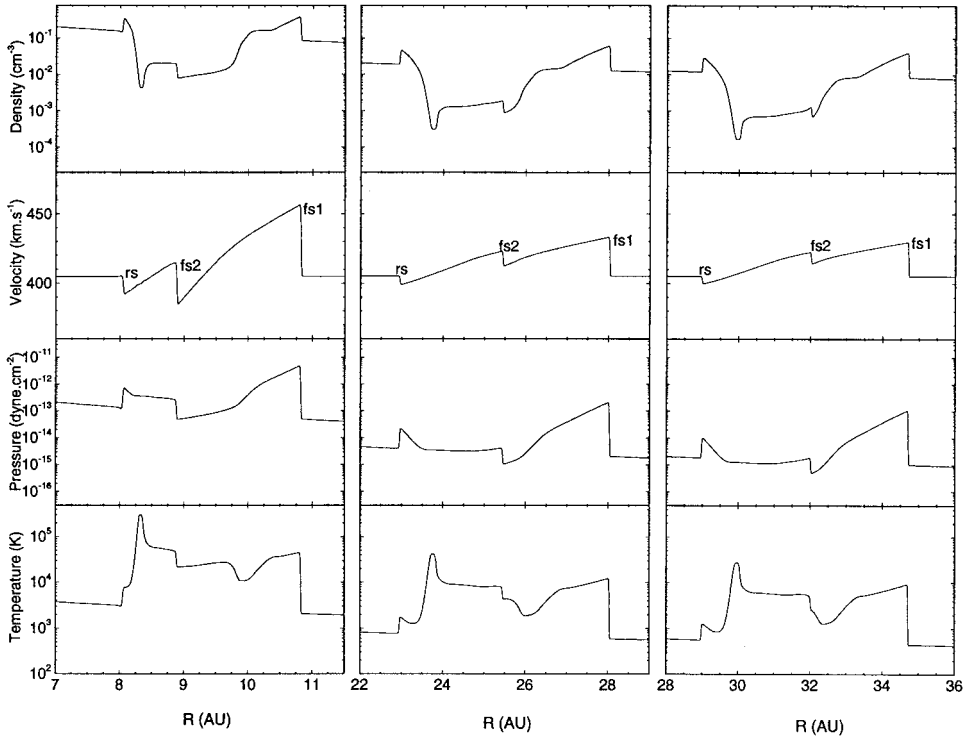

Figure 9.3. Examples depicting the radial evolution of the compound shock wave structure generated by the interaction of streams (case 3) in an adiabatic solar wind ($\gamma = \frac{5}{3}$). (a) 7–11 AU, (b) 22–28 AU, and (c) 28–36 AU. See text for details (Zank and Pauls, 1997.)

mediated heliosphere compared to an adiabatic model. The adiabatic heliospheric case is illustrated in Figure 9.3. By ∼11 AU (Figure 9.3(a)), a strong forward shock (fs1) propagates into the undisturbed solar wind, the head shock possessing the characteristic triangular structure of a shock with an attached rarefaction. A second forward shock (fs2) trails the head shock. Finally, a reverse shock (rs) and attached rarefaction propagate into the shocked solar wind, and a density depletion (analogous to a contact discontinuity) separates the reverse and second forward shock. The region between the two forward shocks consists of a rarefaction (attached to the head shock) and a region of accelerating flow. In Figure 9.3(b), the three shocks that were present at ∼11 AU are still present although damped and further separated from each other. This trend continues essentially unchanged with increasing heliocentric distance, as illustrated in Figure 9.3(c). The leading or head shock closely resembles the structure of the blast wave solutions discussed above, especially in the velocity. Large density depletions are associated with the trailing shock pair and large density enhancements are associated with the head shock.

Consider now Figure 9.4 in which the evolution of the initially square pulse used in Figure 9.3 is illustrated, this time for a pickup ion mediated solar wind.

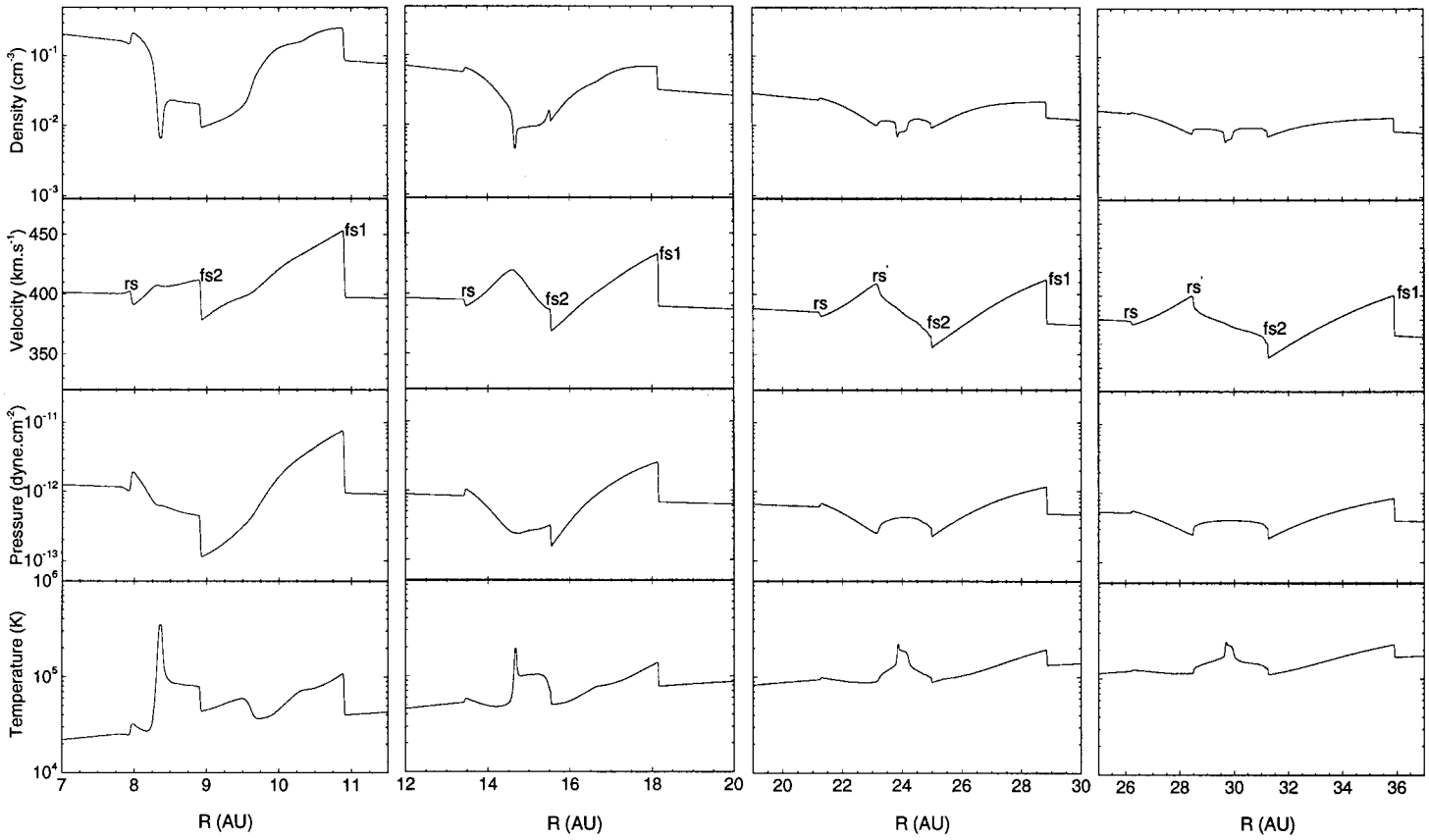

Figure 9.4. The radial evolution of compound shock waves generated by stream-stream interaction (case 3) in a PI-mediated heliosphere ($\gamma = \frac{5}{3}$). (a) 7–11 AU, (b) 12–20 AU, (c) 20–30 AU, and (d) 26–36 AU. See text for details (Zank and Pauls, 1997.)

Figure 9.4(a) depicts the solar wind variables at a time identical to that of Figure 9.3(a). The reverse shock rs and weak forward shock fs2 of the adiabatic case are present in the pickup ion mediated case, but some differences in the velocity and pressure profiles are apparent. Some time later (Figure 9.4(b)), the reverse shock has virtually disappeared, and a large velocity pulse, bounded by the weak fs2 and rs has formed. Figure 9.4(c) and Figure 9.3(b) are for identical times, and the structures are seen to differ significantly in the region trailing the head shock. The head shock fs1 of the PI heliosphere is almost perfectly triangular, has propagated a little further than its adiabatic counterpart and is weaker. The other initial forward shock fs2 is now much weaker and the initial reverse shock rs has almost disappeared. The trailing velocity pulse, in the region of its maximum amplitude, has steepened sufficiently to break with the subsequent formation of a new reverse shock rs′. Thus, by some 36 AU, the initially square pulse representation of a high-speed stream has evolved asymptotically to a double forward- reverse shock pair, very similar structurally to the evolved blast wave structure of Figure 9.2 for the pickup ion mediated heliosphere example.

A basic conclusion to emerge from the Zank and Pauls (1997) study is that interplanetary shock propagation in the outer heliosphere needs to be revisited. The transition from an inner heliosphere (the ionization cavity) to an outer heliosphere dominated by pickup ions leads to dynamical changes in shock evolution. Additional structure can be generated, and the damping/attenuation properties of shocks change. The variation in density fluctuations is not likely to be as well correlated with velocity fluctuation variation in the outer heliosphere as in the inner.

Whang et al. (1995) did not present as detailed an analysis of shock propagation in a pickup ion mediated heliosphere, but they did consider briefly the propagation of a GMIR (a global merged interaction region). They noted that pickup ions increased the temperature, and hence sound speed, so leading to a reduction in Mach number and hence a weakening of the associated shock wave.

9.2. Response of the termination shock to interplanetary disturbances: gas dynamics

Fluctuations in the dynamical pressure of the solar wind result from the presence of interplanetary shock waves or density irregularities. The termination shock responds to collisions with, for example, interplanetary shock waves, by being set into motion. Besides the possibility that the termination shock may pass across a spacecraft several times in the far outer heliosphere, it is not obvious that the resulting structure will identified easily as the termination shock. To properly understand the dynamical response of the termination shock to interplanetary disturbances would require a fully 3D magnetized multi-fluid model (in which the solar wind plasma, pickup ions, interstellar neutrals, and both anomalous and galactic cosmic-rays are treated distinctly). To date, however, this has not been attempted although individual aspects of this program have been considered.

Since a global model is difficult to implement for many problems, one is forced to make certain simplifying assumptions. We are interested in the interaction of the termination shock with interplanetary disturbances and not the complete interaction of the solar wind with the LISM. For this reason, it is assumed typically that the termination shock is stationary with a given strength. In this way, discussion of the heliopause and bow interaction is avoided, and only the states upstream and downstream of the 1D termination shock are considered.

9.2.1. *Analytic Models*

Several analytic and quasi-analytic models have been introduced to study the response of the heliospheric termination shock to interplanetary disturbances. These fall into two categories. The first uses a kinematic model of solar wind temporal disturbances and then calculates the variation in the termination shock location R_{TS} assuming pressure balance between the solar wind and LISM (Seuss, 1990; Belcher et al., 1993). Alternatively, one may analyse the 1D motion of the termination shock using the appropriate Rankine–Hugoniot conditions to determine the post-interaction velocities of the termination shock and the incident disturbance (Barnes, 1993; Naidu and Barnes, 1994a).

Within the termination shock, the solar wind ram pressure essentially balances the LISM pressure, thus

$$\rho_0 u^2 / R_{\mathrm{TS}}^2 \simeq p_{\mathrm{LISM}} \,, \tag{257}$$

where ρ_0 is the solar wind density at 1 AU. Hence,

$$R_{\mathrm{TS}} \propto \rho_0^{1/2} u \,, \tag{258}$$

indicating that the TS location R_{TS} responds more strongly to fluctuations in velocity than in density. Seuss (1990) and Belcher et al. (1993) use (257) to calculate the kinematic variation of R_{TS} in response to interplanetary disturbances. Shown in Figure 9.5 are one day averages of solar wind speed and density as a function of time, taken from Voyager 2 observations. The instantaneous response of the shock is illustrated in Figure 9.6. Clearly, the quasi-static estimate of the TS distance R_{TS} in response to solar wind fluctuations is unreasonable, requiring on occasion relativistic termination shock motions. Belcher et al. (1993) therefore impose an upper limit of 200 km s^{-1} on the speed of the TS, either inward or outward. Three quite different initial starting starting times are chosen for the kinematic model of Belcher et al., corresponding to the dashed, dash-dot, and solid lines plotted in Figure 9.6. All three models converge asymptotically to a similar value of R_{TS} in the middle of 1993. Based on the simplified analysis, maximum termination shock excursions of $\sim$ 27 AU are found to occur. Seuss (1993) arrived at a similar result based on a slightly more sophisticated kinematic model which allowed the TS to accelerate and decelerate.

While the kinematic models evidently suggest that the termination shock is likely to move possibly substantial distances in response to temporal variations

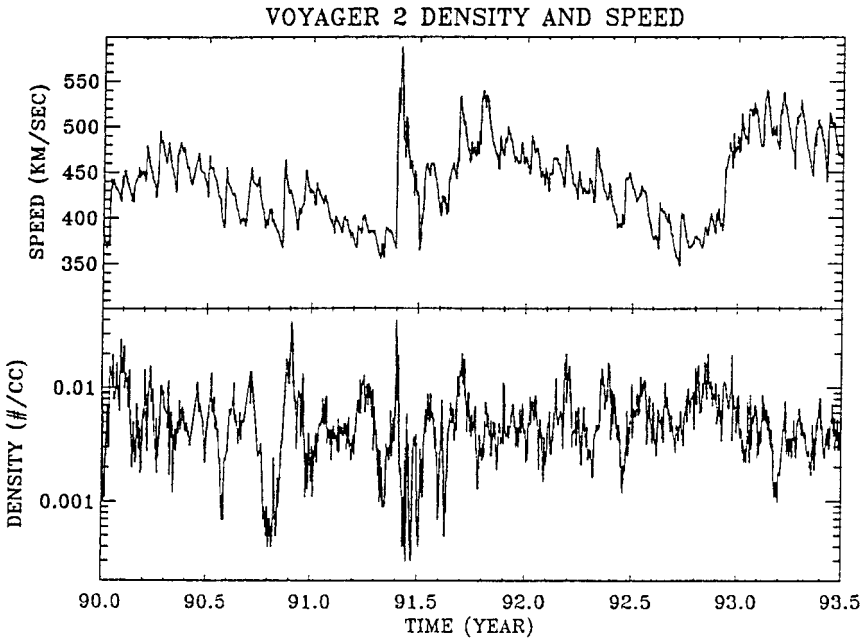

Figure 9.5. One-day averages of solar wind density and speed versus time, from January 3, 1990 to June 30, 1993 (Belcher et al., 1993.)

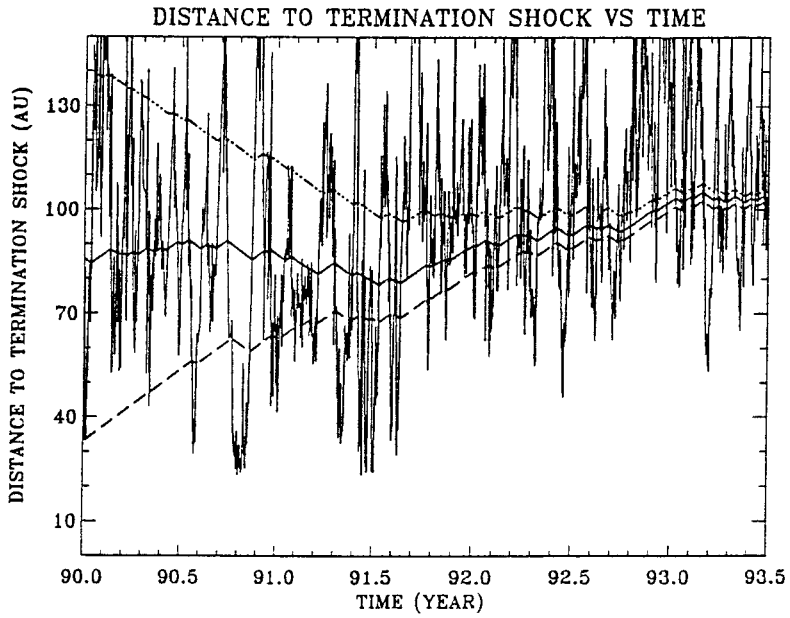

Figure 9.6. Distance to the TS as a function of time, from January 3, 1990 to June 30, 1993, based on an instantaneous response of the shock to variations in ram pressure. Also shown, as smooth curves, are the positions of the shock based on model calculations described in the text (Belcher et al., 1993.)

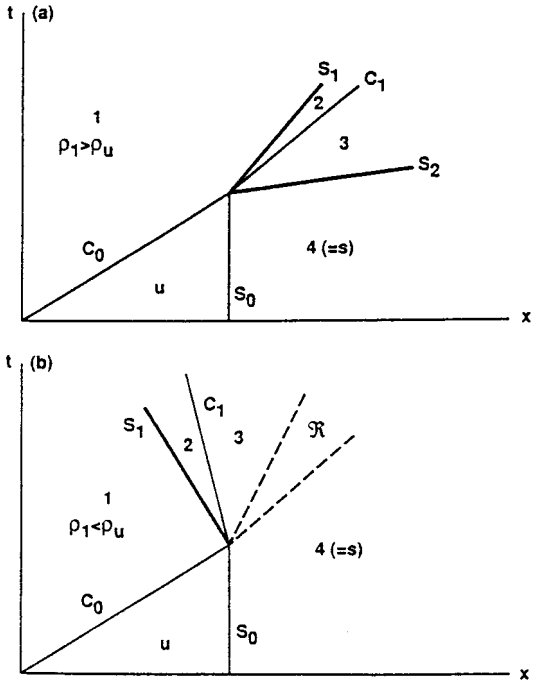

Figure 9.7. (a) Schematic representation in the $x - t$ plane of the interaction of an upstream contact discontinuity C_0 with the termination shock S_0 when $\rho_1 > \rho_u$. After the interaction, two outwardly propagating shock waves S_1 and S_2 result, separated by a contact discontinuity C_1. (b) The same but now for $\rho_1 < \rho_u$. After the collision, there is a single inwardly propagating shock, a contact discontinuity and a simple wave rarefaction $\mathcal{R}$ propagating into the heliosheath (Barnes, 1993.)

in the solar wind, such an approach is clearly extremely limited. Barnes (1993) has considered the response of the TS to solar wind density variations (specifically a contact discontinuity), and has extended this to incident interplanetary shocks (Naidu and Barnes, 1994a). In view of (258), we shall follow the analysis of Naidu and Barnes (1994a), although the contact discontinuity results presented by Barnes (1993) are very similar.

Consider an initially stationary termination shock S_0 (a reverse shock) and let S_i represent an interplanetary forward or reverse shock. Let ρ_u, u_u, p_u and $C_u^2 = \gamma p_u/\rho_u$ denote the fluid variables upstream of S_0, and let ρ_s, u_s, p_s and C_s^2 represent the corresponding downstream variables. Let $M_{u0} \equiv u_u/C_u$ be the Mach number upstream of S_0 and M_{ui} the Mach number upstream of S_i. Clearly, $M_{ui} > 1$ for a forward shock and $M_{ui} < 1$ for a reverse shock. Let the dynamical variables upstream of S_i be distinguished by the subscript 1.

From characteristic theory, one can infer the post-interaction state (Barnes, 1993). In the stationary frame of the TS, the interplanetary shock or contact discontinuity and TS collide at some time t. Thereafter, depending on the ratio ρ_1/ρ_u ($\lessgtr 1$), one has the following possibilities (illustrated graphically in Figure 9.7). (1)

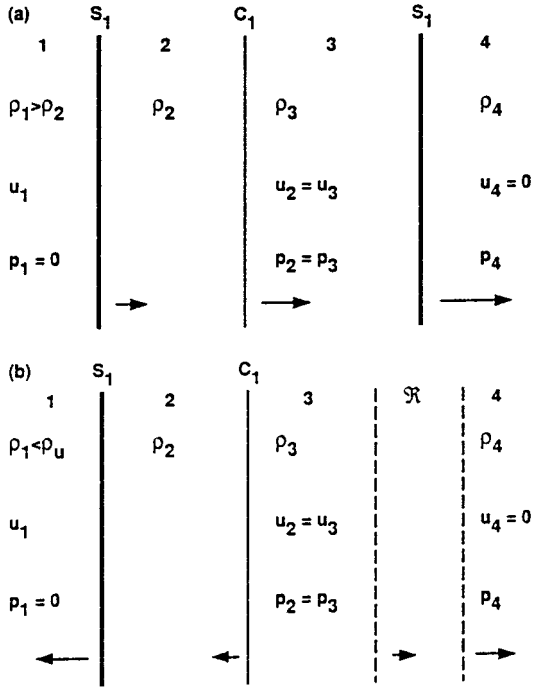

Figure 9.8. Schematic representation of the post-interaction geometry for a reference frame in which the far-downstream gas (at the right of the diagram) is at rest. Arrows indicate the propagation direction of shocks, contact discontinuities and rarefaction fronts. (a) Condition $\rho_1 > \rho_u$. Region 1 contains the unshocked solar wind gas, which passes through the shock S_1 into region 2. Region 2 is separated from region 3 by the contact discontinuity C_1. The shock S_2 propagates into the heliosheath region. (b) Condition $\rho_1 < \rho_u$. The transition between regions 3 and 4 is now accomplished by a rarefaction $\mathcal{R}$ rather than a shock (Barnes, 1993.)

If $\rho_1/\rho_u > 1$, then the post-collision state consists of two outwardly moving shock waves separated by a contact discontinuity. The left shock S_1 corresponds to the displaced strong TS and the right shock S_2 is the transmitted shock propagating into the subsonic heliosheath. (2) If $\rho_1/\rho_u < 1$, the the termination shock S_1 moves inward while a simple wave rarefaction $\mathcal{R}$ propagates into the subsonic flow. Again, a contact discontinuity separates the two states. Possibilities (1) and (2) are shown schematically in Figure 9.8.

A straightforward, if somewhat tedious, calculation allows one to determine the post-shock speed of S_1. The final evaluation of the nonlinear algebraic equation has to be done numerically. Plots of the TS velocity V_1 as a function of ρ_1/ρ_u for various M_{u0} values are illustrated in Figure 9.9. Also shown is the velocity V_2 of the second shock S_2 (if $\rho_1/\rho_u > 1$) or rarefaction (if $\rho_1/\rho_u < 1$). Evidently, if $\rho_1 > \rho_u$, the TS moves outward, whereas for $\rho_1 < \rho_u$, the TS moves inward for reasonable values of M_{u0}. The speed of the termination shock for this simple planar model can be as much as 80–100 km s^{-1} for rather modest compression ratios ρ_1/ρ_u.

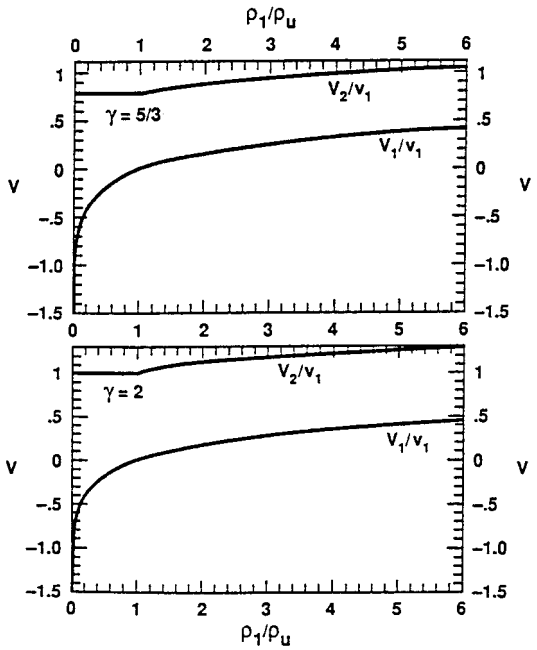

Figure 9.9. Plots of V_1 and V_2 as functions of ρ_1/ρ_u for $\gamma = 5/3$ and $\gamma = 2$. The velocities are computed in the pre-interaction rest frame of the termination shock and scaled to the upstream solar wind speed. V_1 is the velocity of the post-interaction termination shock S_1, and V_2 the velocity of either the rarefaction front (if $\rho_1 < \rho_u$) or the transmitted shock S_2 (if $\rho_1 > \rho_u$) (Barnes, 1993.)

The speed of the emitted shock is predicted to be far larger. The results of Naidu and Barnes (1994a) confirm the simpler analysis of Barnes (1993) in all essential respects.

9.2.2. *Numerical Simulations*

Barnes (1993) and Naidu and Barnes (1994a) considered the interaction of a 1D gas dynamic termination shock with interplanetary disturbances. Their work is primarily analytic and, although quite valid, is limited to a relatively small number of TS-solar wind interactions, beyond which the algebra becomes progressively more complicated. Furthermore, they assume that the waves incident on the TS are perfect discontinuities, on either side of which are constant states. Such conditions are unlikely to prevail in the solar wind. In addition, the results of Barnes are essentially asymptotic in that they consider only the final state of the interaction. It is quite likely that Voyager will encounter the TS during a collision with an interplanetary disturbance. In this case, it will be necessary to understand the detailed structure of the TS region as it evolves. This requires extending the work of Barnes to situations that are not tractable analytically, and for which numerical simulations are necessary. In the context of gas dynamics, we discuss the work of Story and Zank (1995), Ratkiewicz et al. (1996), and Steinolfson (1994). Story and Zank (1995)

considered a planar 1D model, Ratkiewicz et al. (1996) a spherically symmetric 1D model, and Steinolfson (1994) a 2D model. The models are all based on the single-fluid gas dynamic equations (239)–(241) i.e., without the source terms.

Story and Zank (1995) consider the interaction of a Mach 10 gas dynamic termination shock with an increased momentum flux, either in the form of a Gaussian-shaped density pulse advecting into the TS or a Gaussian-shaped 'shock' colliding with the TS. The result of both collisions is the production of two waves which propagate downstream at different speeds. The first is a density spike, with no variation in the pressure or velocity, which is convected downstream at the flow speed. The second is an approximately triangular forward shock pulse leading the density spike. The strength of the secondary shock decreases with time according to the law (Landau and Lifshitz, 1979)

$$\delta v(t) = \frac{\delta v_0}{\sqrt{1 + \left(\frac{1}{2}(\gamma+1)\delta v_0/\ell_0\right) t}} \,, \tag{259}$$

where $\delta v(t)$ is the jump in velocity at the shock front, δv_0 and ℓ_0 are the initial velocity jump and width of the pulse, and the time t is measured from the initial formation of the pulse. It is apparent from the functional form of Equation (259) that for a given δv_0 and ℓ_0, the decay rate of the secondary shock increases with increasing adiabatic index. Similarly, the ratio $\delta v_0/\ell_0$ also controls the secondary shock decay rate.

As was discussed by Barnes (1993) originally, the reason for the similarity between the two collisions described above is that it is the change in the total upstream momentum flux,

$$\Pi \equiv p + \tfrac{1}{2}\rho u^2 \,, \tag{260}$$

that is important, rather than the dynamic or thermal pressure alone. Story and Zank (1995) describe the collision of the TS with both a density enhancement only (the variation in Π due to ρ only) and an incident shock (variation in thermal pressure, velocity and density). They also discuss the role of different values of γ (which can affect p).

Following Story and Zank (1995), consider the collision of a square-shaped density pulse with a Mach 10 termination shock. This allows the detailed dynamics of the collision to be examined more easily. The various stages in the evolution are illustrated in Figure 9.10. The first collision is of $cd2$ with the TS, which results in the production of a forward shock fs' another contact discontinuity cd', and another reverse shock, the once-modified termination shock TS′. This structure propagates downstream until $cd1$ collides with TS′. Since TS′ experiences a decrease in the upstream momentum flux, this collision results in a twice-modified and nearly final termination shock TS″, a rarefaction wave r'', behind which trails a contact discontinuity cd''. The rarefaction wave catches up with and modifies cd', resulting in mcd''. The interaction of r'' with cd' is actually more complicated than

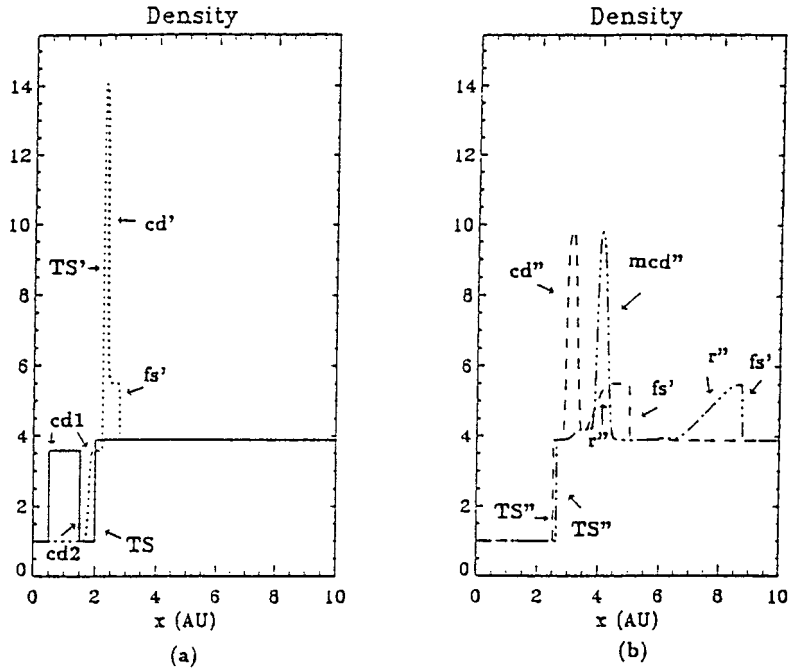

Figure 9.10. Density profiles for the collision of a square density pulse with a Mach 10 termination shock. (a) The initial condition (solid line) and the evolved solution (dotted line). (b) Continued evolution of the dotted line solution of (a). The dashed line is at an earlier time than the dot-dashed line (Story and Zank, 1995.)

this, but the end result is apparent. The r'' then chases and catches fs'. Once the rarefaction reaches fs', the two waves merge into a triangular shock pulse, which then decays. There are no significant differences between the square-pulse example and a Gaussian density pulse. Both collisions result in the production of a density spike and decaying forward shock pulse.

Shown in Figure 9.11 is the speed of the termination shock $V(t)$ as a function of time from the moment a Gaussian density pulse collides with the TS. In the planar 1D simulation, the TS moves a distance of $\sim$ 0.3 AU before coming to rest again. The TS took $\sim$ 17 days to stop moving, and had a peak velocity of ~ 0.07 AU day$^{-1} \simeq 120$ km s^{-1}. The initial compression accelerates the TS away from the impinging pulse. Since the TS is now moving in the same direction as the unshocked portion of the pulse, it takes longer to catch the TS, and so the deceleration of the TS is more gradual than the acceleration. Consequently, the $V(t)$ profile of Figure 9.11 is asymmetric.

Dynamic pressure depletions, in the form of a pulse, colliding with the TS lead asymptotically to an inverse density spike and a triangular shock (Story and Zank, 1995).

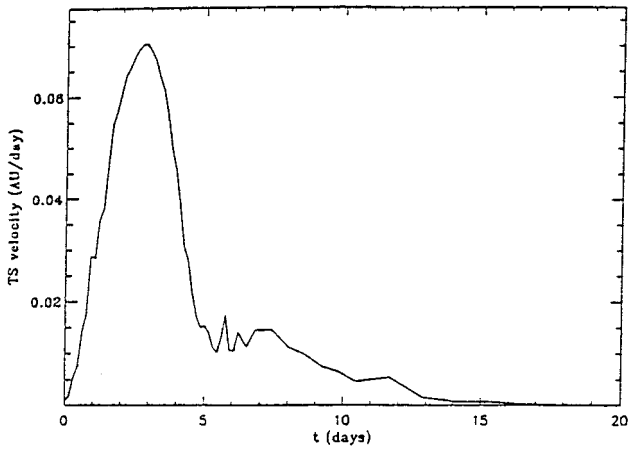

Figure 9.11. Speed of the termination shock as a function of time starting from the point when a Gaussian density pulse first impinges on the initially stationary Mach 10 TS. Here $\gamma = \frac{5}{3}$ (Story and Zank, 1995.)

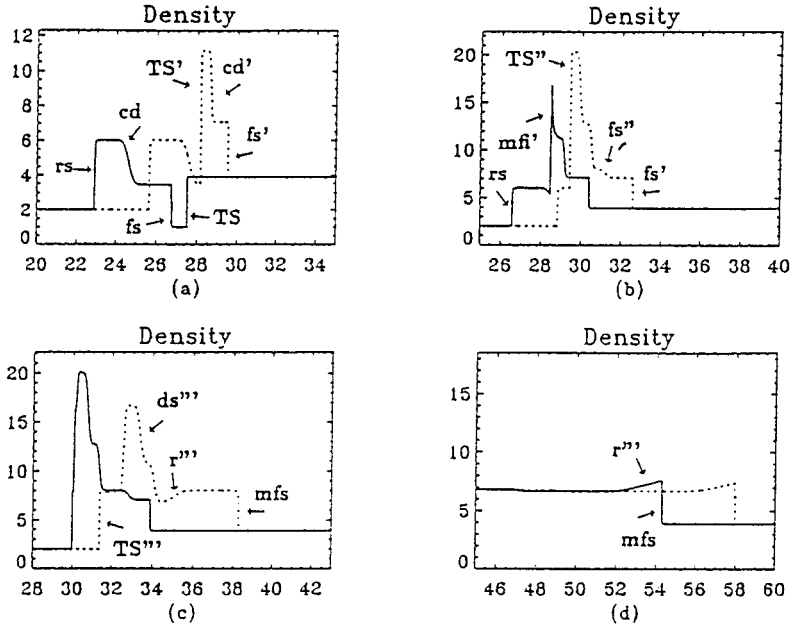

Figure 9.12. Density profile time sequence for the collision of a forward-reverse shock pair with a Mach 10 termination shock, for $\gamma = \frac{5}{3}$. In this example, the far upstream pressure and density are greater than those initially immediately upstream of the then stationary TS. In all figures, the sequence is from the solid to the dotted line, and from (a) to (d) (Story and Zank, 1995.)

More interesting is the collision of a forward-reverse shock pair with the TS (Story and Zank, 1995). Only one case is illustrated, shown in Figure 9.12. Such collisions between the termination shock and compound structures are very complex, and Figure 9.12 shows a time sequence of the interaction. There are three primary collisions. First, the forward shock fs collides with TS, producing the state depicted by the dotted line of Figure 9.12(a). This produces a modified termination shock TS′, a contact discontinuity cd', and a forward shock fs', all moving in a downstream direction. In the second primary collision, cd convects into TS′, producing mfi' (Figure 9.12(b)). In principle, mfi' is composed of a forward shock and contact discontinuity, although this is not easily seen in in Figure 9.12(b). The dotted line solution in Figure 9.12(b) shows the shock portion of mfi' emerging out of cd' after the two have interacted, and is labeled fs''. In fact, the collision of mfi' with cd' should result in a forward shock fs'', a contact discontinuity, and a rarefaction. The rarefaction in this case propagates to the left in the frame of fs'' and is not seen because it quickly interacts with the various density structures in the same region. Eventually, fs'' merges with fs', forming a single stronger shock mfs, illustrated in Figure 9.12(c). Also shown in Figure 9.12(c) is the collision of the reverse shock rs with TS″. A collision of this type produces a modified termination shock TS‴, a contact discontinuity, and a rarefaction. The contact discontinuity adds to the complicated density structure seen in Figure 9.12(c) (labelled ds'''), and the rarefaction r''' propagates through all structures between it and mfs. Eventually, of course, the rarefaction catches up with mfs (Figure 9.12(d), where the remaining solution is not shown), yielding a damped triangular shock. The net result of the complete interaction is a damped forward shock propagating downstream, a very large density enhancement ($\sim$ 16 times the incident solar wind density), and a modification of the original termination shock strength and speed.

Ratkiewicz et al. (1996) extended the 1D planar studies described above by considering interactions of interplanetary disturbances with the TS in the context of a spherically symmetric 1D model. Such a model, while obviously not entirely realistic, provides more insight into the manner in which the termination shock equilibrates after a collision with an interplanetary disturbance. The model requires an outer boundary (a proxy for the heliopause), which acts to reflect disturbances transmitted through the termination shock back to TS. Multiple reflection of waves between the outer boundary and the TS can set up an effective 'ringing' of the outer heliosphere.

A steady-state spherically symmetric model is generated using an inner boundary at 30 AU ($n = 0.01$ cm^{-3}, $u = 400$ km s^{-1} and $T = 9 \times 10^3$ K) and an outer boundary at 400 AU (by specifying a LISM pressure p_∞).

Since a contact discontinuity colliding with the termination shock leads to a qualitatively similar response as that of an incident shock wave, we discuss here the former case only. Plate 9.1 illustrates the results of a density enhancement colliding with the TS in a contour plot format, as a function of radial distance and time. Contour intervals are the ratios with respect to the upstream solar wind parameters

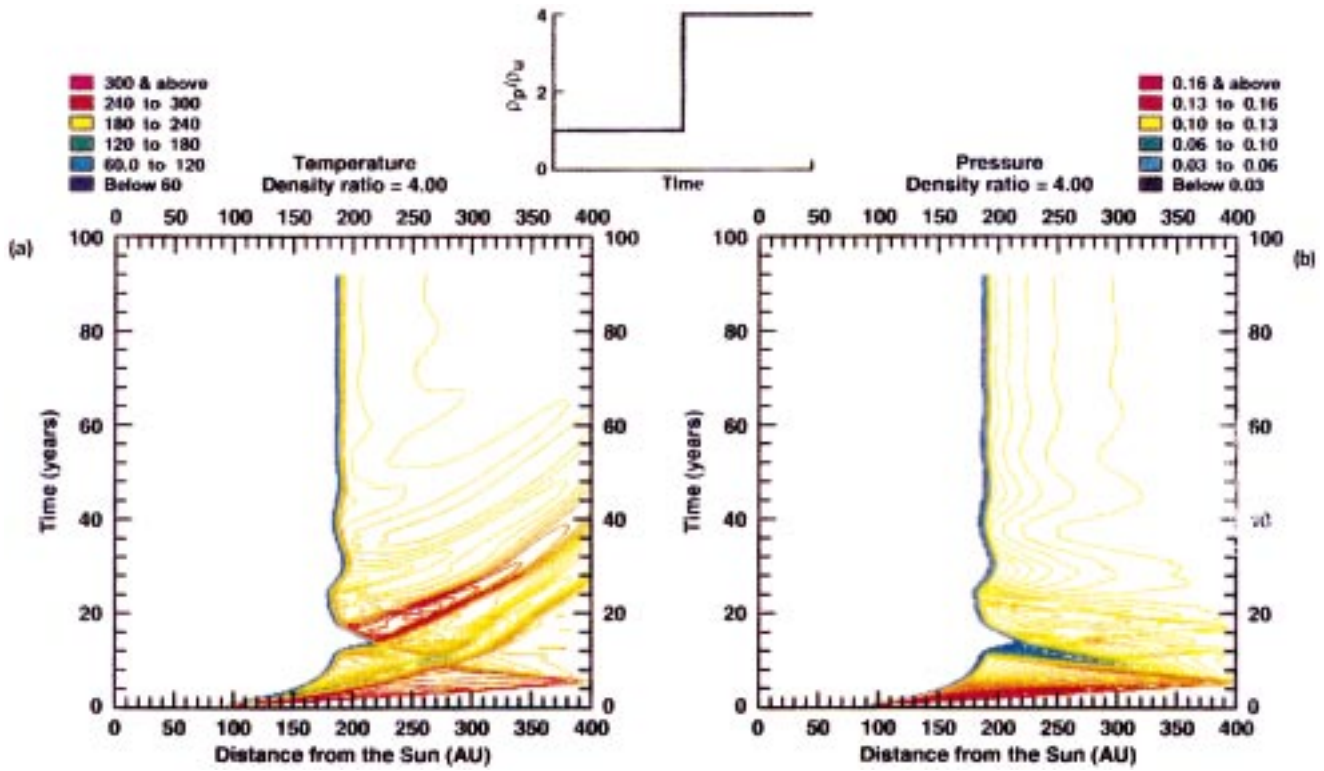

Plate 9.1. (a) Temperature and (b) pressure contour plots. Single density jump at the inner boundary of $\rho_2/\rho_1 = 4$. The outer boundary is located at 400 AU (Ratkiewicz et al., 1996.)

at 30 AU. After the interaction, two shock waves propagate outward – the displaced TS and the emitted forward shock, with a contact discontinuity separating them. Before the TS can settle into a new equilibrium, however, a reflected rarefaction (from the outer boundary) collides with the TS, leading to further outward motion. A period of 'bouncing' occurs for the termination shock, with the oscillations damping away as a new equilibrium is attained. That the wave reflected from the outer boundary is a rarefaction is a consequence of assuming a fixed boundary pressure and different boundary conditions may well yield different results. The initial speeds of the perturbed TS and the emitted shock are consistent with the analytical estimates of Barnes (1993).

The 2D response of the termination shock to solar wind disturbances has been addressed by Steinolfson (1994) and Karmesin et al. (1995). The latter paper was discussed briefly in Section 5.3.1 in the context of a variable solar wind ram pressure. Steinolfson (1994) initiated large-scale velocity fluctuations at an inner (10 AU) radial boundary for a one-shock model. The amplitude of the velocity fluctuations was chosen to be 100 km s^{-1}, with a solar wind speed that varied between 200 and 400 km s^{-1} at the boundary with a periodicity of 180 days. The TS oscillates at the same period in response to the variation in ram pressure and the amplitude of the TS motion is $\sim$ 1 AU. The amplitude of the downstream oscillations is substantial (Figure 9.13) but these do not propagate through the heliopause into the LISM apparently. Such displacements of the TS are far smaller than predicted by the analytic models of Barnes (1993) and Naidu and Barnes (1994a), but these estimates were based on step-like discontinuities. The distance moved by the TS appears to more in accord with the shock pulse model interactions described by Story and Zank (1995), where typical TS movements were $\sim$ 0.5 AU.

9.3. RESPONSE OF THE TERMINATION SHOCK TO INTERPLANETARY DISTURBANCES: MHD

The results of Section 9.2 have been extended to MHD, both analytically and numerically. Since the results are not very different in their basic conclusions from those of the gas dynamic models, and since the plasma beta is expected to be large in the outer heliosphere, our discussion here is somewhat brief.

9.3.1. *Analytic Models*

MHD extensions to the analytic models described above have been presented by Naidu and Barnes (1994b), while Baranov et al. (1996) considered a 2D MHD model of the oblique interaction between an interplanetary shock and the TS.

Barnes (1993) observed that for the special case of $\gamma = 2$, the MHD results are isomorphic to the gas dynamic results for flows perpendicular to the magnetic field. Matters are, however, more complicated for other values of γ. Naidu and Barnes (1994b) consider the interaction of a tangential discontinuity with a perpendicular termination shock. Considering only this simpler case is justifiable

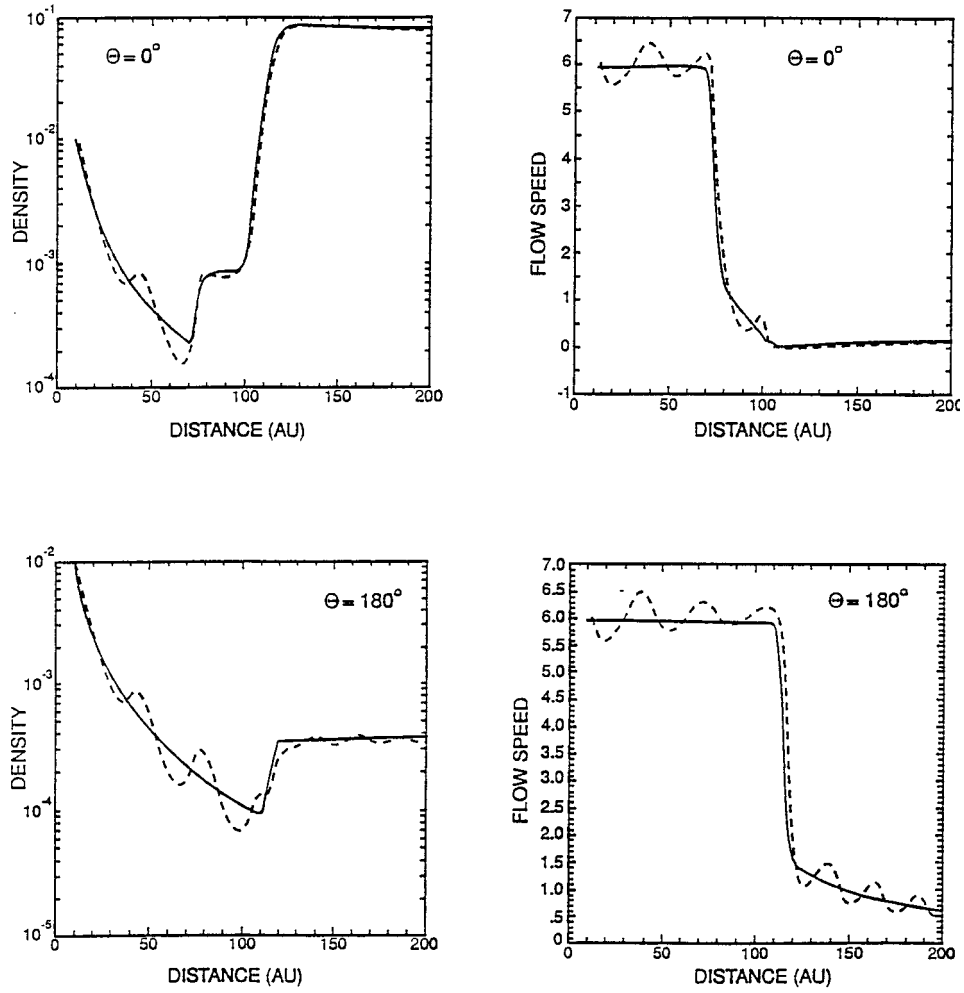

Figure 9.13. Spatial fluctuations in the density and flow speed along the poles ($\theta = 0°, 180°$) at the end of a 2D gas dynamic simulation (dashed lines) superimposed on the stationary equilibrium state (solid lines) (Steinolfson, 1994.)

since, asymptotically, the post-interaction configuration depends primarily on the dynamic pressure associated with the tangential discontinuity.

The Rankine–Hugoniot conditions for a perpendicular shock moving with velocity $V_s\hat{e}_x$ are

$$
\begin{aligned}
&[\rho\,(u - V_s)] = 0\,, \\
&\left[\rho\,(u - V_s)^2 + p + B^2/2\mu\right] = 0\,, \\
&\left[\left(\frac{1}{2}\rho\,(u - V_s)^2 + \frac{\gamma}{\gamma - 1}p + \frac{B^2}{2\mu}\right)(u - V_s)\right] = 0\,, \\
&[B\,(u - V_s)] = 0\,,
\end{aligned}
\tag{261}
$$

where, as usual, the square brackets denote the jump across the shock. For the tangential discontinuity, stationary in the solar wind frame, the jump conditions are simply

$$
[u] = 0\,, \qquad \left[p + B^2/2\mu\right] = 0\,. \tag{262}
$$

Suppose that the termination shock S_0 is at rest initially, with a given upstream state $\Psi_u = (\rho_u, u_u, p_u, B_u)$ and far downstream state Ψ_0. The incident tangential discontinuity T_0 is characterized by Ψ_1. Figure 9.14 illustrates the two possible configurations for the final state, and, as before, the primary factor determining the final state is the ratio ρ_1/ρ_u (Barnes, 1993). If $\rho_1/\rho_u > 1$, then two outwardly propagating shocks, S_1 and S_2, result, separated by a tangential discontinuity T_1. S_1 is the new termination shock. If, however, $\rho_1/\rho_u < 1$, then only S_1, the new termination shock, results and it propagates inward. A tangential discontinuity T_1 and an MHD simple wave $\mathcal{R}$ propagate into the heliosheath. Since the magnetic field is assumed to be transverse, $\mathcal{R}$ is a fast rarefaction wave. The post-interaction geometry for the two possibilities is illustrated in Figure 9.15. The basic calculation is outlined in Naidu and Barnes (1994b).

There are four free parameters in the analysis of Naidu and Barnes (1994b), M_{fu0} (the upstream fast magnetosonic Mach number), ρ_1/ρ_u, β_u, and β_1. For a fixed Mach number and upstream plasma beta M_{fu0} and β_u, Naidu and Barnes (1994b) find that the variation in TS velocity V_1 as a function of ρ_1/ρ_u scarcely depends on the value of β_1, the change in the plasma beta across the tangential discontinuity. Similarly, the same is true of V_1 when M_{fu0} and β_1 are held fixed and β_u is varied. This suggests that termination shock motion may be relatively insensitive to the pressure of pickup ions in the solar wind. By contrast, when β_u and β_1 are held fixed and M_{fu0} is varied, much larger variations in V_1 and V_2 result. This is illustrated in Figure 9.16.

The basic results of the Naidu and Barnes (1994b) analysis are very similar to the simpler gas dynamic case, and the new termination shock attains speeds that are typically $\sim$ 100 km s^{-1}. Thus, MHD, at least in a perpendicular geometry, does not significantly change the response of the TS to upstream disturbances by comparison with gas dynamic models.

For large, extended interplanetary shocks, the interaction with the termination shock cannot be regarded as planar and the problem becomes at least 2D. Thus, one needs to solve instead the more complicated shock interaction problem illustrated

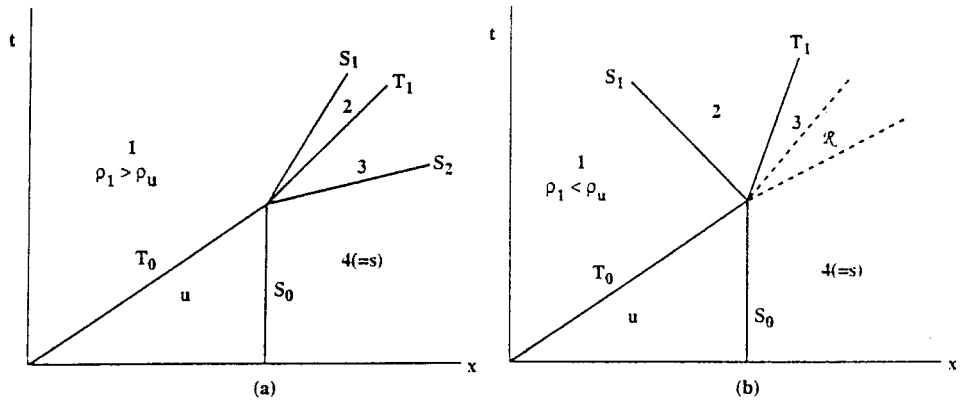

Figure 9.14. (a) Schematic representation in the $x - t$ plane of the interaction of an upstream tangential discontinuity T_0 with the termination shock S_0 when $\rho_1 > \rho_u$. After the interaction, two outwardly propagating shock waves S_1 and S_2 result, separated by a tangential discontinuity T_1. (b) The same but now for $\rho_1 < \rho_u$. After the collision, there is a single inwardly propagating shock, a tangential discontinuity and a simple wave rarefaction $\mathcal{R}$ propagating into the heliosheath (Naidu and Barnes, 1994.)

in Figure 9.17. Barmin and Pushkar (1991) and Pushkar (1995) formulated an analytical-numerical technique for solving the steady-state MHD equations subject to the Rankine-Hugoniot conditions for an oblique shock. This approach was used by Baranov et al. (1996) to examine the interaction of interplanetary disturbances with the TS. The gas dynamic model of Baranov and Malama (1993) was used to prescribe the TS geometry initially. The solution to the interaction problem is determined by the dimensionless parameters

$$M_{\rm TS}, \quad M_{\rm IPS}, \quad \beta, \quad \theta, \quad \text{and} \quad \psi_{\rm TS}\,,$$

which denote the upstream solar wind Mach number (or TS Mach number), the interplanetary shock Mach number, the plasma beta, the angle between the interacting shock and the termination shock, and finally the angle between the TS and the interplanetary magnetic field (Figure 9.17). Baranov et al. (1996) used the method of Pushkar (1995) to solve a set of ordinary differential and algebraic equations for the final MHD state.

Since the number of possible MHD waves is large, the final state after an interplanetary shock and the TS collide can depend sensitively on the parameters (263). For small angles $\psi_{\rm TS} < 40°$, Baranov et al. (1996) find that the collision of a forward interplanetary shock with the TS yields no Alfvén discontinuities, and that the flow corresponds to one of the following diagrams,

$$\overset{\rm TS}{\rightarrow}\ \overset{\rm IPS}{\leftarrow\!\!\Rightarrow}\ \overset{\rm IPS'}{\leftarrow}\ \overset{R^-}{\leftarrow}\ C\ \overset{S^-}{\rightarrow}\ \overset{\rm TS'}{\rightarrow}; \tag{264}$$

$$\overset{\rm TS}{\rightarrow}\ \overset{\rm IPS}{\leftarrow\!\!\Rightarrow}\ \overset{\rm IPS'}{\leftarrow}\ \overset{R^-}{\leftarrow}\ C\ \overset{R^-}{\rightarrow}\ \overset{\rm TS'}{\rightarrow}\ ; \tag{265}$$

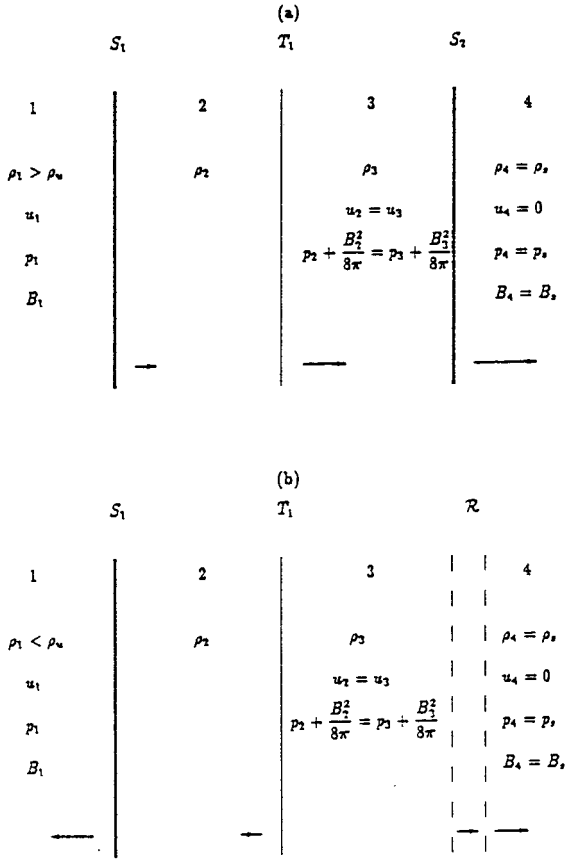

Figure 9.15. Schematic representation of the post-interaction geometry for a reference frame in which the far-downstream gas (at the right of the diagram) is at rest. Arrows indicate the propagation direction of shocks, tangential discontinuities and rarefaction fronts. (a) Condition $\rho_1 > \rho_u$. Region 1 contains the unshocked solar wind gas, which passes through the shock S_1 into region 2. Region 2 is separated from region 3 by the tangential discontinuity T_1. The weak shock S_2 propagates into the heliosheath region. (b) Condition $\rho_1 < \rho_u$. The transition between regions 3 and 4 is now accomplished by an MHD rarefaction wave $\mathcal{R}$ rather than a shock (Naidu and Barnes, 1994.)

$$\overset{\text{TS}}{\rightarrow}\ \overset{\text{IPS}}{\leftarrow\!\!\Rightarrow}\ \overset{\text{IPS}'}{\leftarrow}\ \overset{S^-}{\leftarrow}\ C\ \overset{R^-}{\rightarrow}\ \overset{\text{TS}'}{\rightarrow}\ ; \tag{266}$$

$$\overset{\text{TS}}{\rightarrow}\ \overset{\text{IPS}}{\leftarrow\!\!\Rightarrow}\ \overset{\text{IPS}'}{\leftarrow}\ \overset{S^-}{\leftarrow}\ C\ \overset{S^-}{\rightarrow}\ \overset{\text{TS}'}{\rightarrow}\ . \tag{267}$$

In (264)–(267), the arrows depict the direction of the wave motion with respect to the solar wind (Figure 9.17(a)), the primes denote the post-interaction state, $R^{\pm}$ denotes a fast/slow rarefaction, IPS an interplanetary shock, and S^- and C denote an MHD slow mode shock and a contact discontinuity respectively. The situation (267) appears to occur rarely. Which of the remaining three cases occurs depends on the value of θ and the remaining parameters in a way that is not obvious.

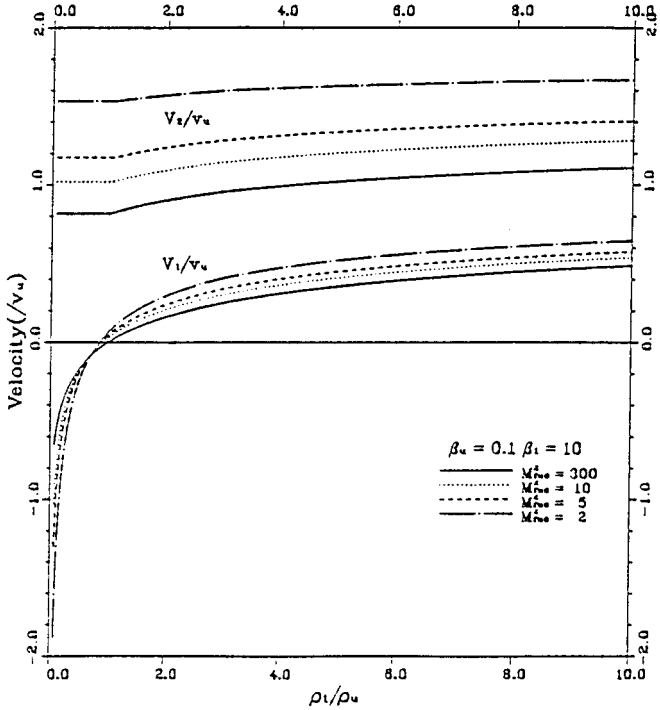

Figure 9.16. Plots of V_1/u_u and V_2/u_u as a function of ρ_1/ρ_u for various values of M^2_{fu0} with $\beta_u = 0.1$ and $\beta_1 = 10$ (Naidu and Barnes, 1994.)

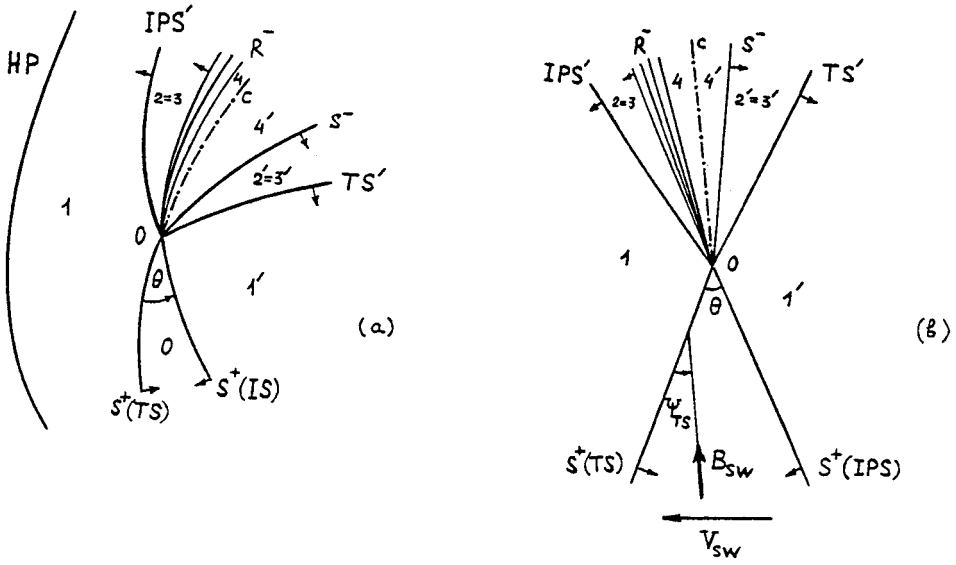

Figure 9.17. (a) Depiction of the 2D interaction of an interplanetary shock IPS colliding with the TS. θ is the angle between the interacting shocks and $\psi_{\rm TS}$ the angle between the TS and the IMF. (b) The pattern of characteristics in the neighbourhood of the intersection point of S^+(TS) and S^+(IPS) (Baranov et al., 1996.)

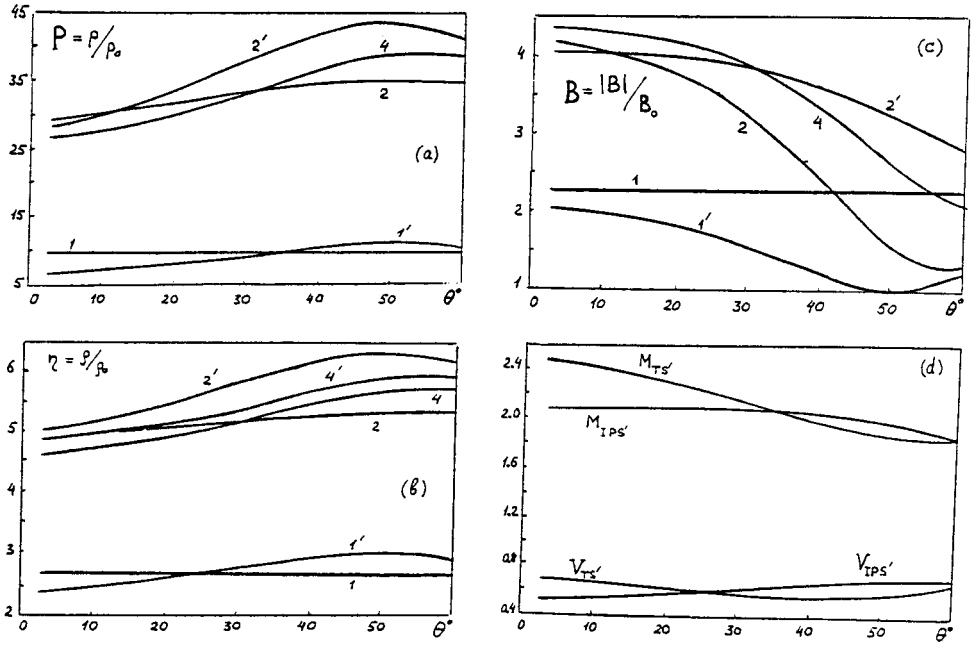

Figure 9.18. The plasma parameters and magnetic field strength behind the discontinuities generated by the collision of of the TS with an interplanetary shock, using $M_{\rm TS} = 3.5$, $M_{IPS} = 3$, $\beta = 1$, $\psi_{\rm TS} = 40°$, and $\gamma = 5/3$. The numbers on the curves correspond to the states in the sense illustrated in Figure 9.17. All quantities have been normalized by the value of the corresponding parameter in the undisturbed solar wind just upstream of the TS (Baranov et al., 1996.)

For large values of $\psi_{\rm TS} \geq\sim 65° - \sim 85°$, the post-interaction flow can include Alfvén discontinuities. Six post-interaction states corresponding to the interaction $\overset{\rm TS}{\rightarrow}\ \overset{\rm IPS}{\leftarrow}$ are now possible (Baranov et al., 1996). Shown in Figure 9.18 is an example of the variation in the plasma beta with the angle θ for $M_{\rm TS} = 3.5$, $M_{\rm IPS} = 3$, $\beta = 1$, and $\psi_{\rm TS} = 40°$. No Alfvén discontinuities are present. The numbering of the curves corresponds to the states behind the wave according to $1 \rightarrow \overset{\rm TS}{\rightarrow}$, $2 \rightarrow \overset{\rm IPS'}{\leftarrow}$, $4 \rightarrow \overset{R^-}{\leftarrow}$ or $\overset{S^-}{\leftarrow}$, $1' \rightarrow \overset{\rm IPS}{\leftarrow}$, $2' \rightarrow \overset{\rm TS'}{\rightarrow}$, and $4' \rightarrow \overset{R}{\rightarrow}$ or $\overset{S^-}{\rightarrow}$. Curves 4 and $4'$ represent the state at different sides of the contact discontinuity C. Hence, with the exception of Figure 9.18(b), 4 and $4'$ coincide since only the density changes across a contact discontinuity. The Mach numbers and normalized (to the solar wind speed) velocities of TS′ and IPS′ are shown in Figure 9.18(d).

Baranov et al. (1996) conclude with an exhaustive study of the variation of the electron number density behind TS′, and the velocities $V_{\rm TS'}$ and $V_{\rm IPS'}$ as functions of θ for various values of the parameters (263). Figure 9.19 shows the dimensionless velocities $V_{\rm IPS'}$ (dashed-dotted lines) and $V_{\rm TS'}$ (dashed curves) as a function of θ for different values of $M_{\rm IPS}$ and $M_{\rm TS} = 5.5$, $\beta = 1$, and $\psi_{\rm TS} = 0$.

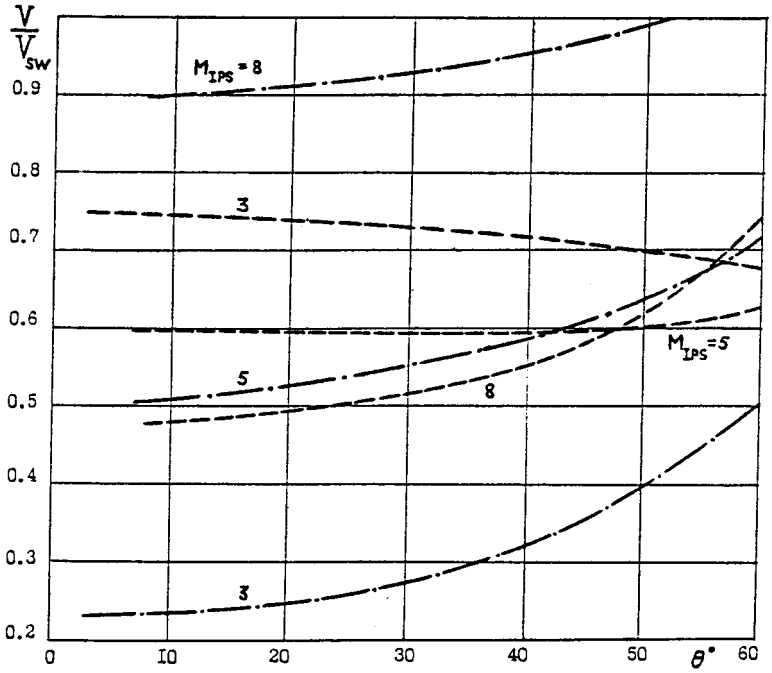

Figure 9.19. The dimensionless velocities of the reflected interplanetary shock ($V_{\mathrm{IPS}'}$, dash-dotted lines) and the new termination shock ($V_{\mathrm{TS}'}$, dashed lines) for $M_{\mathrm{TS}} = 5.5$, $\beta = 1$, $\psi_{\mathrm{TS}} = 0$, and $\gamma = 5/3$ (Baranov et al., 1996.)

9.3.2. *Numerical Simulations*

The response of an MHD termination shock to interplanetary disturbances has been considered numerically by Whang and Burlaga (1993), Whang et al. (1995), and Story and Zank (1997).

Whang and Burlaga (1993) and Whang et al. (1995) assume that the termination shock is a perpendicular MHD shock, for which the Rankine–Hugoniot relations are given by (261). The shock speed V_s, an unknown variable, is therefore related to the ratio of the jumps in mass flux and density, i.e.,

$$V_s = \frac{[\rho u]}{[\rho]} = \frac{r u_2 - u_1}{r - 1}\,, \tag{268}$$

where r is the shock compression ratio. In the downstream region of the TS, Whang et al. (1993, 1995) suggest that the gas dynamical Riemann invariants

$$J_{\pm} = \frac{2C_s}{\gamma - 1} \pm u = \text{const.}, \tag{269}$$

provide a constraint (specifically J_{-}) on the jump conditions at the termination shock. The gas dynamic Riemann invariant is approximately valid downstream since the plasma beta satisfies $\beta \gg 1$.

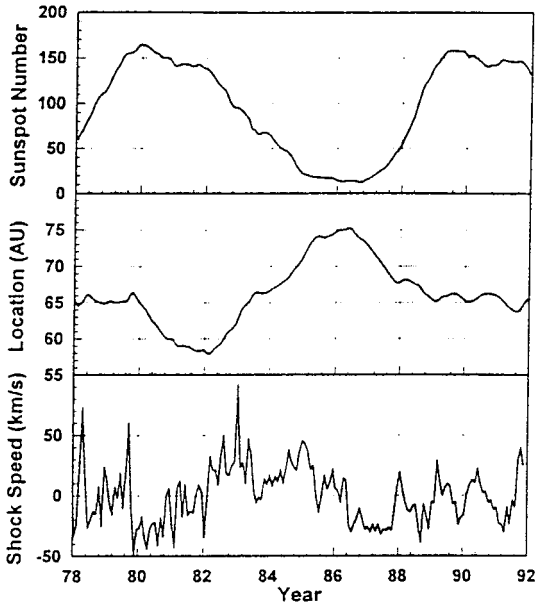

Figure 9.20. Temporal variations of the shock distance R in 1978–1991. The termination shock location is anti-correlated with the sunspot number (Whang et al., 1995.)

On the basis of (261), (268) and (269), Whang et al. (1995) determine the temporal variation in the TS speed V_s and location in response to upstream interplanetary disturbances. The results are plotted in Figure 9.20, together with the sunspot number. Responding to upstream solar wind fluctuations, the termination shock is in motion on timescales greater than the solar rotation period. The shock speed V_s can have relatively large values but the absolute mean speed is ~ 19 km s^{-1}. The location of the TS is anti-correlated with sunspot number.

During the declining phase of the solar cycle, the solar wind has a relatively high speed and the TS moves outward on average. The maximum heliocentric distance of the TS from the sun occurs near solar maximum. Since the solar wind has relatively low average speed during the rising phase of the solar cycle, the TS moves inward on average during this period.

Finally, Whang et al. (1995) consider the interaction of a GMIR (a Global Merged Interaction Region) with the termination shock and heliopause. The leading edge of the GMIR is a strong forward shock, followed by several large increases in the solar wind velocity and magnetic field. Both the TS and transmitted GMIR are weakened after the collision, and the plasma flow between the shocks is separated by a tangential discontinuity.

The most detailed analysis of the MHD wave modes and shock structure generated by the interaction of the termination shock with interplanetary disturbances has been presented by Story and Zank (1997). These authors use a 1D MHD numerical model for both transverse and oblique shocks. The inclusion of a parallel

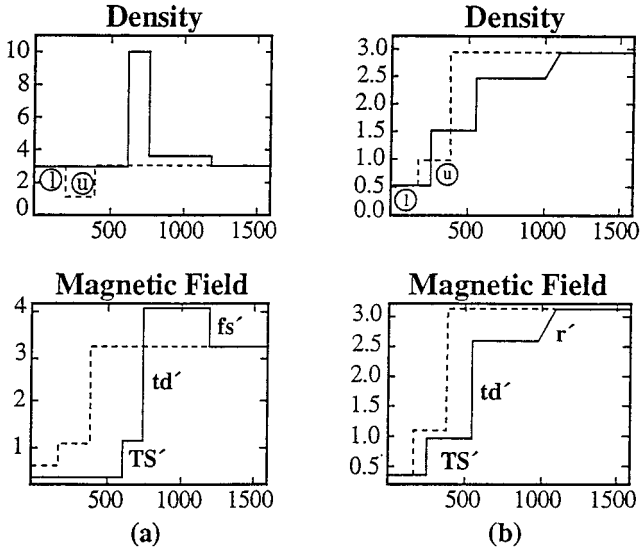

Figure 9.21. Collision of a $\beta_u = 0.1$, $M_{fu}^2 = 10$ termination shock with a tangential discontinuity, for which (a) $\beta_1 = 10$ and $\rho_1/\rho_u = 0.5$ and (b) $\beta_1 = 10$ and $\rho_1/\rho_u = 3.0$ (Story and Zank, 1997.)

magnetic field component can introduce slow-mode rarefactions and shocks as well as the usual fast-mode waves (also Section 9.3.1). This work represents a direct extension of the earlier gas dynamic simulations of Story and Zank (1995) to MHD.

Story and Zank (1997) consider both transverse and oblique MHD shocks for the interaction of the TS with interplanetary disturbances. As in the gas dynamic case, collisions in the transverse MHD limit result in the production of three waves: a modified and moving TS, a tangential discontinuity (rather than a contact discontinuity, as in gas dynamics, for which $[p + B^2/2\mu] = 0$) and an additional secondary wave, the latter of which propagates downstream and away from the TS. The speeds of the resultant modified TS and 'secondary wave' are a function of the strength of the incident disturbance. The secondary waves fall into two categories. When the upstream total pressure $\Pi \equiv \rho u^2 + P + B^2/8\pi$ increases following the collision, as in Figure 9.21(a), a forward shock wave results (fs' in Figure 9.21(a)). In the case that the upstream total pressure decreases after the collision, as in Figure 9.21(b), a rarefaction wave results (r' in Figure 9.21(b)). The two cases above are associated with anti-sunward and sunward movement of the final TS respectively.

In Figure 9.22, a time sequence of density and magnetic field profiles which result from the collision of an initially stationary TS (fast magnetosonic Mach number of 6.85) and a contact discontinuity pulse of amplitude $\rho_1/\rho_u = 2$ and width 5 AU is shown (Story and Zank, 1997). The result of the collision between the leading edge of cd' with TS is qualitatively identical to the result of the collision depicted in Figure 9.21(a) (solid line) and results in a once modified termination

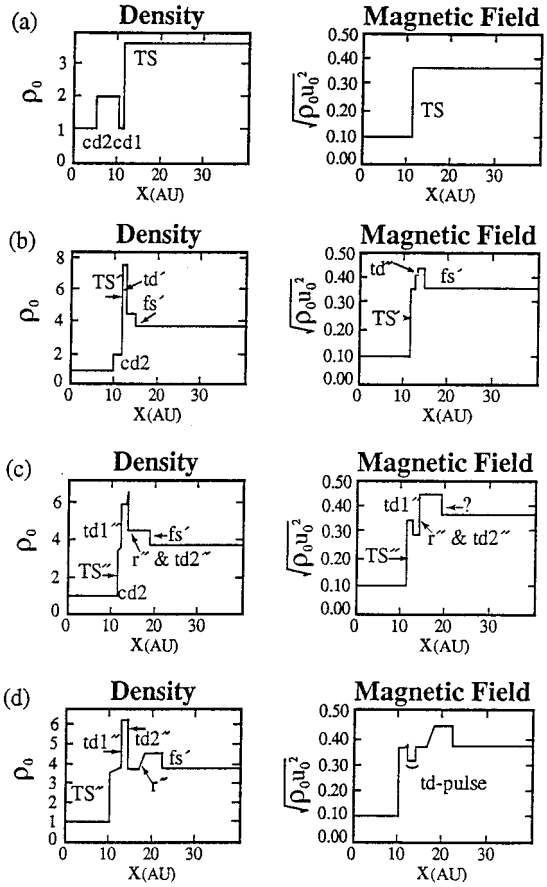

Figure 9.22. Time sequence of the collision of a contact discontinuity pulse with a $M_{fu} = 6.85$ termination shock. The final consequence of the collision is an unmodified (in strength), but displaced termination shock, a tangential discontinuity pulse which travels downstream at the flow speed and a magnetized secondary triangular shock pulse (Story and Zank, 1997.)

shock TS′, a tangential contact discontinuity td' and a forward shock fs'. The second collision, between cd2 and TS′, is different from the first collision because the total pressure upstream of TS′ decreases. Thus, in the absence of the waves td' and fs', the result of the second collision would be qualitatively identical to that shown in Figure 9.21(b). This is in fact what occurs initially but shortly after the second collision, the emitted rarefaction collides with td' and is 'refracted' through. The resultant modified rarefaction wave r'' then chases and catches up with fs'. Behind (sunward of) r'' is a rectangular 'td pulse' and a twice modified, stationary and final termination shock, TS″. TS″ is at rest because the state of the solar wind behind the incident contact discontinuity pulse is the same as that initially upstream of the undisturbed and stationary TS. For times between the cd1-TS collision and the cd2-TS′ collision, the speed of the TS is constant. During the intermediate

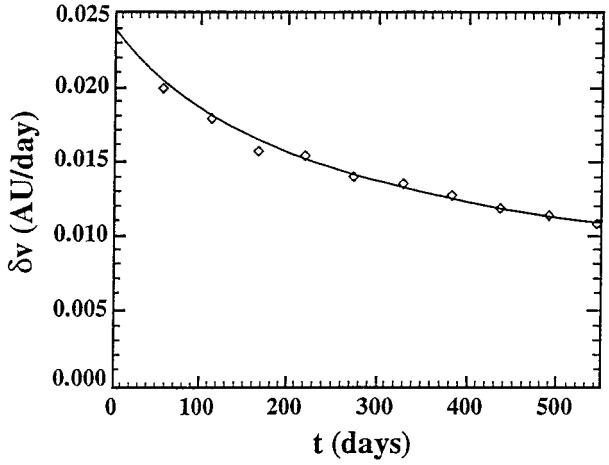

Figure 9.23. Time rate of decay of the triangular shock pulse in Figure 9.22 (Story and Zank, 1997.)

period, the speed of the TS can be found from equation (268), which yields a value of approximately $V \simeq 0.04$ AU day$^{-1} \simeq 70$ km s^{-1}. For the 5 AU wide contact discontinuity pulse in this example, the duration of the interaction (i.e., the period of time during which the TS had a nonzero speed) was slightly less than 40 days. The final termination shock TS$''$ is displaced downstream approximately 1AU from its original position. This displacement is proportional to the width of the pulse. Thus, even though the width of the incident pulse was substantial, the resulting TS movement was relatively small.

After the interaction of the rarefaction and the compound tangential discontinuity, r'' pursues the forward shock fs' and eventually catches it. Prior to the interaction of r'' and fs'', the pressure and density levels behind fs' do not change, but once the leading edge of r'' impinges upon the fs'' interface, these variables begin to decrease, since the rarefaction wave causes the shocked gas to accelerate away from the downstream side of fs'. The structure that forms is a triangular shock pulse. The decay rate of the triangular pulse can be approximated using the same approach described by Story and Zank (1995) for the gas dynamic case.

Story and Zank (1997) show that the triangular shock wave in the heliosheath decays according to

$$\delta v(t) = \frac{\delta v_i}{\sqrt{1 + (\alpha_v \delta v_i)t}}, \quad \alpha_0 \equiv \frac{c_{f0}^2 + \gamma c_{sd0}^2 + 2c_{a0}^2}{2c_{f0}^2}, \tag{270}$$

where δv_i is the initial velocity jump across fs$'$, the 0 subscript denotes the background state of the heliosheath plasma, C_f, C_{sd} and $C_{\rm A}$ the fast, gas dynamic, and Alfvén speeds respectively.

Figure 9.23 is a comparison between the theoretical decay predicted by equation (270) (solid line) and that from simulation (diamonds) (Story and Zank, 1997) and shows good agreement. Subtracting the gas dynamic damping coefficient $\alpha_{gd} =$

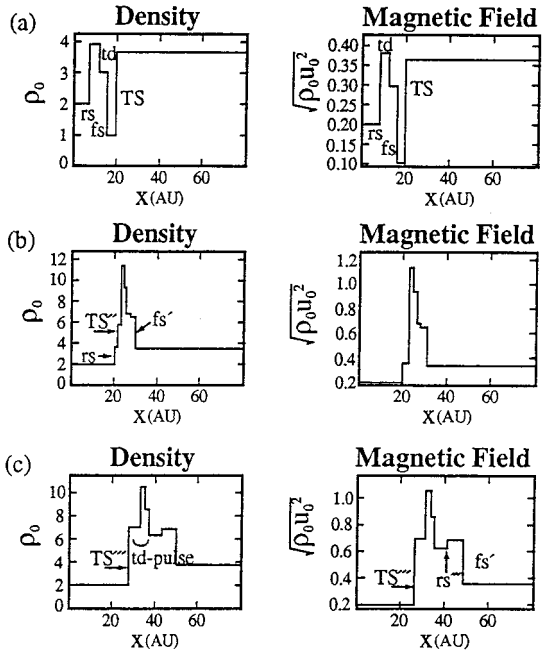

Figure 9.24. Time sequence of the collision between a Mach 6.85 termination shock and a forward reverse shock pair (Story and Zank, 1997.)

$\frac{1}{2}(\gamma + 1)$ from (270), it follows that $\alpha_{\mathrm{MHD}} > \alpha_{gd}$ if and only if $\gamma < 2$. Thus, for $\gamma = \frac{5}{3}$, transverse MHD shock pulses damp away faster than their gas dynamic analogues.

The more realistic possibility of the interaction of a forward-reverse shock pair, separated by a tangential discontinuity, with the TS is illustrated in Figure 9.24. The initial state is shown in Figure 9.24(a). Figure 9.24(b) shows the interaction just after td has collided with the once modified (by fs) termination shock, 49 days after the state shown in Figure 9.24(a), and just prior to the collision between rs and the now twice modified termination shock, TS$''$. At this point, the density has reached a level 11.5 times that initially and immediately upstream of the pre-interaction TS. Figure 9.24(c) shows the final state except for the pursuit and eventual damping of fs' by r'''. The final maximum density associated with the complete profile is 10.5 times that initially and immediately upstream of the pre-interaction TS. At this time, 125 days after time frame (a), the termination shock has been displaced a total distance of 9 AU. However, this is due partially to the nonzero final speed of TS$'''$. The final termination shock speed is nonzero because the final upstream state was not the same as the initial upstream state, resulting in a non-stationary and anti-sunward moving termination shock, with a final speed of $v_{\mathrm{TS}} \simeq 0.07$ AU day^{-1}.

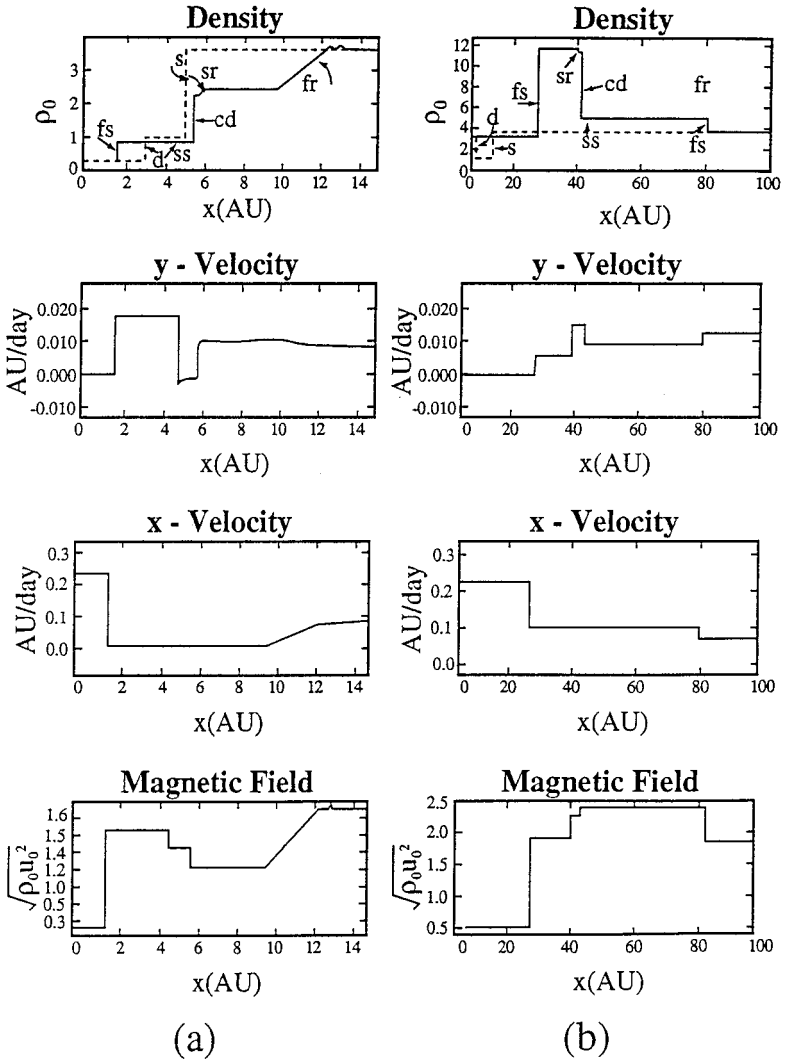

Figure 9.25. (a) Collision of a 60° oblique stationary termination shock (**s**) with a contact discontinuity (**d**), across which the density increases and which is incident from upstream. (b) Collision of a 60° oblique stationary termination shock (**s**) with a contact discontinuity (**d**), across which the density decreases and which is incident from upstream (Story and Zank, 1997.)

As discussed earlier, the IMF in the outer heliosphere is oriented perpendicular to the solar wind flow only on average and one should therefore consider oblique shocks interacting with the termination shock as well. In Figure 9.25, the initial condition (densities only, dashed line) and the result (solid lines) of a collision between an oblique MHD TS ($\theta_{BN} = 60°$) and a contact discontinuity incident from the upstream solar wind is shown. Figure 9.25(a) illustrates the case of a collision with a contact discontinuity in which the upstream dynamic pressure ($P_{dyn} \equiv \rho u^2$)

increases and Figure 9.25(b) depicts the case in which $P_{\rm dyn}$ decreases. Except for the contact discontinuity, the thermal pressure p varies in the same sense as the density. The pressure remains constant across the contact–discontinuity. In both examples, the magnetic field is completely coplanar, with the consequence that no rotational discontinuities occur. The far left and far right states are connected by five waves, which are, in order, a fast shock fs, a slow rarefaction sr, a contact discontinuity cd, a slow shock ss and a fast shock fs.

Figure 9.25 is interesting in that it suggests that slow mode waves may be generated at the TS and propagate in the heliosheath. Specifically, if the TS is sufficiently oblique or if a wave with which it collides is sufficiently oblique, then the result of the interaction includes two slow mode waves which propagate downstream of the TS. Thus, not only might we expect to see slow mode waves generated in the inner solar system (Whang, 1987), but also in the extreme outer heliosphere. Finally, there is is no reason to rule out collisions between non-coplanar structures, which give rise to rotational discontinuities and this too was discussed by Story and Zank (1997).

9.4. Response of the Termination Shock to Interplanetary Disturbances: Cosmic-Ray Hydrodynamics

The termination shock is expected to be a site of anomalous cosmic-ray acceleration (Section 7 and 8). In addition, galactic cosmic-rays of low energy might also act to mediate the termination shock. Both ACRs and GCRs are likely to play a basic role in determining the structure of the TS. Since the cosmic ray mediated termination shock can reasonably be several tenths or more of an AU thick, it would take several days for such structure to move past a spacecraft. Thus, observations of a cosmic-ray mediated TS might be quite unlike those that characterize typical interplanetary shocks or planetary bow shocks. Two approaches have so far been followed in investigating the response of a cosmic-ray mediated TS to interplanetary disturbances. One is to suppose that the energization of ACRs at the termination shock represents an energy sink in the Rankine–Hugoniot conditions, i.e., energy is lost from the thermal solar wind to a massless cosmic-ray population (Barnes, 1994; Ziemkiewicz, 1994). The second approach is to solve the cosmic-ray shock structure equations dynamically as an interplanetary disturbance collides with the TS (Donohue and Zank, 1993; Zank et al., 1994).

9.4.1. *The Cosmic-Ray Modified Rankine–Hugoniot Conditions*

Following Barnes (1994) and Ziemkiewicz (1994), we assume that some fraction ε of the incident kinetic energy is used to accelerate cosmic-rays (note the similarity between this approach and the injection models described in Section 7). The modified gas dynamic Rankine-Hugoniot conditions are therefore

$$[\rho u] = 0\,, \qquad \left[\rho u^2 + p\right] = 0\,, \qquad \left[\frac{1}{2}\rho u^3 + \frac{\gamma}{\gamma - 1} pu\right] = \frac{\varepsilon}{2}\rho_1 u_1^2\,. \quad (271)$$

In (271), the cosmic-rays are assumed to be massless (a reasonable assumption in view of their very low number density) and it assumed that the cosmic-ray pressure is continuous across the shock (this too is reasonable, given the large gyroradii of energetic cosmic-rays).

The Rankine–Hugoniot conditions may be recast in the form

$$\frac{\rho_2}{\rho_1} = \frac{u_1}{u_2} = \frac{\Gamma(\varepsilon\,,\gamma)+1}{\Gamma(\varepsilon\,,\gamma)-1}\,, \tag{272}$$

$$\Gamma(\varepsilon\,,\gamma) \equiv \frac{\gamma + [1+\varepsilon(\gamma^2-1)]^{1/2} + (1-\varepsilon)(\gamma-1)}{\gamma + [1+\varepsilon(\gamma^2-1)]^{1/2} - (1-\varepsilon)(\gamma-1)}\,,$$

if we assume that $p_1 = 0$. Ziemkiewicz (1994) gives a more general expression for $p_1 \neq 0$. Evidently, in the limit that $\varepsilon \to 1$, i.e., all the upstream kinetic energy is used to accelerate cosmic-rays, the compression ratio $r \equiv \rho_2/\rho_1 \to \infty$. Thus, shocks which accelerate cosmic-rays can be comparatively stronger than pure gas dynamic shocks.

By modifying the analysis of Barnes (1993) (Section 9.2.1) in a straightforward fashion (Barnes, 1994; Ziemkiewicz, 1994), one can reduce the problem of the shock-shock interaction to a coupled pair of nonlinear algebraic equations which can be solved numerically. An example showing the post-interaction termination shock speed $V_s = s$ is shown in Figure 9.26(a) as a function of upstream solar wind speed v after a collision with a forward interplanetary shock with speed 600 km s^{-1}. Figure 9.26(b) shows s as a function of the incident forward shock velocity s^{-1} for a given upstream solar wind speed of 600 km s^{-1} (Ziemkiewicz, 1994). Curves 1, 2, and 3 correspond to $\varepsilon = 0.1$, 0.2, and 0.3 respectively. As ε increases, the termination shock velocity s is reduced since a larger fraction of the available solar wind kinetic energy is used to accelerate cosmic-rays. The reduction in ram pressure leads therefore to a corresponding decrease in the speed with which the TS moves outward. One can see that the effect of reverse shock colliding with the TS will be opposite to that just described i.e., s inward will increase as ε increases. This was demonstrated explicitly by Ziemkiewicz (1994).

9.4.2. *Dynamical Structure of a Cosmic-Ray Mediated Shock*

While the use of energy sink terms in the gas dynamic Rankine–Hugoniot equations can model some aspects of a cosmic-ray mediated termination shock colliding with interplanetary disturbances, one should ideally like to study the interaction problem within the framework of the two-fluid cosmic-ray model, using either the cosmic-ray transport equation directly or an integrated form. Donohue and Zank (1993) use the two-fluid cosmic-ray model of Zank et al. (1993) (see Section 8.2) with a cosmic-ray pressure equation to study the collision of interplanetary disturbances with a cosmic-ray mediated TS. Zank et al. (1994) also consider the interaction of a gas dynamical GMIR with a cosmic-ray mediated TS. Figure 9.27 illustrates the initial velocity profile for a two-shock collision. The equilibrium

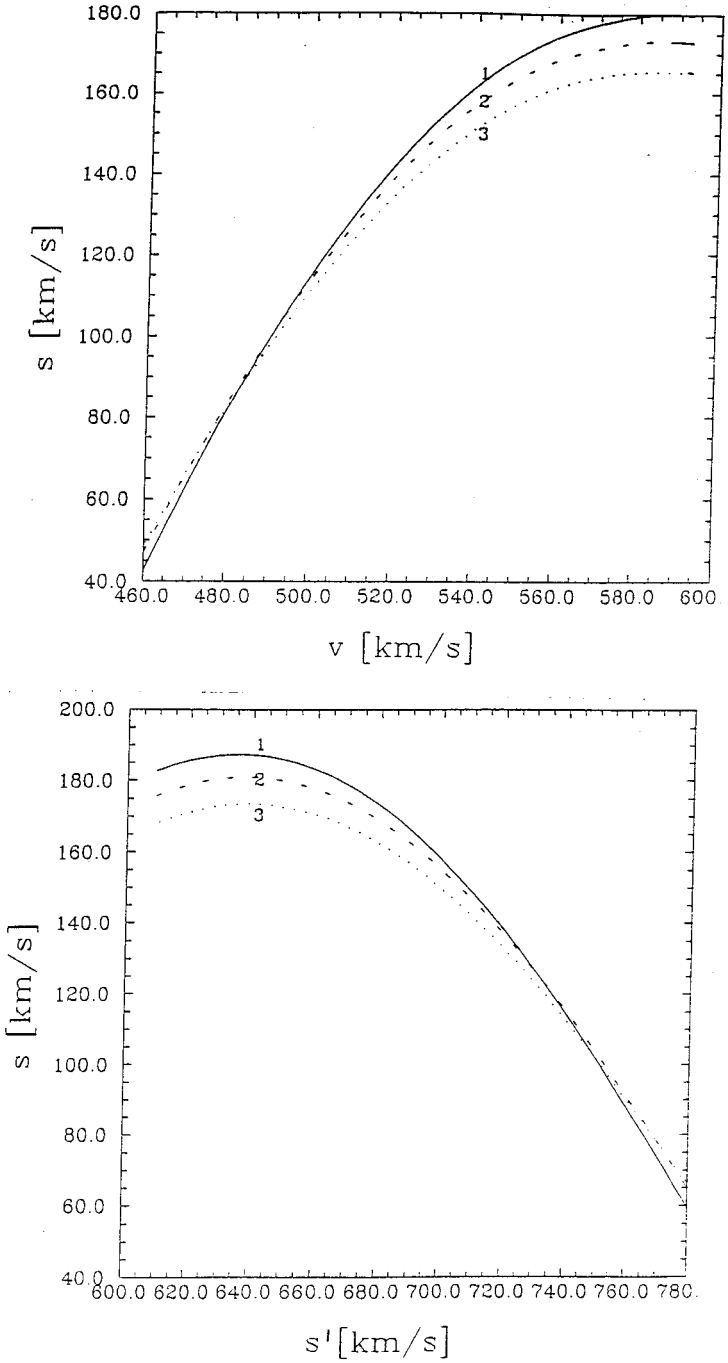

Figure 9.26. Speed of the heliospheric TS as a function of (a) the left state velocity with the primary forward shock velocity $s' = 600$ km s^{-1}; (b) the primary forward shock velocity with the left state velocity $u = 600$ km s^{-1}. Cases 1, 2, and 3 correspond to $\varepsilon = 0.1$, 0.2, and 0.3 (Ziemkiewicz, 1994.)

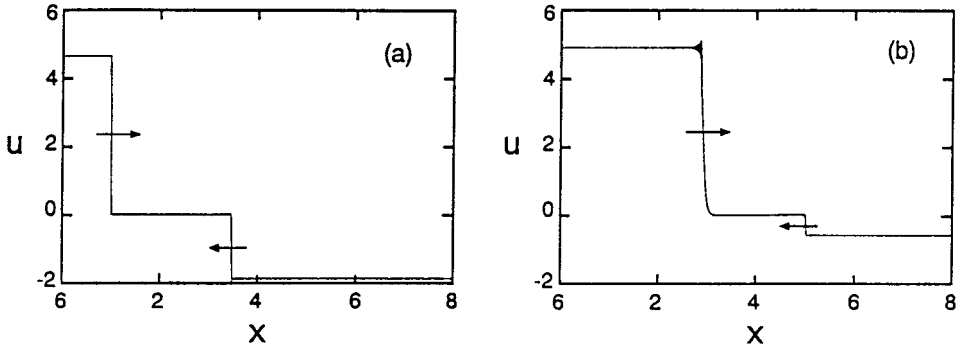

Figure 9.27. Initial velocity profile for the collision of a forward travelling shock with the reverse termination shock. Arrows depict the direction of shock motion relative to the undisturbed solar wind. (a) A one-fluid gas dynamic simulation, and (b) a two-fluid cosmic ray-mediated TS colliding with an interplanetary shock (Donohue and Zank, 1993.)

termination shock is on the left. The travelling shock front is to the right. The direction of motion of each shock relative to the unshocked gas between the two is indicated by the arrows. The travelling shock has a jump in pressure of 2.5, compared to the total pressure jump of 50 at the termination shock. The ordinary gas dynamic jump conditions are used to calculate the density and velocity jumps at the travelling shock. The termination shock of Figure 9.27(b) is in equilibrium with the cosmic-ray population, unlike the travelling disturbance which is not mediated. For comparison, a similar collision of two, ideal gas dynamic shock fronts is shown in Figure 9.27(a). The gas dynamical calculation employs the same computational model as used for the cosmic-ray calculation but with the cosmic ray pressure $p_c = 0$.

Figure 9.28 shows the velocity, density and pressure fields for both shock collisions well after the collision. The purely gas dynamic collision (Figures 9.28(a–c)) shows the forward and reverse shocks separating with a contact discontinuity between, leaving behind an expanding zone of higher pressure and constant flow velocity. The cosmic ray-modified shock collision, illustrated in Figures 9.28(d–g), produces a substantially different structure. As the travelling shock propagates downstream away from the termination shock, cosmic-rays are trapped and accelerated in the turbulence convecting with the transmitted shock. An enhanced cosmic-ray pressure therefore trails the travelling shock, as shown in Figure 9.28(g). It should be noted that the post-collision time interval is sufficiently large that the travelling shock has reached a steady state, smoothing the overall shock transition. Since the transmitted shock is much weaker than the TS, the diffusion scale length κ / V_{sh}, which defines the precursor scale, is much broader. This, however, reflects a limitation of the simulation which uses a constant diffusion coefficient κ.

Unlike the contact discontinuity of gas dynamics, the structure of the contact discontinuity within the cosmic-ray model is quite different. In the example of Figure 9.28(e), the gas is compressed to the left of the sharp density discontinuity.

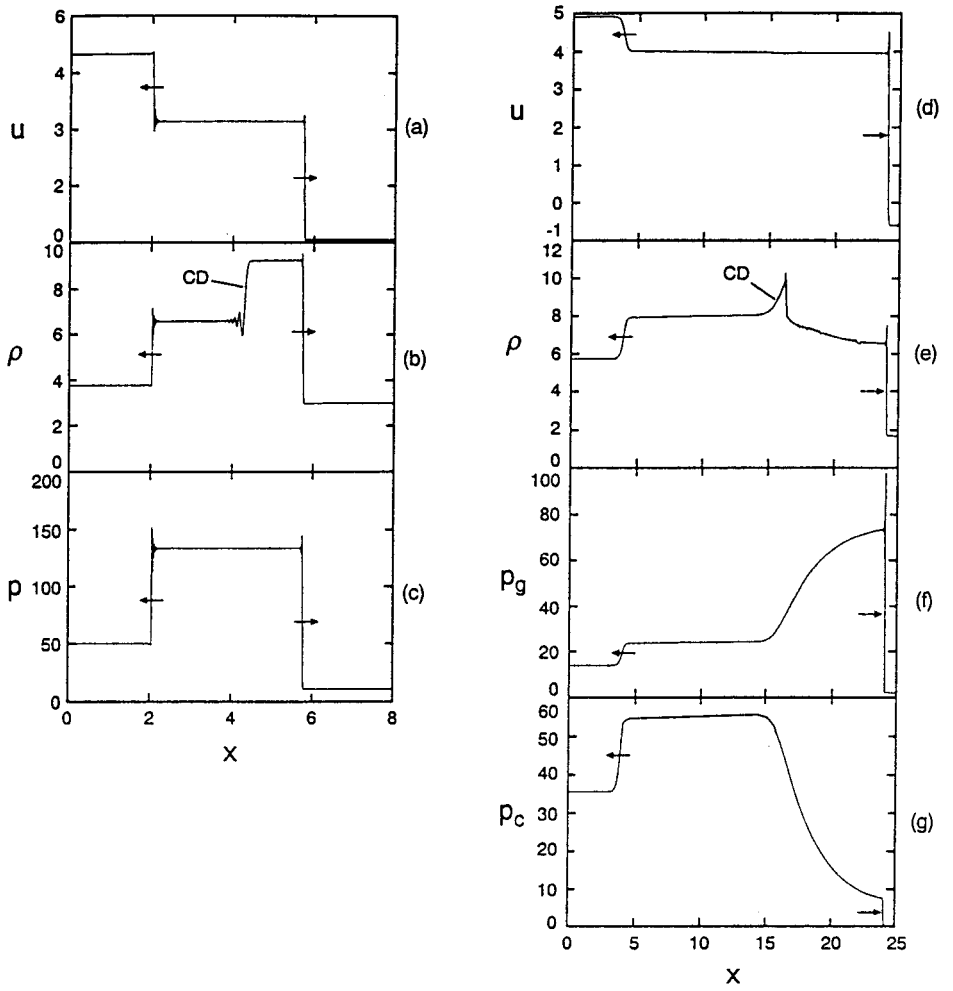

Figure 9.28. The fluid state following the shock front collision depicted in Figure 9.27. The TS is now to the right of the travelling disturbance as the two separate. (a)–(c) The gas dynamic calculation. (d)–(g) The cosmic ray-modified result. The contact discontinuities (CD) are labelled in the density profiles (Donohue and Zank, 1993.)

The additional degree of freedom provided by the cosmic-ray pressure allows the thermal gas compression to be adiabatic ($p_g/\rho^{\gamma_g} = \text{const.}$) and smoothed. Such an adiabatic compression can occur because the total pressure $P = p_c + p_g$ remains constant across the structure. The adiabatic compression reaches a maximum, after which it experiences a discontinuous jump in density. Unlike the gas dynamic case, the density decreases across the jump, this to adjust the fluid to the new downstream state of the termination shock. The new downstream state is determined by the presence of a cosmic-ray population. The state of a cosmic-ray-mediated shock of the strength used in Figure 9.28 is either a cosmic-ray dominated shock or

a pure gas dynamic shock (Section 8.2.2). In the case shown here, the response of the TS is to approach the latter. The decrease in cosmic-ray pressure at the contact discontinuity not only permits the adiabatic compression, but is necessary to connect the two downstream states. The travelling shock, in effect, sweeps up the cosmic-ray population downstream of the TS. The diffusive flux back to the TS is insufficient to maintain a non-zero cosmic-ray pressure in the steady state. The cosmic-ray-modified termination shock then approaches the gas dynamic limit on a long timescale. Thus, a sudden change in the state of the solar wind may alter the steady state of the termination shock from a cosmic-ray dominated to a gas dynamical state. However, this possibility depends strongly on the radial extent of the disturbance, the size of the heliosheath, and the assumed upstream state.

Of course, the shock collisions described so far are highly idealized, and one needs to consider shock transitions of limited spatial extent. Donohue and Zank (1993) considered a variety of shock pulse collisions. Figure 9.29 shows the collision of a forward Gaussian-shaped shock pulse with the TS. Figure 9.29 shows the initial state (solid line) and an intermediate time before the collision (dotted line). The structure resembles that seen in interplanetary data. Figures 9.29(b–e) show the structure well after the collision. The cosmic ray-mediated shock has now returned to its pre-interaction steady state. As was discussed above, a cosmic-ray-modified shock of this magnitude has two stable states. In the example of Figure 9.28, the duration of the disturbance was sufficiently long as to induce the shock to converge to the gas dynamic state. The pulse of finite spatial extent, however, only temporarily disturbs the state of the shock. Downstream of the termination shock, a triangular forward shock is transmitted. The emitted pulse carries an equilibrium cosmic-ray distribution (the structure has reached a steady state) which was swept up from the background cosmic-ray population in the heliosheath. The pulse is thus smoothed, as before.

A contact discontinuity which resembles that of Figure 9.28 is formed by the interaction of the TS with a shock pulse. Since the TS recovers eventually to a cosmic-ray-mediated state, the density behind the contact discontinuity recovers, unlike the infinite duration interaction.

Pulse-like disturbances do not induce a permanent change in state at the termination shock unless they are quite long in comparison to the precursor scale (Donohue and Zank, 1993). The primary effect is to introduce new structure downstream of the termination shock.

The role of reverse interplanetary shocks colliding with the TS was considered too by Donohue and Zank (1993). The longer interaction time of such a collision leads to some modification in the time scales for the TS to reach an equilibrium state.

The temporal evolution of the TS following the collision of forward or reverse shock pulses was explored by Donohue and Zank (1993). The above examples considered only the intial and final states of the interaction. However, one can follow the cosmic-ray pressure at the TS as a function of time subsequent to the

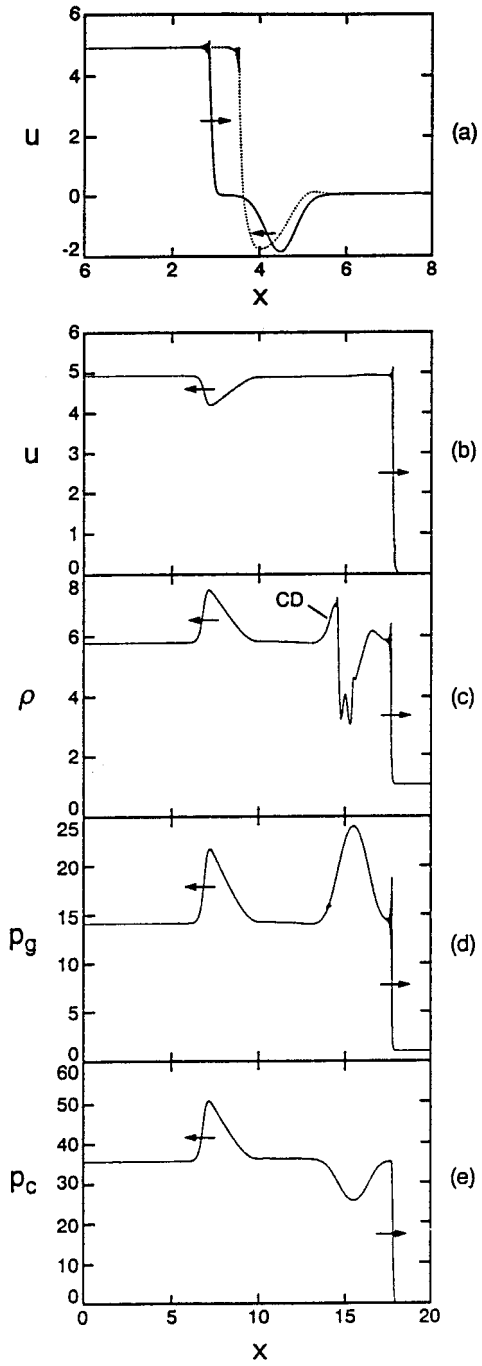

Figure 9.29. The interaction between a forward shock pulse and the cosmic ray-mediated TS. (a) The initial velocity distribution. The dashed profile is at an intermediate time step just before the collision. (b)–(e) The final steady state (Donohue and Zank, 1993.)

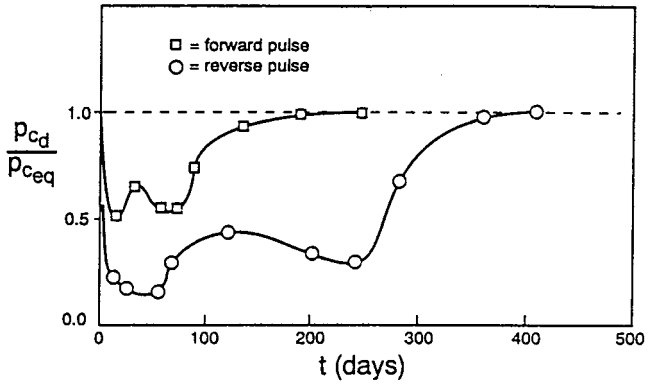

Figure 9.30. A plot of the cosmic ray pressure just downstream of the termination shock as a function of time following the pulse interactions (Donohue and Zank, 1993.)

pulse-TS interaction. The results are shown in Figure 9.30 for both forward and reverse pulse interactions. Although the numbers are very approximate, it takes $\sim$ 190–240 days for the termination shock to reform and reach a cosmic-ray-dominated state following the forward-pulse interaction. Roughly 360–410 days are required for the reformation following the reverse pulse interaction. A slightly more meaningful way of measuring the TS recovery times is to use either diffusion times or the duration time for the pulse to convect through the TS. One finds then that the above recovery time scales correspond to either $\sim$ 44–55 and $\sim$ 83–95 diffusion times or 7–8 and 15–20 duration times for forward and reverse shock pulses, respectively. The incident forward and reverse shock pulses took some 12 and 53 days to convect through the cosmic-ray-mediated TS.

Some further implications of a dynamical cosmic-ray-mediated TS were discussed by Zank and Donohue (1993). These relate to a variable source for the ACR component and a leaky boundary for galactic cosmic-rays.

The unusual nature of the contact and pressure-balanced structures found in the simulations of Donohue and Zank (1993) prompted Webb et al. (1995) to investigate these structures further. Here we discuss the simplest example of a pressure-balanced structure associated with the 1D two-fluid cosmic-ray equations (217)–(221). Consider travelling wave solutions in which the fluid velocity u is constant. Solutions to the two-fluid cosmic-ray equations may then be expressed as

$$p_g = p_g(\xi)\,, \quad \rho = \rho(\xi)\,, \quad p_c = p_c(\xi)\,, \quad \xi = x - ut\,. \tag{273}$$

It follows immediately that one has the total momentum balance integral

$$p_c + p_g = P_0\,, \tag{274}$$

where P_0 denotes the constant total pressure of the cosmic-rays and thermal gas. The cosmic-ray energy equation (217) and (274) yield a steady-state form of the heat equation

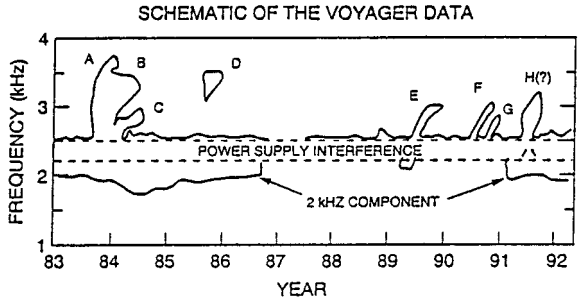

Figure 9.31. A schematic illustration of the 2 kHz and transient events observed until 1992 (Zank et al., 1994.)

$$\frac{\mathrm{d}}{\mathrm{d}\xi}\left(\kappa\frac{\mathrm{d}p_g}{\mathrm{d}\xi}\right) = -\frac{\mathrm{d}}{\mathrm{d}\xi}\left(\kappa\frac{\mathrm{d}p_c}{\mathrm{d}\xi}\right) = 0\,, \tag{275}$$

which governs the variation of p_g and p_c throughout the structure.

By way of example, using $\kappa = \kappa_0 \cosh^2(\xi/\xi_0)$ and the boundary conditions $p_g \to p_{g\infty}^{\pm}$ as $\xi \to \pm\infty$, Webb et al. (1995) obtain

$$p_g(\xi) = p_{g\infty}^{-} + \frac{p_{g\infty}^{+} - p_{g\infty}^{-}}{2}\left[1 + \tanh(\xi/\xi_0)\right]\,,$$

$$p_c(\xi) = P_0 - p_g(\xi)\,. \tag{276}$$

By assuming the functional form $p_g/\rho^{\gamma_g} = \text{const.}$ throughout the flow, one obtains the density profile

$$\rho = \rho_{\infty}^{+}\left(p_g/p_{g\infty}^{+}\right)^{1/\gamma_g}\,. \tag{277}$$

The solutions (276) and (277) show the same qualitative behaviour as seen in Figures 9.28 and 9.29. The density ρ is an arbitrary function of ξ and need not in fact be compressed adiabatically.

9.5. RADIO EMISSION AND THE HELIOSPHERIC BOUNDARIES

The detection of low-frequency radio emission in the outer heliosphere beyond 11 AU (Kurth et al., 1984; Gurnett et al., 1993) offered the possibility that the heliospheric boundaries may have been detected. Unfortunately, a satisfactory quantitative theory has yet to be advanced which relates the radio observations to any of the heliospheric boundaries, nor can definitive estimates for the distance to these boundaries be inferred from the data. Here we do no more than describe the observations briefly and list some of the models that have been developed to explain the emissions. Almost all models involve the propagation of interplanetary shocks and their interaction with one or more of the heliospheric boundaries.

As illustrated in Figure 9.31, any model attempting to explain the Voyager radio observations (Kurth et al., 1984; Cairns et al., 1992; Gurnett et al., 1993) must

account for (i) the simultaneous existence of two classes of emissions: a relatively steady 2kHz 'continuum' component and 'transient events' which can last for as long as two hundred days; (ii) the rarity of transient events and their highly variable rate of upward frequency drift (1–3 kHz year^{-1}); (iii) the evident clumping (e.g., events A, B and C and events F and G) and filamentation of the transient events; (iv) the very high plasma frequencies (up to $\sim$ 3.6 kHz) achieved by the transient events; (v) the apparent disappearance during 1987–1991 of the continuum emission, and (vi) the width of the steady 2kHz band and the variation of the bounding frequencies together with the absence of discernable drifts.

Five basic mechanisms have been suggested to explain the observations shown in Figure 9.31. (1) Czechowski and Grzedzielski (1990a, b) considered the temporal evolution of electromagnetic radiation trapped in the outer heliosphere by the heliopause. As solar wind density fluctuations are convected outward, the trapped radiation may be reflected and scattered. The net transfer in energy from the solar wind fluctuations to the trapped radiation results in an upward drift of the radiation frequency at the rate of $\sim$ 1 kHz year^{-1}. Such a model, while theoretically very attractive, has great difficulty explaining most of the features of Figure 9.31, such as the non-rising continuum, the highly variable drift rate of the transient events, and the sporadic nature of the emission. (2) Cairns and Gurnett (1992) and Cairns et al. (1992) suggested, by analogy with type II solar radio bursts in the corona, the inner solar wind, and the Earth's bow shock, that Langmuir waves produced by an electron beam instability in the TS foreshock might generate electromagnetic radiation at multiples of the plasma frequency f_p. They suggested that density variations of order 4–10 above the ambient solar wind density could increase the source frequency upstream of the termination shock sufficiently to account for the observed frequencies. Unfortunately, as estimates increase for the distance to the TS, this model faces increasing difficulties in generating the observed source frequencies. (3) Fahr et al. (1986) suggested that the heliopause might be unstable, but the generated plasma wave modes appear to have frequencies that are too low. An 'electrostatically turbulent heliopause layer' was also suggested as a possibility, but this requires further elucidation. (4) Gurnett et al. (1993) and Steinolfson and Gurnett (1994) suggested what is presently the most popular interpretation. They suggested that the rising radio frequencies result from the f_p and $2f_p$ emission by an interplanetary shock propagating up the heliopause ramp and beyond. The 3 kHz cutoff is explained naturally by the high density of the interstellar plasma. A variation on this model has been proposed by Czechowski and Grzedzielski (1995). These authors considered more carefully the structural modification to the heliopause that results when charge exchange is included in the plasma model of the heliosheath region (Section 5.5). The increased smoothing of the heliopause can extend the duration of the rising frequency but generally the Gurnett et al. (1993) model and its variations do not appear to offer an explanation for the duration of the long-lived transients. Whang et al. (1995) further modified the Gurnett et al. model by suggesting that an interplanetary shock, as well as being transmitted

through the heliopause, may also experience some reflection at the heliopause and propagate back into the heliosheath region towards the TS. The 1.8 kHz emission is generated downstream of the reflected shock, taking advantage of the increased plasma density, and the 3 kHz emission is generated in the downstream region of the transmitted shock. This mechanism does not appear to be consistent with our current understanding of type II bursts at interplanetary shocks. (5) A final alternative was introduced by Zank et al. (1994). This model uses a cosmic-ray mediated TS which experiences numerous collisions by interplanetary disturbances, each of which generate new shocks propagating into the heliosheath. The continuum emission was suggested to result from the radio emission produced in the foreshock region of the many travelling shocks in the heliosheath. The rising frequencies were suggested to result from the interaction of the heliosheath shocks with large density enhancements, such as GMIRs, which were transmitted through the TS. This model too has difficulty explaining the long-lived transients and, as estimates for the distance to the TS increase, the level of the continuum emission.

None of these models is completely satisfactory. The data itself remains difficult to interpret, especially in terms of the inferred direction of the source, since density irregularities scatter the radio waves, affecting the apparent angular size, intensity, and direction of the radio source, as well as temporal and spectral variability of the radiation. Some discussion of these issues has been presented by Cairns (1996).

10. Concluding Remarks

The LISM influences the outer heliosphere in a profound and complicated way and this theme has been pursued here in as self-contained a fashion as possible. Only those topics for which a direct connection exists or has been made between the physics of the solar wind and the LISM have been addressed. This has led unfortunately to the omission of many interesting areas which are related to the general theme of this review. Much more, for example, can be said about the subject of cosmic ray modulation and Section 7 scarcely does justice to the subject.

Little has been said about spacecraft observations too. This reflects two factors. The first is that the review deliberately adopts a theoretical perspective in an effort to summarize the very extensive body of work that has been developed over the last 2–3 decades and which has yet to be coherently and comprehensively summarized. Secondly, the absence of observations reflects to some extent the very limited data sets with which we can work. The Pioneer and Voyager spacecraft have been and are hardy stalwarts, returning data from the outer heliosphere for many years. This data has proved invaluable, but, of course, the instrumentation is aged and was not designed for the extreme plasma conditions that prevail in the very distant heliosphere. Furthermore, the instruments were not designed to address questions that are particularly pertinent to the outer heliosphere, questions related to pickup ions and interstellar neutrals. With *Ulysses*, we have been given a taste of what

more recent instruments can measure and the results for pickup ions, interstellar neutrals, solar wind composition, and the 3D solar wind structure have been very exciting, leaving us with, regrettably, more questions than answers. Unfortunately, the *Ulysses* observations were made within the heliospheric ionization cavity and suffer accordingly from this limitation. Other ingenious efforts have been devised to study pickup ions locally in the vicinity of the Earth. Finally, our knowledge of the most basic LISM parameters is very limited and this represent one of the greatest impediments to the further development of the field.

Nonetheless, in spite of the limited data that is available to address questions about the plasma physics of the outer heliosphere, progress has been made theoretically in many areas. It is fair to say, however, that the field awaits considerable advances on almost all fronts before we can claim a reasonable understanding of the interaction of the solar wind with the LISM. This makes this area of space physics especially exciting and attractive.

In concluding, one should not lose sight of the fact that the interaction of the solar wind with the LISM represents only one, admittedly important, astrophysical example of the interaction of a stellar wind with a partially ionized interstellar medium. This is a subject that has been studied somewhat cursorily yet it may prove fundamental in determining both the asymptotic evolution of stellar winds in such an environment and the evolution of the interstellar medium itself. The expansion of a stellar wind from late-type stars into a partially ionized or cloudy interstellar medium has been considered by Wood and Linsky (1998) using Goddard High Resolution Spectrograph observations of the Lyman-α and Mg II absorption lines towards nearby stars. These authors use the possible detection of a hydrogen wall about nearby stars to infer the existence of a stellar wind and its concomitant properties. The results presented by Wood and Linsky (1998) exemplify the fundamental nature of the solar wind interaction with the LISM and demonstrate that it is truly a subject at the interface of space physics and astrophysics.

Acknowledgements

The support of the NSF, NASA and Bartol Research Institute is gratefully acknowledged. This work was supported in part by an NSF Young Investigator Award ATM-9357861, an NSF award ATM-9713223, a NASA award NAG5-6469, a NASA Delaware Space Grant NGT5-40024, and JPL contract 959167. I should like to thank my many many colleagues for their help, patience and encouragement, especially W. I. Axford, I. H. Cairns, D. J. Donohue, H. J. Fahr, M. A. Forman, P. C. Frisch, K. G. Gayley, T. I. Gombosi, D. T. Hall, T. E. Holzer, P. A. Isenberg, J. R. Jokipii, I. Kh. Khabibrakhmanov, J. A. le Roux, M. A. Lee, A. S. Lipatov, T. R. Story, W. H. Matthaeus, N. F. Ness, H. L. Pauls, R. Ratkiewicz, C. W. Smith, G. M.

Webb, L. L. Williams. Finally, I should like to thank Lorraine Zank for her help with some of the figures.

References

Achterberg, A., Blandford, R. D., and Periwal, V.: 1984, *Astron. Astrophys.* **132**, 97.
Adams, J. H. and Liesing, M. D.: 1991, *Proc. 22rd Int. Cosmic-ray Conf., Dublin*, Paper SH4.2.8.
Adams, T. F. and Frisch, P. C.: 1977, 'High-Resolution Observations of the Lyman Alpha Sky Background', *Astrophys. J.* **212**, 300.
Ajello, J. M. et al.: 1987, 'Solar Cycle Study of Interplanetary Lyman-Alpha Variations: Pioneer Venus Orbiter Sky Background Results', *Astrophys. J.* **317**, 964.
Allen, C. W.: 1973, *Astrophysical Quantities*, The Athlone Press, London.
Armstrong, T. P., Pesses, M. E., and Decker, R. B.: 1985, 'Shock Drift Acceleration', in B. T. Tsuratani and R. G. Stone (eds), *Collisionless Shocks in the Heliosphere: Reviews of Current Research, Geophys. Res. Monogr. Ser., 35*, p. 271, AGU, Washington, D.C.
Axford, W. I.: 1965, 'The Modulation of Galactic Cosmic-Rays in the Interplanetary Medium', *Planetary Space Sci.* **13**, 115.
Axford, W. I.: 1972, 'The Interaction of the Solar Wind with the Interstellar Medium', *Solar Wind, NASA Spec. Publ.* **SP-308**, 609.
Axford, W. I. and Newman, R. C.: 1965, *Proc. 15th Int. Conf. Cosmic-Ray Conf.* **1**, 173.
Axford, W. I., Dessler, A. J., and Gottlieb, B.: 1963, *Astrophys. J.* **137**, 1268.
Axford, W. I., Leer, E., and Skadron, G.: 1977, 'The Acceleration of Cosmic-Rays by Shock Waves', in *Proc. 15th Int. Cosmic-Ray Conf., Plovdiv* **11**.
Axford, W. I., Leer, E, and McKenzie, J. F.: 1982, 'The Structure of Cosmic-Ray Shocks', *Astron. Astrophys.* **111**, 317.
Babayan, V. K. and Dorman, L. I.: 1977, *Proc. 15th Int. Conf. Cosmic-Ray Conf.* **3**, 107.
Barmin, A. A. and Pushkar, E. A.: 1991, *Izv. USSR Acad. Sci. Fluid Dyn.* **26**, 428.
Banaszkiewicz, M. and Ziemkiewicz, J.: 1997, *Astron. Astrophys.* **000**, 000.
Baranov, V. B.: 1990, 'Gasdynamics of the Solar Wind Interaction with the Interstellar Medium', *Space Sci. Rev.* **52**, 89.
Baranov, V. B., Krasnobaev, K., and Kulikovsky, A.: 1971, *Soviet Phys. Dokl.* **15**, 791.
Baranov, V. B., Ermakov, M. K., and Lebedev, M. G.: 1981, 'Three-Component Gasdynamic Model of the Interaction of the Solar Wind with the Interstellar Medium', *Soviet Astron. Letters* **7**, 206.
Baranov, V. B., Lebedev, M. G., and Malama, Yu. G.: 1991, 'The Influence of the Interface between Heliosphere and the Local Interstellar Medium on the Penetration of the H-Atoms to the Solar System', *Astrophys. J.* **375**, 347.
Baranov, V. B. and Malama, Y. G.: 1993, 'Model of the Solar Wind Interaction with the Local Interstellar Medium: Numerical Solution of Self-Consistent Problem', *J. Geophys. Res.* **98**, 15 157.
Baranov, V. B. and Malama, Y. G.: 1995, 'Effect of Local Interstellar Medium Hydrogen Fractional Ionization on the Distant Solar Wind and Interface Region', *J. Geophys. Res.* **100**, 14 755.
Baranov, V. B. and Malama, Y. G.: 1996, *Space Sci. Rev.* **78**, 305.
Baranov, V. B. and Zaitsev, N. A.: 1995, *Astron. Astrophys.* **304**, 631.
Baranov, V. B., Barmin, A. A., and Pushkar, E. A.: 1996, *J. Geophys. Res.* **101**, 27 465.
Baranov, V. B., Fahr, H. J., and Ruderman, M. S.: 1992, *Astron. Astrophys.* **261**, 341.
Baring, M. G., Ogilvie, K. W., Ellison, D. C., and Forsyth, R. J.: 1997, *Astrophys. J.* **476**, 889.
Barnes, A.: 1970, *Cosmic Electrodyn.* **1**, 90.
Barnes, A.: 1993, 'Motion of the Heliospheric Termination Shock: a Gasdynamic Model', *J. Geophys. Res.* **98**, 15 137.

Barnes, A.: 1994, 'Motion of the Heliospheric Termination Shock: 2. Energy Loss due to Energetic Particle Acceleration', *J. Geophys. Res.* **99**, 6553.
Barnes, A.: 1998, *J. Geophys. Res.* **103**, 2015.
Belcher, J. W., Lazarus, A. J., McNutt, R. L. Jr., and Gordon, G. S. Jr.: 1993, 'Solar Wind Conditions in the Outer Heliosphere and the Distance to the Termination Shock', *J. Geophys. Res.* **98**, 15 177.
Bell, A. R.: 1978a, 'The Acceleration of Cosmic-Rays in Shock Fronts – 1', *Monthly Notices Roy. Astron. Soc.* **182**, 147.
Bell, A. R.: 1978b, 'The Acceleration of Cosmic-Rays in Shock Fronts – 2', *Monthly Notices Roy. Astron. Soc.* **182**, 443.
Bertaux, J.-L., Lallement, R., Kurt, V. G., and Mironova, E.: 1985, 'Characteristics of the Local Interstellar Hydrogen Determined from Prognoz 5 and 6 Interplanetary Lyman-α Line Profile Measurements with a Hydrogen Absorption Cell', *Astron. Astrophys.* **150**, 1.
Bieber, J. W. et al.: 1994, 'Proton and Electron Mean Free Paths: the Palmer Consensus Revisited', *Astrophys. J.* **420**, 294.
Bieber, J. W., Burger, R. A., and Matthaeus, W. H.: 1995, 'The Diffusion Tensor throughout the Heliosphere', *Proc. 24th Int. Cosmic-Ray Conf.* **4**, 694.
Bieber, J. W., Wanner, W., and Matthaeus, W. H.: 1996, 'Dominant Two-Dimensional Solar Wind Turbulence with Implications for Cosmic-Ray Transport', *J. Geophys. Res.* **101**, 2511.
Bieber, J. W. and Matthaeus, W. H.: 1997, 'Perpendicular Diffusion and Drift at Intermediate Cosmic-Ray Energies', *Astrophys. J.* **485**, 655.
Blandford, R. D. and Ostriker, J. P.: 19778, 'Particle Acceleration by Astrophysical Shocks', *Astrophys. J.* **221**, L29.
Blum, P. W. and Fahr, H. J.: 1970, 'Interaction between Interstellar Hydrogen and the Solar Wind', *Astron. Astrophys.* **4**, 280.
Blum, P. W., Gangopadhyay, P., Ogawa, H. S., and Judge, D. L.: 1993, *Astron. Astrophys.* **272**, 549.
Bogdan, T. J., Lee, M., and Schneider, P.: 1991, 'Coupled Quasi-Linear Wave Damping and Stochastic Acceleration of Pickup Ions in the Solar Wind', *J. Geophys. Res.* **96**, 161.
Brinca, A. L. and Tsurutani, B. T.: 1988, 'Survey of Low-Frequency Electromagnetic Waves Stimulated by Two Co-Existing Newborn Ion Species', *J. Geophys. Res.* **93**, 48.
Burlaga, L. F., Ness, N. F., Belcher, J. W., Szabo, A., Isenberg, P. A., and Lee, M. A.: 1994, 'Pickup Protons and Pressure-Balanced Structures: Voyager 2 Observations in Merged Interaction Regions near 35 AU', *J. Geophys. Res.* **99**, 21 511.
Cairns, I. H.: 1996, in *Solar Wind 8, AIP Conference Proceedings 382*, AIP Press, New York, p. 582.
Cairns, I. H. and Gurnett, D. A.: 1992, 'Outer Heliospheric Radio Emissions, 1. Constraints on Emission Processes and the Source Region', *J. Geophys. Res.* **97**, 6235.
Cairns, I. H., Kurth, W. S., and Gurnett, D. A.: 1992, 'Outer Heliospheric Radio Emissions, 2. Foreshock Source Models', *J. Geophys. Res.* **97**, 6245.
Chassefiére, E., Dalaudier, F., and Bertaux, J.-L.: 1988, *Astron. Astrophys.* **201**, 113.
Chalov, S.: 1990, *Astrophys. Space Sci.* **164**, 183.
Chalov, S.: 1996, *Astron. Astrophys.* **308**, 995.
Chalov, S. and Fahr, H. J.: 1994, *Astron. Astrophys.* **288**, 973.
Chalov, S., Fahr, H. J., and Izmodenov, V.: 1995, 'Spectra of Energized Pick-Up Ions Upstream of the Heliospheric Termination Shock, I, The Role of Alfvénic Turbulence', *Astron. Astrophys.* **304**, 609.
Chalov, S., Fahr, H. J., and Izmodenov, V.: 1997, 'Spectra of Energized Pick-Up Ions of the Two-Dimensional Heliospheric Termination Shock, II, Acceleration by Alfvénic Turbulence and by Large-Scale Solar Wind Turbulences', *Astron. Astrophys.* **320**, 659.
Chandrasekhar, S.: 1961, *Hydrodynamic and Hydromagnetic Stability*, Oxford University Press, New York.
Christian, E. R.: 1989, PhD Thesis, California Institute of Technology, USA.
Christian, E. R., Cummings, A. C., and Stone, E. C.: 1988, *Astrophys. J.* **334**, L77.

Clarke, J. T., Lallement, R., Bertaux, J.-L., and Quemerais, E.: 1995, 'HST/GHRS Observations of the Interplanetary Medium Downwind and in the Inner Solar System', *Astrophys. J.* **448**, 893.
Coleman, P. J.: 1968, 'Turbulence, Viscosity and Dissipation in the Solar Wind Plasma', *Astrophys. J.* **153**, 371.
Cranfill, C.: 1971, PhD Thesis, Univ. California, San Diego.
Cummings, A. C. and Stone, E. C.: 1988, *Astrophys. J.* **334**, L77.
Cummings, A. C. et al.: 1987, *Geophys. Res. Letters* **14**, 174.
Cummings, A. C. et al.: 1995, *Geophys. Res. Letters* **22**, 341.
Cummings, A. C., Stone, E. C., and Webber, W. R.: 1994, 'Distance to the Solar Wind Termination Shock and the Source Flux of Anomalous Cosmic-Rays During 1986–1988', *J. Geophys. Res.* **99**, 11 547.
Czechowski, A. and Grzedzielski, S.: 1990a, 'Frequency Drift of 3 kHz Interplanetary Radio Emissions: Evidence of Fermi Accelerated Trapped Radiation in a Small Heliosphere', *Nature* **344**, 640.
Czechowski, A. and Grzedzielski, S.: 1990b, *Nature* **344**, 640.
Czechowski, A. and Grzedzielski, S.: 1990b, in *Physics of the Outer Heliosphere*, Pergamon Press, Oxford, p. 281.
Czechowski, A. and Grzedzielski, S.: 1995, 'Can a Charge-Exchange Induced Density Rise at the Heliopause Explain the Frequency Drift of the 3 kHz Voyager Signal?', *Geophys. Res. Letters*.
Dalgarno, A.: 1960, *Proc. Phys. Soc.* **75**, 374.
Danby, J. M. A. and Bray, T. A.: 1967, 'Density of Interstellar Matter near a Star', *Astron. J.* **72**, 219.
Danby, J. M. A. and Camm, G. L.: 1957, 'Statistical Dynamics and Accretion', *Monthly Notices Roy. Astron. Soc.* **117**, 50.
Davis, L. E.: 1955, 'Interplanetary Magnetic Fields and Cosmic-Rays', *Phys. Rev.* **100**, 1440.
Decker, R. B.: 1988, 'Computer Modeling of Test Particle Acceleration at Oblique Shocks', *Space Sci. Rev.* **48**, 195.
Dessler, A. J.: 1967, *Rev. Geophys.* **5**, 1.
Donohue, D. J. and Zank, G. P.: 1993, 'The Steady State and Dynamical Structure of a Cosmic-Ray-Modified Termination Shock', *J. Geophys. Res.* **98**, 19 005.
Donohue, D. J., Zank, G. P., and Webb, G. M.: 1994, 'Time-Dependent Evolution of Cosmic-Ray-Modified Shock Structure: Transition to Steady-State', *Astrophys. J.* **424**, 263.
Drury, L. O'C.: 1983, 'Introduction to the Theory of Diffusive Shock Acceleration', *Rep. Prog. Phys.* **46**, 973.
Drury, L. O'C. and Falle, S. A. E. G.: 1986, *Monthly Notices Roy. Astron. Soc.* **223**, 353.
Drury, L. O'C. and Völk, H. J.: 1981, *Astrophys. J.* **248**, 344.
Eichler, D.: 1979, *Astrophys. J.* **229**, 419.
Eichler, D.: 1984, *Astrophys. J.* **277**, 429.
Ellison, D. C. and Eichler, D.: 1984, *Astrophys. J.* **286**, 691.
Ellison, D. C., Baring, M. G., and Jone, F. C.: 1995, *Astrophys. J.* **453**, 873.
Fahr, H. J.: 1968, 'Neutral Corpuscular Energy Flux by Charge-Transfer Collisions in the Vicinity of the Sun', *Astrophys, Space Sci.* **2**, 496.
Fahr, H. J.: 1971, *Astron. Astrophys.* **14**, 263.
Fahr, H. J.: 1979, *Astron. Astrophys.* **77**, 101.
Fahr, H. J.: 1996, *Space Sci. Rev.* **78**, 199.
Fahr, H. J. and Ripken, H. W.: 1984, *Astron. Astrophys.* **139**, 551.
Fahr, H. J. and Scherer, K.: 1990, *Astron. Astrophys.* **232**, 556.
Fahr, H. J. and Ziemkiewicz, J.: 1988, The Behavior of Distant Heliospheric Pick-Up Ions and Associated Solar Wind Heating, *Astron. Astrophys.* **202**, 295.
Fahr, H. J. et al.: 1986, *Space Sci. Rev.* **43**, 329.
Fahr, H. J., Ruciński, D., and Nass, H. U.: 1987, *Ann. Geophys.* **5A**, 255.
Fahr, H. J., Grzedzielski, S., and Ratkiewicz, R.: 1988, *Ann. Geophys.* **6**, 337.

Fahr, H. J., Fichtner, H., and Grzedzielski, S.: 1992: 'The Influence of the Anomalous Cosmic-Ray Component on the Dynamics of the Solar Wind', *Sol. Phys.* **137**, 355.
Fahr, H. J., Osterbart, R., and Ruciński, D.: 1995, 'Modulation of the Interstellar Oxygen-to-Hydrogen Ratio by Heliospheric Interface Plasma', *Astron. Astrophys.* **294**, 587.
Falle, S. A. E. G. and Giddings, J. R.: 1987, *Monthly Notices Roy. Astron. Soc.* **225**, 399.
Fichtner, H. et al.: 1994, *Astron. Astrophys.* **284**, 599.
Fichtner, H., de Bruijn, H., and Sreenivasan, S. R.: 1996a, *Geophys. Res. Letters* **23**, 1705.
Fichtner, H., le Roux, J. A., Mall, U., and Rucinski, D.: 1996b, *Astron. Astrophys.* **314**, 650.
Fisk L. A., Kozlovsky, B., and Ramaty, R.: 1974, 'An Interpretation of the Observed Oxygen and Nitrogen Enhancements in Low-Energy Cosmic-Rays', *Astrophys. J.* **190**, L35.
Fisk, L. and Goldstein, M.: 1978, 'On the Assimilation of Interstellar Ions into the Solar Wind', unpublished manuscript.
Fisk, L. A.: 1979, 'The Interactions of Energetic Particles with the Solar Wind', in C. F. Kennel, L. J. Lanzerotti, and E. N. Parker, *Solar System Plasma Physics*, Vol. 1, North-Holland, Amsterdam.
Fite, W. L., Smith, A. C. H., and Stebbings, R. F.: 1962, 'Charge Transfer in Collisions Involving Symmetric and Asymmetric Resonance', *Proc. Roy. Soc. London* **A268**, 527.
Forman, M. A.: 1977, 'The Velocity Correlation Function in Cosmic-Ray Diffusion Theory', *Astrophys. Space Sci.* **49**, 83.
Forman, M. A., Jokipii, J. R., and Owens, A. J.: 1974, 'Cosmic-Ray Streaming Perpendicular to the Mean Magnetic Field', *Astrophys. J.* **192**, 535.
Formisano, V.: 1977, 'The Physics of the Earth's Collisionless Shock Wave', *J. Phys.* **38**, C6–65.
Forsyth, R. J., Horbury, T. S., Balogh, A., and Smith, E. J.: 1996, 'Hourly Variances of Fluctuations in the Heliospheric Magnetic Field out of the Ecliptic Plane', *Geophys. Res. Letters* **23**, 595.
Frisch, P. C.: 1994, 'Morphology and Ionization of the Interstellar Cloud Surrounding the Solar System', *Science* **265**, 1423.
Frisch, P. C.: 1995, *Space Sci. Rev.* **72**, 499.
Frisch, P. C., Welty, D. E., Pauls, H. L., Williams, L. L., and Zank, G. P.: 1996, *Bull. Am. Astron. Soc.* **28**, 760.
Fujimoto, Y. and Matsuda, T.: 1991, 'KUGD91-2, Dept. Aeronautical Engineering', Kyoto University, preprint.
Gaffey, J. D. Jr., Winske, D., and Wu, C. S.: 1988, 'Time Scales for Formation and Spreading of Velocity Shells of Pickup Ions in the Solar Wind', *J. Geophys. Res.* **93**, 5470.
Galeev, A. A. et al.: 1987, 'MHD Turbulence in the Solar Wind Flow Interacting with Comets', *JETP* **192**, 2090.
Galeev, A. A., Lipatov, A. S., and Sagdeev, R. Z.: 1988, 'Alfvén Waves in a Space Plasma and its Role in the Solar Wind Interaction with Comets', *Astrophys. Space Sci.* **144**, 427.
Galeev, A. A., Lipatov, A. S., and Sagdeev, R. Z.: 1987, 'Two-Dimensional Numerical Simulation of the Relaxation of Cometary Ions and MHD Turbulence in the Flow of the Solar Wind Around a Cometary Atmosphere', *Soviet J. Plasma Phys.* **13** (5), 323.
Galeev, A. A. et al.: 1991, 'Quasilinear Theory of the Ion Cyclotron Instability and its Application of the Cometary Plasma', in A. D. Johnstone (ed.), *Cometary Plasma Processes*, Geophysical Monograph 61, American Geophysical Union.
Galeev, A. A.: 1991, in *Comets in the Post-Halley Era*, Vol. 2, Kluwer Academic Publishers, Dordrecht, Holland, p. 1145.
Garcia-Munoz, M., Mason, G. M., Simpson, J. A.: 1973, *Astrophys. J.* **182**, L81.
Gary, S. P.: 1991, 'Electromagnetic Ion/Ion Instabilities and their Consequences in Space Plasmas: a Review', *Space Sci. Rev.* **56**, 373.
Gary, S. P. and Madland, C. D.: 1988, 'Electromagnetic Ion Instabilities in a Cometary Environment', *J. Geophys. Res.* **93**, 235.
Gary, S. P., Hinata, S., Madland, C. D., and Winske, D.: 1986, The 'Development of Shell-Like Distributions from Newborn Cometary Ions', *Geophys. Res. Letters* **13**, 1364.

Gary, S. P., Madland, C. D., Omidi, N., and Winske, D.: 1988, 'Computer Simulation of Two Pickup Ion Instabilities in a Cometary Environment', *J. Geophys. Res.* **93**, 9584.
Gary, S. P., Akimoto, K., and Winske, D.: 1989, 'Computer Simulations of Cometary Ion/Ion Instabilities and Wave Growth', *J. Geophys. Res.* **94**, 3513.
Gazis, P. R.: 1994, 'Pioneer and Voyager Observations of Solar Cycle Variations in the Outer Heliosphere', *Geophys. Res. Letters* **21**, 1743.
Gayley, Zank, G. P., Pauls, H. L., Frisch, P. C., and Welty, D. E.: 1997, 'One-Shock or Two-Shock Heliosphere: Lyman-α Observations and Measurements', *Astrophys. J.* **487**, 259.
Gazis, P. R. et al.: 1994, 'Solar Wind Velocity and Temperature in the Outer Heliosphere', *J. Geophys. Res.* **99**, 6561.
Geiss, J., Gloeckler, G. et al.: 1994, *Astron. Astrophys.* **282**, 924.
Ghosh, S. and Goldstein, M. L.: 1997, 'Anisotropy in Hall MHD Turbulence due to a Mean Magnetic Field', *J. Plasma Phys.* **57**.
Giacalone, J. and Jokipii, J. R.: 1996a, *J. Geophys. Res.* **101**, 11 095.
Giacalone, J. and Jokipii, J. R.: 1996b, in *Solar Wind 8*, AIP Conference Proceedings 382, AIP Press, p. 380.
Giacalone, J., Jokipii, J. R., and Kóta, J.: 1994, Ion Injection and Acceleration at Quasi-Perpendicular Shocks, *J. Geophys. Res.* **99**, 19 351.
Gilardini, A.: 1972, *Low Energy Electron Collisions in Gases*, Wiley and Sons, New York.
Glassmeier, K.-H. et al.: 1989, 'Spectral Characteristics of Low-Frequency Plasma Turbulence Upstream of Comet P/Halley', *J. Geophys. Res.* **94**, 37.
Gleeson, L. J. and Axford, W. I.: 1967, 'Cosmic-Rays in the Interplanetary Medium', *Astrophys. J.* **149**, L115.
Gloeckler, G.: 1996, *Space Sci. Rev.* **78**, 335.
Gloeckler, G.: 1997, *Nature* **386**, 374.
Gloeckler, G., Geiss, J., Balsiger, H., Fisk, L.A., Galvin, A.B., Ipavich, F.M., Ogilvie, K. W., von Steiger, R., and Wilken, B.: 1993, 'Detection of Interstellar Pick-Up Hydrogen in the Solar System', *Science*, **261**, 70.
Gloeckler, G., Geiss, J., Roelof, E. C., Fisk, L. A., Ipavich, F. M., Ogilvie, K. W., Lanzerotti, L. J., von Steiger, R., and Wilken, B.: 1994, 'Acceleration of Interstellar Pickup Ions in the Disturbed Solar Wind Observed on *Ulysses*', *J. Geophys. Res.* **99**, 17 637.
Gloeckler, G., Schwadron, N., Fisk, L. A., and Geiss, J.: 1995, *Geophys. Res. Letters* **22**, 2665.
Golstein, M. L., Lepping, R. P., Lee, M. A., and Fitch, C. A.: 1993, Abstract, *EOS Trans. AGU* **74**, 483.
Gosling, J. T., Thomsen, M. F., Bame, S. J., Feldman, W. C., Paschmann, G., and Sckopke, N.: 1982, 'Evidence for Specularly Reflected Ions Upstream from the Quasi-Parallel Bow Shock', *Geophys. Res. Letters* **9**, 1333.
Gray, P. C., Pontius, D. H. Jr., and Matthaeus, W. H.: 1996, 'Scaling of Field-line Random Walk in Model Solar Wind Fluctuations', *Geophys. Res. Letters* **23**, 965.
Gray, P. C., Smith, C. W., Matthaeus, W. H., and Otani, N. F.: 1996, 'Heating of the Solar Wind by Pickup Ion Driven Alfvén Ion Cyclotron Instability', *Geophys. Res. Letters* **23**, 113.
Greenstadt, E. W.: 1974, in C. T. Russell (ed.), 'Structure of the Terrestrial Bow Shock', *Solar Wind 3*, University of California Press, Los Angeles, p. 440.
Grzedzielski, S. and Page, D. E. (eds): 1989, *Physics of the Outer Heliosphere*, Pergamon Press, Oxford, p. 169.
Grzedzielski, S., Fahr, H. J., and Fichtner, H.: 1992, in E. Marsch and R. Schwenn (eds), *Solar Wind 7*, Pergamon Press, Oxford, p. 173.
Gurnett, D. A., Kurth, W. S., Allendorf, S. C., and Poynter, R. L.: 'Radio Emission from the Heliopause Triggered by an Interplanetary Shock', *Science* **262**, 199.
Hall, D. T.: 1992, 'Ultraviolet Resonance Radiation and the Structure of the Heliosphere', PhD Thesis, Univ. of Arizona.

Hall, D. T., Shamansky, D. E., Judge, D. L., Gangpadhyay, P., and Gruntman, M. A.: 1993, 'Heliospheric Hydrogen beyond 15 AU: Evidence for a Termination Shock', *J. Geophys. Res.* **98**, 15 185.

Hartle, R. E. and Wu, C. S.: 1973, 'Effects of Electrostatic Instabilities on Planetary and Interstellar Ions in the Solar Wind', *J. Geophys. Res.* **78**, 5802.

Hockney, R. W. and Eastwood, J. W.: 1988, *Computer Simulation using Particles*, Adam Hilger, IOP Publishing Ltd, Bristol.

Hollweg, J. V.: 1974, 'Transverse Alfvén Waves in the Solar Wind: Arbitrary $\mathbf{k}$, $\mathbf{V_0}$, $\mathbf{B_0}$ and $|\delta\mathbf{B}|$', *J. Geophys. Res.* **79**, 1539.

Holzer, T. E.: 1970, 'Stellar Winds and Related Flows', PhD Thesis, University of California, San Diego.

Holzer, T. E.: 1972, 'Interaction of the Solar Wind with the Neutral Component of the Interstellar Gas', *J. Geophys. Res.* **77**, 5407.

Holzer, T. E.: 1989, 'Interaction between the Solar Wind and the Interstellar Medium', *Ann. Rev. Astron. Astrophys.* **27**, 199.

Holzer, T. E.: 1979, 'The Solar Wind and Related Astrophysical Phenomena', in C. F. Kennel, L. J. Lanzerotti, and E. N. Parker (eds), *Solar System Plasma Physics*, Vol. 1, p. 101.

Holzer, T. E. and Axford, W. I.: 1970, 'The Theory of Stellar Winds and Related Flows', *Ann. Rev. Astron. Astrophys.* **8**, 31.

Holzer, T. E. and Axford, W. I.: 1971, 'Interaction between Interstellar Helium and the Solar Wind', *J. Geophys. Res.* **76**, 6965.

Holzer, T. E. and Banks, P. M.: 1969, *Planetary Space Sci.* **17**, 1074.

Hovestadt, D., Vollmer, O., Gloeckler, G., Fan, C. Y.: 1973, *Phys. Rev. Letters* **31**, L650.

Huddleston, D. E. and Johnstone, A. D.: 1992, 'Relationship between Wave Energy and Free Energy from Pickup Ions in the Comet Halley Environment', *J. Geophys. Res.* **97**, 12 217.

Hundhausen, A. J.: 1968, *Planetary Space Sci.* **16**, 783.

Hundhausen, A. J.: 1985, in R. G. Stone and B. T. Tsurutani (eds), 'Some Macroscopic Properties of Shock Waves in the Heliosphere', *Collisionless Shocks in the Heliosphere: A Tutorial Review*, AGU Monograph 34, p. 37.

Ip, W.-H. and Axford, W. I.: 1985, 'Estimates of Galactic Cosmic-Ray Spectra at Low Energies', *Astron. Astrophys.* **149**, 7.

Ip, W.-H. and Axford, W. I.: 1990, in W. F. Huebner (ed.), *Physics and Chemistry of Comets*, Springer-Verlag, Berlin, p. 177.

Isenberg, P. A.: 1986, 'Interaction of the Solar Wind with Interstellar Neutral Hydrogen: Three-Fluid Model', *J. Geophys. Res.* **91**, 9965.

Isenberg, P. A.: 1987, 'Evolution of Interstellar Pickup Ions in the Solar Wind', *J. Geophys. Res.* **92**, 1067.

Isenberg, P. A.: 1987, 'Energy Diffusion of Pickup Ions Upstream of Comets', *J. Geophys. Res.* **92**, 8795.

Isenberg, P. A.: 1995, 'Interstellar Pickup Ions: Not Just Theory Anymore', *U.S. Nat. Rep. Int. Union Geod. Geophys. 1991–1994, Rev. Geophys.* **33**, 623.

Isenberg, P. A.: 1997, *Geophys. Res. Letters* **000**, 000.

Isenberg, P. A. and Lee, M. A.: 1995, 'Effects of Time-Dependent Photoionization on Interstellar Pickup Ions', *J. Geophys. Res.* **100**, 17 053.

Isenberg, P. A. and Lee, M. A.: 1996, 'A Dispersive Analysis of Bispherical Pickup Ion Distributions', *J. Geophys. Res.* **101**, 11 055.

Isenberg, P. A., Chih, P. P., and Fisk, L. A.: 1985, 'The Heating of the Solar Wind by the Interstellar Neutral Gas', *J. Geophys. Res.* **90**, 12 040.

Jokipii, J. R.: 1966, 'Cosmic-Ray Propagation, 1, Charged Particles in a Random Magnetic Field', *Astrophys. J.* **146**, 480.

Jokipii, J. R.: 1986, 'Particle Acceleration at a Termination Shock 1. Application to the Solar Wind and the Anomalous Component', *J. Geophys. Res.* **91**, 2929.
Jokipii, J. R.: 1987, 'Rate of Energy Gain and Maximum Energy in Diffusive Shock Acceleration', *Astrophys. J.* **313**, 842.
Jokipii, J. R.: 1990, in S. Grzedzielski and D. E. Page (eds), 'The Anomalous Component of Cosmic-Rays, *Physics of the Outer Heliosphere*, Pergamon Press, Oxford, p. 169.
Jokipii, J. R.: 1992, 'Constraints on the Acceleration of Anomalous Cosmic-Rays', *Astrophys. J.* **393**, L41.
Jokipii, J. R.: 1996, 'Theory of Multiply Charged Anomalous Cosmic-Rays', *Astrophys. J.* **466**, L47.
Jokipii, J. R. and Giacalone, J.: 1996, *Space Sci. Rev.* **78**, 137.
Jokipii, J. R. and Kota, J.: 1989, 'The Polar Heliospheric Magnetic Field', *Geophys. Res. Letters* **16**, 1.
Jokipii, J. R. and Morfill, G.: 1985, *Astrophys. J.* **290**, L1.
Jokipii, J. R. and Parker, E. N.: 1968, 'Random Walk of Magnetic Lines of Force in Astrophysics', *Phys. Rev. Letters* **21**, 44.
Jokipii, J. R. and Parker, E. N.: 1969, 'Stochastic Aspects of Magnetic Lines of Force with Application to Cosmic-Ray Propagation', *Astrophys. J.* **155**, 777.
Jokipii, J. R., Kota, J., and Giacalone, J.: 1993, *Geophys. Res. Letters* **20**, 1759.
Jokipii, J. R. et al.: 1995, *Geophys. Res. Letters* **22**, 3385.
Johnstone, A., Huddleston, D., and Coates, A.: 1991, 'The Spectrum and Energy Density of Solar Wind Turbulence of Cometary Origin', *Cometary Plasma Processes*, Geophysical Monograph 61, American Geophysical Union, Washington DC.
Jones, F. C.: 1990, 'The Generalized Diffusion-Convection Equation', *Astrophys. J.* **361**, 162.
Jones, F. C. and Ellison, D. C.: 1991, 'The Plasma Physics of Shock Acceleration', *Space Sci. Rev.* **58**, 259.
Jones, F. C., Jokipii, J. R., and Baring, M. G.: 1998, *Astrophys. J.*, in press.
Kang, H. and Jones, T. W.: 1990, *Astrophys. J.* **353**, 149.
Kang, H. and Jones, T. W.: 1995, 'Diffusive Shock Acceleration Simulations: Comparison with Particle Methods and Bow Shock Measurements', *Astrophys. J.* **447**, 944.
Karman, T. von and Howarth, L.: 1938, 'On the Statistical Theory of Isotropic Turbulence', *Proc. R. Soc. London* **164**, 192.
Karmesin, S. R., Liewer, P. C., and Brackbill, J. U.: 1995, *Geophys. Res. Letters* **22**, 1153.
Kennel, C. F., Edmiston, J. P., and Hada, T.: 1985, in R. G. Stone and B. T. Tsurutani (eds), *Collisionless Shocks in the Heliosphere: A Tutorial Review*, Geophys. Monogr. Ser. 34, AGU, Washington, D.C., p. 1.
Khabibrakhmanov, I. Kh. and Summers, D.: 1996, *J. Geophys. Res.* **101**, 7609.
Khabibrakhmanov, I. Kh., Summers, D., Zank, G. P., and Pauls, H. L.: 1996a, 'Solar Wind Flow with Interstellar Hydrogen Pick-up', *Astrophys. J.* **469**, 921.
Khabibrakhmanov, I. Kh., Summers, D., Zank, G. P., and Pauls, H. L.: 1996b, 'Analytical Model of the Heliopause', *J. Geophys. Res.* **101**, 20 003.
Klecker, B.: 1995, *Space Sci. Rev.* **72**, 419.
Ko, C. M. and Webb, G. M.: 1987, *Astrophys. J.* **323**, 657.
Ko, C. M. and Webb, G. M.: 1988, *Astrophys. J.* **325**, 296.
Ko, C. M., Jokipii, J. R., and Webb, G. M.: 1988, *Astrophys. J.* **326**, 761.
Ko, C.-M., Chan, K.-W., and Webb, G. M.: 1997, 'Cosmic-Ray-Modified Shocks with Injection in the Hydrodynamic Approach. Part 1. Injection Linear in the Thermal Pressure', *J. Plasma Phys.* **57**, 677.
Kyrölä, E., Summanen, T., and Raback, P.: 1994, *Astron. Astrophys.* **288**, 299.
Krymsky, G. F.: 1977, 'A Regular Mechanism for the Acceleration of Charged Particles on the Front of a Shock Wave', *Dokl. Akad. Nauk. SSR.* **234**, 1306.

Kucharek, H. and Scholer, M.: 1995, 'Injection and Acceleration of Interstellar Pickup Ions at the Heliospheric Termination Shock', *J. Geophys. Res.* **100**, 1745.
Kulsrud, R. M.: 1983, in A. A. Galeev and R. N. Sudan (eds), *Basic Plasma Physics I*, North-Holland, New York, p. 115.
Kurth, W. S. et al.: 1984, 'Detection of a Radio Emission at 3 kHz in the Outer Heliosphere', *Nature* **312**, 27.
Lallement, R., Bertaux, J.-L., and Clarke, J. T.: 1993, 'Deceleration of Interstellar Hydrogen at the Heliospheric Interface', *Science* **260**, 1095.
Lallement, R.: 1996, *Space Sci. Rev.* **78**, 361.
Landau, L. D. and Lifshitz, E. M.: 1987, *Fluid Mechanics–Course of Theoretical Physics*, Vol. 6, Butterworth–Heinemann.
Landsman, W. B., Henry, R. C., Moos, H. W., and Linsky, J. L.: 1984, *Astrophys. J.* **285**, 801.
Lazarus, A. J. and McNutt, R. L. Jr.: 1990, in S. Grzedzielski and D. E. Page (eds), 'Plasma Observations in the Distant Heliosphere: A View from Voyager', *Physics of the Outer Heliosphere*, Pergamon Press, London.
Lean, J. L. and Skumanich, A.: 1983, *J. Geophys. Res.* **88**, 5751.
Lee, M. A.: 1971, 'Self-Consistent Kinetic Equations and the Evolution of Relativistic Plasma in an Ambient Magnetic Field', *Plasma Phys.* **13**, 1079.
Lee, M. A.: 1989, in B. T. Tsuratani and H. Oya (eds), 'Ultra-Low Frequency Waves at Comets', *Plasma Waves and Instabilities at Comets and in Magnetospheres*, Geophysical Monograph 53, American Geophysical Union, p. 13.
Lee, M. A.: 1996, in J. R. Jokipii, C. P. Sonnett, and M. S. Giampapa (eds), *Cosmic Winds and the Heliosphere*, University of Arizona, Tucson.
Lee, M. A. and Ip, W.-H.: 1987, 'Hydromagnetic Wave Excitation by Ionized Interstellar Hydrogen and Helium in the Solar Wind', *J. Geophys. Res.* **92**, 11041.
Lee, M. A. and Axford, W. I.: 1988, 'Model Structure of a Cosmic-Ray Mediated Stellar or Solar Wind', *Astron. Astrophys.* **194**, 297.
Lee, M. A., Shapiro, V. D., and Sagdeev, R. Z.: 1996, 'Pickup Ion Energization by Shock Surfing', *J. Geophys. Res.* **101**, 4777.
Le Roux, J. A. and Fichtner, H.: 1997, *J. Geophys. Res.* **8**, 17 365.
Le Roux, J. A. and Ptuskin, V. S.: 1998, 'Self-Consistent Stochastic Pre-Acceleration of Interstellar Pickup Ions in the Solar Wind Including the Effects of Wave Coupling and Damping', *J. Geophys. Res.* **103**, 4799.
Leroy, M. M. et al.: 1982, *J. Geophys. Res.* **87**, 5081.
Leroy, M. M.: 1983, 'Structure of Perpendicular Shocks in Collisionless Plasma', *Phys. Fluids* **26**, 2742.
Liewer, P. C., Omidi, N., and Goldstein, B. E.: 1993, 'Hybrid Simulations of the Effects of Interstellar Pickup Hydrogen on the Solar Wind Termination Shock', *J. Geophys. Res.* **98**, 15 211.
Liewer, P. C., Rath, Sharadini, and Goldstein, B. E.: 1995, 'Hybrid Simulations of the Interstellar Pickup Ion Acceleration at the Solar Wind Termination Shock', *J. Geophys. Res.* **100**, 19 809.
Liewer, P. C., Karmesin, S. R., and Brackbill, J. U.: 1996, 'Hydrodynamic Instability of the Heliopause Driven by Plasma-Neutral Charge-Exchange Interactions', *J. Geophys. Res.* **101**, 17 119.
Linde, T., Gombosi, T. I., Roe, P. L., Powell, K. G., DeZeeuw, D. L.: 1998, 'The Heliosphere in the Magnetized Local Interstellar Medium: Results of a 3D MHD Simulation', *J. Geophys. Res.* **103**, 1889.
Linsky, J. L.: 1996, 'GHRS Observations of the LISM', *Space Sci. Rev.* **78**, 157.
Linsky, J. L. et al.: 1995, *Astrophys. J.* **451**, 335.
Linsky, J. L. and Wood, B. E.: 1996, 'The α Cen Line of Sight: D/H Ratio, Physical Properties of Local Interstellar Gas, and Measurement of Heated Hydrogen near the Heliopause', *Astrophys. J.* **463**, 254.

Lipatov, A. S.: 1996, '3D and 2.5D Hybrid Multiscale Simulation Technology: Application to Study of Forced Nonstationary Processes at Tangential Discontinuities', *STEP SIMPO Newsletter* **5** (16), 11.

Lipatov, A. S. and Zank, G. P.: 1999, *Phys. Rev. Letters* **84**, 3609.

Lipatov, A. S., Zank, G. P., and Pauls, H. L.: 1998, 'The Interaction of Neutral Interstellar *H* with the Heliosphere: A 2.5D Particle-Mesh Boltzmann Simulation', *J. Geophys. Res.* **103**, 20 631.

Lipatov, A. S., Zank, G. P., and Pauls, H. L.: 1998, 'The Acceleration of Pickup Ions at Shock Waves: Test-Particle-Mesh Simulations', *J. Geophys. Res.*, in press.

Liu, S., Marsch, E., Livi, S., Woch, J., Wilken, B., von Steiger, R., and Gloeckler, G.: 1995, 'Radial Gradients of Ion Densities and Temperatures Derived from SWICS/*Ulysses* Observations', *Geophys. Res. Letters* **22**, 2445.

Lotz, W.: 1967, *Z. Physik* **206**, 205.

McDonald, F. B. and Lal, N.: 1986, *Geophys. Res. Letters* **13**, 781.

McDonald, F. B., Webber, W. R., Teegarden, B. J., and Trainor, J. H.: 1974, *Astrophys. J.* **187**, 105.

McKibben, R. B., Pyle, K. R., and Simpson, J. A.: 1979, *Astrophys. J.* **227**, L147.

McLoud, W. S. and Moraal, H.: 1990, 'Acceleration of Charged Particles in Quasi-Perpendicular Magnetohydrodynamic Shocks', *J. Plasma Phys.* **44**, 123.

Maher, L. and Tinsley, B.: 1977, 'Atomic Hydrogen Escape Rate due to Charge Exchange with Hot Plasmaspheric Ions', *J. Geophys. Res.* **82**, 689.

Malama, Yu. G.: 1991, 'Monte-Carlo Simulation of Neutral Atoms Trajectories in the Solar System', *Astrophys. Space Sci.* **176**, 21.

Matsuda, T., Fujimoto, Y., Shima, E., and Inaguchi, T.: 1989, *Prog. Theor. Phys.* **81**, 810.

Matthaeus, W. H., Goldstein, M. L., and Roberts, D. A.: 1990, 'Evidence for the Presence of Quasi-Two-Dimensional Nearly Incompressible Fluctuations in the Solar Wind', *J. Geophys. Res.* **95**, 20 673.

Matthaeus, W., Oughton, S., Pontius, D., and Zhou, Y.: 1994, 'Evolution of Energy-Containing Turbulent Eddies in the Solar Wind', *J. Geophys. Res.* **99**, 19 267.

Matthaeus, W. H., Gray, P. C., Pontius, D. H., Jr., and Bieber, J. W.: 1995, 'Spatial Structure and Field-Line Diffusion in Transverse Magnetic Turbulence', *Phys. Rev. Letters* **75**, 2136.

Meier, R. R.: 1977, *Astron. Astrophys.* **55**, 211.

Mellott, M. M.: 1985, in B. T. Tsuratani and R. G. Stone (eds), 'Subcritical Collisionless Shock Waves', *Collisionless Shocks in the Heliosphere: Reviews of Current Research*, Geophys. Res. Monogr. Ser. 35, AGU, Washington, D.C., p. 131.

Mewaldt, R. et al.: 1996, *Astrophys. J.* **466**, L43.

Miller, R. H., Gary, S. P., Winske, D., and Gombosi, T. I.: 1991, 'Pitch Angle Scattering of Cometary Ions into Monospherical and Bispherical Distributions', *Geophys. Res. Letters* **18**, 1063.

Möbius, E.: 1996, *Space Sci. Rev.* **78**, 375.

Moraal, H.: 1993, *Nucl. Phys. B Proc. Suppl.* **33** (A,B), 161.

Morfill, G. E., Richter, A. K., and Scholer, M.: 1979, 'Average Properties of Cosmic-Ray Diffusion in Solar Wind Streams', *J. Geophys. Res.* **84**, 1505.

Mullan. D. J. and Arge, N.: 1995, *J. Geophys. Res.* **101**, 2535.

Murphy, N. et al.: 1995, 'Further Studies of Waves Accompanying the Solar Wind Pick-Up of Interstellar Hydrogen', *Space Sci. Rev.* **72**, 447.

Naidu, K. and Barnes, A.: 1994a, 'Motion of the Heliospheric Termination Shock: 3. Incident Interplanetary Shocks', *J. Geophys. Res.* **99**, 11 553.

Naidu, K. and Barnes, A.: 1994b, 'Motion of the Heliospheric Termination Shock 4. MHD Effects', *J. Geophys. Res.* **99**, 17 673.

Nerney, S. F., Suess, S. T., and Schmahl, E. J.: 1991, *Astron. Astrophys.* **250**, 556.

Nerney, S. F., Suess, S. T., and Schmahl, E.J.: 1993, *J. Geophys. Res.* **98**, 15 169.

Nerney, S. F., Suess, S. T., and Schmahl, E.J.: 1995, *J. Geophys. Res.* **100**, 3463.

Osterbart, R. and Fahr, H. J.: 1992, 'A Boltzmann-Kinetic Approach to Describe the Entrance of Neutral Interstellar Hydrogen into the Heliosphere', *Astron. Astrophys.* **264**, 260.
Owocki, S. P. and Zank, G. P.: 1990, 'The Effect of Viscosity on Steady Transonic Flow with a Nodal Solution Topology', *Astrophys. J.* **368**, 491.
Parker, E. N.: 1958, 'Dynamics of Interplanetary Gas and Magnetic Fields', *Astrophys. J.* **123**, 644.
Parker, E. N.: 1963, *Interplanetary Dynamical Processes*, Interscience, New York.
Parker, E. N.: 1965, *Planetary Space Sci.* **13**, 9.
Patterson, T. N. L., Johnson, F. S., and Hanson, W. B.: 1963, *Planetary Space Sci.* **11**, 767.
Pauls, H. L. and Zank, G. P.: 1996, 'Interaction of a Nonuniform Solar Wind with the Local Interstellar Medium', *J. Geophys. Res.* **101**, 17 081.
Pauls, H. L. and Zank, G. P.: 1997, 'Interaction of a Nonuniform Solar Wind with the Local Interstellar Medium. 2. A Two-Fluid Model', *J. Geophys. Res.* **102**, 19 779.
Pauls, H. L. and Zank, G. P.: 1997, 'Modelling the Solar Wind/Interstellar Wind Interaction', *Proc. 25th Int. Cosmic-Ray Conf.* **2**, 241.
Pauls, H. L., Zank, G. P., and Williams, L. L.: 1995, 'Interaction of the Solar Wind with the Local Interstellar Medium', *J. Geophys. Res.* **100**, 21 595.
Pauls, H. L., Zank, G. P., Williams, L. L., and Hall, D. T.: 1996, Solar Wind – Local Interstellar Medium Interaction Including Charge Exchange with Neutral Hydrogen', in *Proc. Solar Wind* **8**, 605.
Pauls, H. L., Zank, G. P., Moraal, H., and Steenkamp, R.: 1997, 'Cosmic-Ray Modulation Calculated from a Self-Consistent Diffusion Tensor', *Proc. 25th Int. Cosmic-ray Conf.* **1**, 233.
Pauls, H. L. and Zank, G. P.: 1997, 'Comment on "Hydrodynamic Instability of the Heliopause driven by Plasma-Neutral Charge-Exchange Interactions" by Paulett C. Liewer, S. Roy Karmesin and J. U. Brackbill', *J. Geophys. Res.* **102**, 9835.
Pesses, M. E., Jokipii, J. R., and Eichler, D.: 1981, 'Cosmic-Ray Drift, Shock Wave Acceleration, and the Anomalous Component of Cosmic-Rays', *Astrophys. J.* **256**, L85.
Phillips, J. L., Bame, S. J., Feldman, W. C., Goldstein, B. E., Gosling, J. T., Hammond, C. M., McComas, D. J., Neugebauer, M., Scime, E. E., and Suess, S. T.: 1995, '*Ulysses* Solar Wind Plasma Observations at High Southerly Latitudes', *Science* **268**, 1030.
Phillips, J. L., Bame, S. J., Feldman, W. C., Goldstein, B. E., Gosling, J. T., Hammond, C. M., McComas, D. J., Neugebauer, M.: 1996, '*Ulysses* Solar Wind Plasma Observations from Peak Southerly through Perihelion and Beyond', *Solar Wind 8*, Am. Inst. of Phys., New York, p. 416.
Pogorelov, N. V. and Semenov, A. Y.: 1997, *Astron. Astrophys.* **321**, 330.
Pogorelov, N. V. and Matsuda, T.: 1998, *J. Geophys. Res.* **103**, 237.
Potgieter, M. S.: 1997, *Adv. Space Res.* **000**, 000.
Pushkar, E. A.: 1995, *Izv. Russ. Acad. Sci. Fluid Dyn.* **30**, 912.
Quémerais, E., Sandel, B. R., Lallement, R., and Bertaux, J.-L.: 1995, 'A New Source of Lyα Emission Detected by Voyager UVS: Heliospheric or Galactic Origin', *Astron. Astrophys.* **299**, 249.
Rand, R. J. and Kulkarni, S. R.: 1989, *Astrophys. J.* **343**, 760.
Ratkiewicz, R.: 1992, in E. Marsch and R. Schwenn (eds), *Solar Wind* **7**, 251.
Ratkiewicz, R., Barnes, A., Molvik, G. A., Spreiter, J. R., and Stahara, S. S.: 1996, *J. Geophys. Res.* **101**, 27 483.
Ratkiewicz, R., Barnes, A., Molvik, G. A., Spreiter, J. R., Stahara, S. S., Vinokur, M., and Venkateswaran, S.: 1998, 'Effect of Varying Strength and Orientation of Local Interstellar Magnetic Field on Configuration of Exterior Heliosphere: 3D MHD Simulations', *Astron. Astrophys.* **335**, 363.
Reinecke, J. P. L. and Moraal, H.: 1992, *Astrophys. J.* **392**, 272.
Richardson, J. D.: 1997, *Geophys. Res. Letters* **24**, 2889.
Richardson, J. D., Paularena, K. I., Lazarus, A. J., and Belcher, J. W.: 1995, 'Radial Evolution of the Solar Wind from Imp 8 to Voyager 2', *Geophys. Res. Letters* **22**, 325.

Ripkin, H. L. and Fahr, H. J.: 19983, 'Modification of the Local Interstellar Gas Properties in the Heliospheric Interface', *Astron. Astrophys.* **122**, 181.
Roberts, D. A., Goldstein, M. L., Matthaeus, W. H., and Ghosh, S.: 1992, 'Velocity Shear Generation of Solar Wind Turbulence', *J. Geophys. Res.* **97**, 17 115.
Ruciński, D.: 1985, PhD Thesis, Warsaw University, Poland.
Ruciński, D. and Bzowski, M.: 1995, 'Modulation of Interplanetary Hydrogen Density Distribution During the Solar Cycle', *Astron. Astrophys.* **296**, 248.
Ruciński, D. and Bzowski, M.: 1996, 'Modelling of the Interstellar Hydrogen Distribution in the Heliosphere', *Space Sci. Rev.* **78**, 265.
Sagdeev, R. Z., Shapiro, V. D., Shevchenko, V. I., and Szego, K.: 1986, 'MHD Turbulence in the Solar Wind-Comet Interaction Region', *Geophys. Res. Letters* **13**, 85.
Savopulos, M. and Quenby, J. J.: 1997, *Solar Phys.* **000**, 000.
Savopulos, M., Quenby, J. J., and Bell, A. R.: 1995, *Solar Phys.* **157**, 349.
Schwartz, S. J., Thomsen, M. F., Bame, S. J., and Stansberry, J.: 1988, 'Electron Heating and the Potential Jump Across Fast Mode Shocks', *J. Geophys. Res.* **93**, 12 923.
Schlickeiser, R.: 1989, 'Cosmic-Ray Transport and Acceleration, II, Cosmic-Rays in Moving Cold Media with Application to Diffusive Shock Wave Acceleration', *Astrophys. J.* **336**, 264.
Sckople, N.: 1995, *Adv. Space Res.* **15** (8/9), 261.
Scudder, J. D. et al.: 1986, *J. Geophys. Res.* **91**, 11 019.
Semar, C. L.: 1970, *J. Geophys. Res.* **75**, 6892.
Sharma, O. P. and Patel, V. L.: 1986, 'Low-Frequency Electromagnetic Waves driven by Gyrotropic Gyrating Ion Beams', *J. Geophys. Res.* **91**, 1529.
Skilling, J.: 1975, *Monthly Notices Roy. Astron. Soc.* **172**, 557.
Skilling, J.: 1975, *Monthly Notices Roy. Astron. Soc.* **173**, 245.
Skilling, J.: 1975, *Monthly Notices Roy. Astron. Soc.* **172**, 255.
Smith, E. J.: 1993, 'Observations of Waves Generated by the Pickup of Interstellar Hydrogen Ions (abstract)', *Eos Trans. AGU*, **74** (16), Spring Meet. Suppl., p. 234.
Smith, E. J., Murphy, N., Tsurutani, B., Balogh, A., Gloeckler, G., Geiss, J., and Isenberg, P. A.: 1994, 'Hydromagnetic Waves and Interstellar Pickup Ions: Recent *Ulysses* Observations', *Eos Trans. AGU* **75** (16), Spring Meet. Suppl., p. 297.
Smith, E. J., Marsden, R. G., and Page, D. E.: 1995, '*Ulysses* Above the Sun's South Pole: An Introduction', *Science* **268**, 1005.
Sousk, S. F. and Lenchek, A. M.: 1969, *Astrophys. J.* **158**, 781.
Spitzer, L.: 1978, *Diffuse Matter in Space*, Interscience, New York.
Steenberg, C. D. and Moraal, H.: 1996, 'An Acceleration/Modulation Model for Anomalous Cosmic-Ray Hydrogen in the Heliosphere', *Astrophys. J.* **463**, 776.
Steenberg, C. D., Moraal, H., and McDonald, F. B.: 1997, *Proc. 25th Int. Cosmic-Ray Conf.* **5**, 233.
Steinolfson, R. S.: 1994, *J. Geophys. Res.* **99**, 13 307.
Steinolfson, R. S., Pizzo, V. J., and Holzer, T.: 1994, 'Gas Dynamic Models of the Solar Wind/Interstellar Medium Interaction', *Geophys. Res. Letters* **21**, 245.
Steinolfson, R. S. and Gurnett, D. A.: 1995, *Geophys. Res. Letters* **22**, 651.
Stone, E. C., Cummings, A. C., and Webber, W. R.: 1996, 'The Distance to the Solar Wind Termination Shock in 1993 and 1994 from Observations of Anomalous Cosmic-Rays', *J. Geophys. Res.* **5**, 11 017.
Story, T. R. and Zank, G. P.: 1995, 'The Interaction of a Gasdynamic Termination Shock with Interplanetary Disturbances', *J. Geophys. Res.* **100**, 9489.
Story, T. R. and Zank, G. P.: 1997, 'The Interaction of an MHD Termination Shock with Interplanetary Disturbances', *J. Geophys. Res.* **102**, 17 381.
Suess, S. T.: 1990, 'The Heliopause', *Rev. Geophys.* **28**, 97.
Suess, S. T.: 1993, *J. Geophys. Res.* **98**, 15 147.
Suess, S. T. and Dessler, A. J.: 1985, 'Probing the Local Interstellar Medium', *Nature* **317**, 702.

Suess, S. T. and Nerney, S.: 1990, 'Flow Downstream of the Heliospheric Terminal Shock, 1, Irrotational Flow', *J. Geophys. Res.* **95**, 6403.
Suess, S. T. and Nerney, S.: 1991, *J. Geophys. Res.* **96**, 1883.
Thomas, G. E. and Krassa, R. F.: 1971, *Astron. Astrophys.* **11**, 218.
Thomas, G. E.: 1978, 'The Interstellar Wind and its Influence on the Interplanetary Environment', *Ann. Rev. Earth Planetary Sci.* **6**, 173.
Tinbergen, J.: 1982, *Astron. Astrophys.* **105**, 53.
Toptygin, I. N.: 1985, *Cosmic-Rays in Interplanetary Magnetic Fields*, D. Reidel Publ. Co., Dordrecht, Holland.
Vallerga, J.: 1996, *Space Sci. Rev.* **78**, 277.
Vasyliunas, V. M. and Siscoe, G. L.: 1976, 'On the Flux and the Energy Spectrum of Interstellar Ions in the Solar System', *J. Geophys. Res.* **81**, 1247.
Wallis, M.: 1971, *Nature* **233**, 23.
Wang, C. and Belcher, J. W.: 1998, *J. Geophys. Res.* **103**, 247.
Washimi, H.: 1993, 'MHD Modeling of the Outer Heliosphere', *Adv. Space Sci.* **13** (6), 227.
Washimi, H. and Tanaka, T.: 1996, '3-D Magnetic Field and Current System in the Heliosphere', *Space Sci. Rev.* **78**, 85.
Webb, G. M., Axford, W. I., and Terasawa, T.: 1983, 'On the Drift Mechanism for Energetic Charged Particles at Shocks', *Astrophys. J.* **270**, 537.
Webb, G. M., Brio, M., Zank, G. P., and Story, T. R.: 1995, 'Contact and Pressure-Balanced Structures in Two-Fluid Cosmic-Ray Hydrodynamics', *Astrophys. J.* **442**, 822.
Webb, G. M., Zank, G. P., Ko, C. M., and Donohue, D. J.: 1995, 'Multi-Dimensional Green's Functions and the Statistics of Diffusive Shock Acceleration', *Astrophys. J.* **453**, 178.
Webb, G. M., Brio, M., Zank, G. P., and Story, T. R.: 1997, Wave-Wave Interaction in Two-Fluid Cosmic-Ray Hydrodynamics', *J. Plasma Phys.* **57**, 631.
Webb, G. M., Zakharian, A., and Zank, G. P.: 1998, 'Wave Mixing and Instabilities in Cosmic-Ray Modified Shocks and Flows', *J. Plasma Phys.*, in press.
Whang, Y. C.: 1987, 'Slow Shocks and Their Transition to Fast Shocks in the Inner Solar Wind', *J. Geophys. Res.* **92**, 4349.
Whang, Y. C.: 1991, 'Shock Interactions in the Outer Heliosphere', *Space Sci. Rev.* **57**, 339.
Whang, Y. C. and Burlaga, L. F.: 1993, 'Termination Shock: Solar Cycle Variations of Location and Speed', *J. Geophys. Res.* **98**, 15 221.
Whang, Y. C. and Burlaga, L. F.: 1994, 'Interaction of GMIR Shock with the Heliopause and its Relation to the 2- and 3-kHz Radio Emissions', *J. Geophys. Res.* **99**, 21 457.
Whang, Y. C., Burlaga, L. F., and Ness, N. F.: 1995, *J. Geophys. Res.* **100**, 17 015.
Whitham, G. B.: 1956, 'On the Propagation of Weak Shock Waves', *J. Fluid Mech.* **1**, 290.
Whitham, G. B.: 1974, *Linear and Nonlinear Waves*, John Wiley,, New York.
Williams, L. L. and Zank, G. P.: 1994, 'The Effect of Magnetic Field Geometry on the Wave Signature of the Pickup of Interstellar Neutrals', *J. Geophys. Res.* **99**, 19 229.
Williams, L. L., Zank, G. P., and Matthaeus, W. H.: 1995, 'Dissipation of Pick-Up Induced Waves: A Solar Wind Temperature Increase in the Outer Heliosphere?', *J. Geophys. Res.* **100**, 17 059.
Williams, L. L., Hall, D. T., Pauls, H. L., and Zank, G. P.: 1996, 'Self-Consistent Dynamical Interaction of the Solar Wind and Local Interstellar Cloud: a Multi-Fluid Hydrogen Model', *Proc. Solar Wind* **8**, 609.
Williams, L. L., Hall, D. T., Pauls, H. L., and Zank, G. P.: 1997, 'The Heliospheric Hydrogen Distribution: A Multi-Fluid Model', *Astrophys. J.* **476**, 366.
Winske, D.: 1985, in R. G. Stone and B. T. Tsurutani (eds), *Collisionless Shocks in the Heliosphere: Reviews of Current Research*, Geophys. Monogr. Ser. 35, AGU, Washington, D.C., p. 225.
Winske, D., Wu, C. S., Li, Y. Y., Mou, Z. Z., and Guo, Y. S. Y.: 1985, 'Coupling of Newborn Ions to the Solar Wind by Electromagnetic Instabilities and their Interaction with the Bow Shock', *J. Geophys. Res.* **90** (3), 2713.

Winske, D. and Gary, P. S.: 1986, 'Electromagnetic Instabilities Driven by Cool Heavy Ion Beam', *J. Geophys. Res.* **91**, 6825.
Witte, M. et al.: 1992, *Astron. Astrophys. Suppl. Ser.* **92**, 333.
Witte, M., Banaszkiewicz, M., and Rosenbauer, H.: 1996, *Space Sci. Rev.* **78**, 289.
Wood, B. E. and Linsky, J. L.: 1998, *Astrophys. J.*, in press.
Wu, C. S. and Davidson, R. C.: 1972, 'Electromagnetic Instabilities Produced by Neutral-Particle Ionization in Interplanetary Space', *J. Geophys. Res.* **77**, 5399.
Wu, C. S. and Hartle, R. E.: 1974, 'Further Remarks on Plasma Instabilities Produced by Ions Born in the Solar Wind', *J. Geophys. Res.* **79**, 283.
Wu, C. S., Hartle, R. E., and Ogilvie, K. W.: 1973, 'Interaction of Singly Charged Interstellar Helium Ions with the Solar Wind', *J. Geophys. Res.* **78**, 306.
Wu, C. S., Winske, D., and Gaffey, J. D.: 1986, 'Rapid Pick-Up of Cometary Ions due to Strong Magnetic Turbulence', *Geophys. Res. Letters* **13** (8), 865.
Wu, F. S. and Judge, D. L.: 1979, 'Temperature and Flow Velocity of the Interplanetary Gases along Solar Radii', *Astrophys. J.* **231**, 594.
Ye, G. and Cravens, T. E.: 1991, 'Combined Energy and Pitch Angle Diffusion of Pickup Ions at Comet Halley', *J. Geophys. Res.* **96**, 5479.
Yoon, P. H., Ziebell, L. F., and Wu, C. S.: 1991, 'Self-Consistent Pitch Angle Diffusion of Newborn Ions', *J. Geophys. Res.* **96**, 5469.
Zank, G. P. and Matthaeus, W. H.: 1992, 'Waves and Turbulence in the Solar Wind', *J. Geophys. Res.* **97**, 17 189.
Zank, G. P. and Matthaeus, W. H.: 1993, 'Nearly Incompressible Fluids, II, Magnetohydrodynamics, Turbulence, and Waves', *Phys. Fluids* **A5**, 257.
Zank, G. P. and McKenzie, J. F.: 1987, 'Short-Wavelength Compressive Instabilities in Cosmic-Ray Shocks and Heat Conduction Flows', *J. Plasma Phys.* **37**, 347.
Zank, G. P. and Pauls, H.L.: 1996, 'Modelling the Heliosphere', *Space Sci. Rev.* **78**, 95.
Zank, G. P. and Pauls, H. L.: 1997, 'Shock Propagation in the Outer Heliosphere I. Pickup Ions and Gasdynamics', *J. Geophys. Res.*, **102**, 7037.
Zank, G. P., Axford, W. I., and McKenzie, J. F.: 1990, 'Instabilities in Energetic Particle Modified Shocks', *Astron. Astrophys.* **233**, 275.
Zank, G. P., Cairns, I. H., Donohue, D. J., and Matthaeus, W. H.: 1994, 'Radio Emissions and the Heliospheric Termination Shock', *J. Geophys. Res.* **99**, 14 729.
Zank, G. P., Cairns, I. H., and Webb, G. M.: 1995, 'The Termination Shock: Physical Processes, *Adv. Space Sci.* **15**, No. 8/9, 453.
Zank, G. P., Khabibrakhmanov, I. Kh., and Story, T. R.: 1992, 'The Structure of Mass-Loading Shocks', *J. Geophys. Res.* **98**, 5645.
Zank, G. P., Matthaeus, W. H., and Smith, C.W.: 1996, 'Evolution of Turbulent Magnetic Fluctuation Power with Heliospheric Distance', *J. Geophys. Res.* **101**, 17 081.
Zank, G. P., Matthaeus, W. H., Bieber, J. W., and Moraal, H.: 1998, 'The Radial and Latitudinal Dependence of the Cosmic-Ray Diffusion Tensor in the Heliosphere', *J. Geophys. Res.* **103**, 2085.
Zank, G. P., Pauls, H. L., Cairns, I. H., and Webb, G. M.: 1996, 'Interstellar Pick-up Ions and Perpendicular Shocks: Implications for the Termination Shock and Interplanetary Shocks', *J. Geophys. Res.* **101**, 457.
Zank, G. P., Pauls, H. L., Williams, L. L., and Hall, D.T.: 1996, 'Interaction of the Solar Wind with the Local Interstellar Medium: A Multifluid Approach', *J. Geophys. Res.* **101**, 21 639.
Zank, G. P., Pauls, H. L., and Williams, L. L.: 1996, 'Modelling the Heliosphere', in *Proc. Solar Wind* **8**, 599.
Zank, G. P., Pauls, H. L., Hall, D., and Williams, L. L.: 1996, 'Multi-Dimensional Modelling of the Solar Wind – LISM Interaction including Neutrals: a Boltzmann Approach', in *Proc. Solar Wind* **8**, 654.

Zank, G. P., Story, T. R., and Neubauer, F. M.: 1994, 'The Structure of Mass-Loading Shocks. I. Comets', *J. Geophys. Res.* **99**, 13 335.

Zank, G. P., Webb, G. M., and Donohue, D. J.: 1993, 'Particle Injection and the Structure of Energetic-Particle-Modified Shocks', *Astrophys. J.* **406**, 67.

Ziebell, L. F. and Yoon, P. H.: 1990, 'Pitch Angle and Velocity Diffusion of Newborn Ions by Turbulence in the Solar Wind', *J. Geophys. Res.* **95**, 21, 203.

Ziebell, L. F., Yoon, P. H., Wu, C. S., and Winske, D.: 1990, 'Pitch Angle and Velocity Diffusion of Newborn Ions due to Intrinsic Turbulence in the Solar Wind', *J. Geophys. Res.* **95**, 17 075.

Ziemkiewicz, J.: 1994, *Astron. Astrophys.* **292**, 677.

Ziemkiewicz, J. and Banaszkiewicz, M.: 1996, *Adv. Space Res.* **000**, 000.

Zilbersher, D. and Gedalin, M.: 1997, 'Pickup Ion Dynamics at the Structured Quasi-Perpendicular Shock', *Planetary Space Sci.* **45(6)**, 693.